Surender K. Sharma   *Editor*

Spinel Nanoferrites

Synthesis, Properties and Applications

Springer

Topics in Mining, Metallurgy and Materials Engineering

Series Editor

Carlos P. Bergmann, Federal University of Rio Grande do Sul, Porto Alegre, Rio Grande do Sul, Brazil

"Topics in Mining, Metallurgy and Materials Engineering" welcomes manuscripts in these three main focus areas: Extractive Metallurgy/Mineral Technology; Manufacturing Processes, and Materials Science and Technology. Manuscripts should present scientific solutions for technological problems. The three focus areas have a vertically lined multidisciplinarity, starting from mineral assets, their extraction and processing, their transformation into materials useful for the society, and their interaction with the environment.

** Indexed by Scopus (2020) **

More information about this series at http://www.springer.com/series/11054

Surender K. Sharma
Editor

Spinel Nanoferrites

Synthesis, Properties and Applications

Springer

Editor
Surender K. Sharma 🄳
Department of Physics
Federal University of Maranhão
São Luis, Maranhão, Brazil

Department of Physics
Central University of Punjab
Bathinda, India

Preface

Ferrites have raised considerable interest in basic research as well as potential applications due to their broad range of novel and enhanced physio-chemical properties. As an important family of magnetic materials, spinel ferrites in nanostructured form with diverse morphology and physio-chemical properties have attracted increasing attention. This is due to their unique characteristics of spinel structure to form an extremely wide variety of total solid solutions, which leads to appealing applications especially in the field of advanced electronics, microwave devices, biotechnology as well as biomedical sciences. There are many literatures available where different spinel nanoferrites and their applications in different area of industry exist but only in scattered manner. However, complete information where this important class of materials, their structures, physio-chemical properties and use for advanced applications is missing.

This book is aimed at highlighting the complexity of the spinel nanoferrites, their synthesis, physio-chemical properties and prospective applications in the area of advanced electronics, microwave devices, biotechnology as well as biomedical sciences. It will serve as an overview of spinel nanoferrites: synthesis, properties and applications for a wide audience: from beginners and graduate-level students up to advanced specialists in both academic and industrial sectors.

São Luis, Brazil   Surender K. Sharma

Contents

Progress in Ferrites Materials: The Past, Present, Future and Their Applications

Anita Manhas, Mahavir Singh, Muhammad Irfan Hussain, Yasir Javed, and Surender K. Sharma

Abstract Ferrite is a magnetic substance consist essentially of an oxide of iron combined with one or more other metals such as manganese, copper, nickel, or zinc. They are being routinely utilized especially in electronic devices owing to its good magnetic properties along with high resistivity.

Keywords Ferrites · Composition · Crystal structure · Magnetism · Applications

1 History of Ferrites

Ferrites, in the broader sense, are magnetic materials. Magnetism and magnetic materials have a long and eminent history. Ancient peoples discovered the property of magnetism around 600 BC. The oldest identified references to magnetic properties were established by sixth century BC by Greek philosopher Thales of Miletus [1]. Some naturally occurring stone-like materials were found with inherent characteristics of being magnetized and the ones that attract iron. That magnetic material is "magnetite", named after their production in the Magnesia region of Thessaly, Greece. Magnetite is one of the main iron ores, with the chemical formula Fe_3O_4 [2]. Later, the naturally-magnetized piece of magnetite was named as a "lodestone" used by ancient navigators to invent the magnetic compass and is considered a "ferrite"

A. Manhas · M. Singh
Department of Physics, Himachal Pradesh University, Shimla 171005, H.P., India

M. I. Hussain
Institute of Materials Science and Advanced Ceramics, University of Science and Technology, Xueyuan Road 30th, BeijingHaidian District, Beijing, China

Y. Javed
Department of Physics, Magnetic Materials Laboratory, University of Agriculture, Faisalabad, Pakistan

S. K. Sharma (✉)
Department of Physics, Federal University of Maranhao, Sao Luis, Brazil
e-mail: surender.sharma@cup.edu.in; surender.sharma@ufma.br

Department of Physics, Central University of Punjab, Bathinda 151401, India

by both engineers and geologists. The term "Ferrite" emanates with the Latin word, 'Ferrum', meaning that Iron. Different scientists have considered ferrite in different ways. According to geologists, ferrites belong to the family of rock minerals with certain utilization of iron oxide. For scientists and electrical engineers, ferrites were like a treasure, since for them ferrites are a group of promising materials based on iron oxide with interesting magnetic and dielectric properties to be employed in electronic industries. In this way, the journey of ferrites begun, which today, influences every essential area of interest to modern human society from health to communication applications and will continue in the future with its incredible contributions to the cutting-edge scientific technologies.

Ferrite is known to exist for hundreds of years. In 1909, one of the earliest scientific studies on genetic and constitutive correlations in magnetic properties of ferrites and iron oxides reported from Hilpert [3]. It is worth mentioning, Hilpert had explained theories on the origin of magnetic properties like ferromagnetism and their correlation with the structure of ferrites. He had successfully synthesized various spinel ferrites by substituting them with different elements such as Zn, Cu, Mg, Mn and Co, as well as alkaline-earth and lead ferrites [4]. Furthermore, in 1909, Hilpert took out a German patent on the manufacturing method of magnetic materials having small electric conductivity for electric and magnetic devices [5]. Hilpert gave pioneer results about high resistivity of ferrites as the eddy current losses were negligible but in response to magnetic properties, results were not desirable as ferrites showed low permeability with high total losses. Thereafter, the essential study on chemistry of ferrites and its magnetic properties was attempted by Forestier in 1928 [6] by synthesizing different compositions of ferrites to measure saturation magnetization with Curie temperature. In the same year (1928), Herroun and Wilson [7] also reported permeability, susceptibility and coercive force for copper and magnesium ferrites in the compressed form. However, copper ferrite has obtained a high maximum permeability, but it was still far below that of the pure magnetite. Till that time, the magnetic properties of ferrites were not improved effectively to that of a commercial level for electronic industries.

The innovative research of Kato and Takei in 1930 paved a new path for the applicability of ferrites, [8] by performing experiments on sinter powder-compacted ferrite at high temperature with a sufficient level of magnetic permeability and loss properties especially for electronic devices and high-frequency applications. They have achieved good magnetic power in zinc ferrite at high temperatures by precisely accessing with temperature, compositions of ferrites and their magnetization, which was well presented in their research paper in 1930 [8]. Furthermore, in 1933, Kato and Takei [9] were performed experiments, by paying specific attention to the consequences of heat treatment, on the magnetostriction and the anisotropy of cobalt ferrites in single-crystal as well as in polycrystal forms to obtained permanent magnets [10, 11]. They developed ferrites from a commercial point of view from their knowledge that the ferrite's magnetic properties are not only greatly affected by its chemical composition but also by its microstructure [12].

In the period 1933–1945, extensive work has been performed on magnetic materials and developed theories of ferromagnetism by taking into account magnetostrictive strains and crystal anisotropy, which has been employed in form of core material in loading coils in various laboratories all over the world especially by Snoek [13], Kleis [14], Williams [15], Becker and Döring [16], McKeehan and Grabbe [17] and Rathenau and Snoek [18]. The research performed by these researchers and other scientists became important factors to determine the permeability of ferrites to be used at high frequencies.

Since 1933, for Snoek and other Philips, the ferrites had been turned into the field of extensive investigations, at the Philips Research Laboratories Netherland, especially for its uses at high-frequency applications. In 1936, Snoek has reported the values of resistivity, coercivity and saturation magnetization of Mn, Cu, Ni, Mg ferrites, mixed ferrites and iron oxides [19]. In 1938, he measured permeability with time, i.e. with magnetic aging [20]. Snoek and other researchers at Philips renewed interest for obtaining such types of ferrites, which hold higher frequencies with superior permeability at low-loss factor. By 1945, Snoek had laid down the foundation of physics and technology of practical ferrite materials.

In 1947, Snoek published his book, "New developments in ferromagnetic materials" [21] and reported in his research paper [22] the "Ferroxcube" (a mixture of nickel ferrite and zinc ferrite, and a mixture of manganese ferrite and zinc ferrite) material exhibited excellent magnetic properties, high electrical resistivity and also explained their high-frequency possible permeability with low relaxation losses at which absorption and dispersion set in by giving practicable frequency range limits for the utilization of ferrite named as "Snoek Limit" [22]. Within the Snoek's limits, the permeability and resonant frequency can be changed within a feasible range by optimizing synthesizing methods, varying the sintering temperature and compositions of ferrites by proper selection of substituents. As a consequence of this Snoek's work has brought about very fast growth in the ferrite core industry for electronic materials and for future ferrite applications.

In 1948, Néel enlightened with an idea of Kramers [23] about the theory of exchange interaction between metal ions through the intermediate non-magnetic oxygen ions and developed a new theory for antiferromagnetism oxides and later for ferrites. Néel gave a molecular-field theory of magnetic ordering for explaining the mechanism of magnetization in those magnetic systems which comprise non-equivalent substructures of magnetic ions. This theory named "Néel theory of ferrimagnetism" [24]. Later, in 1950, Anderson [25] refined Kramers's theory based on calculus, which now specified with "Superexchange interaction". In 1952, Yafet and Kittel [26] extended Néel's theory and method of calculation, based on a Weiss molecular field theory of exchange interactions in spinel ferrites, exists in different spin lattices by suggesting the presence of non-collinear or canted spin arrangements on sublattices and calculating the canting angle between them. Also, in the meantime, Rado et al. [27] explained the mechanism of dispersion in ferrites at very high frequencies. The magnetoplumbite ferrites having hexagonal structure, also named as hexagonal ferrites or hexaferrite, were first invented by Went, Ratenau, Gorter and van Oosterhout in 1952 [28].

Through this journey and combined efforts of various scientific communities all over the world, ferrites came into the existence in the research world for the betterment of basic human life necessities. This remarkable progress leads to the diversification of ferrite industry especially for electronic industries, globe-girdling with intercontinental telecommunication applications at higher frequencies as well as in the health sector which is using till date and will be using after that.

2 Composition of Ferrites

The general chemical formula of ferrite is $MeFe_2O_4$, as it is clear from the definition of ferrite that "*Ferrite is a magnetic substance consist essentially of an oxide of iron combined with one or more other metals*", where 'Me' represents divalent metal ion, with ionic radius approximately was 0.6 to 1 Å. 'Me' can be chosen as Mn, Fe, Co, Ni, Zn, Mg, Cu and Cd element to form simple ferrites or a combination of cations which have an average valency of two. A combination of these ions led to the formation of a large variety of ferrites solid solutions or of mixed ferrites. One can easily interpret that the formula of ferrite ($MeFe_2^{3+}O_4$) derived from Magnetite, Fe_3O_4 or $Fe^{2+}Fe_2^{3+}O_4$, by replacing Fe^{2+} ions by suitable 'Me' cation. Furthermore, Fe^{3+} can also be replaced by a trivalent cation (Me'). Consequently, the general chemical formula of ferrite can be extended to $MeFe_{2-x}^{3+}Me'_xO_4$, for modification of the chemical properties of ferrites for specific applications, where Me' can also completely or partly be substituted with trivalent cation or a combination of cations with an average valency of three. In ferrite composition formula, the variable "x" can take any values from zero to two, provided x cannot be exactly two, otherwise, these oxides would not remain ferrites anymore.

The possible uniqueness in ferrites due to their exceptional magnetic and dielectric properties, obtained essentially via synthesizing ferrites with proper combinations of chemical constituents, researchers were inspired to synthesize a variety of simple ferrites and mixed ferrites. In the early synthesized simple ferrites, where "$x = 0$", 'Me' can be represented as a combination of ions with an average valency of two such as Li^{1+}–Fe^{3+} in lithium ferrite, $Li_{0.5}Fe_{2.5}O_4$ [29] and Cu^+–Fe^{3+} in copper ferrite, $Cu_{0.5}Fe_{2.5}O_4$ [30]. The $MgFe_2O_4$ [19, 31, 32], $NiFe_2O_4$ [19, 33, 34], $MnFe_2O_4$ [19, 35] and $CoFe_2O_4$ [36] have been prepared and studied. Initially, while synthesizing different compositions the much attention of the scientists has been drawn to the magnetic behaviours of the ferrites being its inherent magnetic nature. Many experiments have been performed by scientists and researchers. Of these, the important discovery is to obtain the enhanced value of magnetic saturation in the solid solution or mixed ferrites of magnetic ferrites with Zn substitution, which had also predicted by the Neel theory of ferrimagnetism [24]. For enhancing magnetic properties for electronic industries, Zn substituted ferrite like Fe-Zn [37, 38], Cu–Zn [39, 40], Mn–Zn [21] and Ni–Zn [41, 42] have been studied. Zn and Cd are diamagnetic elements and Cd ferrite has been discovered to be the same as Zn ferrite, Cd substituted ferrite like Cu–Cd [39], Ni–Cd [43], Co–Cd [44] and Mn–Cd ferrites [45] have been

synthesized and investigated with good magnetic properties. Me also represented Mn–Mg in Mn–Mg ferrite [46]. Of these, Mn–Zn ferrite and Ni–Zn ferrite is substituted ferrimagnet which has long been the topic of much theoretical and experimental investigation for the power applications, magnetic heads and magnetic recording due to their high saturation magnetization and for telecommunications and microwave applications due to high permeability with low loss.

The partial substitution of Fe^{3+} ion by trivalent ions, i.e. Me′=Al, Cr, Ga, Rh and V were reported by researchers, whereas the formation of solid solutions by complete substitution of Fe^{3+} ion by these trivalent ions is also possible, resulting mixed crystals with aluminates and chromites [47]. Additionally, mixed ferrites have also been reported in which when Fe^{3+} ion partially substituted by tetravalent ion, the valency of an equal part of Fe^{3+} ions is lowered by one, i.e. the formation of mixed ferrites with the substitutions of tetravalent ions Ti^{4+} and Ge^{4+} in combination with divalent ions Fe^{2+}, Ni^{2+}, Co^{2+} or Mn^{2+} has been existed. Different series of $V_xFe_{3-x}O_4$, by partially substituting Fe^{3+} ion by trivalent ion V^{3+} in magnetite Fe_3O_4, has reported by Nivoix and Gillot [48]. The $CaFe_2O_4$ ferrite has been synthesized by substituting Fe^{2+} by Ca^{2+}, the maximum value of the atomic percentage of Ca^{2+} is 20% [49].

Another important ferrimagnet is a cubic spinel structure of γ-Fe_2O_3, maghemite, with a large number of vacant positions distributed over the cation lattice sites of the spinel. Its chemical formula can be written as $\Upsilon_{1/3}Fe_{2/3}^{3+}Fe_2^{3+}O_4$, where a symbol Υ representing a vacant site. This formula revealed the special case of the divalent Me-substitution, representing the combination of 2/3 Fe^{3+} ion and 1/3 vacancies [50, 51]. Later, in 1967, γ-Fe_2O_3 is reported as the best material for magnetic recording tape. Then, the development of high-density recording material has grown and a high storage magnetic material came into consideration. In response to this, a small amount of cobalt was added to γ-Fe_2O_3 particles to obtain a new type of highly coercive (high storage) Co-γ-Fe_2O_3 particles [52–54].

Different compositions have been synthesized from years for achieving different properties such as higher curie temperature, lower hysteresis losses, negligible eddy current losses, large anisotropy field, high impedance, high resonance frequency obtaining ferrites with good resistivity, that could potentially more desirable results for high-frequency dielectric behaviour and number of other important characteristics as per requirements for different applications. The applications of ferrites will be mentioned in the "Applications of the spinel ferrites" section, in this chapter.

A variety of ferrites, with certain combinations of chemical constituents, can be synthesized by determining the valency of metal ions through an analysis of the oxygen concentrations. However, in some cases of mixed ferrites or solid solutions of ferrites the oxygen analysis is not sufficient to reveal the valency of constituent ions that occur with multiple valency state. Besides, the possible chemical formula may be determined by magnetic properties, i.e. saturation magnetization, based on the Néel theory, as the saturation moment is related in a simple manner to the distribution of magnetic ions among the available lattice sites with particular valency. There are plentiful research papers on the different types of the composition of solid solutions between spinel ferrites which reveal that the formation of different ferrimagnetic

iron oxides, by selecting a suitable different variety of the chemical composition, is possible. This wide variety in the composition of ferrites with its large range of physical and chemical properties makes it a significant magnetic material and of remarkable interest by altering these properties for significant utilization.

3   Structure of Ferrites

The structure of ferrite is spinel, named after the mineral spinel $MgAl_2O_4$, which crystallizes in the cubic system. In 1915, Bragg and Nishikawa [55, 56] were first reported that magnetite, Fe_3O_4, is a member of this spinel group of crystals. The structure has cubic symmetry and belongs to the space group of Fd3m. The unit cell of the spinel lattice contains eight "molecules" of $MeFe_2O_4$ and, therefore, 32 Oxygen ions are there in the unit cell (Verwey and Heilmann [57]) The relatively large oxygen ions (anions) form a cubic close-packed (or face-centred cubic, fcc) structure with a large number of interstices between them, which are partially filled with the smaller metal ions (cations). These interstitial sites can be categorized into two types based on closed packed structure; first is known as tetrahedral site, which positioned at the centre of a tetrahedron surrounded by oxygen ions, i.e. 4 oxygen ions at the corner sites of tetrahedral (Fig. 1a) and the other is octahedral site, as the oxygen ions around it occupy the corners of an octahedron i.e. the octahedral sites are surrounded by 6 oxygen ions (Fig. 1b). As illustration in the cubic unit cell, it depicts 64 tetrahedral sites and 32 octahedral sites. Of these, only 8 tetrahedral (represented as A sites) and 16 octahedral (represented as B sites) sites involved for cations in full unit cell, respectively.

The dimensions of the unit cell are measured in units of Angstrom which are equivalent to 10^{-8} cm. The lengths "a" of a unit cell of some spinel ferrites are listed in Table 1.

(a) Tetrahedral A site   (b) Octahedral B site
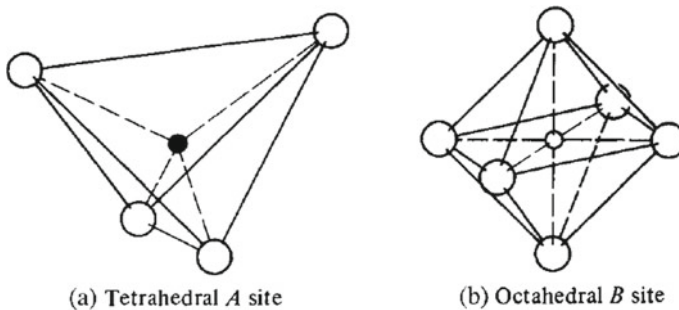
Fig. 1 (**a**) Tetrahedral and (**b**) octahedral sites in the cubic close-packed structure

Table 1 Unit cell lengths of some spinel ferrites.

Ferrite	Unit cell length (Å)
Zinc ferrite	8.44
Manganese ferrite	8.51
Ferrous ferrite	8.39
Cobalt ferrite	8.38
Nickel ferrite	8.34
Magnesium ferrite	8.36

Taken from Goldman [58]

Fig. 2 The elementary cube of edge "*a*" represents the unit cell of the spinel ferrite. The four shaded and the four non-shaded octants are filled with metal ions in the similar way as shown in Fig. 3
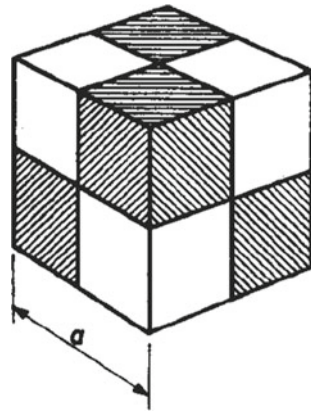
To understand the unit cell of the spinel ferrite, it is convenient to consider it as an elementary cube of edge a. This cube consists of 8 octants with edge 1/2a, as shown in Fig. 2.

Each octant comprised with four oxygen ions (anions) which form the corners of a tetrahedron and in all octants, the anions are located in the same way but there are two types of octants, shaded and non-shaded (Fig. 2), with different locations for the cations as is shown in Fig. 3.

The edge of the fcc oxygen lattice is 1/2a. In Fig. 3, the locations of the anions and cations are specified in two adjacent octants. In one of the octants, cations occupied A sites located in the centre and on four of the eight corners of the octant, whereas, in the adjacent octant the site in the centre is unoccupied by a cation, because of translational symmetry, four of the eight corners of the octant are again occupied. The A sites form two interpenetrating fcc lattices with an edge a, displaced relative to each other over the distance $1/4a \sqrt{3}$ in the direction of the body diagonal of the cube and all octahedral ions collectively placed on four interpenetrating fcc lattices having an edge a, which are shifted relative to each other over the distance $1/4a \sqrt{2}$ in the directions of the face diagonals of the cube.

The oxygen ions (anions) create fcc lattice but in this fcc structure, a slight distortion does occur due to the presence of cations. All A sites are expanded, as A sites
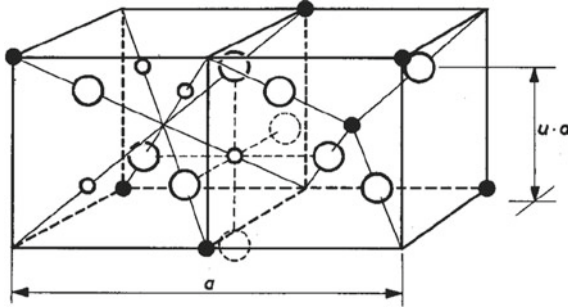
Fig. 3 The spinel structure reveals two octants. The oxygen ions (anions) represented by large size spheres. As indicated the metal ions (cations) with small black and white spheres also verifies the tetrahedral and octahedral sites, respectively. A pioneering work [47] reported on "Ferrites, Philips technical library." Eindhoven

are often smaller than B sites to accommodate a metal ion, by equally shifting of four anions outwards along the body diagonals of the cube as shown in Fig. 3. Besides, it was found that these four anions continued to hold the corners with expanded tetrahedron which in turn holds the same cubic symmetry for each A ion. The four anions in the octahedral octants are displaced in such a way as to shrink the size of the octahedral cell by the same amount as the A site first expands as depicted in Fig. 3. As a consequence of this, the sizes of the two-interstitial sites become more equal as the displacements of the anions mentioned-above make the A sites larger and the B sites smaller in size. In Fig. 4, the anions move along the arrow. The displacement of the tetrahedral oxygen is denoted by a quantity called the oxygen parameter "u" which means distance (as shown in Fig. 3) between an anion and the face of the cube edge along the cube diagonal of the octant, expressed as "au". The ideal distance (u_{ideal}) or
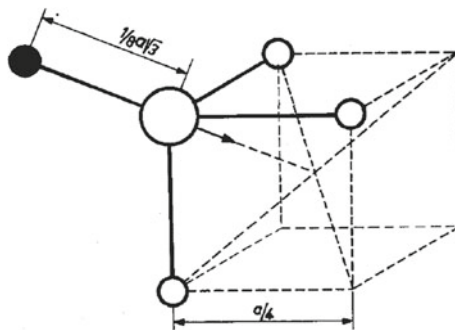
Fig. 4 Demonstration of nearest neighbours of an oxygen ion (anion) in the spinel structure. The octahedral (B) sites denoted by small white spheres represented the metal ions (cations). The tetrahedral (A) site denoted by black sphere exhibiting metal ion (cation). The arrow indicates the direction in which the oxygen ion is displaced, where $u > 3/8$. Taken from [47] reported work on "Ferrites, Philips technical library." Eindhoven

fcc parameters (if there is no enlargement of the tetrahedrons) is theoretically equal to 3/8. Thus, in the above-mentioned slightly distorted structure, the distance "u" is greater than u_{ideal}. Table 2, listed some ferrites with the values of oxygen parameter "u" which is found by using the X-ray or neutron diffraction. Owing to these small displacements, the radii of the spheres in both types of interstitial sites are determined by performing simple calculations which are given as [47]:

$$r_A = (u - 1/4)\, a\sqrt{3} - R_0$$

$$r_B = (5/8 - u)\, a - R_0$$

Table 2 Crystallographic parameters of 'stoichiometric' spinel ferrites

Ferrite	Lattice parameter (Å)	Cation distribution	Oxygen parameter	Density (g/cm^3)
Fe_3O_4	8.398	$Fe^{3+}[Fe^{2+}\ Fe^{3+}]$	0.379	5.193
$AlFe_2O_4$	8.263	$\sim Fe^{2+}_{1-\delta}Fe^{3+}_{\delta}$	0.385	4.77
		$[Fe^{2+}_{\delta}Fe^{3+}_{1-\delta}Al^{3+}]$		
$CdFe_2O_4$	8.70	$Cd[Fe_2]$	0.390	5.81
$CoFe_2O_4$	8.381	$Co_{\delta}Fe_{1-\delta}$	0.3852	5.294
		$[Co_{1-\delta}Fe_{1+\delta}]$		
		$0.07 < \delta < 0.24$		
$Cu_{0.5}Fe_{2.5}O_4$	8.413	$Cu_{0.22}Fe_{0.78}[Cu_{0.28}Fe_{1.72}]$	0.388	5.25
$CrFe_2O_4$	8.396	$Fe^{3+}_{0.3}Fe^{2+}_{0.7}$	0.385	5.11
		$[Fe^{2+}_{0.3}Fe^{3+}_{0.7}Cr^{3+}]$		
$Li_{0.5}Fe_{2.5}O_4$	(o) 8.3143	$Fe[Li_{0.5}\ Fe_{2.5}]$		4.79
	(d) 8.2923	$Fe[Li_{0.5}\ Fe_{2.5}]$	0.382	4.82
$MgFe_2O_4$	8.372	$Mg_{\delta}Fe_{1-\delta}$	0.3856	4.53
	8.398	$[Mg_{1-\delta}Fe_{1+\delta}]$		4.49
		$0.14 < \delta < 0.26$		
$MnFe_2O_4$	8.525	$Mn_{1-\delta}Fe_{\delta}$	0.390	4.94
	8.515	$[Mn_{\delta}Fe_{2-\delta}]$		4.96
		$0.07 < \delta < 0.23$		
$MoFe_2O_4$	8.509	$Fe[FeMo]$	0.383	5.86
$NiFe_2O_4$	8.337	$Fe[FeNi]$	0.386	5.38
$TiFe_2O_4$	8.538	$Fe[FeTi]$	0.390	4.77
VFe_2O_4	8.418	$Fe^{2+}_{0.4}Fe^{3+}_{0.6}$	0.378	5.05
		$[Fe^{2+}_{0.6}Fe^{3+}_{0.4}V^{3+}]$		
$ZnFe_2O_4$	8.443	$Zn[Fe]$	0.387	5.32

Reproduced with permission from [73]

where R_0 is the radius of the anion i.e. oxygen ion.

So far, it has been cleared to the readers that in the unit cell of the spinel ferrites eight tetrahedral (A) and sixteen octahedral (B) sites are occupied by the metal ions. It is significant to know, the distribution of divalent and trivalent metal ions over these two A and B interstitial sites present in the unit cell of spinel ferrites. Researchers or scientists over the world worked progressively and working even today, experimentally and theoretically, by using various technological tools like X-ray diffraction or Neutron diffraction to understand the different possible distributions of cations. To begin with, it was believed that each site is simply occupied by one type of cation which means that tetrahedral sites comprised with all divalent ions and octahedral sites with all trivalent ions and thus this type of cation distribution is named as a normal distribution. In 1932, Barth and Posnjak [59] have drawn everyone's attention by reporting the ground-breaking work on the structure of spinel ferrites with the inverse distribution of cations. In this inverse distribution, the octahedral sites are formed with divalent ions and the trivalent ions are uniformly distributed over the remaining octahedral and tetrahedral sites, and, thus, such ferrites are called inverse spinels.

The distribution of cations in ferrites has long been of significant interest. Initially, researchers acquire information about the distribution of ions over A and B sites, from the general understanding of magnetic interactions by obtaining the magnitude of the saturation magnetization of spinel ferrites and more specifically in connection with the Néel theory of ferrimagnetism [60]. However, in some cases of ferrites, it is not feasible to understand the distributions by magnetic interactions. For instance, Mn^{2+} and Fe^{3+} possessed same electronic configurations, so the preference between alternative cations distributions based on saturation magnetization measurements is not feasible. Apart from that, the cation distribution has been determined by frequently using saturation magnetization data at 4 K, provided the spin configuration or magnetic structure must be known exactly. For example, Li et al. [61] carried out the magnetic studies on $Fe_{3-x}Ti_xO_4$ specimen by performing high field magnetization measurements which revealed that for a higher concentration of Ti ion spin canting occurs but for low concentration of Ti, i.e. $x = 0.5$, the spin configuration is of collinear Néel type (magnetization in A and B antiparallel). This indicates that the cation distribution determined from saturation magnetization is only valid for the lower concentrations of Ti ions [61]. For the experimental investigation of structural studies, some direct techniques have been used. The most often used techniques were X-ray diffraction, neutron diffraction, and Mössbauer spectroscopy. In the X-ray technique, the scattering power of atoms is determined by the number of electrons in the atom. Thus, transition elements have only a small difference in the scattering cross-section of atoms, which in turn, create uncertainty regarding the distribution of cations as it is incapable of reasonably distinguishing between transition elements and, thus, unsuitable to a determination of cation distribution among the spinel sublattices. The spinel ferrites which had studied by the X-Ray diffraction technique, further studied by neutron diffraction. In the neutron diffraction technique, the scattering power is obtained by the nuclear magnetic moment of the atom, because of the simultaneous interaction of neutron spin. This can give sufficient information

on the cation distribution of transition elements on two spinel sublattices as it distinguishes for the atoms even possessed equal number of electrons. It can also use to find the "chemical" details and relevant oxygen parameter "u", in addition to that, its sensitivity of effective magnetic scattering measures the average moment to be related with each kind of spinel sublattice. This helps in comparing the magnitude and relative orientation about average and individual magnetic moments of the ions, according to the Néel theory to determine suitable alternative cation distributions. Mössbauer spectroscopy is a powerful technique to obtain the cation distribution of ferrites, as it possesses the great differences between the hyperfine parameters of Fe^{2+} and Fe^{3+} ions. Experimentally, by using these different ways researchers have studied and reported various spinel ferrites with their suitable cation distributions. However, X-ray diffraction experiments had not been sufficient, so, latter workers developed an indirect method in which, indirect derivations from the lattice constants helped in distinguish between normal and inverse spinels, which was further largely confirmed by neutron scattering power. It has been shown by Barth and Posnjak [59] and by Verwey and Heilmann [57] from a discussion of the lattice constants that Mn, Fe, Co, Ni, Cu and Mg ferrites possess the inverse structure, whereas Zn and Cd ferrites possess the normal structure. They point out that the lattice parameter "a" increases by an amount equal to 0.04 to 0.06 Å for all ferrites, amongst which are those of Mg and Cu with a known inversed structure, and the normal spinels structure information especially for Cd and Zn confirmed by X-ray data, for which the increase in "a" is 0.12 Å. This was confirmed by neutron diffraction. Also, in 1953, Hastings and Corliss [33] found, by using neutron diffraction, that $ZnFe_2O_4$ is normal spinel and $NiFe_2O_4$ is certainly inverse spinel ferrite. In 1972, Abe et al. [62] has reported $MoFe_2O_4$ with a lattice parameter, $a = 8.509$ Å which were determined from both X-ray and neutron diffraction experiments and exhibits completely inverse spinel structure.

The general cation distribution for completely normal, completely inverse and mixed spinel ferrites can be represented as:

$$Me_{\delta}^{2+}Fe_{1-\delta}^{3+}\left[Me_{1-\delta}^{2+}Fe_{1+\delta}^{3+}\right]O_4^{2-},$$
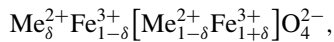
where the cations on tetrahedral (A) sites are given in front of the square brackets comprising the tetrahedral sublattices, while the cations enclosed by the square bracket occupy octahedral (B) sites comprising the octahedral sublattices and the quantity δ is the inversion parameter as it is a measure of the inversions occur in the structure of spinel ferrites. In general, for an inverse spinel $\delta = 0$ and on other case for a normal spinel $\delta = 1$, instead of this, for completely random distribution or mixed spinel, $0 < \delta < 1$. In some ferrites, the extent to which this process of inversion occurs depend on the method of preparation which reported by Bertaut [63] by using X-ray diffraction and, Néel [64] and Pauthenet [65] by using magnetization measurements on $CuFe_2O_4$ and $MgFe_2O_4$ ferrites quenched from various temperatures. They showed that the inversion or cation distribution in these ferrites is temperature dependent and results validated by the Boltzmann distribution law:

$$\frac{\delta(1+\delta)}{(1-\delta)^2} = e^{-E/KT},$$

where E value is approx. 0.14 eV. The dependence of inversion parameters on the condition of preparation is also shown by Weil et al. in 1950 [66] by reporting that $CuFe_2O_4$ has a distorted spinel structure. They obtained that the temperature of the specimen was heated above 760 °C and then quenched to ambient temperature, which reveals cubic structure instead of normal and inverse spinel. It was rather a disordered structure, that reveals two types of ion in both sites. In 1956, the same distortion in the structure was reported by Prince and Treuting [67] by indicating that $CuFe_2O_4$ is a tetragonally distorted inverse spinel. Also, F. G. Brockman in 1950 [68] published that the distribution in Cu ferrite is not simply $Fe[FeCu]O_4$ but even estimated the most random distribution as $Fe_{2/3}Cu_{1/3}[Fe_{4/3}Cu_{2/3}]O_4$ when Cu ferrite is quenched and may be $Fe_{0.82}Cu_{0.18}[Fe_{1.18}Cu_{0.82}]O_4$ for slowly cooled Cu ferrite and, i.e., when neither Cu^{2+} nor Fe^{3+} is positioned preferentially in A or B sites. In 1953, Corliss et al. [32] have reported the dependence of the degree of inversion on condition of preparation, by performing neutron diffraction studies of $MgFe_2O_4$ and discussed that if the degree inversion is 0.88, the fraction of A sites occupied by Fe^{3+} ions is 0.88 and the fraction of B sites occupied by Fe^{3+} is 0.56 which yielded the value of δ equal to 0.16. In 1956, Hastings and Corliss [69] have reported the results for $MnFe_2O_4$ obtained by different preparations and found that the value for the fraction of tetrahedral sites comprised with Mn^{2+} are found to be around 0.80, which substantially reveals that manganese ferrite is more nearly normal than inverted, corresponding to the formula $Mn_{0.8}Fe_{0.2}[Mn_{0.2}Fe_{1.8}]O_4$. In 1968, Sawatzky et al. [70] proved by using Mössbauer spectroscopy that $CoFe_2O_4$ spinel is not completely inverse and heat treatment of the sample can play a vital role for the degree of inversion. The cation distributions for the slowly cooled and for the quenched cobalt ferrite are $Co_{0.04}Fe_{0.96}[Co_{0.96}Fe_{1.04}]O_4$ and $Co_{0.21}Fe_{0.79}[Co_{0.79}Fe_{1.21}]O_4$, respectively.

The cation distribution of spinel ferrites over the A and B sites are determined by some significant factors such as ionic size, the short-range Born repulsion energy, the Coulomb energy of the charged ions in the lattice, crystal field effects, the ordering of the cations and covalency, and polarization effects.

Initially, the ionic size believed to be one of the important factors as the simple geometry reveals that the smaller cations would prefer the smaller tetrahedral sites. Trivalent ions often have a smaller ionic radius as comparison of divalent ion. Accordingly, the trivalent ion will occupy tetrahedral sites which favour the inverse spinel structure. This indicates that for normal spinel, where trivalent ions will occupy octahedral sites, other factors are leading to the distribution of cations.

The cation distribution of certain ferrite is determined by the total crystal energy and one of the contributions to the crystal energy initiates from the Coulomb interactions between the charged ions. This interaction which determines the distribution of cations also named "Madelung energy". Verwey et al. [71] determined the Madelung constants as a function of the oxygen parameter "u" for cations distribution. They reported that normal spinels have the highest Madelung constant for oxygen parameter "u" larger than the ideal value, which means that these spinels are

electrostatically most favourable. It was concluded from the calculations made by Verwey and Heilmann [57] and De Boer et al. [72] for the complete lattice that the inverse spinels, comprising divalent and trivalent cations, is electrostatically more stable or has the lowest lattice energy for oxygen parameter "u" less than 0.379, even though the normal spinel is electrostatically more stable for "u" more than 0.379. After the results reported by Verwey et al., many researchers reconfirmed electrostatic stability in cation arrangement and there were small differences between the results obtained by other methods by various researchers which the reader can find in detail in Chap. 3 published by Brabers [73] in "Handbook of magnetic materials" book [73]. However, in Table 2, the worth noting that the normal spinel structure of Zn and Cd ferrite are in agreement with the high oxygen parameter (Zn – 0.387 and Cd – 0.390) but the inverse distribution of cations in Ni ferrite and intermediate distributions in Mn, Co, Cu and Mg ferrite is not in agreement with oxygen parameter as it has larger values. This reveals that there are other factors, which are competing with the Madelung energy, contributing to the total energy of the crystal. These factors are the short-range Born repulsion energy and crystal field effects.

Various researchers Kriessman and Harrison [74], Miller [75], Driessens [76], O'Neill and Navrotsky [77] worked on short-range force term in the crystal energy and McClure [78] and Dunitz and Orgel [79] explained the crystal field stabilization for octahedral and tetrahedral symmetry of the transition metals ions from optical spectra. If the reader goes profoundly in a study reported by O'Neill and Navrotsky [77], it will find that they well-thought-out only on the electrostatic contribution in detail by considering the impractical assumption that all simple ferrites are normal spinels and ignored the crystal field and other effects. Even though, their final deduction, that the enthalpy change accompanying cation disordering was quadratic dependent on the inversion parameter, might be beneficial to explain the temperature dependence of the cation distribution in certain ferrites.

Thereafter, all factors such as electrostatic contribution, short-range Born energy and crystal field effects were considered in the theoretical study of lattice energy calculations reported by Cormack et al. [80], that contributed correct prediction about the cation distribution and structure of various spinels based on "interatomic potentials" which are obtained from the pertinent binary oxides. In this model further modifications have been done by including covalency effects, displacement polarizability and ionic polarizability. However, the existence of short-range cation order in inverse spinels [81] generates an enthalpy contribution which is only partially taken by Cormack et al. They investigated the cation distribution by finding the energy difference between the normal and inverse distribution [73] without including the entropy effects and magnetic interactions. It had been proved already by Anderson in 1956 that the short-range order can be responsible for substitution of divalent ions on the B sites and it is possible to maintain the finite entropy while achieving essentially perfect short-range order.

Till 30 years ago, researchers progressively keep on determined the various significant reasons or parameters for the distribution of cations in spinel ferrites. Now, if readers look over the last 20 years, they will come to know that these years are epicentre around the various methods or techniques to find the cations distributions in

spinels. Most of the researchers obtained cation distribution in spinels by analysing the intensities of reflections obtained from X-ray diffraction (XRD). Bertaut [66] and Furuhashi et al. [82] determined the distribution of cations in spinel ferrite by comparing diffraction intensities of reflections, due to the plane (*hkl*), observed experimentally and those calculated for different types of crystal structures theoretically. The information on the distribution of cation can be acquired to its best by comparing experimental and calculated intensity ratios especially for those reflections having intensities which: (1) are closely independent of the oxygen parameter "*u*", (2) vary with the distribution of cation in an opposite ways, and (3) does not differ significantly. Buerger in 1960 [83] has determined intensity of reflection of the plane (*hkl*) using this equation:

$$I_{hkl} = |F_{hkl}|^2 P.L_{\mathrm{P}}$$

where I_{hkl} indicates the intensity of plane (*hkl*), L_{P} is the Lorentz polarization factor, F_{hkl} indicates structure factor and P is the multiplicity factor. The formulae for the Lorentz polarization factor and multiplicity factor are best explained by B. D. Cullity in his books "Elements of X-Ray diffraction" [84]. The extent of accuracy of cation distribution depends on the closeness of the theoretical and experimental intensity ratio. The most appropriate reflections in spinel ferrite are (220), (400) and (440). Further, Furuhashi et al. in 1973 [82] proposed a formula to decides the finest-simulated structure by investigating the degree of linearity of the equation:

$$\ln\left(I_{\mathrm{hkl}}^{\mathrm{obs}} / I_{\mathrm{hkl}}^{\mathrm{calc}}\right) = \ln k - 2\mathrm{B}_{\mathrm{eff}}\left(\mathrm{Sin}^2\theta/\lambda^2\right),$$

where k is the scale factor, $\mathrm{B}_{\mathrm{eff}}$ is the effective Debye parameter in the effective temperature factor, $I_{\mathrm{hkl}}^{\mathrm{obs}}$ is the observed intensity and $I_{\mathrm{hkl}}^{\mathrm{calc}}$ is the theoretical intensity for the diffraction line *hkl*, and (θ) is the diffraction angle of the line *hkl*, λ indicates wavelength of the incident X-rays.

A number of authors have employed these XRD intensities formulae for obtaining cation distributions till date. Trivedi et al. [85] determine the ionic distribution in $Li_{0.5x}Ni_{1-x}Fe_{2+0.5x}O_4$ ($x = 0.0$–0.8) by using equation suggested by Buerger [83]. They reported the B site preference of Li^{2+}, Ni^{2+} and Fe^{3+} as follows: $Ni^{2+} > Li^{1+} > Fe^{3+}$. Patange et al. [86] found cation distribution in $NiCr_xFe_{2-x}O_4$ ($x = 0.0$–1.0) by Bertaut method [66, 87] of XRD intensities and revealed that Cr^{3+} and Ni^{2+} both have a strong preference towards B site. The same method has utilized by Kavas et al. [88] for investigating Zn^{2+} and Fe^{2+} ions distribution in $Zn_xNi_{1-x}Fe_2O_4$ (x = 0, 0.2, 0.4, 0.6, 0.8 and 1) synthesized by using surfactant polyethylene glycol assisted hydrothermal method. They reported occupancy of Zn^{2+} ions mostly in B site and A site were comprised Fe^{3+} ions, under synthesis conditions utilizing surfactant and low temperature. The samples possess almost inverse-spinel ferrite and validated by the results of the magnetic studies. Also, Gomez et al. [89] reported $Ni_{1-x}Zn_xFe_2O_4$ (x = 0.0, 0.2, 0.4, 0.6, 0.8, 1.0) ferrites synthesized by solid-state reaction technique to show the occupation of Zn^{2+} and Ni^{2+} ions in all samples by using the line intensity ratios of diffraction peaks. They confirmed that in pure Zn ferrite ($x = 1.0$), Zn^{2+} ions

prefer A sites, and in pure Ni ferrite ($x = 0.0$), Ni^{2+} ions prefer B sites. Furthermore, Zn^{2+} and Ni^{2+} ions can occupy both A and B sites on mixing-up the ferrite samples with these two ions. Nikmanesh and Eshraghi [90] synthesized $CoCr_xFe_{2-x}O_4$ (x = 0.0, 0.25, 0.50, 0.75, 1.0) ferrites forming mixed spinel structure in which iron and cobalt ions occupy both A and B sites, while chromium ions reside in the B site.

Cvejic et al. [91] reported cations distribution obtained by using Rietveld refinement for sites orientation to show that in $Fe_{2.85}Y_{0.15}O_4$, Y^{3+} ions with 16d sites and in $Fe_{2.55}In_{0.45}O_4$, In^{3+} ions randomly distributed on both 8a and 16d sites with space group Fd3m and spinel-type structure. Patange et al. [87] has reported cation distribution of $NiFe_{2-x}Al_xO_4$ ($x = 0.0$–1.0) which confirmed through X-ray diffraction and Rietveld refinement method. It was found that Al^{3+} ions prefer B site and force Ni^{2+} ions to migrate at A site. The structure of synthesized ferrites changes to normal spinel with an increase in the concentration of Al^{3+} ion.

Kumar et al. [92] published a paper of $CoFe_2O_4$ powder synthesized by citrate precursor and co-precipitation methods labelled as S1 and S2 ferrite samples, respectively. By refining the structure of both samples, they were showed significant dependence of cation distribution on synthesis conditions as well as annealing. Notably, the nucleation and growth rates can be varying due to synthesis condition. Further, it was well-suited for both the samples that comparatively low thermal energy, because of lower annealing, is insufficient to cross the energy barrier to an ordered (stable) cation distribution. With the increase in annealing temperature, the cation redistribution between A and B sites occur to relax the strain at the sublattice. At comparatively higher annealing temperature, there is sufficient thermal energy which allows the cations to migrate between both sites, which in turn, create an ordered (stable) cation distribution and this transfer of cations continuous until their free energy reached to a minimum value. This alteration of cation distribution also provide modified lattice constant and optimized bond lengths. The random distribution (metastable distribution) of cations of sample S1 over A and B sites are turned to an inverse distribution (stable cation distribution) at high annealing (800 °C). It was visualized that due to annealing the crystallite size of sample S1 increased to 48 nm and the cations distribution over A and B sites is nearly an inverse structure. The most noteworthy of annealing at high temperature is that the sample S1 showed possible variation from nanocrystalline to bulk form if compare with size of the sample S2 (33 nm). However, sample S2, annealed at 800 °C, still remains as mixed (random or metastable distribution) spinel as in the case of nanocrystalline ferrite, the preference of cation over a specific site does not hold good because of surface effects. This clearly reveals that the cation distribution between A and B sites in nanocrystalline form is completely different from that of bulk. As evidence, sample S1 shows a higher degree of inversion than sample S2, under identical annealing conditions.

Many authors determined cation distribution with Mössbauer spectroscopy. Gismelseed et al. [93] reported cation distributions of $NiCr_xFe_{1-x}O_4$ ($0 \leq x \leq 1.4$) ferrites, obtained form the area under the resonance curve of each site in Mössbauer spectra which showed that the ferrite samples are gradually changed from perfect inverse spinel to partially normal spinel structure. Mittal et al. [94] reported Mg^{2+} ion distribution in $Ni_xMg_{1-x}Fe_2O_4$ ($0 \leq x \leq 1$) by using Mössbauer spectroscopy and

the entropy change of the system. In spinel, cation distribution attains equilibrium by achieving minimum Gibbs free energy at a given temperature, represented by the equation:

$$\Delta G = \Delta U - T\Delta S + \Delta(PV)$$

where ΔU is the change in the internal energy, T is temperature, change in entropy is indicated by ΔS and change of the product of pressure and volume is indicated with $\Delta(PV)$. ΔG depends only on ΔU and ΔS. In solid sample cases $\Delta(PV)$ is negligible. The ΔU depends on site preference energy of the cations, which in turn, depends on a number of factors such as cationic radii and charge, crystal field stabilizing energy (CFSE), and electrostatic contribution to lattice energy. By these analyses, they were observed that the higher percentage of Mg^{2+} occupies the A sites with higher Ni^{2+} concentration in spinel. The trend showed saturation for Ni^{2+} content $x < 0.4$ which means that Mg^{2+} % in A site is almost constant. This reveals that Mg^{2+} distribution is mostly controlled by Ni^{2+}. The distribution of Mg^{2+} is elucidated in terms of site preference energy of Ni^{2+}, Mg^{2+} and Fe^{3+} and entropy change associated with the cation distribution. Kumar et al. [95] gave a strong push towards cation distributions of Al-substituted $CoFe_2O_4$–$NiFe_2O_4$ soild solutions prepared by sol gel auto combustion technique. The cation distributions calculated via Rietveld refinement and Mössbauer spectroscopy reveal that Fe^{3+}(tetrahedral)/Fe^{3+}(Octahedral) occupancy-ratio increased with an increase in Al^{3+} content and the preference of Ni^{2+} ions is to occupy B site and, Co^{2+} and Al^{3+} ions redistributed in both A and B sites, in the ratio 2:3.

Tang et al. [96] and Han et al. [97] have been proposed Quantum–mechanical (Q.M.) route for calculating ion distributions in spinel ferrites. This approach is significant for assessing the cation distribution in doped ferrites. The four basic principles of this method are following:

The cation distribution is affected by two significant factors such as the cation ionization energy and the distance between the cation and the anion in an ionic compound. It is to be noted that neighbouring cations and anions established a square potential barrier between them, and the width and the height of this barrier is related to the ionization energy of the last ionized electron and the distance between cation-anion pair, respectively. Thus, the content ratio (R) of the different cations is related to the probability of their last ionized electrons transmitting through the potential barrier and takes the form:

$$R = \frac{T_C}{T_D} = \frac{V_D}{V_C} \exp\left[10.24\left(r_D V_D^{1/2} - cr_C V_C^{1/2}\right)\right],$$

where T_C (T_D) represents the probability of the last ionized electron of C (D) cations, jumping to the anions through the potential barrier with the width r_C (r_D) and height V_C (V_D); V_C and V_D are the ionization energies of last ionized electron of the cations C and D, respectively; and, r_C and r_D are the distances from the cations C and D to the anions, respectively; The parameter c is a barrier shape correcting constant.

- The third important factor is Pauli repulsion energy of the electron cloud between neighbouring cations and anions. It can be taken into consideration utilizing the effective ionic radius, as the smaller ions should be located at the interstitial sites with smaller accessible space in the lattice.
- The divalent ions transfer from sites B to A due to charge density balance forces, overcoming the potential barrier V_{BA}, arises from the Pauli repulsion energy of the electron cloud and the magnetic ordered energy.
- The magnetic sub-lattice substitute with non-magnetic ions resulting in a decrease in the magnetic moment of that sublattice.

Ji et al. [98] reported ionicity of cubic spinel ferrite Fe_3O_4, measured by the density of states calculations with plane–wave pseudopotential density functional theory (DFT) method as implemented in the Cambridge Serial Total Energy Package (CASTEP) program. The experimental magnetic moments were fitted by calculated content ratios between Fe ions at both A and B sites, which resulting in the ionicity of Fe_3O_4 to be 0.879. As an application, the distributions of cations at (A) and [B] sites of $(A)[B]_2O_4$ ferrites, i.e. MFe_2O_4, where M=Fe, Co, Ni, Cu, were measured with the help of current values of ionicity, are listed in Table 3.

Raman spectroscopy reported, as one of the important tools to investigate the cation distribution, by Nandan et al. [99] for analysing $Ni_{1-x}Co_xFe_2O_4$ (x = 0.0, 0.4, 0.5, 0.6, 1.0) ferrites. The results proved that nickel ferrite is a nearly inverse structure (Ni^{2+} ion occupy 96% B sites). In addition, doping of Co^{2+} ion in nickel ferrite leads to the formation of partially inverse mixed structure and in $Ni_{0.5}Co_{0.5}Fe_2O_4$, nearly 18% Co^{2+} ion occupying A sites and in $CoFe_2O_4$, the occupancy of A sites by Co^{2+} ion reaching a maximum of 25%.

Manjunatha et al. [100] reported the composition of $Ni_{1-x}Cd_xFe_2O_4$ (x = 0– 1) ferrite, using ^{57}Fe-Zero Field Nuclear Magnetic Resonance (ZFNMR) carried out at 77K and the spectra are deconvoluted using the Gaussian fit. They found a novel technique of using the NMR signal to quantify the composition of the inverse spinel systems involving both sites. For x = 0, Ni enters B sites, ^{57}Fe NMR of Fe^{3+} ions give two signals of equal integral intensities in spectral lines corresponding to

Table 3 Contents of the various ions at (A) sites and [B] sites per formula of the spinel structure ferrites MFe_2O_4 (M=Fe, Co, Ni, Cu), where M_2 and M_3 are the contents of M^{2+} and M^{3+} ions, respectively; F_2 and F_3 are the contents of Fe^{2+} and Fe^{3+} ions, respectively. "a" is the unit cell constant in nm

M	Unit cell constant "a" (nm)	Cation total valence	(A) Sites		[B] Sites			
			F_3	M_2	M_2	M_3	F_2	F_3
Fe	0.839	7.0320	0.4165	0.5835	0	0	1.3845	0.6155
Co	0.838	6.9052	0.6515	0.3485	0.5904	0.0611	1.1559	0.1926
Ni	0.834	6.8556	0.7594	0.2406	0.7402	0.0192	1.1636	0.0770
Cu	0.837	6.8185	0.8149	0.1851	0.8143	0.0006	1.1821	0.0030

Reproduced with permission from [98]

these lattice positions. Accordingly, the contribution of Fe^{3+} nuclei varies for A and B sub-spectra by doping with Cd^{2+} ion. By determining the distribution of Fe^{3+} ion on A and B sublattices, which are obtained from the relative spectral areas of A and B NMR sub-spectra, the cation distribution is estimated and confirmed by the binomial distribution.

4 Magnetic Studies of Ferrites

The mineral magnetite, Fe_3O_4, comprises of 1 Fe^{2+}, 2 Fe^{3+} and 4 O^{2-} ions, from which it was expected that the saturation moment is come out to be $4 + 5 + 5 = 14 \, \mu_B$. However, the experimental value determined by Weiss and Forrer (1929) is $4.08 \, \mu_B$. After 19 years, the reason behind this discrepancy has been understood by Néel [60]. Néel's theory of ferrimagnetism explained magnetic ordering in the simple ferrites. According to the Néel model, the magnetic exchange interactions between the ions at A and B sites (AB interaction) in ferrites are negative and the interactions between the ions at the same site (AA and BB interaction) are weak. Néel predicted magnetic properties by using Weiss molecular field theory. In spinel ferrites, the metals ions Me and Me$^{'}$ are separated by the O^{2-} ions, thus, there is no direct exchange, rather, the exchange energy in ferrites is of indirect (superexchange) type. The value of the negative exchange forces between two metals ions on different sites based on the distances between these ions and the O^{2-} ions, and on the angle Me–O–Me′; in this way, the electron densities can possibly overlap so as to give exchange interaction. In 1934, Kramers [23] presented theoretically the possibility of indirect exchange interaction between cations via anions when he found that in the crystal structure of MnO, the Mn atoms interact with each other despite having non-magnetic O^{2-} ion between them. Later, Anderson [25] in 1950 worked out Kramer's model. According to Anderson's theory, the indirect (superexchange) interaction is highly persistent for such Me–O–Me′ colinear configurations (180°), in which the net consequence was negative indirect interaction in case of certain 3d-transition metal ions, including Fe^{3+} and that indirect interaction in general decreases with increasing distance. For right-angle configurations (90°), the interaction is weakest. Gorter [101] has given most probable arrangements of metal ion pairs in spinel structure with suitable metal ions and anion distances, and angles for effective magnetic interactions. Figure 5, shows the arrangements of ion pairs occupied sites in the spinel lattice. However, in the spinel structure, the arrangement with 180° angle does not arise, whereas, the 125° A-O-B angle, as shown in Fig. 5, still gives a substantial strong interaction for Fe^{3+} ions, in comparison to the 90° B–O–B interaction. Owing to the smaller angle as well as the larger distance the weakest interaction of A-O-A does not affect the magnetic interaction as far as there are sufficient magnetic ions on the B sites. Consequently, for a significant concentration of Fe^{3+} at both A and B sites in ferrite, the criterion to attain a collinear Néel configuration seems to be satisfied. Experimentally, it has been established that the Néel model can be fitted satisfactorily with the magnetic moment of some simple ferrites [47].

AB   BB   AA

$\varphi =$ 125° 9′   154° 34′   90°   125° 2′   79° 38′

Distances Me-O	Distances Me-Me
$p = a(\frac{3}{8} - u)$	$b = (a/4)\sqrt{2}$
$q = a(u - \frac{1}{4})\sqrt{3}$	$c = (a/8)\sqrt{11}$
$r = a(1 + u)\sqrt{11}$	$d = (a/4)\sqrt{3}$
$s = a(\frac{1}{4}u + \frac{1}{8})\sqrt{3}$	$e = (3a/8)\sqrt{3}$
	$f = (a/4)\sqrt{6}$
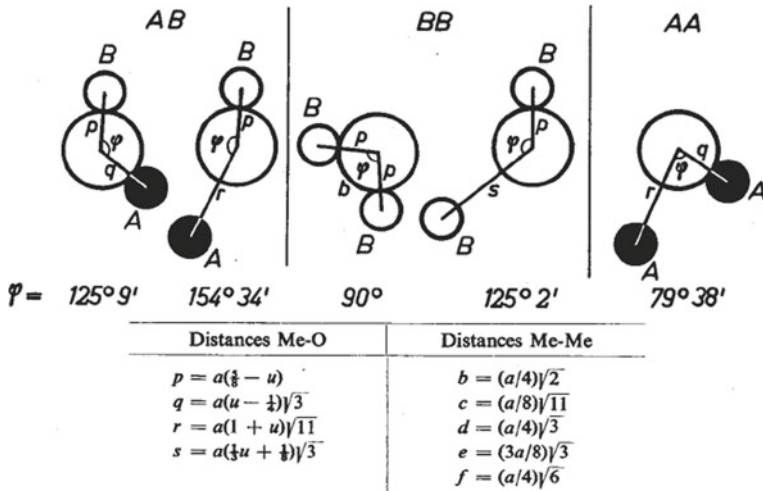
Fig. 5 Representation of the arrangements of ion pairs which possibly make the greatest contributions to the indirect exchange interaction in the spinel lattice. Metal ions A and B are on tetrahedral and octahedral sites, respectively, and oxygen ions indicated with a large open circle. The centre-to-centre distances of the ions, expressed in the lattice constant "a" and oxygen parameter "u" are reported in the attached table below the figure. Taken from Smit and Wijn [47]

As per the Néel Model, AB interactions are dominant over AA and BB interactions. As a consequence of this, the net observed moment should be the difference between the two average sublattice magnetic moments. This theory can also be applicable to the mixed ferrites. With the Néel configuration, the saturation moment at 0 K is given by

$$M_s (\text{in } \mu_B) = M_{(B)} - M_{(A)}$$

where $M_{(B)}$ and $M_{(A)}$ are the magnetic moments at (B) and (A) sites, respectively. When the AB antiferromagnetic interaction is dominant over the other two interactions, then below a transition temperature, A and B will be magnetized in opposite directions with a different magnitude which resulting in a special case of ferromagnetism called as "ferrimagnetism" and orbital magnetic moments are assumed to be quenched. In the cases, where BB interaction is dominant, Néel obtained that the above transition will not occur and decided that the compound remains paramagnetic down to the lowest temperatures. This Néel's predominant conclusion fails as in the presence of strong exchange energy some kind of magnetic ordering may be predicted to occur at low temperatures. Also, discrepancies occur while explaining the behaviour of pure $ZnFe_2O_4$. The ferrite $ZnFe_2O_4$ has a normal spinel structure. As the Zn^{2+} is non-magnetic, the A site has no magnetic moment. Accordingly, BB interaction resulting in the antiferromagnetic ordering in the B site. The discrepancies between the Néel theory and experimental results were attempted to describe by M. A. Gilleo, reported in his paper published in 1958 [102] and 1960 [103],

Table 4 Theoretical and experimental values of the saturaton magnetizaton of simple spinel ferrites in Bohr Magnetons at 0K

Ferrite	Postulated ion distribution		Magnetic moment of tetrahedral ions	Magnetic moment of octahedral ions	Magnetic moment per molecule $MeFe_2O_4$	
	Tetrahedral ions	Octahedral ions			Theoretical	Experimental
$MnFe_2O_4$	$Fe^{3+}_{0.2}$ + $Mn^{2+}_{0.8}$	$Mn^{2+}_{0.2}$ + $Fe^{3+}_{1.8}$	5	$5+5$	5	4.6
Fe_3O_4	Fe^{3+}	Fe^{2+} + Fe^{3+}	5	$4+5$	4	4.1
$CoFe_2O_4$	Fe^{3+}	Co^{2+} + Fe^{3+}	5	$3+5$	3	3.7
$NiFe_2O_4$	Fe^{3+}	Ni^{2+} + Fe^{3+}	5	$2+5$	2	2.3
$CuFe_2O_4$	Fe^{3+}	Cu^{2+} + Fe^{3+}	5	$1+5$	1	1.3
$MgFe_2O_4$	Fe^{3+}	Mg^{2+} + Fe^{3+}	5	$0+5$	0	1.1
$Li_{0.5}Fe_{2.5}O_4$	Fe^{3+}	$Li^+_{0.5}$ + $Fe^{3+}_{1.5}$	5	$0+7.5$	2.5	2.6

Taken from Smit and Wijn [47]

by explaining the superexchange interaction energy through some statistical models by considering linkage approach and by taking into care various nearest magnetic neighbours contributing to the magnetization. Moreover, some changes to the same approach were tried by Ishikawa [104], Nowik [105], Geller [106] etc.

Theoretical and experimental results of simple spinel ferrites elucidate values of the saturation magnetization in Bohr Magnetons at 0 K are depicted in Table 4, in which the average values of the magnetic moments, measured from the value of the saturation magnetization of the polycrystalline sample, are represented. Owing to the relative magnitudes of the magnetic change interactions it has been expected that the spins of the A and B ions in spinel ferrites were oppositely oriented, thus at $T = 0$, there will be two saturated and oppositely magnetized sublattices existing. Accordingly, the net magnetization is the difference between the magnetization of the B sublattices and that of the total A sublattices, by which the first will generally possess the greatest value. This was first proposed by Néel [60] and well-explained through experiments for different simple ferrites, as listed in Table 4, by a number of authors from the value of the saturation magnetization of spinel ferrites at 0 K [65, 101, 107–110].

In Table 4, for $MgFe_2O_4$ and $CuFe_2O_4$, the deviation in the magnetic moment from theoretical values occur. Measured value of saturation magnetization is increased in these spinel ferrites after quenching rather after slow cooling. Also, the ions may possess orbital moment in addition to the spin moment as the orbital moment cannot

Fig. 6 The magnetic moment per formula unit of the mixed $Me_{1-\delta}Zn_\delta Fe_2O_4$ ferrites extrapolated to 0 K. Reproduced with permission from [73]
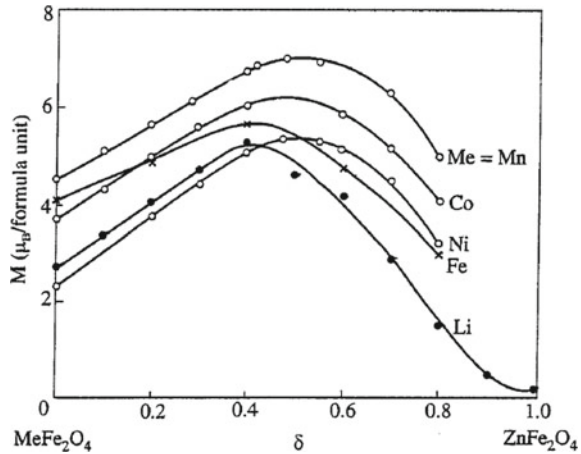
be completely quenched, this especially takes place in cobalt ions [47]. Furthermore, the deviations may be occurred due to the antiparallel orientation of the moments of ions presents at both A and B sites which have been described for $NiFe_2O_4$ by the author Hastings [33] and $MgFe_2O_4$ by Corliss and Bacon [32, 111].

In a variety of technical soft ferrite, the enhancement of saturation magnetization is attained by the substitution of A site's magnetic ion content with non-magnetic Zinc ions. In consequence of this, mixed Zn ferrite shows one of the very important features of ferrimagnetism owing to the preferential occupation of Zn ions (non-magnetic) for A sites, which in turn, leads to the smaller magnetization at A sites than that of simple ferrite and as Fe^{3+} ions possess the largest magnetic moment, at absolute zero point, the magnetization of a mixed ferrite is expected to increase with increasing the Zn concentration. Figure 6 shows the plots of magnetic moment at 0 K for the relevant mixed zinc ferrite series as a function of Zn ion content. The magnetic collinear Néel structure is well-defined for an increase in saturation moment at a small concentration of Zn ion [101, 107, 108], however, does not predict the trend for a higher concentration of Zn ion where saturation magnetization drastically reduced with an increase in Zn content because of the moment of few remaining Fe^{3+} ions on A sites which are not anymore capable to line up all the moments at B sites antiparallel to themselves as it is opposed by negative BB interaction. In this situation, B lattice will then split itself into sublattices, the magnetic moment of which make an angel with each other. The condition for this splitting is that the ions on the same sublattice have lower interaction with each other than the ions on other sublattices. As such, the phenomenal fact emerges that the dilution of magnetic ions in spinel ferrite by non-magnetic ions results in an increase in the saturation magnetization. In addition to Zn^{2+} ion other non-magnetic ions like Cd^{2+} [57], Ga^{3+} [112] and In^{3+} [113] increase the magnetization of spinel ferrites at 0 K, although Ga^{3+} and In^{3+} are less perceptible for A sites and, so, small content is sufficient to increase the magnetization.

Thereafter, in 1952, Yafet and Kittel [26] extended the Néel theory and explained this subdivision of B sublattices by introducing the triangular uniform canting configuration. They took into consideration the antiferromagnetic AA and BB interactions that are not as insignificant as compare to AB interactions. They suggested that in spinel ferrites, if the exchange integral $|J_{AB}|$ is smaller than $3/2 \, |J_{BB}| \, S_B/S_A$, then B sublattice divide into two sublattices with magnetizations making an angle (θ_{YK}) between each other. It means B sublattice splits into two, mostly B_1 and B_2 with an equal moment at an angle (θ_{YK}) with the direction of resultant moment of B sublattices at 0 K owing to the presence of non-magnetic sublattice in one sublattice which creates non-collinear or canted spin configuration on the other sublattice and a net moment antiparallel to the A-site moment. The existence of splitting is obtained by the interactions responsible for the magnetic ordering. Yafet and kittle [26] were developed a split sublattice model to measure the uniform canting angle (θ_{YK}). The modified formula has been written as:

$$M_s(\mu_B) = M_B \mathrm{Cos}\theta_{YK} - M_A$$

with an increase in angle (θ_{YK}), $\mathrm{Cos}\theta_{YK}$ decreases resulting in a decrease in the magnetic moment. Later, in 1962, Lyons et al. [114] noticed that in the case of cubic spinel symmetry, the Yafet-Kittel triangular configuration is not stable but may be stabilized by appropriate tetragonal distortion and that otherwise, a spiral configuration represents the ground state.

Another exchange mechanism is proposed by Zener [115] named as "double exchange", a ferromagnetic interaction that can be found in oxidic spinels. This exchange occurs because of the hopping of electrons between cations in different valence states in one sublattice. In 1977, Lotgering and Van Diepen [116] have reported the existence of the double exchange in the $Zn_{1.5-x}Ti_{0.5+\times} \, Fe^{3+}_{1-2x}Fe^{2+}_{2x}O_4$ sample, which comprises only Fe^{2+} and Fe^{3+} on B sites. The benefit of studying the ZnTi ferrite is that the diamagnetic ions prefer only to occupy A-sublattice, thus, AB and AA superexchange interactions do not interfere. And for a magnetic system with only BB exchange interactions, the condition is more intricate due to the anomalous property of the B sublattice which attains 'perfect' short-range order while maintaining a finite entropy. Anderson [81] has explained that nearest neighbour magnetic interactions may not individually sustain long-range magnetic order, which signifies that along with these interactions other much weaker forces like magnetic anisotropy and dipole interactions are also responsible for the long-range order.

The magnetic characteristics of the simple spinel ferrites are based on the composition of the ferrites. The basic compositions, proper selection of dopants and synthesis conditions determined the magnetic structure of the ferrite systems. Consequently, in order to obtain the physical magnetic properties as per our requirements, like saturation magnetic moment, coercivity, magnetic anisotropy or magnetostriction, etc., the pre-requisite conditions are to choose a suitable composition of ferrites based on intrinsic magnetic properties of the elements comprises a certain composition. For applications, simple spinel ferrites based on Ni, Li, Cu, Mg, Co and Mn are found to be

very significant from their high saturation magnetization values obtained by various researchers. However, ferrite with a high content of Co has high magnetocrystalline anisotropy resulting in low value of permeability, which makes Co ferrite not appropriate for the high permeability applications. Various researchers and authors have reported numerous magnetic properties of different simple ferrites by performing a number of experiments. Here, readers can go through some simple ferrites which are highlighted revealing their interesting magnetic properties.

Initially, the magnetic structure of that $NiFe_2O_4$ has found to be a collinear having complete inverse structure reported by Leung et al. in 1973 [117], whereas Morel in 1967 [118] proposed ferromagnetic interaction between octahedral Fe^{3+} and Ni^{2+} ions. If we consider the past 20 years, it will be interesting to know the valuable magnetic properties of Ni ferrites. Chinnasamy et al. in 2002 [119] published work on nanocrystalline $NiFe_2O_4$ spinel ferrites and ascribed increase in magnetization value to the cation redistribution in the crystal lattice when particles are in nano range. Owing to the cation redistribution, ultra-fine $NiFe_2O_4$ exhibits an 8% more saturation magnetization, compared with the theoretically predicted value. In 2009 Alarifi et al. [120] prepared $NiFe_2O_4$ nanoparticles via facile and economical route using Ni and Fe nitrates, and glycine. The ferromagnetic behaviour of the $NiFe_2O_4$ ferrite confirmed using magnetization measurements at ambient temperature, obtained saturation magnetization around 2.387–57 emu/g at 15 kOe. In $NiFe_2O_4$ nanoparticles measured coercivity were varied from 65.58 to 148.8 Oe following the change in the ratio between nitrates and glycine. Nawale et al. [121] have reported saturation magnetization and coercivity values of the ferromagnetic nanoparticles of nickel ferrite which relying on the different operating parameters. The high saturation magnetization i.e. 48 emu/g has been obtained due to the high degree of crystallinity, high temperature during the growth, and the redistribution of the cation. The high value of coercivity e.g. 115 Oe is dependent on the possible lattice defects arising from the redistribution of the cation. Similarly, Zabotto et al. [122] reported specimen of nickel ferrite sintered at 1200 °C exhibited a coercive field verging on superparamagnetic values, yet keeping the high values of saturation magnetization, as a consequence of the possible formation of a mixed spinel structure. The work presented by Thakur et al. [123] has shown magnetic properties of $Ni_{0.58}Zn_{0.42}Fe_2O_4$ at different pH values (<9.6, 9.6, 10.96 and 11.40) prepared by reverse micelle method. All the samples show superparamagnetic behaviour at ambient temperature (300 K) and negligible hysteresis at low temperature (5 K). The low value of saturation magnetization is explained based on spin canting.

Lithium-based ferrite reported by Dormann et al. [124], revealed that in the ordered as well as in the disordered crystallographic structure, $Li_{0.5}Fe_{2.5}O_4$ appeared to be a collinear Néel ferrimagnet. Further, in 2006, K. U. Kang et al. fabricated ordered Li ferrites via sol–gel method and reported magnetic properties [125]. They reported that for the sample which is annealed below 500 °C, obtained 46 emu/g saturation magnetization and drastically raised up to 63.3 emu/g during annealed at 700 °C, while the coercivity of the samples has obtained maximum value of 152.5 Oe at 500 °C. The ordered cation distribution by the local symmetry reduction of sublattice reveals a practical interpretation of the magnetic characteristics of nanoparticles. The

detailed study by George et al. [126] on fine particles of lithium ferrite achieved a large value of saturation magnetization (75 emu/g) as compared with the value proposed by Neel's two sublattice model. This difference in value is quite obvious as Neel's model is known to obeyed by $Li_{0.5}Fe_{2.5}O_4$ in the bulk. There are a number of factors for the occurrence of deviation in the value of saturation magnetization. Among them, most prominent factors are surface effects/surface spins/cation redistribution. Various researchers have stated this deviation by giving different hypothesis and theories to describe the tuned magnetic properties for ultra-fine particles. In ultra-fine range, when surface-to-volume ratio increases then the bulk properties determined by the surface contribution. However, the variation in magnetization is not only occurred through the grain size variation. In the ulta-fine range, the increase in saturation magnetization is due to the ultra-fine grains. But, a further decrease in magnetization values may be attributed to a number of other factors. $Li_{0.5}Fe_{2.5}O_4$ sample sintered at 300 °C has a saturation magnetization of 42.8 emu/g and the sample sintered at 600 °C drops to 40.8 emu/g. This reduction is owing to the volatilization of lithium and oxygen. The loss of Li_2O results in the formation of α-Fe_2O_3. Thus, the occurrence of haematite which is antiferromagnetic in nature considerably leads to a reduction in the saturation magnetization. Also, Anantharaman et al. [127] and Shenoy et al. [128] have reported that the ultra-fine particles of zinc ferrite become magnetic because of surface effects as the contribution to the total magnetization of the ultra-fine Zinc ferrite occurred from the surface spins.

Copper ferrite ($CuFe_2O_4$) can exist in two crystallographic structures and the magnetic structures remain collinear down to 4.2 K in a field of 6 T reported by Janicki et al. in 1982 [129] and Hannoyer et al. in 1985 [130]. However, Narayanasany and Hagström in 1983 stated a small canting in lower fields of 4 T. $CuFe_2O_4$ is one of the significant spinel ferrites owing to its structural phase transformation and reduction of the crystal symmetry, which is, known as Jahn–Teller effect [131]. This distortion effect occurs when Fe^{3+} ion substitute by Cu^{2+} ion at the (A) tetrahedral site, which in turn, leads to a magnetic dilution that causes the cubic spinel to have a tetragonal distortion [132]. Furthermore, Abdellatif et al. [133] reported that the magnetic ordering in $CuFe_2O_4$ is identified which associated with the domain interaction, under presence of a large fraction of volume of domain boundary in the $CuFe_2O_4$ powder. They presented that in $CuFe_2O_4$ nanoparticles, in addition to the Jahn-Teller effect there appears another type of anisotropy, which probably due to the surface state of the magnetic ions in the crystal field. The interaction energy between two magnetic ions varies with the angle between the spontaneous magnetization and the line linking the two magnetic ions in a crystal field. Chatterjee et al. [134] reported that the field-dependent magnetization studies for the iso-oriented uniform spherical ensembles of $CuFe_2O_4$ nanoparticles, prepared by solvothermal method, at low temperature shows a step-like rectangular hysteresis loop ($M_R/M_S \sim 1$), which signifies the presence of cubic anisotropy in the system. The variation in the coercive field shows dependence on temperature, which is associated with the variation of effective anisotropy (K_E). A high-temperature improvement of K_E and so as coercivity agrees well with strong spin–orbit coupling in the sample which is

further proved by important alteration of Cu/Fe–O bond distances. The nanocrystals at the mesoscopic scale with the spherical arrangement, aligned easy axis of magnetization along the direction of the applied magnetic field which results in a step-like rectangular hysteresis loop. A detailed neutron diffraction study of copper ferrite is reported by Balagurov et al. [135]. They performed experiments in a broad temperature range from 2 to 820 K and observed a completely inverted tetragonal spinel $CuFe_2O_4$ with space group $I4_1/amd$ up to a $T_C \approx 660$ K, where a cubic phase of $CuFe_2O_4$ with space group $Fd3m$ emerges and up to $T \approx 700$ K, both structural phases of $CuFe_2O_4$ coexist. Structure deformation corresponds to the Jahn–Teller effect. Néel ferrimagnetic model, a ferromagnetic ordering of the moments of Fe^{3+} ion at A sites and moments of Cu^{2+} and Fe^{3+} ions at B sites with magnetization in opposite direction, vanishes at $T_N \approx 750$ K. At $T < 30$ K, the magnetic moment at A sites (Fe^{3+}) are equal to 4.06 (6) μ_B and at B sites ($Fe^{3+} + Cu^{2+}$) are equal to 4.89 (8) μ_B. The difference between these two values agrees with the magnetic moment of Cu^{2+} ions. The magnetic study revealed that the collinear Néel order in $CuFe_2O_4$ stabilized by, antiferromagnetic interaction between A and B sublattices obey the superexchange theory.

The thermal treatment can change the cation distribution in $MgFe_2O_4$ which may influence the magnetic structure of the sample. De Grave et al. [136] observed 94% of the Mg-ions in B sites, for a slowly cooled sample, with a collinear magnetic structure down to 4.2. Aliyan et al. [137] have reported nanoparticles of $MgFe_2O_4$ with saturation magnetization value increased from 8.02 to 13.41 emu/g varying with the calcination temperature from 600 to 700 °C. The maximum saturation of 13.41 emu/g was obtained due to the low degree inversion factor. The reason for high saturation at 700 °C is due to the maximum misbalance of Fe^{3+} ions at A and B sites. However, due to the surface spin canting effect, the saturation magnetization for 700 °C is lower than that of bulk (26.9 emu/g), which prevents the core spins to align along the direction of the field. Thus, the magnetization increases with the increase of crystallite size. Furthermore, the experimentally achieved magneton number by VSM approximately comparable with the calculated magneton number using XRD, approving the collinear magnetic structure. The same concept of reduction in magnetization value for oxide nanoparticles, with respect to the bulk value, has reported by Chandradass et al. [138]. This reduction has been attributed to the existence of spin-glass like behaviour of the surface spins or the presence of a magnetically dead layer on the surface of the particle. Also, Aslibeiki et al. [139] reported saturation magnetization of $MgFe_2O_4$ which increases with the increase of crystallite size. They have explained the temperature dependence of M_s in terms of spin-wave excitations in the core and surface spin canting. They applied a modified Bloch law, $[M_s(T) = M_s(0)(1 - \beta T^\alpha)]$ and concluded a dependence of size on the Bloch constant β and the exponent α. With the decrease in the particle size, the value of β increases and α decreases.

In the case of $CoFe_2O_4$, the measurement of the spin structure is hindered by the existence of high magnetic anisotropy and due to the inversion degree range between 80 and 95%. Initially, the magnetic structure was found to be collinear as per research reported by Prince [140], but Petitt and Forester [141], and Hauet et al.

[142] mentioned non-aligned spins, with canting angles θ_A, ~ θ_B ~ 25°, found at 4 K in magnetic fields up to 6 T. However, Persoons et al. [143] claimed that the non-aligned collinear structure is not because of canted structure but to the non-saturation of the specimen caused by the high magnetic anisotropy and almost equal A- and B-site angles are also substantiating the non-aligned spins. Lopez et al. [144] described magnetic properties of $CoFe_2O_4$ sample at 4.2 K with a coercivity of 14.7 k Oe and saturation magnetization of 27.3 emu/g. The squareness ratio is 0.43, smaller than the predicted value for randomly oriented isolated particles with cubic anisotropy (0.8) and particles with uniaxial anisotropy (0.5), respectively. The squareness ratio caused by the struggle between interparticle interactions and intraparticle anisotropy on the spin relaxation process, which produces frustration. At 4.2 K, the value of effective magnetic anisotropy was obtained to be, $K_{eff} = 6 \times 10^6$ erg/cm^3. In the work of Eshraghi and Kameli [145] the magnetization measurements of the $CoFe_2O_4$ nanoparticles showed that with the increase in the particle size from 3.5 to 7.2 nm, the magnetization and coercivity, at room temperature, increases from 8 to 30 emu/g and from 0 to 152 Oe, respectively. The effective anisotropy constant was obtained as $K_{eff} = 9.2 \times 10^6$ erg/cm^3, which is higher than the bulk value due to the surface effects.

Initially, the magnetic structure of $MnFe_2O_4$ is a topic of controversy as Sawatzky et al. [146] observed no evidence for spin canting of the Fe-ions, however, the magnetic moment at 4.2 K (4.5–4.8 μ_B/formula unit) is too small to justify for a collinear structure (5.0 μ_B/formula unit). The valence state of the Fe^{2+} and Mn^{3+} cations on the B sites have been proposed to induce the lower magnetic moment but Mössbauer investigation performed by Sawatzky et al. [146] and Lotgering and Van Diepen [147], reveal that the Fe^{2+} and Mn^{3+} valences are not the ground state. Sawatzky et al. [146] proposed that only the B sites Mn^{2+} spins are canted, that suggestion was further advanced by Simsa and Brabers [148]. Li et al. [149] have investigated the detailed magnetic studies of $MnFe_2O_4$ nanoparticles treated at 450, 500 and 700 °C, as shown in Fig. 7, with the maximum applied magnetic field is 6 kOe. At room temperature, the $MnFe_2O_4$ nanoparticles obtained at 450 and 500 °C exhibits low coercivity reveals their superparamagnetic nature. If the temperature is lower than the magnetic ordering temperature, thermal energy is enough to alter the magnetization direction of the entire crystallite. Therefore, the M-H curve shows a remnant magnetization and a coercivity that can be almost close to zero. By increasing the calcination temperature to 700 °C, the coercivity increases to about 68 Oe. The Stoner–Wohlfarth theory is employed to explain the magnetocrystalline anisotropy energy of a single-domain particle. The almost normal spinel structure ($[Mn_{0.8}^{2+} Fe_{0.2}^{3+}][Fe_{1.8}^{3+}Mn_{0.2}^{2+}]O_4$) of $MnFe_2O_4$, studied by Mossbauer spectroscopy, reveal that more Mn^{2+} ions enter into the B sites leads to the transfer of Fe^{3+} ions from the B to A sites, which in turn, increase the magnetocrystalline anisotropy constant. With an increase in calcination temperature, the size of magnetic particle increases which results in higher magnetocrystalline anisotropy energy. In comparison to the change in the cation distribution, an increase in the coercivity with an increase in calcination temperature is often ascribed to the larger particle size.
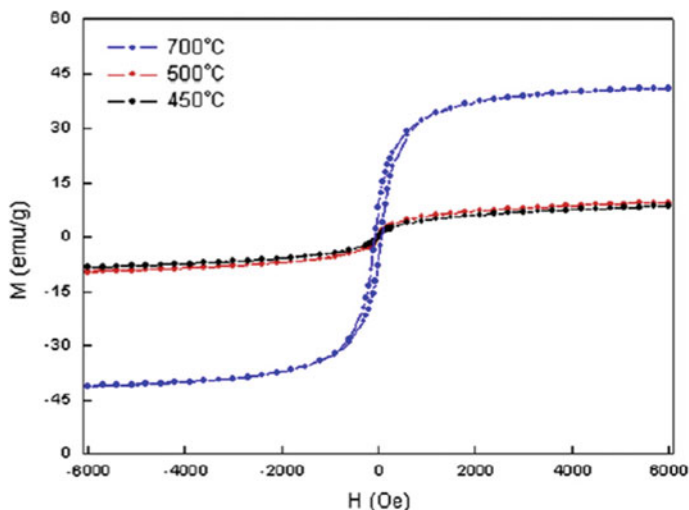
Fig. 7 M-H curve of MnFe$_2$O$_4$ nanoparticles measured at room temperature. Reproduced with permission from [149]

The MnFe$_2$O$_4$ nanoparticles calcined at 450, 500 and 700 °C have a saturation magnetization of 8.5, 9.5 emu/g and 41.5 emu/g, respectively. The decrease of saturation magnetization with decreases in particle size can be attributed to spin canting occur in the disordered surface layer, thus the saturation magnetization of the MnFe$_2$O$_4$ nanoparticles obtained at 450, 500 and 700 °C increases with increase in particle size. Also, with an increase in temperature from 450 to 700 °C, the occupation ratio of Fe^{3+} ions at the B sites decreases from 42.5 to 38.9%, which in turn, leads to an increase in the net moment. However, in their experiments, the particle size is the main aspect affecting the saturation magnetization. The research work presented by Huang and Cheng [150] demonstrated the magnetic orders in MnFe$_2$O$_4$ by using density functional methods. According to them, MnFe$_2$O$_4$ generally crystallizes in a mixed phase comprising of both the inverse-spinel structures with, fitted experimentally obtained, saturation moments of 3 μ_B per formula and normal spinel structures of 5 μ_B per formula. They determine that in the normal spinel the magnetic moment can be attributed by the high-spin Mn^{2+} ions at the A site and in the inverse spinel by the intermediate-spin Mn^{2+} ions at the B site.

5 Applications of Spinel Ferrites

The consistent and great efforts have been made by many researchers and scientists in physics and chemistry since 1936 to establish a firm progress of spinel ferrites for various applications in telecommunications, electrical appliances, automotive and entertainment. In the early practical ferrites, Cu–Zn, Mn–Zn or Ni–Zn have been

widely used for antennas and transformers. Later, of these, the Mn–Zn and Ni–Zn ferrites constitute a vast majority, even at present, in the industrial products of core materials. The Mn–Zn ferrite has found its extensive applications in the 1960s [151] based on its basic characteristic. Its high initial permeability value with low loss leads to the formation of wideband and pulse transformers and, inductors and telecommunications parts. Also, utilized as ferrite electromagnetic wave absorbers which have been used to reduce the echoes in ship's radar signals and leakage of electromagnetic waves from a variety of electrical equipment. In the 1970s, Ni–Zn ferrite [151] has been used as microwave ferrites to enhance the development in microwave communication through mobile and satellite communications. This microwave application of ferrites encouraged researchers over the world to develop ultra-low loss microwave devices which are economically favourable. Thereafter, spinel ferrite of Mn–Mg–Zn, as well as lithium ferrites [152], also comes into consideration as microwave ferrites.

The important material for magnetic recording media is γ-Fe_2O_3 which has been utilized to produce high-quality magnetic recording tapes [153]. Thereafter, in 1974 Philips corporation was established systems for optical recording. The demand for optical recording systems had been rapidly increased in the market which gradually lowered the demand of magnetic heads using high-density Mn–Zn or single-crystal Mn–Zn ferrite. Consequently, Mn–Zn ferrite magnetic heads have been substituted by magnetic resistance (MR) heads or giant magnetic resistance (GMR) heads [154]. Also, ferrites with rectangular hysteresis loop, i.e. material with more coercivity are being utilized for memory in digital computers. For this memory application, Mn–Mg ferrites were also considered as potential candidates, which totally disappeared in the 1980s.

In the 1990s the miniaturization of electronic components has been begun. The concept of miniaturization led to rapid technology evolution for competing systems, especially, integrated circuits. This, in consequence, resulted into the development of multilayer ferrite chip inductors to be utilized in television receivers, hard disk drive systems, headphone stereos, personal computers, automobile parts, etc. [155]. In response to this, Ni–Cu–Zn ferrite has been synthesized for useful applications including multilayer chip components and also used in noise filters and rotary transformers [156].

Presently, if look over the last few years, readers will find the importance of these different compositions of ferrites in various sectors. In the last 20 years, wide applications of ferrites have been developed. The Mn–Zn ferrites have their significant application in the wireless sensor networks and also used in power Electronics Integrated LC Filters [157]. Ferrites are established as well-known materials for fabricating different types of sensors. For instance, Mg-doped $ZnFe_2O_4$ nanoparticles can be used for relative humidity sensors [158], Mn-doped $CuFe_2O_4$ nanoparticles also used in liquefied petroleum gas sensor applications [159].

Sample of Mn–Zn ferrite containing zirconia (ZrO_2) and calcia (CaO) reported, by Waqas et al. [160], as one of the best materials appropriate for high-frequency applications owing to its high resonance frequency and high magnetic impedance. It has a potential application to be utilized for the fabrication of compact and lightweight cores [160]

Ni–Cu–Zn ferrite found its extensive applications in various electromagnetic devices due to high resistivity, high permeability with low magnetic losses. Wide research on Ni–Cu–Zn ferrite systems illustrates improved performance with $Ni_{0.35}Cu_{0.15}Zn_{0.50}Fe_2O_4$ compositions, reported by Huq et al. [161]. Also, Ni–Zn–Cu–Co ferrites are excellent composition of soft ferrites owing to their complex permeability along with their low core losses, which in turn, led to the fabrication of miniaturized magnetic components without lowering down the efficiency. These requirements are necessary to achieve in the field of next-generation high-frequency Switched-Mode Power Supplies [162].

For recording media applications, Nd-doped Lithium cobalt ferrites nanocrystals play a very significant role reported by Gilani et al. [163]. Its improved dielectric properties with doping make Li–Co ferrite beneficial for fabricating high-frequency devices and an increase in magnetization and coercivity make this material to be used in high-density recording media.

Nanoparticles of $Li_{0.5}Fe_{2.5-x}Gd_xO_s$ ferrite studied by Abdullah Dar et al. [164] and nanoparticles of Mn Doped Mg–Zn Ferrite investigated by Sharma et al. [165] are reported as a best potential candidate for microwave device application. Gaba et al. [166] revealed the super-paramagnetic nature of La-doped Mg ferrite which is useful for microwave absorbance purposes. Bhongale et al. [167] investigated electromagnetic properties of nanocrystalline Mg–Cd ferrites and reported the variation of real permittivity (4.2–6.12), real permeability (0.6–1.12) and, dielectric loss tangent (2.9 $\times 10^{-1}$–6 $\times 10^{-2}$) and magnetic loss tangent (4.5 $\times 10^{-1}$–2 $\times 10^{-3}$) with frequency and concentration of Mg in X-band frequency range. The variation of reflection loss with frequency revealed that Mg–Cd ferrites samples are a potential candidate for microwave applications in X-band.

Ferrite material plays a tremendous role in the health sector for human well-being. In recent years, remarkable growth has been observed in the biomedical application of nanostructured biomaterials. The spinel ferrite, MFe_2O_4 (where M=Co, Zn, Mg, Mn etc.), as magnetic materials are a significant class for biomedical applications. For instance, Wu et al. [168] indicated $CoFe_2O_4$ nanoparticles prepared by solvothermal synthesis loaded on multiwalled carbon nanotubes for magnetic resonance imaging (MRI) and drug delivery. Cai et al. [169] reported the bio-inspired formation of 3D hierarchical $CoFe_2O_4$ porous microspheres for drug release systems. Nanoparticles of $ZnFe_2O_4$ and $ZnO/ZnFe_2O_4$ composites possessing bifunctional properties useful for MRI and catalytic applications. Also, the drug release application of $ZnFe_2O_4$ hollow microsphere core/mesoporous silica shell composite particles are very significant [170]. Das et al. [171] investigated the superparamagnetic nature of the Mg ferrite nanosphere for hyperthermia applications.

Furthermore, the knowledge of synthesizing ferrites with polymer has opened up an immense possibility for various medical applications by harnessing the magnetic characteristics of the ferrites. Ferrite magnetic material itself is very significant for hyperthermia applications. In ferrites, Mn dopant, i.e. $MnFe_2O_4$ ferrite came into the limelight for biomedical applications due to its thought-provoking magnetic properties with better chemical stability. Mn ferrite exhibited significant properties, which are useful to defines the needful applications, such as the Mn ferrite surface offers

great adaptability for ligand functionalization and exhibiting high reactivity toward several organic groups. Consequently, a keen curiosity has been developing among researchers to find a different technique to coat $MnFe_2O_4$ particles for utilizing their complete potential in various biomedical applications especially magnetic hyperthermia, drug or gene delivery systems including MRI and protein immobilization. In response to this many researchers have reported well-established results for health sector applications. Arana et al. [172] reported a sample of $Mn_{0.4}Zn_{0.6}Fe_2O_4$ nanoparticles which were coated with chitosan for the preparation of a biocompatible ferrofluid. The magnetic nanofluid showed good stability for 12 h with better performance for hyperthermia according to Intrinsic Loss Parameter (ILP) results ((0.40 $\pm$ 0.03) nH m^2 kg^{-1}). Thus, this fluid is an outstanding substitute to the other usual fluids and other commercially existing ferrofluids of Fe-oxides in biomedical applications. In the year 2019, Monfared et al. [173] reported $Mn_{0.6}Zn_{0.4}Fe_2O_4$ magnetic nanoparticles coated with thermo-responsive copolymer *N*-isopropylacrylamide co-acrylic acid co acrylamide P by mini-emulsion method, which is used to synthesize intelligent ferrogels (these gels comprise of functional hydrogel incorporating ferrite magnetic nanoparticles). This ferrogel are being employed in controlled drug delivery systems along with magnetic fluid hyperthermia applications.

Anupama et al. [174] has published work on Mn–Zn ferrite ($Mn_{0.7}Zn_{0.3}Fe_2O_4$) powder comprising irregular-shaped particles, prepared by solution combustion method, which is a magnetically soft material with high saturation magnetization. By dispersing these magnetic particles in silicone oil, a magnetorheological fluid (MRF) was prepared. Magnetorheological fluids (MRFs) are smart fluids owing to their interesting mechanical properties which can be precisely and instantaneously controlled by an external magnetic field. Great yield strength of the MRFs makes it highly desirable for device applications and MRFs is a potential candidate for state-of-the-art mechanical shock mitigators and vibration isolators.

Presently, among all the nanomaterial-based adsorbents, nanocomposites of graphene and graphene-based metal ferrites having compositions MFe_2O_4 (where M can be Co, Ni, Fe, Mn, etc.) finds its extensive applications for the removal of organic pollutants, for waste water treatment, gas sensors and in numerous other applications. The synthesized Reduced graphene oxide (rGO)/Mn–Zn ferrite nanocomposite holds interesting photocatalytic activity under UV light owing to its properties such as efficient charge separation and magnetic separation, adsorption enhanced photocatalysis, the small amount required, low leaching of catalyst, oxygen vacancy and bandgap in the visible spectral range. The nanocomposite of rGO-based ferrite effectively photo decomposes the compound of acid dye in water [175]. Mylarappa et al. [176] have reported samples of $Mn-ZnFe_2O_4$ and rGO/Mn–$ZnFe_2O_4$ nanocomposite synthesized from the waste battery using the hydrometallurgical method and studied their electrochemical and photochemical activity. rGO/Mn–$ZnFe_2O_4$ nanocomposite is a thermally more stable material and utilized in optoelectronics or device applications. Zhou et al. [177] have reported rGO/$Ni_{0.7}Zn_{0.3}Fe_2O_4$ composite having exceptional broad range absorption potential in GHz, leading to several benefits for research field in particular EM-wave absorbing materials.

6 Future Prospects of Spinel Ferrites

Readers can understand the importance of ferrites, as it is described in the chapter, how progressively production and consumption of ferrites have been increased each year for numerous applications for different social purposes. The scientists and researchers who are interested to contribute in the advanced technologies for society by using magnetic characteristics, they can research and investigate further the immense possibilities of ferrites based on its history. For that, the potential of ferrite material can be enhanced by making its composites with other materials like polymers, two-dimensional material like graphene oxide (GO) or reduced graphene oxide (rGO). For example, Sreeprasad et al. [178] have reported that nickel ferrite-GO composite is a better reaction media than iron ferrites, because of having higher catalytic and electron transfer efficiency through the Ni^{2+} in the nickel ferrite. Furthermore, many other reports have revealed the remarkable removal of impurities/chemicals by using ferrite magnetic nanoparticles/graphene or GO composites. Recently, Ligamdinne et al. [179] have published some papers on the significant research of removing Co, Pb, Cr, As and radionuclides, U and Th from water, by synthesizing "nanocomposite of nickel ferrite-GO". Consequently, in the future, the magnetic ferrite-GO based nanocomposites are economically favourable, promising and can be separated by the external magnetic field.

For future research, we have to go deeper to investigate the precise chemical and physical knowledge of ferrites. The innovation becomes outstanding when experimental studies of ferrites match well with their theoretical studies. For example, let's suppose, the UV optical absorption studies of ferrites investigated experimentally must be authenticated by the theoretical studies performed quantum mechanically or by density functional theory, etc. In one of the latest published (2020) research papers, the authors Gharibshahi, et al. [180] reported theoretical studies for the optical absorption with different size of $CoFe_2O_4$ ferrite nanoparticles and equated the experimentally observed results with the predicted properties of optical absorption based on quantum mechanical principles, assisted via the finite element simulations using COMSOL Multiphysics. They demonstrated that the predicted band gap has good consistencies with band gap energies derived experimentally. This consistency in obtained results enhances the authenticities, which will provide window to tune the structure of $CoFe_2O_4$ nanoparticles using facile pathways and effective strategies for practical applications where it wildly exploits for example sensors, electronic and microwave devices.

Moreover, it seems that the research field of ferrite is almost towards saturation as there is no basic research of physics and chemistry of ferrites left to be investigated, but they are even useful in the field of permanent magnets. Permanent-magnet materials will play a central role in the advancement of future science and technology in societal development such as wind power generators, wind energy turbines, automobile sectors like electric cars and smart mobile phones. It will be a great initiation towards generating renewable energy sources because the present high-performance permanent-magnet materials are synthesized by using compounds

comprising rare-earth, in particular Nd–Fe–B and Sm–Co and rare-earth elements bound the applications due to their scarcity and high cost, as dispersed in small contents and expensive to extract from ore. Also, only a few countries have access to rare-earth elements. In the world, the reservoir of rare earths is existing in China, California, India, Brazil, Australia, South Africa and Malaysia. At the global level, China has rare-earth elements production rate within 80 to 95% that play a significant role in the progress of revolutionary technologies in the research fields of energy, defence, medical devices and information and communication technology [181, 182]. Consequently, the growth of new permanent magnets with lower content of rare-earth elements becomes most useful need of the present scenario to increase the demands of permanent magnets at a large industrial scale for energy conversion applications. The permanent-magnet materials can be synthesized as nanocomposites by combing soft and hard ferrites and we can work on this to increase the energy product. Also, we can enhance the area of hysteresis loss or coercivity of soft ferrite up to the range exhibited by rare-earth magnets. In response to this, some recent work has been reported by Li et al. [183]. They synthesized nanocomposite of hard and soft magnetic material to fabricate a novel bi-morphological anisotropic bulk nanocomposite for investigating ultra-strong permanent magnets with lesser content of expensive rare-earth elements. The nanocomposite has been regarded as one of the most promising for energy product (28 MGOe), owing to exceed energy product up to 58% with less rare-earth elements as compared to pure rare-earth magnets. The role of pure permanent-magnet amendment to make a viable type next-generation stronger nanocomposite at lower costs leads to many other innovative approaches. Also, inspiring progress has been made toward increasing the energy product of nanoscale exchange-spring compositions. Torkian and Ghasemi [184] have reported ferrite based hard-soft magnetic nanocomposites presenting energy product enhancement in single-phase exchange spring-coupled behaviour with high coercivity as well as high saturation. The synthesized nanocomposite comprises of soft phase (15 wt%) exhibited a 10.5% increase in the high energy product in comparison with the pure hard phase and approaches a maximum value of 29.5 kJ/m^3 which is a maximum value of $(BH)_{max}$.

A comprehensive review presented by Radulescu [185] based on the design analysis of unique spoke-type ferrite-magnet generator topologies for suitable use in micro-wind power applications.

Furthermore, ferrites work as a catalyst to transform solar energy into hydrogen energy which will be a breakthrough in hydrogen energy technologies. Few authors have presented research articles on Hydrogen production. Bhosale [186] reported Ni-ferrite based such thermodynamic analysis, where the splitting of H_2O converts to H_2 under solar thermochemical cycle. Goikoetxea et al. [187] have explained thermochemical water-splitting cycles based on Ni and Co ferrites for hydrogen production.

In this way, with deep research and investigation, which is growing faster than before, the future prospects of ferrites will be becoming even more thought-provoking and motivating than what is happening now and will become the topic of great research among researchers throughout the globe. There will be smart connected

devices from communication to the health sector and renewable energy sources which will touch almost every aspect of human life.

References

1. Ida N (2015) Engineering electromagnetics. Springer, London. ISBN 3319078062
2. Melfos V, Helly B, Voudouris P (2011) The ancient Greek names "Magnesia" and "Magnetes" and their origin from the magnetite occurrences at the Mavrovouni mountain of Thessaly, central Greece. A mineralogical–geochemical approach. Archaeol Anthropol Sci 3(2):165–172
3. Hilpert S (1909) Correspondence as to structure and origin in magnetic properties of ferrite and iron oxide (in Ger.), Ber. Dtsch. Chem Ges 42:2248–61
4. Hilpert S, Lindner A (1933) Ferrites. II. Akaline, alkaline-earth, and lead ferrites (in Ger.), Z. Phys Chem B22:395–405
5. Hilpert S (1909) Manufacturing method of magnetic materials having small electric conductivity for electric and magnetic apparatus. German Pat. Nos. 226,347 and 227,787
6. Forestier H (1928) Magnetic transformations of the sesquioxide of iron, of its solid solution and of its ferromagnetic combinations (in Fr.). Ann Chim (Paris) 9:316–401
7. Herroun EF, Wilson E (1928) Ferromagnetic ferric oxide. Proc Phys Soc 41(1):100
8. Kato Y, Takei T (1930) Studies on zinc ferrite. its formation, composition, and chemical and magnetic properties. Trans. Am. Electrochem. Soc. **57**(1):297
9. Kato Y, Takei T (1933) Characteristics of metallic oxide magnet. J Inst Electr Eng Jpn 53:408–412
10. Iida S, Sekizawa H, Aiyama Y (1958) Uniaxial anisotropy in iron-cobalt ferrites. J Phys Soc Jpn 13(1):58–71
11. Williams HJ, Heidenreich RD, Nesbitt EA (1956) Mechanism by which cobalt ferrite heat treats in a magnetic field. J Appl Phys 27(1):85–89
12. Okamoto A (2009) The invention of ferrites and their contribution to the miniaturization of radios. In: 2009 IEEE Globecom workshops. IEEE, pp 1–6
13. Snoek JL (1936) On the Permalloy problem. Nature 137(3464):493–493
14. Kleis JD (1936) Ferromagnetic anisotropy of nickel–iron crystals at various temperatures. Phys Rev 50(12):1178
15. Williams HJ (1937) Magnetic properties of single crystals of silicon iron. Phys Rev 52(7):747
16. Becker CR, Döring W (1939) Ferromagnetismus. Springer, Berlin, p 101
17. McKeehan LW, Grabbe EM (1939) Ferromagnetic anisotropy in nickel-iron crystals. Evidence for superstructure near Ni_3Fe. Phys Rev 55(5):505
18. Rathenau GW, Snoek JL (1941) Magnetic anisotropy phenomena in cold rolled nickel–iron. Physica 8(6):555–575
19. Snoek JL (1936) Magnetic and electrical properties of the binary systems MO. Fe_2O_3. Physica 3(6):463–483
20. Snoek JL (1938) Time effects in magnetization. Physica 5(8):663–688
21. Snoek JL, Went JJ (1947) New developments in ferromagnetic materials. Elsevier
22. Snoek JL (1948) Dispersion and absorption in magnetic ferrites at frequencies above one Mc/s. Physica 14(4):207–217
23. Kramers HA (1934) L'interaction entre les atomes magnétogènes dans un cristal paramagnétique. Physica 1(1–6):182–192

24. Smart JS (1955) The Néel theory of ferrimagnetism. Am J Phys 23(6):356–370
25. Anderson PW (1950) Antiferromagnetism. Theory of superexchange interaction. Phys. Rev. 79(2):350
26. Yafet Y, Kittel C (1952) Antiferromagnetic arrangements in ferrites. Phys Rev 87(2):290
27. Rado GT, Wright RW, Emerson WH (1950) Ferromagnetism at very high frequencies. III. Two mechanisms of dispersion in a ferrite. Phys Rev 80(2):273
28. Went JJ, Ratenau GW, Gorter EW, van Oosterhout GW (1952) Ferroxdure, a class of new permanent magnet materials. Philips Tech. Rev. 13:194–208
29. Folen VJ (1960) Influence of ionic order on the magnetocrystalline anisotropy and crystalline field parameters in lithium ferrite monocrystals. J Appl Phys 31(5):S166–S167
30. Simsa Z (1969) Distribution of cations and phase transition in ferrite $Cu_{0.5}Fe_{2.5}O_4$. IEEE Trans Magn 5(3):592–595
31. Bacon GE, Roberts FF (1953) Neutron-diffraction studies of magnesium ferrite–aluminate powders. Acta Crystallogr A 6(1):57–62
32. Corliss LM, Hastings JM, Brockman FG (1953) A neutron diffraction study of magnesium ferrite. Phys Rev 90(6):1013
33. Hastings JM, Corliss LM (1953) Neutron diffraction studies of zinc ferrite and nickel ferrite. Rev Mod Phys 25(1):114
34. Kedem D, Rothem T (1967) Internal fields in nickel ferrite. Phys Rev Lett 18(5):165
35. Sawatzky GA, Van der Woude F, Morrish AH (1967) Note on cation distribution of $MnFe_2O_4$. Phys Lett A 25(2):147–148
36. Hasegawa K, Satō T (1967) Particle-size distribution of $CoFe_2O_4$ formed by the coprecipitation method. J Appl Phys 38(12):4707–4713
37. Dobson DC, Linnett JW, Rahman MM (1970) Mössbauer studies of the charge transfer process in the system $Zn_xFe_{3−x}O_4$. J Phys Chem Solids 31(12):2727–2733
38. Srivastava CM, Shringi SN, Srivastava RG, Nanadikar NG (1976) Magnetic ordering and domain-wall relaxation in zinc-ferrous ferrites. Phys Rev B 14(5):2032
39. Evans BJ, Hafner (1968) Mössbauer resonance of Fe^{57} in oxidic spinels containing Cu and Fe. J Phys Chem Solids 29(9):1573–1588.hhh
40. Kulkarni RG, Patil VU (1982) Magnetic ordering in Cu–Zn ferrite. J Mater Sci 17(3):843–848
41. Wilson VC, Kasper JS (1954) Neutron diffraction studies of a nickel zinc ferrite. Phys Rev 95(6):1408
42. Daniels JM, Rosencwaig A (1970) Mössbauer study of the Ni–Zn ferrite system. Can J Phys 48(4):381–396
43. Globus A, Pascard H, Cagan V (1977) Distance between magnetic ions and fundamental properties in ferrites. Le Journal de Physique Colloques 38(C1):C1–163
44. Eissa NA, Sallam HA, Fayek MK, Salah SH, Hassaan MY (1981) Study of magnetic properties and lattice dynamics of the $Cd_xCo_{1−x}$ ferrite system by Mössbauer effect. Acta Physica Academiae Scientiarum Hungaricae 51(3):313–318
45. Mazen SA, Abd-el-Rahlem AE, Sabrah BA (1987) The structure and electrical conductivity of Mn–Cd ferrite. J Mater Sci 22(11):4177–4180
46. Wieser E, Povitskii VA, Makarov EF, Kleinstück K (1968) Mössbauer investigations of Mg, Mn, and Mg–Mn ferrites in external magnetic fields. Physica Status Solidi (b) 25(2):607–611
47. Smit J, Wijn HPJ (1959) Ferrites, Philips technical library. Eindhoven, The Netherlands, p 278
48. Nivoix V, Gillot B (1998) Preparation, characterization and reactivity toward oxygen of new nanosized vanadium–iron spinels. Solid State Ionics 111(1–2):17–25
49. Gerardin R, Bonazebi A, Millon E, Brice JF, Evrard O, Sanchez JP (1989) Etude des magne' tites dope' esala chaux: Substitution du fer par le calcium en site te' trae' drique. J Solid State Chem 78(1):154–163
50. Hägg G (1935) Die Kristallstruktur des magnetischen Ferrioxyds, γ-Fe_2O_3. Z Phys Chem 29(1):95–103
51. Verwey EJW (1935) The crystal structure of γ-Fe_2O_3 and γ-Al_2O_3. Zeitschrift für Kristallographie-Crystalline Materials 91(1–6):65–69

52. Sumiya K, Watatani S, Hayama F, Naono H, Matsumoto T (1979) Studies on recording magnetic materials and magnetic composite. 1. Incorporation of cobalt into acicular gamma-Fe_2O_3 particles. Nippon Kagaku Kaishi 8:1033–1038

53. Sumiya K, Matsumoto T, Watatani S, Hayama F (1979) Crystal growth of Co ferrite on fine acicular γ-Fe_2O_3 particles. J Phys Chem Solids 40(12):1097–1102

54. Kishimoto M, Sueyoshi T, Hirata J, Amemiya M, Hayama F (1979) Coercivity of γ-Fe_2O_3 particles growing iron-cobalt ferrite. J Appl Phys 50(1):450–452

55. Bragg WH (1915) XXX. The structure of the spinel group of crystals. Lond Edinburgh Dublin Philos Mag J Sci 30(176):305–315

56. Nishikawa S (1915) Structure of some crystals of spinel group. In: Proceedings of the Tokyo mathematico-physical society, 2nd series, vol 8, no 7, pp 199–209

57. Verwey EJW, Heilmann EL (1947) Physical properties and cation arrangement of oxides with spinel structures I. Cation arrangement in spinels. J Chem Phys 15(4):174–180

58. A. Goldman, *Modern ferrite technology*. Springer Science & Business Media, 2006.

59. Barth TFW, Posnjak E (1932) Spinel structures: with and without variate atom equipoints. Zeitschrift Für Kristallographie-Crystalline Materials 82(1–6):325–341

60. Néel L (1948) Propriétés magnétiques des ferrites; ferrimagnétisme et antiferromagnétisme. Annales de physique 12(3):137–198

61. Li X, Barbers VAM, De Boer FR (1992) In: Proceedings of 6th international conference on ferrites, Tokyo/Kyoto, Japan, p 674

62. Abe M, Kawachi M, Nomura S (1972) X-ray and neutron diffraction studies in spinel Fe_2MoO_4. J Phys Soc Jpn 33(5):1296–1302

63. Bertaut EF (1951) Sur quelques progrès récents dans la cristallographie des spinelles, en particulier des ferrites. J de Phys Rad 12:252–255

64. Néel L (1950) Aimantation a saturation de certains ferrites. CR Acad Sci Paris 230:190–194

65. Pauthenet R (1950) Variation Thermique de l' Aimantation Spontanée des Ferrites de Nickel, Cobalt, Fer et Manganése. Compt R Ac Sc Paris 230:1842–1843

66. Weil L, Bertaut EF, Bochirol L (1950) Propriétés magnétiques et structure de la phase quadratique du ferrite de cuivre. J de Physique et le Radium 11(5):208–212

67. Prince E, Treuting RG (1956) The structure of tetragonal copper ferrite. Acta Crystallogr A 9(12):1025–1028

68. Brockman FG (1950) The cation distribution in ferrites with spinel structure. Phys Rev 77(6):841

69. Hastings JM, Corliss LM (1956) Neutron diffraction study of manganese ferrite. Phys Rev 104(2):328

70. Sawatzky GA, Van Der Woude F, Morrish AH (1968) Cation distributions in octahedral and tetrahedral sites of the ferrimagnetic spinel $CoFe_2O_4$. J Appl Phys 39(2):1204–1205

71. Verwey EJW, De Boer F, Van Santen JH (1948) Cation arrangement in spinels. J Chem Phys 16(12):1091–1092

72. De Boer F, Van Santen JH, Verwey EJW (1950) The electrostatic contribution to the lattice energy of some ordered spinels. J Chem Phys 18(8):1032–1034

73. Brabers VAM (1995) Progress in spinel ferrite research. Handb Magn Mater 8:189–324

74. Kriessman CJ, Harrison SE (1956) Cation distributions in ferrospinels. Magnesium-manganese ferrites. Phys Rev 103(4):857

75. Miller A (1959) Distribution of cations in spinels. J Appl Phys 30(4):S24–S25

76. Driessens FCM (1968) Thermodynamics and defect chemistry of some oxide solid solutions Part III. Defect equilibria and the formalism of pair interactions. Ber Bunsenges Phys Chem 72(9–10):1123–1133

77. O'Neill HSC, Navrotsky A (1983) Simple spinels; crystallographic parameters, cation radii, lattice energies, and cation distribution. Am Miner 68(1–2):181–194

78. McClure DS (1957) The distribution of transition metal cations in spinels. J Phys Chem Solids 3(3–4):311–317

79. Dunitz JD, Orgel LE (1957) Electronic properties of transition-metal oxides—I: distortions from cubic symmetry. J Phys Chem Solids 3(1–2):20–29

80. Cormack AN, Lewis GV, Parker SC, Catlow CRA (1988) On the cation distribution of spinels. J Phys Chem Solids 49(1):53–57
81. Anderson PW (1956) Ordering and antiferromagnetism in ferrites. Phys Rev 102(4):1008
82. Furuhashi H, Inagaki M, Naka S (1973) Determination of cation distribution in spinels by X-ray diffraction method. J Inorg Nucl Chem 35(8):3009–3014
83. Buerger MG (1960) Crystal structure analysis. Wiley, New York
84. Cullity BD (1956) Elements of X-ray diffraction. Addison-Wesley Publishing
85. Trivedi UN, Jani KH, Modi KB, Joshi HH (2000) Study of cation distribution in lithium doped nickel ferrite. J Mater Sci Lett 19(14):1271–1273
86. Patange SM, Shirsath SE, Toksha BG, Jadhav SS, Shukla SJ, Jadhav KM (2009) Cation distribution by Rietveld, spectral and magnetic studies of chromium-substituted nickel ferrites. Appl Phys A 95(2):429–434
87. Patange SM, Shirsath SE, Jangam GS, Lohar KS, Jadhav SS, Jadhav KM (2011) Rietveld structure refinement, cation distribution and magnetic properties of Al^{3+} substituted $NiFe_2O_4$ nanoparticles. J Appl Phys 109(5):053909
88. Kavas H, Baykal A, Toprak MS, Köseoğlu Y, Sertkol M, Aktaş B (2009) Cation distribution and magnetic properties of Zn doped $NiFe_2O_4$ nanoparticles synthesized by PEG-assisted hydrothermal route. J Alloy Compd 479(1–2):49–55
89. Gómez CAP, Meneses CAB, Matute A (2018) Structural parameters and cation distributions in solid state synthesized Ni–Zn ferrites. Mater Sci Eng, B 236:48–55
90. Nikmanesh H, Eshraghi M (2019) Cation distribution, magnetic and structural properties of $CoCr_xFe_{2-x}O_4$: effect of calcination temperature and chromium substitution. J Magn Magn Mater 471:294–303
91. Cvejic Z, Rakic S, Kremenovic A, Antic B, Jovalekic C, Colomban P (2006) Nanosize ferrites obtained by ball milling: crystal structure, cation distribution, size-strain analysis and Raman investigations. Solid State Sci 8(8):908–915
92. Kumar L, Kumar P, Narayan A, Kar M (2013) Rietveld analysis of XRD patterns of different sizes of nanocrystalline cobalt ferrite. Int Nano Letters 3(1):8
93. Gismelseed AM, Yousif AA (2005) Mössbauer study of chromium-substituted nickel ferrites. Phys B 370(1–4):215–222
94. Mittal VK, Chandramohan P, Bera S, Srinivasan MP, Velmurugan SVNS, Narasimhan SV (2006) Cation distribution in $Ni_xMg_{1-x}Fe_2O_4$ studied by XPS and Mössbauer spectroscopy. Solid State Commun 137(1–2):6–10
95. Kumar RV, Anupama AV, Kumar R, Choudhary HK, Khopkar VB, Aravind G, Sahoo B (2018) Cation distributions and magnetism of Al-substituted $CoFe_2O_4$–$NiFe_2O_4$ solid solutions synthesized by sol-gel auto-combustion method. Ceram Int 44(17):20708–20715
96. Tang GD, Ji DH, Yao YX, Liu SP, Li ZZ, Qi WH, Han QJ, Hou X, Hou DL (2011) Quantum-mechanical method for estimating ion distributions in spinel ferrites. Appl Phys Lett 98(7):072511
97. Han QJ, Ji DH, Tang GD, Li ZZ, Hou X, Qi WH, Liu SR, Bian RR (2012) Estimating the cation distributions in the spinel ferrites $Cu_{0.5-x}Ni_{0.5}Zn_xFe_2O_4$ ($0.0 \leq x \leq 0.5$). J Magn Magn Mater 324(12):1975–1981
98. Ji DH, Tang GD, Li ZZ, Hou X, Han QJ, Qi WH, Liu SR, Bian RR (2013) Quantum mechanical method for estimating ionicity of spinel ferrites. J Magn Magn Mater 326:197–200
99. Nandan B, Bhatnagar MC, Kashyap SC (2019) Cation distribution in nanocrystalline cobalt substituted nickel ferrites: X-ray diffraction and Raman spectroscopic investigations. J Phys Chem Solids 129:298–306
100. Manjunatha M, Reddy GS, Damle R, Mallikarjunaiah KJ, Ramesh KP (2019) Estimation of structural composition of the inverse spinel ferrites using ^{57}Fe-Zero Field Nuclear Magnetic Resonance. Ceram Int 45(7):9245–9253
101. Gorter EW (1954) Saturation magnetization and crystal chemistry of ferrimagnetic oxides. I. II. Theory of ferrimagnetism. Philips Res Rep 9:295–320
102. Gilleo MA (1958) Superexchange interaction energy for Fe^{3+}–O^{2-}–Fe^{3+} linkages. Phys Rev 109(3):777

103. Gilleo MA (1960) Superexchange interaction in ferrimagnetic garnets and spinels which contain randomly incomplete linkages. J Phys Chem Solids 13(1–2):33–39
104. Ishikawa Y (1962) Magnetic properties of ilmenite-hematite system at low temperature. J Phys Soc Jpn 17(12):1835–1844
105. Nowik I (1969) Saturation moments of mixed ferrites: a simple theory. J Appl Phys 40(2):872–874
106. Geller S (1969) "Comments on" molecular-field theory for randomly substituted ferrimagnetic garnet systems "by I. Nowik." Phys Rev 181(2):980
107. Guillaud C, Creveaux H (1950) Preparations et properietes magnetiques des ferrites de manganese et de cobalt. Compt R Ac Sc Paris 230(13):1256–1258
108. Guillaud C (1951) Propriétés magnétiques des ferrites. J de Physique et le Radium 12(3):239–248
109. Guillaud C, Sage M (1951) Proprietes Magnetiques des Ferrites Mixtes de Magnesium et de Zinc. Compt R Ac Sc Paris 232:944–946
110. Pauthenet R, Bochirol L (1951) Aimantation spontanée des ferrites. Journal de Physique et le Radium 12(3):249–251
111. Bacon GE (1975) Neutron diffraction. Clarendon (1975)
112. Maxwell LR, Pickart SJ (1953) Magnetization in nickel ferrite-aluminates and nickel ferrite-gallates. Phys Rev 92(5):1120
113. Maxwell LR, Pickart SJ (1954) Magnetic and crystalline behavior of certain oxide systems with spinel and perovskite structures. Phys Rev 96(6):1501
114. Lyons DH, Kaplan TA, Dwight K, Menyuk N (1962) Classical theory of the ground spin-state in cubic spinels. Phys Rev 126(2):540
115. Zener C (1951) Interaction between the d-shells in the transition metals. II. Ferromagnetic compounds of manganese with perovskite structure. Phys Rev 82(3):403
116. Lotgering FK, Van Diepen AM (1977) Electron exchange between Fe^{2+} and Fe^{3+} ions on octahedral sites in spinels studied by means of paramagnetic Mössbauer spectra and susceptibility measurements. J Phys Chem Solids 38(6):565–572
117. Leung LK, Evans BJ, Morrish AH (1973) Low-temperature Mössbauer study of a nickel-zinc ferrite: $Zn_xNi_{1-x}Fe_2O_4$. Phys Rev B 8(1):29
118. Morel JP (1967) Etude par l'effet mössbauer de l'aimantation spontanee des deux sous-reseaux de fer dans le ferrite $NiFe_2O_4$. J Phys Chem Solids 28(4):629–634
119. Chinnasamy CN, Narayanasamy A, Ponpandian N, Chattopadhyay K, Shinoda K, Jeyadevan B, Tohji K, Nakatsuka K, Furubayashi T, Nakatani I (2001) Mixed spinel structure in nanocrystalline $NiFe_2O_4$. Phys Rev B 63(18):184108
120. Alarifi A, Deraz NM, Shaban S (2009) Structural, morphological and magnetic properties of $NiFe_2O_4$ nano-particles. J Alloy Compd 486(1–2):501–506
121. Nawale AB, Kanhe NS, Patil KR, Bhoraskar SV, Mathe VL, Das AK (2011) Magnetic properties of thermal plasma synthesized nanocrystalline nickel ferrite ($NiFe_2O_4$). J Alloy Compd 509(12):4404–4413
122. Zabotto FL, Gualdi AJ, Eiras JA, Aparecido de Oliveira AJ, Garcia D (2012) Influence of the sintering temperature on the magnetic and electric properties of $NiFe_2O_4$ ferrites. Mater Res 15(3):428–433
123. Thakur S, Katyal SC, Singh M (2009) Structural and magnetic properties of nano nickel–zinc ferrite synthesized by reverse micelle technique. J Magn Magn Mater 321(1):1–7
124. Dormann JL, Tomas A, Nogues M (1983) Cation ordering in $LiFe_5O_8$ studied by Mössbauer spectroscopy and X-ray crystallography. Physica Status Solidi (a) 77(2):611–618
125. Kang KU, Hyun SW, Kim CS (2006) Size-dependent magnetic properties of ordered $Li_{0.5}Fe_{2.5}O_4$ prepared by the sol-gel method. J Appl Phys 99(8):08M917
126. George M, Nair SS, John AM, Joy PA, Anantharaman MR (2006) Structural, magnetic and electrical properties of the sol-gel prepared $Li_{0.5}Fe_{2.5}O_4$ fine particles. J Phys D: Appl Phys 39(5):900
127. Anantharaman MR, Jagatheesan S, Malini KA, Sindhu S, Narayanasamy A, Chinnasamy CN, Jacobs JP, Reijne S, Seshan K, Smits RHH, Brongersma HH (1998) On the magnetic properties of ultra-fine zinc ferrites. J Magn Magn Mater 189(1):83–88

128. Shenoy SD, Joy PA, Anantharaman MR (2004) Effect of mechanical milling on the structural, magnetic and dielectric properties of coprecipitated ultrafine zinc ferrite. J Magn Magn Mater 269(2):217–226

129. Janicki J, Pietrzak J, Porębska A, Suwalski J (1982) Mössbauer study of copper ferrites. Physica Status Solidi (a) 72(1):95–98

130. Hannoyer B, Lenglet M, Chopova R, Tellier JC (1985) Contribution de la spectrometrie mössbauer et de la spectrometrie d'absorption XA l'etude de la non-stoechiometrie de $CuFe_2O_4$. Mater Chem Phys 13(5):449–465

131. Hoque SM, Choudhury MA, Islam MF (2002) Characterization of Ni–Cu mixed spinel ferrite. J Magn Magn Mater 251(3):292–303

132. Kimura S, Mashino T, Hiroki T, Shigeoka D, Sakai N, Zhu L, Ichiyanagi Y (2012) Effect of heat treatment on Jahn-Teller distortion and magnetization in Cu ferrite nanoparticles. Thermochim Acta 532:119–122

133. Abdellatif MH, Innocenti C, Liakos I, Scarpellini A, Marras S, Salerno M (2017) Effect of Jahn-Teller distortion on the short-range magnetic order in copper ferrite. J Magn Magn Mater 424:402–409

134. Chatterjee BK, Bhattacharjee K, Dey A, Ghosh CK, Chattopadhyay KK (2014) Influence of spherical assembly of copper ferrite nanoparticles on magnetic properties: orientation of magnetic easy axis. Dalton Trans 43(21):7930–7944

135. Balagurov AM, Bobrikov IA, Pomjakushin VY, Sheptyakov DV, Yushankhai VY (2015) Interplay between structural and magnetic phase transitions in copper ferrite studied with high-resolution neutron diffraction. J Magn Magn Mater 374:591–599

136. De Grave E, Govaert A, Chambaere D, Robbrecht G (1979) A Mössbauer effect study of $MgFe_2O_4$. Physica B + C 96(1):103–110

137. Aliyan N, Mirkazemi SM, Masoudpanah SM, Akbari S (2017) The effect of post-calcination on cation distributions and magnetic properties of the coprecipitated $MgFe_2O_4$ nanoparticles. Appl Phys A 123(6):446

138. Chandradass J, Jadhav AH, Kim KH, Kim H (2012) Influence of processing methodology on the structural and magnetic behavior of $MgFe_2O_4$ nanopowders. J Alloy Compd 517:164–169

139. Aslibeiki B, Varvaro G, Peddis D, Kameli P (2017) Particle size, spin wave and surface effects on magnetic properties of $MgFe_2O_4$ nanoparticles. J Magn Magn Mater 422:7–12

140. Prince E (1956) Neutron diffraction observation of heat treatment in cobalt ferrite. Phys Rev 102(3):674

141. Petitt GA, Forester DW (1971) Mössbauer study of cobalt-zinc ferrites. Phys Rev B 4(11):3912

142. Hauet A, Teillet J, Hannoyer B, Lenglet M (1987) Mössbauer study of Co and Ni ferrichromites. Physica Status Solidi A Appl Res 103(1):257–261

143. Persoons RM, De Grave E, De Bakker PMA, Vandenberghe RE (1993) Mössbauer study of the high-temperature phase of co-substituted magnetites, $Co_xFe_{3-x}O_4$ II. $x \geq 0.1$. Phys Rev B 47(10):5894

144. López JL, Pfannes, H-D, Paniago R, Sinnecker JP, Novak MA (2008) Investigation of the static and dynamic magnetic properties of $CoFe_2O_4$ nanoparticles. J Magnet Magnet Mater 320(14):e327–e330

145. Eshraghi M, Kameli P (2011) Magnetic properties of $CoFe_2O_4$ nanoparticles prepared by thermal treatment of ball-milled precursors. Curr Appl Phys 11(3):476–481

146. Sawatzky GA, Van Der Woude F, Morrish AH (1969) Mössbauer study of several ferrimagnetic spinels. Phys Rev 187(2):747

147. Lotgering FK, Van Diepen AM (1973) Valencies of manganese and iron ions in cubic ferrites as observed in paramagnetic Mössbauer spectra. J Phys Chem Solids 34(8):1369–1377

148. Simsa Z, Brabers V (1975) Influence of the degree of inversion on magnetic properties of $MnFe_2O_4$. IEEE Trans Magn 11(5):1303–1305

149. Li J, Yuan H, Li G, Liu Y, Leng J (2010) Cation distribution dependence of magnetic properties of sol-gel prepared $MnFe_2O_4$ spinel ferrite nanoparticles. J Magn Magn Mater 322(21):3396–3400

150. Huang JR, Cheng C (2013) Cation and magnetic orders in $MnFe_2O_4$ from density functional calculations. J Appl Phys 113(3):033912
151. Sugimoto M (1999) The past, present, and future of ferrites. J Am Ceram Soc 82(2):269–280
152. Wei F, Baoshun L, Jizhong Y, Xi L, Muyu Z (1998) Synthesis and microwave absorptive properties of lithium ferrite nanocrystals. J Magnet Soc Jpn 22(S1):366–368
153. Bertaut F, Forrat F (1956) Structure des ferrites ferrimagnetiques des terres rares. Comptes Rendus Hebdomadaires Des Seances De L Academie Des Sciences 242(3):382–384
154. Tsang C, Chen MM, Yogi T, Ju K (1990) Gigabit density recording using dual-element MR/inductive heads on thin-film disks. IEEE Trans Magn 26(5):1689–1693
155. Nomura T, Takaya M (1987) Passive components and hybrid technology. Hybrids 3(1):16–19
156. Nakamura T, Okano Y (1997) Low temperature sintered Ni–Zn–Cu Ferrite. Le J de Physique IV 7(C1): C1–91
157. Li L, Fang YK, Liu YJ (2015) Preparation and application on antenna of soft ferrite core for wireless sensor networks. IEEE Trans Magn 51(11):1–3
158. Patil SN, Pawar AM, Tilekar SK, Ladgaonkar BP (2016) Investigation of magnesium substituted nano particle zinc ferrites for relative humidity sensors. Sens Actuators, A 244:35–43
159. Kumar E, Ranjith R, Jayaprakash, Sarala Devi G, Siva Prasada Reddy P (2014) Synthesis of Mn substituted $CuFe_2O_4$ nanoparticles for liquefied petroleum gas sensor applications. Sens Actuat B Chem 191:186–191
160. Waqas H, Qureshi AH, Subhan K, Shahzad M (2012) Nanograin Mn–Zn ferrite smart cores to miniaturize electronic devices. Ceram Int 38(2):1235–1240
161. Huq MF, Saha DK, Ahmed R, Mahmood ZH (2013) Ni-Cu-Zn ferrite research: A brief review. J Sci Res 5(2):215–234
162. Lebourgeois R (2014) Low losses ferrites for high integration level in power electronics. J Jpn Soc Powder Powder Metallurgy 61(S1): S211–S213
163. Gilani ZA, Warsi MF, Anjum MN, Shakir I, Naseem S, Riaz S, Khan MA (2015) Structural and electromagnetic behavior evaluation of Nd-doped lithium–cobalt nanocrystals for recording media applications. J Alloy Compd 639:268–273
164. Dar MA, Majid K, Najar MH, Kotnala RK, Shah J (2016) Synthesis and characterization of $Li_{0.5}Fe_{2.5-x}Gd_xO_4$ ferrite nano-particles as a potential candidate for microwave device applications. Mater Des 90:443–452
165. Sharma R, Thakur P, Sharma P, Sharma V (2018) Mn^{2+} doped Mg–Zn ferrite nanoparticles for microwave device applications. IEEE Electron Device Lett 39(6):901–904
166. Gaba S, Kumar A, Rana PS, Arora M (2018) Influence of La^{3+} ion doping on physical properties of magnesium nanoferrites for microwave absorption application. J Magn Magn Mater 460:69–77
167. Bhongale SR, Ingawale HR, Shinde TJ, Pubby K, Narang SB, Vasambekar PN (2017) Nano-crystalline magnesium substituted cadmium ferrites as X-band microwave absorbers. J Magnet Magnet Mater 441:475–481
168. Wu H, Gang L, Wang X, Zhang J, Chen Y, Shi J, Yang H, Hu H, Yang S (2011) Solvothermal synthesis of cobalt ferrite nanoparticles loaded on multiwalled carbon nanotubes for magnetic resonance imaging and drug delivery. Acta Biomater 7(9):3496–3504
169. Cai B, Zhao M, Ma Y, Ye Z, Huang J (2015) Bioinspired formation of 3D hierarchical $CoFe_2O_4$ porous microspheres for magnetic-controlled drug release. ACS Appl Mater Interfaces 7(2):1327–1333
170. Amiri M, Salavati-Niasari M, Akbari A (2019) Magnetic nanocarriers: evolution of spinel ferrites for medical applications. Adv Coll Interface Sci 265:29–44
171. Das H, Sakamoto N, Aono H, Shinozaki K, Suzuki H, Wakiya N (2015) Investigations of super-paramagnetism in magnesium ferrite nano-sphere synthesized by ultrasonic spray pyrolysis technique for hyperthermia application. J Magn Magn Mater 392:91–100
172. Arana M, Bercoff PG, Jacobo SE, Zélis PM, Pasquevich GA (2016) Mechanochemical synthesis of MnZn ferrite nanoparticles suitable for biocompatible ferrofluids. Ceram Int 42(1):1545–1551

173. Monfared AH, Zamanian A, Sharifi I, Mozafari M (2019) Reversible multistimuli-responsive manganese–zinc ferrite/P (NIPAAM-AAc-AAm) core-shell nanoparticles: a programmed ferrogel system. Mater Chem Phys 226:44–50

174. Anupama AV, Kumaran V, Sahoo B (2019) Synthesis of highly magnetic Mn-Zn ferrite ($Mn_{0.7}Zn_{0.3}Fe_2O_4$) ceramic powder and its use in smart magnetorheological fluid. Rheol Acta 58(5):273–280

175. Zahid M, Nadeem N, Hanif MA, Bhatti IA, Bhatti HN, Mustafa G (2019) Metal ferrites and their graphene-based nanocomposites: synthesis, characterization, and applications in wastewater treatment. In: Magnetic nanostructures, pp 181–212. Springer, Cham

176. Mylarappa M, Lakshmi VV, Vishnu Mahesh KR, Nagaswarupa HP, Raghavendra N Synthesis and characterization of $Mn–ZnFe_2O_4$ and $Mn–ZnFe_2O_4$/rGO nanocomposites from waste batteries for photocatalytic, electrochemical and thermal studies. Mater Res Express 4(11):115603

177. Zhou X, Chuai D, Zhu D (2019) Electrospun synthesis of reduced graphene oxide (RGO)/NiZn ferrite nanocomposites for excellent microwave absorption properties. J Supercond Novel Magn 32(8):2687–2697

178. Sreeprasad TS, Maliyekkal SM, Lisha KP, Pradeep T (2011) Reduced graphene oxide–metal/metal oxide composites: facile synthesis and application in water purification. J Hazard Mater 186(1):921–931

179. Koduru JR, Karri RR, Mubarak NM () Smart materials, magnetic graphene oxide-based nanocomposites for sustainable water purification. In: Sustainable polymer composites and nanocomposites. Springer, Cham, pp 759–781

180. Gharibshahi E, Young B, Bhalla A, Guo R (2020) Theory, simulation and experiment of optical properties of cobalt ferrite nanoparticles. J Mater Sci Technol

181. Goldman JA (2014) The US rare earth industry: its growth and decline. Journal of Policy History 26(2):139–166

182. Seaman J (2019) Rare earths and China. A review of changing criticality in the new economy

183. Li X, Lou L, Song W, Huang G, Hou F, Zhang Q, Zhang HT, Xiao J, Wen B, Zhang X (2017) Novel bimorphological anisotropic bulk nanocomposite materials with high energy products. Adv Mater 29(16):1606430

184. Torkian S, Ghasemi A (2019) Energy product enhancement in sufficiently exchange-coupled nanocomposite ferrites. J Magn Magn Mater 469:119–127

185. Radulescu MM (2019) Novel spoke-type ferrite-magnet generators for micro-wind power applications. In: 2019 6th International symposium on electrical and electronics engineering (ISEEE). IEEE, pp 1–6

186. Bhosale RR (2019) Thermodynamic analysis of Ni-ferrite based solar thermochemical H_2O splitting cycle for H_2 production. Int J Hydrogen Energy 44(1):61–71

187. Goikoetxea NB, Gómez-Mancebo MB, Fernández-Saavedra R, Borlaf F, García-Pérez F, Jiménez JA, Llorente I, Rucandio I, Quejido AJ (2019) Understanding water-splitting thermochemical cycles based on nickel and cobalt ferrites for hydrogen production. Int J Hydrogen Energy 44(33):17578–17585

Low Loss Soft Ferrites Nanoparticles for Applications Up to S-band

Sucheta Sharma, Ramesh Verma, Mahavir Singh, and Surender K. Sharma

Abstract This chapter aims at providing a better understanding of soft ferrites and their role in ultra-high-frequency applications. In wireless communication industry trends of miniaturized, highly efficient and wide-band antenna become the new research areas of the antenna technology. Antenna miniaturization cannot be achieved by simply changing the structural design, and it is important to improve the material characteristics of antenna substrates. Furthermore, to improve the antenna efficiency, almost matched permittivity and permeability values and low magnetic as well as dielectric loss tangents are required especially at ultra-high frequency (UHF), L-band, and S-band frequency range. For efficiency improvement and miniaturization of antennas, magneto-dielectric materials have significant advantages with matching permittivity and permeability values along with sufficiently low magnetic and dielectric loss tangents. Ferrites with very high resistance have been reported as the best host materials to produce low loss magneto-dielectric materials for high-frequency antenna applications as they present moderate permeability and permittivity values. In this chapter, the emphasis is given on the soft ferrites Mn–Zn, Ni–Zn spinel ferrite, and Co_2Z type barium hexaferrite. The chapter also explains the effect of substitution of different dopant ions on the properties of soft ferrites.

Keywords Ferrites · Permittivity · Permeability · High frequency · Hexaferrite · Spinel · Saturation magnetization

S. Sharma (✉) · R. Verma · M. Singh
Department of Physics, Himachal Pradesh University, Shimla 171005, India

S. K. Sharma
Department of Physics, Federal University of Maranhao, Sao Luis, Brazil

Department of Physics, Central University of Punjab, Bathinda 151401, India

S. K. Sharma
e-mail: surender.sharma@ufma.br; surender.sharma@cup.edu.in

1 Introduction

Nanoferrites with specific features like low eddy current losses, high electric resistivity, quantum size effect, superparamagnetic behavior, and magnetic tunneling effect have been fascinating due to their wide applications in several areas such as energy storage, environmental protection, biotechnology, wastewater treatment, microwave devices, and communication technology. Beside these unique characteristics, they possess intriguing properties like high permeability, high permittivity, and low losses at ultra-high frequencies and reported as the best host materials for variety of commercial and defence-related applications [1–4] as they present both permeability and permittivity values. Based on their magnetic properties, ferrites are often classified as; "Soft Ferrite" and "Hard Ferrite" which refer to their low and high magnetic coercivity, respectively. The classification of soft and hard ferrites is based upon some important features like [5]:

1. The remanent magnetization M_R, magnetization left behind in the material after removing the magnetic field.
2. Saturation magnetization M_S, the maximum magnetic field that can be induced in the materials.
3. Coercivity H_C, the external magnetic field that brings to magnetization to zero when the magnetic field is applied in the opposite direction.

Soft Ferrites Soft ferrites are the class of magnetic materials which can be easily magnetized/ demagnetized and possess very low value of H_C. They are used in electronics industry to make efficient magnetic core called ferrite core for high-frequency inductors, antennas, transformers, and in microwave components. In general, the chemical composition of soft ferrites can be written as MFe_2O_4 where M is a divalent metal ion such as Zn^{2+}, Ni^{2+}, Mg^{2+}, Mn^{2+} or a combination of these ions. The most common examples of soft ferrites are $NiFe_2O_4$, $MnFe_2O_4$, $(MnZn)Fe_2O_4$, $(NiZn)Fe_2O_4$ ferrites; all these exhibit higher resistivity, higher permeability, and moderate magnetization [6–9] and having a cubic crystal structure and categorized as spinel ferrites.

Hard Ferrites Hard ferrites with hexagonal crystal structure are permanent magnetic materials and have large M_S, high H_C relatively high value of anisotropy constant. These hard ferrites with hexagonal structure are also referred to as hexaferrites or hexagonal ferrites. They are magnetically very stable and difficult to demagnetize either by external magnetic fields or by mechanical shock. They are broadly used as permanent magnets with have high H_C. Hexagonal ferrites were first identified by Went, Rathenau, Gorter, and Van Oostershout in 1952 and Jonker, Wijn, and Braun 1956 [10]. Hexagonal ferrites are referred to as hard ferrites, as the direction of magnetization cannot be changed easily from easy direction to another. These hexagonal ferrites can be classified as M-, W-, U, X-, Y-, and Z-type ferrites according to their crystal structure and arrangement of respective S, R, and T-blocks. Hexagonal ferrites have gained considerable technological importance in recent years because

Table 1 Subclasses of hexaferrites with their chemical formulae

S. No	Hexaferrite type	Chemical formula	Crystallographic build-up
1	M	$AFe_{12}O_{19}$	RSR*S* (MM*)
2	W	$AMe_2Fe_{16}O_{27}$	MSM*S*
3	X	$A_2Me_2Fe_{28}O_{46}$	MM*S
4	Y	$A_2Me_2Fe_{12}O_{22}$	3TS
5	Z	$A_3Me_2Fe_{24}O_{41}$	MYMY
6	U	$A_4Me_2Fe_{36}O_{60}$	MM*Y*

of their good electromagnetic performance, higher resonance frequency, high electrical resistivity, and relatively high permeability. Table 1 shows the subclasses of hexaferrites with their chemical formulae, where A denotes Ba, Pb or Sr, and Me may be divalent transition metal ion or a combination of metal ions as in spinels or may be Mg, Zn, Co, Ni, etc**.**

If Me is cobalt, then these hexagonal ferrites can be abbreviated as Co_2Y, Co_2W, Co_2X, Co_2U, and Co_2Z [11]**.** The complex crystal structures of all hexaferrites can be considered as a superposition of S, R, and T-blocks along the hexagonal c-axis and related to each other. S block represents a spinel block which consists two oxygen layers with composition Fe_6O_8. R is a three-oxygen layer block with composition $BaFe_6O_{11}$. T is a block of four layers of oxygen ions with composition $Ba_2Fe_8O_{14}$. In these ferrites, metal ions at some layers are present with same ionic radii as that of oxygen ions, and the oxygen ions are in the spinel structure and are closely packed. Most of these larger metal ions are barium (Ba^{2+}), strontium (Sr^{2+}), or lead (Pb^{2+}) that replaces oxygen ions in the lattice [12].

The most common examples of hexagonal ferrites are strontium ferrites, $SrFe_{12}O_{19}$ ($SrO.6Fe_2O_3$) and Barium ferrite, $BaFe_{12}O_{19}$ ($BaO.6Fe_2O_3$). Due to microwave device applications, they have received much consideration in the recent years. Because of high uniaxial anisotropy and large resistivity of barium hexaferrite is of great interest for use in monolithic microwave integrated circuits, hybrid microwave devices, even as a future replacement for yttrium iron garnet [13]. The upcoming magnetic microwave devices such as circulators, isolators, phase shifters, and filters will be low loss, self-biased, planar, and operate better than today's devices [14]. The applications of hexaferrites include DC-DC converters, EMI filters, current sensors, switch mode power supplies, handheld devices, computers and communication systems, automobiles, and ignition coils common mode chokes, peripherals. [15].

Among the hexagonal ferrites, Co_2Z type hexaferrite $Ba_3Co_2Fe_{24}O_{41}$ has lately attracted great deal of attention and considered to be a promising candidate for the commercial use in high-frequency operation above 1 GHz [16–20]. This is the only material in the hexaferrite family with planar magneto-crystalline anisotropy at room temperature exhibiting soft magnetic character and good electromagnetic

properties at higher frequencies especially high ferromagnetic resonance frequencies up to 3 GHz compared with the low resonance frequency below 300 MHz for spinel ferrites [21]. Therefore, Z-hexaferrites are in great demand for hyper frequency communication applications and in microwave region for inductor cores.

In Co_2Z type hexaferrite with large permeability and high resonance frequency, the easy magnetization direction lies in the basal plane (c-plane) of the hexagonal structure at room temperature. Co_2Z has a c-plane anisotropy with a small in-plane anisotropy field of about 120 Oe and a large out-of-plane anisotropy field of 12,000 Oe [22, 23]. Here, a small field is sufficient for the moment in the c-plane. Hence, these materials with very small coercivity (H_C) values are magnetically "soft" in the c-plane. Co_2Z thus can be considered for use as electromagnetic materials with broad bandwidth at microwave frequency [24, 25].

2 Crystal Structure of Soft Ferrites

Spinel Ferrites The structure of spinel ferrites is derived from that of the mineral spinel $MgOAl_2O_3$. An ideal spinel structure comprises of a cubic close-packed (fcc) array of oxygen anions in which 32 oxygen ions form the unit cell. In this face centered cubic arrangement, there are two kinds of spaces between anions: tetrahedrally coordinated sites (A), surrounded by four nearest oxygen atoms, and octahedrally coordinated sites (B), surrounded by six nearest neighbor oxygen atoms. In total, there are 64 tetrahedral sites and 32 octahedral sites in the unit cell, of which one eighth of the tetrahedral (A) sites and one half of the octahedral (B) sites are occupied, resulting in a structure that is electrically neutral [26, 27]. One-unit cell consists of eight formula units AB_2O_4, with 64 tetrahedral sites, 16 octahedral sites [28].

The factors such as the electrostatic energy of the spinel lattice, ionic radii, the electronic configuration of the metal ions, and more recently the preparation condition can influence the distribution of the metal ions over tetrahedral and octahedral sites [29, 30]. The distribution of metal ions in spinel lattice may be represented by Eq. (1)

$$\left(M_x^{2+}Fe_{1-x}^{3+}\right)\left[M_{1-x}^{2+}Fe_{1+x}^{3+}\right]O_4^{2-} \tag{1}$$
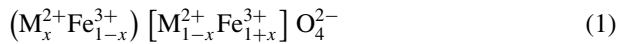
where the cations in the parenthesis occupy tetrahedral sites comprising the tetrahedral sublattice, while the cations in the square bracket occupy octahedral sites comprising the octahedral sublattice. Here, x is the inversion parameter and $x = 0$ and 1, stand for the inverse and normal spinel, respectively, and for mixed spinel, $0 < x < 1$. Figure 1 shows crystal structure of a cubic ferrite with the tetrahedral A site, octahedral B site where metal ions occupy only 1/8th of the A sites and 1/2 of the B sites.

Z-type Hexaferrite The crystal structure of Co_2Z type hexagonal ferrite is the superposition of four S-blocks, two T-blocks, and one R block shown in Fig. 2. The struc-
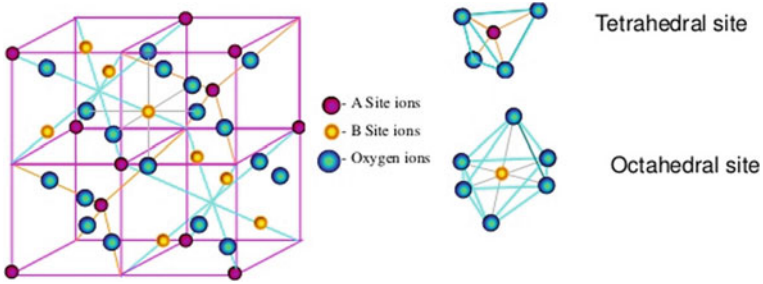
Fig. 1 Crystal structure of spinel ferrite

ture may be designated as a stack of blocks S, T, R, S*, T* and R*, where spinel S block, hexagonal R block, and hexagonal T block are independent, and asterisk (*) shows that the corresponding block is rotated 180° around the hexagonal c-axis. The stacking order is STSRS*T*S*R*. Z-type hexaferrite is composed of two simple
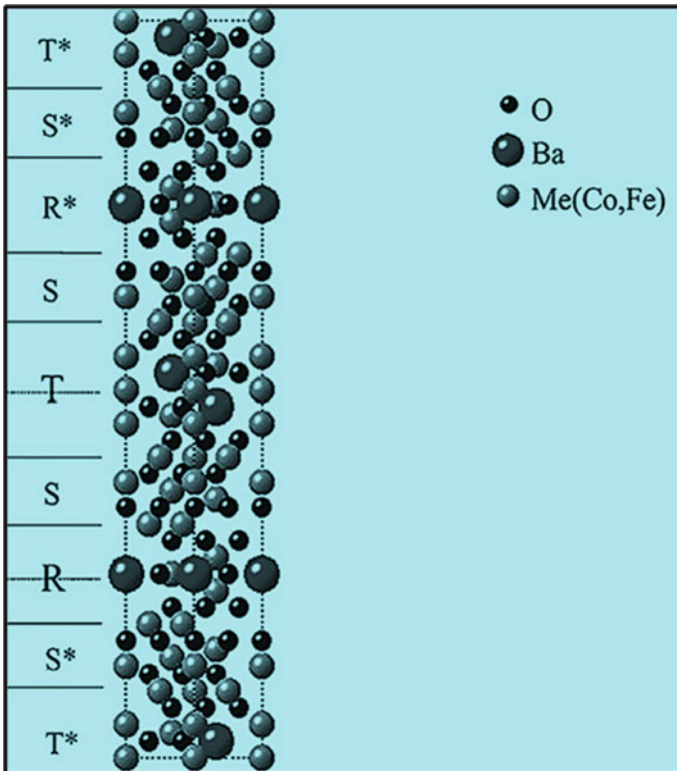
Fig. 2 Crystal structure of Z-type barium hexaferrite. Reproduced with permission from [34] Copyright (2003) Elsevier

hexaferrites, namely M-type ($BaFe_{12}O_{19}$) and Y-type ($Ba_2Co_2Fe_{12}O_{22}$) [31]. Here, the divalent and trivalent metallic ions are distributed among 10 different lattice sites in a complex crystal structure of Z-type hexaferrite, and the unit cell comprises 140 atoms (two formula units) and belongs to the P63/mmc space group. The Wyckoff notations for the 10 different sublattices are $12k_{VI}$ (corresponding to R-S block), $2d_V$ and $4f_{VI}$ (corresponding to R block), $4f_{VI}*$, $4e_{IV}$ and $4f_{IV}$ (corresponding to S block), $2a_{VI}$, $4e_{VI}$, $4f_{IV}*$ (corresponding to T block), and $12k_{VI}*$ (corresponding to T-S block). The subscript IV, V, and VI signifies the corresponding coordination for the sublattices, which is tetrahedral, fivefold, and octahedral, respectively. Co_2Z type hexaferrite with planar hexagonal structure involves high temperature upto 1300 °C synthesis (Z-phase cannot be formed below 1200 °C) is one of the most complex compounds in hexaferrite family from the crystallographic point of view. Zhang et al. testified that Z-type hexaferrite particles were hexagonal with an average size of 5.0 μm, formed at 1200 °C [32]. The complexity of the structure of Co_2Z type hexaferrite mainly due to large Ba^{2+} ions, Ba^{2+} prefers the oxygen site rather than the interstitial sites because the ionic radii of Ba^{2+} ions is comparable to that of O^{2-} ions. Metal ions Fe^{2+}, Fe^{3+}, Co^{2+}, and Cu^{2+}, however, are located in ten non-equivalent interstitial sites. The presence of strongly anisotropic Co^{2+} ions and extremely large unit cell of Co_2Z hexagonal ferrite gives rise to the complexity of its electromagnetic properties [33].

3 Low Loss Soft Ferrites

Ferrite materials possess moderate to high values of magnetization, permeability, permittivity, and low losses at high frequencies which make them potential candidate for microwave devices and modern communication. Soft spinel ferrites have high saturation magnetization, high resistivity, initial high permeability, and low magnetic anisotropy field. The applications of soft ferrites can be divided into two fields according to the demand of application frequency range. One is the field with frequency range less than 300 MHz where high permeability and low power loss are required, whereas other is the microwave region with frequency range 300 MHz or higher where magnetic resonance is required. Among the soft ferrites, Ni–Zn and Mn–Zn have been widely utilized in microwave application below 1 GHz. Ni–Zn and Mn–Zn ferrite materials allow the use of soft ferrites from audio frequencies to several hundred megahertz and are used in modulators, pulse transformers, antennas inductances and reflection coils, etc. [35]

The basic difference between these two soft ferrites is that Mn–Zn has higher permeability, and Ni–Zn has higher resistivity. Mn–Zn ferrites are primarily used for applications such as filter cores, magnetic recording head, inductor and transformer core, etc., at frequencies less than 2 MHz, whereas Ni–Zn ferrites can be used in low- and high-frequency applications and are one of the versatile, low cost magnetic materials. Ni–Zn ferrite can operate from 1–2 MHz to several hundred megahertz because

of high resistivity and used in applications such as transformer or electromagnetic cores at frequencies higher than for Mn–Zn ferrites.

High performance devices with miniaturized structure is highly demanded in modern wireless communication systems. For antenna substrate materials, the ideal parameters are high permeability with equivalent permittivity and low magnetic/dielectric losses [36–44]. Such materials enable miniaturization and enhancing antenna gain and bandwidth. The literature reveals that spinel ferrites (NiZn) and Z-type hexaferrites (Co$_2$Z) with excellent electromagnetic properties are the potential candidates for high-frequency microwave antenna applications. NiZn ferrites have been widely used for high-frequency applications. However, these ferrites cannot be used above 300 MHz because they exhibit relatively low cut-off frequencies and therefore limits their applications at high-frequency range. When used in the high-frequency range, spinel ferrites cannot provide high permeability due to the Snoek's limit also their Snoek product is much lower than that of hexagonal ferrites. Hexaferrites have moderate to high saturation magnetization, high magnetic anisotropy field, high electrical resistivity, and moderate Curie temperature. Due to the unique property of high magnetic anisotropy field compared with spinel ferrites, hexaferrites with high cut-off frequency in gigahertz (GHz) range have superiorities for use in microwave region for inductor cores and ultra-high-frequency communications [45–49].

The Snoek product of spinel ferrites can be expressed as [50]

$$(\mu' - 1)f_0 = (1/3\pi)\gamma M_s \tag{2}$$

where f_0 is the cut-off frequency, γ is the gyromagnetic ratio, M_s is the saturation magnetization.

For hexagonal ferrites, the Snoek product is much higher than that of spinel ferrites and is expressed as [50]

$$(\mu' - 1)f_0 = (1/4\pi)\gamma M_s \sqrt{\frac{H_k^\theta}{H_k^\phi}} \tag{3}$$

where f_0 is the cut-off frequency, γ is the gyromagnetic ratio, M_s is the saturation magnetization, H_k^θ is the anisotropy field for deflection in the vertical direction, and H_k^ϕ is the anisotropy field for deflection in the horizontal direction. Literature revels that among the hexaferrite (hard ferrite) family (M, W, Y, U, X, and Z), Z-type hexaferrite shows soft magnetic characteristics, i.e., low coercive field and is therefore called soft ferrite among other hard ferrites. Recent studies on Co$_2$Z type hexaferrites have shown that this material with high permeability and high ferromagnetic resonance frequency can be used for electromagnetic noise absorbers, inductor cores, antenna cores, and other microwave devices that send receive and manipulate electromagnetic signals in high-frequency region above 1 GHz [18, 42, 51, 52].The soft magnetic properties and high ferromagnetic resonance frequency

are unbeatable features for microwave applications as antenna substrates, inductor cores, and electromagnetic band gap (EBG) structures at high-frequency range.

Co_2Z hexaferrite and Ni–Zn ferrites materials have advantages depending on the tunable application frequency, and Co_2Z hexaferrite is a promising material for microwave devices, whereas NiZn ferrites are still technologically and commercially important from application point of view. Regardless of the type of soft ferrites, it is very difficult to reduce the magnetic and dielectric losses at the same time, but it is relatively easy to match the permeability and permittivity. The later will therefore be the focus of future research in such kind of materials at higher frequencies up to S-band. Magnetic and dielectric losses are critical parameters for microwave device performance [53]. The imaginary part of the permittivity expressed the dielectric loss (due to damping of the vibrating electric dipole moments). Magnetic loss comes from the magnetic damping related with ferromagnetic resonance and domain wall motion and expressed by the imaginary part of the permeability. Ferrite materials with high permeability and low magnetic loss are ideal candidates for microwave high-frequency antenna substrates and inductors applications. Hexaferrites, such as Co_2Z with planar anisotropy, have relative high permeability and higher resonance frequency compared to spinel structures. In polycrystalline ferrites, the frequency dispersion of permeability is affected by two main resonance mechanisms, namely the natural resonance and domain wall resonance [54]. Since microwave devices with ferrite materials like antennas and inductors are operated in off-resonance condition, the operating frequency and magnetic loss of the devices are affected by the resonance frequency and resonance linewidth of the ferrite materials, respectively. Decreasing the grain sizes of ferrite materials will reduce the domain wall resonance effect, which will help to lower the magnetic loss. However, it may decrease the real permeability value at the same time.

Because of high magneto-crystalline anisotropy fields and high permeability, cobalt substituted Z-type (Co_2Z) has much higher ferromagnetic resonance frequencies of above 1.0 GHz [55–57]. Studies on microwave properties of Z-type hexaferrites, represented by complex permittivity and permeability, have been reported [58–61]. The most important technological properties for good performance in low- and high-frequency applications are electric and magnetic losses, saturation magnetization (M_S), initial permeability (μ_i), and coercive force (H_C). If the magneto-dielectric materials used for antenna substrates have same permittivity (ε') and magnetic permeability (μ') over a much wider bandwidth, then it is easy for antenna designers to simply fabricate and enhance antenna efficiency. Both the electromagnetic band gap (EBG) structures and antenna can be miniaturize by the magneto-dielectric materials, however, using moderate values of permittivity and permeability ($n = \sqrt{\varepsilon'\mu'}$) compared to the dielectric-only materials with high permittivity. The use of matching ε' and μ' values has two benefits: it produces better band gap rejection levels for multi-layer EBG structures, [11]; for antennas, an equivalent ε' to μ' allows for ease of impedance matching over a much wider bandwidth, which gives more flexibility of antenna design in order to simply fabrication and efficiency of antennas. It has been very challenging to use such materials at ultra-high frequency (UHF) and S-band.

At the same time, for antenna applications, it is a major challenge to realize low magnetic and dielectric losses of magneto-dielectric materials.

By varying the compositions or adding additives or by selecting the proper synthesis technique, one can to a large extent control most parameters for any particular applications. Keeping in view the major challenges, the researchers are trying to synthesize low loss nanoferrites with enhanced permittivity and permeability values for high-frequency antenna applications in GHz region. It is reported that substitution of divalent or trivalent ions may improve the dielectric and magnetic properties of hexaferrites such as permittivity, permeability, saturation magnetization, and coercivity [62–67]. It has been reported that the properties of Ni–Zn spinel ferrite and Co_2Z hexaferrite can be tailor-made for suitable applications by substituting them with different divalent ion dopants such as Co^{2+}, Mg^{2+}, Mn^{2+}, Cu^{2+}, Zn^{2+}, Ni^{2+} etc.

To reduce the sintering temperature of Co_2Z nano hexaferrite and Z-phase formation, partial substitution of Co^{2+} ions with Cu^{2+} ions have been suggested [68]. It is well documented that the substitution of Zn^{2+} ions in Co_2Z nanohexaferrite improves the magnetic properties [69]. B. B. V. S. Vara Prasad has reported the effect of indium substitution on the electrical and magnetic properties of Ni–Zn ferrite [70]. Parvatheeswara and Rao [71] have studied the doping of indium ions in the Ni–Zn ferrite. They found that for a certain concentration of indium ions, the saturation magnetization increases slightly thereafter it decreases. This type of anomalous behavior of saturation magnetization as a function of indium ions concentration in Ni–Zn ferrite systems was confirmed by Lakshman et al. [72] and Ghosh et al. [73] in their experiments on indium substituted Mg–Mn ferrite. They interpreted this effect in terms of distribution of the indium ions behavior at tetrahedral and octahedral sites.

4   Microwave Properties of Soft Ferrites

For high-frequency applications, both the dielectric properties as well as magnetic properties are very important, particularly in microwave devices and wireless communication systems. The central properties of interest for many applications are permittivity, resistivity, and permeability, which in general at higher frequencies should be as high as possible. There have been several investigations on electromagnetic properties of soft ferrites represented by complex permittivity and permeability spectra. Complex permittivity ($\varepsilon = \varepsilon' - j\varepsilon''$) and complex permeability ($\mu = \mu' - j\mu''$) represent the dielectric and dynamic magnetic properties of magnetic materials. The real parts of ε and μ symbolize the storage capability of electric and magnetic energy. The imaginary parts represent the loss of electric and magnetic energy through $\tan \delta M = \mu''/\mu'$ and $\tan \delta D = \varepsilon''/\varepsilon'$.

Electron hopping between Fe^{2+} and Fe^{3+} leads to the conduction mechanism in ferrites. Electric dipoles are formed by the metal cations and the oxygen anions, creating an intrinsic dielectric polarization. Due to the damping of vibrations of electrical dipoles, dielectric losses occur in polycrystalline materials, and the crystal

structure causes intrinsic losses, while the extrinsic losses are due to grain boundaries in polycrystalline materials, impurities, and porosity, dominate at higher frequencies, causing an excessive decrease of permittivity in most materials at microwave frequencies. Nevertheless, the effective magnetic permeability μ_{eff} is virtually independent of frequency, but there is a critical frequency f_c, above which μ_{eff} falls rapidly as a function of frequency due to eddy current losses. This generally has a lower value for materials with a higher permeability, but also related to the resistivity and thickness of the material. The critical frequency is given by Eq. (4)

$$f_c = \frac{4R}{\pi \mu_i d^2} \tag{4}$$

where R is the specific electrical resistance of the piece of material, μ_i the initial permeability, and d the thickness. Despite being resistive materials, however, the ferrites still have a limiting frequency f_c because in ferrites f_c is also connected to magnetic spin effects, so there is a gyromagnetic critical frequency, f_g, also known as the spin relaxation frequency. This is determined by the gyromagnetic ratio, γ, which is the ratio of the magnetic moment to torque for an electron and is therefore independent of the dimensions of the sample. The gyromagnetic ratio f_g is given by Eq. (5) where M_s is the saturation magnetization.

$$f_g = \frac{0.1\gamma M_s}{\mu_i} \tag{5}$$

It has been shown that if f_g is plotted against M_s or μ_i over a range of frequencies, a variation in f_g is observed, caused by Bloch wall movement and/or the rotation of magnetic domains. If both phenomena have an effect of ferromagnetic resonance (FMR), the resonances due to spin rotation occur at high frequencies than domain wall resonances. At a point where μ_i increases slightly before dropping, these phenomenon occur, resulting in a resonance frequency around f_g, which is called ferromagnetic resonance or FMR. If a plot is made of the two components of the complex permeability, the real permeability μ', and the imaginary permeability, μ'' this resonance can be seen. In a static field, μ'' is lower than μ', and the two values remain constant at low frequencies, rising slowly to a peak. As the magnetic losses μ'' increase at higher frequencies, μ' suffers a sudden decrease, but remains constant at this point until it also drops at a slightly higher frequency. Just before μ'' drops, it experiences a slight increase from the FMR around the critical frequency f_g, giving it a maximum value. This maximum in μ'' should occur at the same frequency at which μ' has dropped to half of its original value, and this is the FMR frequency, f_r, and it should equal or be very close to f_g [12].

MnZn Ferrite De Fazio et al. have investigated the influence of lithium substitution on structural, magnetic, and dielectric properties of MnZn soft ferrite $Li_{0.5x}Mn_{0.4}Zn_{0.6-x}Fe_{2+0.5x}O_4$ ($0.0 \leq x \leq 0.4$) prepared by ceramic method [74]. Complex permeability of toroids and complex permittivity of pallets were measured

by material analyzer from 1 to 1800 MHz (1.8 GHz). The complex relative permeability spectra of the studied ferrites (Fig. 3) show that until the frequency is raised up to a certain value, the real part of permeability (μ') remains almost constant. The imaginary permeability (μ'') gradually increases with the frequency; at a certain frequency, the real permeability rapidly decreases and imaginary permeability (μ'') presents a broad maximum (natural resonance). It was observed that in the low-frequency region below 10 MHz, the real permeability increases with increasing Li substitution. The natural resonance frequency (the value where the imaginary permeability has a maximum value) shifts toward a lower frequency (from 52 to 17 MHz) as x is increased. It is reported that as the Li concentration (x) increases, the imaginary permeability in the low-frequency region below 100 MHz also increases. This is attributed to two mechanisms domain wall movement and spin rotation contributing to the permeability spectra.

Various factors influence the dielectric properties of the ferrite samples such as synthesis approach, chemical composition, grain size, sintering conditions, etc. The microwave permittivity spectra (ε') of these ferrites indicate that the real parts do not change with frequency in the studied range as shown in Fig. 4. The ε' values decrease from 7.2 to 4.6 for $x = 0$ to $x = 0.4$. For the permittivity dispersion, two mechanisms are responsible: electron polarization and ion polarization. Li addition modifies the original Fe^{3+}/Mn^{2+} ratio (refer to the stoichiometric formula) so permittivity decreases, while resistivity slightly increases from 2.1×10^{-7} to 4.4×10^{-7} Ω cm for $x = 0$ to $x = 0.4$, respectively. Permittivity losses profiles (ε'') show that resonant phenomena occur at frequencies higher than 1.9 GHz.
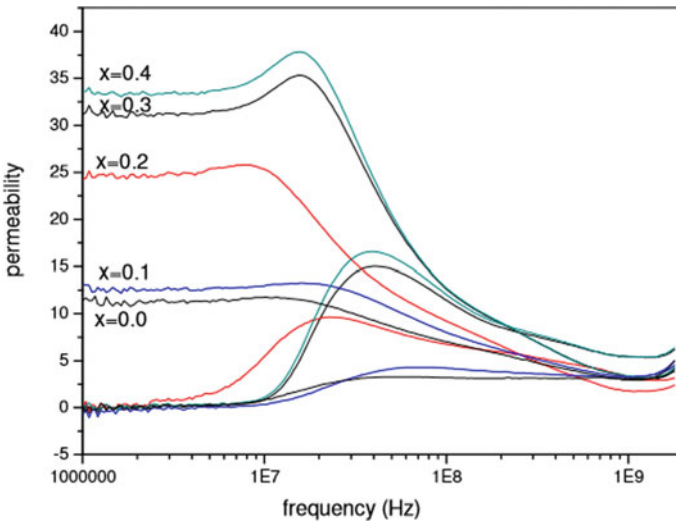
Fig. 3 Real and imaginary permeability of the studied samples in 1 MHz–1.8 GHz range. Reproduced with permission from [74] Copyright (2011) Elsevier
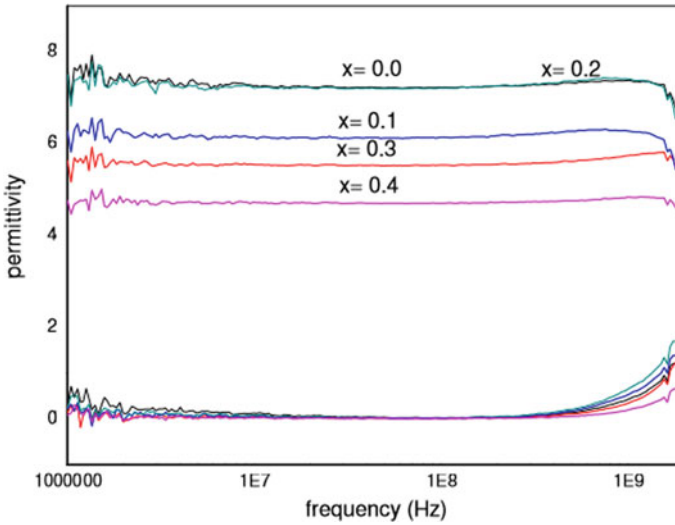
Fig. 4 Real and imaginary permittivity of the studied samples in 1 MHz-1.8 GHz range. Reproduced with permission from [74] Copyright (2011) Elsevier

The electromagnetic wave absorption (reflection loss) characteristics of polycrystalline Li–Mn–Zn ferrite is shown in Fig. 5. It was found that the samples exhibit the potential of relatively wide-band absorption in the frequency region from 140 MHz to 1.8 GHz. The center frequency shifted to lower values as x is increased, and it can be tunable in the range from 150 to 304 MHz. These ferrites can be used as EMI shielding between 10–40 MHz in order to achieve an absorption greater than 20 dB (>99% absorption). Lithium inclusion for $x = 0.4$ enhances microwave absorption with a maximum reflection loss of 45 dB at 140 MHz. These characteristics suggest that high-frequency devices such as single-layered electromagnetic wave absorbers can be designed using these polycrystalline Li–Mn–Zn ferrites.

Ni–Zn Ferrite An investigation by Jacobo et al. [75] on the microwave absorption properties of yttrium (Y^{3+}) substituted $Ni_{0.5}Zn_{0.5}Y_yFe_{2-y}O_4$ ($0.01 \leq y \leq 0.05$) ferrites show that with yttrium content, the dielectric constant decreases and showing a constant behavior in the explored frequency range in the frequency range 1 MHz to 1.8 GHz. Also with yttrium inclusion, the maximum of the magnetic losses diminishes and shifts to higher frequencies. These Yttrium-substituted Ni–Zn ferrites (with Y content ≤0.05 per formula unit) prepared by sol-gel method can be considered as good attenuator materials in the explored microwave frequency range 1 MHz to 1.8 GHz. It is clear from Fig. 6 that the undoped sample (Ni–Zn ferrite) has the maximum value of permittivity (ε), which means it has both a maximum polarization as well as a maximum valence exchange. As with yttrium substitution, the dielectric constant decreases, showing a constant behavior in the explored frequency range. It is reported that the hopping of electrons between ions of the same element, but in different oxidation state leads to the mechanism of polarization in polycrystalline
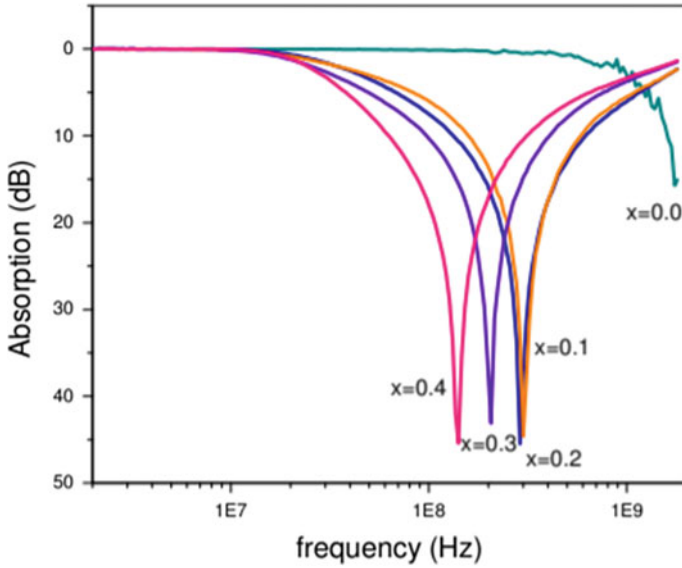
Fig. 5 Calculated absorption spectra of $Li_{0.5x}Mn_{0.4}Zn_{0.6-x}Fe_{2+0.5x}O_4$. Reproduced with permission from [74] Copyright (2011) Elsevier
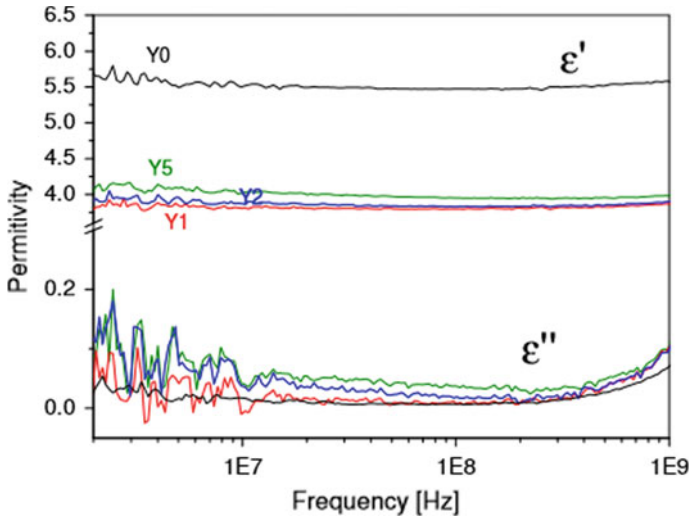
Fig. 6 Dependence of complex permittivity ε (real (ε') and imaginary (ε'') contributions) of the yttrium ferrite samples as a function of frequency (1 MHz–1.8 GHz). Reproduced with permission from [75] Copyright (2016) Elsevier

ferrites such as $Fe^{2+} \rightarrow Fe^{3+}$ [76, 77]. Interfacial polarization is caused when an electric field is applied the electrons reach the grain boundaries, they pile up and a charge build-up takes place. The possibility that ions exist in different valance states is rather low because the ferrites are sintered at a relative low temperature during a short time, which reduces the probability of electron hopping and hence of polarization, resulting in a low dielectric constant. It was found that with yttrium content in $Ni_{0.5}Zn_{0.5}Y_yFe_{2-y}O_4$ electrical conductivity decrease, which is correlated to the decrease in permittivity [78]. Yttrium ions block the Fe^{2+}–Fe^{3+} transformation and do not participate in the conduction process hence limit the degree of Fe^{2+}–Fe^{3+} conduction and decrease in conductivity. The probable reason for this behavior is that the more electric dipoles are induced by substitution, so the imaginary part of the relative complex permittivity increases [79]. It is usually believed that the dielectric loss mainly consists of the electron polarization, the ion polarization, and the electric dipolar polarization. For electron and ion polarizations, the losses are relatively weak in the microwave range and strongly occur at higher frequencies [80]. Thus, it is concluded that the dielectric loss of all the studied samples results mainly from the electric dipolar polarization. As magnetic losses are related to the absorption effect, tan δ_M profiles versus frequency were analyzed (Fig. 7). For all compositions, tan δ_M steeply increases for frequencies higher than 1 GHz.

Sharma et al. investigated the microwave properties of doped nanocrystalline $Ni_{0.58} Zn_{0.42} Co_{0.15} Cu_{0.05} Fe_{1.8}O_4$ (Ni–Zn) spinel ferrite prepared by sol-gel autocombustion method and reported the low dielectric and magnetic loss values close to zero [81]. Microwave properties were measured using cavity perturbation technique in the frequency range 1.6–3.5 GHz. Figure 8a, b illustrated the frequency depen-
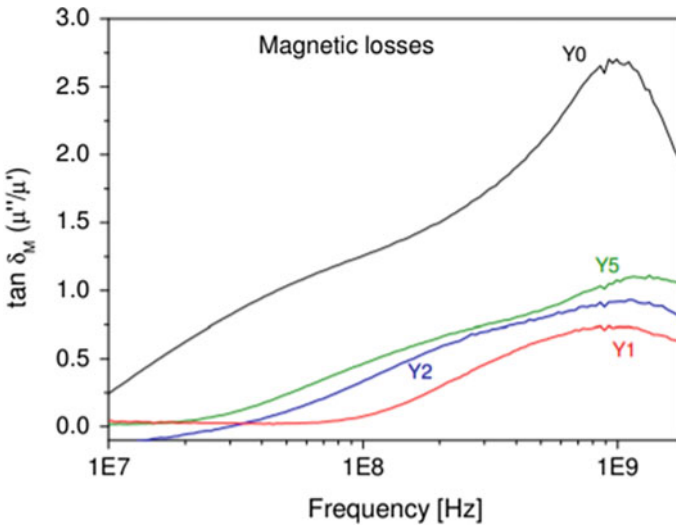
Fig. 7 Dependence of magnetic losses (tan $\delta_M = \mu''/\mu'$) with frequency. Reproduced with permission from [75] Copyright (2016) Elsevier

dence of real part of permittivity and permeability (ε' and μ') of NiZn spinel ferrite over the frequency range 1.6–3.5 GHz. The dielectric behavior of ferrites can be explained by Verway hopping mechanism [82] of electrons/holes transfer between Fe^{2+}–Fe^{3+}, Co^{3+}–Co^{2+}, Ni^{3+}–Ni^{2+} and Cu^{3+}–Cu^{2+} pairs of ions. The permittivity of nanoferrites at higher frequencies is due to the atomic and electronic polarization. The microstructure, grain size, impurities, and density of the sample also affect the permittivity of nanoferrites. The variation of complex permittivity at higher frequencies is explained by Maxwell-Wagner theory [83]. The low values of permittivity (ε') and permeability (μ') as shown in figure for the prepared NiZn spinel ferrite are explained due to the blocking of Verwey hopping mechanism in the system and the spin rotation, respectively, as the grain size is much lower. It is well known that the permeability of polycrystalline ferrites results from two different magnetizing mechanisms: spin rotation and domain wall motion [84].

Figure 9a, b illustrates the frequency dependence of imaginary part of permittivity and permeability (ε'' and μ'') of $Ni_{0.58}$ $Zn_{0.42}$ $Co_{0.15}$ $Cu_{0.05}$ $Fe_{1.8}O_4$ (NiZn) spinel ferrite over the frequency range 1.6 GHz to 3.5 GHz. It is clear that over the whole measured frequency range 1.6–3.5 GHz, both electric and magnetic losses remain

Fig. 8 a, b Frequency dependence of ε' and μ' of NiZn spinel ferrite. Reproduced with permission from [85] Copyright (2016) Ph.D. thesis
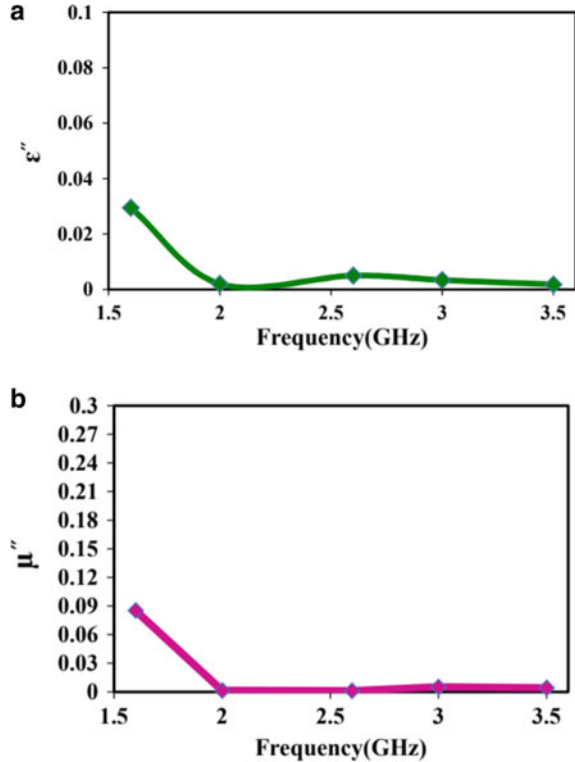
very low close to zero. At frequency 3.5 GHz, the reported electric and magnetic losses (ε'' and μ'') for nanocrystalline NiZn spinel ferrite are 0.0018 and 0.004. The impurities and imperfections present in the ferrite structure cause higher magnetic and dielectric losses. The low dielectric and magnetic loss values measured at such higher frequencies 1.6–3.5 GHz are attributed to the uniform and homogeneous structure of the prepared NiZn nanoparticles by sol-gel auto-combustion method.

Ba Hexaferrites Microwave properties of sol-gel auto-combustion processed Co_2Z barium hexaferrites were investigated by Sharma et al. using cavity perturbation technique [86]. They reported how the Zn^{2+} ions substitution for Co^{2+} ions affect the values of real part of permittivity (ε') and permeability (μ') for all the samples over the high frequencies from 1.6 - 4 GHz. The results shown in Fig. 10a, b clearly indicates an increase of ε' and μ' with the addition of Zn^{2+} ions. The best results obtained were $\varepsilon' = 3.07$, $\mu' = 2.59$ at frequency 2 GHz, and $\varepsilon' = 2.33$, $\mu' = 2.94$ at frequency 2.5 GHz for the composition $Ba_3Co_1Cu_{0.2}Zn_{0.7}Ni_{0.1}Fe_{24}O_{41}$ (sample Z2). The striking point in this investigation was the enhancement in real part of permittivity and permeability with controlled electric and magnetic losses close to zero over such a high-frequency range 1.6–4 GHz. It has been reported that ε' decreases with increasing frequency beyond frequency 2 GHz. Such type of dispersion is a normal
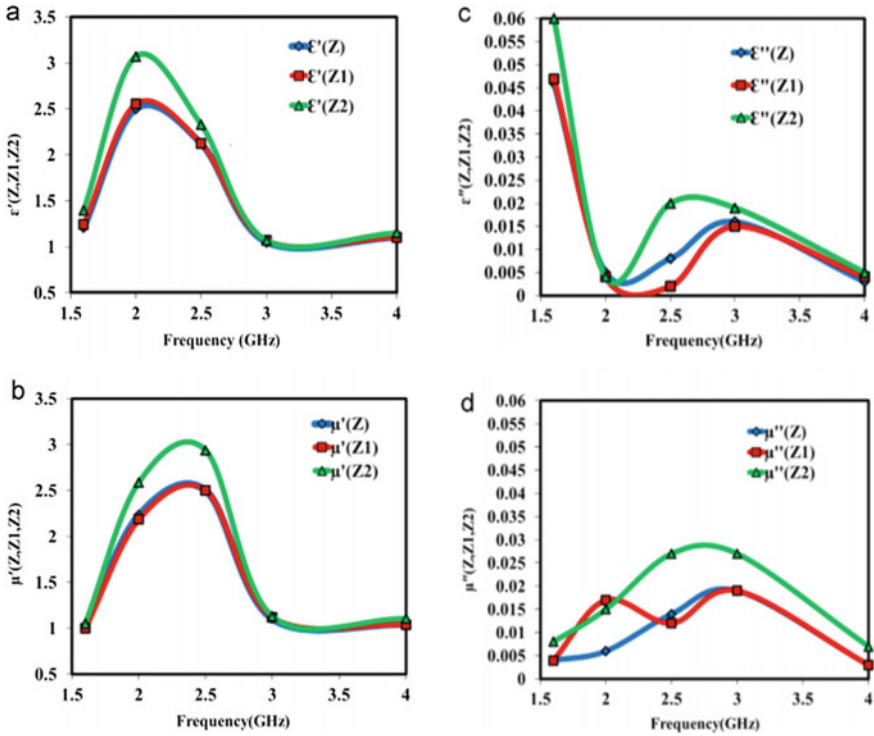
Fig. 10 **a**, **b** Frequency spectra of ε' and μ' of Co_2Z-hexaferrites. **c**, **d** Frequency spectra of ε'' and μ'' of Co_2Z-hexaferrites. Reproduced with permission from [85] Copyright (2015) Elsevier

dielectric dispersion behavior of all ferrites which is due to Maxwell and Wagner type interfacial polarization in accordance with Koop's phenomenological theory [87, 88]. The electron hopping between Fe^{3+} ions and Fe^{2+} ions cannot follow the alternating electric field above a certain frequency and results in a decrease of ε' with increasing frequency. Beyond 2.5 GHz, with increasing frequency, the permeability μ' is found to decreased due to the decrease in domain wall motion and spin rotation effect. At higher frequencies, when the domain wall motion reduces, spin rotation plays a relatively more important role [89].

It is evident from Fig. 10c, d that at all frequencies from 1.6 to 4 GHz, the imaginary part of permittivity and permeability remain very low close to zero. The low values of electric and magnetic losses may be attributed to the homogeneity and uniformity of the prepared nanoparticles at the structural level by the sol-gel auto-combustion method. The experimental results obtained clearly indicate that among the sol-gel auto-combustion processed Co_2Z-hexaferrites, sample Z2 with improved high-frequency electromagnetic properties and low loss tangent ($\tan\delta$) at frequencies 2 and 2.5 GHz could be very useful to the miniaturization of antennas for mobile handheld wireless communication devices.

5   Summary

To summarize, we have discussed the electromagnetic properties of MnZn, NiZn spinel ferrites and Co_2Z type barium hexaferrite, and the effect of substitution of diverse dopant ions on their properties. Our investigations showed that the soft ferrites have very useful electromagnetic properties, i.e., real part of permittivity and permeability (ε' and μ') and low electric as well as magnetic losses (ε'' or μ'') for high-frequency applications.

Li-doped Mn–Zn ferrites synthesized by ceramic method showed good microwave absorption properties from 1 MHz to 1.8 GHz. Real permeability (over 1 MHz) is increased with Li inclusion while as the Li content increases the natural resonance frequency shifts to lower values. The results showed that the samples with higher Li content ($x = 0.4$) have maximum resistivity (~4.4×10^7 Ω cm) and minimum dielectric constant (~4.65) values. Microwave absorption with a maximum reflection loss of 45 dB at 140 MHz for $x = 0.4$ was found to enhanced by Li inclusion. Therefore, these polycrystalline Li–Mn–Zn ferrites can be used for microwave devices such as single-layered electromagnetic wave absorbers. Microwave measurements done by Jacobo et al. showed that Yttrium (Y^{3+}) plays an important role in Ni–Zn ferrites in modifying the saturation magnetization, permeability, and permittivity in the explored frequency range 1 MHz to 1.8 GHz. As with yttrium content, dielectric constant was found to decrease, showing a constant behavior in the explored frequency range, and with yttrium substitution, the maximum of the magnetic losses diminishes and shifts to higher frequencies. Yttrium-substituted Ni–Zn ferrites (with Y content ≤ 0.05 per formula unit) can be considered as good attenuator materials for microwave devices. Microwave measurements of substituted Ni–Zn nanoferrites by cavity perturbation method confirmed that the prepared composition has low magnetic and electric losses close to zero over the frequency range 1.6–3.5 GHz that make these nanoferrites ideally suitable for high-frequency antenna applications. High-frequency electromagnetic properties of soft Ni–Zn ferrite are controlled by the variety of dopants and optimized physical conditions. At frequency 3.5 GHz, the reported magnetic and electric losses are 0.004, 0.0018, respectively. Also, solution combustion processed Co_2Z barium hexaferrite showed almost matched real part of permittivity and permeability (ε' and μ') along with controlled electric and magnetic losses (ε'' or μ'') close to zero over a wide frequency range from 1.6 to 4 GHz. The results showed that with the addition of Zn^{2+} ions, the real part of permeability increases. These electromagnetic properties, in particular the controlled electric and magnetic losses close to zero in the frequency range from 1.6 to 4 GHz make these nanoferrites probable candidates for miniaturization of antennas for mobile handheld wireless communication devices.

References

1. Kawano K, Sadurai N, Kusumi S, Kishi H (2006) Magnetic permeability and microstructure of the B_i, S_i oxides-doped NiZnCu ferrite composite material. J Magn Magn Mater 297(1):26–32
2. Tang X, Zhang H, Su H, Zhong Z, Bai F (2011) Influence of microstructure on the DC bias superposition characteristics of NiZn ferrites. IEEE Trans Magn 47(10):4332–4335 (2011)
3. Moon KS, Wong CP, Kim SH (2007) Ferrite polymer composite for improving the electromagnetic compatibility of semiconductor packaging. J Electron Mater 36(12):1711–1718
4. Kavanlooee M, Hashemi B, Maleki Ghaleh H, Kavanlooee J (2012) Effects of annealing on phase evolution,microstructure and magnetic properties of nanocrystalline Ball-Milled LiZnTi ferrite. J Electron Mater 41:3082–3086 (2012)
5. Kladnig WF, Zenger M (1992) Modern ferrites technologies and products. UNIDO
6. Lazarevic ZZ, Jovalekic C, Milutinovic A, Romcevic MJ, Romcevic NZ (2012) Preparation and characterization of nano ferrites. Acta Phys Pol, A 121(3):682
7. Shahane GS, Zipare KV, Pant RP (2013) Synthesis and characterization of superparamagnetic Fe_3O_4 nanoparticles for ferrofluid applications. Magneto Hydrodyn 49(3–4):317–321
8. Shahane GS, Kumar A, Arora M, Pant RP, Lal K (2010) Synthesis and characterization of Ni-Zn ferrite nanoparticles. J Magn Magn Mater 322(8):1015–1019
9. Sharma US, Sharma RN, Shah R (2014) Physical and magnetic properties of Manganese Ferrite Nanoparticles. Int J Eng Res Appl 4(8):14–17
10. Standley KJ, Oxide magnetic materials, 2nd edn. Oxford University Press
11. Caffarena VR, Ogasawara T, Capitaneo JL, Pinho MS (2007) Magnetic properties of Z-type $Ba_3Co_{1.3}Zn_{0.3}Cu_{0.4}Fe_{24}O_{41}$ nanoparticles. Mater Chem Phys 101:81–86
12. Pullar RC (2012) Hexagonal ferrites: A review of the synthesis properties and applications of hexaferrite ceramics. Prog Mater Sci 57(7):1191–1334
13. Fang HC, Ong CK (1999) Epitaxy barium ferrite thin films on $LiTaO_3$ substrate. J Appl Phys 86(4):2191
14. Harris, Chen VG, Chen Z, Yoon Y, Sakai S, Gieler T, Yang A, He A, Ziemer Y, Sun KS, Vittoria NX (2006) Ba-hexaferrite films for next generation microwave devices. Carmine J Appl Phys 99(8):08M911
15. Rakshit SK, Parida SC, Dash S, Singh Z, Sen BK, Venugopal V (2007) Thermodynamic studies on $SrFe_{12}O_{19}(s)$, $SrFe_2O_4(s)$, $Sr_2Fe_2O_5(s)$,and $Sr_3Fe_2O_6(s)$. J Solid State Chem 180(2):523–532
16. Autissier D, Podembski A, Jacquiod C (1997) Microwave properties of M and Z type Hexaferrites. J Phys IV 7(C1):409–412
17. Lubitz P, Rachford FJ (2002) Z-type Ba hexagonal ferrites with tailored microwave properties. J Appl Phys 91(10):7613–7615
18. Wang X, Li L, Su S, Gui Z (2005) Novel ferrimagnetic material for fabricating multilayer chip inductors low-temperature sintered Ba_3Co_2-$xZnxFe_{24}O_{41}$ hexaferrites. J Am Ceram Soc 88(2):478–480
19. Töpfer J, Kračunovska S, Barth S, Müller E (2009) Co_2 Z hexagonal ferrites for multilayer inductors. Advanc Appl Ceram 108(5):280–284
20. Zhang L, Puri A, Serte K, Volakis JL, Verweij H (2011) Low loss Z-type $Ba_3Co_2Fe_{24}O_{41}$ Hexaferrites for Antennas and RF devices. IEEE Trans Magn 47(8):2149–2152
21. Smit J, Wijn HPJ (1959) Ferrites: physical properties of ferrimagnetic oxides in relation to their technical applications. Philips' Technical Library, Eindhoven, The Netherlands
22. Verwell J (1971) In: Smit (ed) Magnetic properties of materials. Mc Graw Hill, New York, p 64
23. Jacquiod C Autissier D (1992) Rare-earth substitutions in Z-type hexaferrites. J Magn Magn Mater 104–107:419–420
24. Braden RA, Gordon I, Harvey RL (1966) Microwave properties of planar hexagonal ferrites. IEEE Trans Magn 2(1):43–47
25. Nakamura T, Hankui E (2003) Control of high frequency permeability in polycrystalline(Ba,Co)- Z-type hexagonal ferrite. J Magn Magn Mater 257(2–3):158–164

26. Goldman A (1990) Modern ferrite technology. Van Nostrand Reinhold, New York
27. Spaldin N (2003) Magnetic materials: fundamental and device applications. Cambridge University Press, Cambridge
28. Wahba AM, Mohamed MB (2014)Structural,magnetic and dielectric properties of nanocrystalline Cr-substituted $Co_{0.8}Ni_{0.2}Fe_2O_4$ ferrite. Ceram Int 40(4):6127–6135
29. Corliss LM, Hasting JM, Verwey E (1953) J Jr Chem Phys 90:1013
30. Sawataki GA, Wounde FVD, Morish AH (1962) Cation distributions in Octahedral and Tetrahedral sites of the ferrimagnetic Spinel $CoFe_2O_4$. J Appl Phys 39(2):1204
31. Xu JJ, Yang CM, Zou HF, Song YH, Gao GM, An BC, Gan SC (2009) Electromagnetic and microwave absorbing properties of Co_2 Z-type hexaferrites doped with La^{3+}. J Magn Magn Mater 321:3231–3235
32. Zhang H, Yao X, Wu M, Zhang L (2003) Complex permittivity and permeability of Zn-Co substituted Z type hexaferrite prepared by citrate sol-gel process. Br Ceram Trans 102(1):10–15
33. Hankiewicz JH, Pajak Z, Murakhowski AA (1991) Nuclear magnetic resonance in $Ba_3Co_2Fe_{24}O_{41}$ ferrite. J Magn Magn Mater 101(1–3):134–136
34. Tachibanaa T, Nakagawa T, Takada Y (2003) X-ray and neutron diffraction studies on iron-substituted Z-type hexagonal barium ferrite $Ba_3Co_{2-x}Fe_{24+x}O_{41(x=0-0.6)}$. J Magn Magn Mater 262(2):248–257
35. Murty VRK, Vishwanathan B (1990) Ferrites materials: science and technology. Narosa Publishing House, Mumbai
36. Pozar DM (1989) Microwave engineering. Wiley, Hoboken, pp 92–98
37. Vittoria C (2011) Magnetics, dielectrics, and wave propagation with MATLAB(R) codes. Taylor and Francis Group LLC, Boca Raton, FL, pp 281–333
38. Chen Y, Daigle A, Fitchorov T, Bolin H, Geiler M, Geiler A, Vittoria C, Harris VG (2011) Electronic tuning of magnetic permeability in Co_2 Z hexaferrite toward high frequency electromagnetic device miniaturization. Appl Phys Lett 98:202502
39. Daigle AP, Geiler AL, DuPrel E, Chen Y, Parimi PV, Vittoria C, Harris VG (2011) Numeric simulations of a novel wideband electromagnetic Band Gap Metamaterial utilizing oriented Cobalt-substituted Z-type Barium Hexaferrites. IEEE Magn Lett 2:0500104
40. Harris VG, Chen Z, Chen Y, Yoon SD, Sakai T, Geiler A, Yang A, He Y, Ziemer KS, Sun N, Vittoria C (2006) Ba-hexaferrites films for next generation microwave devices. J Appl Phys 99:08M911
41. Harris VG (2012) Modern microwave ferrites. IEEE Trans Magn 48(3):1075
42. Harris VG, Geiler A, Chen Y, Yoon S, Wu M, Yang A, Chen Z, He P, Parimi PV, Zuo X, Patton CE, Abe M, Acher O, Vittoria C (2009) Recent advances in processing and applications of microwave ferrites. J Magn Magn Mater 321(14):2035–2047
43. Su Z, Bennett S, Hu B, Chen Y, Harris VG (2014) Magnetic and microwave properties of U-type hexaferrite films with high remanence and low ferromagnetic resonance linewidth. J Appl Phys 115(17):17A504
44. Su Z, Chen Y, Hu B et al (2013) Crystallographically textured self-biasedW-type hexaferrites for X-band microwave applications. J Appl Phys 113:17B305
45. Li ZW, Lin GQ, Chen LF, Wu YP, Ong CK (2005) Size effect on the static and dynamic magnetic properties of W-type barium ferrite composites: From microparticles to nanoparticles. Appl J Phys 98(9):094310
46. Singh P, Babbar VK, Razdan A, Puri RK, Goel TC (2000) Complex permittivity, permeability, and X-band microwave absorption of CaCoTi ferrite composites. J Appl Phys 87(9):4362
47. Ruan SP, Xu BK, Suo H, Wu FQ, Xiang SQ, Zhao MY (2000) Microwave absorptive behavior of Zn-Co substituted W-type Ba hexaferrite nanocrystalline composite material. J Magn Magn Mater 212(1–2):175–177
48. Sugimoto S, Haga K, Kagotani T, Inomata K (2005) Microwave absorption properties of Ba M-type ferrite prepared by a modified coprecipitation method. J Magn Magn Mater 290(2):1188–1191
49. Heck C (1974) Magnetic materials and their application. Butterworths, London, pp 511–517

50. Su H, Tang X, Bai F, Zhang H, Jing Y (2014) Low-loss Magneto-dielectric materials: Approaches and Developments. J Electron Mater 43:299–307
51. Harris VG, Chen Z, Chen Y, Yoon SD, Sakai T, Gieler A, Yang A, He Y, Ziemer KS, Sun NX, Vittoria C (2006) J Appl Phys 99(8):08M911
52. Bae S, Hong YK, Lee JJ, Jalli J, Abo GS, Lyle A, Nam IT, Seong WM, Kum JS, Park SH (2009) New synthetic route of Z-type (Ba$_3$Co$_2$Fe$_{24}$O$_{41}$) Hexaferrite Particles. IEEE Trans Magn 45(6):2557–2560
53. Ozgur U, Alivov Y, Morkoc H (2009) Microwave ferrites, part1: fundamental properties. J Mater Sci: Mater Electron 20:789–834
54. Wu YP, Li ZW, Chen LF, Wang SJ, Ong CK (2004) Effect of doping SiO$_2$ on high frequency magnetic properties for W-type barium ferrite. J Appl Phys 95(8):4235
55. Jeong J, Cho KW, Hahn DW, Moon BC, Han YH (2005) Synthesis of Co$_2$ Z Ba-ferrites. Mater Lett 59(29):3959–3962
56. Zhang H, Li L, Zhou J, Yue Z, Ma Z, Gui Z (2001) Microstructure characterization and properties of chemically synthesized Co$_2$ Z hexaferrite. J Eur Ceram Soc 21(2):149–153
57. Nakamura T, Hankui E (2003) Control of high- frequency permeability in polycrystalline (Ba,Co)-Z-type hexagonal ferrite. J Magn Magn Mater 257(2):158–164
58. Tachibana T, Nakagawa T, Takada Y, Shimada T, Yamamoto T (2004) Influence of ion substitution on the magnetic structure and permeability of Z-type hexagonal Ba-ferrites: Ba$_3$Co$_{2-x}$Fe$_{24+x-y}$Cr$_y$O$_{41}$. J Magn Magn Mater 284:369–375
59. Matters-Kammerer M, Mackens U, Reimann K, Pietig R, Hennings D, Schreinemacher B, Mauczok R, Gruhlke S, Martiny C (2006) Material properties and RF applications of high k and ferrite LTCC ceramics. Microelectron Reliab 46(1):134–143
60. Li ZW, Wu YP, Lin GQ, Chen LF (2007) Static and dynamic magnetic properties of CoZn substituted Z-type barium ferrite Ba$_3$Co$_x$Zn$_{2-x}$Fe$_{24}$O$_{41}$ composites. J Magn Magn Mater 310(1):145–151
61. Kracunovska S, Töpfer J (2009) Preparation, thermal stability and permeability behaviour of substituted Z-type hexagonal ferrites for multilayer inductors. J Electroceram 22:227–232
62. PiresJúnior GFM, Rodrigues HO, Almeida JS, Sancho EO, Góes JC, Costa MM, Denardin JC, Sombra ASB (2010) Study of the dielectric and magnetic properties of Co2Y, Y-type hexaferrite (Ba$_2$Co$_2$Fe$_{12}$O$_{22}$) added with PbO and Bi2O3 in the RF frequency range. J Alloys Compd 493(1):326–334
63. Iqbal MJ, Ashiq MN, Hernández-Gómez P, Muχñoz JMM, Cabrera CT (2010) Influence of annealing temperature and doping rate on the magnetic properties of Zr-Mn substituted Sr-hexaferrite nanoparticles. J Alloys Compd 500(1):113–116
64. Zi ZF, Liu HY, Liu YN, Fang L, Liu QC, Dai JM, Zhu XB, Sun YP (2010) Magnetic properties of c-axis oriented Sr$_{0.8}$La$_{0.2}$Fe$_{11.2}$Co$_{0.2}$O$_{19}$ ferrite film prepared by chemical solution deposition. J Magn Magn Mater 332(22):3638–3641
65. Chen Z, Yang A, Mahalingam K, Averett KL, Gao J, Brown GJ Vittoria C, Harris VG (2010) Structure, magnetic and microwave properties of thick Ba-hexaferrite films epitaxially grown on GaN/Al$_2$O$_3$ substrates. Appl Phys Lett 96(24):242502 (2010)
66. Kim YJ, Kim SS (2010) Magnetic and microwave absorbing properties of Ti and Co substituted M- hexaferrites in Ka-band frequencies (26.5-40GHz). J Electroceram 24:314–318
67. Wang LX, Song J, Zhang QT, Huang XG, Xu NC (2009) The microwave magnetic performance of Sm^{3+} doped BaCo$_2$Fe$_{16}$O$_{27}$. J Alloys Compd 481(1):863–866
68. Wang X, Ren T, Li L, Gui Z, Su S, Yue Z, Zhou J (2001) Synthesis of Cu modified Co$_2$ Z hexaferrite with planar structure by a citrate precursor method. J Magn Magn Mater 234(2):255–260
69. Wang X, Li L, Yue Z, Su S, Gui Z, Zhou J (2002) Preparation amd magnetic characterization of the ferroxplana ferrites Ba$_3$Co$_{2-x}$Zn$_x$fe$_{24}$O$_{41}$. J Magn Magn Mater 246(3):434–439
70. Vara Prasad BBVS (2015) Effect of indium substitution on the electrical and magnetic properties of Ni-Zn ferrite. J Theor Appl Phys 9:267–272
71. Parvatheeswara B, Rao KH (2005) Distribution of In^{3+} ions in indium substituted Ni-Zn-Ti ferrites. J Magn Magn Mater 292:44–48

72. Lakshman A, Rao KH, Mendiratta RG (2002) Magnetic properties of In^{3+} and Cr^{3+} substituted Mg-Mn ferrites. J Magn Magn Mater 250:92–97
73. Ghosh S, Nambissan PMG, Bhattacharya R (2004) Positron annihilation and Mossbauer spectroscopic studies of In3+ substitution effects in bulk and nanocrystalline $MgMn_{0.1}Fe_{1.9-x}InxO_4$. Phys Lett A 325(3):301–308
74. De Fazio E, Bercoff PG, Jacobo SE (2011) Electromagnetic properties of manganese -zinc ferrite with lithium substitution. J Magn Magn Mater 323(22):2813–2817
75. Jacobo SE, Bercoff PG (2016) Structural and electromagnetic properties of yttrium-substituted Ni-Zn ferrites. Ceram Int 42(6):7664–7668
76. Amer MA, Hemeda OM, Olofa SA, Henaish MA (1994) Thermal properties of the ferrite system $Co_{0.6}Zn_{0.4}CuxFe_{2-x}O_4$. Appl Phys Comm 13(3–4):255–263
77. Reddy PV, Seshagiri Rao T (1982) Dielectric behaviour of mixed Li-Ni ferrites at low frequencies. J Less-Common Met 86:255–261
78. Jacobo SE, Fano WG, Razzitte AC (2002) The effect of rare earth substitution on the magnetic properties of $Ni_{0.5}Zn_{0.5}MxFe_{2-x}O_4$ (M: rare earth). Phys B 320(1–4):261–263
79. Chen N, Gu M (2012) Microstructure and microwave absorption properties of Y-substituted Ni-Zn ferrites. Open J Metal 2(2):37–41
80. Thakur A, Mathur P, Singh M (2007) Ultra low loss soft magnetic nanoparticles for applications up to S-band. J Phys Chem Solids 68(3):378–381
81. Sharma S, Daya KS, Sharma S, Singh M (2013) Ultra low loss soft magnetic nanoparticles for applications up to S-band. Applied Phys Lett 103(11):112402
82. Verwey EJW, De Boer JH (1936) Cation arrangement in a few oxides with crystal structures of the spinel type. Recl Trav Chim Pays-Bas 55:531
83. Wagner KW (1913) The theory of incomplete dielectricity. Ann Phys 345:817–855
84. Tsutaoka T, Ueshima M, Tokunaga T, Nakamura T, Hatakeyama K (1995) Frequency dispersion and temperature variation of complex permeability of NiZn ferrite composite materials. J Appl Phys 78(6):3983
85. Sharma S (2016) Ph.D. thesis: Synthesis and characterization of magnetic nanoparticles for antenna applications
86. Sharma S, Daya KS, Sharma S, Singh M (2015) Sol-gel auto combustion processed soft Z-type hexa naoferrites for microwave antenna miniaturization. Ceram Int 41(5):7109–7114
87. Shaikh PA, Kambale RC, Rao AV, Kolekar YD (2010) Structural, magnetic and electrical properties of Co-Ni-Mn ferrites synthesized by co-precipitation method. J Alloys Compd 492(1–2):590–596
88. Koop CG (1951) On the dispersion of resistivity and dielectric constant of some semiconductors at audio frequencies. Phys Rev 83:121
89. Gama AM, Rezende MC, Dantas CC (2011) Dependence of microwave absorption properties on ferrite volume fraction in MnZn-ferrite/rubber radar absorbing materials. J Magn Magn Mater 323(22):2782–2785

Wet Chemical Synthesis and Processing of Nanoferrites in Terms of Their Shape, Size and Physiochemical Properties

Sarveena, Gagan Kumar, Neha Kondal, Mahavir Singh, and Surender K. Sharma

Abstract Nanoferrites are found to showcase superior and substantially distinct properties due to the ease with which they can be synthesized and modified chemically. The nanoparticles are synthesized by various methods classified primarily into two categories: top-down and bottom-up methods. Wet chemical synthesis methods offer unlimited control over size distribution and shape of nanoparticles and provide the opportunity of scale-up for production of nanomaterials in bulks for practical application. This chapter covers sol-gel, solvothermal, co-precipitation, thermal decomposition and microwave-assisted methods for the production of nanoferrites. A variety of nanoferrites and its composites with remarkable properties can be synthesized by these methods mentioned in this chapter.

Keywords Nanoferrites · Bottom-up approach · Thermal decomposition · Sol-gel · Ethylene glycol

1 Introduction

Nanoferrites enriched with multifunctional properties have emerged as forefront materials due to their promising applications in wide arenas like nano-electronics, communication technology, magnetic devices, microwave devices, biomedicine, material engineering, wastewater treatment, astronomy and environmental protection [1]. To explore the wide range of applications of nanoferrites, one of the most indispensable aspects is to comprehend many possible synthesis techniques to discover the optimum conditions to produce application oriented nanoparticles (NPs) [2]. Many

Sarveena (✉) · G. Kumar · N. Kondal
Department of Physics, Chandigarh University, Gharuan, Mohali, Punjab, India

M. Singh
Department of Physics, Himachal Pradesh University, Shimla, HP 171005, India

S. K. Sharma (✉)
Department of Physics, Universidade Federal de Marahano, Sao Luis, Brazil
e-mail: surender.sharma@cup.edu.in

Department of Physics, Central University of Punjab, Bathinda 151401, India

methods are employed to advance the properties, reproducibility and to shrink the production costs. The top-down and bottom-up methodologies are the two universal approaches employed to make NPs. Two methods are distinguished on the basis of starting material of nanoparticle preparation. In top-down methods, the bulk material is used as starting material, and particle size is reduced to nano range by using different processes [3]. Both top-down and bottom-up synthesis techniques have their own merits and demerits, and the bottom-up method is simple, scalable and constructive approach of NPs synthesis. Bottom-up methods are based on wet chemical synthesis which provides better control over morphology of the resulting NPs.

The wet chemical route has evolved as most talented method due to its reasonable cost, reproducibility and efficiency to produce high yield nanoferrites [4]. This method helps to control and tune various parameters like surfactant, type of precursor, pH temperature and concentration of substrate. The most commonly used wet or liquid phase-based chemical methods for synthesis of metal oxide nanoparticles are sol-gel, thermal decomposition, solvothermal, reverse micelle, microwave-assisted method, co-precipitation and flow synthesis [5]. This chapter will mainly cover sol-gel, solvothermal, co-precipitation, thermal decomposition and microwave-assisted hydrothermal method.

2   Sol-gel Method

Sol-gel method also called as sol-gel auto-ignition/combustion/auto-combustion method is a widely used to make a range of nanomaterials. It offers various advantages such as low crystallization temperature, possibility of shape and size control, which provide final product with better chemical homogeneity [6, 7]. The synthesis in sol-gel method takes place in two steps; first is the synthesis of sol followed by gel formation. Cross-linkage of sol results in the formation of gel structure. The method develops its name due to formation of a gel from the sol. The sol is comprised of dispersed colloidal suspension of nanoparticles in a solvent, and gel consists of a rigid network. The interactions between colloidal nanoparticles are conquered by Van der Waals forces and undergo Brownian motion in the liquids. These solutions can be used to make the polymers or particles from which can be used to synthesize the ceramic materials [8]. This method involves mainly five steps; hydrolysis, polycondensation, aging, drying and thermal decomposition [9]. Different processing techniques are employed to synthesize the different materials like powder, films, dense ceramics, bulk and nanoparticles.

Step 1 Hydrolysis
Hydrolysis process takes place in either water or alcohols. It is identified as aqueous sol-gel route if water is used as reaction medium and non-aqueous sol-gel route if the organic solvent is used as reaction medium. An acid or a base helps in the process of hydrolysis. In hydrolysis reaction, the OH^- ion is involved to the metal ions (M), as in the reaction [8].

$$M(OR)_4 + H_2O \rightarrow HO - M(OR)_3 + ROH \tag{1}$$

where M = metal; R = alkyl group (C_nH_{2n+1}).

Completion of the reaction depends upon the amount of water and catalyst; the hydrolysis is complete when OH replaces the all OR.

$$M(OR)_4 + 4H_2O \rightarrow M(OH)_4 + 4ROH \tag{2}$$
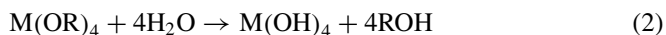
During the condensation, if the amount of water is high, it produces a more branched and polymerized structure. Completion of hydrolysis depends upon the various parameters like the amount of water and the presence of hydrolysis catalysts such as acetic acid or hydrochloric.

Step 2 Condensation

The condensation is accompanied by the production of small water or alcohol molecule along with linkage of metal oxide and polymer networks which grow to colloidal dimensions in the liquid state. Partial hydrolysis may also stop the reaction and results in intermediate species $M(OR)_{4-x}(OH)_x$. Two intermediate species can combine in a condensation reaction, for example,

$$(OR)_3M - OH + HO - M(OR)_3 \rightarrow (OR)_3M - O - M(OR)_3 + H_2O \tag{3}$$
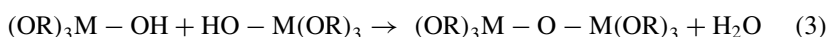
Condensation or polycondensation increases the viscosity of solvent and results in formation of porous structure which helps to maintain the liquid phase known as gel. Gels are noncrystalline and can be crystallized by appropriate heat treatment. The size and the bonding between the colloidal particles are highly dependent upon the pH of solution and precursor [9].

Step 3 Aging

Aging brings the changes in the properties and structure and of the gel. Mother solution is used to age the gel which helps in increasing the gel strength to resist cracking during drying. In aging process, the polycondensation and reprecipitation of the gel network take place, which results in increase of thickness and decreases of porosity between colloidal particles [10].

Step 4 Drying

The solvent is detached from pore network of gel by the process of aging. In this process of drying, the challenge is to keep the structure intact by preventing the cracking and subsequent shrinkage of the dried gel during the removal of water and organic components. There are diverse drying processes: ambient pressure drying/subcritical drying, supercritical drying and freeze drying [9, 11].

An alternative drying process known as supercritical drying process helps to preserve the gel structure and prevent the presence of any intermediate vapor–liquid transition and surface tensions in the gel pores, preventing the pore collapsing of the

gel structure. In freeze-drying process, the solvent is removed by when the temperature of the gel is decreased below, the crystallization temperature of the solvent and cryogel is obtained. Ambient pressure/subcritical drying is popular as it is resourceful and significantly inexpensive. In the ambient pressure, drying of gel takes place at ambient pressure and is dependent upon the processes of surface modification [12].

Step 5

In the final step, the residues and water molecules from the anticipated sample are removed by thermal treatment or calcinations. The calcination temperature plays crucial role in controlling the density of the material [9].

In the sol-gel process, the starting material used are nitrates precursor of the essential metal ions, an appropriate chelating agent (or fuel), namely as urea/glycine/citric acid, as they are effortlessly soluble in water. In general, the ratio of metal nitrate to citrate acid (1: x) used is 1:3. The flowchart of the method is given schematically in Fig. 1.

There are various synthesis parameters like type of fuel/chelating agent, ratio of fuel to nitrate, and pH which affects the properties of prepared nanoferrites. It is

Fig. 1 Flowchart of the sol-gel auto-combustion method
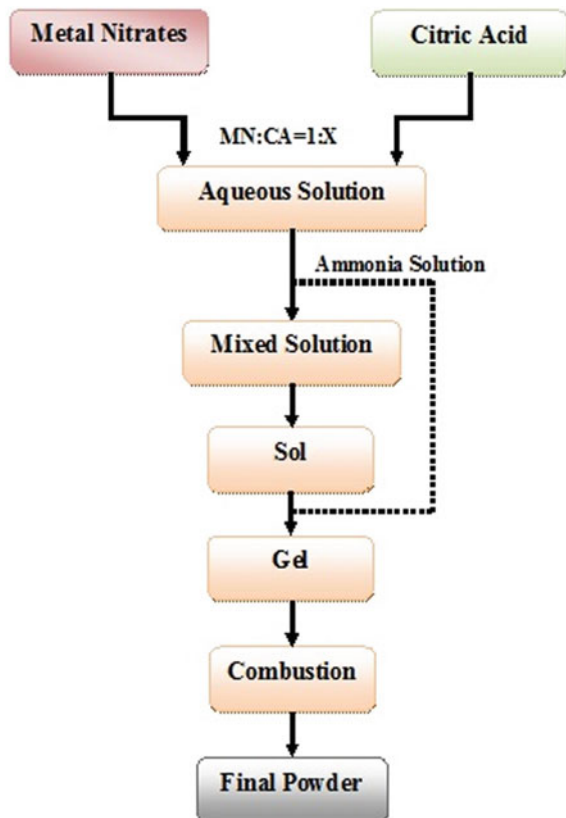
very important to choose the right fuel to nitrate ratio because it affects the magnetic properties and size of the nanoferrites. Nasir et al. [13] synthesized the high-purity Zn-doped $NiFe_2O_4$ nanoparticles without water and surfactants (WOWS) method and studied the effect of molar ratio of ethylene glycol to metal salts. The molar ratio of 14:1 of ethylene glycol to metal salts helped in dissolving the salts uniformly. Single-phase spinel cubic structure with spherical shapes was obtained.

The another parameter which influences the combustion rate and the morphology of nanoparticles is the pH value. Aurelija et al. [6] have reported the synthesis of the different nanoferrites by an aqueous sol-gel procedures. At low sintering temperature (up to $1000\,°C$), single-phase metal ferrites were obtained. The particle size was found to depend upon the nature of transition metal ($CoFe_2O_4 > ZnFe_2O_4 > NiFe_2O_4$).

Sagar et al. [14] synthesized $CoDy_{0.1}Fe_{1.9}O_4$ nanoparticles by sol-gel-based auto-combustion technique at diverse pH values from 2.5 to 10. The combustion rate was found to increase with increasing pH 2.5–7.5, afterward decreased for pH = 10. The best results were obtained at pH = 7.5, where the combustion rapidly propagated to form ferrite powders and single-phase nanoferrites was obtained. The particle size was found to increase with increasing pH till 7.5 and further increase in pH value resulted in decrease of particle size. Pradeep et al. [15] synthesized the $NiFe_2O_4$ nano-ferrites by sol-gel auto-combustion technique at pH values of 7 and 8 and reported the pH 8 which was the optimum for the preparation of the $NiFe_2O_4$ nanoferrites. The formation of the single-phase cubic spinel nanoparticles with a high degree of crystallinity was obtained at a pH of 8, whereas $NiFe_2O_4$ nanoferrites prepared at pH 7 showed the presence of impurity phases.

Seyedeh et al. [16] reported synthesis of $CoFe_2O_4$ nanoparticles by sol-gel auto-combustion in the presence of ethylene glycol (EG) and agarose as complexing agents and analyzed their influence on the structural and magnetic properties. Figure 2 shows the field emission scanning electron microscopy images of the prepared $CoFe_2O_4$ nanoparticles samples A (agent-free sample) and B (with chemical reagents/Nitrates
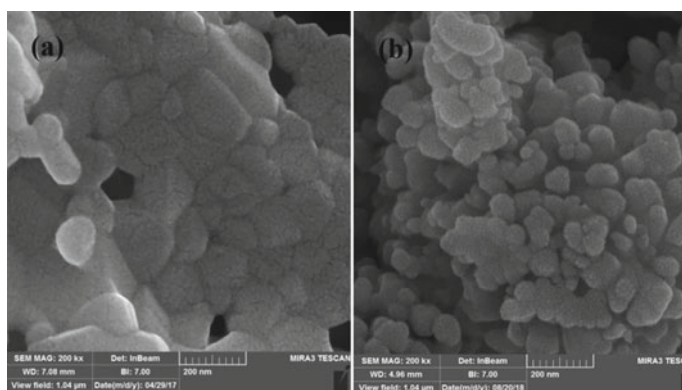
Fig. 2 FE-SEM images of **a** sample A (agent-free sample) and **b** sample B (with chemical reagents/Nitrates = 0.25). Reproduced with permission from SM Hashemi et al. [16]

= 0.25). In sample B, the nanoparticles are less agglomeration as compared with sample A. The average crystallite size and agglomeration between nanoparticles were found to decrease, whereas the coercivity and saturation magnetization enlarged by the appropriate addition of EG and agarose.

The properties of the nanoferrites are affected by the combustion process which depends upon the fuel or chelating agents. Dumitrescu et al. [17] synthesized $NiFe_2O_4$ nanoferrite by the sol-gel auto-combustion method, using cellulose different chelating/fuel agents; cellulose–citric acid mixture, hexamethylenetetramine, citric acid, tartaric acid, glycine and urea. Effect of these chelating/fuel agents on combustion process, and hence, on the structure, morphology and catalytic activity was studied. The combustion process takes longer time when cellulose–citric acid mixture, citric acid, tartaric acid and cellulose are used, whereas in the case of urea, it completes in 2 min. Glycine and hexamethylenetetramine induce instantaneous and an extremely violent combustion process. Higher catalytic activity was observed for the nanostructured $NiFe_2O_4$ obtained by hexamethylenetetramine, urea and tartaric acid as chelating/fuel agents. Tamara Slatineanu et al. [18] analyzed the impact of the chelating/combustion agents on structural and magnetic properties of $ZnFe_2O_4$. Six chelating/combustion agents: citric acid, glucose, egg white, tartaric acid, glucose, glycine and urea were used to obtain monophase Zn nanoferrite by sol-gel auto-combustion method. The intensity of the reaction and thermal treatment duration is influenced by the nature of fuel, which affects the structural and magnetic properties of zinc nanoferrite. At low calcination temperature (973 K) citric acid, glycine, tartaric acid and egg white can be considered as good chelating/combustion agents to obtain single phase Zn ferrite nanoparticles. Glycine or glucose can be considered as a good candidate to achieve the ferrimagnetic behavior and egg white to obtain the paramagnetic behavior.

3   Solvothermal Method

Solvothermal synthesis method is an interesting variation of the hydrothermal method. Hydrothermal and solvothermal methods are both different with only a small difference and so called depending upon the solvent utilized during the synthesis process. In the hydrothermal method, solvent used is water, whereas in the solvothermal method, organic solvents are used. Different types of organic solvent having high boiling temperature can be used in solvothermal method. It can have higher reaction temperatures than hydrothermal method. In this method, not only acid or bases but also large variety of surfactants are employed to control size, shape, morphology and properties of nanomaterials [19].

The solvothermal synthesis is performed in a sealed container known as autoclave at a temperature exceeding the boiling point of the solvents. The solvent will be automatically generated in high pressure which helps to promote the reaction and enhance the crystallinity of the synthesized nanomaterials. The increase of both the temperature and pressure facilitates the solubility and the reactivity of the

reagents [20]. Since the reactions occur in a sealed autoclave, it is difficult to analyze the growth mechanism of this synthesis process. Experimental conditions highly affect the solvothermal method; hence, the crystallization and growth of particles can be controlled by various process parameters such as concentration of precursors, solvents, surfactants and/or polymers, temperature, pressure and time [21, 22]. Oxides of Group II–VI, III–V and IV, transitional-metal NPs and metal-organic frameworks (MOFs), are prepared by this method [23]. It offers various advantages such as low processing temperature, less energy consumption, simple reaction conditions and short synthesis time which helps in producing highly crystalline nanomaterials and with controlled morphology and size. The precursors which are sensitive to water can be handled in solvothermal process, and the products obtained are free from foreign anions.

Solvothermal synthesis is commonly carried out in a reaction vessel known an autoclave, as shown in Fig. 3 [24]. These autoclaves are fabricated from high strength alloy, such stainless steel, cobalt-based super alloys, nickel, iron, titanium and its alloys, to tolerate the pressure developed during the reaction. In general, the autoclave has an extra beaker, can or tube made of Teflon, gold, platinum or silver a liner which makes them chemically inert vessel for the reaction and also protect them from corrosion. Sometimes, a Bourdon gage is fixed to the autoclaves to directly monitor the pressure, and stirring accessories are used to minimize the concentration gradient. Depending on the degree of autoclave filling, pressures of some hundred bar can be obtained, even at low temperatures. For the reactor selection, the parameters like temperature, pressure and corrosive resistance are the very important. To ensure the safety, it is important to estimate the pressures generated in a sealed container and control it below the strength of martials of autoclave [23].

Recently, solvothermal method has received much attention for its improvement with new mixing technologies such as microwave solvothermal synthesis methods
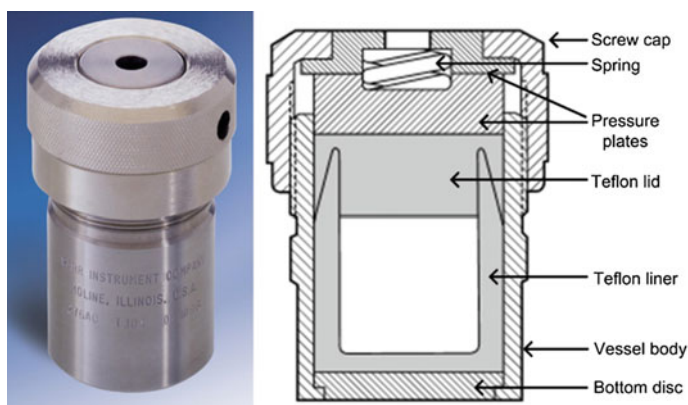
Fig. 3 Autoclave (acid digestion vessel). Reproduced with permission from Nunes et al. [24]

which are used in different systems. Synthesis in solvothermal method is a crystallization process directly from solutions that involve two steps: crystal nucleation and subsequent growth. The compound dissociates in solution to produce the precursor atoms, and then, precipitation occurs to form the nanocrystals. In precipitation process, the nucleation is followed by a crystal growth [24]. The second step plays crucial role in controlling the size and shape of the NPs by controlling processing variables, such as reactant concentrations, temperature, pH and additives.

The crystals growth takes place sequentially or concurrently by a series of methods which involve the incorporation of growth units. The different procedures can be largely categorized into four major steps: transport of units through solution, addition of units to the surface, movement of units on the surface and addition of units to growth sites.

Wang et al. [25] reported fabrication of $NiFe_2O_4$ nanoparticles by modest solvothermal method using EG as solvent and NaAc as electrostatic stabilization. The diameter of the NPs was controlled from 6 to 170 nm by fine-tuning the various experimental parameters such as initial concentration of the reactants, reaction duration, amount of protective reagents and the type of acetates. EG is the high-boiling point solvent (197.5 °C) and is preferred for variable-temperature synthesis, which is desirable to control the reaction rate and to obtain products with enhanced crystallinity. It served not only as solvent, reducing agent and complexing agents for the nickel (α) and iron(β) reactants but also as stabilizing agents to obtain the nanocrystalline nickel ferrite. Agglomeration of particle was prevented by using NaAc as electrostatic stabilizer.

Wen et al. [26] synthesized the Dy^{3+} doped Co–Ni–Zn ferrites ($Co_{0.5}Ni_{0.25}Zn_{0.25}Dy_xFe_{2-x}O_4$ ($0.0 \leq x \leq 0.24$) at altered temperature using the solvothermal process in glycol–water solution. The prepared nanoparticles exhibit rod-like morphology at higher temperature (900 and 1000 °C) and composed of many end-connected spherical particles. This phenomenon was observed due to the glycol which interfere the hydrogen bonding and cohesive forces between water molecules and also lowers surface tension and improves wettability on a hydrophobic surface. Certain oxalates crystal facets became more stable, results in the synthesis of higher aspect ratio oxalates particles. $Co_{0.5}Ni_{0.25}Zn_{0.25}Dy_{0.16}Fe_{1.84}O_4$ composition of Co–Ni–Zn ferrites and calcination temperatures of 1000 °C were found to be appropriate for high- act as a reducindensity data storage devices.

There are various publications on the synthesis of nanoferrites by solvothermal synthesis [27–29]. The choices of solvent, surfactant, temperature affect the physiochemical properties of nanoparticles. Solvothermal processes are characterized by mild temperature conditions. Gérard Demazeau [30] has reviewed various factors which affect the solvothermal synthesis process in detail. Solvothermal synthesis is used for scalable production with controlled size and shape.

4 Thermal Decomposition Method

A chemical procedure in which metal precursor is heated at high refluxing temperatures in high-boiling point organic solvents is known as thermal decomposition. Among all wet chemical methods, the thermal decomposition method is an innovative, simple, convenient and low-cost method to synthesize stable monodisperse NPs with high purity. This method offers many advantages such as no need of solvent, no particular stabilizing agent (stabilizer), low energy consumption, control of process conditions, simple reaction technology, high yield and synthesis at low temperature [31, 32]. The force of reaction with the ligands in coordination compounds and nature of metallic ion impacts the pressure and temperature at which thermal decomposition method occurs.

Thermal decomposition method has also been used for those systems which use high boiling point solvents where one of the reactants acts as a reducing agent both in the presence and absence of a polyol [33]. Several parameters such as nature and amount of organometallic compounds, types of surfactants, reaction time, temperature, stabilizers, reactants concentration and capping agents (surfactants) can alter the structure, morphology, size and hence the properties of the prepared nanoferrites [34, 35]. The narrow size distributions of nanoparticles can be further improved by subsequent precipitation, re-dispersion and centrifugation [36].

The appropriate precursors for this method are mainly organometallic compounds, metal salts, metal ion complexes or chelates. Metal acetylacetonates $[M(acac)_n]$ where M: transition metal such as Fe, Mn, Co, Ni, Cr and $n = 2$ or 3, cupferronates (M_xCup_x) where cup: N nitrosophenylhydroxylamine $(C_6H_5N(NO)O)$, carbonyls, for example, iron pentacarbonyl $[Fe(CO)_5]$, etc., are most commonly used organometallic compounds. The surfactants which are generally used in this method are as follows: oleic acid, oleylamine, fatty acids and hexadecylamine. Diphenyl ether, octylamine, diethylene glycol, octyl ether, hexadecanediol, 1-octadecene and 1-hexadecene are more often used as high-boiling point organic solvents. The polymers or macromolecules such as polyvinyl alcohol (PVA), oleic acid (OA), triphenylphosphine (TPP), polyethylene glycol (PEG) and oleylamine (OAm)(C18H37N) can also be used as capping agents [37, 38]. The capping agents prevent the uncontrolled particle aggregation by avoiding interaction of NPs with one another and make the NPs biocompatible to be used in various biomedical applications. The ratios of the surfactant, organometallic compounds and solvent are crucial parameter to obtain the NPs with controlled morphology and size.

The synthesis setup for thermal decomposition process involves of a three-neck round-bottom flask which is mounted on a heating/stirring plate equipped with condenser. During the reaction, inert atmosphere is maintained in order to prevent any unwanted side reactions (e.g., oxidation of oleic acid) by the continuous flow of nitrogen or argon gas. A thermometer mounted on the heating/stirring plate which is immersed in silicon oil's beaker can be used to monitor the temperature.

Thermal decomposition method is generally used to synthesize variety of nanostructures including metal oxides, metals and sulfides, etc. Varieties of nanoferrites,
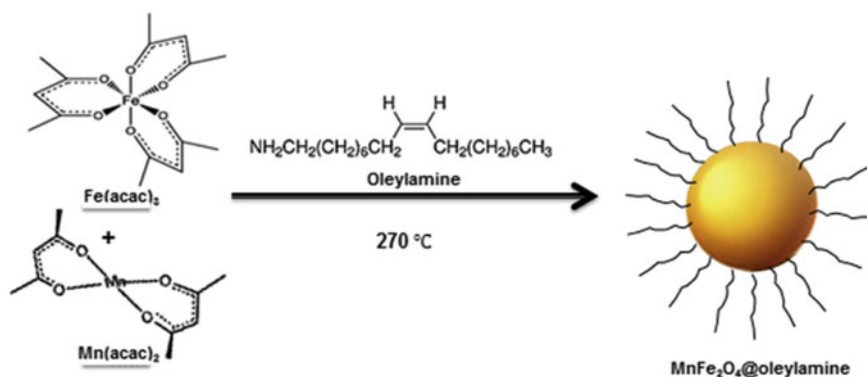
Fig. 4 Synthetic process to obtain $MnFe_2O_4$ Oleyl amine capped nanoparticles. Reproduced with permission from Singh et al. [39]

composites and hybrid system with different morphologies as per the applications have been synthesized using this method. Singh et al. [39] synthesized $MnFe_2O_4$ nanoferrites by thermal decomposition method passing inert gas (N_2) and used oleylamine to control the size/shape of $MnFe_2O_4$ nanoparticles. Figure 4 shows the synthetic procedure to obtain manganese ferrite ($MnFe_2O_4$) Oleyl amine capped nanoparticles.

The molar ratio of 3:3:5 of oleic acid, oleylamine and 1,2-hexadecandiol was used. The oleic acid-acetylacetonate solution was stabilized by using oleylamine as a surfactant. Crystalline $MnFe_2O_4$ nanoferrite with pure cubic spinel structure was obtained with spherical shape and the average crystallite size of 22.7 nm.

Mahhouti et al. [40] studied the role of reagents such as oleic acid or oleylamine and hexadecanediol on the synthesis of $CoFe_2O_4$ nanoparticles by decomposition of acetylacetonate precursors at high temperatures. Highly monodisperse $CoFe_2O_4$NPs which are nearly spherical were obtained. These NPs were surfaced by organic molecules and were stabilized in an organic solvent. The fine dispersion of the NPs in hexane was accomplished with the help of surfactants. Hexadecanediol originated the reaction by stimulating the decomposition of the metal precursor's acetylacetonates. The equation of the reaction is as follows

$$Co(C_5H_7O_2)_2 + Fe(C_5H_7O_2)_3 \rightarrow CoFe_2O_4 + CH_3COCH_3 + CO_2 \qquad (4)$$

Equation shows that the thermal decomposition of acetylacetonates of cobalt and iron produced $CoFe_2O_4$ nanoparticles with acetone and CO_2 as by-products in the presence of oleic acid, oleylamine and 1,2-hexadecanediol. The benzylether proved to be a appropriate solvent for this process due to its higher boiling temperature (298 °C) than the decomposition temperature of precursors.

In our work, Sarveena et al. [41] synthesized the iron oxide and Au–iron oxide nanocomposites by a thermal decomposition method by passing pure oxygen at different temperatures (125–250 °C). A organized improvement in the morphology

Fig. 5 HRTEM images of Au–iron oxide nanoparticles (AIONPs) oxidized at **a** 125 °C, **b** 150 °C, **c** 200 °C and **d** 250 °C for 30 min during cooling from 315 °C [41]
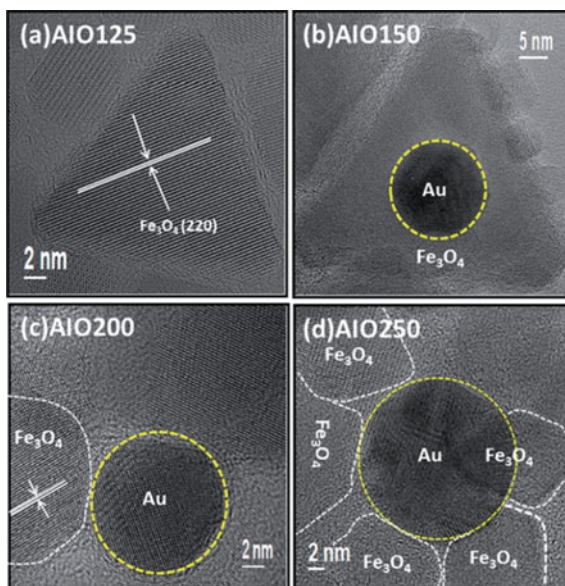
was observed by tuning the reaction time as well as the oxidizing temperatures. Figure 5 shows the HRTEM images of Au–iron oxide nanoparticles (AIONPs) oxidized at (a) 125 °C, (b) 150 °C, (c) 200 °C and (d) 250 °C for 30 min during cooling from 315 °C. Morphology of the particles was found to change with increasing oxidization temperature, and fully grown core–shell heterostructures were obtained at higher oxidation temperature. Magnetic properties showed strong dependence on particle morphology (or shape anisotropy). Prepared iron oxide nanoparticles remained intact showing no aging effect. Hence, thermal decomposition method provides long-term stabilization to the nanoparticles so that they can be used in various applications. The calorimetric study shows the potential of these nanoparticles for hyperthermia application.

Oleic acid and ethylene glycol were used as capping agent and solvent, respectively, in the synthesis of $NiFe_2O_4$ nanoparticles by a thermal decomposition [42]. Ethylene glycol resulted in well-dispersed $NiFe_2O_4$ nanoparticles and oleic acid controlled the morphology and size. Spherical-shaped single nanocrystalline $NiFe_2O_4$ nanoparticles with an average particle diameter of 12.3 ± 0.69 nm were obtained.

5 Co-precipitation Method

Co-precipitation is a well-established classical method for preparing of nanoferrites and their composites. In this method, precipitation of NPs takes place a continuous

fluid solvent [43]. Various advantages of co-precipitation method are rapid synthesis, low cost, simple process, control in pH value, low-temperature synthesis, control over particle crystalline size morphology and composition [44–46]. In co-precipitation process, nucleation, growth, coarsening and/or agglomeration processes take place simultaneously [47]. Morphology and size can be controlled by controlling the rates of nucleation and growth during synthesis or by annealing the sample at higher temperature.

Co-precipitation method can be summed up in three steps [48]:

1. solution preparation in the liquid phase with chemical composition
2. thermal treatment that directly affects the crystallinity, structure and morphology of the NPs
3. adding a precipitation agent (e.g., NaOH, NH$_4$OH, Na$_2$CO$_3$, or urea).

For synthesis of nanoparticles of metal ferrite, the aqueous solutions of Fe(III) and M(II) salts (where M(II) is a d-block transition metal) are usually mixed in an alkaline solution which produces the magnetic precipitate. The chemical reaction which takes place during the co-precipitation method can be described as [45]:

$$M^{2+}(aq) + 2Fe^{3+}(aq) + 8HO^-(aq) \rightarrow MFe_2O_4(s) + 4H_2O(l) \qquad (5)$$
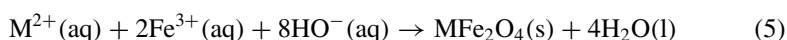
Inorganic metal salt, such as chloride and nitride, is dissolved in water. The metal cations are added to basic solutions, such as NaOH or NH$_4$OH, hydrolyzed species condense, which are then washed, filtered, dried and calcined to obtain the final product [43].

In order to obtain the size- and shape-controlled NPs, it is important to control the various reaction parameters such as the type of precursors, molarity of the precursors, pH value, reaction temperature, ionic strength, type or concentration of alkaline agent and if the process is homogenous or heterogeneous [45, 49]. Since there is a tendency of agglomeration which can affect the size distribution, the use of various organic additives (such as gluconic, citric or oleic acid) or polymer surface complexing agents (carboxydextran, dextran, starch or polyvinyl alcohol) during the formation of nanoparticles help in controlling the size distribution.

During the chemical reactions in co-precipitation method, the pH of the precursor solution is a important factor which control the particle size, morphology and hence the their properties [50–53]. Lamdab et al. [54] synthesized the MnFe$_2$O$_4$ nanoparticles by a co-precipitation method with varying pH values of 9.0, 9.5 and 10.0 and analyzed pH effect on its adsorption properties. MnFe$_2$O$_4$ nanoparticles synthesized at pH 10.5 exhibit highest efficiency of RhB removal which was attributed to large pore size and surface charge of MnFe$_2$O$_4$ nanoparticles. Iranmaneshs et al. [55] synthesized NiFe$_2$O$_4$ nanoferrites by one-step capping agent-free co-precipitation route and analyzed the effect of pH value on its structural, optical and magnetic properties. The particle size increased with increasing pH from 9 to 11 which may be due to the large ions in reaction medium which decreases the surface by lowering the interfacial tension. Increase in pH increased the magnetization and band gap value of Ni ferrite nanoparticles which is the indication of pronounced surface effects in

the small nanoparticles. The reaction temperature affects the crystallite size of nano-ferrites. When reaction temperature increases, the rate of nucleation increases which improves the crystallite size at higher reaction temperatures. Hence, the crystallite size of nanoferrites increased with increasing the reaction temperature [56–62].

Surfactant additives have shown great impact on the dispersion property, purity, crystallite size and agglomeration of the particles [63–66]. The addition of surfactant has shown great potential in controlling and improving nucleation and growth by creation of polarization on the surface of the NPs, which restrict coalescence process of the first nuclei resulting in improvement of crystallite size [67]. Lu et al. [68] prepared the nano-strontium ferrite ($SrFe_{12}O_{19}$) by co-precipitation method using different types of dispersants such as cationic surfactant (CTAB), anionic surfactant (SDS) and nonionic surfactant (PEG-6000). These surfactants helped in lowering the size of aggregates and improving the dispersibilty of the strontium ferrite nanoparticles owing to the steric hindrance and stabilization properties of surfactants. Figure 6 shows the TEM micrographs of $SrFe_{12}O_{16}$ powders: (a) without surfactant, (b) SDS as surfactant, (c) CTAB as surfactant and (d) PEG-6000 as surfactant. Severe aggregation of sample without surfactant is seen in Fig. 6a while in Fig. 6b–d, when surfactant is used, particles with little aggregation can be observed.
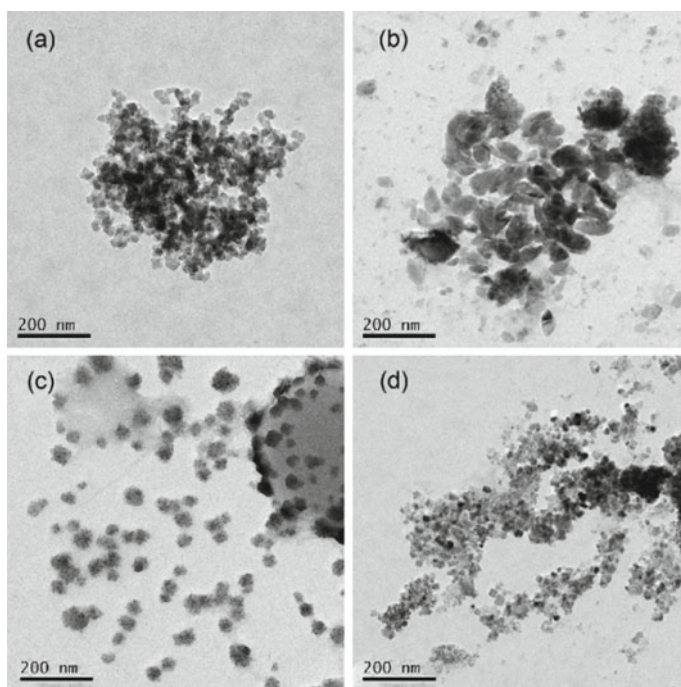
Fig. 6 TEM images of $SrFe_{12}O_{16}$ powders: **a** without surfactant, **b** SDS as surfactant, **c** CTAB as surfactant and **d** PEG-6000 as surfactant. Reproduced with permission from Lu et al. [68]

The particle size is smallest in case of surfactant CTAB, moderate in case of PEG-6000 and poorest in case of SDS. This variation in particle size may be due to different types of charge possessed by these surfactants. The cationic surfactants such as CTAB can be simply absorbed on the surface of the precipitate particles and form a molecular film on the surface of the particles to avoid the aggregation. Macromolecular surfactants (such as PEG) are good water-soluble surfactant and also play certain steric hindrance effect. In anionic surfactant such as SDS, the repulsive force results in poor absorption and aggregation.

6   Microwave-Assisted Method

In the recent past, the microwave-assisted method has revolutionized chemical synthesis and has been successfully applied for nanomaterial synthesis. They have been used to synthesize different inorganic materials such as metallic nanoparticles, semiconductors, amorphous and nanoporous materials, bioceramics, core–shell particles, pure and mixed metal oxides [69–73]. Microwave-assisted synthesis has several advantages over conventional reactions. Generally, the chemical reactions are faster than traditional convection heating methods and penetrate inside the material where heat is generated through direct microwave-material interaction. Microwave-assisted methods provide excellent control over reaction optimization and rapid analogue synthesis, high yield and less side products. It uses less energy and solvent, can selectively heat either the solvent or the precursor molecules for nanomaterials, which is an attractive attribute [47, 74].

The heating is based upon the direct interaction of microwaves at a certain frequency with the charged particles of materials which produces heat by collision or by conduction sensation. The microwave energy changes its polarity in each cycle simultaneously which produces heat by rapid orientation and reorientation of the molecule [75]. Microwave dielectric heating phenomena such as dipolar polarization, ionic conduction mechanisms and interfacial polarization produce heating [75, 76]. Interfacial polarization is a combination of the dipolar polarization and ionic conduction. When the applied field oscillates, the dipole or ion field tends to realign itself with the alternating electric field and molecular friction and dielectric loss results in the heat loss. The amount of heat which is produced during the process is associated with the frequency of the field and how quickly molecules align [69, 74]. The capability of a specific solvent to convert microwave energy into heat at a given frequency and temperature is determined by the loss factor tan δ. This loss factor is expressed as [77]:

$$\tan \delta = \frac{\epsilon''}{\epsilon'}$$

where ϵ'' is dielectric loss and represents the efficiency with which electromagnetic radiation is converted into heat, and ϵ' is the dielectric constant or relative permittivity

and describes the ability of molecules to be polarized by the electric field. For efficient absorption, a reaction medium with a high tan δ value is required which facilitate the rapid heating. The solvents used in microwave heating can be classified on the basis of their loss tangent (tan δ): low (tan δ < 0.1), high (tan δ > 0.5), medium (tan δ ≈ 0.1–0.5) [35]. Solvents having high microwave-absorbing capacity like water and alcohol give high heating rates. Ionic liquids have high ionic conductivity and polarizability which makes them very good microwave-absorbing agents and can be used for the preparation of metal nanostructures.

Microwave-assisted synthesis has been performed in many ways. In early days of microwave-assisted synthesis, domestic household oven has been also used for synthesis as they were easily available and inexpensive. But this type of synthesis poses risk to user and also lack of control in microwave synthesis led to many accidents. One solution to this was to carry out synthesis without solvent. Solvent free approach provides safety by avoiding low boiling solvent. The use of such apparatus cannot be recommended, and it is good to use dedicated apparatus for microwave-assisted synthesis.

Nowadays, for the synthesis, commercially available dedicated microwave reactors are used which have in-built magnetic stirrers, direct temperature control of the reaction mixture with the help of fiber optic probes or infrared (IR) sensors and software that enables online pressure/temperature control by regulating microwave power output. The microwave instruments can be classified into two types: multimode and monomode reactors [78, 79]. They differ from each other in a way that in monomode systems typically only one vessel can be irradiated at a time, whereas in multimode cavities, various reaction vessels can be irradiated simultaneously in multi-vessel rotors (parallel synthesis), and high electromagnetic field densities can be developed inside the cavity causing higher heating rates in monomode systems as compared to multimode system. Figure 7 shows multimode and monomode applicators.

The multimode applicators are generally in the form of rectangular closed metal box called cavity. As the microwaves get reflected from the cavity walls, there exists a large number of resonance modes inside the cavity. The reflections from the cavity walls result in multiple modes of the electromagnetic waves which interact with the
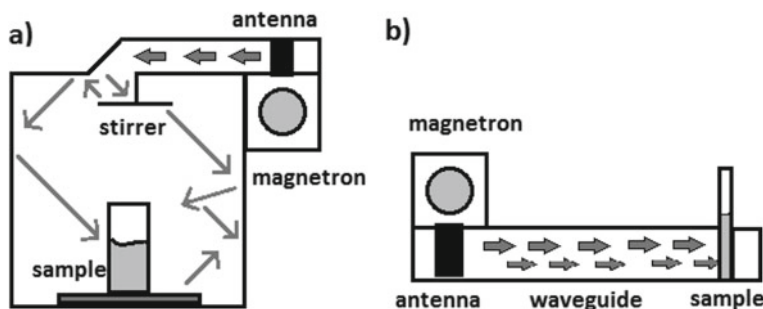
Fig. 7 **a** Multimode microwave applicator and **b** monomode microwave applicator [80]

cavity material (load). The heated material (load) is subjected to a microwave field which is highly non-uniform regardless of the application of a mode stirrer or a rotating disk to support the load. only one mode is present in monomode microwave reactor and is used for small scale synthesis. In the monomode applicators., more stable single-standing wave is generated inside the cavity. Usually, the irradiated material is kept in one of the maxima of the electromagnetic field which implies that their volume and the material load are strictly limited in size [81].

In microwave cavity when reactions are carried out under pressure are benefited from the rapid heating and remote heating of microwave dielectric heating. Multimode cavity microwave can be used when using higher volume, and an alternate approach is to use the continuous flow system. In continuous flow system, the same heat profile can be maintained even for large-scale synthesis. Continuous or stop-flow reactors are available for both single and multimode cavities that enable the synthesis of kilograms of materials by microwave technology where the reaction mixture is passed through a relatively small microwave heated flow cell, which prevents penetration depth problems [82–84]. The rapid transition from laboratory research platforms to industrial research development is possible with these continuous flow processes with the merits of flow synthesis, such as the ability to observe the reaction in real time and make changes to reaction conditions accordingly [85].

Bensebaa et al. [86] reported the preparation of cobalt ferrite nanoparticles by microwave-assisted method under reflux conditions. The synthesis conditions produced stable and above yield particles with an average size of about 5 nm that is much smaller than the critical size for single-domain $CoFe_2O_4$ of about 70 nm. Ahmed Shebl [87] used simple template-free microwave-assisted hydrothermal green synthesis technique to produce manganese zinc ferrite ($Mn_{0.5}Zn_{0.5}Fe_2O_4$) nanoparticles at different temperatures (100, 120, 140, 160 and 180 °C). The prepared manganese zinc ferrite nanoparticles were appropriate for use as fertilizer. The particle size increased with the increase in microwave temperature, and shape of NPs was cubic. As the synthesis temperature was increased, the pore size distribution and surface area of nanoferrites decreased. Nano-fertilizer prepared at 160 °C (T-160) has highest fruit yield of squash per hectare (54.8 and 55.2 t/ha).

Zhenyu et al. [88] prepared $MnZnFe_2O_4$ nanoparticles by low temperature microwave-assisted method. Microwave can accelerate reaction to prepare nanoparticles in short time due its high heating efficiency. In the presence of the microwave, the energy was transmitted directly to the reactants due to localized high temperatures, and more energized molecules were formed rapidly. Average particle size obtained was 10 nm, and longer microwave heating resulted in increased particle size of nanoparticles. The samples which have nanoparticles of small size can absorb more water as compared to those samples prepared at longer heating time.

Manikandan et al. [89] showed that the microwave-assisted synthesis is a quick process. Spinel $Co_xMn_{1-x}Fe_2O_4$ (x = 0.0, 0.2, 0.4, 0.6, 0.8 and 1.0) nanoferrite were synthesized in microwave oven at microwave energy of 2.45 GHz multimode cavity at 850 W in 10 min. The prepared nanoferrites were analyzed for catalytic activity. Chen et al. [90] reported one-step microwave-assisted ball milling method for low-temperature synthesis of $MgFe_2O_4$ nanoferrites. They observed

that the coupling effect of microwave and ball milling plays crucial role in the preparation of the $MgFe_2O_4$ nanoparticles along with the intermediate product $Mg_6Fe_2CO_3(OH)_{16}\cdot3H_2O$. The formation of the final product $MgFe_2O_4$ at low temperature is due the microwave which stimulates the microscopic incorporation of Fe ions into the lattices of magnesium compounds at the sheared interfaces. There are various publications on successful application of microwave-assisted method for the synthesis of nanoferrites and their composites [91–96].

7 Conclusion

This chapter has provided a summary of the various wet chemical synthesis methods for the nanoferrites. Each synthesis technique has its own strengths and limitations. To select, the suitable synthesis technique is of prime importance to prepare the application-oriented nanoferrites. In many applications, the NPs with certain morphologies are preferred; thus, the concept of shape and size-controlled synthesis has been vastly studied. Controlled and large-scale production of nanoferrites require more attention to understand the role of each parameter influencing the synthesis of nanoferrites and hence their properties. Hence, it is very important to discover the optimum conditions to enhance the reproducibility and the quantity of nanoferrites.

References

1. Tsay CY, Chiu YC, Lei CM (2018) Hydrothermally synthesized Mg-based spinel nanoferrites: Phase formation and study on magnetic features and microwave characteristics. Mater 11 2274
2. Dhand C, Dwivedi N, Loh XJ, Ying ANJ, Varma NK, Beuerman RW (2015) Methods and strategies for the synthesis of diverse nanoparticles and their applications: A comprehensive overview. RSC Adv 5:105003
3. Jamkhande PG, Ghule NW, Bamer AH, Kalaskar MG (2019) Metal nanoparticles synthesis: An overview on methods of preparation, advantages and disadvantages, and applications. J Drug Deliv Sci Technol 53:101174
4. Tan C, Zhang H (2015)Wet-chemical synthesis and applications of non-layer structured two-dimensional nanomaterials. Nat Commun 6:7873
5. Nikam AV, Prasad BLV, Kulkarni AA (2018) CrystEngComm 20:5091–5107
6. Gatelyte A, Jasaitis D, Beganskiene A, Kareiva A (2011) Sol-gel synthesis and characterization of selected transition metal nano-ferrites. Medziagotyra 17:302–307
7. Sharifianjazi F, Moradi M, Parvin N, Nemati A, Jafari Rad A, Sheysi N, Abouchenari A, Mohammadi A, Karbasi S, Ahmadi Z, Esmaeilkhanian A, Irani M, Pakseresht A, Sahmani S, Shahedi Asl M (2020) Magnetic $CoFe_2O_4$ nanoparticles doped with metal ions: A review. Ceram Int 46:18391–18412
8. Shirsath SE, Jadhav SS, Mane ML, Li S (2018) In: Klein L, Aparicio M, Jitianu A (eds) Handbook of sol-gel science and technology. Springer, Cham
9. Parashar M, Shukla VK, Singh R (2020) Metal oxides nanoparticles via sol–gel method: a review on synthesis, characterization and applications. J Mater Sci Mater Electron 31:3729
10. Hench LL, West JK (1990) The Sol-gel process. Chem Rev 90:33–72

11. González JA, Andrés JP, López Antón R, De Toro JA, Normile PS, Muniz P, Riveiro JM, Nogués J (2017) Maximizing exchange bias in Co/CoO Core/Shell nanoparticles by lattice matching between the shell and the embedding matrix. Chem Mater 29:5200–5206

12. Dervin S, Pillai SC (2017) An introduction to sol-gel processing for aerogels. In: Pillai S, Hehir S (eds) Sol-gel materials for energy, environment and electronic applications. Springer, Cham, pp 1–22

13. Amin N, Ul Hasan MS, Majeed Z, Latif Z, Ajaz un Nabi M, Mahmood K, Ali A, Mehmood K, Fatima M, Akhtar M, Arshad MI, Bibi A, Iqbal MZ, Jabeen F, Bano N (2020) Structural, electrical, optical and dielectric properties of yttrium substituted cadmium ferrites prepared by Co-precipitation method Ceram Int 46:20798–20809

14. Shirsath SE, Mane ML, Yasukawa Y, Liu X, Morisako A (2013) Chemical tuning of structure formation and combustion process in $CoDy_{0.1}Fe_{1.9}O_4$ nanoparticles: Influence@pH. J Nanoparticle Res 15:1–13

15. Pradeep A, Priyadharsini P, Chandrasekaran G (2008) Production of single phase nano size $NiFe_2O_4$ particles using sol-gel auto combustion route by optimizing the preparation conditions. Mater Chem Phys 112:572–576

16. Hashemi SM, Hasani S, Ardakani KJ, Davar FT (2019) The effect of simultaneous addition of ethylene glycol and agarose on the structural and magnetic properties of $CoFe_2O_4$ nanoparticles prepared by the sol-gel auto-combustion method. J Magn Magn Mater 492:165714

17. Dumitrescu AM, Samoila PM, Nica V, Doroftei F, Iordan AR, Palamaru MN (2013) Study of the chelating/fuel agents influence on NiFe2O4 samples with potential catalytic properties. Powder Technol 243:9–17

18. Slatineanu T, Diana E, Nica V, Oancea V, Caltun OF, Iordan AR, Palamaru MN (2012) The influence of the chelating/combustion agents on the structure and magnetic properties of zinc ferrite. Cent Eur J Chem 10:1799–1807

19. Arienzo MD, Scotti R, Credico B Di, Redaelli M (2017) Synthesis and characterization of morphology-controlled TiO_2 nanocrystals : Opportunities and challenges for their application in photocatalytic materials. In: Fornasiero P, Cargnello M (eds) Morphological, compositional, and shape control of materials for catalysis. Elsevier, pp 477–540 (2017)

20. Mohammad SN (2020) Nanomaterials synthesis routes. In: Synthesis of nanomaterials. Springer, Cham, pp 13–26

21. Grabowska E, Marchelek M, Paszkiewicz-gawron M, Zaleska-medynska A (2018) Metal oxide photocatalysts. In: Zaleska-Medynska A (ed) Metal oxide-based photocatalysis fundamentals and prospects for application. Elsevier, pp 51–209

22. Parvez K (2019) Two-dimensional nanomaterials: crystal structure and synthesis. In: Nurunnabi M, McCarthy JR (eds) Biomedical applications of graphene and 2D nanomaterials. Elsevier, pp 1–25

23. Li J, Wu Q, Wu J (2015) Synthesis of nanoparticles via solvothermal and hydrothermal methods. In: Aliofkhazraei M (ed) Handbook of nanoparticles. Springer, Cham, pp 1–28

24. Nunes D, Pimentel A, Santos L, Barquinha P, Pereira L, Fortunato E, Martins R (2019) Synthesis, design, and morphology of metal oxide nanostructures. In: Nunes D, Pimentel A, Santos L, Barquinha P, Pereira L, Fortunato E, Martins R (eds) Metal oxide nanostructures. Elsevier, pp 21–57

25. Wang J, Ren F, Yi R, Yan A, Qiu G, Liu X (2009) Solvothermal synthesis and magnetic properties of size-controlled nickel ferrite nanoparticles. J Alloys Compd 479:791–796

26. Chen W, Liu D, Wu W, Zhang H, Wu J (2017) Structure and magnetic properties evolution of rod-like $Co_{0.5}Ni_{0.25}Zn_{0.25}Dy_xFe_{2-x}O_4$ synthesized by solvothermal method.J Magn Magn Mater 422:49–56

27. Ji R, Cao C, Chen Z, Zhai H, Bai J (2014) Solvothermal synthesis of $Co_xFe_{3-x}O_4$ spheres and their microwave absorption properties. J Mater Chem C 2:5944–5953

28. Yan W, Jiang W, Zhang Q, Li Y, Wang H (2010) Structure and magnetic properties of nickel-zinc ferrite microspheres synthesized by solvothermal method. Mater Sci Eng B Solid-State Mater Adv Technol 171:144–148

29. de Medeiros F, Madigou V, Lopes-Moriyama AL, de Souza CP, Leroux C (2020) ynthesis of CoFe$_2$O$_4$ nanocubes. Nano-structures and nano-objects 21:100422
30. Demazeau G (2010) Solvothermal processes : definition, key factors governing the involved chemical reactions and new trends. Z Naturforsch 65b:999–1006
31. Sheikhhosseini E, Ranjbar M (2017) Solid-state thermal decomposition method for synthesis and characterization Mg/carbon nanocomposites and investigation of optical investigation. J Mater Sci Mater Electron 28:6201–6207
32. Odularu AT (2018) Metal nanoparticles: Thermal decomposition, biomedicinal applications to cancer treatment, and future perspectives. Bioinorg Chem Appl 2018
33. Varanda LC, Souza CGS, Moraes DA, Neves HR, Souza Junior JB, Silva MF, Bini RA, Albers RF, Silva TL, Beck W (2019) Size and shape-controlled nanomaterials based on modified polyol and thermal decomposition approaches. An Acad Bras Cienc 91:1–32
34. Shahjuee T, Masoudpanah SM, Mirkazemi SM (2019) Thermal decomposition synthesis of MgFe$_2$O$_4$ nanoparticles for magnetic hyperthermia. J Supercond Nov Magn 32:1347–1352
35. Niraula G, Shrivastava N, Akhtar K, Javed Y, Coaquira JAH, Sharma SK (2020) Liquid-phase synthesis of multifunctional nanomaterials: a recent update. In: Javed SKS and Y (ed) Magnetic nanoheterostructures, nanomedicine and nanotoxicology. Springer, pp 1–56
36. Umut E (2016) Surface modification of nanoparticles used in biomedical applications. In: Aliofkhazraei M (ed) Modern surface engineering treatments. INTECH Open Access, p 13 (2016)
37. Khan LU, Khan ZU (2017) Bifunctional nanomaterials: magnetism, luminescence and multimodal biomedical applications. In: Sharma SK (ed) Complex magnetic nanostructures: synthesis, assembly and applications. Springer, pp 1–464
38. Fereshteh Z, Salavati-Niasari M (2017) Effect of ligand on particle size and morphology of nanostructures synthesized by thermal decomposition of coordination compounds. Adv Colloid Interface Sci 243:86–104
39. Singh G, Chandra S (2018) Electrochemical performance of MnFe$_2$O$_4$ nano-ferrites synthesized using thermal decomposition method. Int J Hydrogen Energy 43:4058–4066
40. Mahhouti Z, El Moussaoui H, Mahfoud T, Hamedoun M, El Marssi M, Lahmar A, El Kenz A, Benyoussef A (2019) Chemical synthesis and magnetic properties of monodisperse cobalt ferrite nanoparticles. J Mater Sci Mater Electron 30:14913–14922
41. Sarveena, Muraca D, Zelis PM, Javed Y, Ahmad N, Vargas JM, Moscoso-Londõno, Knobel M, Singh M, Sharma SK (2016) Surface and interface interplay on the oxidizing temperature of iron oxide and Au – iron oxide. RSC Adv 6:70394–70404
42. Babu LK, Reddy YVR (2020) A novel thermal decomposition approach for the synthesis and properties of superparamagnetic nanocrystalline NiFe$_2$O$_4$ and Its antibacterial, electrocatalytic properties. J Supercond Nov Magn 33:1013–1021
43. Prasad S, Kumar V, Kirubanandam S, Barhoum A (2018) Engineered nanomaterials: nanofabrication and surface functionalization. In: Barhoum A, Makhlouf ASH (eds) Emerging applications of nanoparticles and architectural nanostructures: current prospects and future trends. Elsevier, pp 305–340
44. Shoba M, Kaleemulla S, Krishnamoorthi C (2020) Structural, dielectric and magnetic properties of ZnFe$_{2-x}$Sr$_x$O$_4$ nanoparticles prepared by co-precipitation method. Phys B Condens Matter 583: 412018
45. Cruz IF, Freire C, Araújo JP, Pereira C, Pereira AM (2018) Multifunctional ferrite nanoparticles: From current trends toward the future. In: El-Gendy AA, Barandiarán JM, Hadimani RL (eds) Micro and nano technologies, magnetic nanostructured materials. Elsevier, pp 59–116
46. Nasir Z, Shakir ML, Wahab R, Shoeb M, Alam P, Khan RH, Mobin M (2017) Co-precipitation synthesis and characterization of Co doped SnO$_2$ NPs, HSA interaction via various spectroscopic techniques and their antimicrobial and photocatalytic activities. Int J Biol Macromol 94:554–565
47. Rane AV, Kanny K, Abitha VK (2018) Thomas S Methods for synthesis of nanoparticles and fabrication of nanocomposites. In: Bhagyaraj SM, Oluwafemi OS, Kalarikkal N, Thomas S (eds) Micro and nano technologies, synthesis of inorganic nanomaterials. Woodhead Publishing, pp 121–139

48. de Oliveira Sousa Neto V, Freire TM, Saraiva GD, Muniz CR, Cunha MS, Fechine PBA, do Nascimento RF (2019) Water treatment devices based on zero-valent metal and metal oxide nanomaterials. In: do Nascimento RF Ferreira OP, De Paula AJ, de Neto VOS (eds) Advanced nanomaterials: nanomaterials applications for environmental matrices. pp 187–225

49. Varanda LC, de Souza CGS, Perecin C, Moraes D, de Queiróz DF, Neves HR, Junior JBS, da Silva MF, Albers RF, da Silva TL (2019) Inorganic and organic–inorganic composite nanoparticles with potential biomedical applications: synthesis challenges for enhanced performance. In: Grumezescu AM, Grumezescu V (eds) Materials for biomedical engineering. Elsevier, pp 47–99

50. Goh KW, Johan MR, Wong YH (2016) Effect of pH variation on the stability and structural properties of In(OH)$_3$ nanoparticles synthesized by co-precipitation method. Appl Phys A Mater Sci Process 122:1–9

51. Praveena K, Sadhana K (2015) Ferromagnetic properties of Zn substituted spinel ferrites for high frequency applications. Int J Sci Res Publ 5:1–21

52. Mascolo MC, Pei Y, Ring TA (2013) Room temperature Co-precipitation synthesis of magnetite nanoparticles in a large pH window with different bases.Materials (Basel) 6:5549–5567

53. Chen X, Li Y, Huang L, Zou D, Wu E, Liu Y, Xie Y, Yao R, Liao S, Wang G, Zheng F (2017) Effects of precipitant and pH on coprecipitation of nanosized Co-Cr-V alloy powders. Materials (Basel) 10:1108

54. Lamdab U, Wetchakun K, Kangwansupamonkon W, Wetchakun N (2018) Effect of a pH-controlled co-precipitation process on rhodamine B adsorption of MnFe$_2$O$_4$ nanoparticles. RSC Adv 8:6709–6718

55. Iranmanesh P, Tabatabai Yazdi S, Mehran M, Saeednia S (2018) Superior magnetic properties of Ni ferrite nanoparticles synthesized by capping agent-free one-step coprecipitation route at different pH values. J Magn Magn Mater 449:172–179

56. Prabhakaran T, Mangalaraja RV, Denardin JC, Jiménez JA (2017) The effect of reaction temperature on the structural and magnetic properties of nano CoFe$_2$O$_4$. Ceram Int 43:5599–5606

57. Amer MA, Meaz TM, Mostafa AG, El-Ghazally HF (2015) Influence of annealing process on phase transition of Cu–Al nanoferrites synthesized by a coprecipitation method. Mater Sci Semicond Process 36:49–56

58. Sinkó K, Manek E, Meiszterics A, Havancsák K, Vainio U, Peterlik H (2012) Liquid-phase syntheses of cobalt ferrite nanoparticles. J Nanoparticle Res 14:894

59. Kim Y Il, Kim D, Lee CS, Phys B (2003) Synthesis and characterization of CoFe$_2$O$_4$ magnetic nanoparticles prepared by temperature-controlled coprecipitation method. Condensed Matter 337:42–51

60. Kader SS, Paul DP, Hoque SM (2014) Effect of temperature on the structural and magnetic Properties of CuFe2O4 Nano particle prepared by chemical Co-precipitation method. Int J Mater Mech Manuf 2:5–8

61. Yakubu A, Abbas Z, Ibrahim N, Hashim M (2015) Effect of temperature on structural, magnetic and dielectric properties of Cobalt ferrite nanoparticles prepared via co-precipitation method. Phys Sci Int J 8:1–8

62. Saragi T, Depi BL, Butarbutar S, Permana B, Risdiana (2018) The impact of synthesis temperature on magnetite nanoparticles size synthesized by co-precipitation method. J Phys Conf Ser 1013:012190

63. Huang GY, Xu SM, Li LY, Wang XJ (2014) Effect of surfactants on dispersion property and morphology of nano-sized nickel powders. Trans Nonferrous Met Soc China 24:3739–3746

64. Zafar K, Aadil M, Shahi MN, Sabeeh H, Nazar F, Iqbal M, Yousuf MA (2020) Physical, structural and dielectric parameters evaluation of new Mg$_{1-x}$Co$_x$Ni$_y$Fe$_{2-y}$O$_4$ nano-ferrites synthesized via wet chemical approach. AAAFM Energy 1:36–44

65. Powar RR, Phadtare VD, Parale VG, Pathak S, Sanadi KR, Park HH, Patil DR, Piste PB, Zambare DN (2020) Effect of zinc substitution on magnesium ferrite nanoparticles: Structural, electrical, magnetic, and gas-sensing properties. Mater Sci Eng B 262:114776

66. Vaidyanathan G, Sendhilnathan S (2008) Characterization of $Co_{1-x}Zn_xFe_2O_4$ nanoparticles synthesized by co-precipitation method. Phys B Condens Matter 403:2157–2167
67. El Foulani AH, Aamouche A, Mohseni F, Amaral JS, Tobaldi DM, Pullar RC (2019) Effect of surfactants on the optical and magnetic properties of cobalt-zinc ferrite $Co_{0.5}Zn_{0.5}Fe_2O_4$. J Alloys Compd 774:1250–1259
68. Lu HF, Hong RY, Li HZ (2011) Influence of surfactants on co-precipitation synthesis of strontium ferrite. J Alloys Compd 509:10127–10131
69. Mirzaei A, Neri G (2016) Microwave-assisted synthesis of metal oxide nanostructures for gas sensing application: A review. Sens Actuat B Chem 237:749–775
70. Lagashetty A, Havanoor V, Basavaraja S, Balaji SD, Venkataraman A (2007) Microwave-assisted route for synthesis of nanosized metal oxides. Sci Technol Adv Mater 8:484–493
71. Baghbanzadeh M, Carbone L, Cozzoli PD, Kappe CO (2011) Microwave-assisted synthesis of colloidal inorganic nanocrystals. Angew Chem Int Ed 50:11312–11359
72. Polshettiwar V, Nadagouda MN, Varma RS (2009) Microwave-assisted chemistry: A rapid and sustainable route to synthesis of organics and nanomaterials. Aust J Chem 62:16–26
73. Thongtem T, Phuruangrat A, Thongtem S (2010) Microwave-assisted synthesis and characterization of $SrMoO_4$ and $SrWO_4$ nanocrystals. J Nanoparticle Res 12:2287–2294
74. Chikan V, McLaurin EJ (2016) Rapid nanoparticle synthesis by magnetic and microwave heating. Nanomaterials 6:85
75. Gupta D, Jamwal D, Rana D, Katoch A (2018) Microwave synthesized nanocomposites for enhancing oral bioavailability of drugs. In: Inamuddin, Asiri AM, Mohammad A (eds) Applications of nanocomposite materials in drug delivery. Woodhead Publishing, pp 619–632
76. Gude V, Patil P, Martinez-Guerra E, Deng S, Nirmalakhandan N (2013) Microwave energy potential for biodiesel production. Sustain Chem Process 1:5
77. Dallinger D, Kappe CO (2007) Microwave-assisted synthesis in water as solvent. Chem Rev 107:2563–2591
78. Kappe CO (2006) Microwave-assisted chemistry. Compr Med Chem II 3:837–860
79. Leadbeater NE (2014) Microwave-assisted synthesis: general concepts. In: Hoogenboom R, Schubert US, Wiesbrock F (eds) Microwave-assisted polymer synthesis. Springer, Cham, pp 1–44
80. Dąbrowska S, Chudoba T, Wojnarowicz J, Łojkowski W. (2018) Current trends in the development of microwave reactors for the synthesis of nanomaterials in laboratories and industries: A review. Crystals 8:379
81. Stefanidis GD, Muñoz AN, Sturm GSJ, Stankiewicz A (2014) A helicopter view of microwave application to chemical processes: Reactions, separations, and equipment concepts. Rev Chem Eng 30:233–259
82. Lidstrom P, Tierney J, Wathey B, Westman J (2001) Microwave-assisted organic synthesis-a review. Tetrahedron 57:9225–9283
83. Nishioka M, Miyakawa M, Daino Y, Kataoka H, Koda H, Sato K, Suzuki TM (2013) Single-mode microwave reactor used for continuous flow reactions under elevated pressure. Ind Eng Chem Res 52:4683–4687
84. Glasnov TN, Kappe CO (2007) Microwave-assisted synthesis under continuous-flow conditions. Macromol Rapid Commun 28:395–410
85. Gawande MB, Shelke SN, Zboril R, Varma RS (2014) Microwave-assisted chemistry: Synthetic applications for rapid assembly of nanomaterials and organics. Acc Chem Res 47:1338–1348
86. Bensebaa F, Zavaliche F, Ecuyer PL, Cochrane RW, Veres T (2004) Microwave synthesis and characterization of Co–ferrite nanoparticles. J Colloid Interface Sci 277:104–110
87. Shebl A, Hassan AA, Salama DM, El-aziz MEA, Abd MSA (2020) Template-free microwave-assisted hydrothermal synthesis of manganese zinc ferrite as a nanofertilizer for squash plant (Cucurbita pepo L). Heliyon 6:e03596
88. Zhenyu L, Guangliang X, Yalin Z (2007) Microwave assisted low temperature synthesis of MnZn ferrite nanoparticles. Nanoscale Res Lett 2:40–43
89. Manikandan A, Durka M, Antony SA (2014) A novel synthesis, structural, morphological, and opto magnetic characterizations of magnetically separable spinel $Co_xMn_{1-x}Fe_2O_4$ ($0 \leq x \leq 1$) Nano catalysts. J Supercond Nov Magn 27:2841–2857

90. Chen D, Zhang Y, Chen B, Kang Z (2013) Coupling effect of microwave and mechanical forces during the synthesis of ferrite nanoparticles by microwave-assisted ball milling. Ind Eng Chem Res 52:14179
91. Kane SN, Verma R, Tiwari P, Mazaleyrat F (2019) Preparation condition , composition and post-preparation thermal treatment assisted control of structural and magnetic properties of spinel nano ferrites. In: AIP conference proceedings, p 020003
92. Singh C, Sai R, Raland RD, Shivashankar SA (2020) Mapping solution loss-tangent dependent deposition rate of MnZn-ferrite via microwave-assisted solvothermal processing. In: AIP conference proceedings, p 030080
93. Tiwari P, Kane SN, Verma R, Mazaleyrat F (2019) Preparation condition assisted modification of structural and magnetic properties of $MgFe_2O_4$ nano ferrite. In: AIP conference proceedings, p 160003
94. Azam A (2012) Microwave assisted synthesis and characterization of Co doped Cu ferrite nanoparticles. J Alloys Compd 540:145–153
95. Vilvanathaprabu A, Ravikumar B, Perumal S (2020) Synthesis of vanadium ferrite nanoparticles by microwave assisted technique. In: Journal of Physics: Conference Series 1644:012034
96. Sadanandan AM, Khatri PK, Jain SL (2020) Highly efficient microwave assisted synthesis of magnetically separable $GO\text{-}CoFe_2O_4$ nanocomposite for visible light induced oxidative coupling of benzyl amines. J Photochem Photobiol A Chem 400:112697

Modern Applications of Ferrites: An Important Class of Ferrimagnetic System

Gabriel Alves Gomes, Kanwal Akhtar, Gisela Lara da Costa, Yasir Javed, and Surender K. Sharma

Abstract Magnetic nanoparticles (MNPs) have been used in engineering applications for different purposes in the last few decades, increasing their relevance recently on biomedical studies, with alternative treatments to most complex diseases, and microelectronic fields, as an excellent way to improve aspects such as thermal and electric conductivity. The use of nanomagnetic ferrite particles in cancer therapy and to control antibacterial agents is also noteworthy, because of their advantages in terms of resistance to temperature variations, chemical stability, and long-term durability. One of the promising applications of these nanoparticles includes water-purifying systems. In this chapter, those outstanding aspects of nanoparticle ferrites were treated since their very applicable point-of-view. In this sense, the structure properties of this class of materials are a very important matter to discuss, investigating how their unique ferrimagnetic face centered behavior could directly influence their potential in technological fields and innovative medical treatments.

Keywords Nanomagnetic ferrites · Synthesis · Surface functionalization · Biomedical & bioengineering · Technological and physical field

1 Introduction

Ferrites are usually ferrimagnetic ceramic compounds, a metallic oxide mixture with 70% of this composition constituted with hematite (Fe_2O_3) and the remains

G. A. Gomes (✉) · G. L. da Costa
Biochemical and Taxonomy Laboratory, Oswaldo Cruz Foundation, Rio de Janeiro 21040-360, Brazil

K. Akhtar · Y. Javed
Department of Physics, Magnetic Materials Laboratory, University of Agriculture, Faisalabad, Pakistan

S. K. Sharma (✉)
Department of Physics, Federal University of Maranhao, Sao Luis, Brazil
e-mail: surender.sharma@ufma.br; surender.sharma@cup.edu.in

Department of Physics, Central University of Punjab, Bathinda 151401, India

30% filled with other bivalent transition metals. Those nanoparticles show structural formula MFe_2O_4, which M represents an bivalent ion (as Ni^{2+}, Mn^{2+}, Cu^{2+} etc.), and the crystal structure is classically composed by divalent and trivalent ions on an atomic packing with face-centered cubic symmetry where the oxygen ions occupies positions in tetrahedral and octahedral symmetry sites [1].

Spinel ferrites XFe_2O_4 (where X=Al, Co, Mg, Mn, Fe, etc.) have cubic crystal structure. Spinel ferrites have two interstitial sites that are entitled as tetrahedral and octahedral sites. Tetrahedral sites are predominantly filled with divalent ions while octahedral sites occupied with trivalent ions [2]. Unit cell is equanimous of 64 tetrahedral and 32 octahedral sites, from which un-occupied sites are 56 tetrahedral and 16 octahedral sites [3]. Spinel ferrites are diversified into normal spinel-structure and inverse spinel-structure to mixed (partial) spinel structures. Structural formula of normal spinel is $Me^{2+}[Fe_2^{3+}]O_4^{2-}$. In normal spinel structures, tetrahedral and octahedral sites is occupied by divalent and trivalent cations respectively. Structural formula of inverse ferrites are $Fe^{3+}[Me^{2+}Fe^{3+}]O_4^{2-}$. Magnetic moments of inverse spinels are remunerated mutually leads resulting moments because of cations magnetic moments. In inverse spinel structures, octahedral site is consists upon divalent cations while trivalent cations are distributed indiscriminately on octahedral and tetrahedral sites. Mixed spinels have structural formula $Me_{1-\delta}^{2+}Fe_\delta^{3+}[Me_\delta^{2+}Fe_{2-\delta}^{3+}]O_4^{2-}$ (*here δ represents degree of freedom*). In Mixed (partial) spinel ferrites, divalent and trivalent cations are distributed arbitrarily [3–5]. Fe^{2+} cations are present on 1/8 tetrahedral sites while ½ octahedral sites are filled by Al^{3+} cations. This degree of inversion can be varied by varying synthesis techniques.

With wide possibilities of structural symmetry, ferrites can be natural and found in certain minerals or artificially produced in research laboratories. These materials ratify their extreme importance in various science fields due to the uniqueness of their optical, magnetic, and electric properties [6]. Although ferrites are composed of a mixture of oxides, their electrical and magnetic characteristics are derived from the metals that compose it. In general, they present great permeability, high magnetization saturation, and high magnetocrystalline anisotropy [6, 7]. Among the alternatives of magnetic materials, spinel ferrites are usually particularly attractive for physical and biological applications due to their unique properties, such as chemical and thermal stability, guaranteed by their cubic crystalline structure [8]. Several promising applications such as catalysis, sensors, storage systems, thin films, magnetic fluids, and medical treatments are already in use, with new solutions in growing development emerging every day [9].

Saturation magnetization values of magnetic ferrites are smaller as compared to ferromagnetic alloys. Properties of ferrites such as higher corrosion resistance and greater heat resistance make them promising candidates towards many applications [7, 10]. In recent years, spinel ferrite NPs have been of great interest in biomedical applications, need precise control on morphology, dispersion, and particle size, as well as of other prompting factors that influence these types of properties.

2 Synthesis and Fabrication of Nanomagnetic Ferrites

On nano scale, materials having low dimensional structures with advanced morphological features are extensively attracted towards potential applications due to their distinctive properties in magnetic, optical, and electronic devices. Hybrid nanomaterials exhibiting additive effects and facilitate as multifunctional have been fabricated through different techniques [11]. Several techniques are reported for synthesizing spinel ferrite nanoparticles including solid-state reaction, microemulsion, combustion, sol–gel, mechanical milling, chemical coprecipitation, and microwave synthesis (Fig. 1) [12]. Each one of that processes exhibits excellent results in terms of physical and chemical properties, and some of that synthesis techniques offers greater control over homogeneity, powder morphology and elemental composition.

2.1 Solid-State Reaction Method

This method is a relatively novel progress and possesses great advantages likewise their extreme simplicity and the fact that give a high yield of products. In addition, this method involves less solvent, which is preponderant to reduce contamination under the products. Several authors [12, 14] reported Ni ferrite nanoparticles
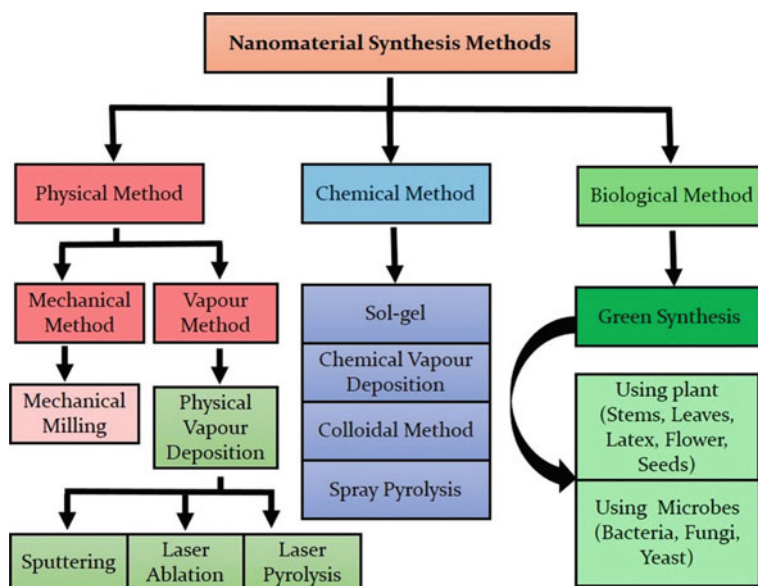
Fig. 1 Synthesis protocols for nanomagnetic ferrites. Reprinted with permission from [13]

produced through this method, annealing Ni and Fe nanoparticles in ambient conditions [12] or using NaCl as dispersant in an ambient with calculated proportions of sodium hydroxide, ferrous and nickel sulfate [15]. Superparamagnetic Zn [16] and Mn–Zn [17] ferrites are reported to be synthesized by a low-temperature solid-state reaction (LTSSR) method. In each case, a simple stoichiometric mixture was applied using simple reagents such as ferric chloride, sodium hydroxide (NaOH), manganese chloride and zinc chloride.

2.2 Microemulsion Method

The microemulsion involves the thermodynamically stable dispersions of relatively immiscible two liquids stabilized by surfactant methods [9]. Some main recompences of this method include the variety of synthesis paths only varying the combination of surfactants, co-surfactant, and oil–water ratio, which leads to an effective particle size control. This method is also one of the most cost-effective routes to obtain ferrite nanoparticles with a refined control over impurities [9]. This reaction is favorable and eco-friendly, which can be perform even at low temperatures. This type of synthesis protocol allows reuse of surfactants for many times during preparation method, which lead towards their use in commercial products [8]. This leads striking aspect about microemulsion is that stable nanosized ferrites can be produced, and the fact that method permits for the reuse and recovery of oil and surfactants oil for NPs synthesis cycles [9]. However, the particles obtained sometimes exhibits a poor crystalline nature due to prerequisite of large amounts of solvents involved and are more polydisperse due to the slow nucleation proportion at low temperatures [17]. There are two major categories of this method: the reverse water-in-oil and normal oil-in-water and monodisperse nanometric droplets are shown in the dispersed phase, which offers a curbed environment for the preparation of nano-scale particles. Some reported nanoparticles synthesized by the microemulsion method involve $Fe_2Mn_{0.5}Zn_{0.5}O_4$ [18, 19], and Fe_3O_4 [20].

2.3 Combustion Solution Method

The solution combustion synthesis (SCS) drives other methods for the synthesis of nanoparticles maintaining its owing characteristics. This technique is very known for oxide materials; however, it is no very common to produce superparamagnetic materials which were reported recently for the first time [21]. This technique can synthesize homogeneously form particles through atomization of the liquid before the explosive flora of the reaction itself. Firstly, a homogeneity must be achieved in the system between the hydrate nitrates precursors and the complexing agent (commonly citric acid, glycine, or urea), which is achieved by stoichiometric balance. Given that the system is mixed on an atomic scale in solution leading to a diffusion this process

is restricted to the size of the liquid drop before drying [22]. A chemical pyrolization occurs in the fluid compound powder, usually a mixture of metal oxides as the eventual result of the method. The triumph of the process is because of an excellent blending amid the constituents using an appropriate fuel through an exothermic redox reaction of complexing agent in an aqueous medium between oxidizer Magnetite (Fe_3O_4), Maghemite (α-Fe_2O_3) and fuel were reported to be produced by the SCS method with dissimilar fuel-to-oxidant molar ratios with urea as a fuel and ferric nitrate as oxidizer [21]. Copper-silver ferrites ($Cu_{1-x}Ag_xFe_2O_4$) were synthesized for the first time by a modification of the SCS using glycine ($C_2H_5NO_2$) as reducing agent [22]. It is noticed that a major effect in regulating particle size and microstructure of the artifact for combustion depends on different fuel-to-oxidant ratios. One of the most advantages in using the combustion solution synthesis is that be very economical, fast, and practical. The self-sustained combustion process occurs on the entire volume and normally taken no more than a few minutes to be reached, lead towards high-volume powder with dark precipitates distinct by the amount of oxides present in the samples.

2.4 Sol–gel

The sol–gel synthesis method is an attractive and widely used technique for the preparation of metal oxide nanosized particles. This technique normally includes the use of metal alkoxide solutions and exhibits some interesting advantages such as great stoichiometric control and the manufacturing of ultrafine particles with a slight size distribution in a comparatively short processing time at lesser temperatures [17, 23]. In this method, the metal solution undergoes condensation polymerization reactions and hydrolysis to form a gel at room temperature [4]. The reaction temperature in sol–gel varies between 25 and 200 °C, which is very interesting due to the possibilities to synthesize NPs with narrow size distribution and controlled shape. In order to obtain the final crystalline state, any volatile impurities that may appear during synthesis could be removed further by heat treatment after the combination reaction [23]. This lack of purity of the final product could be understood as one of the major limitations of the sol-gel technique, and thus heat treatment is needed after the production to attain the high purity state [24]. Other advantages of the sol-gel synthesis method include the fact that it functions under low temperature, cost-effective and no special instruments are needed to carry it on. The ease in terms of synthesis procedures merged with these advantages makes the sol-gel method a very attractive route for synthesize nanocomposites. Normally citric acid is used as conventional chelating agent, but other reagents like polyacrylic acid (PAA) which is reported to being additional carboxylic acid groups to formulize chelates with mixed cations could be used to produce superparamagnetic ferrites such as $NiFe_2O_4$ [23] and $CoFe_2O_4$ [25, 26]. Because of these outstanding benefits, sol–gel is one of the preferred synthesis methods to achieve homogeneity, composition control,

microstructure, particle size, and particle distribution of NP, by regulating different limitations such as sol concentration, stirring rate, and annealing temperature [9, 16].

2.5 Mechanical Milling

The mechanical milling technique, as reported by its name, is a recurrent method used for the preparation of nanoparticles and involves a top-down approach. This method is a low-cost alternative for a rapid and simple synthesis route and offers the possibility to obtain a large-scale quantity of materials for various applications. Some ferrimagnetic nanoparticles synthesized by this method include $CuFe_2O_4$ [27–29] and nickel-substitute manganese ferrite ($Ni_{1-x}Mn_xFe_2O_4$) [23, 29]. One of the disadvantages of this technique is frequent contamination of nanoparticles during longtime milling, which in turn will change the stoichiometry of the obtained NPs. Also, some studies show that increasing the calcination temperature the saturation magnetization M_s from almost 10 emu g^{-1} and a decrease in coercivity from above 25 Oe, which changes the average size to about 15 nm. These results demonstrate the impact of synthesis method on the magnetic properties and shows that refining the synthesis technique is one of the most required conditions to get ferrites nanoparticles with higher crystallinities and outstanding superparamagnetic properties [27].

2.6 Coprecipitation

The chemical coprecipitation method is one of the most frequently applied techniques to synthesize magnetic oxides, due to its simplicity, good control of grain size, and uniformity of NPs produced. However, some reports [30] observed that some undesirable intermediate phases could be found among the other metallic phases, which led to poor magnetic properties and irregular shape for the derived ferrite particles. This method employs a solution mixture of divalent to trivalent transition metals soluble salts, bonded in 1:2 molar ratio commonly adjustable in an alkaline medium. It is notable that this synthesis method needs a controlled monitoring of pH solution, which is usually attuned through ammonium solution or sodium hydroxide solution [8]. The coprecipitation method involves synthesize of mixed FNPs with different magnetic properties, such as by doping rare earth metals (Nd, Eu, and Gd) into $CoFe_2O_4$ [12, 30]. The major disadvantage of this method is the low crystallinity of prepared superparamagnetic ferrites and hence following heat treatment is essential in order to attain better crystallinity [31].

3 Surface Functionalization of Magnetic Nano Ferrites

One of the crucial steps involved in the fabrication of nanodevices is surface functionalization of synthesized nanomagnetic ferrites, as functionalization controls many physio-chemical processes which tune electrical, optical, and magnetic properties according to the requirement. However, in situ functionalizations of prepared ferrite NPs can be done through many synthetic methods. Many environmental and biomedical applications required different types of hydrophilic coatings possessing definite chemical groups [32, 33]. one of the important features for surface functionalization is accessibility of superficial transition metals with d orbitals working ass Lewis acids in existence of donor ligands. Spinel ferrite surface behave reactive towards different chemical groups, which provide a chamber for multiple combinations. Ligands provide many high and low-weight compounds. For surface complexation, many functional groups are available including amides, hydroxamic acids, carboxylic acids, phosphonic, and hydroxyl [34, 35].

Three major approaches are involved to make NPs hydrophilic in nature: (1) polymer coatings, (2) silica coatings, and (3) ligand exchange reaction. Ligand exchange reactions efficiently transfer many hydrophobic particles to the aqueous medium by replacing hydrophobic ligands without changing magnetic core considerably with different hydrophilic ligands. Silica coatings provide an excellent chemical stability and also prevent magnetic interactions, which denigrated the colloidal stability. Stober established the hydrolysis-condensation method to attain silica shells with meticulous thickness by adding tetraethyl orthosilicate to the dispersion of NPs without appearing single silica particles for enhancing the magnetic interactions. Silica coatings can be used with many organosilanes consisting groups such as -NH and -SH [36, 37]. Two major possibilities for polymer coatings of NPs are: (i) NPs surface functionalization with a molecule which acts as initiator for controlled-interfacial polymerization and (ii) preparation of polymer following the first step by surface anchoring. Second route is more simpler and allows variety of macromolecules for surface binding with suitable functional groups. Former route is more laborious and possess the advantage of controlling surface density by monitoring the length of chains and grafting the polymer [38].

Zhao et al., synthesized hydroamic acide coated Fe_3O_4/poly(acrylaide) nanocomposites (PAM). Authors treated amide bonds with the hydroxylamine solution [39]. While, Zhao et al., familiarized amine groups by ethlenediamine with epoxy moieties consisting polymer attached with the Fe_3O_4 NPs [15]. A similar method was also reported with the addition of NaSH into episulfide moieties. Ester and amide formations are good strategies to achieve better conjugation of NPs; carbodiimides are used as a coupling agent in these reactions. Ren et al., fused EDTA ligands with Fe_3O_4@silica@chitosan particles through amide bonding between NH_2 groups and EDTA-COO^- moieties in chitosan shells (Fig. 2) [40]. Ge et al., introduced polycarboxylic acid in amine coated magnetite [41].
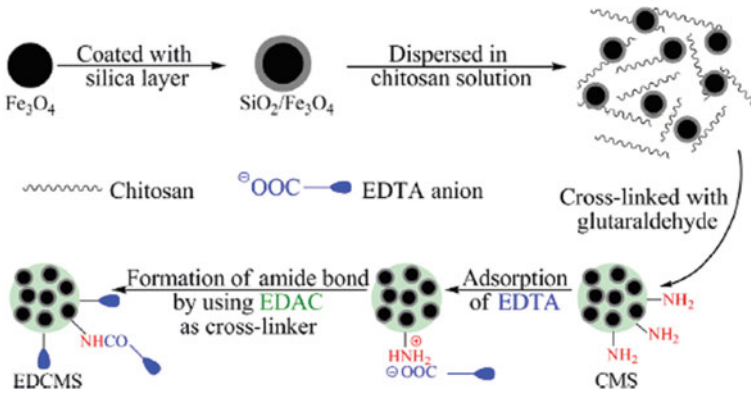
Fig. 2 Synthesis protocol followed for EDTA-consisting nano ferrites by amidation of chitosan. Reprinted with permission from [40]

4 Applications of Magnetic Ferrites

Magnetic semiconductors, heusler alloys, and metal oxides are amidst materials that are considered auspicious candidates for wide applications in spintronics (Fig. 3). Exceedingly essential requirements for appropriate and multi-functioning of these devices are high curie temperature, low eddy currents, and high spin polarization. Ferrites are not regarded conventionally as magnetic materials but they are considered as magnetic in nature due to their advanced magnetic/structural properties, high degree of freedom, flexibility, high resistivity ranges, low leakage inductances, less eddy current losses, and multiple functionalities that motivate scientists to search for such type of materials [2, 3, 42, 43].

4.1 Applications in Biomedical and Bioengineering Fields

Magnetic nanoparticles show tremendous potential in several applications owing to their unique material properties. The use of magnetic nanoparticles for clinical and biological applications is one of the most thought-provoking research areas in the field of nanomagnetism [17, 44]. The ability to precisely control the behavior of the material using an externally applied magnetic field has made MNPs a promising nano agent in biosensors, magnetic separation, antibacterial control, targeted drug delivery, magnetic hyperthermia, magnetic resonance imaging (MRI) (Fig. 4) [45, 46]. In that way, the use of MNPs for drug delivery in cancer therapy has gained recent attention as a more effective tool than the usual chemotherapy and radiotherapy treatments [47].

Advancements in technology provide many targeted approaches in NPs domain uptake in tissues, assembling the complexes to target specific tissues [48]. This
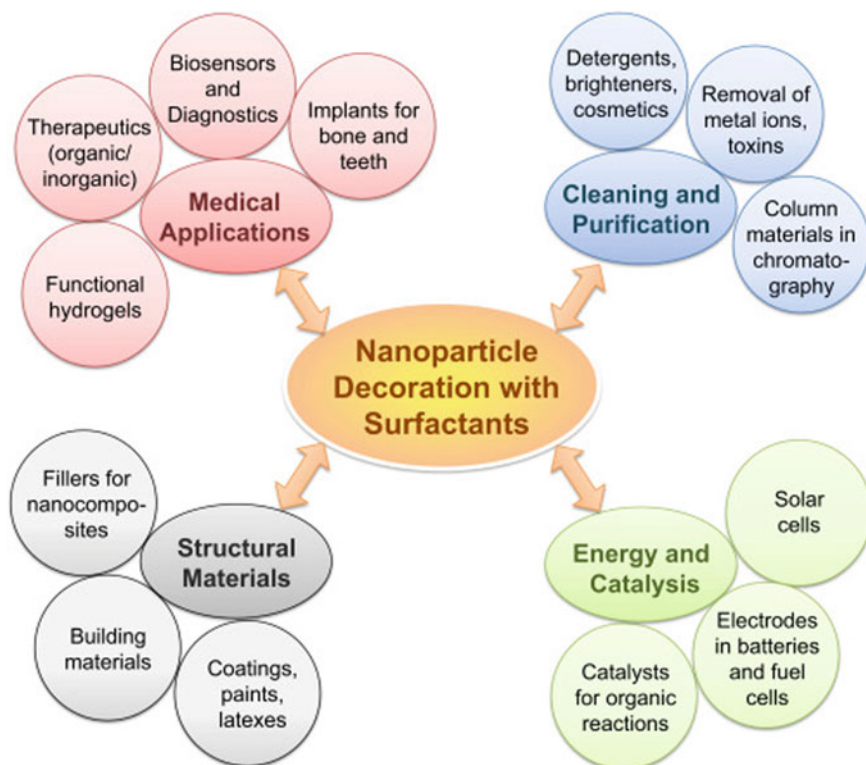
Fig. 3 Modern applications of nanoferrites [1]

research area is considered as a novel, with the increasing attention of different research groups around the world that have been exploring the role of different NPs in the treatment of cancer. Iron oxide nanoparticles such as Fe_3O_4 and γ-Fe_2O_3 show great therapeutic potential, which make them a good candidate for magnetic hyperthermia due to excellent superparamagnetic properties, nontoxicity, and higher biocompatibility [48]. Different types of agents are administrated during chemotherapy, which affects transcription phenomenon and DNA replication in dividing cells [46, 48].less side effects have been generated during targeted delivery systems, which enhances the capability of administrated therapeutic agents linked with their ligands. These NPs are functionalized with different types of cancer-specific antibodies/folic acid [49]. While drug delivery efficiency can be enhanced, NPs synthesis is required with responsive pH, rendering to different types of body tissues. These nanomaterials have many advantages which make them attractive candidate in drug carrier materials, which accumulates in tumor tissues, easy penetration by cellular membranes in different types of intracellular environments with higher specific surface area, which result in efficient drug loading [47].
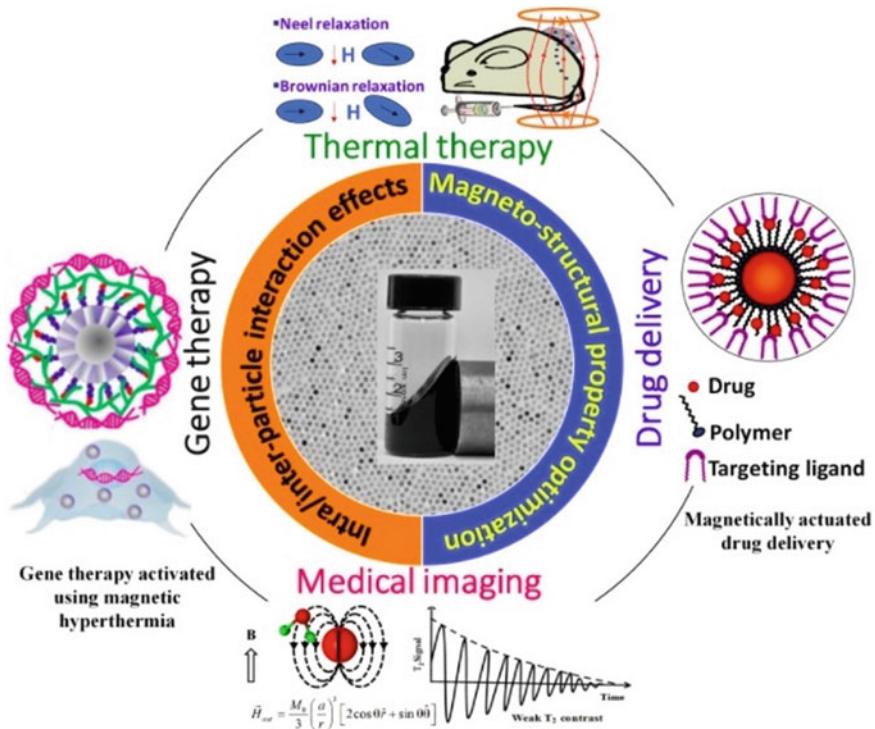
Fig. 4 Due to heat activity of ferrimagnetic nanoferrites have been used in gene therapy, drug carrier, and cancer treatment. Magnetic NPs also utilized as contrast agents in magnetic resonance imaging and magnetic particle imaging [55]

Hyperthermia is a treatment performed through heat generation at a specific site and focused on regional, local, and whole body. Among different types of hyperthermia, local hyperthermia is gaining much attention in which tumor cells are treated between 42 and 46 °C heat produced through spinel ferrite NPs. Tumor cells are sensitive towards hyperthermic effects as compared to the normal healthy cells because of higher metabolic rates [50–54].

4.2 Applications in Technological and Physical Field

Spinel ferrites were focused from the last few years for technical applications such as remote monitoring, computers, industrial automation, and communication technologies. Ferrites are considered as excellent materials for their use in electrochemical biosensing due to their greater sensing accuracy, quick analysis, and low detection levels of different analytes (Fig. 5). For optimization in electronic devices, nanomaterials specially ferrites are used widely due to higher permeability, saturation
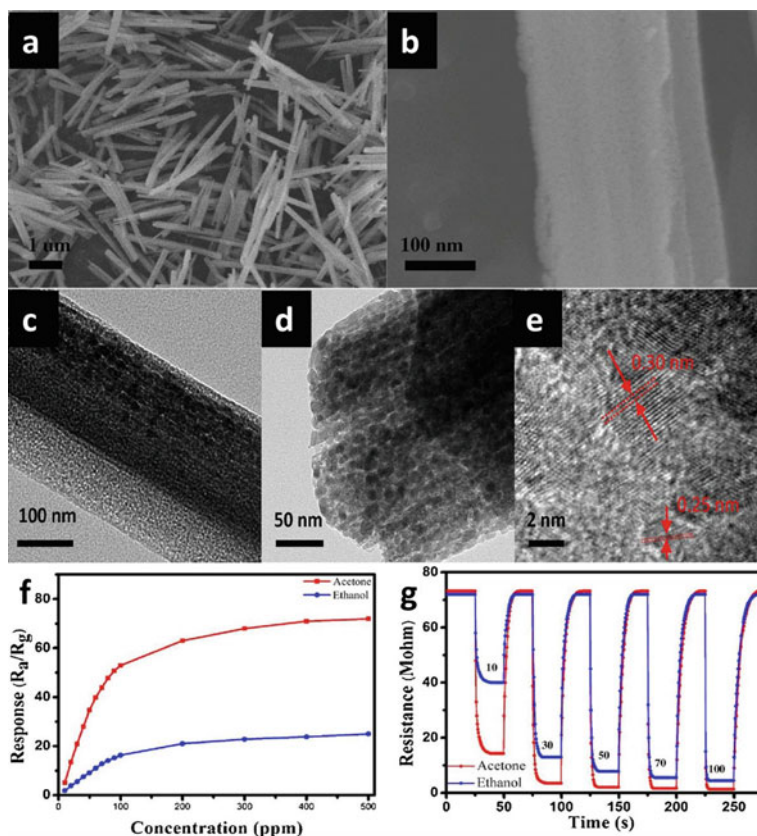
Fig. 5 Zinc ferrite nanorods as gas sensors for ethanol and acetone detection: **a–e** TEM images of nanorods. **f** Response of zinc ferrite nanorods as gas sensor for different acetone and ethanol concentration. **g** Response curve for acetone and ethanol for different times at 260 °C. Reprinted with permission from [57]

magnetization, and greater magnetic relaxation frequency. These types of ferrites are used in electrical and electronic industries especially magnetic recording heads, transducers, magnetic memory chips and transformers, etc. [56].

Ferrites also play an important role as multilayer chip inductor and wire-wound chip inductor magnetic materials, used primarily for microwave gyromagnetic devices, capacitors, transformers, and components in electronic products like cell phones, wireless communication systems, and laptops [58]. Additionally many other metal ferrites composites, like $CoFe_2O_4$ and $SnFe_2O_4$ among others, have been largely used in supercapacitors applications, such charge storage applications, due to their outstanding electrochemical activity [58]. Other applications of ferrite materials include electromagnetic microwave absorption [58] and photocatalysis studies [59] and storage devices [60].

Removal of Organic and Inorganic Contaminants by Using Different Adsorption Techniques For removal of toxic elements from waste/drinking water, majorly due to high efficiency and simplicity; basic advantage is sorbent separation during adsorption process, which is more energy consuming and tedious. For adsorption, use of magnetic materials make this task easier through magnetic decantation with the help of a permanent magnet. At room temperature, higher surface area of ferrites-based NPs enhances the binding specificity and superparamagnetic properties for strong binding of functional groups at the surfaces of NPs, which makes them the ideal candidates for the development of many innovative adsorption techniques [61].

Heavy Metal Cations In waste/natural water, heavy metal cations are present due to many industrial activities, consist of many toxic substances with high impact on humans. Here we focus on those studies which concentrate on two aspects: (1) on adsorption mechanism, shedding light at atomic and molecular level (2) improving selectivity and adsorption capacity towards certain contaminant through surface functionalized ferrite NPs [62]. Ren et al., noticed the adsorption capacity of metal-EDTA complex stability: $Cu(II) > Pb(II) > Cd(II)$. Authors verified the metal-carboxl.coated NPs through Fourier transform infrared spectroscopic measurements. Carboxyl-coated NPs from crotonic and acrylic acid copolymer were tested for Pb(II), Cd(II), Cu(II), and Zn(II). However, authors did not provide the spectroscopic evidences based on metal-carboxylated interactions, adsorption capacity increases with the increment in hardness of Lewis acid. Mahdavian et al., discussed adsorption properties of Cd(II), Cu(II), Ni(II), and Pb(II) with a nanoplatform containing chains of polyacrylic acid grown on magnetite NPs surface. pH increased with metal uptake, suggested the formation of chelates [36, 40].

Oxidation Technology Oxidation technology comprises upon assisted degradation mechanism of pollutant through the use of highly transient oxidizing species. These species can be activated through substances which can act as catalyst. Since toxicity, removal, and reuse of catalysts are the main concerns, studies have been reported on the synthesis of heterogeneous magnetic materials which can efficiently active the oxidizing mechanism of pollutants and as well minimize some contamination events. Because of these major reasons, ferrite NPs are becoming potential candidates towards many applications: (1) onset superparamagnetic properties activate the facile removal of catalysts; (2) catalytic activity enhanced due to large surface to volume ratio; (3) chemically stable ferrite structure avoids metal leakage in the environment and (4) ferrite compositions versatility enhances photodegradation mechanisms. Improved catalytic properties can be achieved using rGo and multiwall carbon nanotubes. This synergic effect is the result of large surface-to-volume ratio of the synthesized composites with enhanced electronic properties as evidenced in the figure below. Fu et al., reported $CoFe_2O_4/rGo$ nanocomposites with concentration greater than 40% of GO, no H_2O_2 was needed to achieve catalytic degradation. For dye degradation mechanism, $CoFe_2O_4TiO_2$ nanocomposites were required.

Inductors magnetic ferrites are promisingly sued in inductors as inductive components in different electronic circuits such as voltage-controlled oscillators, low noise

amplifiers, impedance matching networks, and filters. Their applications in inductors possess general trend in integration and miniaturization for multi-functional electronic devices. This multilayer technology has become important for the mass production of multilayered integrated devices, which allow high degree of integration density. Multilayered capacitors are introduced few decades ago in the market, while inductors penetrated in 1980s [63]. Basic components such as metallic coils and soft ferrites are used to produce inductance. Ferrites-based thin films are used to produce higher permeability at the given operational frequency. Such type of films can be produced through sputtering, but composition and accuracy is difficult to control. Pulsed laser deposition provide high-quality thin films, while method involving the synthesis protocol for ferrite films by a combination of spin coating and sol-gel seems cost-effective and easier [64].

Electromagnetic Interference Suppression (EMI) Many electronic equipments such as digital camera, digital high-speed interface based notebooks, scanners, and computers in small areas has enhanced technology by electromagnetic interference. Fast development in the field of wireless communications led towards the interference produced by magnetic and electric fields. Electromagnetic interference is the degradation in electronic systems produced by the electromagnetic disturbance. Noise produced by the electric devices produced at higher frequency than circuit signals. To reduce/avoid the EMI, different types of suppressors worked at low-pass filters in circuits to block higher frequency signals [65, 66].

5 Conclusions

In this chapter, ferrite nanoparticles were presented as one of the most interesting materials applicable in several applications, for very distinguished areas of science and technology. In this way, magnetic spinel nanoparticles attract attention due to their possibility to be manipulated under application of an external magnetic field. These properties lead spinel ferrites to be utilized on electronic devices, gas sensors, bacterial inactivation, smart drug delivery, photocatalysts, and others. The crystal structure, magnetic and optical properties of spinel ferrites depend on the preparation method, and some usual synthesis methods (microemulsion, sol-gel, combustion solution, coprecipitation, etc.) could be employed depending on the refinement or property optimization required. The efficiency of spinel ferrites in different kinds of science fields shows that those materials are highly versatile products, which makes the ferrite nanoparticles suitable for many biomedical and technological applications.

References

1. Heinz H et al (2017) Nanoparticle decoration with surfactants: molecular interactions, assembly, and applications. Surf Sci Rep 72(1):1–58
2. Goldman A (2012) Handbook of modern ferromagnetic materials. Springer, US
3. Riaz S et al (2014) Magnetic and magnetization properties of iron aluminum oxide thin films prepared by sol-gel. IEEE Trans Magn 50(8):1–4
4. Cullity BD, Graham CD (2011) Introduction to magnetic materials. Wiley
5. Naseri MG, Saion EB (2012) Crystalization in spinel ferrite nanoparticles. In: Advances in crystallization processes, pp 349–380
6. Kumar GR, Kumar KV, Venudhar YC (2012) Synthesis, structural and magnetic properties of copper substituted nickel ferrites by sol-gel method
7. Murthy Y, Rao TK, Singh R (2010) Synthesis and characterization of nano silver ferrite composite. J Magn Magn Mater 322(14):2071–2074
8. Tatarchuk T et al (2016) Spinel ferrite nanoparticles: synthesis, crystal structure, properties, and perspective applications. In: International conference on nanotechnology and nanomaterials. Springer
9. Kefeni KK, Msagati TA, Mamba BB (2017) Ferrite nanoparticles: synthesis, characterisation and applications in electronic device. Mater Sci Eng B 215:37–55
10. Hanini A et al (2018) Ferrite nanoparticles for cancer hyperthermia therapy. Handbook of nanomaterials for industrial applications. Elsevier, pp 638–661
11. Shi D et al (2012) Controlled nanostructuring of multiphase core-shell nanowires by a template-assisted electrodeposition approach. Nanotechnology 23(30):305601
12. Sanpo N et al (2013) Transition metal-substituted cobalt ferrite nanoparticles for biomedical applications. Acta Biomater 9(3):5830–5837
13. Goutam SP et al (2020) Green synthesis of nanoparticles and their applications in water and wastewater treatment. Bioremediation of industrial waste for environmental safety. Springer, pp 349–379
14. Low C, Wills R, Walsh F (2006) Electrodeposition of composite coatings containing nanoparticles in a metal deposit. Surf Coat Technol 201(1–2):371–383
15. Zhao Y-G et al (2010) Synthesis, characterization and properties of ethylenediamine-functionalized Fe_3O_4 magnetic polymers for removal of Cr (VI) in wastewater. J Hazard Mater 182(1–3):295–302
16. Li F et al (2007) Magnetic properties of $ZnFe_2O_4$ nanoparticles produced by a low-temperature solid-state reaction method. J Magn Magn Mater 309(2):295–299
17. Amiri GR et al (2011) Magnetic properties and microwave absorption in Ni–Zn and Mn–Zn ferrite nanoparticles synthesized by low-temperature solid-state reaction. J Magn Magn Mater 323(6):730–734
18. Pemartin K et al (2014) Synthesis of Mn–Zn ferrite nanoparticles by the oil-in-water microemulsion reaction method. Colloids Surf A 451:161–171
19. Zeng S et al (2014) Magnetically separable $Ni_{0.6}Fe_{2.4}O_4$ nanoparticles as an effective adsorbent for dye removal: synthesis and study on the kinetic and thermodynamic behaviors for dye adsorption. Chem Eng J 258:218–228
20. Ai Z et al (2010) Facile microwave-assisted synthesis and magnetic and gas sensing properties of Fe_3O_4 nanoroses. J Phys Chem C 114(14):6237–6242
21. Toniolo J et al (2007) Synthesis by the solution combustion process and magnetic properties of iron oxide (Fe_3O_4 and α-Fe_2O_3) particles. J Mater Sci 42(13):4785–4791
22. Gomes GA, da Costa GL, da Silva Figueiredo AB-H (2018) Synthesis of ferrite nanoparticles $Cu_{1-x}Ag_xFe_2O_4$ and evaluation of potential antibacterial activity. J Mater Res Technol 7(3):381–386
23. Chen D-H, He X-R (2001) Synthesis of nickel ferrite nanoparticles by sol-gel method. Mater Res Bull 36(7–8):1369–1377
24. BV, D.C. and D. HYDRAULICS (1962). Absorption spectroscopy

25. Meron T et al (2005) Synthesis and assembly of high-quality cobalt ferrite nanocrystals prepared by a modified sol-gel technique. J Magn Magn Mater 292:11–16

26. Avazpour L, Toroghinejad M, Shokrollahi H (2015) Synthesis of single-phase cobalt ferrite nanoparticles via a novel EDTA/EG precursor-based route and their magnetic properties. J Alloy Compd 637:497–503

27. Marinca TF, Chicinaş I, Isnard O (2013) Structural and magnetic properties of the copper ferrite obtained by reactive milling and heat treatment. Ceram Int 39(4):4179–4186

28. Manova E et al (2004) Mechano-synthesis, characterization, and magnetic properties of nanoparticles of cobalt ferrite, $CoFe_2O_4$. Chem Mater 16(26):5689–5696

29. Zhang Z et al (2013) Synthesis and Characterization of $NiFe_2O_4$ Nanoparticles via Solid-State Reaction. Int J Appl Ceram Technol 10(1):142–149

30. Zi Z et al (2009) Synthesis and magnetic properties of $CoFe_2O_4$ ferrite nanoparticles. J Magn Magn Mater 321(9):1251–1255

31. Akhtar K et al (2020) Functionalized cobalt ferrite cubes: toxicity, interactions and mineralization into ferritin proteins. Appl Nanosci 10(9):3659–3674

32. Baldi G et al (2007) Synthesis and coating of cobalt ferrite nanoparticles: a first step toward the obtainment of new magnetic nanocarriers. Langmuir 23(7):4026–4028

33. Dai Q et al (2010) Monodisperse cobalt ferrite nanomagnets with uniform silica coatings. Langmuir 26(22):17546–17551

34. Deligöz H et al (2012) Synthesis, structural and electrical properties of triethylene glycol (TREG) stabilized $Mn_{0.2}Co_{0.8}Fe_2O_4$ NPs. Mater Res Bull 47(3):537–543

35. Duan H et al (2008) Reexamining the effects of particle size and surface chemistry on the magnetic properties of iron oxide nanocrystals: new insights into spin disorder and proton relaxivity. J Phys Chem C 112(22):8127–8131

36. Odio OF, Reguera E (2017) Nanostructured spinel ferrites: Synthesis, functionalization, nanomagnetism and environmental applications. In: Magnetic spinels-synthesis, properties and applications, pp 185–216

37. Ge J et al (2007) One-step synthesis of highly water-soluble magnetite colloidal nanocrystals. Chem Euro J 13(25):7153–7161

38. Costa FBT et al (2019) Highly magnetizable crosslinked chloromethylated polystyrene-based nanocomposite beads for selective molecular separation of 4-aminobenzoic acid. ACS Omega 4(3):5640–5649

39. Zhao F et al (2015) Green synthesis of magnetic EDTA-and/or DTPA-cross-linked chitosan adsorbents for highly efficient removal of metals. Ind Eng Chem Res 54(4):1271–1281

40. Ren Y et al (2013) Magnetic EDTA-modified chitosan/SiO_2/Fe_3O_4 adsorbent: preparation, characterization, and application in heavy metal adsorption. Chem Eng J 226:300–311

41. Ge F et al (2012) Effective removal of heavy metal ions Cd^{2+}, Zn^{2+}, Pb^{2+}, Cu^{2+} from aqueous solution by polymer-modified magnetic nanoparticles. J Hazard Mater 211:366–372

42. Bakshi UA, Bakshi VU (2009) Electrical circuits and machines. Technical Publications

43. Pervaiz E, Gul I, Virk MS (2014) Magnetic and RF-electromagnetic absorbing study of aluminum doped nickel ferrites prepared by two techniques. Mater Res Exp 1(1):016104

44. Hussain MI et al (2020) Ferrite nanoparticles for biomedical applications. Magnetic nanoheterostructures. Springer, pp 243–265

45. Javed Y et al (2017) MRI based on iron oxide nanoparticles contrast agents: effect of oxidation state and architecture. J Nanopart Res 19(11):1–25

46. Srinivasan SY et al (2018) Applications of cobalt ferrite nanoparticles in biomedical nanotechnology. Nanomedicine 13(10):1221–1238

47. Hajba L, Guttman A (2016) The use of magnetic nanoparticles in cancer theranostics: toward handheld diagnostic devices. Biotechnol Adv 34(4):354–361

48. Karponis D, Azzawi M, Seifalian A (2016) An arsenal of magnetic nanoparticles; perspectives in the treatment of cancer. Nanomedicine 11(16):2215–2232

49. Huang HS, Hainfeld JF (2013) Intravenous magnetic nanoparticle cancer hyperthermia. Int J Nanomed 8:2521

50. Organization WH (2014) Antimicrobial resistance: global report on surveillance. World Health Organization
51. Raffi M et al (2010) Investigations into the antibacterial behavior of copper nanoparticles against *Escherichia coli*. Annals of microbiology 60(1):75–80
52. Hundáková M, Dědková K, Martynková GS (2017) Decoration of inorganic substrates with metallic nanoparticles and their application as antimicrobial agents. Metal nanoparticles in pharma. Springer, pp 295–336
53. Lin L et al (2013) Ag–$CuFe_2O_4$ magnetic hollow fibers for recyclable antibacterial materials. J Mater Chem B 1(21):2719–2723
54. Gong P et al (2007) Preparation and antibacterial activity of Fe_3O_4 @ Ag nanoparticles. Nanotechnology 18(28):285604
55. Mohapatra J, Xing M, Liu JP (2019) Inductive thermal effect of ferrite magnetic nanoparticles. Materials 12(19):3208
56. Praveena K et al (2016) Enhanced magnetic domain relaxation frequency and low power losses in Zn^{2+} substituted manganese ferrites potential for high frequency applications. J Magn Magn Mater 420:129–142
57. Li L et al (2017) Porous $ZnFe_2O_4$ nanorods with net-worked nanostructure for highly sensor response and fast response acetone gas sensor. Sens Actuat B Chem 248:85–91
58. Stergiou CA, Litsardakis G (2016) Y-type hexagonal ferrites for microwave absorber and antenna applications. J Magn Magn Mater 405:54–61
59. Casbeer E, Sharma VK, Li X-Z (2012) Synthesis and photocatalytic activity of ferrites under visible light: a review. Sep Purif Technol 87:1–14
60. Shad NA et al (2019) Photocatalytic degradation performance of cadmium tungstate ($CdWO_4$) nanosheets-assembly and their hydrogen storage features. Ceram Int 45(15):19015–19021
61. Gómez-Pastora J, Bringas E, Ortiz I (2014) Recent progress and future challenges on the use of high performance magnetic nano-adsorbents in environmental applications. Chem Eng J 256:187–20s4
62. Hua M et al (2012) Heavy metal removal from water/wastewater by nanosized metal oxides: a review. J Hazard Mater 211:317–331
63. Ahmed MAA (2017) A review on the properties and uses of ferrite magnet. Sudan University of Science and Technology
64. Yang C et al (2006) Fully integrated ferrite-based inductors for RF ICs. Sens Actuators A 130:365–370
65. Stojanovic G et al (2006) High-performance zig-zag and meander inductors embedded in ferrite material. J Magn Magn Mater 297(2):76–83
66. Feng Y-B et al (2006) Electromagnetic and absorption properties of carbonyl iron/rubber radar absorbing materials. IEEE Trans Magn 42(3):363–368

Potential of Iron Oxide Nanoparticles as Drug Delivery Vehicle

Muhammad Aamir Hassan, Aqib Zafar Khan, Muhammad Munir Sajid, Yasir Javed, Asmat Ullah, Naveed Akhtar Shad, Surender K. Sharma, Muhammad Shafique, and Muhammad Sarwar

Abstract Nanotechnology has introduced new techniques and therapeutic approaches for the treatment of different cancer types. Current cancer-curing drugs have many limitations such as use of high concentrations, effects on other cells, and non-confinement at cancer sites, which reduce the efficacy of drugs and also induce toxic effects in other normal cells. Nanomaterials have provided new ways to increase the efficacy of already used cancer drugs by providing drug delivery systems. Anticancer drugs can be encapsulated/attached with the nanomaterials and delivered at specific sites and cells under certain microenvironment conditions. Among metallic oxide nanoparticles, iron-based particles have shown great potential in drug delivery and at the same time for cancer treatment by producing localized heat. Therefore, researchers have focused on iron oxide nanoparticles as drug delivery vehicles. This chapter highlights the synthesizing methods of iron oxide nanoparticles such as co-precipitation, thermal decomposition, microemulsion, sol–gel, and additional chemical methods including hydrothermal, sonochemical decomposition, and electrochemical for their wide range of biomedical applications. It also provides a brief

M. A. Hassan · M. Sarwar
National Institute for Biotechnology and Genetic Engineering (NIBGE), Faisalabad, Pakistan

A. Z. Khan
State Key Laboratory of Microbial Metabolism, Joint International Research Laboratory of Metabolic and Developmental Sciences, School of Life Sciences and Biotechnology, Shanghai Jiaotong University, Shanghai 200240, China

M. M. Sajid · N. A. Shad (✉)
Agricultural Biotechnology Division, National Institute for Biotechnology & Genetic Engineering (NIBGE), Faisalabad, Pakistan

Y. Javed · A. Ullah
Department of Physics, University of Agriculture, Faisalabad, Pakistan

S. K. Sharma
Department of Physics, Federal University of Maranhao, Sao Luis, Brazil

Department of Physics, Central University of Punjab, Bathinda 151401, India

M. Shafique
Department of Microbiology, Government College University Faisalabad, Faisalabad, Pakistan

overview of recent developments in iron oxide nanoparticles, some limitations in the explored research areas. and suggests future directions to overcome these limitations.

Keywords Iron oxide nanoparticles · Drug delivery · Biocompatibility · Surface modification · Antibodies

1 Introduction

Cells in the human body grow systematically; however, sometimes there might be abnormal growth, which leads toward unwanted cells in the body. These cells can be toxic in nature and move freely to other parts of the body to cause a malady called cancer. The uncontrolled multiplication of these cells takes many forms to make tumor masses [1]. When the masses are detected to be small or at an early stage, surgical approaches can be considered the best for their removal, but some tissues or organs are very sensitive such as brain and pancreatic tissue due to the presence of number of healthy tissues nearby [2–4]. Once a cancerous cell starts to grow, it moves from the source site and migrates to nutrient-rich and suitable environment to develop more conveniently. According to World Health Organization (WHO), it is the second global death causing disease with an estimation of about 9.8 million people in 2018 [5].

The cancer cells are mostly removed from the infected area at an early stage by surgery, radiotherapy, and chemotherapy so that these will not be harmful to other cells; however, early detection is one of the limitations in the case of cancer. Although early detection is now possible, most of the time these strategies are not very viable due to their side effects [6, 7]. Therefore, scientists have started working to find some sustainable solutions for cancer treatment and then some useful therapies come in this field such as hormonal therapies [8], checkpoint-inhibitor therapy, photodynamic therapy (PDT) [9], and photothermal therapy (PTT) [10, 11]. There are some hormone-sensitive cancers such as breast, prostate, adrenal gland, and endometrium. In hormone therapeutic approach, hormone related to cancer is used for destroying the cancer cells. Checkpoint-inhibitor treatment hits immune checkpoints, which is responsible for significant regulators of the immune system that when stimulated can inhibit the immune response for the stimulus. Some cancers can protect themselves from attack by stimulating immune checkpoint targets. Checkpoint therapy can block inhibitory checkpoints by restoring immune system function. Photothermal and photodynamic therapies are light-based treatment approaches to kill cancer cells by thermal (infrared rays) and oxidative stress, respectively.

Diseases are commonly started by disturbing cellular activities at molecular level, which needs to be reconnoitered for diagnostic, treatment, and prevention. The production of substances as nanoscale helps in this area with the advancement of nanotechnology approaches. Most common types of nanoparticles are metallic, metal oxide, and carbon-based nanoparticles, used for cancer treatment.

Size of the employed nanomaterial is important for their activity while nanoscale materials especially 1–100 nm are emerged due to their applications in sensors and medical devices. Structure, synthesis approaches, and manipulation are other important factors for nanoparticles. For medical applications, the particles should be non-toxic for normal cells, can absorb light-specific wavelength, target-specific, and degradable. Many nanoparticles change their structure during photothermal approach to ameliorate their treatment value. While for target-specific, sometimes, a biological signal molecule is attached, which leads the particles to target-specific site [12].

Among metal oxide NPs, iron-based particles show their great potential in cancer treatment as shown in further sections. Iron-based nanoparticles are commonly used in two oxidation forms called magnetite (Fe_3O_4) and maghemite (γ-Fe_2O_3). Both of these structures are media-based to let the particles a stable form, which may be further modified by the addition of organic acids, hydrophilic, or polysaccharide molecules [13–15].

2 Synthesis Methods

Confirmation and morphology are two characteristics on which magnetic properties of iron oxide nanoparticles (IONP) are dependent. Therefore, selection of an appropriate approach to construct these nanoparticles is important for the surety of cell size, shape, and size distribution. Chemical, physical, and biological synthesis are the three approaches used for IONP synthesis [16–19]. Control of particle size by physical method is hard in nanometer size range [19]. Microbes and plants are good in utilization of salts for themselves via enzyme and phytochemicals, respectively, and convert the salt molecules into nanoparticles. This biological means of nanoparticle production is eco-friendly, and the products attained by means of such trials incline to demonstrate virtuous biocompatibility. The size ranges are diverse in this approach along with low productivity. Chemical approach is most commonly used, which is more than 90% of all approaches to produce nanoparticles [16].

2.1 Co-Precipitation

This is the most commonly used laboratory approach to synthesize IONP, where Fe^{2+} and Fe^{3+} aqueous salt solutions are precipitated at the same time in the presence of a base. However, type of base, salt, temperature, and pH are main parameters, which influence size, shape, and magnetic properties of NPs. Yield of NPs is quite high in this approach, but higher polydispersity and low degree of crystallinity are drawbacks which lower their activity. Since easy use in commercial aspects, co-precipitation is modified to overcome their drawbacks, which includes utilization of magnetic field, ultrasound succor, special base solutions such as alkanolamines,

in situ co-precipitation in a carboxyl-functionalized polymer matrix, and finally, co-precipitation of $FeC_{l3} \cdot 6H_2O$, $FeSO_4 \cdot 7H_2O$, and $Gd(NO_3)_3$ aqueous solutions by the addition of NaOH [20–24].

2.2 Thermal Decomposition

When organic iron salt and stabilizing surfactants are mixed with organic solvent, then organic iron salt is thermally decomposed, which results in the production of nanoparticles with fine-size dispersal and virtuous crystallinity [25, 26]. Surfactant molecules are mostly amphiphilic in nature, which improve nucleation and growth kinetics of particles. Oleic acid, oleylamine, fatty acids, and hexadecyl amine are some of the known examples. While this approach is beneficial in terms of size and crystal morphology, but on other side, due to utilization of toxic chemicals in the reaction, makes it non-environmentally friendly. For biomedical application of nanoparticles, manufacturing via this approach also requires water-dispersible and biocompatibility. Three major factors which influence the size and morphology of particles are heating time, temperature, and precursor-to-surfactant ratio [27].

2.3 Micro-Emulsion

In this method of NPs formation, isotropic scattering of two or more immiscible liquids is stabilized thermodynamically. There are two methodologies used in microemulsion, i.e., reversed micelles (water in oil) and normal micelles (oil in water). For the synthesis of nanoparticles, dispersion phase is used because liquid phases deliver suitable medium for nucleation of controlled growth. There are numerous types of amphiphilic surfactants such as polyethoxylates, SDS (sodium dodecyl sulfate), DSS (dioctyl sodium dodecyl sulfate), and CTAB (cetyltrimethylammonium bromide) [28] utilized during the reaction. Microemulsion method has advantages over other nanoparticle fabrication methods due to its ability to produce superparamagnetic iron oxide nanoparticles. In this method, the size of nanoparticles is controlled by changing the micelles' size. However, the size of nanoparticles is improved by the polydispersity of comparative homozygous-sized micelles. In microemulsion, a relatively lower temperature is used during the fabrication process as compared to other methods, which is the main drawback of this technique. The low-temperature-based fabrication methods give poor crystal structure, abnormal morphology, and lower yield. Therefore, high temperature and thermal annealing are being used for IONPs synthesis, which improves the yield and structural characteristics [29, 30]. Complications associated with uncomplimentary properties and larger quantities of surfactant residual severely affects the characteristics of the IONPs [18].

2.4 Sol–gel

This approach is commonly used for formation of IONPs coated by silica due to colloidal solutions. This colloidal solution is formed by condensation and hydrolysis of two different solutions such as 30% aqueous H_2O_2 with Fe^{3+} solutions and TEOS (tetraethyl orthosilicate) in ethanol. Three-dimensional iron oxide network can be obtained due to chemical reaction or solvent extraction. Additional crushing step is required for obtaining iron nanoparticles. Another way to obtain nanoparticles is the addition of surfactant, which lowers the system energy and would not proceed to crystallization of particles and formed nanoparticles instead of formation of a 3D network. Monodisperse and moderately bigger sized particles are obtained in this approach with good yield. The reaction is mostly conducted at room temperature; therefore, post-treatment is required for proper crystal formation. Different types of byproducts are also formed during the reactions, which need to be extracted for purification of IONP. The pH and temperature are the main restrictions for solvent, whereas concentration of salt precursors impacts the assembly and the characteristics of the IONPs. The viscosity of the silica shell is archetypally tweaked by monitoring the volume of TEOS and ammonia [31–33].

2.5 Additional Chemical Methods

With the advancement in research on nanomaterials and drawbacks as mentioned above, scientists are trying to find more suitable methods for development so that high yield, sustainability, stable structure, and environment-friendly nanoparticles can be obtained. Hydrothermal, sonochemical, and electrochemical are some of those methods more frequently used.

2.5.1 Hydrothermal

In this method, the solution of iron salt is put into teflon-lined stainless-steel auto-clave and then kept there till the temperature will cross 200 °C for different times. As the temperature enhances, the pressure inside the container also enhances. This high temperature and high pressure cause synergistic effect on iron salt, which improves their magnetic and morphological characteristics. Temperature, pressure, salt concentration, and reaction time are key factors, playing an important role in formation and size of nanoparticles. However, this is not easy to achieve the target size, and many times polydisperse particles are obtained via this method [18, 19, 34].

2.5.2 Sono-Chemical Decomposition

In this method, ultrasonic radiations are used for creating heat in the solution to around 5000 °C. Transformation of monodisperse nanostructures is with a diversity of forms under suitable environments and without the requisite of long or high thermal conditions. It is commonly observed that high temperature causes low crystal structure. Although in sonochemical approach, enormous chilling rate of cavitation's through quenching avoids the IONP crystallization. The resultant nanoparticles can be further treated in powder form at high temperatures for crystallization [18, 19, 34–36].

2.5.3 Electrochemical

In this method, electric current is used for making nanoparticles. This current is passed through a solution that contains anode and cathode. Metal ion species are oxidized from anode and move via electrolyte toward cathode where cathode reduces these ions. Stabilizer is also present in electrolyte, which provides controls growth process of the nanoparticles. In this way, the highest purity nanoparticles are obtained while the size can be manipulated by changing the voltages. This method does not require high temperature, thus, forming byproducts. Commercialization of this approach is quite difficult due to the requirement of large amount of electricity [16, 37].

3   Surface Modification of Iron Oxide Nanoparticles

After finding a suitable approach for the formation of nanoparticles, next step is to find an appropriate molecule for their stability in biological fluids. Some approaches provide this step during synthesis reaction while others do not. This modification is important so that the molecules would not be oxidized, and the biocompatibility of nanoparticles is enhanced. It is also done by using some functional molecules so that it can target only specific cancerous cells.

There are some common examples of constituents used to coat IONPs (Fig. 1); polymers [18, 35, 38], such as amino acids (cysteine, lysine, tyrosine, phenylalanine, and arginine) [39–41], fatty acids (dodecylphosphonic acid, lauric acid, stearic acid, and oleic acid) [42–46], metals (silver, gadolinium, and gold) [47–49], and oxides (TiO_2 and silica) [50–52]. Polymers are undoubtedly the utmost common coating materials among these materials. Recently, there are numerous synthetic and natural polymers used during the fabrication methods of superparamagnetic IONPs; synthetic polymers such as PLGA (polylactic-co-glycolic acid), dendrimers [53, 54] (polyvinyl alcohol) [55], PVA, PEG (polyethylene glycol) [56–59], and PVP (polyvinyl pyrrolidone) [60], while natural polymers are casein [61], chitosan [62, 63], dextran [64–66], albumin [67], alginate [62, 68], polydopamine [69, 70], starch [71], and gelatin [72].
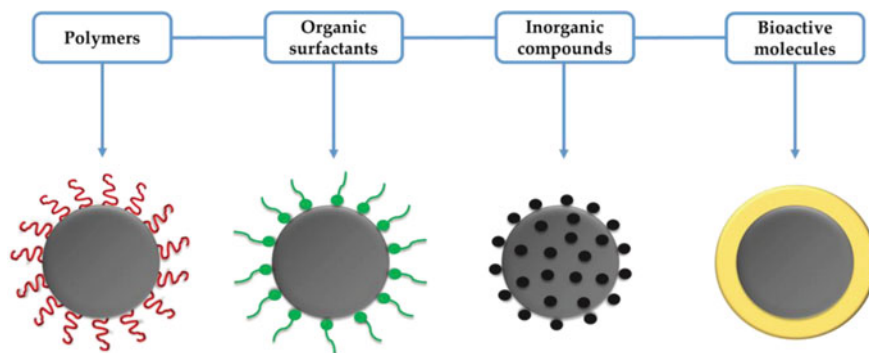
Fig. 1 Different functional moieties used for enhancing biocompatibility of IONPs [73]

Manipulation of nanoparticles with polymer coating is common. For selecting an appropriate polymer, the following two features must be considered [74, 75].

(i)   Obligation as GRAS (generally regarded as safe)
(ii) After transformed intravenously, macrophages existing in liver and spleen should not detect it and avoid producing antibodies before reaching target site.

Polyether and their derivative molecules are exceedingly compatible for surface manipulation and remain intact during vascular circulation of nanoparticles. Most common polyether compounds are PEG and PEGylated starch. Cytotoxicity, circulation time in the arteries, and stability of IONPs depend on PEG molecular weight and density of surface [71, 76]. Another type of molecules commonly used for compatibility is dextran or their derivates (such as carboxydextran and carboxydmethyl-dextran), which itself is not causing any toxicity to cells, but when it will be metabolized, their degraded part may cause disturbances in cellular activity [28, 65, 75, 76].

Along with these ordinary polymers, countless exertions have participated in recent times in evolving stimuli-responsive polymeric (SRP) coatings. The SRP manipulates the inflammation behavior and proceeds toward reversible phase transition under environmental stress. The stress acts as stimuli, which may be any abiotic factor such as enzymes, light, pH, ionic strength, magnetic field, electric field, and temperature. Temperature and pH are common stimuli among all, which are mostly studied. A polymer with temperature stimuli factor depends on lower critical solution temperature (LCST), whose characteristics may be varied due to nearby environmental temperature. They are distended in solution media when the temperature is lower than LCST and experience a phase transition after the temperature is augmented above the LCST. However, pH-sensitive coating depends on the presence of weak acidic group on polymer, which varies during external pH due to carboxyl group protonation manipulation [77–82].

Polymeric micelles and liposomes are two types of vesicles that capture IONPs inside themselves [83–90]. Polymeric micelles are core–shell materials, containing

hydrophobic section. Environmental conditions are apposite for hydrophobic IONPs and provide stability to nanoparticles in the presence of chemical or biological media. The liposome is an amphiphilic bilayer structure of phospholipids whose middle layer is resonating. This area can capture IONPs of hydrophobic nature [83–91].

4   Characterization of Iron Oxide Nanoparticles

There are numerous analytical approaches used to analyze the physiochemical characteristics of IONPs (iron oxide nanoparticles). The flame atomic-absorption spectrometry, ICP-MS, and 1, 10-phenanthroline assay have been used for the measurement of iron concentrations in samples. The morphology, core size distribution, and core size of IONPs can be determined by atomic force microscopy and transmission electron microscopy [92, 93]. The superparamagnetic IONPs crystallographic phase and composition can be determined by XRD, high-resolution TEM, and selected area electron diffraction (SAED) [94]. The nanoparticle tracking analysis (NTA) and dynamic light scattering (DLS) techniques are used for the measurement of hydrodynamic size distribution and hydrodynamic diameter of IONPs. These techniques also are used for identification of aggregation behavior and colloidal stability of IONPs in suspension. However, DLS is very sensitive to large aggregates present in the solution; therefore, proper dispersion is very important before measurement. The NTA has a narrow spectrum identification limit as compared to DLS [95].

The X-ray photoelectron spectroscopy, Fourier transform infrared spectroscopy, and nuclear magnetic resonance are used to identify the elemental composition, functional groups, surface-to-volume ratio, and size with size distribution of IONPs, respectively. The size with size distribution, shape, and pore sizes of IONPs can be identified by employing ultra-small angle X-ray scattering and small-angle X-ray scattering. [96]. Superconducting quantum interference measurement device is used for the analysis of magnetic characteristics of IONPs [92].

To examine the application of superparamagnetic IONPs for magnetic resonance-based imaging, T_2^* (effective transverse), T_2 (transverse), and T_1 (longitudinal) relaxation time with consistent relaxation rates such as R_2^*, R_2, and R_1 (these are the inverse of T_2^*, T_2, and T_2), respectively, are identified by NMR spectroscopy and MR scanners. The measurement of changes in the contrast agents (R_1 and R_2) in MRI have functions according to the concentration used and matching relaxivity r_1 and r_2 are identified according to concentration of contrasting agents. The concentrations of contrast agents in MRI are measured in $mM^{-1} s^{-1}$. There are various constraints of IONPs which have collective impact on transverse and longitudinal relaxivity such as size, size distribution, coating of nanoparticles, morphology, hydrodynamic diameter, and core size of IONPs. r_2 exhibits linear direct relation to the core size of NPs, it varies from 5 to 18 nm. On the other hand, r_1 remains slightly in-variant as compared to r_2, i.e., the core size of particle is greater than 8 nm.

The r_2 progressively increases with the increment in hydrodynamic diameter for smaller cluster up to the 80 nm in diameter because the superparamagnetic IONPs

have the capability to steadily distribute in aqueous medium and diffusion of proton into the magnetic cores. If the hydrodynamic diameter is higher than the 90 nm, the r_2 gradually decreases because of the surface accessibility reduction by arising of the proton exchange rate with aqueous medium. The characteristics of contrast agents and their relaxivity itself depend on various parameters such as dispersion of contrast agent into biological fluid, temperature, and magnetic field to be applied [97–100].

The full width at half maximum (FWHM), point-spread function (PSF) as well as signal-to-noise ratio (SNR) in blood, water, and serum can be evaluated on the basis of measurement of magnetic particle imaging (MPI). The capability of IONPs for delivering the attired imaging in MPI is by adopting SNR parameter. The SNR is known as the ratio of power of background noise with power of sample signal. The SNR identification for tracer requirements is to be standardized with concentrations of iron because of the different MPI tracers comprise of various quantities of iron. These changes are the modifications as the purpose of applied drive field for the identification of magnetization changes by PSF of IONPs. However, Schmale et al. [101, 102] have reported the technique used for the identification of spectroscopic magnetic particle imaging from PSF. The Δx (spatial resolution) that is attainable in the devise of MPI is acquired by FWHM of PSF, and FWHM is inversely proportional to the spatial resolution. Higher spatial resolution in MPI linked with lower values of FWHM. Likewise, other MPI also disparagingly depends on various parameters that influence the magnetization expression such as size and size distribution of IONPs [101, 102].

The SPION can be exposed to microwaves, ultrasound waves, radiofrequency, or any other medium. The specific absorption rate (SAR) is defined as the magnetic power absorbed per unit mass of magnetic specie for the assessment hyperthermia presentation. The SAR is also associated to the amplitude of magnetic field, magnetic characteristics, monodispersity, structural, frequency, and size of IONPs. The SAR values are typically in various ranges from 4 to 100 W/ g for IONPs dispersions commercially available. The amplitude of magnetic field and frequency rather than composition and structure of IONPs play a significant role in SAR and generation of heat [103, 104].

5   Analysis of the Biocompatibility of Iron Oxide Nanoparticles

The significant clinical use of IONPs requires cautious evaluation of their toxicological traits particularly for healthy as well as patients. Consequently, each constraint used in diagnostics requires to be comprehensively estimated with concern to their potential side effects. Generally, if the level of iron is exceeded from normal ranges, then extra quantity of iron ions is a major cause for creation of reactive oxygen species (ROS) by Fenton reaction. If in normal cells, the accumulation of iron is increased, ROS can be created, which enhanced the lipid peroxidation, DNA damage, and ability

of cell's scavenging and ultimately induces cell death by ferroptosis [105]. Rather than cytotoxicity of IONPs, ROS contribute in the regulation of redox reaction in various signaling processes of cells. These ROS triggers the cell motility, proliferation, death, and phagocytic capability and also involve in M_1-like polarization malfunctioning which is responsible for defending of the body from various types of pathogens [106, 107].

There are numerous in vivo and in vitro protocols that have been used for the biocompatibility assessment of IONPs. There is slight cytotoxicity reported at 100 µg/ml when the cell is exposed to IONPs in vitro. Generally, the cytotoxicity depends upon numerous types of factors such as size of the particle, protein-IONPs interaction, hydrodynamic diameter, coating material nature, time of exposure, and dose rate [108–111]. There is the activation of many important pathways of immune system when IONPs is coated with polyethyleneimine (PEI) exposed to cell in vitro. These immunological pathways comprise induction of macrophages by M1-like activation and dendritic cell activation by the exposure of PEI-coated IONPs [112–114]. For cell tracking determinations, when IONPs are loaded with cells, attention should be paid that cataloging does not affect the function, motility, and proliferation of the cells. Previous reports revealed that IONPs coated with sugars present various cellular functions and phenotypic effects on various types of cells such as tumor cells [115], endothelial cells [116, 117], mesenchymal stem cells [118, 119], and dendritic cells [120]. There are various techniques used for the determination of in vitro IONPs cytotoxicity such as analysis of gene expression, immune system marker (necrosis and apoptosis) based staining, assessment of cell membrane integrity by the measurement of lactate dehydrogenase, and MTT or XTT assay for checking the redox activity of mitochondria. These types of IONPs cytotoxicity assays used for in vitro measurement of adverse effects deliver a significant biocompatibility impression for these nanoparticles' formulation. Including these factors, there are many other aspects accounted for in vivo biocompatibility such as cellular accumulations, deposition of IONPs into organ, and distribution of particles.

There are numerous studies that have been reported on intravenous administration of IONPs and have little or no toxic effect on the patient body. A case study has reported on cytotoxicity of administered ferucarbotran and various adverse effects exhibited such as headache, pain, and irritation at the site of injection. In this study, few patients expressed these types of toxic effects by the administration of ferucarbotran [121]. Approximately, there are less than 1% cases of severe side effects comprising hypotension, dyspnea, chest pain, and anaphylatic shock and about 10% to 20% showed moderate side effects such as urticarial, headache, and back pain. The adverse effects of IONPs administration also depend on administration rate, place of injection, and time of injection [122, 123]. Normally, IONPs are accumulated in spleen, liver, high-phagocytic-capacity-containing cells, fenestrated blood vessels, and other tissues having larger vascularization when it is injected intravenously. Generally, these organs accomplish their physical state with the accumulation of IONPs, e.g., liver is a main vital organ and having the ability to store iron in the body [122]. Recently, zebrafish (*Danio rerio*) embryo assay has been developed for detection of biocompatibility-based cytotoxicity analysis with the addition of relatively

high throughput analysis in vivo because this fish has more complicated system as cell culture in case of an intermediate model system [123].

6 Use of Iron Oxide for Drug Delivery

The evaluation of adverse effects of various magnetic nanoparticles acted as nanocarriers coated with drugs in patients revealed that there are not any considerable outcomes obtained, primary to end of medical improvement in phase II/III. An alternate approach for drug delivery into system established on IONPs is the coating of these structures with directing moieties such as targeting peptides, folate, hyaluronic acid, antibodies, transferrin, and aptamers (Fig. 2). These directing moieties can be identified by particular receptors/ integrins that are over regulated precisely on the surface of tumor cell consequential in reducing of the quantity and decreasing off-target. The drug delivery with targeted moieties for the delivery of anticancer drugs, the novel drug delivery system is magnetic nanoparticle with a goal to deliver recommendations on the improvement of IONPs through discussion.

6.1 Transferrin and Its Analogues

An important tumor-targeting ligand is transferrin (Tf), which is an Fe ion-combining blood plasma glycoprotein that participates in the transport of Fe ions and has low immunogenicity [124, 125]. The Tf has a high affinity to the Tf receptor (TfR) overexpressed on diverse tumor cells, most notably breast cancer cells [126]. The overexpression of TfR on tumor tissues has been successfully employed to construct targeted
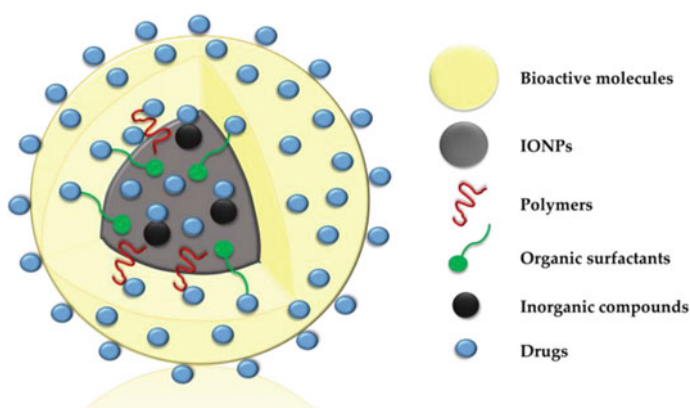
Fig. 2 Graphical description of drug attachment with iron oxide nanoparticles or core–shell nanoparticles

Tf-conjugated delivery systems for cancer therapy in phase I/II clinical trials. Indeed, examples of such use include CALAA-01 (a polymer-based nanoparticle containing siRNA), MBP-426 (TfR-targeted liposomal formulation of oxaliplatin designed by Mebiopharm), SGT-94 (RB94 gene encapsulated by a liposome targeting the TfR single-chain antibody fragment), and SGT-53 (an intravenous, tumor-targeted liposomal p53 delivery system) [127]. As a ligand, Tf also binds to the surface of IONPs to selectively transfer therapeutic drugs [DOX, paclitaxel (PTX), and cisplatin] or genes (CYP2B1, ETR, and LacZ) into cancer cells overexpressing TfR by the TfR-mediated endocytosis pathway [128–130].

Yang et al. [131] developed a tumor-targeting nano-immunoliposome platform to efficiently encapsulate IONPs (scL nanocomplex) without chemical modification. The scL nanocomplex consisted of a diagnostic (MRI contrast agent [132]) or a therapeutic (p53 DNA [133] and anti-HER-2 siRNA [134]) payload and a single-chain antibody Fv fragment (TfR-scFv) [135]. The results exhibited that the scL nanocomplex could specifically deliver the therapeutic payload (p53 DNA and anti-HER-2 siRNA) to the tumors, leading to an increased response to conventional chemotherapy with dramatic tumor growth inhibition compared to the untreated group [131].

Some polymers have been decorated on the surface of Tf-conjugated IONPs for drug and gene delivery. Ghadiri et al. [136] developed a targeted drug delivery system (TDS-NPs) using dextran-spermine biopolymer-modified Tf-conjugated IONPs for capecitabine delivery across the blood–brain barrier (BBB). Compared with dextran-spermine-IONPs and free capecitabine, TDS-NPs with capecitabine displayed remarkable cellular uptake and enhanced cytotoxicity to U87MG cells. Furthermore, in vivo biodistribution and histological studies showed a significant increase in Fe concentration in the brain. Recently, Wang et al. [125] constructed an innovative multifunctional IONPs nanoplatform containing chitosan (CS), an antitumor drug (DOX), tumor-specific ligand Tf, and fluorescent dye rhodamine B isothiocyanate (RBITC) for evaluation of their biological properties in brain tumor cells. The results exhibited that the fluorescent Tf-CS/IONPs containing a contrast agent could be employed as probes for simultaneous MRI and fluorescence imaging. Furthermore, the drug-loaded Tf-CS/IONPs could effectively inhibit cell proliferation and induce cell apoptosis and autophagy. These results display that the Tf-CS/IONPs have high potential as anticancer targeted drug delivery systems and as MRI/fluorescence imaging probes for the therapy and diagnosis of human brain tumors (Fig. 3).

Singh et al. [138] used the epoxide functionality of PGMA to covalently attach Tf onto the surface of Dtxl-Np to obtain Tf-Dtxl-Np. By comparing Tf-free Dtxl-Np and Tf-tethered Dtxl-Np, they demonstrated that the two mechanisms of anticancer targeted delivery systems are active targeting and passive accumulation, which interrelated and dosage dependent. Tf-Dtxl-Np could more efficiently inhibit cell proliferation than Dtxl-Np at lower doses. However, there is no statistical difference in therapeutic efficacy between Dtxl-Np and Tf-Dtxl-Np in the higher dose group, indicating that the EPR effect of cancer tissues is the main factor affecting the efficacy of actively and passively targeted nanomaterials at higher doses. Rajkumar and Prabaharan conjugated iron oxide nanoparticles with DOX, PEG, and folic acid and
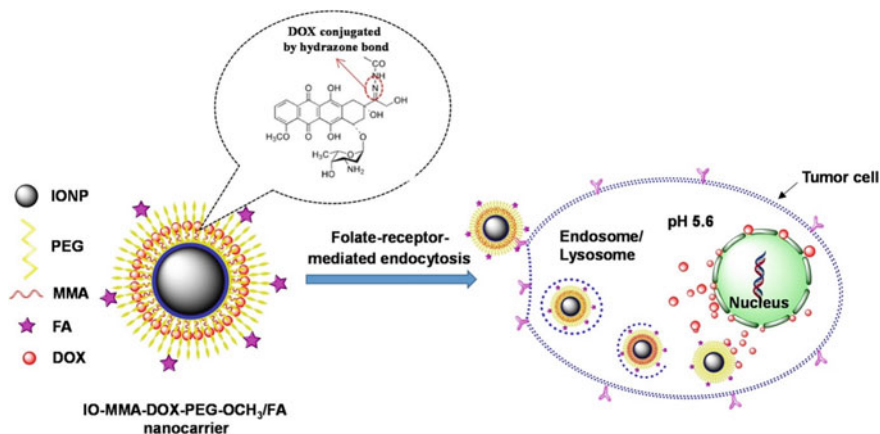
Fig. 3 DOX loaded PEG-folic acid conjugated iron oxide nanoparticles. DOX release was observed at pH 5.6 rather than usual release pH 7.4. Reprinted with permission from [137]

employed for drug delivery and as theranostics. Higher uptake was observed in the presence of folic acid and drug release was observed at pH 5.6. Formulation presented enhanced cytotoxicity against HeLa cells [137].

In addition to polymers, inorganic materials have also been used to modify Tf-conjugated IONPs, resulting in nanoparticles with the significant ability of drug delivery and optical imaging [139]. Chen et al. [140] developed a versatile multi-component nano-system (Fe_3O_4@CNT-HQDs-Trf) containing magnetic nanoparticle (MNP)-filled carbon nanotubes (CNTs), Tf, CdTe quantum dots (QDs), and DOX for the magnetically guided delivery of anticancer agents and targeted optical imaging. In general, the active surface of CNT-conjugated MNPs and QDs can decrease the drug storage capacity and the magnetic-fluorescence dual functionality [141, 142]. Therefore, MNPs were encapsulated inside the CNTs to provide a large effective surface area for improving the drug loading of Fe_3O_4@CNT-HQDs-Trf while avoiding aggregations of MNPs. Tf on the exterior and MNPs in the interior of CNTs could be employed as double-targeted drug delivery systems to penetrate cell membranes, followed by the delivery of DOX to tumor cells by targeting the Tf receptors overexpressed on HeLa cells and magnetically guided targeting by the external magnetic field. These results displayed that Fe_3O_4@CNT-HQDs-Trf has excellent capabilities including magnetically guided tumor-targeted optical imaging and drug delivery [140].

In addition, lactoferrin (LF) is an analog of Tf and belongs to the transferrin family of proteins with a molecular mass of approximately 80,000 Da [143]. The LF is widely found in a variety of body secretions including milk, tears, mucus, blood, and saliva [144]. Furthermore, it has favorable transport properties with a very high affinity for Lf receptors on cancer cells [145]. Thus, some researchers found that the behavior of LF-tethered nanoparticles is similar to that of Tf-tethered analogs. Gupta and Curtis [146] observed that LF-tethered IONPs demonstrated high specificity for

Lf receptors on the cell surface mainly thanks to the ligand–receptor interactions. Thus, they suggested that these nanoparticles might serve as contrast agents for MRI and/or drug delivery in vivo homed cells.

Overall, Tf has been widely applied as a targeting ligand in the active targeting of anticancer agents and IONPs into tumor cells by TfR-mediated endocytosis. However, LF is not internalized by its specific receptor, and it acts by releasing its iron at the plasma membrane without itself being internalized. Regardless of the way Tf or its analogues (e.g., Tf, Rsc, Fv, and LF) enter the cell, they can be conjugated with IONPs and cationic polymers (e.g., CS and PGMA), liposomes, nanoparticles (e.g., QD and CNTs), or other molecules (e.g., RBITC) to achieve targeted drug delivery and/or monitoring in cancer tissues.

6.2 Antibodies

Antibodies are glycoproteins that belong to the superfamily of immunoglobulin. Various antibodies have higher affinity to several receptors or antigens overexpressed on the surface of cancer cells, including epidermal growth factor receptor (EGFR), vascular endothelial growth factor receptor (VEGF), human epidermal receptor-2 (HER-2), hyaluronan receptor (CD44), and PSMA (prostate-specific membrane antigen) [147]. These antibodies or their fragments when combined with nanoparticles can selectively target tumor cells [148].

7 Anti-EGFR Family

It is known that the EGFR family includes HER1 (EGFR and ErbB 1), HER2 and HER3 (ErbB 3), and HER4 (ErbB 4) and have been employed as tyrosine kinase cellular transmembrane receptors that can bind to various closely related ligands such as EGF and transforming growth factor α (TGF-α) [149].

When EGFR is activated by its ligand, the downstream signaling promotes proliferation, migration; consequently, angiogenesis can be triggered [147]. In addition, a high EGFR expression level is strongly correlated with poor prognosis [150]. Furthermore, HER-2 correlates with 16–29% of breast cancers [151], 7–34% of gastric cancers [152, 153], and approximately 30% of salivary duct carcinomas [154], indicating that HER2 is a tumor biomarker and can be considered as a target in cancer treatment. Therefore, several strategies have been already examined in the clinical therapy against cancer, including (i) inhibition of EGFR activation by humanized antibodies such as cetuximab (colorectal and head/neck carcinomas) [155, 156], panitumumab (colorectal carcinomas) [157], nimotuzumab (head/neck carcinomas) [158], and single-chain antibody fragment (ScFv) against EGFR [159] (ScFvEGFR, breast carcinomas) [160], and (ii) HER-2 activation by humanized antibodies such as emtansine and trastuzumab [161, 162] conjugated with nanomaterials [163–165].

Polymers have been combined with cetuximab and IONPs for targeting of therapy and imaging of selective cancer cells [166]. Liao et al. [167] described the preparation of cetuximab-immuno-micelles, in which the thiolated cetuximab has chemically coupled to poly (ethylene glycol)-block-poly(ε-caprolactone) (PEG-PCL) nano-micelles. Cetuximab-immuno-micelles could be effectively loaded with IONPs (16.1%) and DOX (3.8%) and significantly combined with EGFR-overexpressing tumor cells, resulting in a large number of IONPs and DOX being transferred to these cells. Moreover, immuno-micelles are more effective at inhibiting of cell proliferation than their nontargeting counterparts [168]. Recently, cetuximab-modified IONPs (anti-EGFR-PEG-IONPs) are also synthesized as a targeted contrast agent and a synergistic agent for MRI-guided focused ultrasound surgery (MRgFUS) to ablate lung carcinomas (Fig. 4). The result showed that the anti-EGFR-PEG-IONPs could enhance the tumor-ablative efficacy and imaging sensitivity for clinical MRgFUS.

In addition to the complexes of cetuximab to polymer-encapsulated IONPs, cetuximab has been conjugated with lipid-encapsulated IONPs by Chen et al. [169]. They found that such nanoparticles could selectively bind to human glioblastoma (U-251 GBM) cells overexpressing EGFR. Furthermore, the coating of the lipid on the surface of IONPs generated a potent nonfouling performance that could effectively suppress the nonspecific sorption of IONPs.

In addition to cetuximab, nimotuzumab has been combined with MNPs, resulting in efficient uptake of the drug by EGFR-overexpressing tumor cells. Ma et al. [170] synthesized nimotuzumab (mAbh-R3)-labeled core–shell $Fe_3O_4@SiO_2$ nanoparticles ($MNP@SiO_2$-mAbh − R3 NPs), which could significantly improve the cellular uptake and inhibit tumor cell growth in vitro when compared with their nontargeting
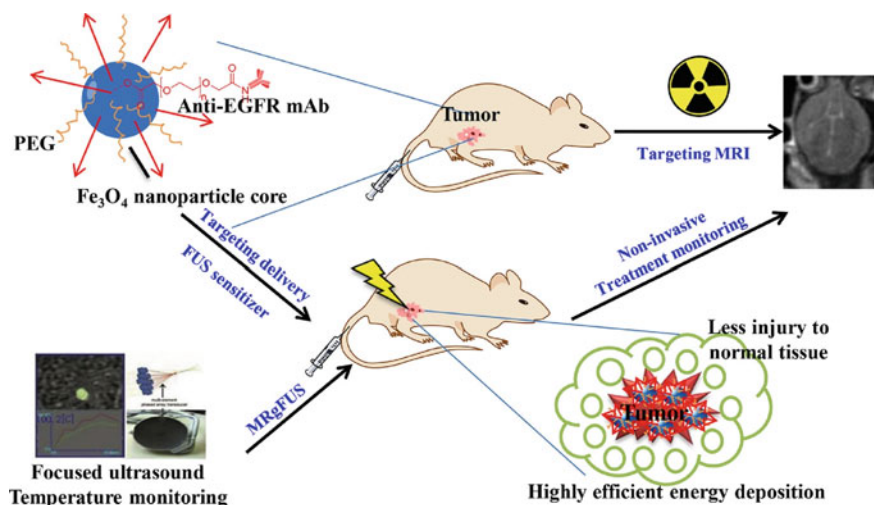
Fig. 4 Schematic representation of the formulation of anti-EGFR-PEG-IONPs for MRI-guided focused ultrasound surgery. Reproduced with permission from [167]

counterparts. mAbh-R3 can promote the uptake rate of $Fe_3O_4@SiO_2$ nanoparticles by EGFR-receptor endocytosis.

Compared with intact EGFR antibody, ScFvEGFR, which contained the specific EGFR-combining region, but lacked the Fc region, possessed several advantages including small size, low molecular weight, less accumulation in normal organs, and immunogenicity [171]. Although the binding affinity of a ScFvEGFR to its receptor is weaker than that of intact antibody, when ScFvEGFR is attached on the surface of the nanoparticles, they could facilitate greater functional affinity [172]. Chen et al. [165] investigated block copolymer poly (ethylene oxide)-block-poly(γ-methacryloxypropyl-trimethoxysilane) (PEO-b-PγMPS)-coated IONPs and conjugate them with ScFvEGFR for forming EGFR-targeted IONPs (ScFvEGFR-IONPs), which interacted strongly with breast tumor cells (MDA-MB-231) overexpressing EGFR, but not with EGFR-negative cells (MDA-MB-453 cells). The results displayed that the signal reduction in the tumor is due to the accumulation of targeted IONPs.

Trastuzumab is the first humanized immunoglobulin type G (IgG) 1 monoclonal antibody approved by the Food and Drug Administration (FDA) for the therapy of breast cancer cells overexpressing HER-2, and it can inhibit the tyrosine kinase activities of HER-2 receptors by signal transduction. Trastuzumab has been conjugated with IONPs to enhance MRI sensitivity for the surveillance of carcinoma markers [173] and improved anticancer efficacy. Lee et al. [174] described an ultrasensitive magnetic resonance probe agent in which trastuzumab was conjugated to IONPs for monitoring small implanted tumors. Similarly, Chen et al. [175] conjugated trastuzumab onto the surface of IONPs containing dextran to form new MRI contrast agents, which could enhance the internalization of nanoparticles by receptor-mediated selectivity in targeting carcinomas, resulting in intensified magnetic resonance signal intensity.

To utilize trastuzumab for a combination therapy against cancer, it has been combined with other drugs (such as DOX and PTX) [176], nanoparticles [177], and micelles [178]. In earlier studies, IONPs, DOX, and trastuzumab-bearing CS have been used by Choi et al. [179] to obtain multipurpose nanocarriers (IONPs/DOX-MFNC). Compared with the nanocarriers without trastuzumab, these nanocarriers can not only increase the diagnostic ability, but also improve antitumor activity by ligand–receptor interactions, providing potential use for early tumor diagnosis and combination treatment for HER2-overexpressing breast cancer. In another study, trastuzumab has been conjugated with pH-sensitive dual-emulsion nanocapsules (DENCs) to simultaneously coat hydrophobic PTX and hydrophilic DOX for combination therapy of HER-2-positive cancers. DENCs combined with magnetic targeted nanoparticles and HER-2-specific trastuzumab (trastuzumab-bound DENCs) showed a remarkable cell uptake in SkBr3 cells overexpressing HER-2. The trastuzumab-bound DENCs have been injected into nude mice bearing SkBr3 tumors, and it inhibited tumor growth more effectively than single-targeted chemotherapy using PTX or DOX. These results indicated that the combination therapy system is a powerful tool in the therapy against tumor, resulting in potential clinical applications [180].

In addition, HER-2-targeting affibody is a small 7000 Da molecule and its performance is similar to that of antibodies. The HER-2-targeting affibody has been combined with IONPs to form a target-specific contrast agent, which can noninvasively image tissues or cells expressing HER-2 by MRI [181]. Similarly, the HER-2 affibody has been also coated on IONPs labeled with NIR830 (a near-infrared dye) to obtain a dual-imaging modality nanoparticle probe, which showed specificity and sensitivity in optical imaging and MRI of primary and metastatic ovarian tumors [182].

Recently, DARPin G3 (ankyrin repeat protein G3), which is a new combining protein containing picomolar appetency for HER-2, has been labeled with fluorescein-5-maleimide to combine with IONPs (IO-G3-5MF) for imaging HER-2. These nanoparticles can selectively bind to and image HER-2-overexpressed breast tumor cells in vivo [183].

7.1 Anti-VEGF antibody

VEGF is an important signaling protein inducing neovascularization, and the major driver of cancer vasculogenesis and angiogenesis [184]. Therefore, anti-VEGF monoclonal antibodies such as bevacizumab, aflibercept and anti-VEGFR2 [185] have been used as drug delivery systems to control the progression of vascular-related diseases by the inhibition of VEGF expression [186–188].

Bevacizumab has been labeled with a radionuclide or a dye to be conjugated with IONPs for cancer multimodality imaging and therapy. Zhao et al. [189] synthesized technetium-99 m (99mTc)-IONPs-bevacizumab nanoparticles which could increase tumor penetration and accumulation. Recently, Lin et al. [190] described a multimodal VEGF-targeted molecular imaging probe (NIR830-bevacizumab-IONPs) including IONPs and NIR830-labeled bevacizumab (Avastin®) for optical imaging and MRI of cancer cells overexpressing VEGF. Compared with nontargeted IONPs, VEGF-targeted NIR830-bevacizumab-IONPs displayed higher accumulation in tumor cells of mice. They recommended to use NIR830-bevacizumab-IONPs as VEGF-targeted double-modality molecular imaging probes and drug delivery systems for the treatment and diagnosis of tumors overexpressing VEGF.

In addition to bevacizumab, other anti-VEGF monoclonal antibodies were conjugated with IONPs for the diagnosis and treatment of tumors [191]. A method for the preparation of vector nanoparticles composed of anti-VEGF monoclonal antibody (anti-VEGF) and IONPs has been established by Abakumov et al. [192], and the nanoparticles could maintain the immunochemical activity of antibody. The resultant nanoparticles containing immunoglobulin could accumulate in the brain tumor after 14 days of tail vein injection. Additionally, stimuli-sensitive polymers have been added to magnetic nanoparticle-based drug delivery systems for enhancing their therapeutic effect. An acid-sensitive polymer, p(aspartate)-graft-p(ethylene glycol)-dodecylamine-hydrazone-(adriamycin-levulinic acid) (PASP-g-PEG-DDAHyd-(ADR-LEV)), has conjugated with IONPs and anti-VEGF to obtain
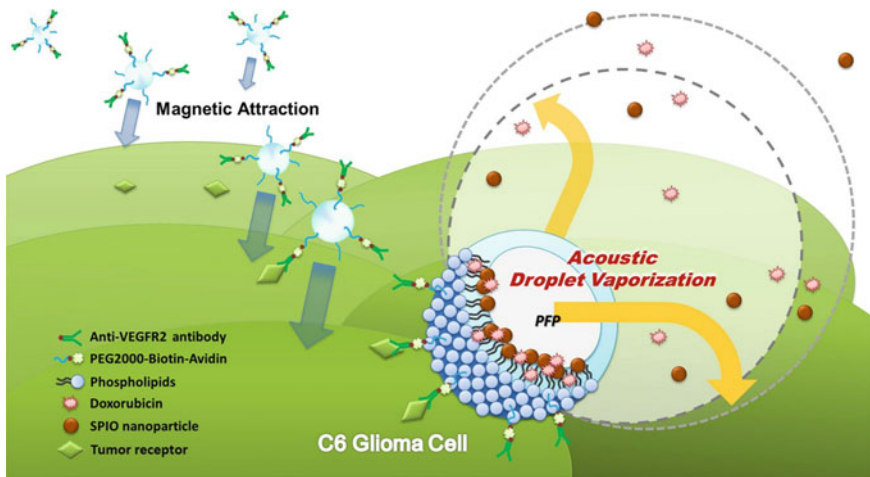
Fig. 5 DOX-loaded IONPs complex conjugated droplets for ultrasound-based targeted drug delivery. Reprinted with permission from [195]

MRI-visible and anti-VEGF-conjugate@IONPs for specific diagnosis and treatment of hepatocellular carcinoma. In vitro drug release studies showed that anti-VEGF-conjugate@IONPs are stable under neutral pH and could be degraded under low pH that mimicked the acidic conditions of endo/lysosomes. Compared with the conjugate@IONPs, the anti-VEGF-conjugate@IONPs could significantly accumulate in liver tumors, indicating their potential application value in MRI detection and treatment of hepatocellular carcinoma [193].

Furthermore, VEGF receptor 2 (VEGFR2) is specifically and highly expressed on vascular endothelial cells of many carcinomas including gliomas [194]. Wang et al. [195] developed a highly integrated droplet system (IO-embedded droplets) composed of anti-VEGFR2 antibodies, IONPs, and DOX to satisfy the multifunctional demands of clinical applications (Fig. 5). Iron oxide embedded droplets possessed the ability of dual-modal imaging including ultrasound imaging and MRI and provided a cocktail treatment strategy by combining with DOX to inhibit tumor growth. This formulation could improve targeting efficiency and cell destruction owing to their capability of magnetism-assisted targeting and insonation-induced acoustic droplet vaporization, suggesting that they are potentially suitable as agents for tumor diagnosis and treatment for clinical applications [196].

8   Conclusion and Future Prospects

Tremendous progress has been made toward the development of multifunctional nanodrug delivery systems for targeted tumor treatment and imaging. Among the drug delivery platforms, targeted delivery systems based on IONPs are particularly

promising. They can be not only accumulated in the cancer cells by the EPR effect and under an external magnetic field due to the superparamagnetic characteristics of IONPs, but also used as tracers to clearly show the location and state of disease in the body because of their excellent MRI-enhancing ability. Furthermore, IONPs can be biodegraded into ferric ions in the human body, especially under the acidic conditions of cells (such as lysosome and endosome), thereby reducing their potential toxicity compared with other inorganic nanoparticles including carbon- and gold-based counterparts. More importantly, the surface of IONPs can be easily functionalized with different types of targeting molecules including Tf, antibodies, aptamers, HA, FA, and targeting peptides through several conjugation strategies. In general, magnetic nanoparticle-based delivery systems with these targeting moieties can be specifically recognized through receptors on the surface of a cell, and they can also enter into tumor cells through both receptor-mediated endocytosis and adsorptive endocytosis pathway.

The Tf has been widely applied as a targeting ligand in conjugation with IONPs in the active targeting of tumor cells by TfR-mediated endocytosis. Its analog, LF, is not internalized by its specific receptor, and the activity of the Lf receptor can be activated by releasing its iron at the plasma membrane. In addition, antibodies are valuable targeting molecules, especially regarding their highest specificity, in the formation of anticancer agent delivery systems including IONPs. However, the difficulty in obtaining regulatory approval, cost, and complexity of preparation can prevent their clinical application. The aptamer mimics the natural properties of the antibody, and at the same time, it contrasts with the antibody. Furthermore, the aptamer exhibits other superior properties including rapid tissue penetration, low toxicity, and immuno-genicity. The interaction of CD44 with HA is often utilized as a tumor marker in some cells, and HA has been employed as a targeting ligand for modifying and conjugating with polymers and IONPs to improve anticancer therapy and imaging. In comparison to targeted macromolecules (including Tf, antibodies, aptamers, and HA), small targeted molecules (FA and some targeted peptides including chloro-toxin, RGD, LHRH, EPPT, CREKA, and CGKRK peptides) attract great attention owing to their many potential advantages including significant simplicity, ease of production, good repeatability, and biodegradability. Thus, targeting tumors using small targeted molecules attracts increasing attention. These small targeted molecules can be conjugated with polymer- or amine-functionalized IONPs, therapeutic drugs, and/or near-infrared fluorescing molecules by either electrostatic interaction or covalent amide bond formation to obtain receptor/integrin-targeted multimodal imaging probes and therapeutic agents.

In summary, drug delivery systems coated with IONPs and targeting molecules are identified as valuable tools for early disease diagnosis, magnetic heat treatment, and delivery of anticancer drugs to target tumor sites, thereby attracting interest in clinical practice. However, to date, various problems are restricting the use of targeted imaging and therapeutics from research labs to clinics, such as inefficient endosomal escape, hematolytic effects, high renal toxicity, and short circulation time. Magnetic nanoparticle-based targeted delivery systems bound to other materials including biocompatible and biodegradable polymeric micelles, modified natural biological

materials including polysaccharides and polypeptides, carbon-based materials, fluo-rescing molecule, and/or siRNA/microRNA may overcome some of the above obsta-cles. In addition, more research should be performed to better characterize these systems, including long-term toxicity and pharmacokinetic studies because these targeted delivery systems are composed of multiple additional components. Further-more, various targeting molecules conjugated with magnetic nanoparticle-based delivery systems may be employed to guide and correct the targeted distribution of therapeutic agents. The development of nanotechnology is integrating all of the above functionalities and new molecular targets identified will lead to changes in traditional tumor treatment and diagnostic approaches.

References

1. Olopade O, Pichert G (2001) Cancer genetics in oncology practice. Ann Oncol 12(7):895–908
2. Gudjonsson B (2016) Pancreatic cancer: 80 years of surgery—percentage and repetitions. HPB Surg 2016
3. Andrén-Sandberg Å, Ivanics T (2018) Pancreatic cancer surgery–what's next? JOP J Pancreas (Online) 19(1):1–2
4. Metellus P et al (2020) Surgery in brain metastasis management: therapeutic, diagnostic, and strategic considerations. Central nervous system metastases. Springer, Berlin, pp 183–190
5. WHO (2019) Facts sheet of cancer 2018. Available from https://www.who.int/news-room/fact-sheets/detail/cancer
6. Cella D, Cherin E (1988) Quality of life during and after cancer treatment. Compr Ther 14(5):69–75
7. Fann JR et al (2008) Major depression after breast cancer: a review of epidemiology and treatment. Gen Hosp Psychiatry 30(2):112–126
8. Zhao, H., et al., *Hormone therapy as a management strategy for lung metastasis after 5 years of endometrial cancer: A case report and literature review.* Medicine, 2017. **96**(51).
9. Yoest JM (2017) Clinical features, predictive correlates, and pathophysiology of immune-related adverse events in immune checkpoint inhibitor treatments in cancer: a short review. ImmunoTargets Ther 6:73
10. Gui C, Cui D-X (2012) Functionalized gold nanorods for tumor imaging and targeted therapy. Cancer Biol Med 9(4):221
11. Singh R, Torti SV (2013) Carbon nanotubes in hyperthermia therapy. Adv Drug Deliv Rev 65(15):2045–2060
12. Doughty AC et al (2019) Nanomaterial applications in photothermal therapy for cancer. Materials 12(5):779
13. Kumar P, Agnihotri S, Roy I (2016) Synthesis of dox drug conjugation and citric acid stabilized superparamagnetic iron-oxide nanoparticles for drug delivery. Biochem Physiol 5(194):2
14. Lassenberger A et al (2017) Individually stabilized, superparamagnetic nanoparticles with controlled shell and size leading to exceptional stealth properties and high relaxivities. ACS Appl Mater Interfaces 9(4):3343–3353
15. Uthaman S et al (2015) Polysaccharide-coated magnetic nanoparticles for imaging and gene therapy. BioMed Res Int 2015

16. Wu W et al (2015) Recent progress on magnetic iron oxide nanoparticles: synthesis, surface functional strategies and biomedical applications. Sci Technol Adv Mater 16(2): 023501

17. Laurent S et al (2008) Magnetic iron oxide nanoparticles: synthesis, stabilization, vectorization, physicochemical characterizations, and biological applications. Chem Rev 108(6):2064–2110

18. Hasany S et al (2012) Systematic review of the preparation techniques of iron oxide magnetic nanoparticles. Nanosci Nanotechnol 2(6):148–158

19. Sodipo BK, Aziz AA (2016) Recent advances in synthesis and surface modification of superparamagnetic iron oxide nanoparticles with silica. J Magn Magn Mater 416:275–291

20. Liu Y et al (2011) Studies of Fe_3O_4-chitosan nanoparticles prepared by co-precipitation under the magnetic field for lipase immobilization. Catal Commun 12(8):717–720

21. Wu S et al (2011) Fe_3O_4 magnetic nanoparticles synthesis from tailings by ultrasonic chemical co-precipitation. Mater Lett 65(12):1882–1884

22. Pereira C et al (2012) 2 O 4(M=Fe Co, Mn) nanoparticles: tuning the particle size and magnetic properties through a novel one-step coprecipitation route. Chem Mater 24:1496–1504

23. Suh SK et al (2012) Synthesis of nonspherical superparamagnetic particles: in situ coprecipitation of magnetic nanoparticles in microgels prepared by stop-flow lithography. J Am Chem Soc 134(17):7337–7343

24. Roy E et al (2016) Stimuli-responsive poly (N-isopropyl acrylamide)-co-tyrosine@ gadolinium: iron oxide nanoparticle-based nanotheranostic for cancer diagnosis and treatment. Colloids Surf B 142:248–258

25. Park J et al (2004) Ultra-large-scale syntheses of monodisperse nanocrystals. Nat Mater 3(12):891–895

26. Hufschmid R et al (2015) Synthesis of phase-pure and monodisperse iron oxide nanoparticles by thermal decomposition. Nanoscale 7(25):11142–11154

27. Sharifi I, Shokrollahi H, Amiri S (2012) Ferrite-based magnetic nanofluids used in hyperthermia applications. J Magn Magn Mater 324(6):903–915

28. Remya N et al (2016) Toxicity, toxicokinetics and biodistribution of dextran stabilized Iron oxide Nanoparticles for biomedical applications. Int J Pharm 511(1):586–598

29. Lee Y et al (2005) Large-scale synthesis of uniform and crystalline magnetite nanoparticles using reverse micelles as nanoreactors under reflux conditions. Adv Func Mater 15(3):503–509

30. Tartaj P, Serna CJ (2002) Microemulsion-assisted synthesis of tunable superparamagnetic composites. Chem Mater 14(10):4396–4402

31. Darmawan A et al (2011) Iron oxide silica derived from sol-gel synthesis. Materials 4(2):448–456

32. Puscasu E et al (2016) Iron oxide-silica nanocomposites yielded by chemical route and sol–gel method. J Sol-Gel Sci Technol 79(3):457–465

33. Fernandes MTC et al (2013) The competing effect of ammonia in the synthesis of iron oxide/silica nanoparticles in microemulsion/sol–gel system. Colloids Surf A 422:136–142

34. Wu W, He Q, Jiang C (2008) Magnetic iron oxide nanoparticles: synthesis and surface functionalization strategies. Nanoscale Res Lett 3(11):397

35. Sodipo BK, Aziz AA (2018) One minute synthesis of amino-silane functionalized superparamagnetic iron oxide nanoparticles by sonochemical method. Ultrason Sonochem 40:837–840

36. Kim EH, Ahn Y, Lee HS (2007) Biomedical applications of superparamagnetic iron oxide nanoparticles encapsulated within chitosan. J Alloy Compd 434:633–636

37. Ramimoghadam D, Bagheri S, Hamid SBA (2014) Progress in electrochemical synthesis of magnetic iron oxide nanoparticles. J Magn Magn Mater 368:207–229

38. Oh JK, Park JM (2011) Iron oxide-based superparamagnetic polymeric nanomaterials: design, preparation, and biomedical application. Prog Polym Sci 36(1):168–189

39. Ebrahiminezhad A et al (2012) Impact of amino-acid coating on the synthesis and characteristics of iron-oxide nanoparticles (IONs). Bull Korean Chem Soc 33(12):3957–3962

40. Ahmadi R, Ranjbarnodeh E, Gu N (2012) Synthesizing cysteine-coated magnetite nanoparticles as MRI contrast agent: Effect of pH and cysteine addition on particles size distribution. Mater Sci-Pol 30(4):382–389

41. Nosrati H et al (2019) Phenyl alanine & tyrosine amino acids coated magnetic nanoparticles: preparation and toxicity study. Drug Res 69(05):277–283
42. Li L et al (2013) Effect of synthesis conditions on the properties of citric-acid coated iron oxide nanoparticles. Microelectron Eng 110:329–334
43. Răcuciu M, Creangă D, Airinei A (2006) Citric-acid-coated magnetite nanoparticles for biological applications. Eur Phys J E 21(2):117–121
44. Bloemen M et al (2012) Improved functionalization of oleic acid-coated iron oxide nanoparticles for biomedical applications. J Nanopart Res 14(9):1100
45. Zhang L, He R, Gu H-C (2006) Oleic acid coating on the monodisperse magnetite nanoparticles. Appl Surf Sci 253(5):2611–2617
46. Mamani J et al (2013) Synthesis and characterization of magnetite nanoparticles coated with lauric acid. Mater Charact 81:28–36
47. Mahmoudi M, Serpooshan V (2012) Silver-coated engineered magnetic nanoparticles are promising for the success in the fight against antibacterial resistance threat. ACS Nano 6(3):2656–2664
48. Silva SM et al (2016) Gold coated magnetic nanoparticles: from preparation to surface modification for analytical and biomedical applications. Chem Commun 52(48):7528–7540
49. Szpak A et al (2014) T 1–T 2 dual-modal MRI contrast agents based on superparamagnetic iron oxide nanoparticles with surface attached gadolinium complexes. J Nanopart Res 16(11):2678
50. Alwi R et al (2012) Silica-coated super paramagnetic iron oxide nanoparticles (SPION) as biocompatible contrast agent in biomedical photoacoustics. Biomed Opt Express 3(10):2500–2509
51. Ye F et al (2012) Uniform mesoporous silica coated iron oxide nanoparticles as a highly efficient, nontoxic MRI T2 contrast agent with tunable proton relaxivities. Contrast Media Mol Imaging 7(5):460–468
52. Stefan M et al (2014s) Synthesis and characterization of Fe_3O_4–TiO_2 core-shell nanoparticles. J Appl Phys 116(11):114312
53. Sun W et al (2016) Dendrimer-based magnetic iron oxide nanoparticles: their synthesis and biomedical applications. Drug Discov Today 21(12):1873–1885
54. Schleich N et al (2013) Dual anticancer drug/superparamagnetic iron oxide-loaded PLGA-based nanoparticles for cancer therapy and magnetic resonance imaging. Int J Pharm 447(1–2):94–101
55. Kayal S, Ramanujan R (2010) Doxorubicin loaded PVA coated iron oxide nanoparticles for targeted drug delivery. Mater Sci Eng, C 30(3):484–490
56. García-Jimeno S, Estelrich J (2013) Ferrofluid based on polyethylene glycol-coated iron oxide nanoparticles: characterization and properties. Colloids Surf A 420:74–81
57. Brullot W et al (2012) Versatile ferrofluids based on polyethylene glycol coated iron oxide nanoparticles. J Magn Magn Mater 324(11):1919–1925
58. Larsen EKU et al (2012) Accumulation of magnetic iron oxide nanoparticles coated with variably sized polyethylene glycol in murine tumors. Nanoscale 4(7):2352–2361
59. Yue-Jian C et al (2010) Synthesis, self-assembly, and characterization of PEG-coated iron oxide nanoparticles as potential MRI contrast agent. Drug Dev Ind Pharm 36(10):1235–1244
60. Huang J et al (2010) Effects of nanoparticle size on cellular uptake and liver MRI with polyvinylpyrrolidone-coated iron oxide nanoparticles. ACS Nano 4(12):7151–7160
61. Huang J et al (2013) Casein-coated iron oxide nanoparticles for high MRI contrast enhancement and efficient cell targeting. ACS Appl Mater Interfaces 5(11):4632–4639
62. Castelló J et al (2015) Chitosan (or alginate)-coated iron oxide nanoparticles: a comparative study. Colloids Surf, A 468:151–158
63. Unsoy G et al (2012) Synthesis optimization and characterization of chitosan-coated iron oxide nanoparticles produced for biomedical applications. J Nanopart Res 14(11):964
64. Gupta AK, Gupta M (2005) Synthesis and surface engineering of iron oxide nanoparticles for biomedical applications. Biomaterials 26(18):3995–4021
65. Tassa C, Shaw SY, Weissleder R (2011) Dextran-coated iron oxide nanoparticles: a versatile platform for targeted molecular imaging, molecular diagnostics, and therapy. Acc Chem Res 44(10):842–852

66. Ayala V et al (2013) Effect of surface charge on the colloidal stability and in vitro uptake of carboxymethyl dextran-coated iron oxide nanoparticles. J Nanopart Res 15(8):1874
67. Vismara E et al (2017) Albumin and hyaluronic acid-coated superparamagnetic iron oxide nanoparticles loaded with paclitaxel for biomedical applications. Molecules 22(7):1030
68. Ma H-L et al (2007) Preparation and characterization of superparamagnetic iron oxide nanoparticles stabilized by alginate. Int J Pharm 333(1–2):177–186
69. Wu M et al (2015) Nanocluster of superparamagnetic iron oxide nanoparticles coated with poly (dopamine) for magnetic field-targeting, highly sensitive MRI and photothermal cancer therapy. Nanotechnol 26(11):115102
70. Lin L-S et al (2014) Multifunctional Fe_3O_4@ polydopamine core–shell nanocomposites for intracellular mRNA detection and imaging-guided photothermal therapy. ACS Nano 8(4):3876–3883
71. Cole AJ et al (2011) Polyethylene glycol modified, cross-linked starch-coated iron oxide nanoparticles for enhanced magnetic tumor targeting. Biomaterials 32(8):2183–2193
72. Gaihre B et al (2009) Gelatin-coated magnetic iron oxide nanoparticles as carrier system: drug loading and in vitro drug release study. Int J Pharm 365(1–2):180–189
73. Arias LS et al (2018) Iron oxide nanoparticles for biomedical applications: a perspective on synthesis, drugs, antimicrobial activity, and toxicity. Antibiotics 7(2):46
74. Mojica Pisciotti ML et al (2014) In vitro and in vivo experiments with iron oxide nanoparticles functionalized with DEXTRAN or polyethylene glycol for medical applications: magnetic targeting. J Biomed Mater Res B Appl Biomater 102(4):860–868
75. Yu M et al (2012) Dextran and polymer polyethylene glycol (PEG) coating reduce both 5 and 30 nm iron oxide nanoparticle cytotoxicity in 2D and 3D cell culture. Int J Mol Sci 13(5):5554–5570
76. Wang Y-XJ (2011) Superparamagnetic iron oxide based MRI contrast agents: Current status of clinical application. Quant Imaging Med Surg 1(1):35
77. Vega-Chacón J et al (2017) pH-responsive poly (aspartic acid) hydrogel-coated magnetite nanoparticles for biomedical applications. Mater Sci Eng C 77:366–373
78. Cheng R et al (2013) Dual and multi-stimuli responsive polymeric nanoparticles for programmed site-specific drug delivery. Biomaterials 34(14):3647–3657
79. Yang H-M et al (2011) Multifunctional poly (aspartic acid) nanoparticles containing iron oxide nanocrystals and doxorubicin for simultaneous cancer diagnosis and therapy. Colloids Surf, A 391(1–3):208–215
80. Cohin Y et al (2013) Tracking the interfacial dynamics of PNiPAM soft microgels particles adsorbed at the air–water interface and in thin liquid films. Rheol Acta 52(5):445–454
81. Wei W et al (2015) Synthesis and characterization of a novel pH-thermo dual responsive hydrogel based on salecan and poly (N, N-diethylacrylamide-co-methacrylic acid). Colloids Surf, B 136:1182–1192
82. Kamoun EA et al (2018) Thermo-and pH-sensitive hydrogel membranes composed of poly (N-isopropylacrylamide)-hyaluronan for biomedical applications: influence of hyaluronan incorporation on the membrane properties. Int J Biol Macromol 106:158–167
83. Fortin-Ripoche J-P et al (2006) Magnetic targeting of magnetoliposomes to solid tumors with MR imaging monitoring in mice: feasibility. Radiology 239(2):415–424
84. Nappini S et al (2010) Magnetoliposomes for controlled drug release in the presence of low-frequency magnetic field. Soft Matter 6(1):154–162
85. Amstad E et al (2011) Triggered release from liposomes through magnetic actuation of iron oxide nanoparticle containing membranes. Nano Lett 11(4):1664–1670
86. Tai L-A et al (2009) Thermosensitive liposomes entrapping iron oxide nanoparticles for controllable drug release. Nanotechnology 20(13):135101
87. Hu J et al (2012) Drug-loaded and superparamagnetic iron oxide nanoparticle surface-embedded amphiphilic block copolymer micelles for integrated chemotherapeutic drug delivery and MR imaging. Langmuir 28(4):2073–2082
88. Nasongkla N et al (2006) Multifunctional polymeric micelles as cancer-targeted MRI-ultrasensitive drug delivery systems. Nano Lett 6(11):2427–2430

89. Ai H et al (2005) Magnetite-loaded polymeric micelles as ultrasensitive magnetic-resonance probes. Adv Mater 17(16):1949–1952
90. Talelli M et al (2009) Superparamagnetic iron oxide nanoparticles encapsulated in biodegradable thermosensitive polymeric micelles: toward a targeted nanomedicine suitable for image-guided drug delivery. Langmuir 25(4):2060–2067
91. Bulte JW et al (1999) Preparation, relaxometry, and biokinetics of PEGylated magnetoliposomes as MR contrast agent. J Magn Magn Mater 194(1–3):204–209
92. Ali A et al (2016) Synthesis, characterization, applications, and challenges of iron oxide nanoparticles. Nanotechnol Sci Appl 9:49
93. Hajba L, Guttman A (2016) The use of magnetic nanoparticles in cancer theranostics: toward handheld diagnostic devices. Biotechnol Adv 34(4):354–361
94. Woo K et al (2004) Easy synthesis and magnetic properties of iron oxide nanoparticles. Chem Mater 16(14):2814–2818
95. Filipe V, Hawe A, Jiskoot W (2010) Critical evaluation of nanoparticle tracking analysis (NTA) by NanoSight for the measurement of nanoparticles and protein aggregates. Pharm Res 27(5):796–810
96. Li T, Senesi AJ, Lee B (2016) Small angle X-ray scattering for nanoparticle research. Chem Rev 116(18):11128–11180
97. Smolensky ED et al (2013) Scaling laws at the nanosize: the effect of particle size and shape on the magnetism and relaxivity of iron oxide nanoparticle contrast agents. J Mater Chem B 1(22):2818–2828
98. Blanco-Andujar C et al (2016) Design of iron oxide-based nanoparticles for MRI and magnetic hyperthermia. Nanomedicine 11(14):1889–1910
99. Bulte JW, Kraitchman DL (2004) Iron oxide MR contrast agents for molecular and cellular imaging. NMR Biomed Inte J Devoted Dev Appl Magn Reson In Vivo 17(7):484–499
100. Bulte JW (2009) In vivo MRI cell tracking: clinical studies. Am J Roentgenol 193(2):314–325
101. Laurent S et al (2011) Magnetic fluid hyperthermia: focus on superparamagnetic iron oxide nanoparticles. Adv Coll Interface Sci 166(1–2):8–23
102. Schmale I et al (2012) Point spread function analysis of magnetic particles. Magnetic particle imaging. Springer, Berlin, pp 287–292
103. Panagiotopoulos N et al (2015) Magnetic particle imaging: current developments and future directions. Int J Nanomed 10:3097
104. Guardia P et al (2012) Water-soluble iron oxide nanocubes with high values of specific absorption rate for cancer cell hyperthermia treatment. ACS Nano 6(4):3080–3091
105. Latunde-Dada GO (2017) Ferroptosis: role of lipid peroxidation, iron and ferritinophagy. Biochimica et Biophysica Acta (BBA)-General Subj 1861(8):1893–1900
106. Brüne B et al (2013) Redox control of inflammation in macrophages. Antioxid Redox Signal 19(6):595–637
107. Tan, H-Y et al (2016) The reactive oxygen species in macrophage polarization: reflecting its dual role in progression and treatment of human diseases. Oxidative medicine and cellular longevity, vol 2016
108. Ankamwar B et al (2010) Biocompatibility of Fe_3O_4 nanoparticles evaluated by in vitro cytotoxicity assays using normal, glia and breast cancer cells. Nanotechnology 21(7):075102
109. Singh N et al (2010) Potential toxicity of superparamagnetic iron oxide nanoparticles (SPION). Nano reviews 1(1):5358
110. Liu G et al (2013) Applications and potential toxicity of magnetic iron oxide nanoparticles. Small 9(9–10):1533–1545
111. Mahmoudi M et al (2010) A new approach for the in vitro identification of the cytotoxicity of superparamagnetic iron oxide nanoparticles. Colloids Surf B 75(1):300–309
112. Xia T et al (2009) Polyethyleneimine coating enhances the cellular uptake of mesoporous silica nanoparticles and allows safe delivery of siRNA and DNA constructs. ACS Nano 3(10):3273–3286
113. Mulens-Arias V et al (2015) Polyethylenimine-coated SPIONs trigger macrophage activation through TLR-4 signaling and ROS production and modulate podosome dynamics. Biomaterials 52:494–506

114. Blank F et al (2011) Biomedical nanoparticles modulate specific CD4+ T cell stimulation by inhibition of antigen processing in dendritic cells. Nanotoxicology 5(4):606–621
115. Pawelczyk E et al (2006) Expression of transferrin receptor and ferritin following ferumoxides–protamine sulfate labeling of cells: implications for cellular magnetic resonance imaging. NMR Biomed Int J Devoted Dev Appl Magnetic Reson In vivo 19(5):581–592
116. Matuszak J et al (2015) Endothelial biocompatibility and accumulation of SPION under flow conditions. J Magn Magn Mater 380:20–26
117. Polyak B et al (2008) High field gradient targeting of magnetic nanoparticle-loaded endothelial cells to the surfaces of steel stents. Proc Natl Acad Sci 105(2):698–703
118. Arbab AS et al (2005) Labeling of cells with ferumoxides–protamine sulfate complexes does not inhibit function or differentiation capacity of hematopoietic or mesenchymal stem cells. NMR Biomed Int J Devoted Dev Appl Mag Reson In Vivo 18(8):553–559
119. Schmidtke-Schrezenmeier G et al (2011) Labeling of mesenchymal stromal cells with iron oxide–poly (L-lactide) nanoparticles for magnetic resonance imaging: uptake, persistence, effects on cellular function and magnetic resonance imaging properties. Cytotherapy 13(8):962–975
120. De Vries IJM et al (2005) Magnetic resonance tracking of dendritic cells in melanoma patients for monitoring of cellular therapy. Nat Biotechnol 23(11):1407–1413
121. Hamm B et al (1994) Contrast-enhanced MR imaging of liver and spleen: first experience in humans with a new superparamagnetic iron oxide. J Magn Reson Imaging 4(5):659–668
122. Bernd H et al (2009) Safety and tolerability of ultrasmall superparamagnetic iron oxide contrast agent: comprehensive analysis of a clinical development program. Invest Radiol 44(6):336–342
123. Toth GB et al (2017) Current and potential imaging applications of ferumoxytol for magnetic resonance imaging. Kidney Int 92(1):47–66
124. Liu G et al (2013) Transferrin modified graphene oxide for glioma-targeted drug delivery: in vitro and in vivo evaluations. ACS Appl Mater Interfaces 5(15):6909–6914
125. Wang X et al (2016) Transferrin-conjugated drug/dye-co-encapsulated magnetic nanocarriers for active-targeting fluorescent/magnetic resonance imaging and anti-tumor effects in human brain tumor cells. RSC Adv 6(107):105661–105675
126. Thorstensen K, Romslo I (1993) The transferrin receptor: its diagnostic value and its potential as therapeutic target. Scand J Clin Lab Invest 53(sup215):113–120
127. van der Meel R et al (2013) Ligand-targeted particulate nanomedicines undergoing clinical evaluation: current status. Adv Drug Deliv Rev 65(10):1284–1298
128. Högemann D et al (2000) Improvement of MRI probes to allow efficient detection of gene expression. Bioconjug Chem 11(6):941–946
129. Ichikawa T et al (2002) MRI of transgene expression: correlation to therapeutic gene expression. Neoplasia (New York, NY) 4(6):523
130. Qian ZM et al (2002) Targeted drug delivery via the transferrin receptor-mediated endocytosis pathway. Pharmacol Rev 54(4):561–587
131. Yang C et al (2008) Nanoimmunoliposome delivery of superparamagnetic iron oxide markedly enhances targeting and uptake in human cancer cells in vitro and in vivo. Nanomed Nanotechnol Biolo Med 4(4):318–329
132. Pirollo KF et al (2006) A tumor-targeted nanodelivery system to improve early MRI detection of cancer. Mole Imaging 5(1): 7290–2006
133. Xu L et al (1999) Transferrin-liposome-mediated systemic p53 gene therapy in combination with radiation results in regression of human head and neck cancer xenografts. Hum Gene Ther 10(18):2941–2952
134. Pirollo KF et al (2007) Materializing the potential of small interfering RNA via a tumor-targeting nanodelivery system. Can Res 67(7):2938–2943
135. Ponka P, Lok CN (1999) The transferrin receptor: role in health and disease. Int J Biochem Cell Biol 31(10):1111–1137
136. Ghadiri M et al (2017) Transferrin-conjugated magnetic dextran-spermine nanoparticles for targeted drug transport across blood-brain barrier. J Biomed Mater Res Part A 105(10):2851–2864

137. Rajkumar S, Prabaharan M (2018) Multi-functional nanocarriers based on iron oxide nanoparticles conjugated with doxorubicin, poly(ethylene glycol) and folic acid as theranostics for cancer therapy. Colloids Surf B 170:529–537

138. Singh R et al (2016) Dose-dependent therapeutic distinction between active and passive targeting revealed using transferrin-coated PGMA nanoparticles. Small 12(3):351–359

139. El-Fattah MA et al (2015) Studying the effect of organo-modified nanoclay loading on the thermal stability, flame retardant, anti-corrosive and mechanical properties of polyurethane nanocomposite for surface coating. Prog Org Coat 89:212–219

140. Chen M-L et al (2012) Quantum dots conjugated with Fe3O4-filled carbon nanotubes for cancer-targeted imaging and magnetically guided drug delivery. Langmuir 28(47):16469–16476

141. Vermisoglou EC et al (2011) Magnetic carbon nanotubes with particle-free surfaces and high drug loading capacity. Nanotechnology 22(35):355602

142. Yang X et al (2009) Superparamagnetic graphene oxide–Fe 3 O 4 nanoparticles hybrid for controlled targeted drug carriers. J Mater Chem 19(18):2710–2714

143. Elfinger M et al (2009) Self-assembly of ternary insulin−polyethylenimine (PEI)−DNA nanoparticles for enhanced gene delivery and expression in alveolar epithelial cells. Biomacromol 10(10):2912–2920

144. Levay PF, Viljoen M (1995) Lactoferrin: a general review. Haematologica 80(3):252–267

145. Kumari S, Kondapi AK (2018) Receptor-mediated targeted delivery of DNA using Lactoferrin nanoparticles. Int J Biol Macromol 108:401–407

146. Gupta AK, Curtis AS (2004) Lactoferrin and ceruloplasmin derivatized superparamagnetic iron oxide nanoparticles for targeting cell surface receptors. Biomaterials 25(15):3029–3040

147. Fay F, Scott CJ (2011) Antibody-targeted nanoparticles for cancer therapy. Immunotherapy 3(3):381–394

148. Gao Y et al (2014) Nanotechnology-based intelligent drug design for cancer metastasis treatment. Biotechnol Adv 32(4):761–777

149. Aaron JS et al (2006) Increased optical contrast in imaging of epidermal growth factor receptor using magnetically actuated hybrid gold/iron oxide nanoparticles. Opt Expr 14(26):12930–12943

150. Kocbek P et al (2007) Targeting cancer cells using PLGA nanoparticles surface modified with monoclonal antibody. J Control Release 120(1–2):18–26

151. Mitri Z, Constantine T, O'Regan R (2012) The HER2 receptor in breast cancer: pathophysiology, clinical use, and new advances in therapy. Chemother Res Prac 2012

152. Rüschoff J et al (2012) HER2 testing in gastric cancer: a practical approach. Mod Pathol 25(5):637–650

153. Meza-Junco J, Au H-J, Sawyer MB (2011) Critical appraisal of trastuzumab in treatment of advanced stomach cancer. Manag Res 3:57

154. Chiosea SI et al (2015) Molecular characterization of apocrine salivary duct carcinoma. Am J Surg Pathol 39(6):744–752

155. Tejani MA, Cohen RB, Mehra R (2010) The contribution of cetuximab in the treatment of recurrent and/or metastatic head and neck cancer. Biologics Targets Therapy 4:173

156. Melancon MP et al (2011) Targeted multifunctional gold-based nanoshells for magnetic resonance-guided laser ablation of head and neck cancer. Biomaterials 32(30):7600–7608

157. Fakih M, Wong R (2010) Efficacy of the monoclonal antibody EGFR inhibitors for the treatment of metastatic colorectal cancer. Curr Oncol 17(Suppl 1):S3

158. Talavera A et al (2009) Nimotuzumab, an antitumor antibody that targets the epidermal growth factor receptor, blocks ligand binding while permitting the active receptor conformation. Can Res 69(14):5851–5859

159. Yang L et al (2009) Single chain epidermal growth factor receptor antibody conjugated nanoparticles for in vivo tumor targeting and imaging. Small 5(2):235–243

160. Dolatyari M et al (2017) Fluorescence resonance energy transfer between an anti-EGFR antibody and Bi2Se3/SiO2, ZnS/SiO2, and ZnSe/SiO2 nanomaterials for biosensor purposes. Z Anorg Allg Chem 643(21):1564–1571

161. Cho WC, Roukos DH (2013) Trastuzumab emtansine for advanced HER2-positive breast cancer and beyond: genome landscape-based targets. Expert Rev Anticancer Ther 13(1):5–8
162. Kulhari H et al (2015) Biomedical applications of trastuzumab: as a therapeutic agent and a targeting ligand. Med Res Rev 35(4):849–876
163. Ignatiadis M et al (2009) HER-2 as a target for breast cancer therapy. Clin Cancer Res 15(6):1848–1852
164. Capala J, Bouchelouche K (2010) Molecular imaging of HER2-positive breast cancer-a step toward an individualized "Image and Treat" strategy. Curr Opin Oncol 22(6):559
165. Chen H et al (2013) Anti-HER2 antibody and ScFvEGFR-conjugated antifouling magnetic iron oxide nanoparticles for targeting and magnetic resonance imaging of breast cancer. Int J Nanomed 8:3781
166. Liu D et al (2011) Specific targeting of nasopharyngeal carcinoma cell line CNE1 by C225-conjugated ultrasmall superparamagnetic iron oxide particles with magnetic resonance imaging. Acta Biochim Biophys Sin 43(4):301–306
167. Wang Z et al (2017) Active targeting theranostic iron oxide nanoparticles for MRI and magnetic resonance-guided focused ultrasound ablation of lung cancer. Biomaterials 127:25–35
168. Liao C et al (2011) Targeting EGFR-overexpressing tumor cells using cetuximab-immunomicelles loaded with doxorubicin and superparamagnetic iron oxide. Eur J Radiol 80(3):699–705
169. Chen H-L et al (2017) Identification of epidermal growth factor receptor-positive glioblastoma using lipid-encapsulated targeted superparamagnetic iron oxide nanoparticles in vitro. J Nanobiotechnol 15(1):86
170. Ma M et al (2013) Silica-coated magnetite nanoparticles labeled by nimotuzumab, a humanised monoclonal antibody to epidermal growth factor receptor: Preparations, specific targeting and bioimaging. J Nanosci Nanotechnol 13(10):6541–6545
171. Majumdar D, Peng X-H, Shin DM (2010) The medicinal chemistry of theragnostics, multimodality imaging and applications of nanotechnology in cancer. Curr Top Med Chem 10(12):1211–1226
172. Peng X-H et al (2011) Targeted delivery of cisplatin to lung cancer using ScFvEGFR-heparin-cisplatin nanoparticles. ACS Nano 5(12):9480–9493
173. Wang G et al (2017) In vitro and in vivo differences in murine third complement component (C_3) opsonization and macrophage/leukocyte responses to antibody-functionalized iron oxide nanoworms. Front Immunol 8:151
174. Lee J-H et al (2007) Artificially engineered magnetic nanoparticles for ultra-sensitive molecular imaging. Nat Med 13(1):95–99
175. Chen T-J et al (2009) Targeted Herceptin–dextran iron oxide nanoparticles for noninvasive imaging of HER2/neu receptors using MRI. J Biol Inorg Chem 14(2):253
176. Nahta R, Hung M-C, Esteva FJ (2004) The HER-2-targeting antibodies trastuzumab and pertuzumab synergistically inhibit the survival of breast cancer cells. Can Res 64(7):2343–2346
177. Wang Y, Chen J, Irudayaraj J (2011) Nuclear targeting dynamics of gold nanoclusters for enhanced therapy of HER2+ breast cancer. ACS Nano 5(12):9718–9725
178. Lee AL et al (2009) The co-delivery of paclitaxel and Herceptin using cationic micellar nanoparticles. Biomaterials 30(5):919–927
179. Choi WI et al (2015) Targeted antitumor efficacy and imaging via multifunctional nano-carrier conjugated with anti-HER2 trastuzumab. Nanomed Nanotechnol Biol Med 11(2):359–368
180. Chiang C-S et al (2014) Enhancement of cancer therapy efficacy by trastuzumab-conjugated and pH-sensitive nanocapsules with the simultaneous encapsulation of hydrophilic and hydrophobic compounds. Nanomed Nanotechnol Biol Med 10(1):99–107
181. Kinoshita M et al (2010) MR molecular imaging of HER-2 in a murine tumor xenograft by SPIO labeling of anti-HER-2 affibody. Contrast Media Mol Imaging 5(1):18–22
182. Satpathy M et al (2014) Active targeting using her-2-affibody-conjugated nanoparticles enabled sensitive and specific imaging of orthotopic her-2 positive ovarian tumors. Small 10(3):544–555

183. Li D-L et al (2017) Multifunctional superparamagnetic nanoparticles conjugated with fluorescein-labeled designed ankyrin repeat protein as an efficient HER2-targeted probe in breast cancer. Biomaterials 147:86–98

184. Shweiki D et al (1992) Vascular endothelial growth factor induced by hypoxia may mediate hypoxia-initiated angiogenesis. Nature 359(6398):843–845

185. Winkler F et al (2004) Kinetics of vascular normalization by VEGFR2 blockade governs brain tumor response to radiation: role of oxygenation, angiopoietin-1, and matrix metallo-proteinases. Cancer Cell 6(6):553–563

186. Papadopoulos N et al (2012) Binding and neutralization of vascular endothelial growth factor (VEGF) and related ligands by VEGF Trap, ranibizumab and bevacizumab. Angiogenesis 15(2):171–185

187. Thaler S et al (2010) Toxicity testing of the VEGF inhibitors bevacizumab, ranibizumab and pegaptanib in rats both with and without prior retinal ganglion cell damage. Acta Ophthalmol 88(5):e170–e176

188. Nagengast WB et al (2011) VEGF-PET imaging is a noninvasive biomarker showing differential changes in the tumor during sunitinib treatment. Can Res 71(1):143–153

189. Zhao Y et al (2014) Design and preliminary assessment of 99m Tc-labeled ultrasmall super-paramagnetic iron oxide-conjugated bevacizumab for single photon emission computed tomography/magnetic resonance imaging of hepatocellular carcinoma. J Radioanal Nucl Chem 299(3):1273–1280

190. Lin R et al (2018) Bevacizumab and near infrared probe conjugated iron oxide nanoparticles for vascular endothelial growth factor targeted MR and optical imaging. Biomater Sci 6(6):1517–1525

191. Liu H et al (2016) Application of iron oxide nanoparticles in glioma imaging and therapy: from bench to bedside. Nanoscale 8(15):7808–7826

192. Abakumov M et al (2012) Visualization of experimental glioma C6 by MRI with magnetic nanoparticles conjugated with monoclonal antibodies to vascular endothelial growth factor. Bull Exp Biol Med 154(2):274–277

193. Huang H et al (2013) A novel anti-VEGF targeting and MRI-V isible smart drug delivery system for specific diagnosis and therapy of liver cancer. Macromol Biosci 13(10):1358–1368

194. Holmes K et al (2007) Vascular endothelial growth factor receptor-2: structure, function, intracellular signalling and therapeutic inhibition. Cell Signal 19(10):2003–2012

195. Wang C-H, Kang S-T, Yeh C-K (2013) Superparamagnetic iron oxide and drug complex-embedded acoustic droplets for ultrasound targeted theranosis. Biomaterials 34(7):1852–1861

196. Wang C-H, Yeh C-K (2012) Superparamagnetic iron oxide/drug complex-embedded droplets for Bi-model imaging and enhanced targeted therapy. In: 2012 IEEE international ultrasonics symposium. IEEE

Magnetic Nanoflowers: Synthesis, Formation Mechanism and Hyperthermia Application

Gopal Niraula, Mohan Chandra Mathpal, Edher Z. Herrera, Maria A. G. Soler, Jose A. H. Coaquira, and Surender K. Sharma

Abstract Magnetic hyperthermia is becoming a very propitious supplementary technique for cancer treatments such as chemotherapy radiotherapy and radiotherapy. In this regard, magnetic nanoflowers (MNFs) are novel system in terms of morphology showing a structure similar to flower and exhibiting higher stability and enhanced heating efficiency when compared with similar nanoparticles displaying standard formats; enabling them for magneto-hyperthermia applications. In this chapter, different types of nanoflowers such as magnetic-oxide, magneto-plasmonic, and magnetic-organic/inorganic and their applicability are discussed. Moreover, a discussion on the most common chemical routes to design nanoflowers emphasizing hydro/solvothermal techniques, microwave-assisted hydrothermal, co-precipitations, and polyol are highlighted. Furthermore, the nucleation of MNFs and their growing process with a physical parameter are presented. At last, the magnetic hyperthermia properties of MNFs and their recent findings are critically scrutinized along with their future perspectives in biomedicine.

Keywords Magnetic nanoflowers · Synthesis · Nucleation and growth · Magnetic hyperthermia · Biomedicine

G. Niraula · S. K. Sharma (✉)
Department of Physics, Federal University of Maranhao, Sao Luis, Brazil
e-mail: surender.sharma@cup.edu.in; surender.sharma@ufma.br

G. Niraula · J. A. H. Coaquira
Laboratory of Magnetic Materials, Institute of Physics, NFA, University of Brasilia, Brasilia, DF, Brazil

M. C. Mathpal · M. A. G. Soler
Institute of Physics, University of Brasilia, Brasilia, DF, Brazil

E. Z. Herrera
Brazilian Center for Research in Physics- CBPF, Rio de Janeiro, RJ, Brazil

S. K. Sharma
Department of Physics, Central University of Punjab, Bathinda 151401, India

1   Introduction

Nanomaterials (NMs), ultrathin particles in size of less than 100 nm, are extremely reactive and versatile as compared to their bulk counterparts due to their high surface-area-to-volume ratio. These features, in turn, provide excessive possibilities to improve their unique optical, magnetic, and mechanical properties [1, 2]. Particularly, magnetic NPs (MNPs) have enlarged great deal of consideration in biomedicine owing to their multifunction and tunable magnetic behavior and their tendency to be functionalized at both molecular and cellular levels. More precisely, the unique magnetic properties exhibited by MNPs and their biocompatibility as well as less toxicity based upon the size/shape led researchers work with these NPs to explore the potential use in biomedical field [3–10]. Several works have been done to design different morphologies NPs, i.e., nanocubes, nanorods, nanowires, nanodisks, nanorings, nanotubes, nanoflowers, etc. [11–19]. Among such different nanoparticulate systems, nanoflowers (NFs) are novel nanoparticles with structural outlook similar to plant flowers (See Fig. 1a–c) in a scale of 100–500 nm. Like general flowers found in nature, different parts of flowers are given in Fig. 1a. They are made up of distinct layers of petals to encompass a larger surface area in a small scale, considering several applications: magnetic hyperthermia (MH), photodynamic and photothermal therapy (PDT/PTT)). Especially, magnetic nanoflowers (MNFs) have been considered as a prevailing candidate for magnetic hyperthermia (MH) due to their substantial heating properties [20–23]. It is well recognized that higher magnetic losses through hysteresis is found in ferrimagnetic particles than superparamagnetic ones [24–26]. However, remanence (Mr) is a foremost issue which causes the agglomeration in ferrimagnetic nanoparticles, and hence restrict their suitability for biomedical applications. Nevertheless, magnetic nanoflowers can retain their soft magnetic properties even for larger than 50 nm, which led to consider MNFs as appropriate candidates for MH replacing the superparamagnetic NPs [27]. In this article, we have explored different types of magnetic nanoflowers with special
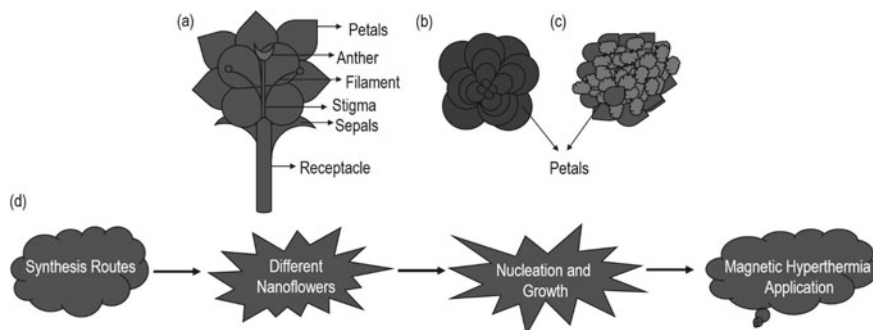
Fig. 1   **a** Flower, **b** microflower, **c** nanoflower, and **d** flow-chart of the chapter

emphasis on their synthesis, nucleation and growth mechanism, and utilization in magneto-hyperthermia application.

2 Synthesis Routes of Magnetic Nanoflowers

The synthetic route is one of crucial factor to design a particular nanoparticle for a specific kind of application, which determine the physico chemical and consequently their magnetic properties. The final morphology depends largely on the synthetic process, where thermodynamic/kinetic features limit the reaction and preferential adsorption of capping molecules to specific facets [28–31]. Nowadays, the synthesis of MNFs has gained more consideration to improve efficiency and stability of surface reaction due to its simple method either from inorganic, or organic materials and sometimes a combination of both. In recent years, a lot of research has been done aiming to develop novel methods to synthesize NFs displaying better properties, with multifunctionality, at lower cost than the existing ones. NFs can be synthesized by joining up atoms, molecules or, clusters, which is usually referred as a 'Bottom-up' method. Bottom-up method effectively covers the several chemical routes to strengthen the performance of nanomaterials having improved properties aiming to get better restraints over the size/shape disseminations as well as surface chemistry. Based upon the structural, compositional, magneto-optical properties important for specific applications of magnetic NFs, the most employed chemical methods are discussed here in the following section:

2.1 Co-precipitation

Co-precipitation is the most widely accepted method for the synthesis of MNPs with controlled sizes/shapes for biomedical applications [32–34]. In co-precipitation, MNPs are generally synthesized by adding a basic solution under an inert atmosphere either at ambient temperature or at high temperature, from aqueous salt solutions [35]. It largely depends on the hydrolysis of a mixture of Fe^{2+} and Fe^{3+} ions which are used to fix the A to B molar ratio in the inverse spinel structure during the synthesize of magnetite. In co-precipitation method, Fe^{2+} and Fe^{3+} ions are usually precipitated in alkaline solutions, such as NH_4OH, KOH or NaOH. In general, the synthesis are performed in the temperature 70–80 °C [36] or at higher temperatures. The influence of different techniques, stirring rate [37], required time [38], pH value and the applied field [39, 40] resulting magnetic properties, on particle size and morphology should be considered important factors. In addition to their great benefits, the main drawback with this synthesis is larger specific surface area and high surface energy due to the formation of extremely small particles which have a tendency to agglomerate. Thus, care should be taken to tackle such issues; for example, the effect of reaction temperature, alkali, and emulsifier, which generally decides the final product [41, 42].
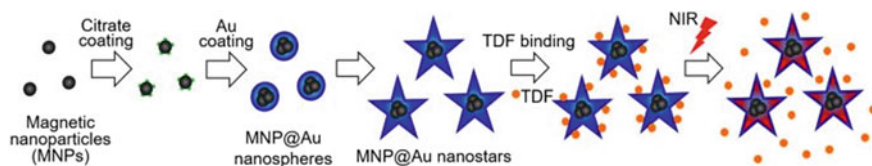
Fig. 2 A schematic design of Fe_3O_4@Au nanostars synthesis stages, drug binding, and NIR-triggered drug release. MNPs (Fe_3O_4) and Tenofovirdisoproxil fumarate (TDF); near-infrared (NIR). (Reprinted with permission from Ref. [43]. Copyright © 2020, Springer Nature)

Tomitaka et al. [43] have synthesized a near-infrared (NIR) responsive Fe_3O_4@Au nanostars using a two-step process as shown in Fig. 2. In the first step, Fe_3O_4 was synthesized by co-precipitation of Fe^{2+} and Fe^{3+} ions and then gold coating of Fe_3O_4 by seed-mediated growth strategy. Here, sodium citrate and Fe_3O_4 was used as a reducing agent whereas seeds for Au^{3+} ions, respectively. The core–shell Fe_3O_4@Au NPs with spherical shapes were obtained. In the second step, Fe_3O_4@Au nanospheres as seeds were used for altering the morphology of these core–shell NPs from spherical to star shape by the thermal annealing process, silver nitrate ($AgNO_3$) plays to give rise to anisotropic growth of Au and L-ascorbic acid as a reducing agent for Au^{3+} ions, and to control the shape of Au nanoparticles, silver ions were utilized in the seed-mediated synthesis as a supplementary to drive the specific shape of nanoparticles. After the reduction of silver ions on the Au surface, the anisotropic growth of Au is evolved and form several branches [44].

2.2 Hydrothermal Synthesis

Hydrothermal synthesis is most easier and a simple possible approach as compared to the operationally complicated micro-emulsion or thermal decomposition processes, which provide highly crystalline NPs with well-defined morphology and crystal phase. This approach is based on the aim of growing dislocation-free crystalline lattices in a sealed container at high vapor pressure (from 0.3 to 4 MPa), high temperatures (130–250 °C), and for long periods of time (an hour to several days). Simply in the hydrothermal routes, distilled water is considered as solvent whereas organic solvent is used in solvothermal routes [45–48]. Hydrothermal approach generally suited helps to prepare metal oxide nanoparticles in subcritical and supercritical water using batch reaction and flow reaction systems [49–51]. The moderate reaction temperature (<300 °C) set to tackle the number of issues, for example, stoichiometry control, rapid growth, etc., which run across in the high-temperature reaction synthesis method.

Ramesh and coworkers [52] have successfully prepared single crystalline Fe_3O_4 nanoflowers (Fig. 3a) with size of ~ 30 nm by simple one-pot surfactant-assisted hydrothermal method using 0.9 g $FeCl_3 \cdot 6H_2O$, ethylene glycol (50 ml) and by adding
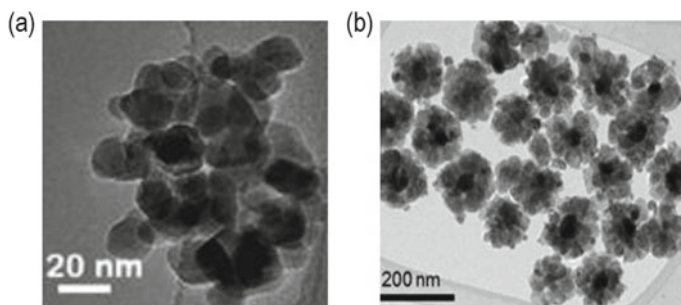
Fig. 3 a, b Transmission electron microscopy (TEM) image of Fe_3O_4 (Reprinted with permission from Ref. [52]. Copyright © 2011 Elsevier B.V. All rights reserved) and Ag/Fe_3O_4 nanoflowers (Reprinted with permission from Ref. [53]. Copyright ©2016 American Chemical Society)

tetraethylene tetramine (TETA) under continuous stirring. Polyhedron to flower-shaped morphology evolution of the Fe_3O_4 nanoparticles were achieved by varying the amount of TETA. The saturation magnetization of Fe_3O_4 nanoflowers was found to be ~66 emu/g. Das et al. [53] have fabricated coreAg@Fe_3O_4 nanoflowers using a one-step solvothermal process; where 1.16 g $Fe(NO_3)_3 \cdot 9H_2O$ was dissolved in 35 ml of ethylene glycol, 2.9 g of sodium acetate, and 0.1 g of $AgNO_3$. The prepared Ag@Fe_3O_4 nanoflowers exhibited an interesting heating efficiency by acting as dual agents for both magnetic hyperthermia (Fe_3O_4) and photothermal therapy (Ag). The morphology of Ag@Fe_3O_4 nanoflowers is shown in Fig. 3b.

2.3 Microwave-Assisted Hydrothermal

The microwave hydrothermal (microwaves and water heat) is a combination of both microwave and hydrothermal methods. Because of many advantages such as shorter reaction time and higher reaction rate, yield, selectivity, supplying swift chemical reactions and quick materials preparation in minutes/seconds, however, conventional heating methods require hours or even days, which leads to relatively inexpensive, energy-economic, and high efficiency for materials-output, therefore microwave heating technology is emerging as an alternative heat source for rapid volumetric heating as compared to the conventional heating methods [54–56]. The generation of microwave (MW) heat is based on electromagnetic fields itself divided into magnetic and electric fields, and follow a different interaction mechanism with materials due to different properties of each fields. The medium is heated by electric field of the microwave and such heating medium is mainly carried out by two mechanisms of ion conduction and dipole polarization. On the other hand, magnetic field heating also affects microwave heating. The effect of the microwave magnetic field is stronger than the one from the electric field in some ferrite based magnetic materials [57]. In addition, there is the popular term "microwave effects" which is a non-thermal

phenomena affect microwave heating [58]. It is important to have an idea of interaction of microwaves with different materials. Depending upon the dielectric loss factor (δ), materials can be divided into three categories: low dielectric loss material also know as transparent materials, non-metallic and polymers; opaque (conductor), such as metals and alloys; absorption (high dielectric loss material), for instance, water [57, 59].

Polshettiwar et al. [60] have synthesized star shape α-Fe$_2$O$_3$ using microwave hydrothermal method by heating the K$_4$[Fe(CN)$_6$]. In the course of reaction, dissociated [Fe(CN)$_6$]$^{4-}$ ion grew rapidly, yielding the α-Fe$_2$O$_3$ materials of diameter 48 nm. The obtained single crystal nanoparticles have morphology similar to a pine tree (Fig. 4a, b), and designated as 'micropine particle'.

A few reports demonstrated the effects of physicochemical parameters on the morphology of nanoflowers and it was found that both are crucial factors to control/tune the flower-shape NPs. Sharpness of branched dendrite particles decreases with an increase in the concentration and finally evolved as branched particles (Fig. 4c–e). Likewise, mild temperatures of 150 °C scaled-up nanoflowers were obtained in 3 h; however, below this temperature (3 h), the formation of nanoparticles needed some extra reaction time. These nanoflowers were prepared using K$_4$[Fe(CN)$_6$] with concentrations of 0.01, 0.02, and 0.03 mol respectively at 150 °C. Higher concentration of K$_4$[Fe(CN)$_6$] produces the thick nanorods branches of the dendrites. Broadening depending on substrate concentration was noted at the temperature of 180 °C. These results suggest that the kinetic parameters (temperature and concentration) are key factors to tune the morphology of flower NPs in MW assisted
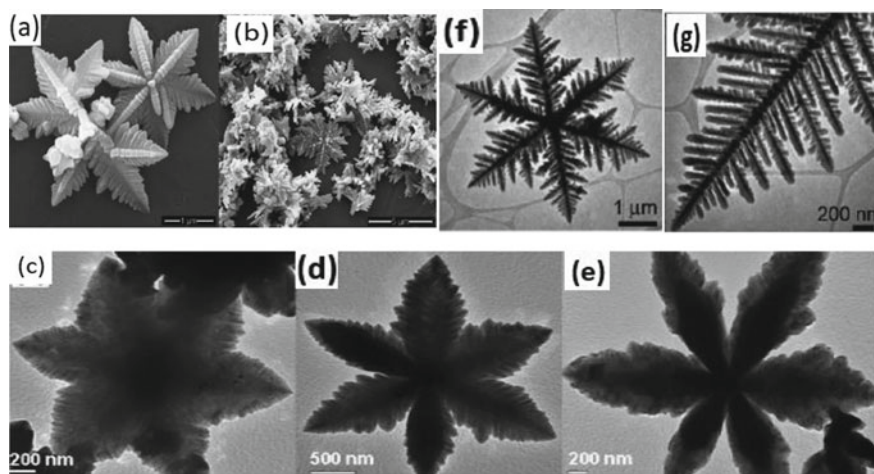
Fig. 4 **a**, **b** Field-emission scanning electron microscopy (FESEM) of dendritic α-Fe$_2$O$_3$, **c–e** represent TEM of α-Fe$_2$O$_3$ particles using **a** 0.01, **b** 0.02, and **c** 0.03 mol of K$_4$[Fe(CN)$_6$] at 150 °C under MW irradiation, and **f** and **g** TEM and HRTEM micrograph of a sixfold-symmetric α-Fe$_2$O$_3$ dendrite. (Reprinted with permission from Ref. [60]. Copyright ©2009 American Chemical Society)

route. Hu et al. [61] demonstrated the single crystalline α-Fe$_2$O$_3$ self-assembled nanoparticles by using an aqueous solution of K$_3$[Fe(CN)$_6$]. Figure 4f show TEM images of a flower-shaped α-Fe$_2$O$_3$ nanoparticles. A closer view showed that the central trunk displayed a pagodas-like instead of a nanorods. Tripod-nanoparticles are considering as a building block in a head-to-head fashion into the central trunk as shown in Fig. 4g.

2.4 Polyol Synthesis

Polyol synthesis is a robust and versatile liquid-phase synthesis for preparation of precise metal NPs in terms of size, shape, phase composition, and crystallinity in high-boiling and multivalent alcohols [5]. Ethylene glycol (EG), commonly solvent and simplest reagent, comprise into two main series of molecules on the basis of EG: (i) diethylene glycol (DEG), triethylene glycol (TrEG), tetraethylene glycol (TEG), and so on up to polyethylene glycol (PEG) and (ii) propanediol (PDO), butanediol (BD), pentanediol (PD), and so on. Usually, a polyol acts as reducing agent, solvent and ligand, to prevent the NPs agglomeration. There are several advantages of polyols synthesis method in various aspects. Polyols has good capabilities to solubilize the starting materials hence allow the use of simple and cheap metal precursors as starting compounds. Polyol have chelating ability which is another beneficial factor to control nucleation and its size evolution, and the cluster formation of the NPs. Despite these superiorities, in case of convective heating for the production of NPs several hours of heating are required. So, it is suggested that microwave heating using polyol could be a unique way to prepare high quality of metal/metal oxide NPs, which not only reduces heating time, but also improves the quality of NPs [62–64].

Ognjanović et al. [65] demonstrated a modified polyol synthesis of iron salts with NaOH in N-methyldiethanolamine (NMDEA) and diethylene glycol (DEG) to investigate flowerlike iron oxide (IO) NPs with sufficient thermal properties where poly-(acrylic acid) (PAA), and poly (ethylene glycol) (PEG), citric acid (CA) were key agents to bind the several radio nuclides efficiently. These coatings increase binding potential, biocompatibility and also prevent aggregation of IONP. The heating efficiency of PAA-coated nanoparticles was higher than other and high radiolabeling production with in number of radionuclides, warrant the further in-vivo experiment to demonstrate their possibility as a theranostic agent. Bender et al. [23] have synthesized a dextran-coated iron oxide nanoflowers and performed a profound analysis connecting the magnetic properties with morphology of nanoflowers. They found that due to an exchange coupling between the cores, the individual nanoflowers had a remanent magnetization, and observed the role of shape anisotropy in preferential magnetization. Hugounenq et al. [21] have developed maghemite (γ-Fe$_2$O$_3$) nanoflowers aiming to be used in efficient magnetic hyperthermia. It is found that the mixture of DEG and NMDEA added in the synthetic process, the alkaline hydrolysis of iron(II) and iron(III) chlorides gave the NPs with flowerlike structure. The assembly of maghemite nanoparticles produces the flowerlike structure of
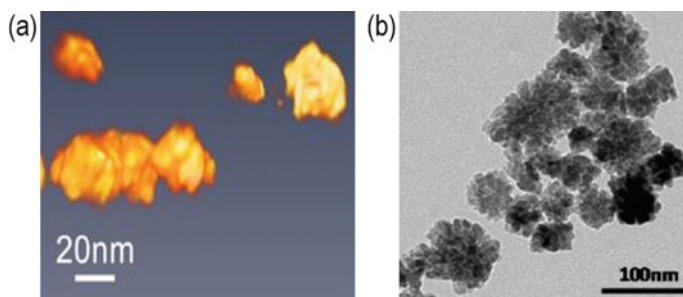
Fig. 5 Electron tomography image of iron oxide nanoflowers (**a**) (Reprinted with permission from Ref. [23]. Copyright ©2018 American Chemical Society) and **b** TEM image of iron oxide nanoflowers (Reprinted with permission from Ref. [21]. Copyright ©2012 American Chemical Society)

the nanoparticles. The synthesis technique allows controlling the size/shape, polycrystallinity, and the magnetic properties which results the enhancement of their hyperthermia properties as compared to conventional approaches (Fig. 5).

3   Different Types of Magnetic Nanoflowers

The increasing curiosity in magnetic nanoparticles for therapy and diagnosis applications [66, 67] is due to their biocompatibility, chemical stability and non-toxicity, and the intense response when exposed to an external magnetic field [68–70]. The shape and size-dependent properties of magnetic nanoflowers and these nanoflowers combined with other materials (such as Au, Ag, organic/inorganic ions etc.) led them to be considered as a potential candidate in thermal therapy applications.
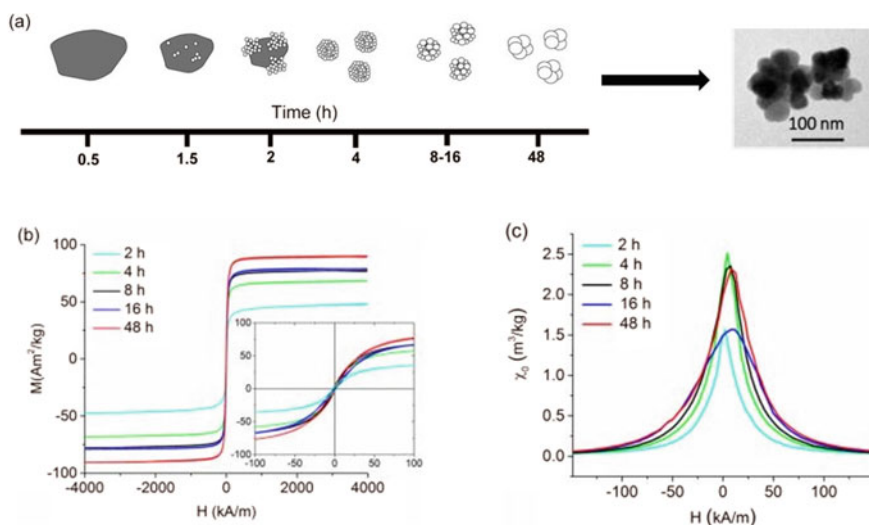
3.1   Magnetic-Oxide Nanoflowers

The witness of magnetic-oxide nanoflowers have shown a remarkable property with higher transverse and longitudinal relaxivities for MRI contrast generation [5] and increased specific absorption rate (SAR) values for magnetic fluid hyperthermia [22]. In the recent year, Fernández et al. [71] have reported monodispersed flower-like superparamagnetic manganese iron oxide NPs controlling the anisotropy of the core and the surface to enhance the hyperthermia properties by tuning: (a) amount of Mn^{2+}, (b) shape to add an additional anisotropy, and (c) maximizing NPs-cell affinity through conjugation with a biological targeting molecule to reach the NPs concentration required to increase the temperature. The developed strategies to optimize particle anisotropy were a favorable direction to ameliorate the thermal properties of these nanoflowers in the different cell line, for example, human glioma

cell line. Further, Nidhin et al. [72] have synthesized $CoFe_2O_4$ nanoflowers (CFNFs) combining the effect of starch; employed as a complexing agent and CTAB; employed as a structure director. From this study, comparatively, CFNF was found more stable as an aqueous dispersion than cobalt ferrite nanoparticles (CFNPs). In addition to the dispersion advantage, CFNF was advantageous as compared to CFNP due to the following reasons: (a) drug carrier in the surface and internal regions, (b) great protection layer that avoids the degradation, (c) exhibits better functioning during imaging. Further, the transverse relaxivities showed that the CFNFs adds the better T2 weighted contrasts as compared to the nanoparticles alone. Their results concluded that the nanoflower contributes toward the increased hyperthermia and magnetic resonance imaging properties. In addition, they suggested multi-core CFNFs assembly could improve drug carriage making the ideal multifunctional nanostructures and also ideal for the functionalization of tumor-targeting antibodies.

Gavilan and co-worker [73] have analyzed the complete synthetic procedure and magnetic behavior of assemble maghemite nanoflowers synthesized via polyol process with average size 63 nm. Figure 6a shows the detail of the formation mechanism and crystallization of NFs. Figure 6b shows the magnetic properties of the nanoflowers for different aging steps from 2 to 48 h in a detail. It was found that the magnetization increased from 48 to 90 A m^2/kg with the time (4, 8, 16, and 48 h), and a high value of coercivity ~0.5–2 kA/m at 290 K (Fig. 6b). The initial mass susceptibility (χ_o) of NF-4, NF-8, and NF-48 are observed in the range of 2.3–2.5 m^3/kg, shown in Fig. 6c. The aggregation of cores resulted in the magnetic susceptibility enhancement and form densely packed nanoflowers [22].


Fig. 6 Maghemite nanoflowers: **a** evolution during the aging process, **b** magnetic properties at 290 K for the samples NF-2-48, **c** mass initial susceptibility (χ_o) for the samples NF-2-48. (Reprinted with permission from Ref. [73]. Copyright ©2017 American Chemical Society)

3.2 Magnetic Plasmonic Nanoflowers

The plasmonic nanomaterials, for example, gold (Au), silver (Ag), and platinum (Pt), etc. have investigated their possibility in several imaging systems, such as biosensing and thermal therapy, owing to the natural biocompatibility, great functionality, and controllable optical properties [53, 74–77]. These materials show an intense absorption of the incident light under the exposure of light illumination caused by the coherent oscillation of conduction electrons on their surface [78]. When surface plasmon resonance (SPR) arises under the magnetic field with the resonance frequency, the most effective absorption is observed. This resonance strongly depends on the particles morphology. The tunability of SPR is very important to achieve efficient penetration into deep tissues and to tackle the delimited penetration of optical imaging systems. The biological window of near-infrared (NIR) light wavelength in between 650 and 900 nm provides increased transparency to water and biological molecules [79, 80]. Therefore, the plasmonic nanomaterials tuned within the NIR have been discussing rigorously for advance optical imaging and photothermal therapy. For image-guided therapy, the nanoparticles which possess dual magneto-plasmonic behavior in a system are highly recommended. For creating a shell on the magnetic core, these plasmonic NPs are used which is chemically inert in the physicochemical system and biocompatible [81]. The core@shell nanoparticles are creating an efficient platform for thermal therapy due to their unique magnetic and optical properties [82]. The inner magnetic core is completely protected from a myriad factor which is the main advantage of these plasmonic surfaces [83]. Taking these an account, magneto-plasmonic nanomaterials allow more practical and clinically result-oriented treatments by incorporating imaging properties into therapeutics.

Recently, Tomitaka et al. [43] have synthesized NIR-responsive magnetic@plasmonic(Fe_3O_4@Au) nanostars, shown in Fig. 7a, for image-guided drug delivery applications. The Fe_3O_4@Au nano stars exhibited multifunctionality combining plasmonic and superparamagnetic properties, as well as drug binding and controlled release capabilities. The magnetization curves of Fe_3O_4 and Fe_3O_4@Au nanostars are shown in Fig. 7b, which showed superparamagnetic behavior. The saturation magnetization of Fe_3O_4 and Fe_3O_4@Au nanostars were 52 emu/g and 3 emu/g, respectively with Au-to-Fe weight ratio of Fe_3O_4@Au nanostars 10.7 (89 wt% Au, 11 wt% Fe_3O_4).

Figure 7c shows NIR-triggered release profile of antiretroviral drug, tenofovir disoproxil fumarate (TDF) from MNP@Au nanostars at different exposure times. TDF release was observed as fast as 5 min of NIR stimulation and increased continuously with the exposure time. The SPR effect created the rise in temperature of Fe_3O_4@Aunanostars under NIR at the wavelength of 808 nm. It was found that the total temperature rise was nearby +4.2 °C from room temperature for 30 min (see Fig. 7d). Such light-to-heat conversion phenomena is a central principle for NIR-triggered controlled release of drugs from gold nanomaterials. It was revealed that the light-to-heat conversion property of Fe_3O_4@Au nanostars is outstanding features that can be used for NIR-triggered controlled release of different types of drugs by
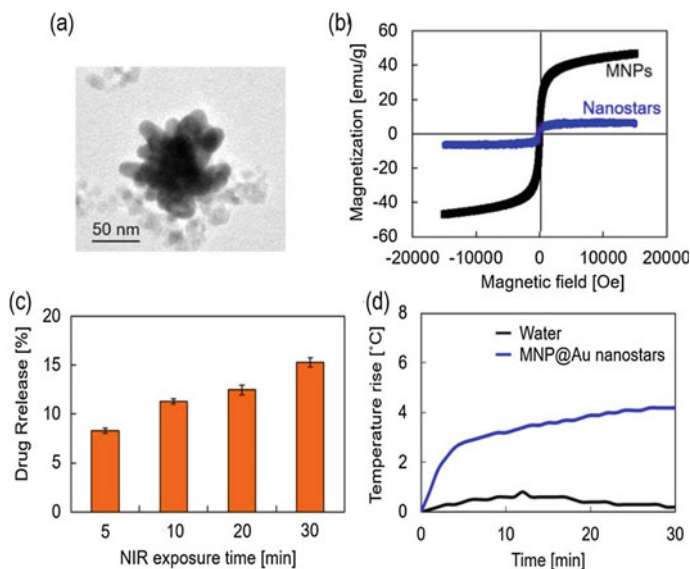
Fig. 7 **a** TEM image Fe_3O_4@Au nanostars, **b** hysteresis loss of Fe_3O_4 and Fe_3O_4@Au nanostars, **c** tenofovir disoproxil fumarate (TDF) release from MNP@Au nanostars after illumination with NIR, **d** time-dependent heating efficiency of MNP@Au nanostars after NIR exposure (Reprinted with permission from Ref. [43]. Copyright © 2020, Springer Nature)

splitting the bonding in between nanostars and the drug at the specific location in the body.

Recently, as a part of nanoflowers/star family, the study of spiky (SP) shapes of magneto-plasmonic nanoflowers is getting attention due to their large optical cross sections for NIR photons necessary in therapy/imaging and drug delivery application [84, 85]. It is believed that on combining the magnetic core with spiky plasmonic shells of Au will significantly improve the cancer diagnosis/therapy [86], imaging [87], DNA analysis [88], and drug delivery [89]. Due to the presence of Au on the surface which contributes to the chemical stability and dielectric properties, Fe_3O_4@Au SPs become well-defined plasmon resonances within the visible and NIR spectra in the high electromagnetic fields. These nanoflowers are considered a highly effective contrast agent in cancer diagnosis and therapeutics due to the spiky-like structure. Plasmon mode dominates the optical response of the spiky SPs and can be rationalized in terms of plasmon hybridization [90]. The hybridization results in a multi peaked optical spectrum where the mode coupling is controlled by the thickness of the intermetallic dielectric layer and red-shifting of the collective plasmon modes can be induced by the petals aperture angle and length effects. Enhancement in extinction cross section is also caused by these petals. For the formation of spiky nanoscale particles in concave shapes, Zhou et al. [91] have demonstrated a new method of self-assembly approach by adding negatively charged Au attached on the surface of previously fabricated negatively charged Fe_3O_4@Au core–shell particles.

The mechanism showed important differences with the detailed overview of the origin of spiky morphology in nanoscale structures.

## 3.3 Magnetic@Organic/Inorganic/Metal Ion Nanoflowers:

The development of advance nanotechnology has explored a number of nanomaterials, such as nanoporous silica [92], electrospun nanofibers [93], and magnetic nanoparticles [94], which have been utilizing in enzyme immobilization. Briefly, it is expected that enzyme reproducibility and reusability can be enhanced by enzyme immobilization. Due to unique magnetic response of immobilized enzyme, they realize several recycling of the enzyme and expand the enzymes life. After immobilization, however, the enzyme functions are limited owing to conformation instability [95], control mass-transfer and preparation complexity [95] which still impedes the number of biomedical applications, for example, nanobiocatalysis. While talking on enzyme immobilization, biomineralization is a central term that needs to be known that depends on the inorganic nanomaterials in the living organisms [96]. Therefore, to enhance the activity of enzymes and operational stability, the development of an easy and effective way for the immobilization of enzymes is desirable. High catalytic activity is found in the hybrid nanoflowers in comparison with most of the reported immobilized enzymes and free enzymes. Moreover, organic–inorganic hybrid nanoflower durable, activity and stability of entrapped organic biomolecules and have received great attention.

Several techniques have been discussed to integrate the multiple enzymes within hybrid nanoflowers to perceive the target analytes. Usually, it is reported that two different enzyme components for the detection of target glucose via the GOx-HRP mediated cascade enzyme reaction [97, 98]; glucose oxidase (GOx) and horseradish peroxidase (HRP) with copper sulfate in phosphate buffered saline (PBS). The organic components, for instance, streptavidin, antibody, or concanavalin, were added to inorganic metal ions and generally used enzymes in order to develop triple component-incorporated hybrid nanoflowers and also have high affinity for their corresponding target molecules [99–101]. The disease-indicating biomarkers or pathogenic bacteria in food can be detected by nanoflowers due to their multifunctionality. These examples show the effectiveness of nanoflowers and diversify their applicability. Cheon et al. [102] have developed the nanoparticle combining the enzyme which allowed for the close proximity of glucose oxidase (GOx) and inorganic MNPs within copper-based nanoflowers. It is observed that for cascade reaction, the MNPs–GOx (Fe$_3$O$_4$–GOx) NFs have highly enhanced peroxidase activity as well as substrate channeling, which leads to a highly specific and sensitive glucose detection system, in addition to the magnetic reusability and excellent operational stability. High level of glucose inhuman blood serum is diagnosed by this new biosensor which demonstrates its analytical utility. Authors conclude that the Fe$_3$O$_4$–GOx NFs has opened up a great potential, for the development of enzyme-inorganic hybrid nanoflowers with

the substrate channeling mechanisms and also applicable in convenient detection of clinically important target molecule and applications like, robust, and in rapid.

Bisphenol A (BPA) is well known organic chemical material which can cause harmful effects in the living organism, such as carcinogenic activities, metabolic disorders, chronic diseases, and obesity, [103]. This is commonly used in the preparation of polycarbonate plastics and epoxy resins into products for most aspects of our lives [93]. Thus, increasing number of techniques were developed in order to remove BPA from the environment. To improve the activity and the recycling performance of the immobilized HRP, recently Han and Group [104] have prepared the magnetic nanoflowers and their application for BSA removal. For this, Fe_3O_4 magnetic nanoparticles were first synthesized and then 3- (methacryloxy)-propyltrimethoxysilane (MPS) were used to modify the surface of Fe_3O_4 magnetic nanoparticles to form numerous double bonds. Subsequently, a facile one-step distillation precipitation polymerization (DPP) of glyceryl methacrylate (GMA) were used to prepare the core/shell structural Fe_3O_4@PMG magnetic nanoparticles. After that, the compound of Fe_3O_4@PMG-IDA was prepared, where IDA is iminodiacetic acid, and then Cu^{2+} was adsorbed to the surface which gives Fe_3O_4@PMG-IDA-Cu^{2+}. The Fe_3O_4@PMG-IDA-Cu^{2+} was added to PBS solution and followed by an incubation at 25 °C for a different time and finally obtained nanoparticles were magnetic nanoflowers. The relationship between enzyme activity of the magnetic nanoflowers and hierarchical structure were fully investigated. The optimization of formation conditions of the magnetic nanoflowers has been analyzed; the effect of the incubation pH, the effect of the HRP concentration, the effect of the incubation time. Figure 8a1–a6 demonstrated that the concentration of HRP affect morphology and size of the magnetic nanoflowers. It is found that the activity recovery of the magnetic nanoflowers increased first and then decreased with the increase of the HRP concentration. According to the results of the activity recovery of the magnetic nanoflowers and morphology, the optimum synthetic concentration of HRP was 0.5 mg/mL, where the activity recovery and the encapsulation efficiency were 182% and 83.21%, respectively.

The effect of the incubation time on the activity recovery of the magnetic nanoflowers consistent with the morphology of magnetic nanoflowers forming with the time evolution, shown in Fig. 8b1–b6. The activity recovery of these magnetic nanoflowers was optimal when the complete hierarchical flower-shape structures were formed. It was observed that 8 h was the optimum incubation time of HRP in which the activity recovery and the encapsulation efficiency were 175% and 84.16%, respectively. Further, Fig. 8c1–c6 showed that at pH ~ 7, the activity recovery reached the maximum value. These results suggested that a synergistic effect between Fe_3O_4@PMA-IDA-Cu^{2+} and HRP immobilized in the magnetic nanoflowers as shown in Fig. 8d. Figure 8e shows the catalytic kinetics, and reaction rate of the oxidization of BPA by free HRP and the magnetic nanoflowers. The reaction rate constants (K) of the nanoflowers and free HRP were 0.2132 min^{-1} and 0.0921 min^{-1}, respectively whereas the enzymatic activity of the magnetic nanoflowers (468.5 U/mg) was approximately 183% higher than free HRP (256 U/mg) in solution.
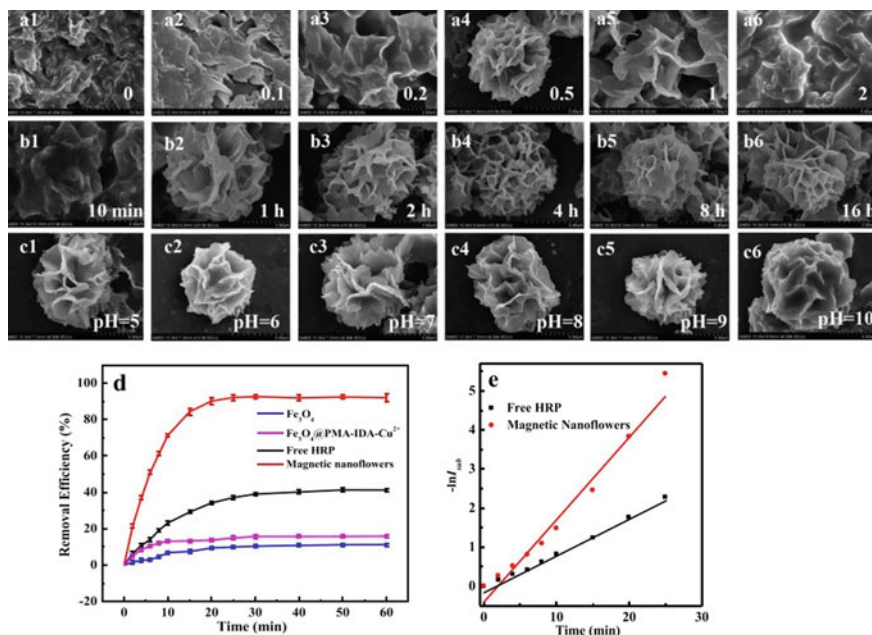
Fig. 8 Effect of different HRP concentrations on the morphologies of the magnetic nanoflowers: **a**1 0.0 mg/mL, **a**2 0.1 mg/mL, **a**3 0.2 mg/mL, **a**4 0.5 mg/mL, **a**5 1.0 mg/mL, **a**6 2.0 mg/mL, and other conditions: 0.1M Cu^{2+}, 0.2M PBS at p^H 7.0, and incubation for 8 h at 25 °C; Effect of different incubation time on the morphologies of the magnetic nanoflowers: **b**1 10 min, **b**2 1 h, **b**3 2 h, **b**4 4 h, **b**5 8 h, **b**6 16 h, and other conditions: 0.1M Cu^{2+}, 0.2M PBS, and 0.5 mg/mL HRP at pH 7.0 at 25 °C; effect of different incubation pH on the morphologies of the magnetic nanoflowers: **c**1 pH = 5, **c**2 pH = 6, **c**3 pH = 7, **c**4 pH = 8, **c**5 pH = 9, **c**6 pH = 10, and other conditions: 0.1M Cu^{2+}, 0.2 M PBS, 0.5 mg/mL HRP and incubation for 8 h at 25 °C, **d** the removal efficiency of BPA catalyzed by Fe$_3$O$_4$, Fe$_3$O$_4$@PMA-IDA- Cu^{2+}, free HRP and the magnetic nanoflowers, and **e** catalytic kinetics and reaction rate of the oxidization of BPA by free HRP and the magnetic nanoflowers. (Reprinted with permission from Ref. [104]. Copyright © 2019 Elsevier B.V. All rights reserved

4 Theory of Nucleation and Formation of Magnetic Nanoflower

Theory of Nucleation: The present cognition on the formation mechanism of uniform nanoparticles is concerning the synthesis of micro/nano scale colloidal nanoparticles. The current understanding of NPs formation is provided by a classical model, which clearly discussed regarding the discrepancy in NPs sizes, shapes and reaction conditions. Nanocrystal formation mechanism is well explained by Ostwald ripening, diffusion-controlled growth, and burst nucleation [30, 31, 105–108]. Let us start with formation of colloidal particles in which monomers are considered as building units of nanocrystals and the first stage of a crystallization process. The obtained solid phase from solution during crystallization is simply called 'Nucleation'. Nucleation is purely considered as a thermodynamic model describes the

process of the physics of first-order phase transition of materials in solutions. It discusses a new phase—the nucleus- in the metastable primary phase. The complete physical process of the reaction in the solution well explained by classical nucleation theory (CNT) [109, 110]. The unique idea of CNT in this process is a thermodynamic system tends to minimize its Gibbs free energy. For growth processes of nanoparticles such as LaMer's theory, this thermodynamic theory was transferred [111–113]. The CNT only describes the nucleation, particle growth is separated as a subsequent process. Growth processes such as Oswald ripening diffusion-limited growth and aggregation can be used for further growth, after nucleation. Further approaches to characterize the particle growth are models using rate equations defining the size evolution of nanoparticles. Formulating and solving (in general numerically) these expressions evolve a size distribution of the nanoparticles with the span of time. The CNT proposes the two types of nucleation based upon the surface energy of particles, i.e., homogeneous and heterogeneous. Nucleation which occurs at nucleation sites on solid surfaces contacting the liquid or vapor are referred to as heterogeneous nucleation. For instance, in seeded-growth syntheses of nanoparticle a heterogeneous nucleation occurs at the surface of particles in solution providing nucleation sites. On the other hand, homogeneous nucleation requires a supercritical state such as a supersaturation, and occurs spontaneously and randomly. A stable nucleating surface is present in heterogeneous nucleation and mostly occurs in liquid phase. By looking at the total free energy of a nanoparticle, the process of homogeneous nuclei formation can be considered thermodynamically.

Volmer and Weber [114] have elaborate the concept of Gibb's free energy (G) which is equal to sum of surface free energy μ_s and volume free energy μ_v (also called bulk free energy). The free surface energy 'μ_s' is directly varied by the interfacial tension 'γ' (defined as the surface free energy per unit area) between the nanocrystal surface and the surrounding solution. This indicates 'γ' increases if the radius of nuclei increases that presides a positive change in free surface energy. The positive term describes an energy unfavorable bonding between a monomer and a cluster or theoretically also in between several monomers leading to an enhance in the free surface energy. The graphical representation of these phenomena is shown in Fig. 9a on the other hand, volume free energy, μ_v is proportional to the negative of volume nucleus. The negative term describes how an energy favorable such bonding overriding to a lowering of the bulk energy. The reduced free energy is considered as driving force for both nucleation and seed-mediated growth. Let C_i, C_o, V_n, and S are the concentration of the solute, equilibrium concentration, atomic volume, and the supersaturation respectively, then bulk free energy ΔG_v per unit volume of solid phase which depends on the concentration of solute and is given by,

$$\Delta G_v = -\frac{kT}{V_n} \ln \frac{C_i}{C_o} \tag{1}$$

where $S = C_i/C_o$, no nucleation if $S = 0$. When $C_i > C_o$, ΔG_v is negative, nucleation occurs at once. Consider r is the radius of spherical nucleus, then Gibbs free energy or volume energy is given by,
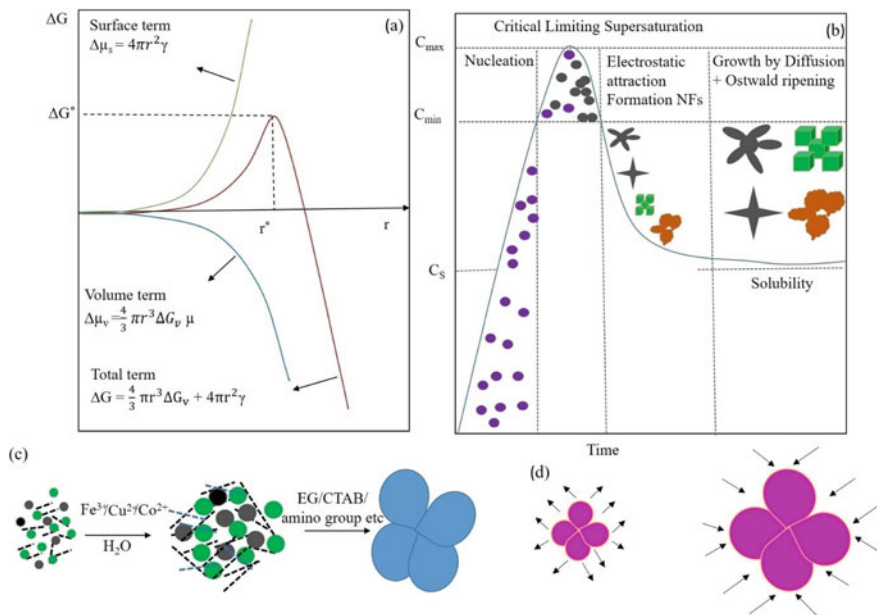
Fig. 9 a Represents the change in volume free energy $\Delta\mu_v$, surface free energy $\Delta\mu_s$, and total free energy ΔG, as functions of radius, **b** schematic diagram showing the processes of nucleation and subsequent growth in solution. (Reprinted with permission from Ref. [115]. Copyright 2012 American Chemical society), **c** schematic mechanism of NFs, and **d** concept of Ostwald's ripening

$$\Delta\mu_v = \frac{4}{3}\pi r^3 \Delta G_v \qquad (2)$$

The surface free energy which balances the reduced energy during the nucleation of particles is given by,

$$\Delta\mu_s = 4\pi r^2 \gamma \qquad (3)$$

Which gives the total free energy of nucleus by adding Eqs. (2) and (3) given by,

$$\Delta G = \frac{4}{3}\pi r^3 \Delta G_v + 4\pi r^2 \gamma \qquad (4)$$

Roughly, surface free energy is proportional to the radius of nucleus,

$$\Delta\mu_s \approx A_n \approx r^2 \qquad (5)$$

And similarly, the volume free energy $\Delta\mu_v$ can be written as

$$\Delta\mu_v \approx V_n \approx r^3 \qquad (6)$$

Here, A_n is surface of nucleus and V_n is volume nucleus.

As shown in the Fig. 9b as long as $S > 1$, the volume term favors the formation of crystals to release the unnecessary free energy of newly formed nucleus and becomes stable if its radius exceeds critical radius $r*$ that resist the dissolution and could evolve further to reach in final state. At $r = r* \frac{d\Delta G}{dr} = 0$ provides critical free energy $\Delta G*$, also referred as barrier energy, that is necessary to defeat in order to get a nucleation of the particles. Thus, we have

$$r* = -\frac{2\gamma}{\Delta G_v} \text{ and } \Delta G* = \frac{16\pi\gamma}{3(\Delta G_v)^2} \tag{7}$$

If the size of nuclei is smaller than a critical radius '$r*$', it cannot evolve further; instead only dissolve back into the solution in the form of monomers to decrease their free energy which is imposed by surface for the formation of nuclei. The critical radius represents the limit on how specific nanoparticles can synthesize understanding the nucleation process. The Gibbs–Thomson equation gives a unique idea regarding the nucleation at maximum supersaturation 'S_m' which varies with the temperature [105, 115].

La Mer's and coworkers [113] proposed the concept of burst nucleation to explore further understanding the mechanism process of nucleation and growth of colloids/nanoparticles on several oil aerosols and sulfur hydrosols. The burst nucleation process favors the simultaneous generation of nuclei and subsequently growth without further nucleation, i.e., it pertains to the configuration of the excessive nuclei rapidly followed by growth without additional nucleation. The burst nucleation concept in nanoparticle formation is to separate the nucleation and growth phenomena. This allows to control the particle size distribution during growth. The complete mechanism shown in Fig. 9b follows several steps: (I) the increased concentration of monomers reach to the critical supersaturation level at a certain time and takes place a homogeneous nucleation; the supersaturation level is the foremost requirement for the homogeneous nucleation. These unknown form of material crystalized during the first nucleation is considered as 'primary nucleation' (II) the saturation level at which the energy barrier (activation energy) can be overcome leading to a rapid self-nucleation, i.e., secondary nucleation [116, 117], and (III) nucleation period is ended due to the burst nucleation and the saturation level fall down immediately below the self-nucleation level. After that, diffusion of further monomers causes heterogeneous nucleation/growth of nanoparticles in solution. The concentration monomers favor the rapid increase in the self-nucleation stage (II) and almost constant during the final stage (III).

Supersaturation is the difference between the chemical potential of the solute molecules in the supersaturated (μ) and saturated (μ_s) states, respectively. In thermodynamic, the chemical potential is also referred to as partial molar free energy [109, 118].

$$\Delta\mu = \mu - \mu_s = k_B T \ln S \tag{8}$$

where S is supersaturation, k_B is Boltzmann constant and T is the temperature and S can be calculated further by taking ratio in between concentration of the solute in solution C_i and saturated/equilibrium concentration of the solute C_o, i.e.,

$$S = \frac{C_i}{c_b} \tag{9}$$

if $S > 1$, nucleus grows and solid phase formed; if $S < 1$, nucleus dissolves and if $S = 0$, nucleus and solution are in equilibrium.

Formation Mechanism of Magnetic Nanoflowers: The magnetic nanoflowers are formed by combinatorial attachment of magnetic nanoparticles to the petal surface of nanoflowers (NFs) due to the electrostatic attraction in between positive and negative charge of MNPs and NFs, respectively. Generally, the organic groups, for instance, amino groups, are used to functionalize the magnetic nanoparticles, which produces large positive charges, while petals of the nanoflowers are negatively charged. Although the interaction between proteins and metals is poorly perceived, the assumptions on the formation of nanoflowers include the following successive steps: nucleation of MNPs, formation of petals, their attachment, and continuous growth as nano flowers. The nucleation process of NPs is already discussed in the aforementioned section and the growth mechanism is discussed in later section. The formation of petals and its attachment with MNPs is a main task to synthesize flower-shape NPs. Usually, sodium acetate (NAOAc), cupper phosphate ($Cu_3(PO_4)_2$), copper sulfate ($CuSO_4$), CTAB and PBS, etc. are used in the solution to develop petals with negative charge. However, concentration of these additives are responsible to develop either as petals or not during the synthesis. In addition, size/length/thickness of petals is also leaned on the concentration of these additives. Fu et al. [18] have synthesized laccase-loaded magnetic nanoflowers where the influence of Cu^{2+} concentration was clearly observed. As per their findings, when Cu^{2+} concentration was below 0.4 mM, (concentration did not reach the point of supersaturation) no plump NFs were observed. The diameters of NFs were increased with increase of Cu^{2+} concentration also the petals became more crisp. Nanoflowers sizes decreased and more number of nucleation sites were available hence petals became more tightly with increase in laccase concentration (i.e., 0.05, 0.1, 0.25, and 0.5 mg/mL). In brief from a mechanistic point of view, Cu^{2+} first formed primary copper phosphate crystals by reacting phosphate groups in phosphate buffered saline (PBS) and then laccase attached to copper phosphate through binding reaction between the amine groups, and Cu^{2+} to assemble NFs that induce the nucleation of copper phosphate primary crystals. The anisotropic growth of these primary particles gives the complete a flowerlike structure. After several experiments, the author's suggested that 0.1 m/mL laccase and 2.6 mM Cu^{2+} in PBS (p^H 6.5) at 4 °C were optimized conditions for the nanoflowers. Nidhin and coworkers [72] prepared cobalt ferrite NFs (CFNFs) in the presence of CTAB as a surfactant which can easily be visualized from the structure of a flower, whose petals assemble from a center. They were able to obtained cobalt ferrite NPs without flower shape in the absence of

surfactant. Here, due to a combined effect of starch employed as a complexing agent and CTAB as a flower-shape structure director the nanoflowers are formed.

5 Growth Mechanism and Ostwald Ripening

Growth Mechanism: As we have discussed above that growth of nanoparticles occurs immediately after the end of nucleation. When the concentration of solutes/monomer's falls below supersaturation, nucleation stops but does not stop a further growth of nanoparticles. Generally, in smaller nanoparticles, the surface to volume ratio is quite high that indicates surface excess energy becomes more important constituting a non-negligible percentage of the total energy. Hence, the thermodynamically non-equilibrium solution allows the formation of larger particles from the combination of smaller ones that decrease the surface energy and favors the further grow of nanoparticles. The particles in the solutions further growth by a sequence of monomer diffusion followed by their reaction on the surface. Coarsening effects, controlled either by mass transport or diffusion, are often termed the Ostwald ripening process. Reiss et al. [119] proposed a growth model called "growth by diffusion" in which the growth rate of spherical particles depends solely on the monomer flux supplied to the particles. Smaller particles will grow faster in presence of larger particles if the diffusional growth depends only on the monomer flux, which leads to a size focusing (narrowing of size distribution). This mechanism does not include other effects such as coalescence or dissolution (Ostwald ripening), aggregation and is, therefore, a very simplified mechanism. In addition, Sugimoto et al. [120] including dissolution effects obtaining a size-dependent growth rate by considering the Gibbs–Thomson equation and extended Reiss's model qualitatively. This diffusion bounded Ostwald ripening phenomena is a principal mechanism of particle growth and was explained collectively by Lifshitz, Slyozov, and Wagner, known as the LSW theory. The growth of nanoparticles consists following mechanisms: (a) diffusion to the surface, and (b) surface reaction.

Let 'r' is radius of spherical particles, J is the total flux of monomers, 'x' is the diffusion layer, D is the diffusion coefficient and C is the concentration at distance 'x', then total flux of the monomers is given by Fick's first law,

$$J = 4\pi D x^2 \frac{dC}{dx} \tag{10}$$

Let C_b be the bulk concentration of monomers, C_i be the concentration of the monomers at solid/liquid interface and δ be the distance between particle surface to bulk concentration of monomers, i.e., thickness of diffusion layer and J is the constant over diffusion layer at steady state, so Eq. (10) can be written as,

$$J = \frac{4\pi D r (r + \delta)}{\delta}(C_b - C_i) \tag{11}$$

Integrating (11) from $r + \delta$ to r, we get,

$$J = 4\pi Dr(C_b - C_i) \tag{12}$$

This flux is the consumption rate of the monomer at the surface of the particle. That is,

$$J = 4\pi Dr^2 k(C_i - C_r) \tag{13}$$

where k is rate of surface reaction and is independent of particle size. But in solution, it is difficult to find out the C_i, so it must be eliminated using the above two equations.

Now if this growth evolution is tuned by the diffusion process of monomers from bulk solution to particle surface, then growth rate is given by,

$$\frac{dr}{dt} = \frac{Dv(C_b - C_r)}{r} \tag{14}$$

where v is the molar volume of the bulk crystal and C_r is the concentration on the surface of solid particle. The growth evolution controlled by such diffusion contributes to the formation of homogeneous size distribution of the particles.

On the other hand, when the diffusion occurs rapidly, the growth rate controlled by surface process and the rate is given by,

$$\frac{dr}{dt} = kv(C_b - C_r) \tag{15}$$

However, in the absence of controlled diffusion and surface reaction, the increase in particle's radius with respect to time can be written as,

$$\frac{dr}{dt} = \frac{Dv(C_b - C_r)}{r + D/k} \tag{16}$$

This shows that the particle radius is sensitive and a key factor for the solubility. According to the Gibbs–Thomson relation, the particles with radius 'r' has extra chemical potential $\Delta\mu$. Thus C_r can be expressed as,

$$C_r = C_b \exp\left(\frac{2\gamma v}{r K_B T}\right) \tag{17}$$

where v is the molar volume of the bulk crystal and C_b is the concentration of the bulk solution. At last, it is worth to express the general equation of growth rate of spherical NPs putting Eq. (17) in (16). We have,

$$\frac{dr^*}{d} = \frac{S - \exp\left(\frac{1}{r^*}\right)}{r^* + K} \tag{18}$$

where dimensionless quantities are defined as, $r^* = \frac{RT}{2\gamma v} r$; $\frac{RT}{2\gamma v}$ is capillary length, $\tau = \frac{K_B^2 T^2 D C_b}{4\gamma^2 v}$ and $K = \frac{K_B T D}{2\gamma v k}$ is Damköhler number. The capillary length measures the size effect of a particle on the chemical potential whereas Damköhler number checks whether the diffusion rate (D) and/or reaction rate (k) influence the growth reaction or not. It is clear from the above growth rate equations that the growth rate of NPs is strongly affected by their size. When the chemical potential of monomers is lower than it is in the solution, the dissolution reaction takes place. On the other hand, the precipitate reaction dominates the surface reaction, for the larger particles. When $K/r^* \gg 1$, In this case, the smaller values of r and k make the surface reaction the rate-determining step in the growth process, and this growth mode is called reaction-controlled growth. In contrast, when $K/r^* \ll 1$, the reaction mode is called diffusion-controlled growth, in which the monomer diffusion is the rate-determining step. In this case, the monomers transported from the bulk solution precipitate immediately onto the surface of the particle. In brief, the crystal growth process in solution consists of nucleation and growth as separate phenomena, which are affected by the intrinsic crystal structure and the external conditions including the capping molecules, temperature, kinetic energy barrier, time, and intrinsic crystal structure. The formation of nanostructures after nucleation in solution relates to two primary mechanisms: the aggregation growth process and the Ostwald ripening process after the 'burst nucleation'. Crystal growth by aggregation can occur by oriented aggregation, and random aggregation, and the Ostwald ripening process involves the growth of larger crystals at the expense of smaller ones [113, 119–121]. Gavilan et al. [73] have prepared a controlled single- and multi-core maghemite NFs which occurred following burst nucleation, growth by aggregation, and recrystallization that takes place over time. The growth of NFs over time is shown in Fig. 10 Sodium acetate was found to be a key parameter governing the self-assembly process in overall reaction. For higher acetate concentration, an author's observed that massive nucleation and growth by diffusion takes place, resulting in single-core particles. The initial nanocrystalline subunits seem to grow by partial aggregation in hollow spheres, as the amount of acetate is reduced. Initial nanocrystalline nuclei are formed on further reduction in acetate and these nanocrystalline nuclei strongly aggregate to produce the final flowerlike particles.

Ostwald ripening: 'Ostwald ripening' is the result of the Gibbs–Thomson relation (smaller particles have a higher chemical potential). It is a final stage of first order
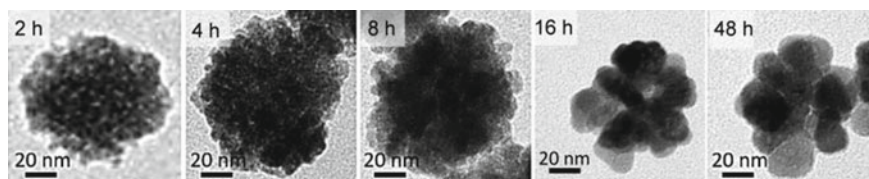
Fig. 10 Growth evolution of maghemite NFs with time. (Reprinted with permission from Ref. [73]. Copyright ©2017 American Chemical Society)

phase transformations following growth stages and nucleation, and is often observed in synthesis of nanoparticles [122], oil–water emulsions,, and during epitaxial growth [106] binary alloys [123], two-phase mixtures composed of second phase in matrix [108], and clusters on surfaces [124]. In the diffusion-controlled growth mode, all of the solute that diffuses onto the crystal surface immediately precipitates when the concentration of the solubility of the particle is much lower than solute. On the other hand, dissolution of the particle occurs and direction of mass transport is reversed with the concentration lower than the solubility of the particle. Some of the particles dissolve when the driving force for crystallization is weak, while others keep growing (Ostwald ripening). The dissolution reaction is faster than the precipitation for the smaller particles when the solute concentration is low. On the other hand, larger particles can grow by receiving solute from the dissolving particles and are so stable. Under the Ostwald ripening process, mean size of the particles increases. While the solute concentration and particle concentration generally decrease. In this way, in Ostwald ripening smaller nanoparticles/clusters of atoms/molecules transfer to bigger clusters, shown in Fig. 9d. and represents the spontaneous and continuous evolution of precipitated nanoparticles/clusters. A driving force is induced because of increased solubility of the smaller particles due to surface tension between the precipitate and the solute. The driving force for the ripening process is the well known curvature dependence of the chemical potential which, assuming isotropic surface energy, is

$$\mu = \mu_0 + \gamma \kappa V_m \tag{19}$$

where κ is the mean interfacial curvature and μ_0 is the chemical potential of an atom at a flat interface, V_m is the molar volume and γ is the surface energy. It is clear from the above Eq. (19) that the flow of atoms will be from high to low curvature regions. This results in an increase in the size scale of dispersed second phase, which is consistent with the necessary decrease in total energy of the two-phase system and disappearance of surfaces possessing high curvature. Typically, the net effect of Ostwald ripening is to broaden the size distribution of nucleated particles [125, 126]. As ripening takes place in epitaxial growth of quantum dot arrays [127–129], in liquid [130–132] and gas-phase [17–20] fabrication of two nanoparticles, and epitaxial growth of quantum dot arrays [127–129], it prevents the highly desirable formation of narrow size distribution of particles. Besides understanding the fundamental growth of nanoparticles/clusters, study of Ostwald ripening is also important in industrial applications to prepare uniform particles in closed system where large seed particles will grow at the expense of large amount of small particles. Such closed system keeps super saturation constant during particle which is its growth advantage and by changing the size of small particles its level can be controlled. The known mechanisms discussed in the literature for narrowing a particle size distribution (PSD) are: (i) digestive ripening [131, 133], and (ii) inverse ripening [134–136].

6 Magnetic Hyperthermia: Recent Findings on Magnetic Nanoflowers

Currently, the critical problem in public health is the treatment of cancer and it challenges not only the medical practitioner but also scientists from physics, chemistry, and biology from designing of material to the implementation in a body. The urgent need of a new approach to assist in rapidly advancing diagnosis and treatment and could be a supplementary technique for existing therapies based on chemotherapy and radiotherapy. To tackle such problems, magnetic nanoparticles are introduced in localized hyperthermia which has been emerging as very promising agents for cancer treatment [76, 137–140]. Radiotherapy and chemotherapy can be replaced by magnetic hyperthermia and photothermal therapy, as over the past two decades, these are becoming very promising techniques. These approaches have substantially amended their ability to execute the controlled treatments delivering the nanoparticles into targeted tumor tissues, which release the therapeutic heat either upon AC magnetic field exposure or laser irradiation [53, 141, 142]. The heat generated by magnetic nanoparticles is prominently depend on the application of ac magnetic field and frequency. Besides this, magnetic properties, i.e., magnetic saturation (M_S), coercive field (H_C) and magnetic remanent (M_R); structural properties, i.e., size, shape, crystallography, composition, defects, etc.; anisotropic properties, i.e., surface and shape anisotropy, etc. [143–145]. Several efforts have been made to design different shapes, such as, nanospheres, nanohexanes, nanooctapodes, nanocubes, nanowires, nanodisks, nanorings, nanoflowers, nanotubes, nanorings, and, etc. tuning the reactants, volume, time, temperatures, and synthesis routes [11, 12, 15, 25, 100, 143, 146–151]. In the recent years, for magnetic hyperthermia (MHT) magnetic nanoflowers have emerged as promising candidates as a nanoheaters. It has been speculated that their phenomenal heating behavior in MHT is primarily a result of an exchange coupling between the cores, which leads to a super-ferromagnetic magnetization state [21, 22, 27]. An unprecedented spiky flower shell around the magnetic core is the main advantage of nanoflowers over other shapes. Such nanohybrids allowed exploring the concept of a tri-therapeutic strategy merging MHT, photothermal therapy (PTT), and photodynamic therapy (PDT). The multiple expected functions of such nanohybrids at increasing degrees of complexity from test tubes to animals were assessed, with the aim to describe acritical comparison with the stand-alone treatments (MHT and PTT), and to provide effective windows of applicability.

In this regard, Gavilan et al. [73] have recently investigated the magnetic hyperthermia properties of citric acid (CA) coated maghemite (γ-Fe_2O_3) NFs. Nanoflowers with a core size of 23 nm (NF-48) have the highest SLP values, for example, yielding 1131.2 W/g Fe for a frequency of 710 kHz. It is observed that SLP values of NF-48 nearly 5 times larger than those of nanoflowers with crystal size of 15 nm (NF-4), nearly 4 times larger than hollow spheres (HS), and 1.5 times larger than single-core (SC) nanoparticles, although these two latter samples (HS and SC) have bigger core sizes of 27 and 36 nm, respectively. These results suggest that heating capacity is influenced by both core sizes and the packing of the cores. Enhanced

heating capacity is offered by nanoflowers with densely packed cores and large cores compare to nanoflowers with smaller crystallite sizes, single-core nanoparticles, and hollow spheres. In the recent past, Di Corato et al. [152] have reported the systematic study of the heating power and magnetic dynamics in a controlled cellular environment, magnetic properties of a broad range of nanomaterials with different sizes, shapes, and in solution. They observed a rapid and systematic fall in the heating capacity of all the nanomaterials tested, as soon as they associated with the cell membrane or were internalized. Whether the nanoparticles were attached to the cell membrane or contained within intracellular vesicles observed drop was the same. Figure 11e, f are iron oxide nanocubes and nanoflowers, and Fig. 11g, h
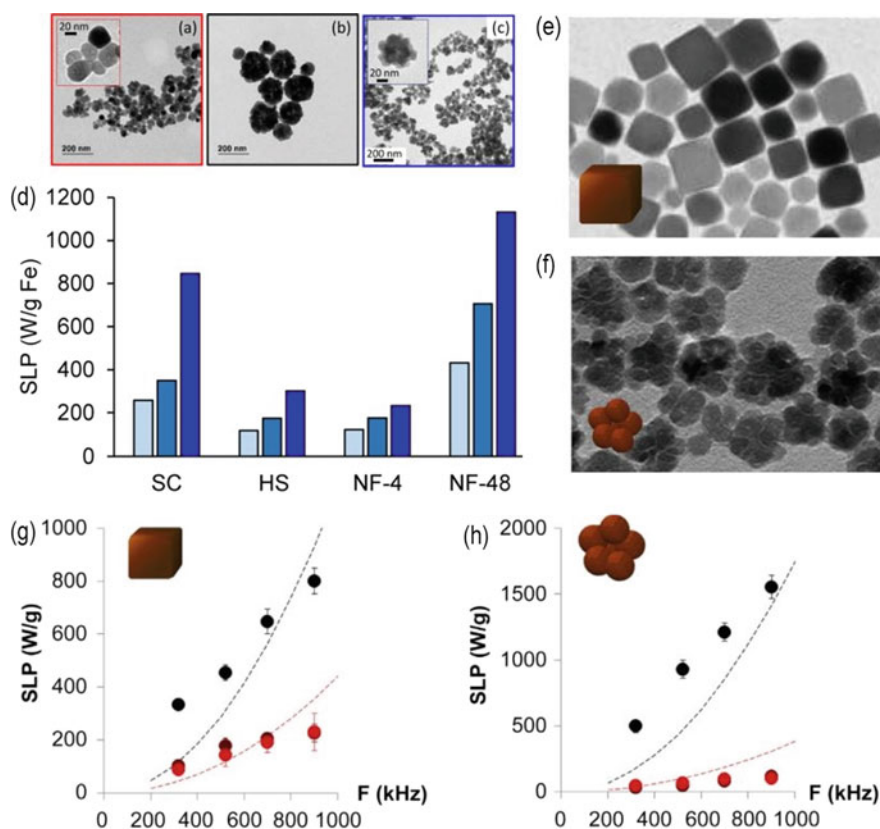

Fig. 11 TEM images of the different structures: **a** single-core (SC) particles, **b** hollow spheres (HS), and **c** nanoflowers (NF), **d** SLP values of samples of citric acid (CA)-coated SC, HS, NF-4, and NF-48 at field amplitude 23.8 kA/m. (Reprinted with permission from Ref. [73]. Copyright ©2017 American Chemical Society). Measurement of heat-generating capacity (in terms of the SLP (W/g)) for **g** iron oxide nanocubes (18 nm), and **h** iron oxide nanoflowers (25 nm), in water and within cell model systems, according to the frequency of the applied magnetic field. (Reprinted with permission from Ref. [152]. Copyright © 2014 Elsevier Ltd. All rights reserved)

are their heating efficiency respectively. The heating efficiency of nanoflowers was observed very high as compared to the nanocubes in water. However, the sharp drop in their heating efficiency when nanocubes and nanoflowers were attached to the cell membrane and internalized with cells. It was found that reduced heating efficiency of nanoflowers is higher than nanocubes, i.e., SLP of nanoflowers reduced by about 10 times, whereas SLP of nanocubes reduced by 4 times on cell membrane and internalized cells as compared to water. In cells, such decrease on SLP was due to magnetic inter-particle interactions as a consequence of confinement of the particles, and/or by the increase of the cellular surrounding viscosity and impeded mobility of the particles.

Hugounenq et al. [21] have developed a maghemite nanoflowers beyond the superparamagnetic size range (24 nm) through polyol synthesis which show highly efficient magnetic hyperthermia properties, i.e., SLP value 1992 ± 34 W/g in compared to other spherical and cubic nanoparticles [153, 154]. The highly enhancement of heating properties was observed due to the size, the polycrystalline character, and the magnetic properties of the nanoflowers along with their colloidal stability in culture medium. Although the exact mechanisms for thermal losses in these nanoflowers remain to be explored, their findings show a very enticing biocompatible nanoscale platform for a variety of applications that rely on magnetic hyperthermia, especially cancer treatment and thermally assisted drug delivery. Curcio et al. [155] have reported an optimize nanohybrid maghemite (γ-Fe$_2$O$_3$@CuS) nanoflowers for cancer tri-therapy featuring a maghemite (γ-Fe$_2$O$_3$) nanoflowers conceived for efficient magnetic hyperthermia (MHT) and photodynamic therapy (PDT), a spiky copper sulfide (CuS) shell for a high near-infrared (NIR) absorption coefficient suitable for photothermal (PTT). In order to study MHT or the PTT modalities individually, or both at the same time, IONF@CuS heating efficiency was then evaluated using either magnetic or photo-stimulation. Typical infrared (IR) images are shown in Fig. 12, after 5 min exposure to alternating magnetic field (Fig. 12a), laser (Fig. 12b), or both (Fig. 12c). In each case, the heating efficiency was measured at different concentrations, equivalent copper concentrations of 20–320 mM and in the range of iron concentrations of 3–50 mM. Figure 12a clearly shows that the temperature elevation increases linearly with the concentration; as a result, the SAR is independent of the concentration, with SAR value reaching ~350 W/g. The SAR was also measured for the bare magnetic IONF core, which featured a SAR of ~500 W/g in the same conditions. Such a value is among the highest values reported for the frequency/field used. Photothermal therapy (PTT) experiments were carried out using a 1064 nm laser and the power density was set to 0.3 W cm^{-2} by positioning the fiber tip at a 4 cm distance from the target. The high efficiency puts these NFs among the most promising materials for PTT. In contrast with MHT, the heating performance tends to saturate when increasing the NFs concentration during PTT. As a result, although the heating at high doses was similar for MHT and PTT, heating efficiency is much higher for PTT at low doses as shown in Fig. 12b. The dual mode AMF and Laser (Fig. 3c) allowed providing a cumulative effect at the full concentration range tested. Indeed, the heating obtained by bi-modal stimulation closely corresponded to the sum of the heating obtained for every single modality. These data prove the versatility of
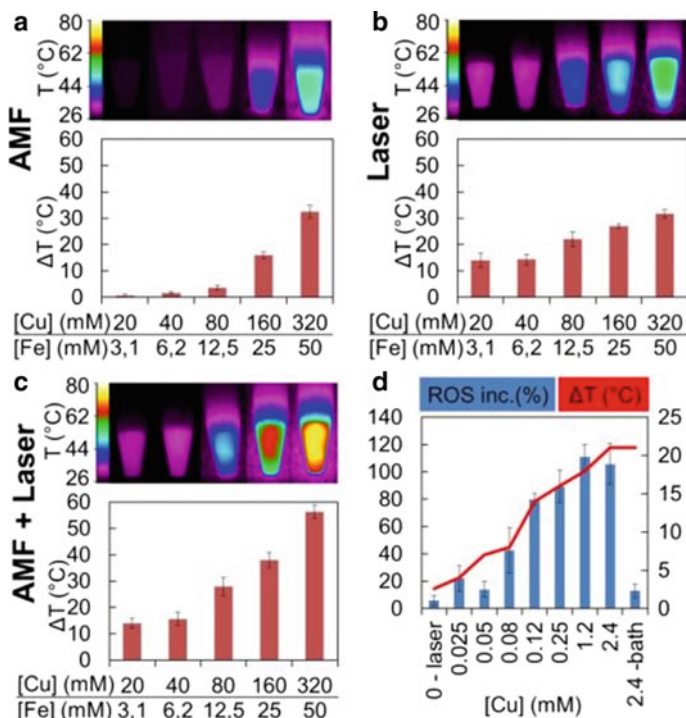
Fig. 12 Heating profiles attained by MHT, PTT, and bi-modal stimulation. Temperature increase of IONF@CuS NFs dispersion at different concentration exposed to **a** alternating magnetic field (AMF) at 471 kHz and 18 mT, **b** 1064 nm laser at the power of 0.3 Wcm^{-2} and **c** the combination of both modalities. In the top panel of each figure, typical infrared images after 5 min heating are displayed. **d** ROS production in NFs dispersions following laser stimulation: the blue columns display the relative ROS increase as a function of Cu concentration after 5 min laser exposure (1064 nm at 1 W cm^{-2}) while the red curve shows the temperature elevation obtained by the NFs. (Reprinted with permission from Ref. [155]. Open access)

NFs and attest to the cumulative effect of the two heating approaches, promising for the delivery of therapeutic heating to cancer tissues. The stability of the nanohybrids was conserved after several heating. cycles. As a result, the heating efficiency was constant for repeated application, and the colloidal stability was retained.

The relative ROS increase was normalized by the signal obtained from the non-irradiated samples. A probe was added to the nanohybrids at a concentration of 1.65 mM to detect the ROS level and provide a fluorescent signal when oxidized by ROS. As a control, the nanohybrids were heated at a similar temperature reached by the highest concentration using a water bath for the same time. Bender et al. [23] have deliberated in-depth study of magnetic hyperthermia properties of iron oxide nanoflowers (size ~39 nm). They found that due to an exchange coupling between the cores, the individual nanoflowers had a remanent magnetization and preferentially magnetized along their longest dimension due to shape anisotropy. The intrinsic

loss power (ILP) of the nanoflowers with (~7 nHm^2/kg Fe) was independent of the viscosity of the surrounding medium and was high compared to conventional iron oxide nanoparticles [156]. The insensitivity to viscosity agreed well with the observation that in the high frequency range, the relaxation dynamics of the nanoflowers were dominated by internal moment relaxation. The average detected ILP value is well described within the linear response theory, and hence the could be directly connected to the quite large value of the imaginary part of the volume susceptibility at high frequencies. The work established that the observed fast relaxation dynamics, which is also resulted in finite values of χ'' at high frequencies, was related to the fact that the nanoflowers constitute disordered spin systems caused by the nanocrystalline structure, but are easily magnetized by external magnetic fields, aided by an exchange coupling.

Recently, Das and co-worker [53] have analyzed the heating efficiency of Ag/Fe$_3$O$_4$ nanoflowers in separate experiment of magnetic hyperthermia, photothermal therapy, and their combined modal. The heating efficiency through combined effect of AC magnetic field and laser was greatly enhanced as compared to distinct magnetic hyperthermia and photothermal therapy. Figure 13a, b represent the heating curves of the nanoflowers under different values of the applied magnetic field intensities, during irradiation with fixed laser power densities of 0.53 W/cm^2 and 0.93 W/cm^2, respectively. For example, for H_{AC} = 400 Oe, the achieved temperature after 5 min of exposure changes from 30.8 °C for $P = 0$ to 41.1 and 48 °C, for 0.53 and 0.93 W/cm^2, respectively. It is worth noting that a magnetic field of 600 Oe is required in absence of laser irradiation (not shown here) for reaching a target temperature of 40 °C. When a laser power density of 0.93 W/cm^2 is simultaneously applied (Fig. 13c), this value decreases by a factor of 3 (200 Oe). This effect is even more obvious in Fig. 13d, where the SAR values for different combinations of magnetic field magnitudes and laser power densities are displayed. When a laser is applied simultaneously, the SAR values increase considerably for all magnetic fields. As a result, the heating ability at H_{AC} = 200 Oe at $P = 0$ increased by more than one order of magnitude (from ~10 W/g to ~130 W/g) for $P = 0.93$ W/cm^2.

Therefore, the combined use of magnetic field and laser exposure is more capable, laser-induced SAR enriched is sharper and it is more appropriate for clinic trials. The above finding support the idea for a new class of efficient hyperthermia agents by designing new hybrid nanostructures with synergic magnetic and plasmonic properties for simultaneous photothermal therapy and magnetic hyperthermia applications. For Ag/Fe$_3$O$_4$ nanosystem, we noted that individually both Ag and Fe$_3$O$_4$ nanoparticles are biocompatible, but the cytotoxicity remains to be examined. Further in- vitro or in-vivo studies of Ag/Fe$_3$O$_4$ nanoparticles are therefore desirable to fully understand their applications in biomedical field. Ognjanović et al. [65] reported citric acid, poly (acrylic acid) (PAA) and poly (ethylene glycol) coated IONPs nanoflowers, 13.5 nm spherically shaped cores and 24.8 nm diameter, and their labeling with three radionuclides, namely, technetium (99mTc), yttrium (90Y), and lutetium (177Lu), with the aim of the potential use in cancer diagnosis and therapy. It was found that best characteristics was shown by PAA-coated NFs (PAA@IONP) as they showed excellent in-vitro stabilities with <10% of radio nuclides detaching after 24 h and
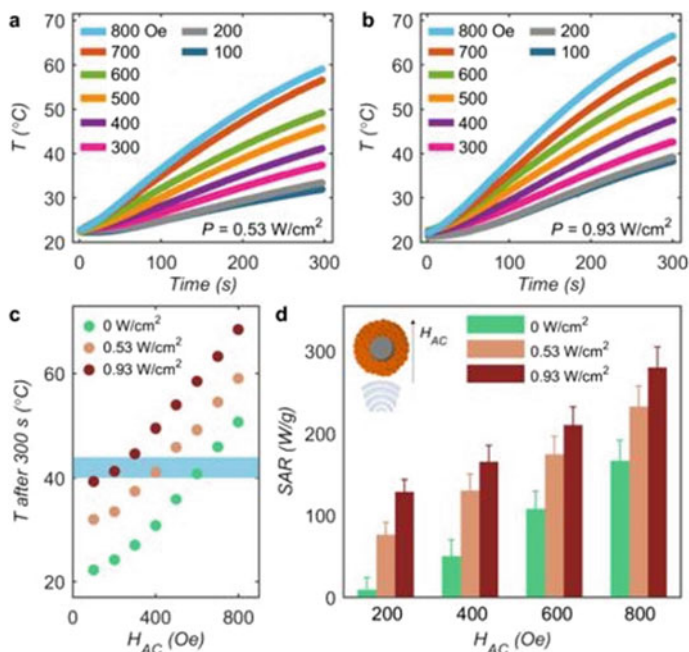
Fig. 13 Magnetic fluid hyperthermia and photothermal therapy. **a**, **b** heating curves (time versus temperature) for the Ag–Fe$_3$O$_4$ nanoflowers under different AC magnetic fields ($100 < H_{AC} < 800$ Oe) at a fixed frequency, $f = 310$ Hz, under irradiation with a 442 nm laser at two different power densities: 0.53 (**a**) and 0.93 (**b**) W/cm^2 (**c**, **d**). Temperature reached after 300 s of heating (**c**) and SAR (**d**) as a function of HAC for different laser power densities. The blue zone in (**c**) evidence the therapeutic temperature window of 40–44 °C. (Reprinted with permission from Ref. [53]. Copyright ©2016 American Chemical Society)

easy radio labeling with very high yields (>97.5%) with all three radio nuclides. In an ac external magnetic field heating ability of PAA@IONP showed intrinsic loss power value of ~7.3 nHm^2/kg, which is higher among the reported values. Additionally, no significant cytotoxicity to the CT-26 cancer cells, reaching IC50 at 60 μg/mL was observed by PAA@IONP. However, they showed hyperthermia-mediated cells killing under the external magnetic field, and correlated with the time of exposure and magnetic field strength. Meanwhile, PAA@IONP with excellent magnetic heat induction are simple and easy to prepare, biocompatible, these nanoparticles radio labeled with high-energy beta emitters 90Y and 177Lu, while radiolabeled with 99mTc could be used in diagnostic imaging and have valuable potential as agent for dual magnetic hyperthermia and radionuclide therapy.

7 Conclusion and Future Perspectives

Magnetic nanoflowers has gained a great attraction as a heat generator and recent studies showed that the heating efficiency has been improved a lot. However, it is still under research and several points, regarding the size and toxicity of nanoflowers, need to be well understood in in-vivo before its clinical trial on humans. For imaging and therapies, the optimum particle size is different, hence different magnetic properties. In addition to the anti-cancer agents, nanoflowers have marvelous potential in pharmaceuticals industry for protein drug delivery, multidrug delivery, bio-separation, and detection of toxicity. For synthesis purpose of nanoflowers, several liquid-phase approaches and biomineralization are used, which are eco-friendly and economical. To increase the stability and durability of enzymes and proteins, eco-friendly methods for synthesizing nanoflowers are being developed in recent years; which can be synthesized without any addition of capping and reducing agents. Via aforementioned chemical routes, nanoflowers can be exploited to scale up production at a large scale, due to the ease of downstream processing. Owing to the interesting magnetic properties of nanoflowers, the applications in biomedicine are can be seen even more than anti-cancer therapeutics heat generators. The granted magnetic properties shown by nanoflowers has to be transferred to the stage of in-vivo animal tests to show practically their excellent performance for several bio-application. To the date, only a few animal studies confirmed the promising heat generation from nanoflowers in magnetic hyperthermia. Thus, based upon these facts, we proposed that magnetic nanoflowers could be an advanced material and can be considered in several biomedical applications.

References

1. Jakubovics JP (1994) Magnetism and magnetic materials , 2nd ed. London Institute of Materials
2. Guimarães AP (2009) Principles of nanomagnetism. Springer, Berlin
3. (2015) Hyaluronic acid-modified Fe_3O_4@Au core/shell nanostars for multimodal imaging and photothermal therapy of tumors. Biomaterials 38:10–21. https://doi.org/10.1016/J.BIO MATERIALS.2014.10.065
4. Xuan S, Lee S-F, Lau JT-F, Zhu X, Wang Y-XJ, Wang F, Lai JMY, Sham KWY, Lo P-C, Yu JC, Cheng CHK, Leung KC-F (2012) Photocytotoxicity and magnetic relaxivity responses of dual-porous γ-Fe_2O_3 @ meso -SiO_2 microspheres. ACS Appl Mater Interfaces 4:2033–2040. https://doi.org/10.1021/am300008x

5. Laurent S, Forge D, Port M, Roch A, Robic C, Vander Elst L, Muller RN (2008) Magnetic iron oxide nanoparticles: synthesis, stabilization, vectorization, physicochemical characterizations, and biological applications. Chem Rev 108:2064–2110. https://doi.org/10.1021/cr068445e

6. Nemati Z, Salili SM, Alonso J, Ataie A, Das R, Phan MH, Srikanth H (2017) Superparamagnetic iron oxide nanodiscs for hyperthermia therapy: does size matter? J Alloys Compd 714:709–714. https://doi.org/10.1016/j.jallcom.2017.04.211

7. Kim T, Momin E, Choi J, Yuan K, Zaidi H, Kim J, Park M, Lee N, Mcmahon MT, Quinones-Hinojosa A, Bulte JWM, Hyeon T, Gilad AA, Morgan RH (2011) Mesoporous silica-coated hollow manganese oxide nanoparticles as positive T 1 contrast agents for labeling and MRI tracking of adipose-derived mesenchymal stem cells. J Am Chem Soc 133:2955–2961. https://doi.org/10.1021/ja1084095

8. Virkutyte J, Varma RS (2011) Green synthesis of metal nanoparticles: biodegradable polymers and enzymes in stabilization and surface functionalization. Chem Sci 2:837–846. https://doi.org/10.1039/C0SC00338G

9. Louie AY, Hüber MM, Ahrens ET, Rothbächer U, Moats R, Jacobs RE, Fraser SE, Meade TJ (2000) In vivo visualization of gene expression using magnetic resonance imaging. Nat Biotechnol 18:321–325. https://doi.org/10.1038/73780

10. Sun C, Lee JSH, Zhang M (2008) Magnetic nanoparticles in MR imaging and drug delivery. Adv Drug Deliv Rev 60:1252–1265. https://doi.org/10.1016/j.addr.2008.03.018

11. Jia C-J, Sun L-D, Luo F, Han X-D, Heyderman LJ, Yan Z-G, Yan C-H, Zheng K, Zhang Z, Takano M, Hayashi N, Eltschka M, Kläui M, Rüdiger U, Kasama T, Cervera-Gontard L, Dunin-Borkowski RE, Tzvetkov G, Raabe J (2008) Large-scale synthesis of single-crystalline iron oxide magnetic nanorings. J Am Chem Soc 130:16968–16977. https://doi.org/10.1021/ja805152t

12. Ferrero R, Manzin A, Barrera G, Celegato F, Coïsson M, Tiberto P (2019) Influence of shape, size and magnetostatic interactions on the hyperthermia properties of permalloy nanostructures. Sci Rep 9:6591. https://doi.org/10.1038/s41598-019-43197-4

13. Kim D-H, Rozhkova EA, Ulasov IV, Bader SD, Rajh T, Lesniak MS, Novosad V (2010) Biofunctionalized magnetic-vortex microdiscs for targeted cancer-cell destruction. Nat Mater 9:165–171. https://doi.org/10.1038/nmat2591

14. Landeros P, Allende S, Escrig J, Salcedo E, Altbir D, Vogel EE (2007) Reversal modes in magnetic nanotubes. Appl Phys Lett 90:102501. https://doi.org/10.1063/1.2437655

15. Gutierrez-Guzman DF, Lizardi LI, Otálora JA, Landeros P (2017) Hyperthermia in low aspect-ratio magnetic nanotubes for biomedical applications. Appl Phys Lett 110. https://doi.org/10.1063/1.4979165

16. Amara D, Grinblat J, Margel S (2012) Solventless thermal decomposition of ferrocene as a new approach for one-step synthesis of magnetite nanocubes and nanospheres. J Mater Chem 22:2188–2195. https://doi.org/10.1039/C1JM13942H

17. Chang M-T, Chou L-J, Hsieh C-H, Chueh Y-L, Wang ZL, Murakami Y, Shindo D (2007) Magnetic and electrical characterizations of half-metallic Fe_3O_4 Nanowires. Adv Mater 19:2290–2294. https://doi.org/10.1002/adma.200602330

18. Fu M, Xing J, Ge Z (2019) Preparation of laccase-loaded magnetic nanoflowers and their recycling for efficient degradation of bisphenol A. Sci Total Environ 651:2857–2865. https://doi.org/10.1016/j.scitotenv.2018.10.145

19. Roca AG, Gutiérrez L, Gavilán H, Fortes Brollo ME, Veintemillas-Verdaguer S, del Morales M, P, (2019) Design strategies for shape-controlled magnetic iron oxide nanoparticles. Adv Drug Deliv Rev 138:68–104

20. Blanco-Andujar C, Ortega D, Southern P, Pankhurst QA, Thanh NTK (2015) High performance multi-core iron oxide nanoparticles for magnetic hyperthermia: microwave synthesis, and the role of core-to-core interactions. Nanoscale 7:1768–1775. https://doi.org/10.1039/c4nr06239f

21. Hugounenq P, Levy M, Alloyeau D, Lartigue L, Dubois E, Cabuil V, Ricolleau C, Roux S, Wilhelm C, Gazeau F, Bazzi R (2012) Iron oxide monocrystalline nanoflowers for highly

efficient magnetic hyperthermia. J Phys Chem C 116:15702–15712. https://doi.org/10.1021/jp3025478

22. Lartigue L, Hugounenq P, Alloyeau D, Clarke SP, Lévy M, Bacri JC, Bazzi R, Brougham DF, Wilhelm C, Gazeau F (2012) Cooperative organization in iron oxide multi-core nanoparticles potentiates their efficiency as heating mediators and MRI contrast agents. ACS Nano 6:10935–10949. https://doi.org/10.1021/nn304477s

23. Bender P, Fock J, Frandsen C, Hansen MF, Balceris C, Ludwig F, Posth O, Wetterskog E, Bogart LK, Southern P, Szczerba W, Zeng L, Witte K, Grüttner C, Westphal F, Honecker D, González-Alonso D, Fernández Barquín L, Johansson C (2018) Relating magnetic properties and high hyperthermia performance of iron oxide nanoflowers. J Phys Chem C 122:3068–3077. https://doi.org/10.1021/acs.jpcc.7b11255

24. Zhang W, Zuo X, Niu Y, Wu C, Wang S, Guan S, Silva SRP (2017) Novel nanoparticles with Cr3+ substituted ferrite for self-regulating temperature hyperthermia. Nanoscale 9:13929–13937. https://doi.org/10.1039/c7nr02356a

25. Yang Y, Liu X, Lv Y, Herng TS, Xu X, Xia W, Zhang T, Fang J, Xiao W, Ding J (2015) Orientation mediated enhancement on magnetic hyperthermia of Fe_3O_4 Nanodisc. Adv Funct Mater 25:812–820. https://doi.org/10.1002/adfm.201402764

26. Liu XL, Yang Y, Ng CT, Zhao LY, Zhang Y, Bay BH, Fan HM, Ding J (2015) Magnetic vortex nanorings: a new class of hyperthermia agent for highly efficient in vivo regression of tumors. Adv Mater 27:1939–1944. https://doi.org/10.1002/adma.201405036

27. Dutz S (2016) Are magnetic multicore nanoparticles promising candidates for biomedical applications? IEEE Trans Magn 52

28. Shields SP, Richards VN, Buhro WE (2010) Nucleation control of size and dispersity in aggregative nanoparticle growth. A study of the coarsening kinetics of thiolate-capped gold nanocrystals. Chem Mater 22:3212–3225. https://doi.org/10.1021/cm100458b

29. Banin U, Ben-Shahar Y, Vinokurov K (2014) Hybrid semiconductor-metal nanoparticles: from architecture to function. Chem Mater 26:97–110. https://doi.org/10.1021/cm402131n

30. Lee D-K, Park S-I, Lee JK, Hwang N-M (2007) A theoretical model for digestive ripening. Acta Mater 55:5281–5288. https://doi.org/10.1016/j.actamat.2007.05.048

31. Polte J, Erler R, Thünemann AF, Sokolov S, Ahner TT, Rademann K, Emmerling F, Kraehnert R (2010) Nucleation and growth of gold nanoparticles studied via in situ small angle X-ray scattering at millisecond time resolution. ACS Nano. https://doi.org/10.1021/NN901499C

32. Soler MAG, Lima ECD, Nunes ES, Silva FLR, Oliveira AC, Azevedo RB, Morais PC (2011) Spectroscopic study of maghemite nanoparticles surface-grafted with DMSA. J Phys Chem A 115:1003–1008. https://doi.org/10.1021/jp1109916

33. Rivera LMR, MacHado JG, Chandra Mathpal M, Chaves NL, Gregurec D, Baó SN, Paterno LG, Moya SE, Azevedo RB, Soler MAG (2020) Functional glucosamine-iron oxide nanocarriers. J Mater Res 35:1726–1737. https://doi.org/10.1557/jmr.2020.121

34. Afiune LAF, Ushirobira CY, Barbosa DPP, de Souza PEN, Leles MIG, Cunha-Filho M, Gelfuso GM, Soler MAG, Gratieri T (2020) Novel iron oxide nanocarriers loading finasteride or dutasteride: enhanced skin penetration for topical treatment of alopecia. Int J Pharm 587:119709. https://doi.org/10.1016/j.ijpharm.2020.119709

35. Bandhu A, Mukherjee S, Acharya S, Modak S, Brahma SK, Das D, Chakrabarti PK (2009) Dynamic magnetic behaviour and Mössbauer effect measurements of magnetite nanoparticles prepared by a new technique in the co-precipitation method. Solid State Commun 149:1790–1794. https://doi.org/10.1016/j.ssc.2009.07.018

36. Ozkaya T, Toprak MS, Baykal A, Kavas H, Köseoğlu Y, Aktaş B, Journal of the less-common metals. Elsevier Pub. Co

37. Valenzuela R, Fuentes MC, Parra C, Baeza J, Duran N, Sharma SK, Knobel M, Freer J (2009) Influence of stirring velocity on the synthesis of magnetite nanoparticles (Fe_3O_4) by the co-precipitation method. J Alloys Compd 488:227–231. https://doi.org/10.1016/j.jallcom.2009.08.087

38. Gnanaprakash G, Philip J, Jayakumar T, Raj B (2007) Effect of digestion time and alkali addition rate on physical properties of magnetite nanoparticles. J Phys Chem B 111:7978–7986. https://doi.org/10.1021/jp071299b

39. Hu D, Wang Y, Song Q (2009) ARTICLE IN PRESS G model weakly magnetic field-assisted synthesis of magnetite nano-particles in oxidative co-precipitation. Particuology. https://doi.org/10.1016/j.partic.2009.03.005

40. Vereda F, Juan de Vicente A, Hidalgo-Álvarez R (2007) Influence of a magnetic field on the formation of magnetite particles via two precipitation methods. Langmuir 23:3581–3589. https://doi.org/10.1021/LA0633583

41. Salavati-Niasari M, Mahmoudi T, Amiri O (2012) Easy synthesis of magnetite nanocrystals via coprecipitation method. J Clust Sci 23:597–602. https://doi.org/10.1007/s10876-012-0451-5

42. Farahmandjou M, Soflaee F (2015) Synthesis and characterization of α-Fe_2O_3 nanoparticles by simple co-precipitation method. Phys Chem Res 3:191–196. https://doi.org/10.22036/pcr.2015.9193

43. Tomitaka A, Arami H, Ahmadivand A, Pala N, McGoron AJ, Takemura Y, Febo M, Nair M (2020) Magneto-plasmonic nanostars for image-guided and NIR-triggered drug delivery. Sci Rep 10:1–10. https://doi.org/10.1038/s41598-020-66706-2

44. He S, Kang MWC, Khan FJ, Tan EKM, Reyes MA, Kah JCY (2015) Optimizing gold nanostars as a colloid-based surface-enhanced Raman scattering (SERS) substrate. J Opt (United Kingdom) 17:114013. https://doi.org/10.1088/2040-8978/17/11/114013

45. Byrappa K, Adschiri T (2007) Hydrothermal technology for nanotechnology. Prog Cryst Growth Charact Mater 53:117–166. https://doi.org/10.1016/J.PCRYSGROW.2007.04.001

46. Rabenau A (1985) The role of hydrothermal synthesis in preparative chemistry. Angew Chemie Int Ed English 24:1026–1040. https://doi.org/10.1002/anie.198510261

47. Morey GW, Niggli P (1913) The hydrothermal formation of silicates, a review. J Am Chem Soc 35:1086–1130. https://doi.org/10.1021/ja02198a600

48. Byrappa K, Yoshimura M (2013) Handbook of hydrothermal technology. William Andrew

49. Yahya RB, Hayashi H, Nagase T, Ebina T, Onodera Y, Saitoh N (2001) Hydrothermal synthesis of potassium hexatitanates under subcritical and supercritical water conditions and its application in photocatalysis. Chem Mater 13:842–847. https://doi.org/10.1021/cm000561p

50. Hakuta Y, Hayashi H, Arai K (2004) Hydrothermal synthesis of photocatalyst potassium hexatitanate nanowires under supercritical conditions. J Mater Sci 39:4977–4980. https://doi.org/10.1023/B:JMSC.0000035349.99273.c7

51. Sue K, Suzuki M, Arai K, Ohashi T, Ura H, Matsui K, Hakuta Y, Hayashi H, Watanabe M, Hiaki T (2006) Size-controlled synthesis of metal oxide nanoparticles with a flow-through supercritical water method. Green Chem 8:634. https://doi.org/10.1039/b518291c

52. Ramesh R, Rajalakshmi M, Muthamizhchelvan C, Ponnusamy S (2012) Synthesis of Fe_3O_4 nanoflowers by one pot surfactant assisted hydrothermal method and its properties. Mater Lett 70:73–75. https://doi.org/10.1016/j.matlet.2011.11.085

53. Das R, Rinaldi-Montes N, Alonso J, Amghouz Z, Garaio E, García JA, Gorria P, Blanco JA, Phan MH, Srikanth H (2016) Boosted hyperthermia therapy by combined AC magnetic and photothermal exposures in Ag/Fe_3O_4 nanoflowers. ACS Appl Mater Interfaces 8:25162–25169. https://doi.org/10.1021/acsami.6b09942

54. Galema SA (1997) Microwave chemistry. Chem Soc Rev 26:233. https://doi.org/10.1039/cs9972600233

55. Bilecka I, Niederberger M (2010) Microwave chemistry for inorganic nanomaterials synthesis. Nanoscale 2:1358. https://doi.org/10.1039/b9nr00377k

56. Kappe CO (2004) Controlled microwave heating in modern organic synthesis. Angew Chemie Int Ed 43:6250–6284. https://doi.org/10.1002/anie.200400655

57. Mingos DMP, Baghurst DR (1991) Tilden lecture. applications of microwave dielectric heating effects to synthetic problems in chemistry. Chem Soc Rev 20:1. https://doi.org/10.1039/cs9912000001

58. de la Hoz A, Díaz-Ortiz A, Moreno A (2005) Microwaves in organic synthesis. Thermal and non-thermal microwave effects. Chem Soc Rev 34:164–178. https://doi.org/10.1039/b411438h

59. Baghbanzadeh M, Carbone L, Cozzoli PD, Kappe CO (2011) Microwave-assisted synthesis of colloidal inorganic nanocrystals. Angew Chemie Int Ed 50:11312–11359. https://doi.org/10.1002/anie.201101274

60. Polshettiwar V, Baruwati B, Varma RS (2009) Self-assembly of metal oxides into three-dimensional nanostructures: synthesis and application in catalysis. ACS Nano 3:728–736. https://doi.org/10.1021/nn800903p

61. Hu X, Yu JC, Gong J (2007) Fast production of self-assembled hierarchical α-Fe$_2$O$_3$ nanoarchitectures. J Phys Chem C 111:11180–11185. https://doi.org/10.1021/jp073073e

62. Jokerst JV, Lobovkina T, Zare RN, Gambhir SS (2011) Nanoparticle PEGylation for imaging and therapy. Nanomedicine 6:715–728. https://doi.org/10.2217/nnm.11.19

63. Cheng Y, Zhao L, Li Y, Xu T (2011) Design of biocompatible dendrimers for cancer diagnosis and therapy: current status and future perspectives. Chem Soc Rev 40:2673. https://doi.org/10.1039/c0cs00097c

64. Shaw SK, Biswas A, Gangwar A, Maiti P, Prajapat CL, Meena SS, Prasad NK (2019) Synthesis of exchange coupled nanoflowers for efficient magnetic hyperthermia. J Magn Magn Mater 484:437–444. https://doi.org/10.1016/j.jmmm.2019.04.056

65. Ognjanović M, Radović M, Mirković M, Prijović Ž, Del Puerto Morales M, Čeh M, Vranješ-Durić S, Antić B (2019) 99mTc-, 90Y-, and 177Lu-labeled iron oxide nanoflowers designed for potential use in dual magnetic hyperthermia/radionuclide cancer therapy and diagnosis. ACS Appl Mater Interfaces 11:41109–41117. https://doi.org/10.1021/acsami.9b16428

66. Ho D, Sun X, Sun S (2011) Monodisperse magnetic nanoparticles for theranostic applications. Acc Chem Res 44:875–882. https://doi.org/10.1021/ar200090c

67. Hufschmid R, Arami H, Ferguson RM, Gonzales M, Teeman E, Brush LN, Browning ND, Krishnan KM (2015) Synthesis of phase-pure and monodisperse iron oxide nanoparticles by thermal decomposition. Nanoscale 7:11142–11154. https://doi.org/10.1039/c5nr01651g

68. Ling D, Lee N, Hyeon T (2015) Chemical synthesis and assembly of uniformly sized iron oxide nanoparticles for medical applications. Acc Chem Res 48:1276–1285. https://doi.org/10.1021/acs.accounts.5b00038

69. Périgo EA, Hemery G, Sandre O, Ortega D, Garaio E, Plazaola F, Teran FJ (2015) Fundamentals and advances in magnetic hyperthermia. Appl Phys Rev 2:041302

70. Okuhata Y (1999) Delivery of diagnostic agents for magnetic resonance imaging. Adv Drug Deliv Rev 37:121–137

71. Del Sol-Fernández S, Portilla-Tundidor Y, Gutiérrez L, Odio OF, Reguera E, Barber DF, Morales MP (2019) Flower-like Mn-doped magnetic nanoparticles functionalized with αvβ3-integrin-ligand to efficiently induce intracellular heat after alternating magnetic field exposition, triggering glioma cell death. ACS Appl Mater Interfaces 11:26648–26663. https://doi.org/10.1021/acsami.9b08318

72. Nidhin M, Nazeer SS, Jayasree RS, Kiran MS, Nair BU, Sreeram KJ (2013) Flower shaped assembly of cobalt ferrite nanoparticles: application as T2 contrast agent in MRI. RSC Adv 3:6906–6912. https://doi.org/10.1039/c3ra23232h

73. Gavilán H, Sánchez EH, Brollo MEF, Asín L, Moerner KK, Frandsen C, Lázaro FJ, Serna CJ, Veintemillas-Verdaguer S, Morales MP, Gutiérrez L (2017) Formation mechanism of maghemite nanoflowers synthesized by a polyol-mediated process. ACS Omega 2:7172–7184. https://doi.org/10.1021/acsomega.7b00975

74. Hu Y, Wang R, Wang S, Ding L, Li J, Luo Y, Wang X, Shen M, Shi X (2016) Multifunctional Fe$_3$O$_4$ @ Au core/shell nanostars: a unique platform for multimode imaging and photothermal therapy of tumors. Sci Rep 6. 10.1038/

75. Bigall NC, Parak WJ, Dorfs D (2012) Fluorescent, magnetic and plasmonic hybrid multifunctional colloidal nano objects. Nano Today 7:282–296. https://doi.org/10.1016/j.nantod.2012.06.007

76. Huang L, Ao L, Hu D, Wang W, Sheng Z, Su W (2016) Magneto-plasmonic nanocapsules for multimodal-imaging and magnetically guided combination cancer therapy. Chem Mater 28:5896–5904. https://doi.org/10.1021/acs.chemmater.6b02413

77. Zhichuan Xu, Yanglong Hou A, Sun S (2007) Magnetic core/shell Fe$_3$O$_4$/Au and Fe$_3$O$_4$/Au/Ag nanoparticles with tunable plasmonic properties. J Am Chem Soc 129:8698–8699. https://doi.org/10.1021/JA073057V

78. Huang X, El-Sayed MA (2010) Gold nanoparticles: optical properties and implementations in cancer diagnosis and photothermal therapy. J Adv Res 1:13–28

79. Hemmer E, Benayas A, Légaré F, Vetrone F (2016) Exploiting the biological windows: Current perspectives on fluorescent bioprobes emitting above 1000 nm. Nanoscale Horizons 1:168–184

80. Pastrana E (2013) Near-infrared probes. Nat Methods 10:36

81. Goon IY, Lai LMH, Lim M, Munroe P, Gooding JJ, Amal R (2009) Fabrication and dispersion of gold-shell-protected magnetite nanoparticles: systematic control using polyethyleneimine. Chem Mater 21:673–681. https://doi.org/10.1021/cm8025329

82. Zhang Y, Ding H, Liu Y, Pan S, Luo Y, Li G (2012) Facile one-step synthesis of plasmonic/magnetic core/shell nanostructures and their multifunctionality. J Mater Chem 22:10779–10786. https://doi.org/10.1039/c2jm16293h

83. Xia Y, Gates B, Yin Y, Lu Y (2000) Monodispersed colloidal spheres: old materials with new applications. Adv Mater 12:693–713. https://doi.org/10.1002/(SICI)1521-4095(200005)12:10%3c693::AID-ADMA693%3e3.0.CO;2-J

84. Dreaden EC, Alkilany AM, Huang X, Murphy CJ, El-Sayed MA (2012) The golden age: gold nanoparticles for biomedicine. Chem Soc Rev 41:2740–2779. https://doi.org/10.1039/c1cs15237h

85. Chen W, Xu N, Xu L, Wang L, Li Z, Ma W, Zhu Y, Xu C, Kotov NA (2010) Multifunctional magnetoplasmonic nanoparticle assemblies for cancer therapy and diagnostics (Theranostics). Macromol Rapid Commun 31:228–236. https://doi.org/10.1002/marc.200900793

86. Godin B, Tasciotti E, Liu X, Serda RE, Ferrari M (2011) Multistage nanovectors: from concept to novel imaging contrast agents and therapeutics. Acc Chem Res 44:979–989

87. Robinson I, Tung LD, Maenosono S, Wälti C, Thanh NTK (2010) Synthesis of core-shell gold coated magnetic nanoparticles and their interaction with thiolated DNA. Nanoscale 2:2624–2630. https://doi.org/10.1039/c0nr00621a

88. Cheng LC, Huang JH, Chen HM, Lai TC, Yang KY, Liu RS, Hsiao M, Chen CH, Her LJ, Tsai DP (2012) Seedless, silver-induced synthesis of star-shaped gold/silver bimetallic nanoparticles as high efficiency photothermal therapy reagent. J Mater Chem 22:2244–2253. https://doi.org/10.1039/c1jm13937a

89. Leung KCF, Xuan S, Zhu X, Wang D, Chak CP, Lee SF, Ho WKW, Chung BCT (2012) Gold and iron oxide hybrid nanocomposite materials. Chem Soc Rev 41:1911–1928. https://doi.org/10.1039/c1cs15213k

90. Halas NJ, Lal S, Link S, Chang W-S, Natelson D, Hafner JH, Nordlander P (2012) A plethora of plasmonics from the laboratory for nanophotonics at rice university. Adv Mater 24:4842–4877. https://doi.org/10.1002/adma.201202331

91. Zhou H, Kim J-P, Bahng JH, Kotov NA, Lee J (2014) Self-assembly mechanism of spiky magnetoplasmonic supraparticles. Adv Funct Mater 24:1439–1448. https://doi.org/10.1002/adfm.201302405

92. Le TB, Han CS, Cho K, Han O (2018) Covalent immobilization of oxylipin biosynthetic enzymes on nanoporous rice husk silica for production of cis(+)-12-oxophytodienoic acid. Artif Cells, Nanomed Biotechnol 46:1523–1529. https://doi.org/10.1080/21691401.2017.1375939

93. Huang R ping, Liu Z hua, Yin H, Dang Z, Wu P xiao, Zhu N wu, Lin Z (2018) Bisphenol A concentrations in human urine, human intakes across six continents, and annual trends of average intakes in adult and child populations worldwide: a thorough literature review. Sci Total Environ 626:971–981

94. Vaghari H, Jafarizadeh-Malmiri H, Mohammadlou M, Berenjian A, Anarjan N, Jafari N, Nasiri S (2016) Application of magnetic nanoparticles in smart enzyme immobilization. Biotechnol Lett 38:223–233

95. Hwang ET, Gu MB (2013) Enzyme stabilization by nano/microsized hybrid materials. Eng Life Sci 13:49–61

96. Lian X, Fang Y, Joseph E, Wang Q, Li J, Banerjee S, Lollar C, Wang X, Zhou HC (2017) Enzyme-MOF (metal-organic framework) composites. Chem Soc Rev 46:3386–3401

97. Li Z, Zhang Y, Su Y, Ouyang P, Ge J, Liu Z (2014) Spatial co-localization of multi-enzymes by inorganic nanocrystal-protein complexes. Chem Commun 50:12465–12468. https://doi.org/10.1039/c4cc05478d

98. Sun J, Ge J, Liu W, Lan M, Zhang H, Wang P, Wang Y, Niu Z (2014) Multi-enzyme co-embedded organic-inorganic hybrid nanoflowers: synthesis and application as a colorimetric sensor. Nanoscale 6:255–262. https://doi.org/10.1039/c3nr04425d

99. Wei T, Du D, Zhu MJ, Lin Y, Dai Z (2016) An improved ultrasensitive enzyme-linked immunosorbent assay using hydrangea-like antibody-enzyme-inorganic three-in-one nanocomposites. ACS Appl Mater Interfaces 8:6329–6335. https://doi.org/10.1021/acsami.5b11834

100. Liu Y, Chen J, Du M, Wang X, Ji X, He Z (2017) The preparation of dual-functional hybrid nanoflower and its application in the ultrasensitive detection of disease-related biomarker. Biosens Bioelectron 92:68–73. https://doi.org/10.1016/j.bios.2017.02.004

101. Ye R, Zhu C, Song Y, Lu Q, Ge X, Yang X, Zhu MJ, Du D, Li H, Lin Y (2016) Bioinspired synthesis of all-in-one organic–inorganic hybrid nanoflowers combined with a handheld pH meter for on-site detection of food pathogen. Small 12:3094–3100. https://doi.org/10.1002/smll.201600273

102. Cheon HJ, Adhikari MD, Chung M, Tran TD, Kim J, Il KM (2019) Magnetic nanoparticles-embedded enzyme-inorganic hybrid nanoflowers with enhanced peroxidase-like activity and substrate channeling for glucose biosensing. Adv Healthc Mater 8:1801507. https://doi.org/10.1002/adhm.201801507

103. Vandenberg LN, Hunt PA, Gore AC (2019) Endocrine disruptors and the future of toxicology testing—lessons from CLARITY–BPA. Nat Rev Endocrinol 15:366–374. https://doi.org/10.1038/s41574-019-0173-y

104. Han J, Luo P, Wang L, Li C, Mao Y, Wang Y (2019) Construction of magnetic nanoflower biocatalytic system with enhanced enzymatic performance by biomineralization and its application for bisphenol A removal. J Hazard Mater 380:120901. https://doi.org/10.1016/j.jhazmat.2019.120901

105. Thanh NTK, Maclean N, Mahiddine S (2014) Mechanisms of nucleation and growth of nanoparticles in solution. Chem Rev 114:7610–7630. https://doi.org/10.1021/cr400544s

106. Taylor P (2003) Ostwald ripening in emulsions: estimation of solution thermodynamics of the disperse phase. Adv Colloid Interface Sci 106:261–285

107. Desai RC, Kapral R (2009) Lifshitz–Slyozov–Wagner theory. Dynamics of self-organized and self-assembled structures. Cambridge University Press, Cambridge, pp 87–95

108. Voorhees PW (1992) Ostwald ripening of two-phase mixtures. Annu Rev Mater Sci 22:197–215. https://doi.org/10.1146/annurev.ms.22.080192.001213

109. Davey RJ, Back KR, Sullivan RA (2015) Crystal nucleation from solutions—transition states, rate determining steps and complexity. Faraday Discuss 179:9–26. https://doi.org/10.1039/C5FD00037H

110. Finney EE, Finke RG (2008) Nanocluster nucleation and growth kinetic and mechanistic studies: a review emphasizing transition-metal nanoclusters. J Colloid Interface Sci 317:351–374. https://doi.org/10.1016/j.jcis.2007.05.092

111. Baumgartner J, Dey A, Bomans PHH, Le Coadou C, Fratzl P, Sommerdijk NAJM, Faivre D (2013) Nucleation and growth of magnetite from solution. Nat Mater 12:310–314. https://doi.org/10.1038/nmat3558

112. Vreeland EC, Watt J, Schober GB, Hance BG, Austin MJ, Price AD, Fellows BD, Monson TC, Hudak NS, Maldonado-Camargo L, Bohorquez AC, Rinaldi C, Huber DL (2015) Enhanced nanoparticle size control by extending Lamer's mechanism. Chem Mater 27:6059–6066. https://doi.org/10.1021/acs.chemmater.5b02510

113. LaMer VK, Dinegar RH (1950) Theory, production and mechanism of formation of monodispersed hydrosols. J Am Chem Soc 72:4847–4854. https://doi.org/10.1021/ja0116 7a001

114. Maris HJ (2006) Introduction to the physics of nucleation. Comptes Rendus Phys 7:946–958. https://doi.org/10.1016/J.CRHY.2006.10.019

115. Zhang R, Khalizov A, Wang L, Hu M, Xu W (2012) Nucleation and growth of nanoparticles in the atmosphere. Chem Rev 112:1957–2011. https://doi.org/10.1021/cr2001756

116. Coquerel G (2014) Crystallization of molecular systems from solution: phase diagrams, supersaturation and other basic concepts. Chem Soc Rev 43:2286–2300. https://doi.org/10.1039/C3CS60359H

117. Mullin JW, John W (2001) Crystallization. Elsevier

118. Denis Mangin F, SV (2009) Polymorphism in processes of crystallization in solution: a practical review. Org Process Res Dev 13:1241–1253. https://doi.org/10.1021/op900168f

119. Reiss H (1951) The growth of uniform colloidal dispersions. J Chem Phys 19:482–487. https://doi.org/10.1063/1.1748251

120. Sugimoto T (1987) Preparation of monodispersed colloidal particles. Adv Colloid Interface Sci 28:65–108. https://doi.org/10.1016/0001-8686(87)80009-X

121. Yin W, Chen X, Cao M, Hu C, Wei B (2009) α-Fe$_2$O$_3$ nanocrystals: controllable SSA-assisted hydrothermal synthesis, growth mechanism, and magnetic properties. J Phys Chem C 113:15897–15903. https://doi.org/10.1021/jp904413m

122. Mantzaris NV (2005) Liquid-phase synthesis of nanoparticles: particle size distribution dynamics and control. Chem Eng Sci 60:4749–4770. https://doi.org/10.1016/j.ces.2005.04.012

123. Porter DA, Easterling KE (1992) Phase transformations in metals and alloys. Springer, US, Boston

124. Zinke-Allmang M, Feldman LC, Grabow MH (1992) Clustering on surfaces. Surf Sci Rep 16:377–463. https://doi.org/10.1016/0167-5729(92)90006-W

125. Lifshitz IM, Slyozov VV (1961) The kinetics of precipitation from supersaturated solid solutions. J Phys Chem Solids 19:35–50. https://doi.org/10.1016/0022-3697(61)90054-3

126. Chakraverty BK (1967) Grain size distribution in thin films—2. non-conservative systems. J Phys Chem Solids 28:2413–2421. https://doi.org/10.1016/0022-3697(67)90027-3

127. Ross FM, Tersoff J, Tromp RM (1998) Coarsening of self-assembled ge quantum dots on Si(001). Phys Rev Lett 80:984–987. https://doi.org/10.1103/PhysRevLett.80.984

128. Ross, Tromp, Reuter (1999) Transition states between pyramids and domes during Ge/Si island growth. Science 286:1931–1934. https://doi.org/10.1126/science.286.5446.1931

129. Tromp RM, Ross FM, Reuter MC (2000) Instability-driven SiGe Island growth. Phys Rev Lett 84:4641–4644. https://doi.org/10.1103/PhysRevLett.84.4641

130. Stoeva S, Klabunde KJ, Sorensen CM, A, Dragieva I, (2002) Gram-scale synthesis of monodisperse gold colloids by the solvated metal atom dispersion method and digestive ripening and their organization into two- and three-dimensional structures. J Am Chem Soc 124:2305–2311. https://doi.org/10.1021/JA012076G

131. Smetana AB, Klabunde KJ, Sorensen CM (2005) Synthesis of spherical silver nanoparticles by digestive ripening, stabilization with various agents, and their 3-D and 2-D superlattice formation. J Colloid Interface Sci 284:521–526. https://doi.org/10.1016/j.jcis.2004.10.038

132. Pan J, El-Ballouli AO, Rollny L, Voznyy O, Burlakov VM, Goriely A, Sargent EH, Bakr OM (2013) Automated synthesis of photovoltaic-quality colloidal quantum dots using separate nucleation and growth stages. ACS Nano 7:10158–10166. https://doi.org/10.1021/nn404397d

133. Prasad BLV, Stoeva SI, Sorensen CM, A, Klabunde KJ, (2002) Digestive ripening of thiolated gold nanoparticles: the effect of alkyl chain length. Langmuir 18:7515–7520. https://doi.org/10.1021/LA020181D

134. Rizza GC, Strobel M, Heinig KH, Bernas H (2001) Ion irradiation of gold inclusions in SiO$_2$: experimental evidence for inverse Ostwald ripening. Nucl Instrum Methods Phys Res Sect B Beam Interact Mater Atoms 178:78–83. https://doi.org/10.1016/S0168-583X(01)00496-7

135. Rizza G, Cheverry H, Gacoin T, Lamasson A, Henry S (2007) Ion beam irradiation of embedded nanoparticles: toward an in situ control of size and spatial distribution. J Appl Phys 101:014321. https://doi.org/10.1063/1.2402351

136. Ramaswamy V, Haynes TE, White CW, MoberlyChan WJ, Roorda S, Aziz MJ (2005) Synthesis of nearly monodisperse embedded nanoparticles by separating nucleation and growth in ion implantation. Nano Lett 5:373–377. https://doi.org/10.1021/nl048077z

137. Hurley KR, Ring HL, Etheridge M, Zhang J, Gao Z, Shao Q, Klein ND, Szlag VM, Chung C, Reineke TM, Garwood M, Bischof JC, Haynes CL (2016) Predictable heating and positive MRI contrast from a mesoporous silica-coated iron oxide nanoparticle. Mol Pharm 13:2172–2183. https://doi.org/10.1021/acs.molpharmaceut.5b00866

138. Neuberger T, Schöpf B, Hofmann H, Hofmann M, Von Rechenberg B (2005) Superparamagnetic nanoparticles for biomedical applications: possibilities and limitations of a new drug delivery system. J Magn Magn Mater. North-Holland, pp 483–496

139. Guibert CC, Dupuis V, Peyre V, Jérô Me Fresnais J (2015) Hyperthermia of magnetic nanoparticles: experimental study of the role of aggregation. doi: https://doi.org/10.1021/acs.jpcc.5b07796

140. Dutz S, Hergt R (2014) Magnetic particle hyperthermia—a promising tumour therapy? Nanotechnology 25:452001

141. Wu C-H, Cook J, Emelianov S, Sokolov K (2014) Multimodal magneto-plasmonic nanoclusters for biomedical applications. Adv Funct Mater 24:6862–6871. https://doi.org/10.1002/adfm.201401806

142. Habib AH, Ondeck CL, Chaudhary P, Bockstaller MR, McHenry ME (2008) Evaluation of iron-cobalt/ferrite core-shell nanoparticles for cancer thermotherapy. J Appl Phys 103:07A307. https://doi.org/10.1063/1.2830975

143. Das R, Alonso J, Nemati Porshokouh Z, Kalappattil V, Torres D, Phan MH, Garaio E, García JÁ, Sanchez Llamazares JL, Srikanth H (2016) Tunable high aspect ratio iron oxide nanorods for enhanced hyperthermia. J Phys Chem C 120:10086–10093. https://doi.org/10.1021/acs.jpcc.6b02006

144. Nemati Z, Das R, Alonso J, Clements E, Phan MH, Srikanth H (2017) Iron oxide nanospheres and nanocubes for magnetic hyperthermia therapy: a comparative study. J Electron Mater 46:3764–3769. https://doi.org/10.1007/s11664-017-5347-6

145. Mehdaoui B, Meffre A, Carrey J, Lachaize S, Lacroix L-M, Gougeon M, Chaudret B, Respaud M (2011) Optimal size of nanoparticles for magnetic hyperthermia: a combined theoretical and experimental study. Adv Funct Mater 21:4573–4581. https://doi.org/10.1002/adfm.201101243

146. Sun W, Yang W, Xu Z, Li Q (2018) Anchoring Pd nanoparticles on Fe_3O_4 @SiO_2 Core-shell nanoparticles by cross-linked polyvinylpyrrolidone for nitrite reduction. ACS Appl Nano Mater 1:5035–5043. https://doi.org/10.1021/acsanm.8b01149

147. Karatutlu A, Sapelkin A (2018) Liquid-phase synthesis of nanoparticles and nanostructured materials. Emerg Appl Nanoparticles Archit Nanostruct 1–28. https://doi.org/10.1016/B978-0-323-51254-1.00001-4

148. Polshettiwar V, Nadagouda MN, Varma RS (2009) Microwave-assisted chemistry: a rapid and sustainable route to synthesis of organics and nanomaterials. Aust J Chem 62:16–26. https://doi.org/10.1071/CH08404

149. Sathya A, Kalyani S, Ranoo S, Philip J (2017) One-step microwave-assisted synthesis of water-dispersible Fe_3O_4 magnetic nanoclusters for hyperthermia applications. J Magn Magn Mater 439:107–113. https://doi.org/10.1016/j.jmmm.2017.05.018

150. Hyeon T (2003) Chemical synthesis of magnetic nanoparticles. Chem Commun 3:927–934. https://doi.org/10.1039/b207789b

151. Sun M, Fu W, Yang H, Sui Y, Zhao B, Yin G, Li Q, Zhao H, Zou G (2011) One-step synthesis of coaxial Ag/TiO_2 nanowire arrays on transparent conducting substrates: enhanced electron collection in dye-sensitized solar cells. Electrochem commun 13:1324–1327. https://doi.org/10.1016/j.elecom.2011.08.003

152. Di Corato R, Espinosa A, Lartigue L, Tharaud M, Chat S, Pellegrino T, Ménager C, Gazeau F, Wilhelm C (2014) Magnetic hyperthermia efficiency in the cellular environment fordifferent nanoparticle designs. Biomaterials 35:6400–6411. https://doi.org/10.1016/j.biomaterials.2014.04.036

153. Alphandéry E, Faure S, Seksek O, Guyot F, Chebbi I (2011) Chains of magnetosomes extracted from AMB-1 magnetotactic bacteria for application in alternative magnetic field cancer therapy. ACS Nano 5:6279–6296. https://doi.org/10.1021/nn201290k

154. Guardia P, Di Corato R, Lartigue L, Wilhelm C, Espinosa A, Garcia-Hernandez M, Gazeau F, Manna L, Pellegrino T (2012) Water-soluble iron oxide nanocubes with high values of specific absorption rate for cancer cell hyperthermia treatment. ACS Nano 6:3080–3091. https://doi.org/10.1021/nn2048137

155. Curcio A, Silva AKA, Cabana S, Espinosa A, Baptiste B, Menguy N, Wilhelm C, Abou-Hassan A (2019) Iron oxide nanoflowers @ cus hybrids for cancer tri-therapy: interplay of photothermal therapy, magnetic hyperthermia and photodynamic therapy. Theranostics 9:1288–1302. https://doi.org/10.7150/thno.30238

156. Kallumadil M, Tada M, Nakagawa T, Abe M, Southern P, Pankhurst QA (2009) Suitability of commercial colloids for magnetic hyperthermia. J Magn Magn Mater 321:1509–1513. https://doi.org/10.1016/j.jmmm.2009.02.075

Superparamagnetic Iron Oxide-Based Nanomaterials for Magnetic Resonance Imaging

Gopal Niraula, Mohan Chandra Mathpal, Jason J. A. Medrano, Manish Kumar Singh, Jose A. H. Coaquira, Ramesh Verma, and Surender K. Sharma

Abstract Magnetic resonance imaging (MRI) is the technique for the visualization of targeted macromolecules or cells in biological system. Nowadays, superparamagnetic iron oxide nanoparticles (SPIONs) have been attracted and remarkably emerging as a negative contrast agent (T_2-weighted) offering sufficient detection sensitivity as compared to positive contrast agent (T_1-weighted). In the present chapter, we first introduce the necessary background of superparamagnetic iron oxide-based nanoparticles and MRI taking into an account to discuss both T_1–T_2-weighted imaging. The liquid-based synthesis methods of SPIONs and their applicability in MRI have been thoroughly revised. Finally, several nanohybrids such as magnetic-silica, magneto-luminescent, magneto-plasmonic along with ferrite-based SPIONs are thoroughly presented in light of MRI application.

Keywords Superparamagnetic iron oxide (SPIONs) · Finite-size effect · Surface effect · Magnetic resonance imaging · T_1–T_2 dual weighted imaging

G. Niraula · S. K. Sharma (✉)
Department of Physics, Federal University of Maranhao, Sao Luis, Brazil
e-mail: surender.sharma@cup.edu.in; surender.sharma@ufma.br

G. Niraula · J. A. H. Coaquira
Laboratory of Magnetic Materials, NFA, Institute of Physics, University of Brasilia, Brasilia, DF, Brazil

M. C. Mathpal · J. J. A. Medrano
Institute of Physics, University of Brasilia, Brasilia, DF, Brazil

M. K. Singh
Department of Physics, The LNM Institute of Information Technology, Jaipur, India

R. Verma
Department of Physics, H. P University, Shimla, India

S. K. Sharma
Department of Physics, Central University of Punjab, Bathinda 151401, India

1 Introduction

Magnetic nanoparticles often possess unique magnetic properties due to their finite-size effect, shapes including core@shell morphology allowing for use in a variety of novel applications ranging from industrial technology, biomedicine, quantum computing, etc., [1–4]. In case of biomedicine, the magnetic properties of these particles provide a great advantage by offering selective binding to functional molecules; magnetic properties conferred by these nanoparticles to the functional molecules help in their manipulation and transportation to the target site under a controlled magnetic field. The biomedical use of the magnetic nanoparticles mostly dependent on the chemical stability, shape, and size [5–7].

For early diagnosis of cancer, a number of exertions made to modify the sensitivity and accuracy of the early detection methods so that the efficiency of the treatment method can be improved. In-vivo imaging techniques viz., computed tomography (CT), magnetic resonance imaging (MRI), nuclear imaging of positron emission tomography (PET), single-photon emission computed tomography (SPECT), and optical (or fluorescence) imaging provide a non-invasive method for the diagnosis of patients [6, 8, 9]. High spatial resolution ($\sim$100 μm), rapid in-vivo acquisition of images, absence of exposure to ionizing radiation, and long effective imaging window of MRI technique offers great benefit over other techniques. The most apparent characteristics of MRI are its excellent intrinsic soft-tissue contrast and radiation safety as low level of radiation. MRI has promising future for in-vivo tracing of cells. Albeit, sensitivity of MRI is generally lower as compared to SPECT and bioluminescence. Thus, the design of MRI contrast agents with high efficiency and sensitivity becomes essential tool to allow successful bioimaging at both cellular and molecular levels.

Use of superparamagnetic iron oxide nanoparticles (SPIONs) in MRI as a contact agent (CA) has substantial advantage because of its high sensitivity and amenability to surface modification. In principle, the iron core of SPIONs is useful as dephasing T_2 contrast agent for MRI. SPIONs are promising as a contrast agent in MRI which is due to the unique size-dependent magnetic properties, small enough to interact in the region of interest, e.g., to promote tissular diffusion, potential in cell targeting, and biocompatible/degradable [7, 10].

The synthesis of SPIONs is a challenging task because the size distribution, crystallinity, stoichiometry, and the surface structure of SPIONs all directly linked with their magnetic properties. Several methods have been utilized to address these issues to improve the quality of nanoparticles further.

In this article, we have started by first discussing the theory of SPIONs viz., finite-size and surface effect, theoretical background of MRI technique. Later part of the article, we have emphasized on the most significant chemical routes to synthesize SPIONs and their nanohybrids including magnetite/maghemite, magnetic@silica/carbon, magnetic@plasmonic, and magnetic@luminescent with particular attention to their utilization in MRI applications.

2 Theory of Superparamagnetism: Finite-Size Effect and Surface Effect

Superparamagnetism (SPM) is a special magnetic phase exist in tiny ferro/ferrimagnetic nanoparticles around the size of few nanometer to a couple of a tenth nanometer [11, 12]. Here, the total magnetic moment of the nanoparticles is composed of all the individual magnetic moments of the atoms that constitute the nanoparticles and can be considered as one giant magnetic moment. As per rule, an assembly of non-interacting single-domain (i.e., size above SPM but below ferromagnetic) isotropic materials exhibits a classical paramagnetic with very larger ($\sim 10^3$–10^4 μ_B) magnetic moment μ per particle, but real particles can be a complex (not uniform) in magnetic structure/behavior. Generally, albeit, the properties shown by a single-domain nanoparticles are not considering an isotropic. The morphology and crystal composition are important physical factor that contributes anisotropically to their energy profile. In the presence external magnetic field to the SPM state, magnetic nanoparticles show quick response to change of magnetic field without remanence (M_R) and coercive field (H_C). Under the influence of temperature, the magnetization of sufficiently small nanoparticles can randomly flip its direction with uniaxial anisotropy. This is due to the fact that below certain critical dimension, the anisotropy barrier energy (ΔE) of a magnetic nanoparticle is decreased to the edge point where this energy can be prevailed by thermal energy $k_B T$ (here, k_B is the Boltzmann constant, and T is the absolute temperature) [13]; this phenomenon is collectively shown in Fig. 1a, b.

The single-domain particle has anisotropy energy and is varies with its volume V. For the uniaxial anisotropy, the energy barrier E_{an} proportionally varies to KV; here, K is anisotropy constant. This anisotropy energy depends on the size and decreases with decrease in the particle size that leads the anisotropy energy very small, either comparable or lower, than the thermal energy $k_B T$ if the nanoparticle size is lower
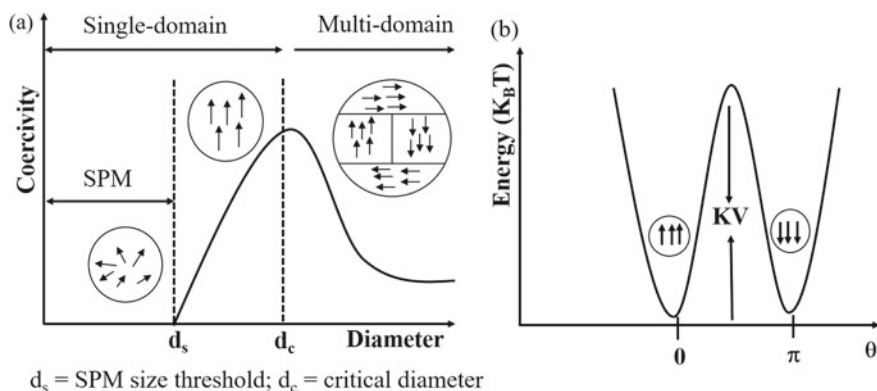
Fig. 1 **a** Schematic picture showing the coercivity (H_c) behavior of magnetic nanoparticles and its relation with diameter and **b** energy barrier for magnetization reversal

than a characteristic value. As a results, the magnetic reversal can be overcome by this energy reinforcing the thermal fluctuation of total magnetic moment, and such magnetic moment is plainly rotated but remain magnetically coupled (ferromagnetically or antiferromagnetically) within the particle. In such case, if external magnetic field or temperature changes, it results in the rapid assembly of nanoparticles approaching to thermal equilibrium. At $H = 0$, the two minima are detached by an energy barrier of height $\Delta E = KV$. The system exhibits like a 'permanent' ferromagnet; if $KV \gg k_B T$, then the moment cannot switch spontaneously. However, if $KV \sim k_B T$ or less, then the natural switching of the 'superspins' can exist on the time scale of the experiment, and the nanoparticles are in SPM state. The magnetic properties of nanoparticles are affected by the measuring time (τ_m) of the specific experimental approach with respect to the relaxation time (τ) that is related with the overcoming of the energy barriers. Magnetic nanoparticles having uniaxial anisotropy can randomly overturn their magnetization direction induced by the thermal energy. The average time required to overturn can be given by the relaxation time [14, 15];

$$\tau = \tau_0 \, e^{-\Delta E / k_B T} \tag{1}$$

where $\Delta E = KV\sin^2\theta$ is the energy barrier, $\tau_0 \sim 10^{-9}$–10^{-12} s is the length of time characteristic of the material, θ is angle between the magnetization and easy axis, and T is absolute temperature [16]. When field is applied, then above Eq. (1) becomes,

$$\tau = \tau_0 \, e^{-\Delta E(H,\theta) / k_B T} \tag{2}$$

with $\Delta E(H, \theta)$ is the field-dependent energy barrier, which can be derived as

$$\Delta E(H, \theta) = \Delta E_0 \cdot \left(1 - \frac{H}{H_{SW}^0}\right) \tag{3}$$

where $\kappa = 0.86 + \frac{1.14 \, H_{SW}^0}{H}$, $H_{SW}^0 = \frac{H_a}{(\sin^{2/3} + \cos^{2/3})^{3/2}}$ and $H_a = \frac{2K}{M_S}$.

The magnetization, in superparamagnetic phase, is zero in the absence of external magnetic field which is linearly varied with the application of field. Every experimental technique has its own measurement time scale τ_m, which can vary from 10^{-8} s to 100 s. There are two conditional state that may explain with relating τ_m and τ, i.e., superparamagnetic and blocking state. The first is when $\tau_m \gg \tau$; if the average time between the spin overturns (flips) smaller than the measurement time, the magnetization appears to fluctuate unless the external field applied. The magnetization appears to be zero, and this magnetic arrangement is known as a superparamagnetic state, whereas $\tau_m \ll \tau$ when the average time between flips is much larger than the measurement time, the system appears to be stuck, and given magnetic field has a fixed magnetization in the field direction. The nanoparticles in this situation are in defined state, known as a blocking state due to the blockage of magnetization in one direction and stop flipping. Simply, the blocking temperature is the transition temperature between blocking state and superparamagnetic state. If $T > T_B$, then

nanoparticle is in superparamagnetic state, and if $T < T_B$, then is in blocking state [17].

The energy required to form the domain walls is an important factor that determines the favorable state; if the energy required in the formation of the domain walls is less than the difference between the magnetostatic energies of the single-domain and multi-domain states, then the multi-domain state is energetically most favorable. When the dimensions of the particles are shrink, the resultant energy of the ferromagnetic particles is changed due to the parallel contributions of the several energies that account the surface energy of domain walls which is more important as compared to the magnetostatic volume energy. As already mentioned above that the particle size in between superparamagnetic and ferromagnetic is single-domain particles. The magnetic behavior of a single-domain particle strongly depends on the particle's shape and magnetic anisotropy; for instance, the total magnetic moment of the spherical particle is zero due to negligible anisotropic properties. It is expected that magnetic moment aligns toward the easy direction if the magnetocrystalline anisotropy is relatively high. The combined contribution from the energy parameters; exchange stiffness constant 'A,' anisotropy constant 'K,' and particle volume energy; introduces characteristic length scales, for example, the exchange length $l_{ex} = (A/M_S)^{1/2}$, the Bloch wall thickness $l_w = (A/|K_1|)^{1/2}$. The relative ordering of the quantities l_{ex}, l_w and the particle size 'l' is of great importance for the critical properties (i.e., exchange coupling/interaction and magnetic properties, etc.) of the nanoparticle. For $l \ll l_w < l_{ex}$, the particle is dominated by the exchange interaction. Finite-size effect arises from the geometric restriction of the particle volume originating due to cutoff of the characteristic length, i.e., exchange length, domain size, etc. As the specimen characteristic dimension l approach to nanosized value and the magnetic correlation length deviates at the critical temperature (T_C), the correlated fluctuating magnetic moments are controlled by the finite size of the specimen [18–20]. With the decrease in the particle size, the Curie temperature also decreases. However, the changes in the crystallography could mask and even inverse this effect [21, 22].

Surface effects have a sort of finite-size effects since the surface influence is highly significant in small nanoparticles. Because of the small size of nanoparticles, a large fraction of all the atoms in a nanoparticle are surface atom, which prompt surface effect. The surface contribution to the magnetization becomes significant when there is an increase in the ratio of surface atom to the bulk atom. The surface atoms have different environment than core because these have been affected by the existence of different types of defect, for instance, changes in the atomic coordination, dangling bonds, atomic vacancies, and lattice disorder. In particular, the reduced atomic coordination at the surface leads to a reduction in the Curie temperature 'T_C' and significant deviation of the temperature dependence of the magnetization in the thermodynamic limit [23]. The surface anisotropy that helps to enhance the magnetic anisotropy which results on cluster demonstrating a significant change in physical/magnetic properties for surface atoms [24, 25]. For example, thermal measurements revealed that the strength of their surface anisotropy and the structure of nanoparticles control their magnetic properties [26]. The magnetization of

oxide nanoparticles decreases for some oxide nanoparticles due to the existence of a magnetically dead layer, canted spins, or the existence of a spin glass-like behavior of the surface spins on the particle's surface [21]. On the other hand, the magnetization of some metallic nanoparticles (cobalt) was reported to increase [27]. A number of experimental studies reported an increase in the effective magnetic anisotropy due to surface effects [24, 27–29].

3 Synthesis of Superparamagnetic Iron Oxide (SPIONs)

Several chemical routes to synthesize SPIONs with various degrees of control over the properties of the final product have been reported. In the past decade, bottom-up chemical synthesis of magnetic nanoparticles has been actively used to design new materials for biomedical applications [6, 30–34]. High-quality iron oxide-based nanoparticles are synthesized by chemical methods viz., coprecipitation [4, 35, 36], thermal decomposition [37–42], sol–gel [43–47], microwave irradiation, and hydrothermal reaction [48–55]. The most commonly used chemical routes are highlighted here.

3.1 Coprecipitation

Coprecipitation is the most widely used; owing to its protocols simplicity, speed, mild operating conditions, the yield of nanoparticles is high, easy to scale up, and relatively low-cost experiment. The only drawback associated with coprecipitation is the lack of control over the uniformity of the nanoparticles [56]. In bioimaging, coprecipitation is usually popular to produce very small nanoparticles, called ultrasmall iron oxide nanoparticles ($D < 5.0$ nm) which show potential in positive MRI imaging [57–59].

Li et al. [60] have prepared a monodispersed water-soluble and biocompatible UIONs through coprecipitation method and used thiol functionalized poly (methacrylic acid), in-situ, as a stabilizers which showed a better control of particle size and their distribution. Later, these magnetic nanoparticles have been tested as efficient T_1—and T_2—contrast agents, by in-vitro and in-vivo experiments comparing with clinically used Gd-DTPA agents. The in-vitro results show that their longitudinal (r_1) and transversal (r_2) relaxivities are 8.3 m M^{-1} s^{-1} and 35.1 m M^{-1} s^{-1}, respectively, which larger than those of Gd-DTPA agent. The in-vivo results demonstrated the better performance in T_1—and T_2—weighted MR imaging than Gd-DTPA. Thus, synthesis of UIONs functionalized with poly (methacrylic acid) has a great potential of UMIONs in dual contrast agents of MRI, especially as an alternative to Gd-based T_1-contrast agents with known clinical risks. Tao and co-worker [61] have used three macromolecule ligands that possessed negative, positive, and neutral charges with carboxylic acid, i.e., poly (acrylic acid) (PAA), amino poly (allylamine hydrochloride), (PAH) and hydroxyl groups, i.e., polyvinyl alcohol (PVA), respectively, as a

stabilizer for the coprecipitation synthesis of small magnetic Fe_3O_4 nanoparticles, where the p^H of PAA, PAH, and PVA in aqueous solution was 2.9, 5.8, and 3.8, respectively. The obtained nanoparticles showed differences in size, water-dispersibilty, cytotoxicity, and T_1-weight contrast performance. The MRI properties of Fe_3O_4-PAA, Fe_3O_4-PAH, and Fe_3O_4-PVA, the T_1-weighted image and longitudinal and transverse relaxation time (T_1 and T_2, respectively) with different concentrations of materials in aqueous solution at 25 °C, have been studied. With the increasing concentration of nanoparticles, all the T_1-weighted images of Fe_3O_4-PAA, Fe_3O_4-PAH, and Fe_3O_4-PVA gradually brightened, indicating that they were able to exhibit T_1-weighted contrast. According to the slope of the relaxometric curves, the longitudinal molar relaxivities (r_1) for Fe_3O_4-PAA, Fe_3O_4-PAH, and Fe_3O_4-PVA were calculated to be 23.6, 60.8, and 30.9 mM^{-1} s^{-1}, respectively. The high r_1 relaxivity of these nanoparticles should be attributed to their small size and high surface decorated with hydrophilic macromolecules, which can facilitate the water exchange rate between the surrounding bulk water molecules and which coordinated with the Fe ions. The transverse molar relaxivities (r_2) for Fe_3O_4-PAA, Fe_3O_4-PAH, and Fe_3O_4-PVA were determined to be 62.3, 232.3, and 224.5 mM^{-1} s^{-1}, respectively. Generally, the r_2/r_1 ratio is a crucial parameter for assessing the T_1 performance of contrast agents. The r_2/r_1 ratio for Fe_3O_4-PAA, Fe_3O_4-PAH, and Fe_3O_4-PVA was calculated to be 2.64, 3.82, and 7.27, respectively. For Fe_3O_4-PAA, the low r_2 and r_2/r_1 ratio indicated that it is adequate as a T_1-weighted contrast agent.

3.2 Thermal Decomposition

The thermal decomposition is greatly preferred to synthesize nanoparticles for MRI application, as this method provides highly uniform, crystallinity, and control over the size of the nanoparticles. The key points to control the magnetic properties, morphologies, size distributions, and particle size are amounts of precursors, solvents, and surfactants. Generally, the reaction is performed in organic solvents (e.g., fatty acids, oleic acid, and hexadecylamine, etc.) and not in aqueous phase which avoids the reactivity of Fe^{3+} and/or Fe^{2+}. Owing to the organic solvents and surfactants remains in the final products which might be crucial for toxicity [31, 33, 62–64]. Therefore, the purification process is required to remove the organic solvents and surfactants from surface of nanoparticles and is a challenging task. Despite this inconvenience, the control over the hydrodynamic size allows the attention of USPIO with potential in positive contrast [65–68]. Wei et al. [69] synthesized the SPIONs from 2.5 to 7.0 nm of a maghemite (γ-Fe_2O_3) core oxidized with trimethylamine *N*-oxide using thermal decomposition of Fe(oleate)$_3$ in the presence of 1-tetradecene, 1-hexadecene, and 1-octadecene. After synthesizing the above inorganic core SPIONs, for the stabilization of nanoparticles in water, the native hydrophobic oleic acid coating was exchanged with a zwitter-ionic dopamine sulfonate (ZDS). The nanoparticles showed a modest relaxivities, i.e., $r_1 = 5.2$ mM^{-1} s^{-1} at 1.5 T and 1.5 mM^{-1} s^{-1} at 7 T. After analyzing the r_2/r_1, it was observed that the positive contrast of this SPIONs is more preferable

than that of other SPION-based MRI contrast agents including Feraheme, Resovist, Feridex, Combidex, Supravist, Clariscan, and others [70–74]. The in-vivo results demonstrated that small SPIONs show kidney clearance, and T_1 contrast power is high enough that these particles can be used for magnetic resonance angiography (MRA) and conventional positive MRI contrast agent. Interestingly, such Gd-free MRI contrast agents that could be used for MRA in a way that is similar to the Gd-based contrast agents (GBCAs). Thus, this nanosystem can be the basis for developing positive Gd-free MRI contrast agents as alternatives to GBCAs in the clinic.

The main drawback of thermal decomposition method is requirement of the surface modification for the transfer of particles into aqueous media [5, 75]. In fact, the thermal decomposition proceeds in the presence of long-chain surfactants which lead to the formation of hydrophobic systems [76, 77]. However, such modification can induce the formation of agglomerates, engendering inevitably a significant rise of the transverse relaxivity alongside a slight decrease of the longitudinal relaxivity, thus limiting their T_1 effect [3, 78]. In order to solve this issue, polyol methods have been developed to synthesize water-soluble iron oxide nanoparticles. The polyol methods are essentially thermal decomposition of organometallic compounds (i.e., precursors) in polyol solvents, which could also be the surfactants and/or reducing agents [39, 79, 80]. Nevertheless, it remains a significant challenge to remove the organic solvents and surfactants. Similar to the thermal decomposition, scale-up is not easy as the removal of the organic solvents and surfactants is non-trivial.

3.3 Microwave-Assisted Hydrothermal

Microwave (MW)-assisted hydrothermal route yields the highly homogeneous/uniform particles in a very short span of time and facilitates for the outcome of best functioning materials mitigating the possible toxic materials. It is difficult to preserve monodispersity of magnetic nanoparticles and hence would spurn the goals of the synthesizing materials; indeed, the route of targeting application depends on every step and the physical parameter involved during the synthesis. The citrate-functionalized iron oxide nanoparticles (C-ESION) were synthesized by MW synthesis route [81]. Later, Pellico et al. [82] reproduced extremely small citrate-functionalized iron oxide nanoparticles (C-ESION), i.e., maghemite, through MW synthesis at reaction temperature 60–140 °C for the investigation of MRI T_1—weighted contrast properties. With the increase in reaction temperature, the size of nanoparticles increases and thus larger at 140 °C, denoted as C-ESION140. The core size of nanoparticles prepared below 120 °C reaction temperature was very small, however, better magnetization, and a thick organic layer formulate them an ideal candidate for T_1 contrast imaging. The relaxometric properties have been altered by tuning the functionalize composition and thickness while keeping same crystallography, magnetic behavior, and core size; yielding for T_1 high-resolution MR imaging. In addition to the T_1 agents, synthesized at 140 °C gives larger crystalline

nanoparticles with a thick-coated layer. CESION140 is tiny nanoparticles that apt the motional regime for T_2 relaxation rates of superparamagnetic nanoparticles. These C-ESION140 maghemite has a great possibility to utilize in standard T_2 contrast by modifying the surface, which enables the full range of dual MRI applications. The surface coating chemistry is crucial factor for the relaxometric properties of these tiny nanoparticles that can be manipulate to engender nanoparticles with radically different contrast natures. Further, the core doping of iron oxide nanoparticles carried out by a microwave-driven protocol, which resulted in the production of extremely small (~2.5 nm) 68 Ga core-doped iron oxide nanoparticles. The method was focused to design nanoparticles for the new generation of hybrid systems, which could use in nanotracer with improved stability, radiolabeling yield, and in-vivo performance in dual PET/MRI [83]. Bhavesh et al. [84] synthesized fluorescein isothiocyanate carboxymethyl (FITC-CM) dextran (4 KDa) functionalized iron oxide nanoparticles (fdIONP) via microwave irradiation to produce extremely small nanoparticles to explore the positive contrast agent. The main advantage of these small nanoparticles is longer circulating times in blood. Here, dextran was used to functionalize the surface composition owing to its biocompatibility, easily degradation in in-vivo, hydrophilicity, and the stealth from the immune system when it considered under circulation. The observed relaxivity values of fdIONP for r_1 and r_2 were 5.97 mM^{-1} s^{-1} and a 27.95 mM^{-1} s^{-1}, respectively, at 1.5 T and 37 °C giving r_2/r_1 ratio of 4.7. The high r_1 value of fdIONP was due to the small size of the magnetic core which leaves a number of Fe^{3+} cations (each with 5-unpaired electrons) on the surface of the nanoparticles. These as-synthesized nanoparticles can be used for in-vitro cell imaging, fluorescence imaging, and in-vivo imaging for magnetic resonance angiography (MRA) due to exhibited fluorescent signal along with T_1 contrast.

Hu et al. [85] synthesized spherical shaped 12–20 nm crystalline iron oxide nanoparticles through a MW-assisted method. The mixture of iron chloride salts (FeCl$_2$ and FeCl$_3$) and sodium hydroxide was irradiated in an MW autoclave reactor adjusting a constant pressure. Bano et al. [86] demonstrated a MW-assisted green synthesis route to prepare superparamagnetic nanoparticles using fruit peel where FeCl$_3$ combined with different fruit peel: lemon pomegranate, apple, and orange. The size of the obtained nanoparticles after functionalization ranged between 17 and 25 nm with almost spherical morphology. The reported nanoparticles were colloidally stabile and water dispersible having a large r_2 value of 225 mM^{-1} s^{-1}. These NPs showed hemocompatible at concentrations as high as 400 µg/mL. Their utilization in photodynamic therapy was assessed in HeLa cells which showed survival of 23%. Further, Williams et al. [87] discussed the synthesis of multifunctional materials comprising several factor such as magnetic cores, a polyelectrolyte stabilizer, and an organic dye for imaging applications. For this, first FeCl$_3$ and FeCl$_2$ were mixed in deoxygenated water. Subsequently, the mixture of rhodamine B polyelectrolyte stabilizer (either poly (sodium 4-styrenesulfonate) (PSSS) or sodium polyphosphate (SPP)) was dissolved in the solution and heated to 80 °C. After all, an ammonia solution was added into the solution and stirred for 20 min and finally transferred to the MW reactor to be heated at 150 °C for 20 min. The dynamic light scattering (DLS) measurements of obtained materials reveal the hydrodynamic mean size of

~100 nm. The zeta potential in the range of -40 mV in those materials clearly indicates the excellent water stability until the last six months. The obtained relaxivities ratio (r_2/r_1) of 8.18 for Fe_3O_4-PSSS and 6.21 for Fe_3O_4-SSP established them as potential candidates for T_2 contrast agents.

4 Magnetic Resonance Imaging: Theoretical Background

MRI is a non-invasive imaging technique used to study the structure and function of tissues in biomedical research and able to obtain highly contrasted images by applying external magnetic fields in the whole body. The term non-invasive relies on the water content to differentiate between diseased tissues from healthy ones. In principle, MRI works depending upon the alignment and interactional behavior of the protons that allow for the tissue imaging with an amplified resolution in both, i.e., space and time in the presence magnetic field. The strong magnetic field (e.g., MRI scanner) allows to polarize the spins of hydrogen nuclei from a chaotic state to ordered state in the direction of the magnetic field. The induced magnetic properties under a perpendicular radio frequency (RF) pulse interact with the receiver coil in which the spin polarization can be observed. The net magnetization will back to its equilibrium position when RF pulse is removed. The time required for the magnetic moments to reach at the equilibrium state, termed as a relaxation time, and is tissue-dependent. In this process, two magnetization processes; the longitudinal and the transverse magnetization have been accounted, which generate magnetic resonance images. The exponential recovery of the longitudinal magnetization corresponds to the T_1 relaxation, and it appears bright in T_1-weighted MR images, whereas on the other hand, the exponential decay of the transversal magnetization corresponds to the T_2 relaxation and appears dark in T_2-weighted MR images.

The relaxivities (r_1 and r_2) determine the efficiency of the contrast agents that can be calculated as,

$$R_i = \frac{1}{T_{i,0}} + r_i C \qquad (4)$$

where $i = 1$ or 2; R_i is the observed relaxation rate (s^{-1}); $T_{i,0}$ is the relaxation time before adding contrast agents (s); r_i is the relaxivity coefficient (mM^{-1}s^1); and C (mM) is the concentration of contrast agents. The $r_1 = 1/T_1$ and $r_2 = 1/T_2$ are contrast agents determined by the slope of a plot ($1/T_1$ and $1/T_2$) versus the concentration.

The distinct number of water protons in various organs is the foremost source of contrast in magnetic resonance images that result in T_1 and/or T_2 relaxation times. After intravenous, the iron oxide nanoparticles can reduce the T_1 and/or T_2 relaxation times of water protons inside several organs, leading to contrast in the MR images [48, 88–90]. The superparamagnetic nanoparticles assembled in the tissue offer the MR contrast enhancement by reducing T_2 relaxation time of its nearby water protons. The superparamagnetic iron oxide nanoparticles (SPIONs) in tissue are subjected to

applied magnetic field; the align magnetic moments generate the heterogeneous field gradients which allow the diffusion of water protons. The main source of the efficient spin dephasing, and to reduce the signal intensity, is the dipolar coupling between the magnetic moments of water protons and the administered nanoparticles.

4.1 T_1-Weighted Imaging

Magnetic spins turn-back to the thermal equilibrium (Boltzmann distribution) condition prior to a disturbance once the spin system is placed in a uniform magnetic field during relaxation and spin–lattice relaxation (T_1 relaxation) resulted by exchanging energy with the thermal reservoir (i.e., lattice) (Fig. 2). In this process, T_1 relaxation reestablishes the state of spin polarization that can be characterized by a net magnetization (M_0). Such net magnetization, obviously, depends on the application of magnetic field (B_0), nuclear spin intensity (I), gyromagnetic ratio (γ), and inversely proportional to the temperature. For a spin half ($I = 1/2$) system, T_1 relaxation reduces the energy of the system because of the quantum transition from high
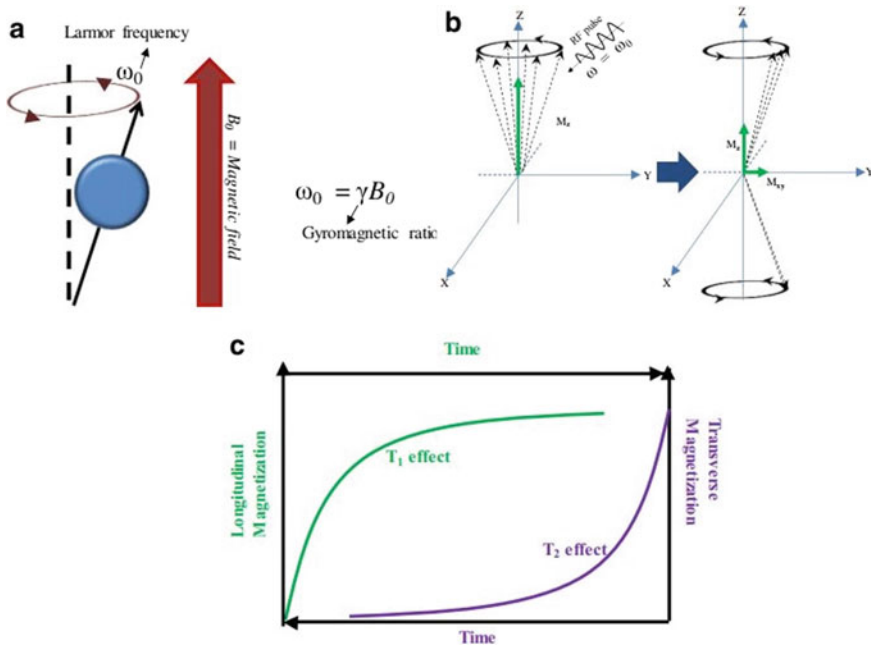
Fig. 2 Overview of MRI principle using IONPs. **a** Alignment of spins in the application magnetic field and precession under Larmor frequency ω_0. **b** Spin relaxation mechanisms of T_1 and T_2 after applying RF pulse. **c** Hypothetical graphs of longitudinal and transverse relaxation with time. (Reprinted with permission from Ref. [101]. Copyright © 2017, Springer Nature)

energy level to the lower one; the energy difference is given by the fundamental equation

$$E = \frac{h\omega_o}{2} = \frac{h\gamma B_o}{2}; \omega_o = \gamma \text{Bo} \tag{5}$$

where ω_o is Larmor frequency, and h is Planck's constant. Further, in T_1 relaxation, the phenomenological equation that shows the evolution of longitudinal magnetization M_Z from the initial $M_Z(0)$ is given by first-order equation,

$$\frac{dM_z}{dt} = -\frac{M_0 - M_z}{T1} \tag{6}$$

Which gives following solution,

$$M_z(t) = M_z(0) \exp^{-\frac{t}{T1}} + M_0\left(1 - \exp^{-\frac{t}{T1}}\right) \tag{7}$$

The protons relaxation times are in the range 0.1–10 s for liquids at room temperatures [91–93]. The off-resonance technique and inversion recovery with on-resonant water suppression are the general techniques that provide the effective T_1 contrast images [1, 94]. The off-resonance technique employs the spectrally selective RF pulses to excite and refocus the off-resonance water nearby SPIONs, whereas inversion recovery with on-resonant water uppression applies the inversion of magnetization in conjunction with a spectrally selective on-resonant saturation prepulse inducing the signal from off-resonant protons in close proximity to SPIONs.

The T_1 contrast effect can be altered by the interaction between the protons and nearby paramagnetic ions; the gadolinium (Gd) is a widely used positive contrast agents [95, 96]. Gadolinium (Gd^{3+}) having seven unpaired electrons provides the intense contrast effect. The Gd^{3+} ions, for example, Gd-chelates Gd diethylenetriaminepentaacetic acid (Gd-DTPA) and tetraazacyclododecanetetraacetic acid (Gd-DOTA), are highly enticed for T_1 contrast agent [97]. All Gd-based contrast agents used in the clinics nowadays are T_1 contrast agents [96]. Nevertheless, Gd^{3+} can be separated from the complexes and induce severe side effects, such as Gd deposition in the human brain [98] and nephrogenic system fibrosis (NSF) [99, 100].

Iron oxide nanoparticles can also be suggested as an alternative of T_1 contrast agents instead of paramagnetic ones because of their high biocompatibility and degradability in the body [7, 102, 103]. Albeit, various factors that are needed to be controlled to consider iron oxide nanoparticles as T_1 contrast agent, for instance, the size, surface state, and phase composition. It is well known that the dimension/magnitude of particles can greatly affect the magnetic behavior; for instance, the magnetic spins of the on surface can be disordered due to the spin-canting effect from where T_1 contrast effect comes from [104, 105]. Thus, the T_1 contrast can be amplified by controlling the dimension/size of nanoparticles. Several investigations have shown that iron oxide nanoparticles with size less than 10 nm (also called ultra-superparamagnetic iron oxide, i.e., USPIOs) are considered as T_1 contrast agent.

Recently, the MR relaxivities of nanoparticles ranging from 3 to 8 nm are studied to investigate how the core size affects the relaxivity [9, 106]. These studies have concluded that r_2 values are strongly affected (very low) due to the size reduction of the nanoparticles which is proportional to the magnetic moment. Consequently, it is clear that low value of r_2 gives a low r_2/r_1 ratio which is necessary factor for T_1 contrast agent. It is worth to mention that the particles size less than 3 nm which consists of the large surface-to-volume ratio significantly affects the quality of T_1 contrast. Iron oxide nanoparticles with size ~2 nm show almost a paramagnetic behavior due to their canted spins and have been reported as T_1 contrast agents [107]. The high r_1 relaxivity of 4.78 mM^{-1} s^{-1} and low r_2/r_1 ratio of 3.67 suggest them as effective positive contrast agents. Further, the oxidation state (surface state or surface composition) of paramagnetic metal ions on the surface is a key factor in T_1 contrast. For example, Kucheryavy et al. [108] have reported the r_1 relaxivities of Fe_3O_4 and γ-Fe_2O_3 nanoparticles where both of them have similar r_1 values. It is believed that enhanced contrast effect of γ-Fe_2O_3 may be attributed to the higher number of unpaired electrons of Fe^{3+} (5 electrons) than that of Fe^{2+} (4 electrons) although the saturation magnetization of γ-Fe_2O_3 is ca. 20% smaller than that of Fe_3O_4 of a similar size. In addition to these factors, authors have suggested that the surface coating of material and their thickness also key factors in the T_1 contrast effect.

4.2 T_2- Weighted Imaging

Spin–spin relaxation (T_2) is the time constant of the exponential decay of transverse magnetization (M_{xy}) after an RF pulse. This is associated to the time precessing's magnetic moments of protons to become randomly aligned in the xy-plane after an RF pulse which provides a net magnetic moment of zero in that plane. After RF pulse, the spins start to interact with their neighbors by exchanging energy in non-dissipative manner without net transfer to the lattice. The coherence established by the RF pulse starts reducing, and the spins develop the phase difference between them in the xy-plane. The dephasing process caused by a combination of local inhomogeneities in the magnetic field owing to magnetic interactions of neighboring molecules and by macroscopic effects related to subtle variations in the external magnetic field. T_2-weighted images are acquired by the elimination the dephasing effects caused by extrinsic magnetic field in homogeneities and thus account for the molecular interactions alone. The enhanced longitudinal magnetization is related with the reduced transverse component, therefore, $T_2 \leq T_1$. The T_2 values for tiny molecules and large water pools are in the range 10 ms–10 s and can be much shorter for solids. The phenomenological description for the transverse relaxation can be given by a first-order equation (in the rotating frame)

$$\frac{\mathrm{d}M_{xy}}{\mathrm{d}t} = -\frac{M_{xy}}{T2} \tag{8}$$

Which gives following solution,

$$M_{xy}(t) = M_{xy}(0) \exp^{-\frac{t}{T_2}} \tag{9}$$

This solution applies for weak and non-interacting spins. For the protons decaying in biological environments and molecules of several dimensions/sizes, the decay is non-exponential that can be described by a two exponential model reflecting compartments and exchange processes; for example, the decay in ice is well described by a Gaussian rather than exponential process [91–93].

The particle size, composition, and crystallinity are three key factors which affect the r_2 relaxivity of SPIONs [109]. The size of SPIONs for effective T_2 contrast agents is above 10 nm. It is established that the magnetization is highly influenced by the particle size/dimensions; larger SPIONs generally have higher magnetization and contribute to the higher T_2 relaxivity. However, superparamagnetic size has certain limit in magnetic iron oxide [110]. Based on several theoretical evidences on how the relaxivity affected by the particle, there are three separate regimes of r_2 with the increase particles size: (a) motional average regime (MAR), (b) static dephasing regime (SDR), and (c) echo limiting regime (ELR) [111–114]. This is a region where value of r_2 relaxivity increases continuously with increase in size of nanoparticles below SPM limit. The magnetic fields are averaged by a rapid diffusion of the protons in MAR due to the quick diffusion of water between particles. The size effect on a T_2 contrast effect in MAR is envisioned with water-soluble superparamagnetic iron oxide nanoparticles (WSIONs); the magnetization is increased with increase in size of the particles and attributed to the higher r_2 relaxivity [115].

The size regime, where the r_2 relaxivity of the particles is constant even with the increase in size within the certain limit and maximum r_2 seems to be a plateau, is called the SDR [111–114]. In principle, magnetic nanoparticles belong in the SDR are usually ferrimagnetic. On the other hand, when nanoparticles are too large (larger than SDR regime), the spin gets dephased rapidly that fewer spins can be refocused by the echo sequence, leading to decrease in the r_2 with increase in the size. This regime is called the ELR in which r_2 depends on the echo time [114]. However, the large nanoparticles in ELR can be used in the gradient echo MR imaging, which is sensitive to the magnetic susceptibility [116]. The aggregation of such nanoparticles is main issue to use in biomedical application due to the remanent magnetization/dipole interaction. Nevertheless, these iron oxide nanoparticles can be utilized to track the bio-distribution of labeled cells along with MRI because the cell size is much larger than the aggregates of nanoparticles [117]. To obtain a better stabilization and well dispersion, surface modification/encapsulation is necessary. Recently, water dispersible ferrimagnetic iron oxide nanocubes were synthesized by the encapsulation with an edge length of 22 nm within PEG phospholipids [118]

To prepare SPIONs with enhancing r_2 relaxivity, the control aggregation method has been reported which maintain the superparamagnetism. However, the SDR of iron oxide nanoparticle clusters is ~100 nm which makes controlled aggregation of nanoparticles difficult to achieve maximum r_2 relaxivity [119, 120]. The controllable

aggregation of nanoparticles into clusters produces the magnetic relaxation switch effect [11, 121–123]. Although clustering of nanoparticles enhances the r_2 relaxivity, their relaxivities are usually lower than the theoretical estimation because of the individual size of the nanoparticles and the fraction of the magnetic nanoparticles in the cluster [119, 120]. Moreover, the crystallinity and the phase composition even in the clusters are important for the relaxivity performance of nanoparticles.

The distribution of Fe^{2+} and Fe^{3+} ion in A- and B-site of iron oxide significantly affects the magnetic properties. The magnetic spins of the ions in the octahedral sites (B-site) are ferromagnetically coupled to each other and antiferromagnetically coupled with tetrahedral sites (A-site). The magnetic spins of Fe^{2+} ions in the octahedral sites contribute to the net magnetic moment. It is well known that the net magnetic moments are proportional to the magnetic spins of divalent ions except for Zn^{2+}. This implies that the magnetic properties of iron oxide nanoparticles can be control replacing Fe^{2+} ions by other divalent transition metal ions, such as Mn^{2+}, Co^{2+}, Ni^{2+}, and Zn^{2+} ions [124–126]. Among the divalent ions, Mn^{2+} ions exhibit the strongest magnetic moment due to five unpaired d-orbital electrons [126]. The relaxivity r_2 value of Fe_3O_4 is 218 mM^{-1} s^{-1}, whereas the r_2 relaxivity of $MnFe_2O_4$ nanoparticles is 358 mM^{-1} s^{-1} because the higher saturation magnetization (magnetic moment) contributed by Mn^{2+}. Lee et al. [126] reported that $MnFe_2O_4$ nanoparticles exhibited the largest magnetic susceptibility and obviously the strongest T_2 shortening effect among the series of metal-doped iron oxide MFe_2O_4 (M = Mn, Fe, Co, or Ni) within the similar size distribution. In contrast to the inverse spinel structures (e.g., Fe_3O_4), $ZnFe_2O_4$ has a normal spinel structure. Owing to the non-magnetic property of Zn^{2+} cations and antiferromagnetic coupling between Fe^{3+} cations, $ZnFe_2O_4$ is unsuitable to be used as an MRI contrast agent. However, partial substitution of Fe^{2+} cations with Zn^{2+} increases the net magnetization [125, 127]. The magnetization of $Zn_xFe_{1-x}Fe_2O_4$ is at maximum when x is approximately 0.4 [127]. The r_2 relaxivity of the $Zn_{0.4}Fe_{2.6}O_4$ nanoparticles is 860 mM^{-1} s^{-1} (Fig. 3).
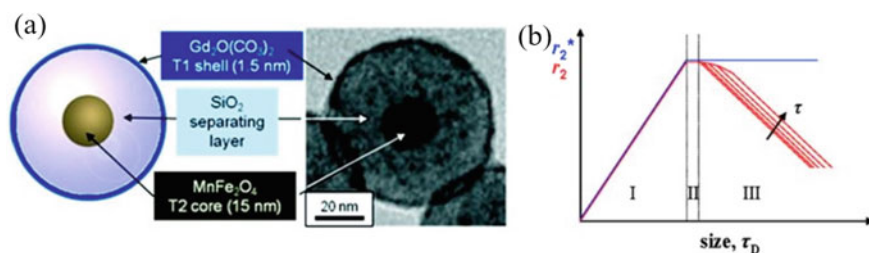
Fig. 3 **a** Schematic and TEM image of the core–shell type dual-mode contrast agents and **b** representation of the r_2 and r_2* varying with size of the nanoparticles in different regimes. (Reprinted with permission from Ref. [88]. Copyright © 2015 American Chemical Society)

4.3 Dual-Modal (T_1- and T_2-) Weighted Imaging

A number of researchers explained theoretical concept of SPIONs T_1 and T_2 contrast effect with some examples. Although the MRI is not a new in biomedical, the clear discussion on several factor that affects the signals in MRI is still lacking; the endogenous artifacts viz., fat, hemorrhage, blood clot, and air could mislead the MRI signals originated from the contrast agents [128, 129]. To overcome these issues and to obtain simultaneously high sensitivity and biocompatibility, a complementary T_1–T_2 dual-modal CA that provides T_1 and T_2 signal and MR images is highly desirable for the diagnosis. Therefore, simultaneous acquisitions of T_1 and T_2 contrasts have been extensively studied to investigate the harmonious information on T_1-weighted and T_2-weighted MRI [130, 131]. However, both T_1 and T_2 contrast agents (CAs) are suffered from their own limitations; thus, finding a new type of CAs is essential. Dual contrast agents (T_1–T_2—weighted) are advantageous that report the more comprehensive information for the diagnosis [132]. Such combined CAs can be achievable; however, it is challenging, by controlling the size and functionalization factors [133, 134].

The T_1–T_2 dual-modal MRI agents can be prepared by direct conjugation/absorption of T_1 chelating agent on the surface of iron oxide nanoparticles. While synthesizing those system, the magnetic nanoparticles and paramagnetic ions should not be in closed contact to avoid the possible signal attenuation due to the presence disturbance in T_1 relaxation by the resultant effect of T_2 contrast magnetic materials. To circumvent such contact between magnetic and paramagnetic ions, the surface modification to separate the layers is necessary which can be done by using polymers/organic/inorganic materials, for instance, polyethylene glycol (PEG) chain, citric acid, and silica shells, etc. [63, 131, 135]. It is worth to mention that the dependency of r_1 and r_2 relaxivities on the thickness of separating layer [130]. Considering this approach, the SPIONs were prepared and coated by a polymer in which later the gadolinium ions were added that provides the combined T_1–T_2 dual mode for imaging [136]. The dual T_1–T_2 contrast agent efficiently lowers the T_1 and T_2 relaxation times and attains effective contrast in animals (mice) for both T_1- and T_2-weighted images. The proper combination of chelating agents, coating polymer, and SPIONs authorizes the acquisition of both highly detailed T_1-weighted anatomical images and pathologically relevant T_2-weighted images in single imaging probes. In addition, such a contrast probe allows enhanced T_1-weighted imaging of brain tumors. However, frequently used gadolinium chelates such as gadolinium diethylenetriamine penta-acetic acid (Gd-DTPA) cannot traverse the blood–brain barrier (BBB) by the use of non-invasive techniques [137, 138], which restricts their application in brain tumor imaging. The large surface area for the efficient addition of biologically active moieties such as BBB-penetrating peptides for a non-invasive brain tumor imaging is beneficial. For instance, the SPIONs labeled with chlorotoxin (CTX) peptide can easily pass the BBB and successfully target the brain tumors in a transgenic mouse model [139–141]. Xiao et al. [142] synthesized PEG functionalized

superparamagnetic iron oxide nanoparticles in the addition of gadolinium as a potential dual-modal CAs for the brain glioma imaging. It was observed that the nanoparticles exhibited a high r_1 value and low r_2/r_1 ratio that supports remark its possibility as a T_1–T_2 dual-modal MRI contrast agent. The in-vivo MRI demonstrated the simultaneous contrast enhancements in T_1- and T_2-weighted MR images toward the glioma bearing mice. In addition, the in-vitro cytotoxicity assays and in-vivo and histological analyses confirmed the biocompatibility of PEG-GdIO nanoparticles. The study encouraged the potentiality of PEG-GdIO NPs in T_1–T_2 dual-modal imaging for brain glioma diagnosis.

Cellulose nanocrystals (CNC) are a type of nanomaterials having a number of appreciable properties such as low cost, biocompatibility, sustainability, high mechanical strength, non-toxicity, hydrophilicity, large surface area, biodegradability, and high stiffness [143]. Torkashvand et al. [144] synthesized a T_1–T_2 dual contrast agent consisting of ultrasmall Fe_3O_4 nanoparticles and cellulose nanocrystals-poly citric acid (CNC-PCA) nanoplatform. The CNC was synthesized through acid-hydrolysis routes incorporating with PCA to obtained dispersible, stable, biocompatible, and hydrophilic substrate. The nanocomposite could be obtained by loading of ultrasmall Fe_3O_4 nanoparticles on CNCPCA nanoplatform. The simultaneous use of ultrasmall iron oxide nanoparticles and cellulose nanocrystals causes to many noteworthy properties for CNC-PCA/ Fe_3O_4 nanocomposites as compared to other iron oxide-based system, for example, high zeta potential, ultrasmall hydrodynamic size, high saturation magnetization (~52.2 emu g^{-1}), colloidal stability, water dispersibility, and hydrophilicity as expected (Fig. 4).

The obtained nanocomposite non-toxic in in-vitro and considerable cellular uptake toward the HeLa cell lines. The CNC-PCA/Fe_3O_4 nanoparticles exhibited an outstanding contrast effect on both T_1- and T_2-weighted MR images providing a high value of r_1 (13.8 mM^{-1} s^{-1}) and r_2 (96.2 mM^{-1} s^{-1}) relaxivity as compared to commercial and clinical agents. Therefore, such biocompatible CNC-PCA/Fe_3O_4 nanocomposites could act as a potential dual contrast agent for MRI and further biomedical applications.

5 Superparamagnetic Nanomaterials for Magnetic Resonance Imaging Applications

5.1 Ferrite-Based SPIONs

The SPIONs are considered as an effective probe for the negative contrast (T_2-contrast agents) because of their magnetic behavior along with size advantages. Albeit, the dark signal detected in the T_2-image may be quite complicated to identify the region of interest, for instance, glioma imaging, calcium deposits, and bleeding. Pellico et al. [82] have developed citrate-coated IO nanoparticles (C-ESION), i.e., maghemite that demonstrated an outstanding positive (T_1 imaging) and negative
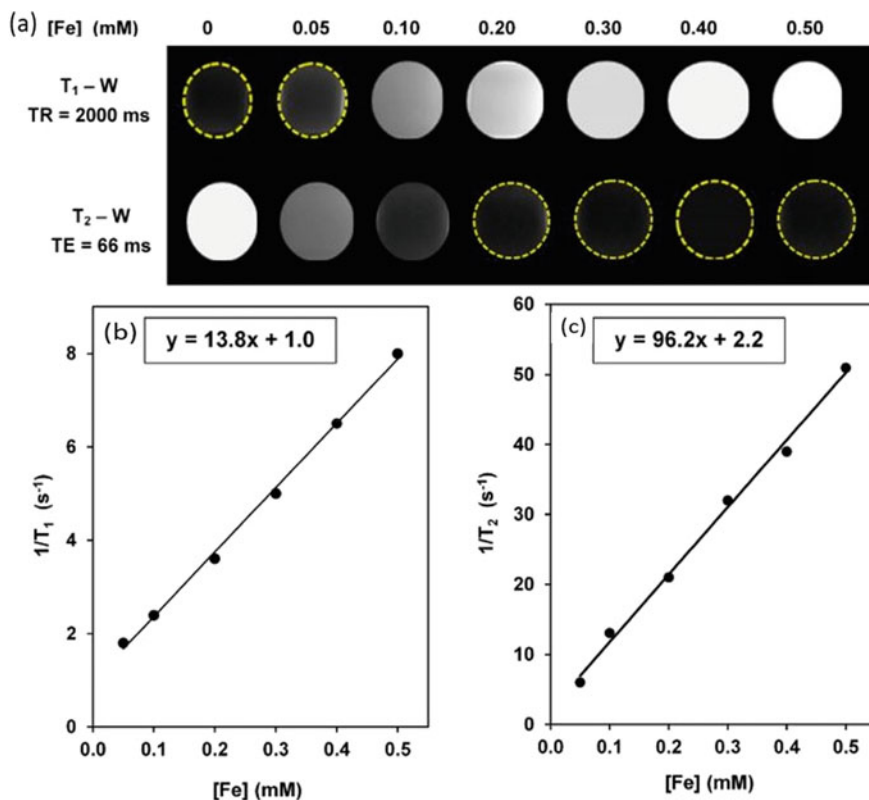
Fig. 4 **a** T_1- and T_2-weighted MRI images of CNC-PCA/Fe_3O_4 at different Fe concentrations (mM) at 3.0 T, and **b**, **c** T_1 and T_2 relaxation rates ($1/T_1$ and $1/T_2$ s^{-1}) as a function of the Fe concentration (mM) for CNC-PCA/Fe_3O_4 nanocomposite at 3.0 T. (Reprinted with permission from Ref. [144]. Copyright © 2019 Elsevier Ltd. All rights reserved.)

contrast through modulating the physiochemical properties, i.e., composition and coating thickness. The relaxometric experiment has shown that sample C-ESION120 has a very large r_1 value of 11.9 mM^{-1} s^{-1} and an r_2/r_1 ratio of 1.9, and the authors claimed that the obtained values are larger than the most traditional Gd-based contrast agents available in the literatures. On the other hand, C-ESION140 nanoparticles exhibited the traditional superparamagnetic properties for T_2-weighted imaging, with r_2 value of 74.9 mM^{-1} s^{-1} and a large r_2/r_1 ratio of 5.9. The reason for this very different behavior was due to increase in synthesis temperature from 120 to 140 °C which led to sharp increase in hydrodynamic size. In addition, the surface coating chemistry and their thickness on nanoparticles surface are important factor to change the relaxometric properties. Two different nanoparticles are favored for different imaging; the C-ESION120 showed T_1-weighed contrast and C-ESION140 showed T_2-contrast signal. The larger coating thickness in C-ESION140 led to slow down the water diffusion that enhances the effect of magnetization on water protons and leading

toward the larger r_2 value. Hence, the modified coating enabled the maghemite NPs for T_1 high-resolution MR angiography and also provided standard T_2 contrast to utilizing them for a full range of applications in MRI.

Lee et al. [126] examined a series of metal-doped magnetism-engineered iron oxide (MEIO) nanoparticles of spinel MFe_2O_4 as shown in Fig. 5a, where M is +2 cation of Mn, Fe, Co, or Ni, in the presence of oleic acid and oleylamine as surfactants, to explore the possible applications in MRI contrast agent. After the synthesis to investigate the metal-doped MEIO nanoparticles modulated MR signal enhancement effect, the spin–spin relaxation time (T_2)-weighted MR images were taken for each sample at 1.5 T. The performance of the MR contrast agent cross-linked iron oxide (CLIO) under identical conditions was also assessed. They found
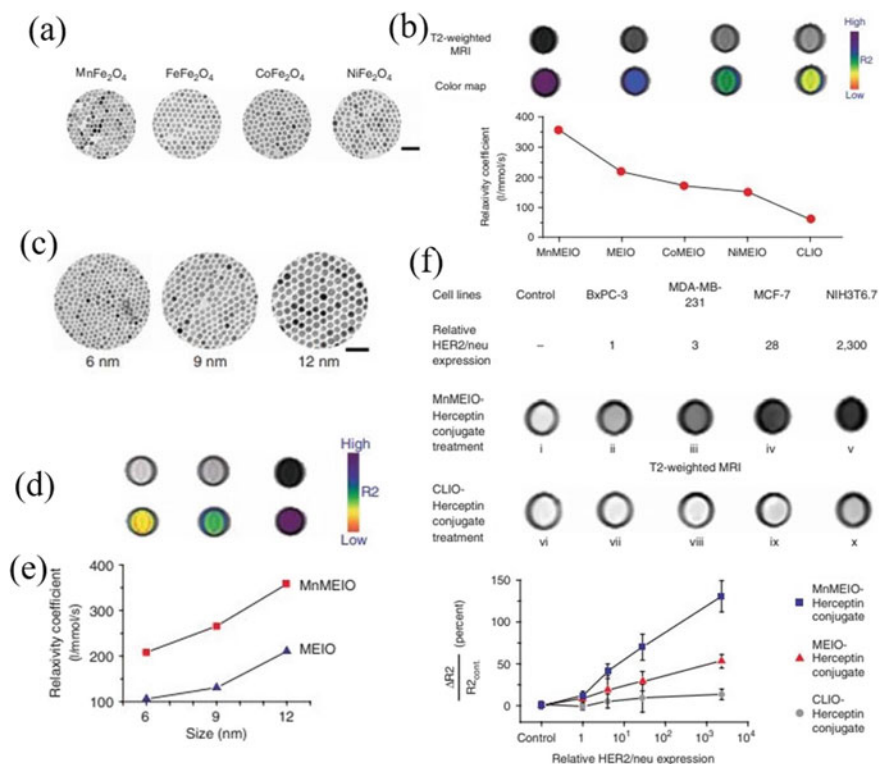
Fig. 5 **a** TEM images of $MnFe_2O_4$ (MnMEIO), Fe_3O_4 (MEIO), $CoFe_2O_4$ (CoMEIO), and $NiFe_2O_4$ (NiMEIO), **b** T_2-weighted spin echo MR images, their color maps and relaxivity (r_2) of a series of MEIO nanoparticles at 1.5 T, **c** size-dependent MR contrast effect of MnMEIO and MEIO nanoparticles TEM images, **d** T_2-weighted MR images and color maps of MnMEIO nanoparticles, **e** a plot of nanoparticle size versus r_2, and **f** Relative HER2/neu expression levels of various cell lines, T_2-weighted MR images of cell lines treated with MnMEIO-Herceptin conjugate or with CLIO-Herceptin conjugate and plot of relative HER2/neu expression level for each cell line versus r_2 enhancement (Reprinted with permission from Ref. [126]. Copyright © 2007, Springer Nature)

that Mn-doped $MnFe_2O_4$ (MnMEIO) exhibited the strongest MR contrast effect (Fig. 5b), with a relaxivity value (r_2) of 358 mM^{-1} s^{-1}. The r_2 values are reduced to 218, 172, 152, and 62 mM^{-1} s^{-1} for the set of $FeFe_2O_4$ (MEIO), $CoFe_2O_4$ (CoMEIO), $NiFe_2O_4$ (NiMEIO), and CLIO, respectively. The color-coded images based on r_2 revealed that the colors changing from violet (high r_2) to blue, green, and yellow (low r_2). Therefore, the tuning of particles composition is critical to modulate the spin–spin relaxation of the protons. Further, their analysis has demonstrated that size dependency of T_2-weighted MR signals of MnMEIO and MEIO. Here, they found that the contrast effectiveness increased with in size of MnMEIO nanoparticles from 6 to 9 to 12 nm (Fig. 5c) corresponding to their r_2 values 208, 265, and 358 mM^{-1} s^{-1} which are consistent with their magnetization values 68, 98, and 110 (emu/mass of magnetic atoms), respectively. From the color-coded images, colors corresponded to the size of the nanoparticles: yellow (6 nm), green (9 nm), and violet (12 nm), respectively, (Fig. 5d). In agreement with the above results, a similar size dependency of the MR signals with MnMEIO and MEIO (Fig. 5e) was observed.

It was concluded that higher relaxivity values proportional to the better MR which means again larger nanoparticles (i.e., larger magnetization value) are responsible for faster spin–spin relaxation processes. Among the several metal-doped MEIO nanoparticles as studied, 12-nm MnMEIO nanoparticles showed the intense MR enhancement effect. In-vitro experiment of these ferrites NPs has been performed in the number of cell lines with different levels of HER2/neu overexpression: Bx-PC-3, MDA-MB-231, MCF-7, and NIH3T6.7 (relative HER2/neu expression levels are 1, 3, 28 and 2300, respectively). With the MnMEIO-Herceptin conjugates, the detection of the BxPC-3 cell line (Fig. 5f) showed noteworthy MR contrast (T_2-weighted MR images). As the relative HER2/neu expression level increase to 3, 28, and 2300, the MR contrast consistently increased by 40%, 70%, and 130% for the MDA-MB-231, MCF-7, and NIH3T6.7 cell lines, respectively. On the other hand, with the CLIO-Herceptin conjugates, only NIH3T6.7 cell line was MR-detectable with an enhanced r_2 by 10%. These results concluded that MnMEIO-Herceptin conjugates provide the better MR contrast effects than MEIO-Herceptin and CLIO-Herceptin conjugates. Gao et al. [145] have studied the T^*-weighted MR imaging of γ-Fe_2O_3 hollow nanoparticles comparing with FePt@Fe_2O_3 yolk-shell nanoparticles and Pt@Fe_2O_3 yolk-shell nanoparticles; γ-Fe_2O_3 hollow nanoparticles exhibit the strongest MR signal attenuation effect. It is well known that MR signals are widely affected by geometry (size and shape) of NPs. It is worthy to mention that the hollow magnetic particles are advantageous in to enhance MR relaxation because of their inside-empty geometry.

5.2 *Magnetic @silica Nanomaterials*

Kim et al. [146] have synthesized uniform iron oxide nanoparticle/mesoporous silica core/shell nanoparticles (Fe_3O_4@mSiO_2) to investigate their potential application in therapy and MRI. The main advantage of these mesoporous nanoparticles was an

ability to immobilized with an organic fluorescence dyes, for instance, fluorescein isothiocyanate (FITC) and rhodamine B isothiocyanate (RITC) offering them as fluorescent imaging probes. The surface functionalization of these NPs with poly (ethylene glycol) (PEG) imparted biocompatibility and colloidal stability under physicochemical conditions. In addition, these functionalized core@shell nanoparticles were well-internalized into cells by endocytosis; the doxorubicin (DOX) loaded nanoparticles were internalized by cancer cells that labeled with Fe_3O_4@$mSiO_2$. These labeled cells observed in the fluorescence image appeared as dark contrast in the MR image due to enhanced T_2 relaxation and intense red emission due to RITC. The multimodal imaging capability of this technique is convenient for both non-invasive diagnosis and to provide the guidance to surgical treatment. The intravenous injection of Fe_3O_4@$mSiO_2$ nanoparticles into the tail vain of tumor-bearing mice resulted in the accumulation of these particles at the tumor sites which were detected via MRI. Based on MR and fluorescence imaging reports, authors suggested as-prepared Fe_3O_4@$mSiO_2$ nanoparticles could be an efficient nanoprobes for the simultaneous cancer diagnosis and therapy.

Sato et al. [147] have designed the superparamagnetic hybrid nanoparticles (HNPs) combining silica and magnetic iron oxides, i.e., magnetite/maghemite with the mean diameter of 3–5 nm. These HNPs provided a good biocompatibility due to the high viabilities of HeLa cells stained with the HNPs. All HNPs were well up-taken by HeLa cells even at high concentration, i.e., 100 µg/mL during the cell culture. It was found that most of nanoparticles were in the cytoplasmic region suggesting that the uptake does not affect the cell viability. The fluorescence imaging of HNPs after the cellular uptake showed dusky-green light. In particular, green fluorescence intensities in the cells for the HNPs with Fe content of 5.3% were relatively weak as compared to those in an aqueous solution. Thus, the biocompatible HNPs can be considered as a potential contrast agent for in-vitro/in-vivo imaging including MRI monitoring, fluorescence optical imaging, and the magnetic field guided targeting in living body.

Chio and co-workers [130] have developed magnetically decouple core − shell concept to produce a dual-mode contrast agent (DMCA) which possesses not only enhanced MR contrast effects but also the unique capability of displaying 'AND' logic signals in both the T_1 and T_2 modes. In principle, the magnetic layer-paramagnetic nanoparticles give the information about T_1–T_2 contrast only if the layer is formed by polymer such as silica shells that control the magnetic coupling between T_1 and T_2 contrast materials. The simultaneous acquisitions of T_1 (positive) and T_2 (negative) contrasts extensively provide the complementary information on T_1-weighted MRI and T_2-weighted MRI. They reported that as the thickness of the separating silica layer increases, the r_1 relaxivity dramatically increased from 2.0 to 32.5 mM^{-1} s^{-1}, while the r_2 relaxivity moderately decreased from 340 to 213 mM^{-1} s^{-1}.

5.3 Magnetic@Plasmonic Nanomaterials

Plasmonic nanoparticles involves surface plasmon resonance phenomena that enables to achieve the intensive selective absorption/scattering of light widely used in photo-thermal therapy, bioassays, diagnostic tools, sensing, photodynamic therapy, etc., as a biomedical application. The combination of magnetic and plasmonic properties supplies the unique possibility to be used in multimodal imaging. The combined modalities of different physical properties in a single technique could provide an extensive and through information for the diagnosis and the treatments of cancers.

Osborne et al. [148] reported the core–shell Fe-Au nanoparticles to investigate their possibility in MRI as a contrast agents. The nanoparticles were able to affect the T_1 and T_2 contrast in a concentration-dependent manner shown in Fig. 6a, b. The decrease in signal intensity is due to increase in particle concentration. The T_2 effect of iron oxide-based nanoparticles typically dominates the relaxation at high field strengths and limits their use as T_1 agents; however, this is not case for Fe–Au nanoparticles. The Fe–Au nanoparticles have shown a great ability to conjugate easily with any biomolecules of interest. The utilization of Fe–Au nanoparticles as a vehicle for bead-based assay technology can be adapted for high-throughput MR, optical or multimodal detection.
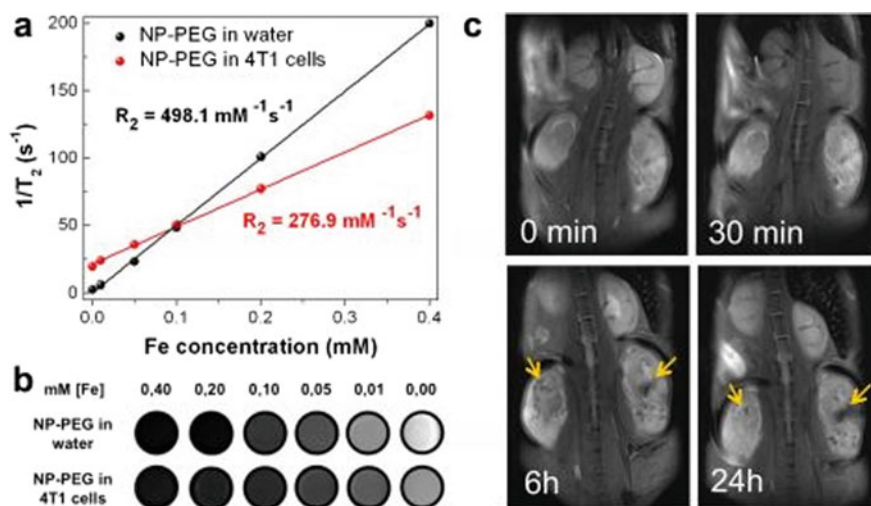
Fig. 6 Fe_3O_4–Au Janus NPs as MRI contrast agents. **a** Proton T_2 relaxation time as a function of iron concentration for NP-PEG in water and in $4T_1$ cells. The R_2 value is determined by the slope of the linear fitting. **b** T_2-weighted images of NPs serial dilutions acquired at TE = 24 ms in water (top panel) and $4T_1$ cells (bottom panel). **c** Representative T_2-weighted images of BALB/c mouse with both flanks grafted $4T_1$ tumors captured before and within 24 h after NPs (6.6 mg kg^{-1} Fe_3O_4). Areas with enhanced tumor contrasting are indicated by arrows. (Reprinted with permission from Ref. [149]. Copyright © 2018, Springer Nature)

Efremova et al. [149] have reported Fe_3O_4–Au hybrid NPs to investigate the contrast effect in MRI. Figure 6a shows the proton $1/T_2$ relaxation time and Fig. 6b phantom images as function of Fe concentration for Fe_3O_4–Au-PEG in water and $4T_1$ cells. A linear relationship reported for both specimens at all the concentrations. In the respective regimes, it was not observed the agglomeration effects nor precipitation during 40 min of measurement at 7 T. The transverse relaxivity coefficient r_2 (the slope in Fig. 6a; represented by R_2) = 498.1 mM^{-1} s^{-1} for Fe_3O_4–Au -PEG in water. Further, the diagnostic capabilities of these hybrid nanoparticles were tested in in-vitro. After incubation of $4T_1$ cells with Fe_3O_4–Au-PEG for 24 h, the obtained r_2 is reduced to 276.9 mM^{-1} s^{-1}; however, it is still reasonably high for imaging. As compared to the literature, the hybrid Fe_3O_4–Au NPs are more efficient than other Janus NPs (r_2 = 125.5–381.4 mM^{-1} s^{-1}) [150–152]. The main reason of this values of r_2 is the perfect crystallinity which leads toward a stronger local magnetic field in the vicinity of NPs. In addition to the stray field strength, the facets of NPs produce strong stray field gradients ΔB, especially near the 6 corners and 8 edges of the magnetic octahedrons. Furthermore, these nanohybrids were tested in in-vivo MRI. $4T_1$-bearing mice or B16-F10-bearing mice was treated with NP-PEG (6.6 mg kg^{-1} Fe_3O_4), and T_2-weighthed images were captured before, 30 min, 6 h, and 24 h after NPs injection as shown in Fig. 6c. Although 30 min after injection assemble NPs was mainly found in liver, later at 6 and 24 h enhanced tumor contrasting was clearly seen. The assemble NPs peak in malignant tissues was around 6 h after injection. The high accumulation efficiency of these hybrid NPs in malignant lesions (up to 3%) coupled with MRI data makes Fe_3O_4–Au hybrid NPs an attractive platform for tumor theranostics.

Wang et al. [153] have synthesized a folic acid functionalized magnetic plasmonic NPs (F-Au@Fe_3O_4), which were based on Au nanocages (AuNCs) and ultrasmall Fe_3O_4 nanoparticles, to associate in one signal nanosystem several different properties, such as tumor targeting, bright T_1 and dark T_2 dual MRI contrast enhancement. It was observed that UV–vis absorption spectra of the Au nanocage and F-AuNC@Fe_3O_4 in aqueous suspension exhibited very strong and broad absorption from 600 to 800 nm with the maximum absorption at around 750 nm. The contrast capability of these F-AuNC@ Fe_3O_4 for T_1 and T_2 weight MRI at different Fe concentrations has been detected and found high relaxation efficiencies r_1 of 6.263 and an r_2 value of 28.117 mM^{-1} s^{-1}. The high r_1 relaxivity of F-AuNC@ Fe_3O_4 all can be attributed to the large number 5 unpaired electrons of Fe^{3+} ions on the ultrasmall Fe_3O_4 nanoparticle surface. In addition, r_2/r_1 ratio is also an important parameter to evaluate the efficiency of T_1 contrast agents. The r_2/r_1 ratio of F-AuNC@ Fe_3O_4 was 4.48 demonstrating that it can be efficient T_1 contrast agents claiming F-AuNC@ Fe_3O_4 which was the first example that exhibits high r_1 relaxivity value for T_1-weight MR enhanced imaging. Figure 7a, b demonstrated the T_1 and T_2 modal MR images of F-AuNC@Fe_3O_4 with different Fe ion concentrations. The signal enhancement progressively increases with increasing of the F-AuNC@ Fe_3O_4 concentrations, which manifests the potential of F-AuNC@ Fe_3O_4 as powerful multifunctional contrast agent for T_1 and T_2 MRI.
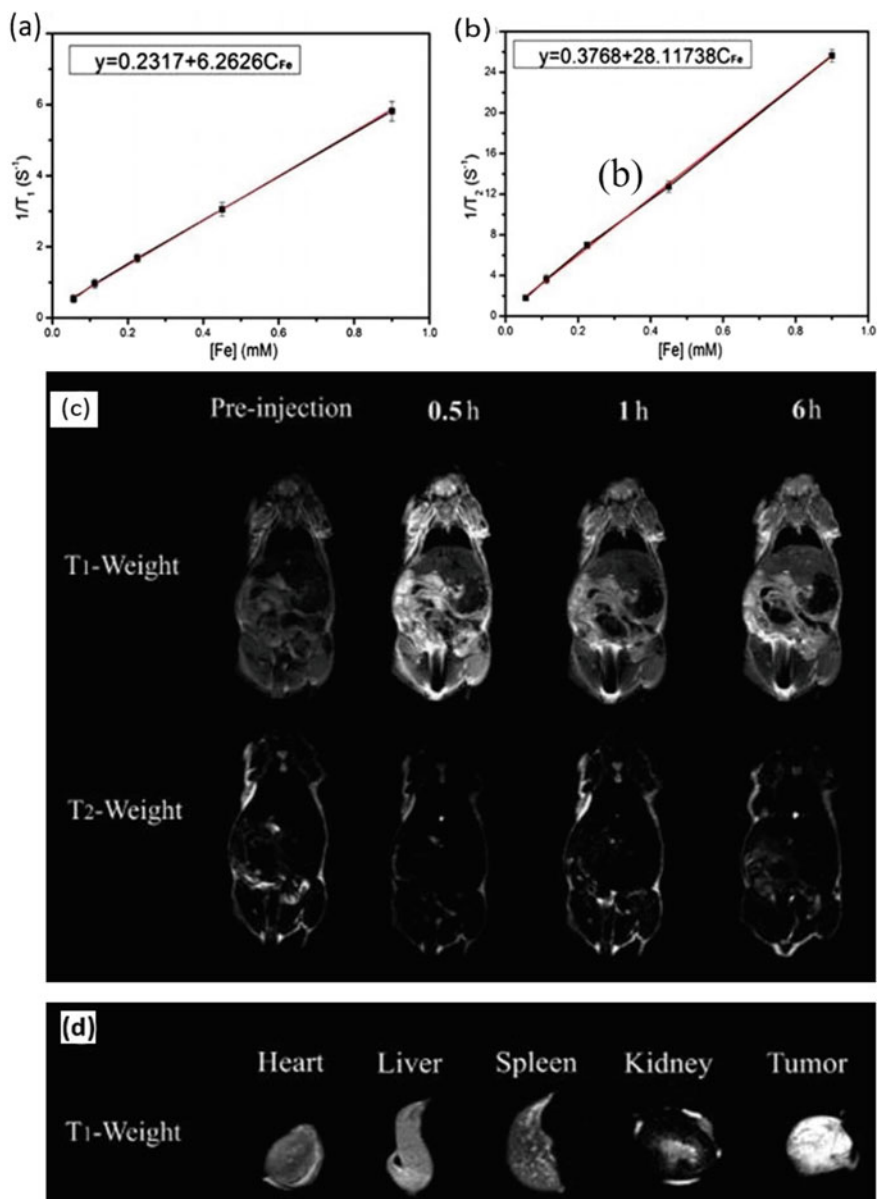
Fig. 7 MRI contrast ability of F-AuNC@Fe$_3$O$_4$. **a**, **b** Plot of $1/T_1$ and $1/T_2$ over Fe concentration, **c** in vivo T_1 and T_2 weight MRI images of nude mice bearing tumor after intravenous injection at different timed intervals, and **d** T_1 and T_2 weighted MR images of various organs from the mice treated with F-AuNC@Fe$_3$O$_4$ after 6 h post-injection. (Reprinted with permission from Ref. [153]. Copyright © 2016, Springer Nature)

Further, for tumor targeting T_1 and T_2 modal MR imaging, T_1 and T_2 modal MRI of tumor-bearing mice were recorded at various time intervals: before injection, 0.5, 1, and 6 h after injection, as shown in Fig. 7c. When compared with pre-injection, a great contrast enhancement (brighten on the T_1-weighted and darken on the T_2 weighted MR images) in the mouse body after post-injection which demonstrates that as-synthesized F-AuNC@ Fe_3O_4 can simultaneously enhance T_1 and T_2 relaxation in the circulating system. The enhanced signal of blood vessel maintained for more than 6 h, which is much longer than that of Gd complex small molecules with a high excrete. It was reported that after 6 h, the T_1 and T_2 contrast intensity in the body of mouse obviously decrease over time, while the contrast intensity in the region of tumor increased over time, which confirm the F-AuNC@Fe_3O_4, has a tendency to be enriched in the tumor tissue. Thus, it is concluded that F-AuNC@ Fe_3O_4 could be used for long-term blood pool T_1 and T_2 modal MRI contrast agent, which is very important in clinical MR imaging. The long-term effect is critical to obtain high-resolution and steady state images. Wu et al. [154] have proposed PEG functionalized magnetic plasmonic NPs, synthesized using sodium dodecyl sulfate (SDS), for their use as multimodal imaging agents. The molecular specificity of the composite nanoparticles was tested on SK-BR-3 breast cancer cells and A-431 keratinocytes and found that the cell-targeting agent demonstrates high cell specificity and was preferentially taken up by cells with the complementary antigen. This biocompatible magneto-plasmonic nanoparticles significantly impacted on the development of point-of-care assays for the detection of circulating tumor cells and in cell therapy with magnetic cell guidance and imaging monitoring.

5.4 Magnetic @Luminescent Nanomaterials

Fluorescent-magnetic nanocomposites can be used simultaneously in confocal fluorescent microscopy and in MRI, so they serve as new dual function contrast agents. In addition, fluorescent-magnetic nanocomposites can be used to perform optical tracking of biological molecules and processes in combination with magnetophoretic manipulation. These multifunctional materials hold great importance as probes and bio-labels for in-vivo cellular imaging. The utilization of multifunctional fluorescent-magnetic nanocomposites as contrast agents has been well reported. These nanocomposites have optimized luminescent behavior and high magnetic or superparamagnetic properties, so these nanohybrids are used as contrast agent in MRI. There is an exponentially increase in the number of new developments per year in the field of nanohybrids and become a fast-evolving branch of science. In magneto-luminescent nanohybrids, it is important to control the spacing between the emitting species and the magnetic, in order to keep both properties unaltered or at least not strongly reduced in the hybrid system. Superparamagnetic NPs (magnetite NPs) and paramagnetic NPs (gadolinium or gadolinium containing NPs) have been synthesized and combined with several emitting species, such as quantum dots, fluorescent metal NPs, fluorescence dyes, or lanthanide doping of either the magnetic NPs themselves

or separate insulating NPs. Paramagnetic Gd^{3+} ions are widely used T_1 MRI contrast agent owing to the existence of seven unpaired 4f electrons. By adding Gd^{3+} and Ln^{3+} ($Ln^{3+} = Er^{3+}, Ho^{3+}, Tm^{3+}$) ions in one nanocrystal, the integration of UCL imaging and MRI has been achieved. Plus, the NCs overcome the leaching of Gd^{3+} ions in Gd^{3+}-chelates contrast agents.

The upconversion nanoparticles (UCNPs) can display both T_1- and T_2-weighted MR imaging if linked with T_2 MR imaging contrast agents. Magnetic NPs such as Fe_3O_4 show a negative T_2 imaging signal with the increase of Fe concentration. Chen et al. [155] prepared PEGylated b-NaGdF4:Yb/Er and b-NaGdF4:Yb/Tm magnetic upconversion nanophosphors with an iron oxide (Fe_3O_4) core, which showed great dual-modal T_1–T_2-weighted MR imaging with the value of r_1 and r_2 being 2.9 mM^{-1} s^{-1} and 204 mM^{-1} s^{-1}, respectively. Interestingly, the positive T_1- and negative T_2-weighted MR imaging become brighter and darker, respectively, with the increase of magnetic UCNPs concentrations. In addition, PEGylated Fe_3O_4@b- NaGdF4: Yb/Tm nanoparticles showed a NIR emission at 800 nm, which is located within 'optical transmission window (700–1000 nm)' of biological tissue. The magnetic upconversion nanoparticles injected into 1 cm thickness of chicken breast displayed extremely bright upconversion photoluminescence, holding excellent projections for MR/UCPL bioimaging. In contrast, Xia and Group [156] investigated the MR imaging potentiality of NaYF4:Tm^{3+},Yb^{3+}@Fe_3O_4 core/shell with shell thickness 5 nm. The r_2 relaxivity of NaYF4:Yb^{3+}, Tm^{3+}@Fe_3O_4 core@shell nanocrystal is 189 mM^{-1} s^{-1}. The second row of Fig. 8a represented a clear view of the negative enhancement effect relative to the concentration, colored T_2-weighted MR images. As the concentration of nanocrystals were increased, colors of the sample changed from orange to green to purple. The T_2 relaxivity coefficient (r_2) of the NaYF4:Yb^{3+}, Tm^{3+}@ Fe_3O_4 nanocrystals could also be calculated from the curve of T_2 versus Fe concentration as shown in Fig. 8b.

Further, Fig. 8c shows a series of in-vivo MR images of lymphatic node tissue over a time sequence at 0, 10, and 30 min, before and after injection with NaYF4:Yb^{3+}, Tm^{3+}@ Fe_3O_4 nanocrystals (1.5 mg/kg diluted in pH 7.2–7.4 PBS. The negative enhanced effect was evident after several minutes of injection and absorbed as the change in the contrast at the lymph node; although the content of the NaYF4: Yb^{3+}, Tm^{3+}@ Fe_3O_4 nanocrystals was low. By comparison of color mapping coronal MR images of the lymphatic node obtained at 0 min (Fig. 8c4), 10 min (Fig. 8c5), and 30 min (Fig. 8c6), it was found that the mean intensity of the signal at the lymph node decreased corresponding to negative enhancements at 10 min and 30 min, respectively.

6   Summary and Future Prospective

To summarize, taking the advantages of the finite-size effect and surface moieties, SPIONs have gained intensive research interest in stem cell labeling as a contrast agent due to their high MR sensitivity, where SPIONs less than 10 nm is utilized as
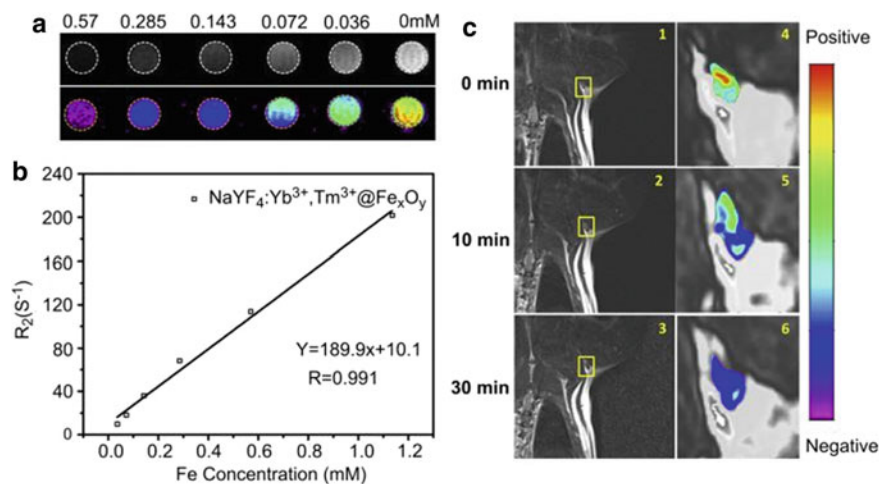
Fig. 8 T2-weighted and color-mapped MR images of various molar concentrations of NaYF4:Yb^{3+}, Tm^{3+}@Fe$_x$O$_y$ nanocrystals. Deionized water (0 mg/mL) used as reference. **b** Relaxation rate R_2 ($1/T_2$) versus various molar concentrations of hydrophilic NaYF4:Yb^{3+}, Tm^{3+}@Fe$_x$O$_y$ nanocrystals at room temperature using a 3 T MRI scanner. **c** MR images of the armpit region after injection with NaYF4:Yb^{3+}, Tm^{3+}@Fe$_x$O$_y$ nanocrystals, and color-mapped coronal images of lymph node at various time. The dose of NaYF4:Yb^{3+}, Tm^{3+}@Fe$_x$O$_y$ nanocrystals is 1.5 mg/kg. (Reprinted with permission from Ref. [156]. Copyright © 2011 Elsevier Ltd. All rights reserved.)

a positive (T_1) contrast agent, and the size between 10 nm to SPM range is utilized as a negative (T_2) contrast agent. To the date, SPIONs-based T_2-CAs for the liver provide dark image as compared to bright MR images of Gd-based T_1-CAs, so were not able to compete against the currently used Gd-based small molecules due to the clinical preference over the dark image of the T_2-CAs [157] and advances in MR sequences and techniques (e.g., dynamic imaging).

Although several advances have been achieved from SPIONs in MRI, still some key elements need to be determined in synthesis and their utilization in in-vivo applications. The liquid phase synthesis methods have resulted in great improvement in size, morphology, crystallinity, and stoichiometry of SPIONs. However, some points need to be tackled in such chemical synthesis routes, which include the enhancement of monodispersity; the more regular and uniform shape/morphology; and the uniform particle size and distribution. These challenges could overcome by reducing the reaction rate (e.g., decrease the reaction temperature and/or concentration of iron precursors) and prolong the reaction time.

Despite the rapid development of different SPIONs, i.e., magnetite/maghemite, magnetic@silica, magnetic@plasmonic, and magnetic@luminescent, advancing their contrast/magnetic properties, several problems remain to be tackled in current technology: (1) the way to detect not only the location but also the function of the labeled cells. This issue could overcome by developing a technique conjugating MRI with other non-invasive imaging modalities, such as positron emission tomography

(PET), single-photon emission computerized tomography (SPECT), ultrasound, and optical imaging [158, 159]; (2) the potential toxicity of SPIONs in vivo after the SPION labeled cells being transplanted into the host, because SPIONs influence not only the labeled cells but also possible to the liver and spleen of the host; and (3) the way to translate cell tracking from pre-clinical models to human. For in-vivo use of SPIONs, pre-clinical studies have to be conducted thoroughly with standardized assays to assess the potential long-term toxicity. Thus, despite recent progress with promising results and approval of SPIONs by the FDA [160], but before moving forward from bench to bedside, the competitiveness with current technologies should be considered. Specially, in case of iron oxide nanoparticles, as Feridex and Resovist were already withdrawn and are no longer commercially available [161]. From a technical point of view, external magnetic setups that can precisely focus on a diseased target located in deep tissue with adequate strength are urgently needed. SPIONs may become a very promising candidates for MRI, and other several forefront applications in biomedicine in the near future if above-mentioned issues are resolved.

References

1. Cunningham CH, Arai T, Yang PC, McConnell MV, Pauly JM, Conolly SM (2005) Positive contrast magnetic resonance imaging of cells labeled with magnetic nanoparticles. Magn Reson Med 53:999–1005. https://doi.org/10.1002/mrm.20477
2. Fan HM, Olivo M, Shuter B, Yi JB, Bhuvaneswari R, Tan HR, Xing GC, Ng CT, Liu L, Lucky SS, Bay BH, Ding J (2010) Quantum dot capped magnetite nanorings as high performance nanoprobe for multiphoton fluorescence and magnetic resonance imaging. J Am Chem Soc 132:14803–14811. https://doi.org/10.1021/ja103738t
3. Matsumoto Y, Jasanoff A (2008) T2 relaxation induced by clusters of superparamagnetic nanoparticles: Monte Carlo simulations. Magn Reson Imaging 26:994–998. https://doi.org/10.1016/j.mri.2008.01.039
4. Babes L, Denizot B, Tanguy G, Le Jeune JJ, Jallet P (1999) Synthesis of iron oxide nanoparticles used as MRI contrast agents: a parametric study. J Colloid Interface Sci 212:474–482. https://doi.org/10.1006/jcis.1998.6053
5. Smolensky ED, Park HYE, Berquó TS, Pierre VC (2011) Surface functionalization of magnetic iron oxide nanoparticles for MRI applications—effect of anchoring group and ligand exchange protocol. Contrast Media Mol Imaging 6:189–199. https://doi.org/10.1002/cmmi.417
6. Ho D, Sun X, Sun S (2011) Monodisperse magnetic nanoparticles for theranostic applications. Acc Chem Res 44:875–882. https://doi.org/10.1021/ar200090c
7. Neuberger T, Schöpf B, Hofmann H, Hofmann M, Von Rechenberg B (2005) Superparamagnetic nanoparticles for biomedical applications: possibilities and limitations of a new drug delivery system. J Magn Mag Mater. North-Holland, pp 483–496

8. Cheng Y, Zhao L, Li Y, Xu T (2011) Design of biocompatible dendrimers for cancer diagnosis and therapy: current status and future perspectives. Chem Soc Rev 40:2673. https://doi.org/10.1039/c0cs00097c

9. Sandiford L, Phinikaridou A, Protti A, Meszaros LK, Cui X, Yan Y, Frodsham G, Williamson PA, Gaddum N, Botnar RM, Blower PJ, Green MA, De Rosales RTM (2013) Bisphosphonate-anchored pegylation and radiolabeling of superparamagnetic iron oxide: long-circulating nanoparticles for in vivo multimodal (T1 MRI-SPECT) imaging. ACS Nano 7:500–512. https://doi.org/10.1021/nn3046055

10. Jung H, Park B, Lee C, Cho J, Suh J, Park JY, Kim YR, Kim J, Cho G, Cho HJ (2014) Dual MRI T1 and T2(*) contrast with size-controlled iron oxide nanoparticles. Nanomed Nanotechnol Biol Med 10:1679–1689. https://doi.org/10.1016/j.nano.2014.05.003

11. Bowen CV, Zhang X, Saab G, Gareau PJ, Rutt BK (2002) Application of the static dephasing regime theory to superparamagnetic iron-oxide loaded cells. Magn Reson Med 48:52–61. https://doi.org/10.1002/mrm.10192

12. Hergt R, Dutz S, Zeisberger M, Gawalek W (2006) Nanocrystalline iron oxide and Ba ferrite particles in the superparamagnetism-ferromagnetism transition range with ferrofluid applications. J Phys Condens Matter 18:2527–2542. https://doi.org/10.1088/0953-8984/18/38/S01

13. M. Benz (2012) Superparamagnetism : theory and applications

14. Jönsson PE (2004) Superparamagnetism and spin glass dynamics of interacting magnetic nanoparticle systems. Adv Chem Phys 128:191–248

15. Brown WF (1963) Thermal fluctuations of a single-domain particle. Phys Rev 130:1677–1686. https://doi.org/10.1103/PhysRev.130.1677

16. Papaefthymiou GC (2009) Nanoparticle magnetism. Nano Today 4:438–447. https://doi.org/10.1016/j.nantod.2009.08.006

17. Benz M (2012) Superparamagnetism : theory and applications-discussion of two papers on magnetic nanoparticles

18. Zheng M, Wu XC, Zou BS, Wang YJ (1998) Magnetic properties of nanosized $MnFe_2O_4$ particles. J Magn Magn Mater 183:152–156. https://doi.org/10.1016/S0304-8853(97)01057-3

19. Vedantam TS, Liu JP, Zeng H, Sun S (2003) Thermal stability of self-assembled FePt nanoparticles. J Appl Phys Am Inst Phys AIP, 7184–7186

20. Skomski R (2004) Nanomagnetic scaling. J Magn Magn Mater 272–276:1476–1481. https://doi.org/10.1016/j.jmmm.2003.12.175

21. Kodama R (1999) Magnetic nanoparticles. J Magn Magn Mater 200:359–372. https://doi.org/10.1016/S0304-8853(99)00347-9

22. Lifshitz IM, Slyozov VV (1961) The kinetics of precipitation from supersaturated solid solutions. J Phys Chem Solids 19:35–50. https://doi.org/10.1016/0022-3697(61)90054-3

23. Binder K (1986) Monte Carlo methods in statistical physics. Springer, Berlin

24. Jamet M, Wernsdorfer W, Thirion C, Dupuis V, Mélinon P, Pérez A, Mailly D (2004) Magnetic anisotropy in single clusters. Phys Rev B 69:024401. https://doi.org/10.1103/PhysRevB.69.024401

25. Eastham DA, Kirkman IW (2000) Highly enhanced orbital magnetism on cobalt cluster surfaces. J Phys Condens Matter 12:L525–L532. https://doi.org/10.1088/0953-8984/12/31/101

26. Yanes R, Chubykalo-Fesenko O, Kachkachi H, Garanin DA, Evans R, Chantrell RW (2007) Effective anisotropies and energy barriers of magnetic nanoparticles with Neel surface anisotropy. https://doi.org/10.1103/PhysRevB.76.064416

27. Respaud M, Broto JM, Rakoto H, Fert AR, Thomas L, Barbara B, Verelst M, Snoeck E, Lecante P, Mosset A, Osuna J, Ely TO, Amiens C, Chaudret B (1998) Surface effects on the magnetic properties of ultrafine cobalt particles. Phys Rev B 57:2925–2935. https://doi.org/10.1103/PhysRevB.57.2925

28. Bødker F, Mørup S, Linderoth S (1994) Surface effects in metallic iron nanoparticles. Phys Rev Lett 72:282–285. https://doi.org/10.1103/PhysRevLett.72.282

29. Luis F, Torres JM, García LM, Bartolomé J, Stankiewicz J, Petroff F, Fettar F, Maurice J-L, Vaurès A (2002) Enhancement of the magnetic anisotropy of nanometer-sized Co clusters: influence of the surface and of interparticle interactions. Phys Rev B 65:094409. https://doi.org/10.1103/PhysRevB.65.094409

30. Kainz QM, Reiser O (2014) Polymer- and dendrimer-coated magnetic nanoparticles as versatile supports for catalysts, scavengers, and reagents. Acc Chem Res 47:667–677. https://doi.org/10.1021/ar400236y

31. Sun S (2006) Recent advances in chemical synthesis, self-assembly, and applications of FePt nanoparticles. Adv Mater 18:393–403

32. Hyeon T (2003) Chemical synthesis of magnetic nanoparticles. Chem Commun 3:927–934. https://doi.org/10.1039/b207789b

33. Yadav SK Nanoscale materials in targeted drug delivery, theragnosis and tissue regeneration

34. Das R, Cardarelli JA, Phan MH, Srikanth H (2019) Magnetically tunable iron oxide nanotubes for multifunctional biomedical applications. J Alloys Compd 789:323–329. https://doi.org/10.1016/j.jallcom.2019.03.024

35. Pereira C, Pereira AM, Fernandes C, Rocha M, Mendes R, Fernández-García MP, Guedes A, Tavares PB, Grenèche J-M, Araújo JP, Freire C (2012) Superparamagnetic MFe_2O_4 (M = Fe Co, Mn) nanoparticles: tuning the particle size and magnetic properties through a novel one-step coprecipitation route. Chem Mater 24:1496–1504. https://doi.org/10.1021/cm300301c

36. Chekina N, Horák D, Jendelová P, Trchová M, Bene MJ, Hrubý M, Herynek V, Turnovcová K, Syková E (2011) Fluorescent magnetic nanoparticles for biomedical applications. J Mater Chem 21:7630–7639. https://doi.org/10.1039/c1jm10621j

37. Miguel-Sancho N, Bomatí-Miguel O, Colom GO, Salvador J-P, Marco M-P, Santamaría J, De Bioingeniería C (2011) Development of stable, water-dispersible, and biofunctionalizable superparamagnetic iron oxide nanoparticles. Chem Mater 23:2795–2802. https://doi.org/10.1021/cm1036452

38. Ye F, Laurent S, Fornara A, Astolfi L, Qin J, Roch A, Martini A, Toprak MS, Muller RN, Muhammed M (2012) Uniform mesoporous silica coated iron oxide nanoparticles as a highly efficient, nontoxic MRI T 2 contrast agent with tunable proton relaxivities. Contrast Media Mol Imaging 7:460–468. https://doi.org/10.1002/cmmi.1473

39. Hachani R, Lowdell M, Birchall M, Hervault A, Mertz D, Begin-Colin S, Thanh K (2016) Polyol synthesis, functionalisation, and biocompatibility studies of superparamagnetic iron oxide nanoparticles as potential MRI contrast agents. Nanoscale 8:3278–3287. https://doi.org/10.1039/c5nr03867g

40. Huang J-H, Parab HJ, Liu R-S, Lai T-C, Hsiao M, Chen C-H, Sheu H-S, Chen J-M, Tsai D-P, Hwu Y-K (2008) Investigation of the growth mechanism of iron oxide nanoparticles via a seed-mediated method and its cytotoxicity studies. J Phys Chem C 112:15684–15690. https://doi.org/10.1021/jp803452j

41. Zhu N, Ji H, Yu P, Niu J, Farooq M, Akram M, Udego I, Li H, Niu X, Zhu N, Ji H, Yu P, Niu J, Farooq MU, Akram MW, Udego IO, Li H, Niu X (2018) Surface modification of magnetic iron oxide nanoparticles. Nanomaterials 8:810. https://doi.org/10.3390/nano8100810

42. Hyeon T, Lee SS, Park J, Chung Y, Na HB (2001) Synthesis of highly crystalline and monodisperse maghemite nanocrystallites without a size-selection process. J Am Chem Soc 123:12798–12801. https://doi.org/10.1021/ja016812s

43. Park C, Walker J, Tannenbaum R, Stiegman AE, Frydrych J, Machala L (2009) Sol−gel-derived iron oxide thin films on silicon: surface properties and interfacial chemistry. ACS Appl Mater Interfaces 1:1843–1846. https://doi.org/10.1021/am900362x

44. Lu Y, Yin Y, Mayers BTA, Xia Y (2002) Modifying the surface properties of superparamagnetic iron oxide nanoparticles through a sol−gel approach. Nano Lett 2:183–186. https://doi.org/10.1021/NL015681Q

45. Park CD, Magana D, Stiegman AE (2007) High-quality Fe and γ-Fe_2O_3 magnetic thin films from an epoxide-catalyzed sol-gel process. Chem Mater 19:677–683. https://doi.org/10.1021/cm0617079

46. Popescu RC, Andronescu E, Vasile BS (2019) Recent advances in magnetite Nanoparticle functionalization for nanomedicine. Nanomater (Basel, Switzerland) 9. https://doi.org/10.3390/nano9121791

47. Itoh H, Sugimoto T (2003) Systematic control of size, shape, structure, and magnetic properties of uniform magnetite and maghemite particles. J Colloid Interface Sci 265:283–295. https://doi.org/10.1016/S0021-9797(03)00511-3

48. Ling D, Lee N, Hyeon T (2015) Chemical synthesis and assembly of uniformly sized iron oxide nanoparticles for medical applications. Acc Chem Res 48:1276–1285. https://doi.org/10.1021/acs.accounts.5b00038

49. Dias CSB, Hanchuk TDM, Wender H, Shigeyosi WT, Kobarg J, Rossi AL, Tanaka MN, Cardoso MB, Garcia F (2017) Shape tailored magnetic nanorings for intracellular hyperthermia cancer therapy. Sci Rep 7:14843. https://doi.org/10.1038/s41598-017-14633-0

50. Cote LJ, Teja AS, Wilkinson AP, Zhang ZJ (2002) Continuous hydrothermal synthesis and crystallization of magnetic oxide nanoparticles. J Mater Res Res 17:2410–2416. https://doi.org/10.1557/JMR.2002.0352

51. Pang YL, Lim S, Ong HC, Chong WT (2016) Research progress on iron oxide-based magnetic materials: synthesis techniques and photocatalytic applications. Ceram Int 42:9–34. https://doi.org/10.1016/j.ceramint.2015.08.144

52. Sheng W, Liu J, Liu S, Lu Q, Kaplan Ac DL, Zhu H (2014) One-step synthesis of biocompatible magnetite/silk fibroin core-shell nanoparticles. J Mater Chem B 2:7394–7402. https://doi.org/10.1039/c4tb01125b

53. Deepak FL, Bañobre-López M, Carbó-Argibay E, Cerqueira MF, Piñeiro-Redondo Y, Rivas J, Thompson CM, Kamali S, Rodríguez-Abreu C, Kovnir K, Kolenko YV (2015) A systematic study of the structural and magnetic properties of Mn-, Co-, and Ni-doped colloidal magnetite nanoparticles. J Phys Chem C 119:11947–11957. https://doi.org/10.1021/acs.jpcc.5b01575

54. Rabenau A (1985) The role of hydrothermal synthesis in preparative chemistry. Angew Chemie Int Ed English 24:1026–1040. https://doi.org/10.1002/anie.198510261

55. Reddy LH, Arias JL, Nicolas J, Couvreur P (2012) Magnetic nanoparticles: design and characterization, toxicity and biocompatibility, pharmaceutical and biomedical applications. Chem Rev 112:5818–5878

56. Ali A, Zafar H, Zia M, ul Haq I, Phull AR, Ali JS, Hussain A (2016) Synthesis, characterization, applications, and challenges of iron oxide nanoparticles. Nanotechnol Sci Appl 9:49–67

57. Hu F, Jia Q, Li Y, Gao M (2011) Facile synthesis of ultrasmall PEGylated iron oxide nanoparticles for dual-contrast T_1 - and T_2 - weighted magnetic resonance imaging. Nanotechnology 22:245604. https://doi.org/10.1088/0957-4484/22/24/245604

58. Li Z, Tan B, Allix M, Cooper AI, Rosseinsky MJ (2008) Direct coprecipitation route to monodisperse dual-functionalized magnetic iron oxide nanocrystals without size selection. Small 4:231–239. https://doi.org/10.1002/smll.200700575

59. Tromsdorf UI, Bruns OT, Salmen SC, Beisiegel U, Weller H (2009) A highly effective, nontoxic T1 MR contrast agent based on ultrasmall PEGylated iron oxide nanoparticles. Nano Lett 9:4434–4440. https://doi.org/10.1021/nl902715v

60. Li Z, Yi PW, Sun Q, Lei H, Li Zhao H, Zhu ZH, Smith SC, Lan MB, Lu GQM (2012) Ultrasmall water-soluble and biocompatible magnetic iron oxide nanoparticles as positive and negative dual contrast agents. Adv Funct Mater 22:2387–2393. https://doi.org/10.1002/adfm.201103123

61. Tao C, Chen Y, Wang D, Cai Y, Zheng Q, An L, Lin J, Tian Q, Yang S (2019) Macromolecules with different charges, lengths, and coordination groups for the coprecipitation synthesis of magnetic iron oxide nanoparticles as T1 MRI contrast agents. Nanomaterials 9:699. https://doi.org/10.3390/nano9050699

62. Kovalenko MV, Bodnarchuk MI, Lechner RT, Hesser G, Friedrich Schäffler A, Heiss W (2007) Fatty acid salts as stabilizers in size- and shape-controlled nanocrystal synthesis: the case of inverse spinel iron oxide. J Am Chem Soc 129:6352–6353. https://doi.org/10.1021/JA0692478

63. Yang H, Zhuang Y, Sun Y, Dai A, Shi Xiangyang X, Wu D, Li F, Hu H, Yang S (2011) Targeted dual-contrast T1- and T2-weighted magnetic resonance imaging of tumors using multifunctional gadolinium-labeled superparamagnetic iron oxide nanoparticles. Biomaterials 32:4584–4593. https://doi.org/10.1016/j.biomaterials.2011.03.018

64. Zhang Q, Yin T, Gao G, Shapter JG, Lai W, Huang P, Qi W, Song J, Cui D (2017) Multifunctional Core@Shell magnetic nanoprobes for enhancing targeted magnetic resonance imaging and fluorescent labeling in vitro and in vivo. ACS Appl Mater Interfaces 9:17777–17785. https://doi.org/10.1021/acsami.7b04288

65. Park J, An K, Hwang Y, Park JEG, Noh HJ, Kim JY, Park JH, Hwang NM, Hyeon T (2004) Ultra-large-scale syntheses of monodisperse nanocrystals. Nat Mater 3:891–895. https://doi.org/10.1038/nmat1251

66. Sun S, Zeng H, Robinson DB, Raoux S, Rice PM, Wang SX, Li G (2004) Monodisperse MFe_2O_4 (M = Fe Co, Mn) nanoparticles. J Am Chem Soc 126:273–279. https://doi.org/10.1021/ja0380852

67. Park J, Lee E, Hwang NM, Kang M, Sung CK, Hwang Y, Park JG, Noh HJ, Kim JY, Park JH, Hyeon T (2005) One-nanometer-scale size-controlled synthesis of monodisperse magnetic iron oxide nanoparticles. Angew Chemie Int Ed 44:2872–2877. https://doi.org/10.1002/anie.200461665

68. Sun S, Zeng H (2002) Size-controlled synthesis of magnetite nanoparticles. J Am Chem Soc 124:8204–8205. https://doi.org/10.1021/ja026501x

69. Wei H, Bruns OT, Kaul MG, Hansen EC, Barch M, Wiśniowska A, Chen O, Chen Y, Li N, Okada S, Cordero JM, Heine M, Farrar CT, Montana DM, Adam G, Ittrich H, Jasanoff A, Nielsen P, Bawendi MG (2017) Exceedingly small iron oxide nanoparticles as positive MRI contrast agents. Proc Natl Acad Sci U S A 114:2325–2330. https://doi.org/10.1073/pnas.1620145114

70. Gaglia JL, Harisinghani M, Aganj I, Wojtkiewicz GR, Hedgire S, Benoist C, Mathis D, Weissleder R (2015) Noninvasive mapping of pancreatic inflammation in recent-onset type-1 diabetes patients. Proc Natl Acad Sci U S A 112:2139–2144. https://doi.org/10.1073/pnas.1424993112

71. Bennett CL, Qureshi ZP, Sartor AO, Norris LB, Murday A, Xirasagar S, Thomsen HS (2012) History of nephrology gadolinium-induced nephrogenic systemic fibrosis: the rise and fall of an iatrogenic disease. Clin Kidney J 5:82–88. https://doi.org/10.1093/ckj/sfr172

72. Bin NH, Lee JH, An K, Il PY, Park M, Lee IS, Nam D-H, Kim ST, Kim S-H, Kim S-W, Lim K-H, Kim K-S, Kim S-O, Hyeon T (2007) Development of a T1 contrast agent for magnetic resonance imaging using MnO nanoparticles. Angew Chemie 119:5493–5497. https://doi.org/10.1002/ange.200604775

73. Hifumi H, Yamaoka S, Tanimoto A, Citterio D, Suzuki K (2006) Gadolinium-based hybrid nanoparticles as a positive MR contrast agent. J Am Chem Soc 128:15090–15091. https://doi.org/10.1021/ja066442d

74. Kim BH, Lee N, Kim H, An K, Il PY, Choi Y, Shin K, Lee Y, Kwon SG, Bin NH, Park JG, Ahn TY, Kim YW, Moon WK, Choi SH, Hyeon T (2011) Large-scale synthesis of uniform and extremely small-sized iron oxide nanoparticles for high-resolution T 1 magnetic resonance imaging contrast agents. J Am Chem Soc 133:12624–12631. https://doi.org/10.1021/ja203340u

75. Wu L, Mendoza-Garcia A, Li Q, Sun S (2016) Organic phase syntheses of magnetic nanoparticles and their applications. Chem Rev 116:10473–10512

76. Hufschmid R, Arami H, Ferguson RM, Gonzales M, Teeman E, Brush LN, Browning ND, Krishnan KM (2015) Synthesis of phase-pure and monodisperse iron oxide nanoparticles by thermal decomposition. Nanoscale 7:11142–11154. https://doi.org/10.1039/c5nr01651g

77. Chen Z (2012) Size and shape controllable synthesis of monodisperse iron oxide nanoparticles by thermal decomposition of iron oleate complex. Synth React Inorganic Met Nano-Metal Chem 42:1040–1046. https://doi.org/10.1080/15533174.2012.680126

78. Roca AG, Veintemillas-Verdaguer S, Port M, Robic C, Serna CJ, Morales MP (2009) Effect of nanoparticle and aggregate size on the relaxometric properties of MR contrast agents based

on high quality magnetite nanoparticles. J Phys Chem B 113:7033–7039. https://doi.org/10.1021/jp807820s

79. Wan J, Cai W, Meng X, Liu E (2007) Monodisperse water-soluble magnetite nanoparticles prepared by polyol process for high-performance magnetic resonance imaging. Chem Commun 5004–5006. https://doi.org/10.1039/b712795b

80. Cheng C, Xu F, Gu H (2011) Facile synthesis and morphology evolution of magnetic iron oxide nanoparticles in different polyol processes. New J Chem 35:1072–1079. https://doi.org/10.1039/c0nj00986e

81. Carenza E, Barceló V, Morancho A, Montaner J, Rosell A, Roig A (2014) Rapid synthesis of water-dispersible superparamagnetic iron oxide nanoparticles by a microwave-assisted route for safe labeling of endothelial progenitor cells. Acta Biomater 10:3775–3785. https://doi.org/10.1016/j.actbio.2014.04.010

82. Pellico J, Ruiz-Cabello J, Fernández-Barahona I, Gutiérrez L, Lechuga-Vieco AV, Enríquez JA, Morales MP, Herranz F (2017) One-step fast synthesis of nanoparticles for MRI: coating chemistry as the key variable determining positive or negative contrast. Langmuir 33:10239–10247. https://doi.org/10.1021/acs.langmuir.7b01759

83. Pellico J, Ruiz-Cabello J, Saiz-Alía M, del Rosario G, Caja S, Montoya M, Fernández de Manuel L, Morales MP, Gutiérrez L, Galiana B, Enríquez JA, Herranz F (2016) Fast synthesis and bioconjugation of 68Ga core-doped extremely small iron oxide nanoparticles for PET/MR imaging. Contrast Media Mol Imaging 11:203–210. https://doi.org/10.1002/cmmi.1681

84. Bhavesh R, Lechuga-Vieco AV, Ruiz-Cabello J, Herranz F (2015) T1-MRI fluorescent iron oxide nanoparticles by microwave assisted synthesis. Nanomaterials 5:1880–1890. https://doi.org/10.3390/nano5041880

85. Hu L, Percheron A, Chaumont D, Brachais CH (2011) Microwave-assisted one-step hydrothermal synthesis of pure iron oxide nanoparticles: magnetite, maghemite and hematite. J Sol-Gel Sci Technol 60:198–205. https://doi.org/10.1007/s10971-011-2579-4

86. Bano S, Nazir S, Nazir A, Munir S, Mahmood T, Afzal M, Ansari FL, Mazhar K (2016) Microwave-assisted green synthesis of superparamagnetic nanoparticles using fruit peel extracts: surface engineering, T2 relaxometry, and photodynamic treatment potential. Int J Nanomed 11:3833–3848. https://doi.org/10.2147/IJN.S106553

87. Williams MJ, Sánchez E, Aluri ER, Douglas FJ, Maclaren DA, Collins OM, Cussen EJ, Budge JD, Sanders LC, Michaelis M, Smales CM, Cinatl J, Lorrio S, Krueger D, De Rosales RTM, Corr SA (2016) Microwave-assisted synthesis of highly crystalline, multifunctional iron oxide nanocomposites for imaging applications. RSC Adv 6:83520–83528. https://doi.org/10.1039/c6ra11819d

88. Lee N, Yoo D, Ling D, Cho MH, Hyeon T, Cheon J (2015) Iron oxide based nanoparticles for multimodal imaging and magnetoresponsive therapy. Chem Rev 115:10637–10689

89. Ling D, Park W, Park SJ, Lu Y, Kim KS, Hackett MJ, Kim BH, Yim H, Jeon YS, Na K, Hyeon T (2014) Multifunctional tumor pH-sensitive self-assembled nanoparticles for bimodal imaging and treatment of resistant heterogeneous tumors. J Am Chem Soc 136:5647–5655. https://doi.org/10.1021/ja4108287

90. Ling D, Hyeon T (2013) Chemical design of biocompatible iron oxide nanoparticles for medical applications. Small 9:1450–1466

91. Callaghan PT (1991) Principles of nuclear magnetic resonance microscopy. Clarendon Press Oxford, Oxford University Press, Oxford

92. Andrew ER (1955) Nuclear magnetic resonance. Cambridge University Press

93. Morris GA (2009) Spin dynamics: basics of nuclear magnetic resonance. In: Levitt MH (ed), 2nd edn. Wiley Chichester. 2008. pp xxv + 714. ISBN 978-0-470-51118-3(hbk) 978-0-470-51117-6 (pbk). NMR Biomed 22:240–241. https://doi.org/10.1002/nbm.1356

94. Stuber M, Gilson WD, Schär M, Kedziorek DA, Hofmann LV, Shah S, Vonken EJ, Bulte JWM, Kraitchman DL (2007) Positive contrast visualization of iron oxide-labelled stem cells using inversion-recovery with ON-resonant water suppression (IRON). Magn Reson Med 58:1072–1077. https://doi.org/10.1002/mrm.21399

95. Bin NH, Hyeon T (2009) Nanostructured T1 MRI contrast agents. J Mater Chem 19:6267–6273. https://doi.org/10.1039/b902685a

96. Caravan P, Ellison JJ, McMurry TJ, Lauffer RB (1999) Gadolinium(III) chelates as MRI contrast agents: structure, dynamics, and applications. Chem Rev 99:2293–2352. https://doi.org/10.1021/cr980440x

97. Caravan P (2006) Strategies for increasing the sensitivity of gadolinium based MRI contrast agents. Chem Soc Rev 35:512–523. https://doi.org/10.1039/b510982p

98. Penfield JG, Reilly RF (2007) What nephrologists need to know about gadolinium. Nat Clin Pract Nephrol 3:654–668

99. McDonald RJ, McDonald JS, Kallmes DF, Jentoft ME, Murray DL, Thielen KR, Williamson EE, Eckel LJ (2015) Intracranial gadolinium deposition after contrast-enhanced MR imaging. Radiology 275:772–782. https://doi.org/10.1148/radiol.15150025

100. Kanal E, Tweedle MF (2015) Residual or retained gadolinium: practical implications for radiologists and our patients. Radiology 275:630–634

101. Javed Y, Akhtar K, Anwar H, Jamil Y (2017) MRI based on iron oxide nanoparticles contrast agents: effect of oxidation state and architecture. J Nanopart Res 19:1–25

102. Levy M, Luciani N, Alloyeau D, Elgrabli D, Deveaux V, Pechoux C, Chat S, Wang G, Vats N, Gendron F, Factor C, Lotersztajn S, Luciani A, Wilhelm C, Gazeau F (2011) Long term in vivo biotransformation of iron oxide nanoparticles. Biomaterials 32:3988–3999. https://doi.org/10.1016/j.biomaterials.2011.02.031

103. Regt de, Dijk van, Mullen van, Schram D, van Dijk J (1995) Components of continuum radiation in an inductively coupled plasma. J Phys D Appl Phys 28:40–46. https://doi.org/10.1088/0022-3727

104. Linderoth S, Hendriksen PV, Bødker F, Wells S, Davies K, Charles SW, Mørup S (1994) On spin-canting in maghemite particles. J Appl Phys 75:6583–6585. https://doi.org/10.1063/1.356902

105. Morales MP, Veintemillas-Verdaguer S, Montero MI, Serna CJ, Roig A, Casas LI, Martínez B, Sandiumenge F (1999) Surface and internal spin canting in γ-Fe$_2$O$_3$ nanoparticles. Chem Mater 11:3058–3064. https://doi.org/10.1021/cm991018f

106. Chan N, Laprise-Pelletier M, Chevallier P, Bianchi A, Fortin MA, Oh JK (2014) Multidentate block-copolymer-stabilized ultrasmall superparamagnetic iron oxide nanoparticles with enhanced colloidal stability for magnetic resonance imaging. Biomacromol 15:2146–2156. https://doi.org/10.1021/bm500311k

107. Lee SH, Kim BH, Bin NH, Hyeon T (2014) Paramagnetic inorganic nanoparticles as T1 MRI contrast agents. Wiley Interdiscip Rev Nanomed Nanobiotechnol 6:196–209. https://doi.org/10.1002/wnan.1243

108. Kucheryavy P, He J, John VT, Maharjan P, Spinu L, Goloverda GZ, Kolesnichenko VL (2013) Superparamagnetic iron oxide nanoparticles with variable size and an iron oxidation state as prospective imaging agents. Langmuir 29:710–716. https://doi.org/10.1021/la3037007

109. Ai H (2011) Layer-by-layer capsules for magnetic resonance imaging and drug delivery. Adv Drug Deliv Rev 63:772–788. https://doi.org/10.1016/j.addr.2011.03.013

110. Shapiro EM, Skrtic S, Sharer K, Hill JM, Dunbar CE, Koretsky AP (2004) MRI detection of single particles for cellular imaging. Proc Natl Acad Sci USA 101:10901–10906. https://doi.org/10.1073/pnas.0403918101

111. Gossuin Y, Gillis P, Hocq A, Vuong QL, Roch A (2009) Magnetic resonance relaxation properties of superparamagnetic particles. Wiley Interdiscip Rev Nanomed Nanobiotechnol 1:299–310. https://doi.org/10.1002/wnan.36

112. Brooks RA (2002) T2-shortening by strongly magnetized spheres: a chemical exchange model. Magn Reson Med 47:388–391. https://doi.org/10.1002/mrm.10064

113. Brooks RA, Moiny F, Gillis P (2002) On T2-shortening by strongly magnetized spheres: a partial refocusing model. Magn Reson Med 47:257–263. https://doi.org/10.1002/mrm.10059

114. Brooks RA, Moiny F, Gillis P (2001) On T2-shortening by weakly magnetized particles: the chemical exchange model. Magn Reson Med 45:1014–1020. https://doi.org/10.1002/mrm.1135

115. Jun YW, Huh YM, Choi JS, Lee JH, Song HT, Kim S, Yoon S, Kim KS, Shin JS, Suh JS, Cheon J (2005) Nanoscale size effect of magnetic nanocrystals and their utilization for cancer diagnosis via magnetic resonance imaging. J Am Chem Soc 127:5732–5733. https://doi.org/10.1021/ja0422155

116. Moroz P, Metcalf C, Gray BN (2003) Histologic analysis of liver tissue following hepatic arterial infusion of ferromagnetic particles in a rabbit tumour model. Biometals 16:455–464. https://doi.org/10.1023/A:1022555431476

117. Lee N, Kim H, Choi SH, Park M, Kim D, Kim HC, Choi Y, Lin S, Kim BH, Jung HS, Kim H, Park KS, Moon WK, Hyeon T (2011) Magnetosome-like ferrimagnetic iron oxide nanocubes for highly sensitive MRI of single cells and transplanted pancreatic islets. Proc Natl Acad Sci U S A 108:2662–2667. https://doi.org/10.1073/pnas.1016409108

118. Lee N, Choi Y, Lee Y, Park M, Moon WK, Choi SH, Hyeon T (2012) Water-dispersible ferrimagnetic iron oxide nanocubes with extremely high r 2 relaxivity for highly sensitive in vivo MRI of tumors. Nano Lett 12:3127–3131. https://doi.org/10.1021/nl3010308

119. Pöselt E, Kloust H, Tromsdorf U, Janschel M, Hahn C, Maßlo C, Weller H (2012) Relaxivity optimization of a pegylated iron-oxide-based negative magnetic resonance contrast agent for T 2-weighted spin-echo imaging. ACS Nano 6:1619–1624. https://doi.org/10.1021/nn204591r

120. Yoon TJ, Lee H, Shao H, Hilderbrand SA, Weissleder R (2011) Multicore assemblies potentiate magnetic properties of biomagnetic nanoparticles. Adv Mater 23:4793–4797. https://doi.org/10.1002/adma.201102948

121. Lan F, Hu H, Jiang W, Liu K, Zeng X, Wu Y, Gu Z (2012) Synthesis of superparamagnetic Fe_3O_4/PMMA/SiO_2 nanorattles with periodic mesoporous shell for lysozyme adsorption. Nanoscale 4:2264–2267. https://doi.org/10.1039/c2nr12125e

122. Perez JM, Josephson L, O'Loughlin T, Högemann D, Weissleder R (2002) Magnetic relaxation switches capable of sensing molecular interactions. Nat Biotechnol 20:816–820. https://doi.org/10.1038/nbt720

123. Liu G, Wang Z, Lu J, Xia C, Gao F, Gong Q, Song B, Zhao X, Shuai X, Chen X, Ai H, Gu Z (2011) Low molecular weight alkyl-polycation wrapped magnetite nanoparticle clusters as MRI probes for stem cell labeling and in vivo imaging. Biomaterials 32:528–537. https://doi.org/10.1016/j.biomaterials.2010.08.099

124. Joshi HM, Lin YP, Aslam M, Prasad PV, Schultz-Sikma EA, Edelman R, Meade T, Dravid VP (2009) Effects of shape and size of cobalt ferrite nanostructures on their MRI contrast and thermal activation. J Phys Chem C 113:17761–17767. https://doi.org/10.1021/jp905776g

125. Bárcena C, Sra AK, Chaubey GS, Khemtong C, Liu JP, Gao J (2008) Zinc ferrite nanoparticles as MRI contrast agents. Chem Commun 2224–2226. https://doi.org/10.1039/b801041b

126. Lee JH, Huh YM, Jun YW, Seo JW, Jang JT, Song HT, Kim S, Cho EJ, Yoon HG, Suh JS, Cheon J (2007) Artificially engineered magnetic nanoparticles for ultra-sensitive molecular imaging. Nat Med 13:95–99. https://doi.org/10.1038/nm1467

127. Jang JT, Nah H, Lee JH, Moon SH, Kim MG, Cheon J (2009) Critical enhancements of MRI contrast and hyperthermic effects by dopant-controlled magnetic nanoparticles. Angew Chemie Int Ed 48:1234–1238. https://doi.org/10.1002/anie.200805149

128. Bulte JWM, Kraitchman DL (2004) Iron oxide MR contrast agents for molecular and cellular imaging. NMR Biomed 17:484–499. https://doi.org/10.1002/nbm.924

129. Ahmed HU, Kirkham A, Arya M, Illing R, Freeman A, Allen C, Emberton M (2009) Is it time to consider a role for MRI before prostate biopsy? Nat Rev Clin Oncol 6:197–206

130. Choi JS, Lee JH, Shin TH, Song HT, Kim EY, Cheon J (2010) Self-confirming "aND" logic nanoparticles for fault-free MRI. J Am Chem Soc 132:11015–11017. https://doi.org/10.1021/ja104503g

131. Shin TH, Choi JS, Yun S, Kim IS, Song HT, Kim Y, Park KI, Cheon J (2014) T 1 and T 2 dual-mode MRI contrast agent for enhancing accuracy by engineered nanomaterials. ACS Nano 8:3393–3401. https://doi.org/10.1021/nn405977t

132. Estelrich J, Sánchez-Martín MJ, Busquets MA (2015) Nanoparticles in magnetic resonance imaging: from simple to dual contrast agents. Int J Nanomed 10:1727–1741. https://doi.org/10.2147/IJN.S76501

133. Niu D, Luo X, Li Y, Liu X, Wang X, Shi J (2013) Manganese-loaded dual-mesoporous silica spheres for efficient T1- and T2-weighted dual mode magnetic resonance imaging. ACS Appl Mater Interfaces 5:9942–9948. https://doi.org/10.1021/am401856w

134. Li F, Zhi D, Luo Y, Zhang J, Nan X, Zhang Y, Zhou W, Qiu B, Wen L, Liang G (2016) Core/shell Fe_3O_4/Gd_2O_3 nanocubes as: T 1- T 2 dual modal MRI contrast agents. Nanoscale 8:12826–12833. https://doi.org/10.1039/c6nr02620f

135. Wang Z, Liu J, Li T, Liu J, Wang B (2014) Controlled synthesis of $MnFe_2O_4$ nanoparticles and Gd complex-based nanocomposites as tunable and enhanced T1/T 2-weighted MRI contrast agents. J Mater Chem B 2:4748–4753. https://doi.org/10.1039/c4tb00342j

136. Bae KH, Kim YB, Lee Y, Hwang JY, Park H, Park TG (2010) Bioinspired synthesis and characterization of gadolinium-labeled magnetite nanoparticles for dual contrast T1- and T2-weighted magnetic resonance imaging. Bioconjug Chem 21:505–512. https://doi.org/10.1021/bc900424u

137. Ding D, Kanaly C, Cummings T, Herndon J II, Raghavan R, Sampson J (2010) Convection-enhanced delivery of free gadolinium with the experimental chemotherapeutic agent PRX321. Neurol Res 32:810–815. https://doi.org/10.1179/174367509X12581069052090

138. Ding D, Kanaly CW, Bigner DD, Cummings TJ, Herndon JE, Pastan I, Raghavan R, Sampson JH (2010) Convection-enhanced delivery of free gadolinium with the recombinant immunotoxin MR1-1. J Neurooncol 98:1–7. https://doi.org/10.1007/s11060-009-0046-7

139. Veiseh O, Sun C, Fang C, Bhattarai N, Gunn J, Kievit F, Du K, Pullar B, Lee D, Ellenbogen RG, Olson J, Zhang M (2009) Specific targeting of brain tumors with an optical/magnetic resonance imaging nanoprobe across the blood-brain barrier. Cancer Res 69:6200–6207. https://doi.org/10.1158/0008-5472.CAN-09-1157

140. Veiseh O, Kievit FM, Fang C, Mu N, Jana S, Leung MC, Mok H, Ellenbogen RG, Park JO, Zhang M (2010) Chlorotoxin bound magnetic nanovector tailored for cancer cell targeting, imaging, and siRNA delivery. Biomaterials 31:8032–8042. https://doi.org/10.1016/j.biomaterials.2010.07.016

141. Veiseh O, Kievit FM, Gunn JW, Ratner BD, Zhang M (2009) A ligand-mediated nanovector for targeted gene delivery and transfection in cancer cells. Biomaterials 30:649–657. https://doi.org/10.1016/j.biomaterials.2008.10.003

142. Xiao N, Gu W, Wang H, Deng Y, Shi X, Ye L (2014) T1–T2 dual-modal MRI of brain gliomas using PEGylated Gd-doped iron oxide nanoparticles. J Colloid Interface Sci 417:159–165. https://doi.org/10.1016/j.jcis.2013.11.020

143. Dufresne A (2013) Nanocellulose: a new ageless bionanomaterial. Mater Today 16:220–227

144. Torkashvand N, Sarlak N, Fe U (2019) Fabrication of a dual T 1 and T 2 contrast agent for magnetic resonance imaging using cellulose nanocrystals/Fe_3O_4 nanocomposite cellulose nanocrystals dual contrast agent magnetic resonance imaging. Cellular uptake. https://doi.org/10.1016/j.eurpolymj.2019.05.048

145. Gao J, Liang G, Cheung JS, Pan Y, Kuang Y, Zhao F, Zhang B, Zhang X, Wu EX, Xu B (2008) Multifunctional yolk-shell nanoparticles: a potential MRI contrast and anticancer agent. J Am Chem Soc 130:11828–11833. https://doi.org/10.1021/ja803920b

146. Kim J, Kim HS, Lee N, Kim T, Kim H, Yu T, Song IC, Moon WK, Hyeon T (2008) Multi-functional uniform nanoparticles composed of a magnetite nanocrystal core and a mesoporous silica shell for magnetic resonance and fluorescence imaging and for drug delivery. Angew Chemie 120:8566–8569. https://doi.org/10.1002/ange.200802469

147. Sato K, Yokosuka S, Takigami Y, Hirakuri K, Fujioka K, Manome Y, Sukegawa H, Iwai H, Fukata N (2011) Size-tunable silicon/iron oxide hybrid nanoparticles with fluorescence, superparamagnetism, and biocompatibility. J Am Chem Soc 133:18626–18633. https://doi.org/10.1021/ja202466m

148. Osborne EA, Atkins TM, Gilbert DA (2006) Gold-coated iron nanoparticles: a novel magnetic resonance agent for T 1 and T 2 weighted imaging related content rapid microwave-assisted synthesis of dextran-coated iron oxide nanoparticles for magnetic resonance imaging. Nanotechnology 17:640. https://doi.org/10.1088/0957-4484/17/3/004

149. Efremova MV, Naumenko VA, Spasova M, Garanina AS, Abakumov MA, Blokhina AD, Melnikov PA, Prelovskaya AO, Heidelmann M, Li ZA, Ma Z, Shchetinin IV, Golovin YI, Kireev II, Savchenko AG, Chekhonin VP, Klyachko NL, Farle M, Majouga AG, Wiedwald U (2018) Magnetite-Gold nanohybrids as ideal all-in-one platforms for theranostics. Sci Rep 8:11295. https://doi.org/10.1038/s41598-018-29618-w

150. Lin J, Zhang W, Zhang H, Yang Z, Li T, Wang B, Huo X, Wang R, Chen H (2013) A multifunctional nanoprobe based on Au-Fe$_3$O$_4$ nanoparticles for multimodal and ultrasensitive detection of cancer cells. Chem Commun 49:4938–4940. https://doi.org/10.1039/c3cc41984c

151. Reguera J, Jiménez De Aberasturi D, Henriksen-Lacey M, Langer J, Espinosa A, Szczupak B, Wilhelm C, Liz-Marzán LM (2017) Janus plasmonic-magnetic gold-iron oxide nanoparticles as contrast agents for multimodal imaging. Nanoscale 9:9467–9480. https://doi.org/10.1039/c7nr01406f

152. Xu C, Xie J, Ho D, Wang C, Kohler N, Walsh EG, Morgan JR, Chin YE, Sun S (2008) Au-Fe$_3$O$_4$ dumbbell nanoparticles as dual-functional. Angew Chemie Int Ed 47:173–176. https://doi.org/10.1002/anie.200704392

153. Wang G, Gao W, Zhang X, Mei X (2016) Au Nanocage functionalized with ultra-small Fe$_3$O$_4$ nanoparticles for targeting T1–T2 dual MRI and CT imaging of tumor. Sci Rep 6:1–10. https://doi.org/10.1038/srep28258

154. Wu C-H, Cook J, Emelianov S, Sokolov K (2014) Multimodal magneto-plasmonic nanoclusters for biomedical applications. Adv Funct Mater 24:6862–6871. https://doi.org/10.1002/adfm.201401806

155. Chen H, Qi B, Moore T, Colvin DC, Crawford T, Gore JC, Alexis F, Mefford OT, Anker JN (2014) Synthesis of brightly pegylated luminescent magnetic upconversion nanophosphors for deep tissue and dual MRI imaging. Small 10:160–168. https://doi.org/10.1002/smll.201300828

156. Xia A, Gao Y, Zhou J, Li C, Yang T, Wu D, Wu L, Li F (2011) Core-shell NaYF4:Yb3+, Tm3+@FexOy nanocrystals for dual-modality T2-enhanced magnetic resonance and NIR-to-NIR upconversion luminescent imaging of small-animal lymphatic node. Biomaterials 32:7200–7208. https://doi.org/10.1016/j.biomaterials.2011.05.094

157. Okuhata Y (1999) Delivery of diagnostic agents for magnetic resonance imaging. Adv Drug Deliv Rev 37:121–137

158. Xu C, Mu L, Roes I, Miranda-Nieves D, Nahrendorf M, Ankrum JA, Zhao W, Karp JM (2011) Nanoparticle-based monitoring of cell therapy. Nanotechnology 22:494001. https://doi.org/10.1088/0957-4484/22/49/494001

159. Ly HQ, Frangioni JV, Hajjar RJ (2008) Imaging in cardiac cell-based therapy: in vivo tracking of the biological fate of therapeutic cells. Nat Clin Pract Cardiovasc Med 5:S96–S102

160. Mahmoudi M, Sant S, Wang B, Laurent S, Sen T (2011) Superparamagnetic iron oxide nanoparticles (SPIONs): development, surface modification and applications in chemotherapy. Adv Drug Deliv Rev 63:24–46

161. Wang Y-XJ (2011) Superparamagnetic iron oxide based MRI contrast agents: current status of clinical application. Quant Imaging Med Surg 1:35–40. https://doi.org/10.3978/j.issn.2223-4292.2011.08.03

Antibacterial Potential of Spinel Ferrites: Current and Future Prospects

Hafeez Anwar, Beenish Abbas, Umair Subhani, and Muhammad Khalid

Abstract This book chapter is organized into three major parts. Firstly, it covers an introduction of spinel ferrite nanoparticles in which an overview of the structure and magnetism of spinel ferrites along with their types. In the second part, details of antibacterial properties are discussed. A discussion on the mechanisms for the antibacterial properties is also presented. The last part highlights the influence of transition metal concentration on the physical properties, and antibacterial property of transition metal substituted cobalt ferrite nanoparticles.

Keywords Spinel ferrites · Antibacterial mechanism · Cobalt ferrites · Doping effects · Hemolysis · Antibacterial properties

1 Ferrites

We are surrounded by magnetic materials that played significant role in various devices of everyday life. Magnetic materials were used in many applications such as audio and video system that give information and entertainment on wide range, cellphone and telecommunication system which linked the continents, data storage system which interpenetrate in every human activity. The historical background of magnetic materials were considered as the birth of man. The unusual properties of magnetic ceramic, i.e., magnetic made military success of an ancient Chinese Emperor [55].

In 1825 H. C. Oersted observed that magnetic field was produced by means of electric current which bring a revolution in the field of magnetism. Many theories, models, and discoveries were developed after this experiment. It was an interesting fact that all variety of magnetic materials and their properties were originated from three elements such as nickel, cobalt, and iron which were ferromagnetic at room temperature.

Ferrites were extensively studied in the last 50 years and many theories or models were established. The varieties of materials were obtained from metallic materials

H. Anwar (✉) · B. Abbas · U. Subhani · M. Khalid
Department of Physics, University of Agriculture Faisalabad, Faisalabad 38040, Pakistan

that can be used in wide range of technological applications. Magnetic ceramics were utilized in every field of daily life. Ferrites were well established, but improvements and innovation were continuously taken place. The exciting interesting theories, applications, and preparation of new materials were currently under development. The scientific study on ferrites at very large scale was held in japan at the occasion of the sixth International Conference in October 1992 in which more than 550 research papers were presented by 1159 authors [56, [57].

The research on spinel ferrites was continued by T. Taki, N. Kawai, and V. Kato in Japan in 1930. J. Snoeck also studies the soft ferrites in Netherland at the same time. J. Snoeck and his colleagues were succeeded to describe the practical ferrites materials which possessed strong magnetic properties, low relaxation losses, and high electrical resistivity. The spinel ferrite was used in LC filters in frequency division multiplexer equipment. It was the first practical application of the soft ferrites. Due to strong magnetic properties and high resistivity, spinel ferrites were core materials for filter operating in the frequency range of 50–450 kHz. Ferrites were used in television as high voltage transformer and electron beam deflection. The spinel ferrites can be used in modern applications such as in automotive markets, medical and cell phones [58].

1.1 Types of Ferrites

The types of ferrites are listed below.

- Spinel ferrites or soft ferrites
- Hexagonal ferrites or hard ferrites
- Garnet ferrites
- Ortho ferrites.

2 Spinel Ferrites

Spinel nano ferrites are very important due to the interesting properties. The most widely used magnetic ceramic are spinel ferrites. The general formula of soft ferrites is $MFeO_4$ or AB_2O_4 were M represent the divalent the metal cations. Naturally occurred ferrite was magnetic (Fe_3O_4) and all other ferrites were man-made. All the soft ferrites possessed a similar crystal structure of $MgAl_2O_4$ magnetic mineral. In the magnetic spinel Mg^{2+} were replaced with divalent metal ions such as nickel, cobalt, manganese, copper, iron, zinc, and their combinations. The trivalent metal cation Al^{3+} can be replaced with Fe^{3+} and combination of Fe^{3+} with other trivalent cations. The spinel ferrites unit cell consists eight metal ions per formula unit and coordinated with four or six oxygen ions which produced two distinct sites named A and B sites.

AB_2O_4 spinel The red cubes are also contained in the back half of the unit cell
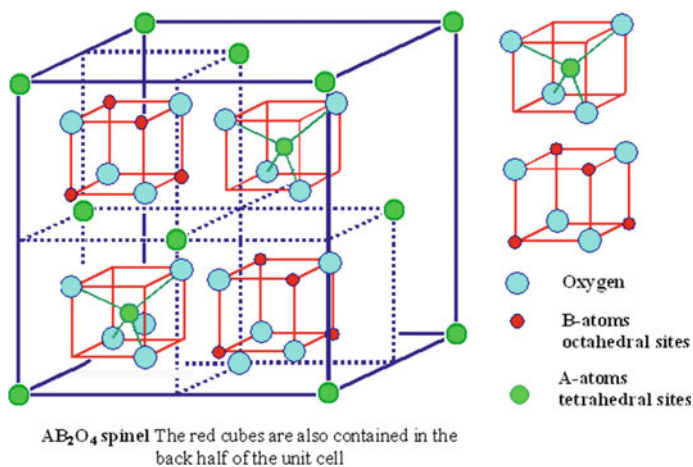
Fig. 1 Unit of spinel ferrites

2.1 Structure of Spinel Ferrites

Bragg and Nishikawa were the first people who determined the crystal structure of spinel ferrites in 1915. They observed that spinel structure was cubic closed packed with oxygen ions layer. The eight A sites while sixteen B sites were filled by cations in the structure of spinel lattice. In tetrahedral site, metal was surrounding by four oxygen ions situated at the center from the tetrahedron. The metal in octahedral site was enclosed of six oxygen ions located at the center of octahedron. The unit of spinel ferrites was shown in Fig. 1. The spinel matrix unit cell contained 64 tetrahedral and 32 octahedral sites. When all the sites were occupied by divalent or trivalent cations then positive charge was much greater than negative charge. So, the structure did not remain electrically neutral. To overcome this effect only 8 A sites out of 64 were occupied by metal cations and out of 32 octahedral sites, only 16 was filled by cations [59].

The oxygen atoms were not located at the exact position of FCC sublattice in the spinel structure. The positions of oxygen ions were determined by oxygen positional parameter u. For an ideal closed-packed spinel structure, the value of oxygen positional parameters was 0.37 or 3/8. The ideal situation did not exist and the value of u for majority of the known spinel was in the range of 0.375–0.385. The value of u increased due to the anions in tetrahedral sites were forcefully moved in the direction of [111] plane. The ratio of tetrahedral cations radii was estimated from *u* value [60, 55].

Ion	Octahedral site	Tetrahedral site
Fe^{2+}	0.78	0.63
Fe^{3+}	0.64	0.49

<div align="right">(continued)</div>

(continued)

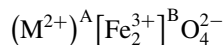| Ion	Octahedral site	Tetrahedral site
Mn^{2+}	0.83	0.66
Zn^{2+}	0.74	0.60
In^{3+}	0.80	0.62

2.2 Types of Spinel Structure

FCC lattices in spinel structure were formed by oxygen ions. Spinel closed pack structure possessed two kinds of crystallographic sites, named as A sites and B sites. All cations resided on these two interstitial sites. The divalent metal cations occupied available A and B sites with oxygen coordination. The cations distributions on these interstitial sites in spinel lattice lead to from three types of structures,

1. Normal spinel
2. Inverse spinel
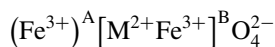3. Intermediate spinel.

2.2.1 Normal Spinel Structure

The spinel structure said to the normal if all the divalent metal cations (Me^{2+}) tend to go A site while trivalent cations (Fe_2^{3+}) reside on B sites in the unit cell. Such type of structure was known as normal spinel. The normal spinel structure was represented by the structure formula (Me^{2+}) [Fe_2^{3+}] O_4^{2-}, The example of normal spinel was $ZnFe_2O_4$ and $CdFe_2O_4$ ferrites.

Degree of inversion δ for normal spinel is one.

$$\left(M^{2+}\right)^A\left[Fe_2^{3+}\right]^B O_4^{2-}$$

2.2.2 Inverse Spinel Structure

When trivalent cations (Fe_2^{3+}) distributed equally among tetrahedral and octahedral sites and all divalent metal cations (Me^{2+}) occupied on octahedral sites. In this crystal structure remaining, cations were randomly distributed. Structural formula of investigated spinel structure was elaborated as (Fe_2^{3+}) [$Me^{2+} Fe^{3+}$] O_4^{2-}. Nickel and cobalt ferrites are the examples of such type of crystal structure. Degree of inversion δ for inverse spinel is zero.

$$\left(Fe^{3+}\right)^A\left[M^{2+}Fe^{3+}\right]^B O_4^{2-}$$

2.2.3 Intermediated Spinel Structure

The proportional of (Me^{2+}) and $\left(Fe_2^{3+}\right)$ cations distributed among both sites such as A sites and B sites represented the mixed spinel structure. The intermediated spinel structure possessed δ between zero and one. Structural formula of mixed ferrite was $Me_{1-\delta}^{2+} Fe_\delta^{3+} [Me_\delta^{2+} Fe_{2-\delta}^{3+}] O_4^{2-}$ The most common example of intermediated spinel is $MnFe_2O_4$ has value of inversion parameter is 0.2. the mixed spinel ferrite [61, 60].

$$\left(M^{3+} x Fe_{1-x}^{3+}\right)^A \left[M_{1-x}^{2+} Fe_{1+x}\right]^B O_4^{2-}$$
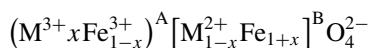
3 Antibacterial Activity

Bacteria can be divided into two parts Gram positive and Gram negative which are based on the structure of the cell wall. Gram positive bacteria contained a thick layer of peptidoglycan around the cell wall and Gram negative contained the thin layer of peptidoglycan with another outer membrane which is called lipopolysaccharide. There is an extra layer of membrane which is known as periplasm [1–5]. Many studies were found that Gram positive bacterial was more resistant for the nanoparticle's mechanisms of action. The reason for this phenomenon was indicating different cell walls. Therefore, Gram-negative bacteria *Escherichia coli* covered the layer of lipopolysaccharides which have the thickness 1–3 μm and peptidoglycans which have the thickness of almost 8 nm. This arrangement was helpful to the nanoparticles to release the ions at the start of the cell. Gram positive such as *Staphylococcus aureus* have a layer of peptidoglycan which is thicker as compared to the Gram-negative bacteria, spanning over 80 nm with covalently attached acids of teichuronic and teichoic shown in Fig. 2.
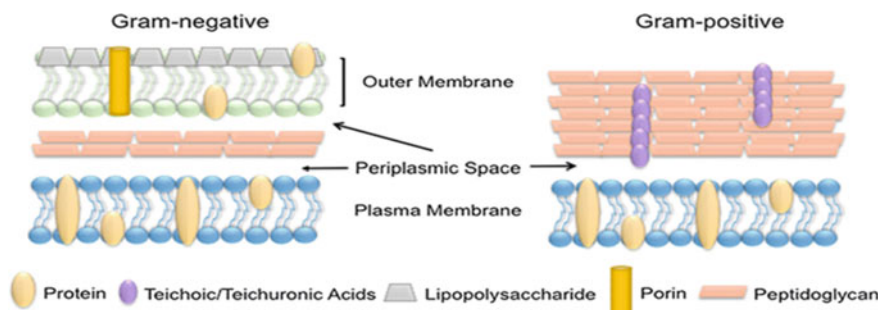

Fig. 2 Comparsion of bacterial cell wall structure

4   Antimicrobial Mechanism of Metallic NPs

For antibacterial mechanism, metal and metallic salts were used for drinking water as a silver spots in 4000 BCE [6, 7]. In the present research in nanophysics capable the scientist to study the properties of antibacterial on many metallic nanoparticles [8, 9]. The toxic mechanisms of antibacterial for the metallic nanoparticles is still under debate. Three main mechanism are included such as,

1.   The formation of reactive oxidative species (ROS)
2.   Releasing process of ions
3.   Interaction of nanoparticles with the cell membrane (Fig. 3)

   Metallic nanoparticles as compared to their salts have increased the potential to combat bacterial infections [10–13]. Mostly, the size of nanoparticles affects the antibacterial mechanism [14–19].

4.1   Entering the Cell

In the first step, mechanism of antibacterial is that metallic ions in the range of nanometer was attached to the cell membrane. When the metallic ions attached to the bacterial cells than it is blocked the channels of transport and producing some change in the structure of cell membrane [4, 20] all processes are depending upon the size. Small size nanoparticles are more efficient but larger nanoparticles have large absolute surface area permitting for better adhesion property of van der Waals forces. So that, nanoparticles may be internalized, within the cell they produced ionization, and damage the structure of intracellular resulting in cell death (Fig. 3) [10].
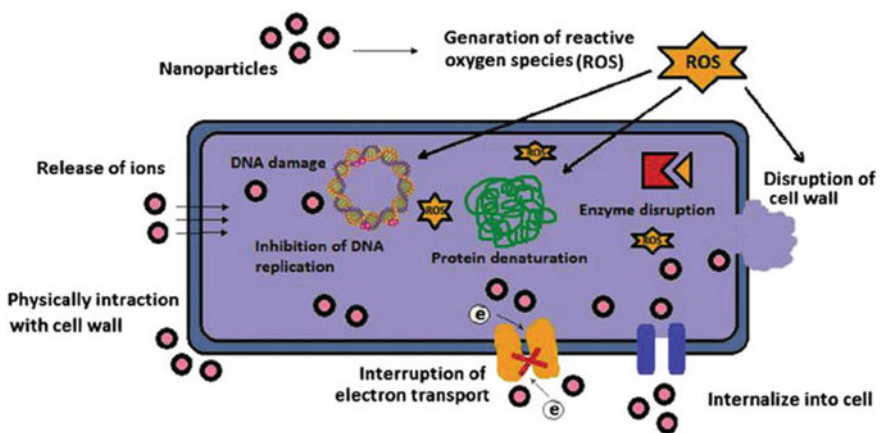

Fig. 3   Various mechanisms of antimicrobial activity of the metal NPs [10]

4.2 Reactive Oxidative Species (ROS) Generation

In antibacterial mechanism, the production of reactive oxidative species (ROS) in metal nanoparticles plays an important role (Fig. 3). Reactive oxidative species was consisting of short-lived oxidants which are known as superoxide radicals (O^{-2}), hydrogen peroxide (H_2O_2), hydroxyl radicals (OH^{-1}), and singlet oxygen (O^{-2}) [21, 22]. Reactive oxidative species was damaging the peptidoglycan and cell membrane, DNA, mRNA, ribosomes, and proteins due to the high reactive of these species [12]. Reactive oxidative species was also preventing the transcription, translation, enzymatic activity, and the chain of electron transport [12, 21]. Some nanoparticles of metal oxide depend on the generation of reactive oxidation species as a main mechanism of toxicity [4, 11, 20].

4.3 Protein Inactivation and DNA Destruction

The atoms of the metal can attach with thiol group of enzymes and damage the function of enzymes. The metals ions are attached to the pyrimidine and purine base pairs and also it is disturbing the hydrogen bonding between the two strands of antiparallel and destruct the molecule of DNA (Fig. 3). Therefore, when the metal ions enter the cell membrane it can attach with the DNA [23].

5 Detection Methods

For the growth of the microbial measurements, there are many direct and indirect methods. In the method of direct some techniques such as plate count, serial dilution, and disk diffusion method. while indirect methods were analyzed by turbidity, dry weight, and by metabolic activity. In short, the description of direct and indirect methods is as follows.

5.1 Viable Plate Count Method

In the method of plate count, for each reading petri dishes was used. The plate of agar was prepared, one plate of inoculums and other plates with inoculum, and the solution of the nanoparticle are spread on the plates with the help of sterile spreader. This plate was incubated for 24 h at 37 °C and then calculated the colonies of each plate. Then, the inhibition percentage growth with each reading is calculated [24, 25].

5.2   Disk Diffusion Method

In this method, the prepared culture of bacteria was mixed in nutrient broth to form liquid culture. Then the solution of nutrient agar was sterile and put into dishes and waited for the solution is solidified. Then, with the help of cork the holes are generated. Holes are filled with the solution metallic nanoparticles and the stabilized. After that, the plates are incubated for 24 h at 37 °C. The zones of inhibition were observed after 24 h and it is calculated with the standard error. For the exact analysis, proper replication of the experiments is done for the study of microbial [26].

5.3   Estimating Bacterial Numbers by Indirect Methods

Indirect methods are known as time-consuming methods, so that large numbers of samples were prepared at a time. A spectrophotometer was used to analyze the process of turbidity by measuring the amount of light that transmits through a bacterial cell suspension. When the transmission occurs through suspension was increased it means that turbidity also decreases, indicating the reduction in bacterial cells and vice versa [27, 28].

6   Antibacterial Activity of Cobalt Ferrite

In Fig. 4. Shows the results of the antibacterial effects of visible light to pure Ag_3PO_4 and the composite such as Ag_3PO_4 towards the *E. coli*. It is shown that under the visible light the number of the *E. coli* was not decreased. Figure 4a clearly show that *the E. coli* was survive in the presence of visible light. In Fig. 4b was confirmed that the numbers of E. coli observed in the dark when the light is on the numbers of the bacteria were decreased. In Fig. 4c. in the dark many bacteria colonies were formed. The results of the antibacterial activities were showed that the 3% of $AgPO_4@NiFe_2O_4$ composites increased the effects of antibacterial against the E. coli as compared to the pure Ag_3PO_4.

El-Shahawy, Abo El-Ela, Mohamed, Eldine, & El Rouby, also studied the antibacterial activity of the $CoFe_2O_4$ and $CoFe_2O_4$ with Chitosan nanohybrid. *S. aureus* and *E. coli* bacteria were used to test. Slants of Muller Hinton agar were used to maintain the tested organisms and incubation was done at temperature 37 °C for time 24 h. Every tested material was prepared by a standard concentration of 10 mg/ml. Cobalt Ferrite with Chitosan and Cobalt ferrite were settled with various concentrations (1000, 500, 250, 125, 62.5, 31.25, 15.6, 7.81, 3.9, 1.95, and 0.9 µg/ml). The antimicrobial action was assessed and calculated using a caliber as the zone diameters zones in millimeters [29]. The antibacterial action was shown by the presence of zones of inhibition around the pores. Both positive control and negative control tube were
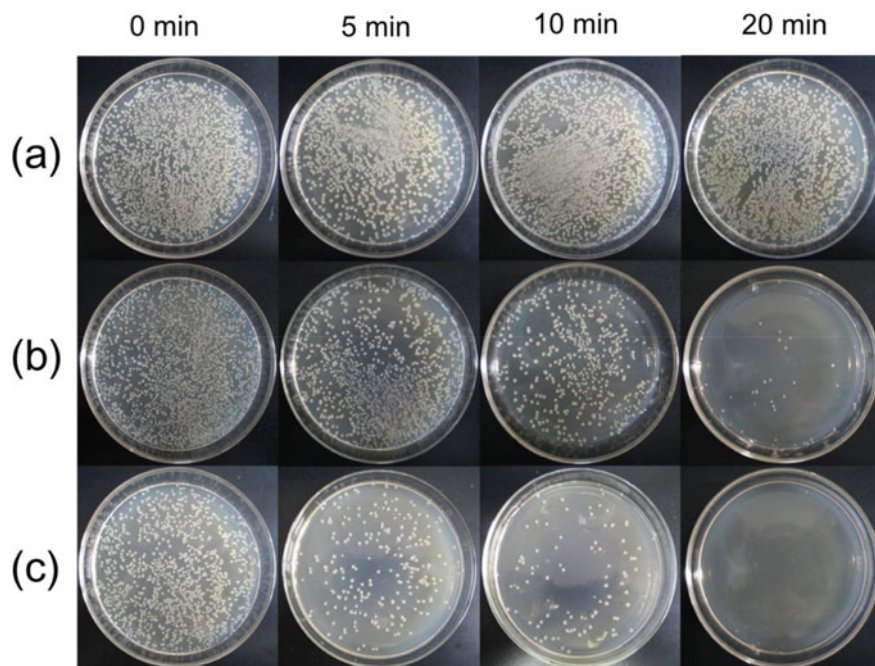
Fig. 4. The photocatalytic antibacterial activities of **a** light only, **b** pure Ag_3PO_4 and **c** 3% $Ag_3PO_4@NiFe_2O_4$ composite against *E. coli* at different irradiation times

used to subculture the isolated organisms on Muller Hinton agar. The incubation of these tested tubes was done for 24 h at 37 °C. Antimicrobial agent inhibits the growth and its low concentration is MIC and to it, results were noted. Muller Hinton agar was used to subculture a tube loop without noticeable growth and incubated for time 24–48 h at temperature 37 °C for the determination of MBC. The subcultured plates were observed for growth after incubation.

Inhibition region against *E. coli* bacteria at various amounts of $CoFe_2O_4$ and $CoFe_2O_4$ with chitosan as shown in Table 1. Results showed that the inhibition zone diameter enhanced by enhancing the concentration of nanoparticles. The nanoparticles of cobalt ferrite do not have antibacterial properties, while chitosan cobalt ferrite has the antibacterial properties. Inhibition region of $CoFe_2O_4$ and chitosan $CoFe_2O_4$ nanoparticles beside *S. aureus* and *E. coli* as shown below in Fig. 5 25.5–28 mm and 10.5 mm was the ZOI of the chitosan cobalt ferrite for a concentration of 1000 μg/ml and 15.6 μg/ml, respectively. Results show values of MIC for chitosan cobalt ferrite at dilutions of (10^7 CFU/ml and 10^8 CFU/ml) were 125 and 1000 μg/ml. For chitosan cobalt ferrite, the tested nanomaterials had MBC values of 250 and 1000 μg/ml.

Inhibition region against *S. aureus* bacteria at various amounts of $CoFe_2O_4$ and $CoFe_2O_4$ with Chitosan as shown in Table 2. Results show that the values of MIC for Cobalt ferrite at bacterial dilutions (10^7 CFU/ml and 10^8 CFU/ml) were >500 μg/ml whereas for cobalt ferrite with Chitosan the MIC values were 125 and 250 μg/ml.

Table 1 Represents the ZOI at various amounts of $CoFe_2O_4$ and $CoFe_2O_4$ covered with Chitosan towards *E. coli* and *S. aureus* bacterial strains

| Sample	Amounts (Ug/ml)	ZOI (mm)				Citation
		E. coli		*S. aureus*		
		10^8 CFU/ml	10^7 CFU/ml	10^8 CFU/ml	10^7 CFU/ml	
Cobalt Ferrite	1000 500 250 125 62.5 31.25 15.6 7.81 3.9 1.95	Bacterial growth	Bacterial growth	Bacterial growth	Bacterial growth	(El-Shahawy et al. 2018)
Cobalt Ferrite with Chitosan	1000 500 250 125 62.5 31.25 15.6	25.5 19.5 16 14 13 12.5 10.5	28*** 21.5*** 19.5*** 16.5*** 15*** 13.5*** 12.5***	32.5 25.5 19 16.5 14.5 13.5 11.5	39.5*** 35.5*** 21*** 19.5*** 17.5*** 15.5*** 13***	

The results written in the table represent the mean values found in triplicate, Meaning: $P \leq 0.001$, $P \leq 0.01$, $P \leq 0.05$

The values of MBC were 62.5 and 125 µg/ml for the chitosan cobalt ferrite and the Cobalt ferrite nanoparticles was >500 µg/ml [30].

7 Doping of Cobalt Ferrites with Metals

7.1 Silver

Mahajan, Sharma, Kaur, Goyal, & Gautam, used the disc diffusion process for testing antibacterial property of silver substitute $CoFe_2O_4$ towards *E. coli*, and *Listeria mono-cytogenes.* In this method used agar plate which is dispersed by analyzing bacteria, and then paper-disks were included which were taken by the prepared nanoparticle. Incubated these plates at 37 °C and after 24 h ZOI was studied for results. Figure 6 represents the antibacterial action of tulsi and garlic-based nanoparticles against *E. coli* and *Listeria manocytogenes.* The ZOI results against bacteria as shown in Table 2. Figure 6a, b shows the antibacterial action in the presence of ZOI. Antibacterial action depends on silver concentration which ZOI presents in Fig. 7. By comparing
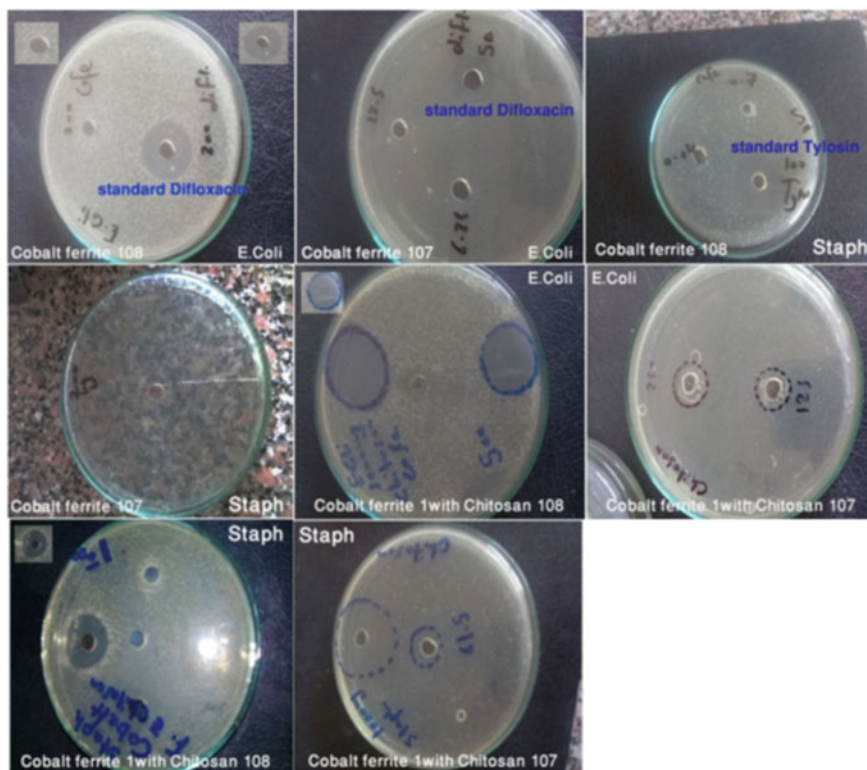
Fig. 5 Antibacterial actions of $CoFe_2O_4$ only, $CoFe_2O_4$ covered with Chitosan towards *S. aureus* and *E. coli*

the dopant concentration in the two methods tulsi mediated synthesis (lower concentration) and garlic mediated synthesis (higher concentration) the first one proved to be the best antibacterial potent shown in Fig. 7a, b [31].

Satheeshkumar et al., also studied the antibacterial action Ag-substituted $CoFe_2O_4$. Well diffusion method was used for testing the antibacterial action of the $CoFe_2O_4$ and the Ag-substituted $CoFe_2O_4$ towards *E. coli*, *S. aureus,* and *C. albicans*. These tests performed on Mueller Hinton agar plates. Vernier caliper was utilized to measure the inhibition zones around the covered samples. Table 1 and Fig. 8 shows the results and images of inhibition zone respectively. A decreased in microbial cultures takes place by increasing nanoparticle concentration. Both nanoparticles were tested with ZOI greater than 7 mm and they show strong antimicrobial action towards *S. aureus, E. coli,* and *C. albicans*. Towards *E. coli* and *C. albicans* $AgCoFe_2O_4$ proved to be more effective than $CoFe_2O_4$. Because antimicrobial action of $AgCoFe_2O_4$ depends on Silver ion concentration which results in distortion of cell and bacterial species [32, 33].
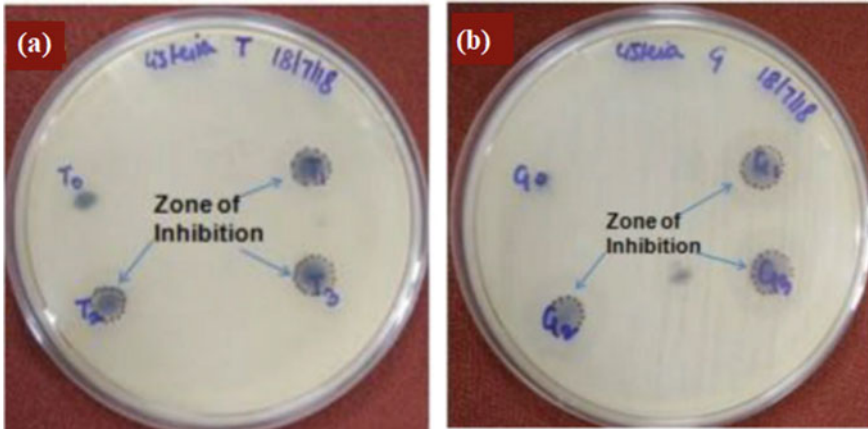
Table 2 Shows the zone of inhibition of different treatments against different bacteria

Sample	Concentration	Zone of inhibition (mm)							Citation
		E.coli	L. monocytogens	S. aureus	C. albicans	S. typhi	B. Subtilis	P. aeruginosa	
C0		6	7						(Mahajan et al., 2019)
C1		7	7						
C2		7	8						
C3		8	9						
T0		7	6						
T1		7	7						
T2		8	8						
T3		9	9						
G0		–	–						
G1		–	7						
G2		5	8						
G3		7	8						
CoFe$_2$O$_3$	100 mg	7.5 ± 0.20		9.0 ± 0.41	8.0 ± 0.08				(Satheeshkumar et al., 2019)
	200 mg	8.0 ± 0.7		9.5 ± 0.01	9.5 ± 0.62				
	300 mg	8.5 ± 0.04		8.5 ± 0.01	10.05 ± 0.23				
	400 mg	9.0 ± 0.8		8.75 ± 0.20	12.5 ± 0.01				
	500 mg	9.5 ± 0.04		10.0 ± 0.41	15.0 ± 0.07				
AgCoFe$_2$O$_4$	100 mg	8.0 ± 0.08		6.5 ± 0.06	8.0 ± 0.04				
	200 mg	8.5 ± 0.06		6.8 ± 0.04	8.5 ± 0.31				
	300 mg	9.3 ± 0.23		7.5 ± 0.01	8.93 ± 0.09				
	400 mg	10.5 ± 0.01		7.86 ± 0.20	16.13 ± 0.18				
	500 mg	10.5 ± 0.08		8.5 ± 0	20.03 ± 0.47				

(continued)

Table 2 (continued)

| Sample	Concentration	Zone of inhibition (mm)							Citation
		E.coli	L. monocytogens	S. aureus	C. albicans	S. typhi	B. Subtilis	P. aeruginosa	
$CoFe_2O_3$	25 Ug/ml			09 ± 0.3		08 ± 0.1			(Madhukara Naik et al., 2019)
	50 Ug/ml			11 ± 0.6		10 ± 0.4			
	100 Ug/ml			19 ± 0.7		16 ± 0.7			
Zn-doped $CoFe_2O_3$	25 Ug/ml			04 ± 0.3		07 ± 0.5			
	50 Ug/ml			09 ± 0.8		12 ± 0.3			
	100 Ug/ml			15 ± 0.5		22 ± 0.8			
$CoFe_2O_4$	5 mg/ml	–		–			–	–	(Kooti et al., 2014)
	10 mg/ml	–		–			–	–	
	20 mg/ml	–		–			–	–	
	40 mg/ml	–		–			–	–	
$CoFe_2O_4$/PANI	5 mg/ml	–		–			–	–	
	10 mg/ml	–		–			–	–	
	20 mg/ml	–		–			–	–	
	40 mg/ml	7		12			11	–	
$CoFe_2O_4$/PANI/Ag	5 mg/ml	14		13			8	7	
	10 mg/ml	14		13			9	8	
	20 mg/ml	15		15			10	8	
	40 mg/ml	16		17			12	11	

Fig. 6 Inhibition zone by prepared Nps using **a** tulsi seed obtain towards *L. monocytogenes*, and **b** garlic obtain, towards *L. monocytogenes*



Fig. 7 Inhibition zone by prepared nanoparticles towards bacteria

7.2 Copper

Samavati and F. Ismail studied the antibacterial activity of Cu-doped $CoFe_2O_3$. Antibacterial action of the nanoparticles synthesized in nanofluids form was investigated by measuring the *E. coli* growth curve preserved in a Luria–Bertani broth method [34]. After incubation for 24 h, the IZD was calculated in millimeters. The *E. coli* bacteria growth curves are shown in Fig. 9 with Nps presence with different
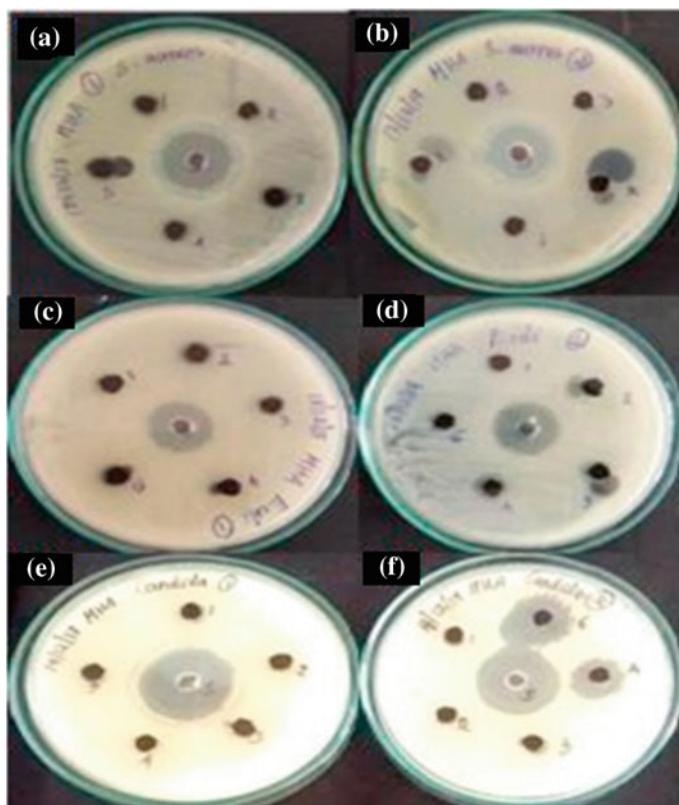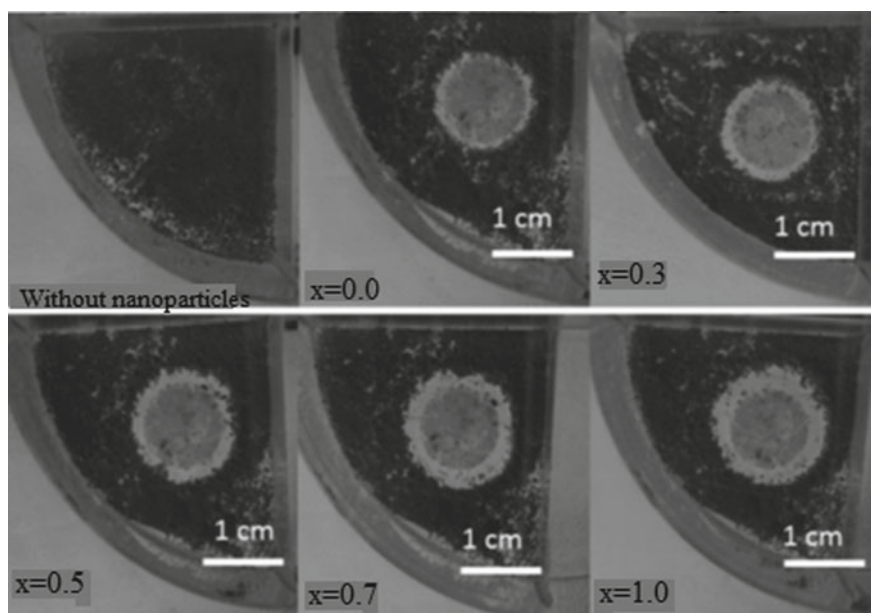
Fig. 8 Antibacterial activity of $CoFe_2O_4$ and $AgCoFe_2O_4$ against *Staphylococcus aureus* (**a**) and (**b**), *E. coli* (**c**) and (**d**), *C. albicans* (**e**) and (**f**)

concentrations of Copper and Cobalt. The optical density shows the bacteria absorption at 600 nm. In the case of Increasing bacteria numbers, light absorption increases. High Copper concentration contributes to improving the antibacterial activity. It is observed from Fig. 10 the substitution of Cobalt and Copper has an evident action on pathogens of bacteria. Figure 10 explains the ZOI diameter for all samples after incubation for 24 h. The samples which were prepared demonstrate antibacterial activity. The IZD findings show that nanoparticle's bactericidal strength is improved with improving the concentration of Cu, as shown in Fig. 10 [35].
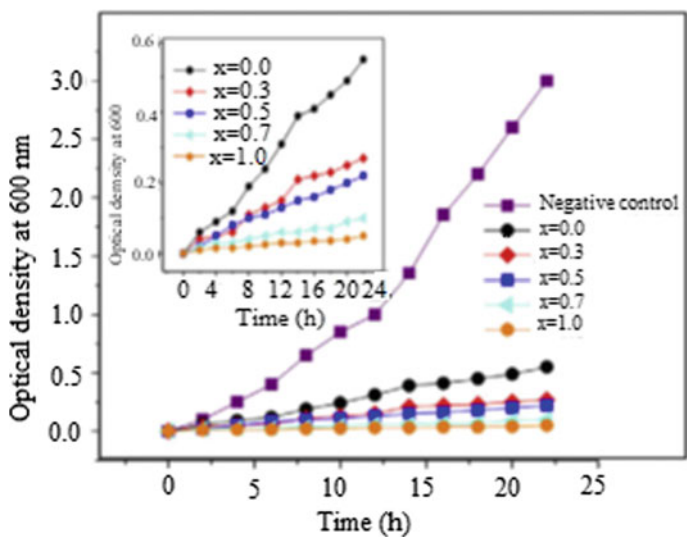
Fig. 9 Copper concentration-dependent antibacterial behavior of Cu-doped CoFe$_2$O$_3$. Enclosure displays the optical density within the 0–0.6 range for good comparison

Fig. 10 Inhibition region formed by copper-doped cobalt ferrite Nps (Co$_{1-x}$Cu$_x$Fe$_2$O$_4$ with x = 0.0, 0.3, 0.5, 0.7, and 1.0) beside *E. coli*

7.3 Cerium

Elayakumar et al., discussed the antibacterial activity of nanoparticles of $CoCe_xFe_{2-x}O_4$ ($x = 0.2, 0.3, 0.4, 0.5$) against *Staphylococcus aureus* and a *Klebsiellapneumoniae*. A culture was adapted to the 0.1 OD for each microorganism and OD was adjusted at 0.1 and washed on Mueller Hilton agar plates. Incubated these plates for 24 h at temperature 37 °C and calculate the ZOI diameter for results. Figure 11a, b indicates that there is no inhibition zone over the control. Figure 12 shows that the bar diagram of change in the inhibition zone diameter. This indicates that the ZOI rises with the rise in the dopant ratio [36, 37]. $CoFe_2O_4$ doping with a
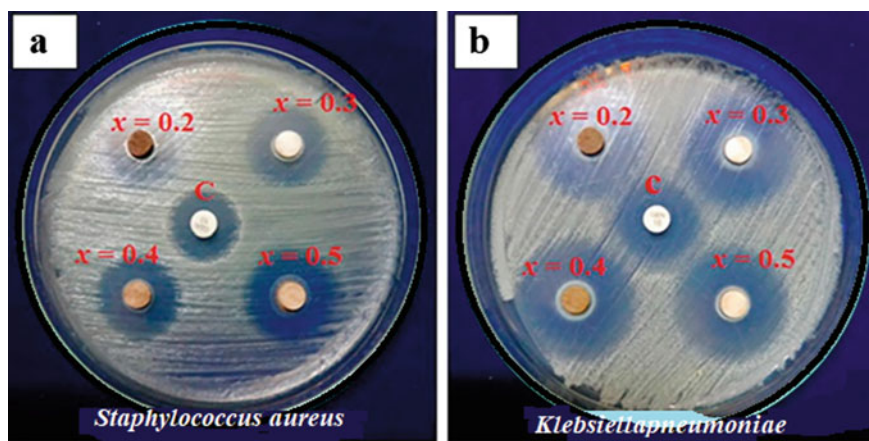
Fig. 11 Antibacterial activity of $CoCe_xFe_{2-x}O_4$ ($x = 0.2, 0.3, 0.4$ and 0.5) towards **a** *S. aureus* and **b** Klebsiellapneumoniae

Fig. 12 Graph of $CoCe_xFe_{2-x}O_4$ ($x = 0.2, 0.3, 0.4$ and 0.5) antibacterial action against *S. aureus* and Klebsiellapneumoniae
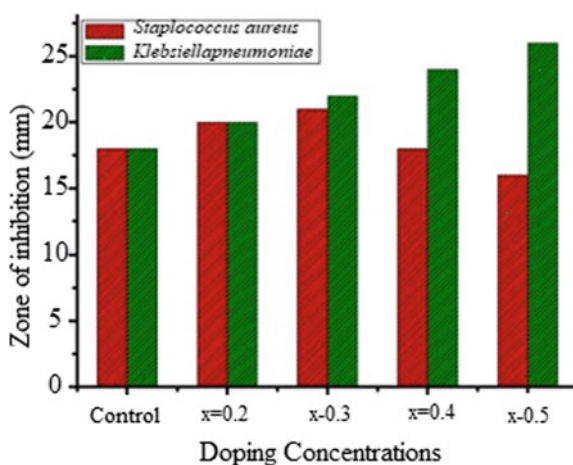
higher concentration of Ce affects higher antibacterial activity compared to Ce lower concentration doped nanopowders [38].

7.4 Iron

Žalnėravičius, Paškevičius, Mažeika, & Jagminas, used the serial dilution method for evaluating the antimicrobial action of iron-doped cobalt ferrite against prokaryotic microorganisms (*S. aureus*, *E. coli*) and eukaryotic microorganisms (*C. albicans, C. parapsilosis*). During these studies, bacteria and yeast cultures were spread in Sabouraud CAF and Nutrient agar medium for 48 h and 24 h at temperature 27 ± 1 °C and 30 ± 1 °C respectively. Microorganisms development was measured for 2–3 days incubation at temperature 30 ± 1 °C and 27 ± 1 °C. Using the field emission scanning electron microscope, the morphological features of nanoparticles exposed to microorganisms were observed.

A Kirby-Bauer procedure established that all $CoFe_2O_4$ nanoparticles had a fungicidal impact against the pathogens evaluated after an incubation 48 h. The maximum inhibition region was reported around the $CoFe_2O_4$ nanoparticles disks saturated with L-lysine (Fig. 13). It has been established that cobalt ferrite nanoparticles doped with Iron often exhibit strong killing performance besides all measured microbes. The antimicrobial property of $CoFe_2O_4$ doped nanoparticles were then further explored by examining the colony-forming units (CFU) against multidrug-resistant clinical pathogens *E. coli*, *S. aureus*, *Candida albicans,* and *C. parapsilosis*. Figure 14 shows the results found from these inquiries. Also, 1 gL^{-1} of Fe_3O_4@Lys and 100 mgL^{-1} of L-lysine nanoparticle samples were incubated and studied. In this way, there was a strong association was found between the overall amount of Co^{2+} in nanoparticles and the microorganism's survival. It is observed that maximum antimicrobial strength was shown by the $CoFe_2O_4$ nanoparticles against all examined microorganisms. Such nanoparticles demonstrated the killing efficiency of 93.1–86.3% and 96.4–42.7% for eukaryotic and prokaryotic strains respectively, as compared with the control sample. The antimicrobial activity decreases by 11–24% and 21–70% of
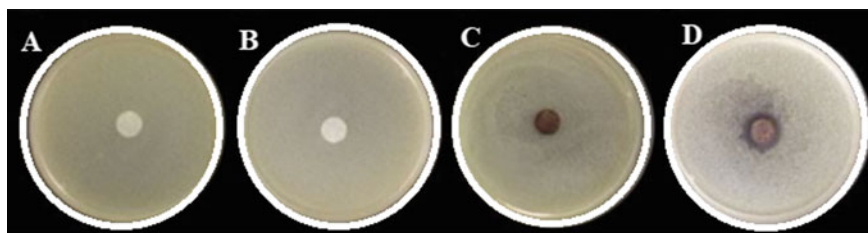


Fig. 13 Inhibitory action of l-lysine (D) functionalized $CoFe_2O_4$ nanoparticles protected filter paper samples towards microorganisms of C. albicans. In left side—control samples: **a**—filter paper, **b**—L-lysine, **c**—Fe_3O_4, and **d**—$CoFe_2O_4$ nanoparticles
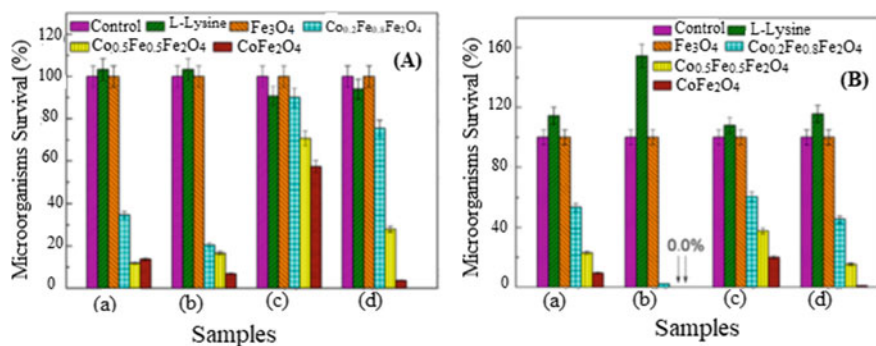
Fig. 14 Antimicrobial actions of the manufactured pure and Fe-doped $CoFe_2O_4$ nanoparticles after **a** 24 h & **b** 72 h cultivation with **a** *C. albicans*, **b** *C. parapsilosis*, **c** *E. coli* and **d** *S. aureus*

$Co_{0.5}Fe_{0.5}Fe_2O_4$ and $Co_{0.2}Fe_{0.8}Fe_2O_4$ respectively, after 24 h incubation compared to $CoFe_2O_4$. The data comparison tests resulted that a huge amount of C. parapsilosis was killed by using the same quantity of $CoFe_2O_4$ and $Co_{0.5}Fe_{0.5}Fe_2O_4$ nanoparticles after cultivating for 72 h. Moreover when S. aureus and E. coli with pure L-lysine for the time of contact 24 h reveals a bactericidal level of potency at 6% and 9%, respectively. After incubation for 72 h in pure L-lysine, the number of microorganisms increased compared to the control sample. Additionally Fig. 15 reveals the quantity of prokaryotic and eukaryotic microorganisms developed on Nutrient and Sabouraud agar plates as a result of Co^{2+}content in the nanoparticles of $CoFe_2O_4$
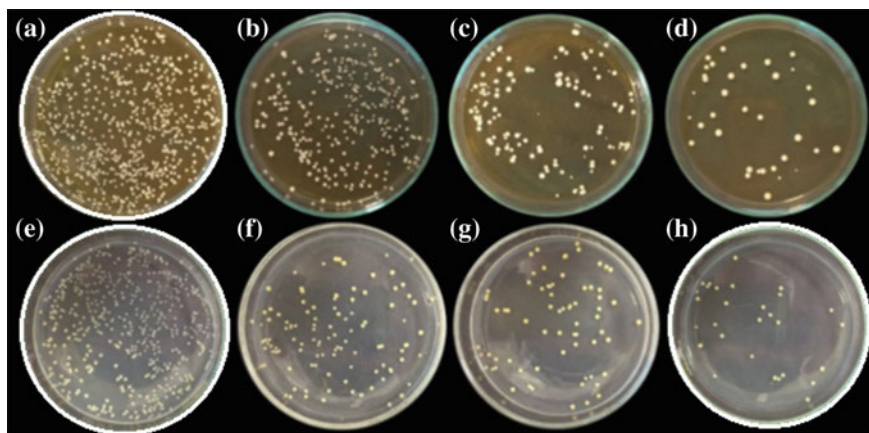
Fig. 15 Images display the antimicrobial action of different Fe-doped $CoFe_2O_4$ nanoparticles for development inhibition of *S. aureus* (bottom row) and *C. albicans* (top row) bacteria cultured in the Nutrient and Sabouraud agar plates, respectively. All bacteria were processed in liquid medium except (**a** & **e**) and by $Co_{0.2}Fe_{0.8}Fe_2O_4$ (**b** & **f**); $Co_{0.5}Fe_{0.5}Fe_2O_4$ (**c** & **g**) or $CoFe_2O_4$ (**d** & **h**) nanoparticles for 24 h. The loading was 10 gmL^{-1}

showing a substantial decrease in colonies with a rise in the amount of Cobalt in iron-doped nanoparticles of $CoFe_2O_4$. After incubation for 24 h with amount 10 g mL^{-1} of nanoparticles of $CoFe_2O_4$, only dozens of two to three bacteria *S. aureus* and *C. albicans* remains feasible instead of thousands. Important substitution of cells of C [39].

7.5 Neodymium

Rehman et al., examined Nd-doped $CeFe_2O_4$ nanopowders i-e $CoNd_xFe_{2-x}O_4$ ($x =$ 0.0, 0.1, 0.15, 0.2) towards *S. aureus, E. coli*, and *Candida albicans* bacteria. The inoculum was formed by inoculating a newly formed single bacterial colony and yeast on Sabauraud Broth and Mueller Hinton Broth, respectively. Incubated these cultures at temperature 37 ± 2 °C for 18 h and temperature 28 ± 2 °C for 48 h. *E. coli* and *S. aureus* colonies were recorded incubating for 18 h, and *Candida albicans* colony for 48 h.

After finding the optical density, *S. aureus* growth was reported to decrease with samples $x = 0.15, 0.2$ and compared with samples $x = 0.0, 0.1$. Whereas the growth pattern of *E. coli* was similar to that of control by a minor change of $x = 0.0$. The development of *Candida albicans* was observed to be minimized by 4 ratios with deep inhibition in a case when controlled with minimum Neodymium ($x = 0.0, 0.1$)) (Fig. 16).

The test organisms viable cell count showed the amount of sustainable *C. albicans* and *S. aureus* was sensibly less than that in a control state (Fig. 17a). In both experiments, all the four concentrations have a major impact on *S. aureus* survival, by a minimum survival percentage of 50%, 45%, 40%, and 30% observed with an enhanced concentration of neodymium in the $x = 0.0, 0.1, 0.15, 0.2$, respectively. All the four concentrations showed a negligible effect on *E. coli* with only 90% survival at $x = 0.0$. But, In case of *C. albicans* evolution, profound inhibition was shown with excellent activity and also shown the survival rate 9, 20, 22, and 40% at all the given four concentrations and $x = 0.0$ and $x = 0.1$ *C. albicans* shows a marginally better inhibition (Fig. 17b).

It was observed that when the concentration of Nd rises to 0.2 from 0.0 it shows increased anti-gram-positive bacterial behavior of nanoparticles while the anti-gram-negative bacterial behavior was observed to be negligible [40].

7.6 Zinc

Sanpo, Berndt, & Wang, analyzed Zn-doped $CoFe_2O_4$ Nps for antimicrobial behavior towards *S. aureus* and *E. coli* bacteria. Solid agar plates with Zn-doped $CoFe_2O_4$Nps were used to perform all the tests. Incubation of these plates took place at temperature 37 °C and after 24 h counted the colonies on the Petri dishes. Antimicrobial effects
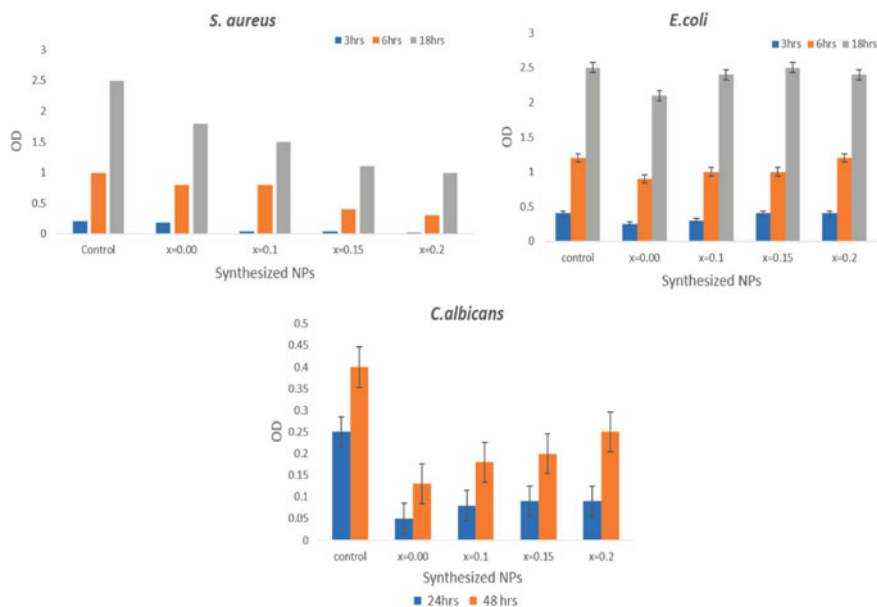
Fig. 16 Development pattern of microbes handled at separate time intervals with amount 1 mg/mL of $CoNd_xFe_{2-x}O_4$ ($x = 0.0, 0.1, 0.15, 0.2$) nanoparticles, control; untreated cells

were assessed by survival percentage and the formula is shown below [41].

$$\text{Survival \%} = \frac{\text{Colony number of treated bacteria}}{\text{Colony number of control bacteria}} \times 100$$

For measuring the inhibition zone, the lysogeny Broth agar plate was used on which samples were put with *E. coli* production, and their incubation was done overnight at 37 °C.

The inhibition region diameter of nanopowders of $CoFe_2O_4$ in the pure state is smaller than zinc doped $CoFe_2O_4$ most probably when increasing the concentration of zinc. The result shows less active interaction biocidal properties of nanopowders of cobalt ferrite in a pure state as related to Zn-substitute $CoFe_2O_4$. Figure 18 shows the antibacterial behavior of $ZnCoFe_2O_4$ towards *S. aureus* and *E. coli*. The development of *S. aureus* and *E. coli* is minimized with nanopowders of $ZnCoFe_2O_4$ in comparison to the control state. The killing rate of *S. aureus* is lesser than that of *E. coli* in nanopowders of $ZnCoFe_2O_4$. When the concentration of Zinc increased, their antibacterial behavior becomes greater [42].

Madhukara Naik et al., also studied the antibacterial action of Zn-doped $CoFe_2O_4$ Nps. Agar well diffusion technique was applied to test the antibacterial action of $CoFe_2O_4$ and Zn-doped $CoFe_2O_4$ NPs towards Salmonella typhi and *S. aureus* bacteria. 100 ml sterilized agar medium gain the volume to 250 ml flask at room temperature. Clinical isolates of Salmonella typhi and Staphylococcus aureus

(a)

(b)
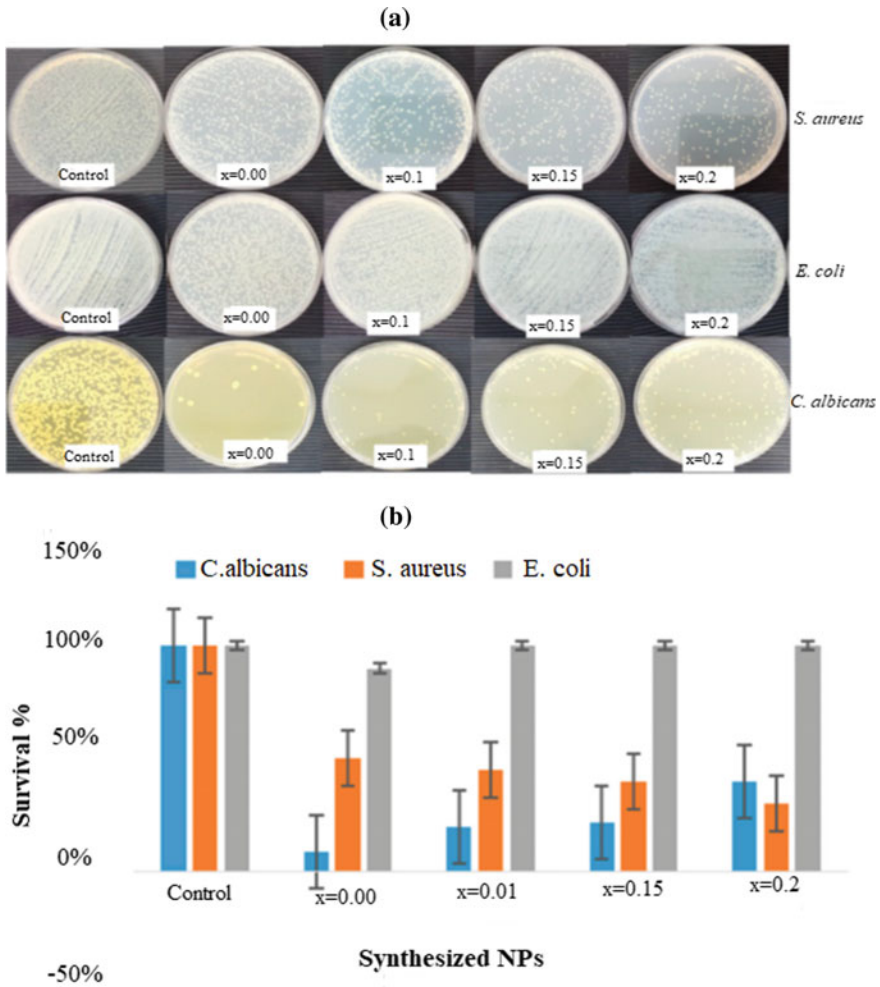
Fig. 17 Culture plates **a** and survival percentage **b** of microbes treated with amount 1 mg/mL of
$CoNd_xFe_{2-x}O_4$ ($0.0 \leq x \leq 0.2$) nanoparticles, control; untreated cells

bacteria were taken at 37 °C for 24 h for sub-culturing the nutrient broth of agar media.
After incubation measured the ZOI for results. Antibacterial action of synthesized
nanoparticles towards the standard antibiotic was less significant than the selected
pathogens as shown in Fig. 18. Table 2 showing the diameter of the inhibition region of
selected pathogens in millimeters. The antibacterial action of Zn $CoFe_2O_4$ nanopar-
ticles towards *S. aureus* (15 mm) was less as compared to *S. typhi* (22 mm) when the
concentration was 100 µg/mL [43].
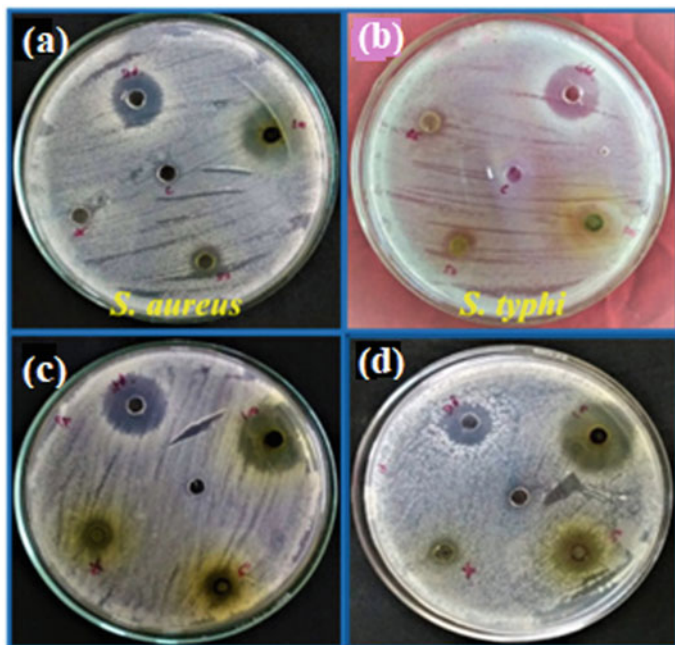
Fig. 18 Antibacterial action images of pure $CoFe_2O_4$ and Zinc doped $CoFe_2O_4$ nanoparticles

7.7 Cu, Zn, Mn

Maksoud et al., selected agar-disc distribution process for testing antimicrobial action of synthesized Fe-doped CFO NPs [44–48]. *Staphylococcus sciuri, Staphylococcus lentus, Staphylococcus vitulinus, S. aureus, Enterococcus columbae,* and *Aerococcus viridians* were bacterial strains. With a fixed UV–Vis. Spectrophotometer at 600 nm and 0.5 McFarland $(1–3) \times 10^8$ cfu/ml bacterial inoculums were set [49]. After incubation for 24 h measured the inhibition region for results [49, 52–54]. The activity of FO nanoparticles was determined by choosing a standard antibiotic disc.

Results show that among all pathogenic bacteria the highest activity was shown by $Zn_{0.75}Co_{0.25}Fe_2O_4$ nanoparticles which are the most potent FO nanoparticles as shown in Table 3. Figure 19 and Table 3 shown the antibacterial activity of CFO and metal-doped CFO nanoparticles towards *S. sciuri*, *S. lentus*, *S. aureus*, *S. vitulinus, E. columbae,* and *A. viridians.* The result shows order of increase in efficiency MCFO < CCFO < ZCFO nanoparticles. $Zn_{0.75}Co_{0.25}Fe_2O_4$ nanoparticles were shown greater efficiency against *S. aureus* by 15 mm, *E. columbae* by 13 mm*,* and *A. viridians* by 12 mm ZOI. The activity of ZCFO nanoparticles maximizes the increase of the amount of Zinc substituted CFO nanoparticles where $x = 0.75 > 0.50 > 0.25$ as noted in Table 3 and shown in Fig. 19a–f. In addition to it the 3-dimensional ZOI images aligned with ZCFO nanoparticles discs (Fig. 19a–f), show the distribution

Table 3 Antibacterial action of $M_xCo_{(1-x)}Fe_2O_4$; (M Zn, Cu, Mn; $x = 0.0, 0.25, 0.50$ and 0.75) nanoparticles (20 ppm), against several pathogenic bacteria as ZOI (mm), [a] Negative means that no ZOI had been measured

Bacterial strains	ZOI of CFO (mm)	ZOI of $Zn_xCo_{1-x}FO$ (mm)			ZOI of $Cu_xCo_{1-x}FO$ (mm)			ZOI of $Mn_xCo_{1-x}FO$ (mm)		
		X = 0.25	X = 0.50	X = 0.75	X = 0.25	X = 0.50	X = 0.75	X = 0.25	X = 0.50	X = 0.75
Staphylococcus lentus	[a]Negative	Negative	11.0d ± 0.763	11.0a ± 0.577	8.0b ± 0.5000	10.0ab ± 0.5000	11.0b ± 0.2886	Negative	Negative	Negative
Staphylococcus sciuri	Negative	7.0a ± 0.5000	7.0a ± 0.7637	11.0a ± 0.2886	Negative	Negative	Negative	7.0ab ± 0.2886	7.0ab ± 0.2886	8.0a ± 0.2886
Staphylococcus vitulinus	8.0[a] ± 0.5000	10.0c ± 0.288	11.0d ± 0.288	11.0a ± 0.2886	7.0a ± 0.2886	9.0a ± 0.7637	11.0bc ± 0.7637	7.0b ± 0.2886	7.0a ± 0.5000	12.0c ± 0.500
Staphylococcus aureus	Negative	8.0ab ± 0.2886	9.0bc ± 0.7637	15.0c ± 0.5773	10.0c ± 0.500	11.0b ± 0.2886	12.0c ± 0.2886	Negative	Negative	11.0b ± 0.500
Aerococcus viridians	8.0[a] ± 0.5773	9.0c ± 0.5773	10.0cd ± 0.866	12.0a ± 1.0408	8.0b ± 0.5000	10.0ab ± 0.8660	10.0a ± 0.5000	Negative	Negative	8.0a ± 0.5291
Enterococcus columbae	7.0[a] ± 0.5000	8.0bc ± 1.0000	8.0ab ± 0.5000	13.0b ± 0.5000	Negative	Negative	7.0a ± 0.5000	7.0a ± 0.5000	7.0ab ± 0.2886	8.0a ± 0.7637
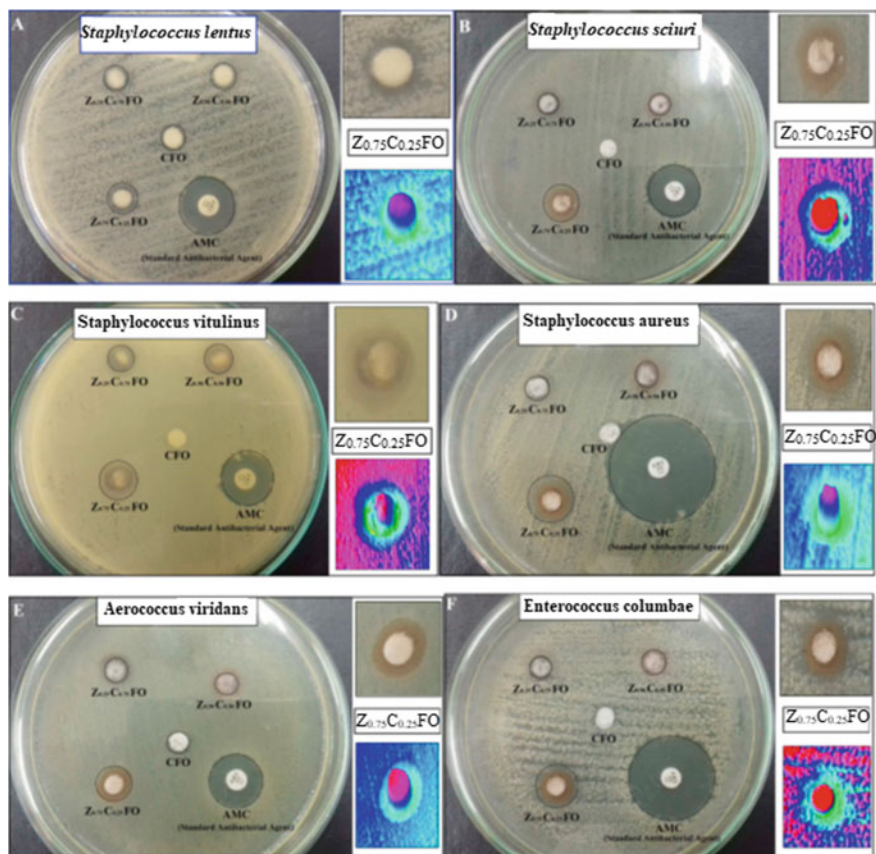
Fig. 19 Antibacterial activity of CFO, $Mn_xCo_{1-x}Fe_2O_4$ nanoparticles; $x = 0.25$, 0.50, and 0.75 versus *S. lentus* (**a**), *S. sciuri* (**b**), *S. vitulinus* (**c**), *S. aureus* (**d**), *A. viridians* (**e**), and *E. columbae* (**f**) as inhibition zone (mm)

effectiveness of the observed ZCFO nanoparticles [62, 53]. Its inevitability signifies that the effectiveness of $Mn_{0.75}Co_{0.25}Fe_2O_4$ was identified as the same as *S. vitulinus* (12.0 mm ZOI), whereas $Cu_{0.75}Co_{0.25}Fe_2O_4$ NPs represents the highest activity against *S. aureus* (12.0 mm ZOI) [50].

7.8 Polyaniline/Ag

Kooti, Kharazi, & Motamedi used magnetic materials for performing an antibacterial test with the help of Kirby–Bauer disk diffusion method. In the above tests, 5, 10, 20, and 40 mg/ml concentration of $CoFe_2O_4$, $CoFe_2O_4$ with polyaniline and $CoFe_2O_4$/polyaniline/silver were dispersed by a method of sonication after being
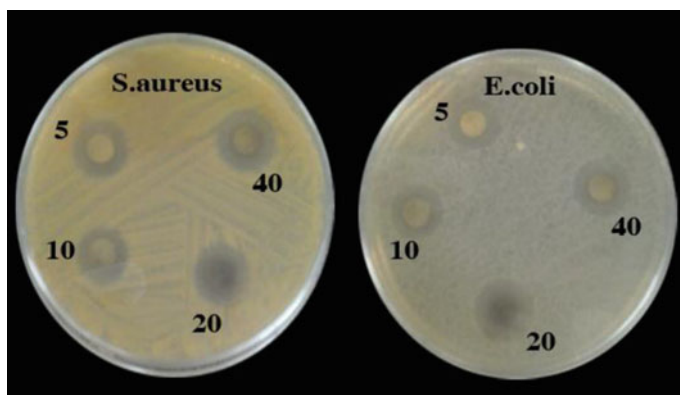
Fig. 20 Images of inhibition region around $CoFe_2O_4$/polyaniline/silver composite for *S. aureus* and *E. coli*

prepared in sterile water. The Gram-negative and Gram-positive bacteria tested included *S. aureus, B. subtilis, E. coli, and P. aeruginosa.* Sterile cotton swabs with 0.5 McFarland turbidity on culture medium for the generation of lawn culture. Then incubated these plates for 24 h at temperature 37 °C and measured and recorded the ZOI around every disk based on mm. Although Ag has a strong antibacterial activity, its potential cytotoxic action towards mammalian cells limits the use of Ag NPs as a therapeutic agent [54]. The inhibition zone diameter (IZD) in disk diffusion test results of this study are shown in Tables 2 and 3 shows that $CoFe_2O_4$/polyaniline/silver nanocomposite antibacterial activity is quite high than $CoFe_2O_4$ and $CoFe_2O_4$/polyaniline nanoparticles. This activity is quite high than a few ordinary antibacterial drugs tested. The calculated value of IZD in the case of *E. coli* is 16 mm and in the case of S. aureus is 17 mm. This shows that the potential biocidal action of magnetic $CoFe_2O_4$/polyaniline/silver composite is nearly the same for different types of bacteria. Figure 20 also shows the images of a zone of inhibition of the nanocomposite $CoFe_2O_4$/polyaniline/silver towards *E. coli* and *S. aureus* for 24 h. Hence, the prepared $CoFe_2O_4$/ polyaniline/silver composite is regarded as an antibacterial substance having a wide spectrum antibacterial capability towards gram-negative bacteria and gram-positive bacteria [51].

8 Conclusion

Pathogenic microbes have become a serious challenge to public health and at the same to the environment. These have the capability to form a biofilm that makes these more dangerous to human beings and cause increased death and mortality rates. Therefore, there is a dire need to develop novel materials that can cope with these issues having enhanced antibacterial properties. Spinel ferrites are extensively investigated for their

antimicrobial potential. These ferrites having various elemental substitutions showed encouraging results regarding the inhibition of various pathogenic microbes. There are still some challenges regarding the controlled growth and careful characterization of these materials for antibacterial applications that need to be addressed. Owing to their antibacterial properties, spinel ferrites hold good potential in pharmaceutical and biomedical applications.

References

1. Feng QL, Wu J, Chen GQ, Cui FZ, Kim TN, Kim JO (2000) J Biomed Mater Res 52:662
2. Kim TH, Kim M, Park HS, Shin US, Gong HM, Kim HW (2012) J Biomed Mater Res A 100:1033
3. Mukha IP, Eremenko AM, Smirnova NP, Mikhienkova AI, Korchak GI, Gorchev VF (2013) Appl Biochem Microbiol 49:199
4. Cavassin ED, de Figueiredo LFP, Otoch JP, Seckler MM, de Oliveira RA, Franco FF (2015) J Nanobiotechnol 13:64
5. Dorobantu LS, Fallone C, Noble AJ, Veinot J, Ma G, Goss GG (2015) J Nanopart Res 17:172
6. Ivask A (2014) J. ACS Nano 8:374
7. Alexander JW (2009) J Surg Infect (Larchmt) 10:289
8. Grass G, Rensing C, Solioz M (2011) J. Appl Environ Microbiol 77:1541
9. Ruparelia JP, Chatterjee A, Duttagupta SP, Mukherji S (2008) J Acta Biomater 4:707
10. Dizaj SM, Lotfipour F, Barzegar-Jalali M, Zarrintan MH, Adibkia K (2014) J Mater Sci Eng C 44:278
11. Zhang L, Jiang Y, Ding Y, Daskalakis N, Jeuken L, Povey M, O'Neill AJ, York DW (2010) J Nanopart Res 12:1625
12. Pelgrift RY, Friedman AJ (2013) J Adv Drug Deliv Rev 65:1803
13. Arias CA, Murray BE (2015) J Med 372:1168
14. Ivask A, Kurvet I, Kasemets K, Blinova I, Aruoja V, Suppi S, Vija H, Ka¨kinen A, Titma T, Heinlaan M, Visnapuu M, Koller D, Kisand V, Kahru A (2014) J PLOS One 9:7
15. Guzman M, Dille J, Godet S (2012) J Nanomed Nanotechnol Biol Med 8:37
16. Azam A, Ahmed AS, Oves M, Khan MS, Memic A (2012) Int J Nanomed 7:3527
17. Kim TH, Kim M, Park HS, Shin US, Gong MS, Kim HW (2012) J Biomed Mater Res-Part A 100:1033
18. Raghupathi KR, Koodali RT, Manna AC (2011) J. Langmuir 27:4020
19. You C, Han C, Wang X, Zheng Y, Li Q, Hu X, Sun H (2012) J Mol Biol Rep 39:9193
20. Dutta RK, Nenavathu BP, Gangishetty MK, Reddy AVR (2012) J Colloids Surf B Bio Interfaces 94:143
21. Raffi M, Hussain F, Bhatti TM, Akhter JI, Hameed A, Hasan MM (2008) J Mater Sci Technol 24:192
22. Baek YW, An YJ (2011) J Sci Total Environ 409:1603
23. Jung WK, Koo HC, Kim KW, Shin S, Kim SH, Park YH (2008) J Appl Environ Microbiol 74:2171
24. Madigan MT, Martinko JM, Stahl DA, Clark DP (2006) Pearson Prentice Hall Inc., San Francisco J vol 129, 130
25. Ben-David A, Davidson CE (2014) J Microbiol Methods 107:214
26. Ceramics M, Valenzuela R (2005) J. Cambridge University Press, New York, vol 188, 765
27. Pommerville JC (2011) Jones and Bartlett Publishers; LLC, Canada, vol 105
28. Zafar N, Shamaila S, Nazir J, Sharif R, Rafique MS, Hasan J, Ammara S, Khalid H (2016) J Mater Sci Technol 32:721
29. Arnaud TMS, De Barros Neto B, Diniz FB (2010) J Dent 38:848

30. El-Shahawy AAG, Abo El-Ela FI, Mohamed NA, Eldine ZE, El Rouby WMA (2018) J Mater Sci Eng C 91:361
31. Mahajan P, Sharma A, Kaur B, Goyal N, Gautam S (2018) J Vacuum 161:389
32. Biswas P, Bandyopadhyaya R (2017) J Environ Sci Nano 4:2405
33. Satheeshkumar MK, Kumar ER, Srinivas C, Suriyanarayanan N, Deepty M, Prajapat CL, Sastry DL (2019) J J Mag Magn Mater **469**, 691 (2019).
34. Zhang L, Jiang Y, Ding Y, Povey M, York D (2007) J J Nanoparticle Res 9:479
35. Samavati A, Ismail F (2017) J Particuol 30:158
36. Chitra K, Reena K, Manikandan A, Antony SA (2015) J Nanosci Nanotechnol 15:4984
37. Bomila R, Srinivasan S, Gunasekaran S, Manikandan A (2018) J Supercond Novel Magn 31:855
38. Elayakumar K, Dinesh A, Manikandan A, Palanivelu M, Kavitha G, Prakash S, Baykal A (2019) J Magn Magn Mater 476:157
39. Žalnėravičius R, Paškevičius A, Mažeika K, Jagminas A (2018) J Appl Surf Sci 435:141
40. Rehman S, Ansari MA, Alzohairy MA, Alomary MN, Jermy BR, Shahzad R, Alsalem ZH (2019) J. Processes 7:1
41. Lu Z, Li CM, Bao H, Qiao Y, Toh Y, Yang X (2008) J Langmuir 24:5445
42. Sanpo N, Berndt CC, Wang J (2012) J Appl Phys 112:1
43. Madhukara Naik M, Bhojya Naik HS, Nagaraju G, Vinuth M, Vinu K, Viswanath R (2019) J Nano-Struct Nano-Objects 19:100322
44. Batal E, Ibrahim A, El-Sayyad GS, El-Ghamery A, Gobara M (2017) J Cluster Sci 28:1083
45. Baraka A, Dickson S, Gobara M, El-Sayyad GS, Zorainy M, Awaad MI, Tawfic AF (2017) J. Chem Papers 71:2271
46. Batal E, Ibrhaim A, Hashem AAM, Abdelbaky NM (2013) J Springer Plus 2:1
47. Batal E, Ahmed I, Mosalam FM, Ghorab MM, Hanora A, Elbarbary AM (2018) J Int J Biol Macromolec 107:2298
48. Batal E, Ahmed I, Al-Hazmi NE, Mosallam FM, El-Sayyad GS (2018) J Microbial Pathog 118:159
49. Balouiri M, Sadiki M, Ibnsouda SK (2016) J Pharm Anal 6:71
50. Batal E, Ahmed I, Hashem AAM, Abdelbaky NM (2013) J SpringerPlus 2:1
51. Maksoud MIAA, El-Sayyad GS, Ashour AH, El-Batal AI, Elsayed MA, Gobara M, El-Okr MM (2019) J Microbial Pathog 127:144
52. Kooti M, Kharazi P, Motamedi H (2014) J Taiwan Inst Chem Eng 45:2698
53. Mosallam FM, El-Sayyad GS, Fathy RM, El-Batal AI (2018) J Microbial Pathog 122:108
54. Yan W, Wang R, Xu Z, Xu J, Lin L, Shen Z, Zhou Y (2006) J Molec Catal A Chem 255:81
55. Valenzuela A, Dornbusch S (1994) J Soc Sci Quarterly 75:36
56. Boll R, Hilzinger H (1983) J IEEE Trans Magn 19:5
57. Buschow K (1991) J RepO Prog Phys 54:1123
58. Relva M, Nunez M, Simberloff D (2010) J Biol Invasions 12:311
59. Goldman V, Santos M, Shayegan M, Cunningham J (1990) J Phys Rev Lett 65:2189
60. Smith J, Wijn H (1959) Phillips Technical Library Eindhoven
61. Golden T (2006) J Occup Organ Psychol Behav 27:340
62. El-Batal A, Al-Hazmi N, Mosallam F, El-Sayyad G (2018) J Microb pathog 118:169

Toxicity Assessment of Nanoferrites

Mariana Tasso, Fiorela Ghilini, Marilina Cathcarth, and Agustin S. Picco

1 Introduction to the Toxicity of Nanomaterials

This section opens with a brief introductory foreword about the aim and scope of this chapter and about the areas in the field of nanoferrites that will be covered. Here, we deal with the toxicity of nanomaterials whose main final projected application is in the **nanomedicine field**. Nanomaterials destined to regenerative therapies, implants, catalysis, bioremediation, ecological and occupational toxicity, coatings, and additives in food, cosmetics or clothing, among others, are excluded from consideration.

The focus here is placed on the toxicity of a subgroup of magnetic nanomaterials, the (nano)ferrites, which have attracted increasing attention in the nanomedicine field in the last years. The **ferrites** represent a novel avenue to the obtainment of magnetic nanostructures of eventually enhanced properties as compared to their closest relatives, the iron oxides magnetite (Fe_3O_4) and maghemite (γ-Fe_2O_3). These pure iron oxide nanoparticles, though of proven efficacy in disease diagnostics and therapy, are oftentimes limited by their capacity to induce reactive oxygen species *in vitro* and *in vivo,* by their high Curie temperature that prohibits self-regulating hyperthermia [1] and by the fact that their iron atoms are rapidly incorporated into hemoglobin, thereby potentially altering the iron homeostasis in the cells [2, 3]. By adding other ions, such as Ni^{2+}, Mn^{2+} and Co^{2+} to Fe_3O_4 nanoparticles (NPs), ferrites of a wide range of magnetic and biomedical properties can be obtained.

M. Tasso (✉) · F. Ghilini · M. Cathcarth · A. S. Picco (✉)
Instituto de Investigaciones Fisicoquímicas Teóricas y Aplicadas (INIFTA), Departamento de Química, Facultad de Ciencias Exactas, Universidad Nacional de La Plata (UNLP), CONICET, Diagonal 113 y 64, (1900), La Plata, Argentina
e-mail: mtasso@inifta.unlp.edu.ar

A. S. Picco
e-mail: apicco@inifta.unlp.edu.ar

Ferrites have low inherent toxicity, can be easily synthesized, have high physical and chemical stabilities, and low production costs [4].

This chapter begins with a general description of nanomaterials for nanomedicines and their potential routes of uptake and administration in animals and humans. Then, the fate of the nanomaterial in the body and the consequent physiological response to it will be discussed depending on the exposure pathway. A broad array of possible cell-nanomaterial interactions will be presented based on the nanomaterial physico-chemical characteristics. Cellular responses to stress and prominent nanoparticle features responsible for nanotoxicological effects will be subsequently described. Finally, a brief description of the most accepted and reported methods to evaluate the in vitro and in vivo toxicity of nanomaterials is presented. This introduction to the toxicity of nanomaterials does not intend to be comprehensive but rather to lay the foundations for a better comprehension of the following sections. For a detailed description of these aspects, the reader is conveyed to other references [5–9].

1.1   Nanomaterials and Nanomedicine

The International Organization for Standardization (ISO) defines "nanomaterial" as a "material with any external dimension in the nanoscale or having internal structure or surface structure in the nanoscale" and "nano object" as a "discrete piece of material with one, two or three external dimensions in the nanoscale", with nanoscale being in the 1–100 nm range [10]. Nanoscale objects present a higher proportion of surface atoms compared to those in the core (or the surface-to-volume ratio), a fact that can lead to thermodynamic instability and enhanced surface reactivity, propelling dissolution processes, redox reactions or the generation of Reactive Oxygen Species (ROS) [11]. These properties, together with other innate nanoparticle attributes, such as size, shape or the presence of surface ligands could constitute leading driving forces for undesirable cellular responses that may result in cellular and organ toxicity [12–14]. Given their small size, nanoparticles can interact with the cell membrane, the cytoplasm and the organelles in ways that could not be accessible to larger particles. These interactions may result in cellular stress and could therefore end up being toxic [15, 16].

Nanomedicine comprises any sort of material, like proteins, polymers, dendrimers, micelles, liposomes, emulsions, nanoparticles, and nanocapsules that falls within the range of 5–250 nm [17] and that is proposed for an application in the medical field, mostly as an analog of a medicament. Drug delivery nanosystems and the magnetic nanomaterials that are since long being used as contrast agents in magnetic resonance imaging (MRI) and that are also proposed as therapeutic tools in hyperthermia or as carriers for (image-guided) drug/gene delivery, they all belong to the nanomedicine field [18–20].

1.2   The Nanomaterials' Journey in the Body

Nanomaterials present in the air can naturally enter the human body through the airways and the mucosae. Some nanoparticles can penetrate the lung, intestinal or dermal skin barriers and translocate to the circulatory, lymphatic and nervous systems [12, 21]. This translocation may result in nanoparticles reaching most body tissues and organs, such as the brain, potentially disrupting cellular processes and causing disease [8, 15, 22, 23]. The immune system provides then the main orchestrated response to the presence of foreign objects inside the body. Immune cells present in the airway and digestive mucosae, as well as in the skin, are the first to intercept nanomaterials upon natural or accidental exposure. If the nanomaterial is administered intravenously, injected inside a target organ or instilled through the airways, the immune cells present in blood, in the muscle tissue, in the liver, spleen and kidney are those who will mainly interact with the nano-objects [8, 24, 25]. If an immune response is set in place, a cascade of events is launched to rapidly eliminate the NPs via phagocytic, metabolic and degradative processes in immune cells.

The **mononuclear phagocytic system** (MPS), also known as reticuloendothelial system (RES), comprises a family of cells that play a vital role in the defense against microorganisms, micro/nano-objects and in immunity. Bone marrow progenitors, blood monocytes and macrophages located in different organs, such as liver, spleen, lymph nodes, bone marrow, lung and brain belong to the RES [26–28]. **Tissue macrophages**, notably those residing in the liver and spleen, are the most relevant cells in the clearance of NPs from blood circulation, being able to remove NPs from the bloodstream within seconds of intravenous administration [25, 29]. Macrophage recognition of the NPs is feasible thanks to the unspecific adsorption of opsonin proteins, blood serum proteins that mark foreign objects for phagocytosis [30, 31]. **Opsonization**, the process related to the deposition of opsonins, is a major obstacle for nanomedicines as it reduces blood circulation time and diminishes the likelihood of arrival to the target site [31, 32]. Phagocytes eventually degrade the opsonized NPs and, if that is not completely feasible, undigested material will either be removed by the renal system (NPs < 10 nm) [25] or sequestered and stored in one of the MPS organs [30, 31, 33].

If opsonization can be reduced (by, for instance, modifying the surface of the NPs with certain ligands) [29, 34] and the MPS evaded, such NPs of longer circulation times may still need to trespass the vascular endothelium barrier to reach target organs. If that is achieved, nanomaterials out of circulation will be exposed to the extracellular matrix, where they may move through its water channels or be spontaneously internalized by cells, mostly by the mechanisms of endocytosis [17, 35]. NPs uptaken by the cells usually end up in the lysosome, where they are exposed to high concentrations of a wide variety of hydrolytic enzymes active on proteins, polysaccharides and nucleic acids [36, 37]. NPs are then finally degraded in the lysosome and exocytosed [38].

1.3 Cell-Nanomaterial Interactions and Cell Stress

As referred to above, there is a moment in the NPs' journey through the body in which NPs (already surface-modified by their interaction with biological fluids) come into contact with cells, in particular with the cell membrane. Since NPs are, due to their high surface-to-volume ratio, thermodynamically unstable, more surface reactive and more biologically active, their presence in the cellular environment represents a potential for inflammatory and pro-oxidant, but also antioxidant capacity [12].

The most commonly cited and explored mechanisms of nanoparticle-mediated cytotoxicity are: oxidative stress (reactive oxygen and nitrogen species), inflammation, cell membrane damage, genotoxicity, immune system response, autophagy and lysosomal dysfunction, ultrastructural changes in cell or cell organelle morphology, lactate dehydrogenase release, inhibition of cell growth and cell death, among others [37, 39–42]. A brief description of the most relevant mechanisms of nanoparticle-mediated cytotoxicity follows.

(a) **Reactive Oxygen Species** (ROS) are a number of reactive molecules and free radicals derived from molecular oxygen, like superoxide anion, hydrogen peroxide and nitric oxide, that are continually produced during cell metabolic processes, though their generation is normally counterbalanced by the action of antioxidant enzymes and other molecules. **Glutathione** may be the most important intra-cellular non-enzymatic small molecule that acts to counterbalance the damaging effects of ROS [39]. The generation of ROS and the related oxidative stress responses by the cells are frequent causes of nanoparticle toxicity, from metal oxides to semiconductor and carbon nanomaterials, among others [9, 13, 24]. Most of the metal-based nanoparticles (Fe, Si, Cu, Ni) elicit oxidative stress through the generation of free radicals following Fenton-type reactions [39, 43, 44]. Intracellularly-produced free radicals have adverse effects on cell components, like proteins (protein oxidation), lipids (lipid peroxidation) and DNA (DNA strand breaks) and also alter mitochondrial membrane potential to the point of inducing a mitochondrial dysfunction and finally cell death [39, 45, 46].

(b) **Inflammation** is the process through which the body repairs tissue damage and defends itself against foreign materials. Tissue resident macrophages participate in the primary immune response of tissues, producing various cytokines and immune regulators. The interaction of NPs with these macrophages can polarize the latter towards pro-inflammatory or anti-inflammatory phenotypes and that polarization may alter the natural equilibrium between macrophage-produced pro- and anti-inflammatory cytokines [42]. Acute and chronic inflammation can result from this unbalance [47, 48].

(c) **Cell membrane damage** can be a consequence of cell-NP interactions and typically depends on nanoparticle attributes, such as size, surface charge or hydrophilicity [14, 49, 50]. It has been well reported that NPs can cause cell and organelle membrane disruptions and, eventually, cell death [15, 22, 50–52].

(d) **Genotoxicity** refers to DNA damage induced by the presence of the NPs, which includes genome rearrangements, strand breaks and the formation of modified DNA bases. These DNA lesions can lead to gene mutations, chromosomal aberrations, apoptosis, carcinogenesis or cellular senescence if left unrepaired [53]. A wealth of evidence supports the idea of a potential genotoxic risk associated to many different NPs [8, 46, 54–56].

(e) **Other negative physiological effects** that can partially or completely impair normal cell and organ functioning have been reported for NPs in the nanomedicine field [9, 45, 57]. Among them, autophagy and lysosomal dysfunction have been proposed as mechanisms of nanomaterial toxicity, notably if the NPs are not biodegradable and accumulate in the lysosomes without plausible exit [37, 58]. NPs can also adsorb on cell membranes and block cellular ducts, cause structural changes to the membranes, or inhibit mobility and nutrient or ion intake and result in cell death.

1.4 Nanomaterial Properties and Cytotoxicity

The interactions between nanomaterials and cells are intimately controlled and defined by the nature and properties of the nano-object. The major interactions, such as the adsorption of biomolecules like proteins or opsonins, the uptake by the cells, the in vivo fate and biodistribution of the NPs and their overall toxicity, tightly depend on the physico-chemical properties of the nanomaterial. Some relevant NP properties include size, size uniformity, shape, composition, surface area, surface charge, state of aggregation, degree of crystallinity, aspect ratio, surface functionalization, aging in biological media, and the potential to generate ROS [8, 14, 35, 36, 59, 60]. A brief description of these elements and their relationship to cytotoxicity is provided below. A more comprehensive review of this topic can be found elsewhere [8, 16, 25, 60, 61].

(a) **Size** is possibly the most relevant property influencing the toxicity of a material and its distribution within the body, the organs and the cell [29, 62–64]. Iron oxide NPs with a hydrodynamic diameter higher than 100 nm quickly accumulate in the liver and spleen while NPs below 10–15 nm are likely to be eliminated through the kidneys [25, 65]. Noteworthy, NP size dictates the likelihood of NP extravasation and accumulation in tumors through their leaky vasculature [66, 67].

(b) **Size uniformity, shape, composition and surface charge.** Size uniformity and low polydispersity index are very much desirable properties for any nanomaterial to be proposed for nanomedicine applications. The shape of the nano-object is of critical importance to determine relevant properties, such as blood circulation times [25], rapid accumulation in certain organs and clearance route [68], rapid entrance to the cell [69], or interaction with the cytoskeleton [70]. Composition is another source of eventual toxicity, though iron and iron oxide

nanomaterials are considered biocompatible and non-toxic since their dissolution yields iron ions which can be metabolized by the cells [71]. Nevertheless, excess iron can induce a dysfunction in the mitochondrial iron homeostasis mechanism and, as previously discussed, participate in the generation of ROS and consequently of oxidative stress [72]. Surface charge, on the other hand, strongly influences protein adsorption and the formation of a protein corona, hence determining cell-NPs interactions and their blood circulation time [29, 51, 73, 74].

(c)   **Surface functionalization** may refer to both, the addition of a surface ligand, such as a polymer, biomacromolecule, short peptide or other, and to the deposition of a shell around the nanoparticle core. Given their susceptibility to oxidation, pure metals, like Fe, Co, Mn, Ni and their metal alloys, are usually covered with a **shell** to avoid exposure of the metal ions to oxidizing species and a potential ion release. The deposition of inorganic components, like silica, carbon, precious metals (Au, Ag) or oxides has been extensively reported, with some of these shells also serving the purpose of carrying a drug or fluorescent label [75–77].

The deposition of a shell or a **ligand** is typically associated with an enhancement in NP colloidal stability and with a higher level of control over NPs' interactions (hence diminishing NP aggregation) as well as over the interactions between NPs, biomolecules and cells. Certain ligands are added to promote a specific, desirable interaction between NPs and cells and could be defined as target-binding units, e.g. folic acid added to iron oxide NPs and proposed for imaging and therapy of various cancer types [78–80]. Polymer ligands are frequently conceived to carry anchoring groups, spacing groups (e.g. polyethylene glycol, PEG, or zwitterions to prevent protein/biomolecule adsorption), and biofunctionalization groups [65, 81–83]. Anchoring groups ensure a strong binding between the ligand and the nanoparticle surface, which diminishes the probability of ligand desorption, its displacement by competitive species present in biological media, and the consequent particle aggregation. Long-term colloidal stability under dilute conditions, high salt concentrations and elevated temperatures is a sine qua non condition for the use of NPs as nanomedicines [65].

(d)   **Aging in biological media.** Besides the almost inevitable formation of a protein corona upon NP interaction with biological fluids that confers a new biological identity on NPs distinct from the bare NP one [32, 84–86], long-term exposure can result in nanoparticle partial degradation and continuous modifications of its physicochemical properties, thereby altering the biological response. Ligand destabilization, nanoparticle dissolution and aggregation, dynamic exchange of biomolecules onto the destabilized nanoparticle surface, catalytic processes, among others, are all characteristic of long-term nanomaterial aging in biological environments.

1.5 *In Vitro and in Vivo Methods for Toxicological Examination of Nanoparticles*

The extensive list of methods frequently employed to evaluate the toxicity of materials and, in particular, of nanomaterials includes in vitro and in vivo assays, as well as oftentimes in vitro assays employing 3D cellular models of various kinds. Here, a brief description of the most cited in vitro methods will be presented. The focus is placed on in vitro methods given their higher prevalence in the literature as a preamble for further in vivo toxicological evaluations. For a more comprehensive review about the toxicological assessment methods in vivo and in 3D cellular models, the reader is conveyed to consult other sources [5, 87–89].

In vitro evaluation of nanomaterials and other compounds refers to their screening in the context of cellular systems, such as conventional cell cultures and 3D cellular models, but also of tissues, whole organs, subcellular organelles and uni- and multicellular small organisms, like bacteria or nematodes as *C. elegans*. In vitro toxicological evaluation of nanomaterials provides the required preamble for a further in vivo evaluation and enables the obtainment of valuable information in terms of possible adverse effects onto cells and permitted concentration ranges together with the appropriate environment to assess the molecular mechanisms associated to cell stress and cellular response [7, 90]. One very relevant outcome parameter of in vitro assays is the **half maximal inhibitory concentration, IC$_{50}$,** which represents the concentration of a nanomedicine that results in a 50% inhibition of a given biological or biochemical function after a defined exposure time to the cells. **Cytotoxicity** is a term that refers to the potential of a compound or treatment to cause cell damage or death [91, 92]. Alterations in cell growth rate, cell adhesion, morphology, metabolic activity, secretion of biomolecules, DNA expression, out of equilibrium production of enzymes or genes, among others, are considered examples of cytotoxicity manifestations [93]. There are several methods described in the literature to evaluate cell viability and cytotoxicity, that either directly determine the percentage of viable cells (e.g. Trypan blue exclusion assay) or assess any other parameter that could be linked to an impaired cellular function, such as cell metabolic activity (e.g. MTT test) or incipient cell membrane damage (e.g. LDH assay).

Cell metabolic activity is usually determined with the **MTT**, **MTS** and resazurin assays [94, 95]. MTT (3-(4,5-dimethylthiazol-2-yl)-2,5-diphenyltetrazolium bromide) is a yellow dye that upon intracellular reduction forms a purple formazan product [96]. Since the formazan product is insoluble and intracellularly-confined, cell lysis with detergent solutions and solubilization of formazan with organic solvents enables formazan resuspension in solution for its further absorbance determination. Besides MTT, other assays based on this principle have been developed, such as the MTS [95], XTT, WST-1 or WST-8, though for them the formazan product is chemically-modified to be rendered soluble. **Resazurin**, on the other hand, is a blue dye that is converted by metabolically-active cells to resorufin, a pink-colored dye that is fluorescent [97, 98]. Both, resazurin and resorufin are water soluble and able to diffuse through the cell membrane.

Cell viability can be ascertained by determining the capacity of the cells to produce **ATP**, adenosine triphosphate, the most important energy carrier molecule in cells. Dead cells do not synthesize ATP while the existing ATP is rapidly depleted by endogenous ATPases [99]. The quantification of cell viability through ATP is carried out by exploiting the ability of the firefly **luciferase** enzyme to oxidize the pigment D-luciferin in the presence of ATP. This oxidation produces oxyluciferin, other subproducts and emitted light (luminescence). The latter is proportional to the amount of ATP present in the sample and hence to the number of viable cells. The **ATP-luciferase** assay is one of the most sensitive tests to evaluate cell viability, being able to detect between 4 and 5 cells in a well in 384 well plates [91, 100].

An alternative to the ATP-luciferase assay is the **Neutral Red Uptake (NRU)** assay. Neutral red (3-amino-7-dimethylamino-2-methylphenazine hydrochloride) is a dye able to penetrate the cell membrane at physiological pH. Thanks to the capacity of the cells to maintain pH gradients through the production of ATP, the dye accumulates in lysosomes from where it is then recovered by addition of a destaining solution usually containing ethanol and acetic acid [101, 102]. Since dead cells do not produce ATP and cannot maintain a correct pH gradient, they lack the dye and will therefore not contribute to the measured signal.

The protein mass present in cells can be indicative of the total cell number and, hence, of **cytotoxicity** [103]. The **Sulforhodamine B (SRB)** assay enables the determination of total protein mass in fixed cells thanks to the use of a bright pink dye that binds to basic amino acid residues in proteins under mild acidic conditions [104, 105]. The dye is afterwards released from proteins under basic conditions and resuspended for spectrophotometric reading (absorbance or fluorescence). The amount of extracted dye is proportional to cell mass/number and that value can be used as indicative of the cytotoxicity of a given compound.

Damage to the cell membrane (and eventually, cell lysis) can be assessed with the **Lactate Dehydrogenase (LDH)** assay [106, 107]. The intracellularly-located LDH enzyme catalyzes the conversion of pyruvate to lactate and, depending on the conditions, is also able to catalyze the reverse reaction. If the cell membrane is damaged, the enzyme can be found in the cell medium surrounding the cells. Exposing that medium to an enzymatic substrate enables the formation of a cherry red formazan product that can be quantified by its absorbance at 492 nm. The product concentration is proportional to LDH amount/activity and that in turn correlates with the number of damaged/dead cells. Used as explained, the LDH assay reveals cytotoxicity. However, if undamaged cells are lysed and the LDH enzyme released from them is recovered, the LDH assay can also be used to assess cell viability [99, 100].

Oxidative stress can be viewed as an indicator of cytotoxicity, but also of cell viability if its repercussions result in cell death. As discussed in the previous subsections, all aerobic cells produce **Reactive Oxygen Species (ROS)** during normal oxygen metabolism. Whenever ROS production exceeds the neutralizing action of cell-borne antioxidants, a state of oxidative stress develops, which may trigger apoptosis, DNA damage and lipid peroxidation [39, 41, 72]. Direct detection of ROS and other free radicals is difficult because these molecules are short-lived and highly

reactive [108]. That's why indirect detection of secondary products of ROS, such as DNA damage, lipid peroxidation and protein oxidation are usually preferred [108, 109]. In direct detection, ROS can be measured following staining with **DCFDA** (5-(and -6)-carboxy-2,7-dichlorodihydrofluorescein diacetate) or its analogue **DCFH-DA** (dichloro-dihydro-fluorescein diacetate) [110, 111]. This membrane-permeable reagent can be hydrolyzed by intracellular esterase to DCFH, which then reacts with H_2O_2 to give a fluorescent product, DCF (2,7-dichlorofluorescein). The amount of peroxide produced by the cells can then be estimated from the DCF fluorescence [110, 111]. Alternatively, superoxide molecules (O_2^-) can be quantified by staining with the fluorescent probe **DHE**, dihydroethidium. Inside the cells, DHE is oxidized by O_2^- yielding a fluorescent product, ethidium bromide [109, 110]. An analogue is **NBT, nitroblue tetrazolium**, though its oxidation produces a stable intermediate whose formation can be monitored spectrophotometrically (absorbance) [109].

On the other hand, **protein damage due to oxidation** can be measured using the 2,4-dinitrophenylhydrazine (**DNPH**) method [112]. **Lipid peroxidation (LPO)** is mainly scrutinized by measuring its major end products, the free aldehydes **malondialdehydes (MDA)**, 4-hydroxy-trans-2-nonenal, isoprostanes and Acrolein [109, 110]. Single- and double-stranded breaks in the DNA are also generated during oxidative stress conditions, as well as other types of **DNA damage**, like thymidine glycol. DNA breaks can be detected using the comet assay, which will be introduced below.

Besides the quantification of ROS species and the evaluation of their resulting damaging effects onto lipids, proteins and DNA, it is possible to monitor the overall redox status of a cell by measuring the **activity of antioxidant enzymes and the levels of antioxidant compounds** present in the cellular milieu. The activities of superoxide dismutase (SOD), catalase, glutathione peroxidase and **glutathione S-transferase (GST)**, as well as the levels of **glutathione (GSH)**, and vitamins A, C and E can be measured to elucidate the redox status of the cell [110].

Finally, **genotoxicity** can also result as a consequence of cell-nanomaterial interactions. Genotoxicity refers to damage induced in the genetic material, which may involve small lesions at DNA level (e.g. strand breaks, adducts, point mutations) or abnormalities in chromosomes (e.g. alterations in the number of chromosomes (aneuploidy) or chromosome fragmentation (clastogenicity) [46, 113, 114]. The comet and micronucleus assays are the most popular tools for the screening of the genotoxic potential of nanomaterials [40, 89]. The **comet assay** informs about primary DNA damage while the **micronucleus assay** ascertains chromosomal alterations in proliferating cells. Lesions detected with the comet assay are still potentially reversible while those found with the micronucleus assay are irreversible.

In vitro toxicological evaluation of nanocompounds is by no means conclusive, though if carried out comprehensibly and over the wide range of cells that are expected to be in contact with the nanocompound in its journey through the body, it can provide very valuable and insightful information. Specially, it can unveil the molecular mechanisms behind the observed cytotoxicity and/or viability loss and it provides a first-order approximation to the problem of optimizing a nanocompound for its safe use as nanomedicine. The passage to 3D cell culture systems prior to

in vivo assays is very much recommended as 3D cell systems possess features of organized cellular arrangements that could better mimic cancer tissue and organs than conventional 2D cell cultures.

2 Toxicity of Iron Oxide Nanomaterials

Iron oxides are the closest relatives to ferrites and therefore the material whose main attributes may then be partially reflected in the physico-chemical and biological characteristics of the ferrites. Iron oxide is modified at various degrees to obtain ferrites: from the iron oxides magnetite (Fe_3O_4) and maghemite (γ-Fe_2O_3) to **ferrites in the form $M_xFe_{2-X}O_4$, $M_3Fe_5O_{12}$, $MFe_{12}O_{19}$, $MFeO_3$ or $M_{1-x}N_xFe_2O_4$, were M and N are co-ions** [2, 4, 115]. These various levels of substitution can drastically change the physico-chemical properties of iron oxides and, eventually also, their interaction with cells, tissues, organs and whole organisms [116–119]. Nevertheless, some of the toxicological issues associated to iron oxide nanomaterials are also shared by ferrites, e.g. induction of ROS and incidence in the cellular iron homeostasis process.

This chapter begins with a brief introduction about iron oxides and their toxicological issues and ends with a succinct description of the application areas of magnetic nanomaterials (iron oxides and ferrites included) in the biomedical field.

2.1 Iron Oxides

Iron, one of the most abundant metallic elements in living organisms, is essential for various biological processes, such as oxygen transport by hemoglobin, cellular respiration by redox enzymes, DNA synthesis, and metabolic energy [120]. Iron oxide nanomaterials are a source of iron since their dissolution under acidic conditions produces Fe^{3+} ions that can be fed into the natural iron homeostasis pathways. If the dissolved iron concentrations exceed the capacity of the cell to restore iron levels to an acceptable equilibrium, iron unbalance becomes cytotoxic. Toxicity is here related to the capacity of iron to naturally interconvert between ferrous (Fe^{2+}) and ferric (Fe^{3+}) forms and to generate free radicals [72]. Besides this potential drawback, and compared to many other NPs, iron oxide nanomaterials are still considered benign, non-toxic and biologically tolerated. They are one of the few nanomaterials that can be administered to the body, naturally degraded and fed into metabolic pathways in mammals [71].

Iron oxides are also one of the most common biocompatible magnetic nanomaterials nowadays employed in the medical field (e.g. Ferumoxytol for the treatment of iron deficiency) [121] and assiduously proposed for further applications. Pure iron oxides maghemite (γ-Fe_2O_3) and magnetite (Fe_3O_4) together with other iron-based magnetic NPs are particularly attractive for in vivo therapy and diagnostics thanks

to the combination of their high magnetization, well-described cellular metabolism and relatively low toxicity [3, 66, 122–124]. Worth a note, iron oxide NPs under ~ 30 nm are superparamagnetic and possess no residual magnetization in the absence of an externally applied magnetic field. These superparamagnetic NPs, named **SPIONs** (superparamagnetic iron oxide nanoparticles) can be transiently magnetized in the presence of an alternating magnetic field, hence only inducing heat generation in magnetic hyperthermia when the magnetic field is applied [125]. In particular for magnetic hyperthermia applications, ferrites are preferred to conventional iron oxide NPs given their lower Curie temperatures that permit self-regulating hyperthermia [1].

Finally, regarding the synthesis methods of iron oxide NPs and their physico-chemical properties, several synthesis protocols have been proposed resulting in nano-objects of various sizes, shell types, ligands, and diverse interactions with biological fluids, cells and organs [20, 65, 71, 77].

2.2 Magnetic Nanomaterials in Nanomedicine

Magnetic nanomaterials have plentiful applications in the biomedical field that comprise cell labeling and separation, cell tracking and magnetically-guided transport of magnetically-labeled cells or nano-objects, for therapeutic purposes in hyperthermia and drug delivery, and for diagnostics, e.g. as contrast agents for magnetic resonance imaging (MRI) or photodynamic therapy (PDT) [19, 65, 126–128]. Biosensing, alignment of cells for tissue engineering approaches and DNA transfer are further examples of application areas of magnetic nanomaterials [18, 19, 129]. In DNA transfer, nucleic acid molecules are bound to the nanomaterial and transported to the target site by application of a magnetic field [130]. Alternatively named magnetofection, this method has been used to deliver DNA and siRNA bound to SPIONs to cancer cells and cancer tissue [131, 132]. For the siRNA, Fang et al. demonstrated that the siRNA strategy inhibited as expected the proliferation, invasion and in vivo tumorigenicity of CD133$^+$ human glioma stem cells [132].

In the imaging field, iron oxide nanomaterials present qualities that make them advantageous for in vivo determinations since they are biocompatible, biodegradable and have deeper imaging penetration in tissues than, for instance, fluorescent probes. Nevertheless, as explained in Sect. 1, they can be opsonized and rapidly cleared from the body by phagocytes. In that respect, certain ultrasmall superparamagnetic iron oxide (**USPIO**) were found to present extended residence times in the bloodstream, which enables long-term vasculature imaging as well as the arrival and retention of higher numbers of NPs in areas of leaky vasculature, as those found in tumors [25, 133]. Thanks to USPIOs' accumulation in tumors, valuable information can be extracted about cancer stage and potential for metastasis, increased neovascularization and vascular leakiness [66]. Furthermore, USPIOs, such as ferumoxytol and ferumoxtran-10, have shown excellent potential for brain tumor imaging because of tumor's impaired blood brain barrier [133]. Last but not least, magnetic materials

have been combined with other types of materials to generate multimodal nano-objects. For instance, SPIONs were combined with fluorescent nanoparticles for dual magnetic and fluorescence imaging [75, 134, 135], while magnetic and photothermal [117, 128, 136], optoacoustic [137], and plasmonic [138] modalities also exist. These multimodal variants are flourishing these days and show great promise for enhanced diagnostics and therapy [139]. For further examples about magnetic nanoparticle applications, the reader is conveyed to a series of review articles [18, 19, 65, 66, 71, 125, 140].

3 Toxicity of Nanoferrites

This chapter section provides a detailed description about the toxicity of the nanoferrites most represented in the literature thereafter followed by a brief discussion about their most salient toxicological features. This section is divided in different subsections describing ferrites sorted by specific (co-)ions. In addition to toxicity, details on nanoferrites' structure, properties and main applications are mentioned. The information presented here is based on the analysis of the available literature corresponding to each type of ferrite. The Scopus database was preferred, though others like PubMed were also analyzed. Queries containing combined terms like "ferrite AND nanoparticle AND toxicity" or specifying specific ions (e.g. "cobalt ferrite AND toxicity") in the title, abstract or keywords were firstly performed. From the initial screening, scientific publications matching the searched terms and referring to applications mostly in the biomedical field were retained. From those, most of conference and proceedings papers were excluded, as well as reports that work with micron-size particles instead of nanoparticles and those that present toxicological results only in bacteria, yeast, algae or similar (unless deemed relevant from a nanomedicine point of view). Furthermore, only reports referring to nanoparticles with chemical formulae corresponding to the ferrites: MFe_2O_4 (or $M_xFe_{3-X}O_4$), $M_3Fe_5O_{12}$ (garnets), $MFe_{12}O_{19}$ (hexaferrites) or $MFeO_3$ (orthoferrites) were retained, were M is the co-ion [115]. The mixed ferrites with formula $M_{1-x}N_xFe_2O_4$ (or even containing more than two mixed co-ions) were also included. Once this selection was made, the resulting scientific publications were sorted by co-ion. The mixed ferrites were treated equally.

Regarding the subsections, a total of seven are presented below. Five of them (Sects. 3.1 to 3.5) are devoted to nanoferrites containing the most represented divalent co-ions (Co, Cu, Mn, Ni, Zn) in the literature; one (Sect. 3.6) groups those containing less frequent co-ions (Bi, Gd, Sr, etc.) and the final Sect. (3.7) accounts for mixed ion ferrites (e.g. NiZn). Most of the referred articles used spinel ferrites of the kind MFe_2O_4 (or $M_xFe_{3-X}O_4$). However, there are few works presenting results in non-spinel ferrites, like the ones from Zioni [141] and Alvino [142] and their co-workers who used Sr- and Ba-based hexaferrites.

Each subsection discusses in vitro and in vivo toxicity of the corresponding type of ferrite. Results from in vitro tests are summarized in one table per subsection. In

the analysis of in vitro results, more attention is given to cytotoxicity and cellular viability results, whereas the assessment of oxidative stress and genotoxicity is mentioned more succinctly. Presenting this information divided by co-ion may enable the intra- and inter-comparison among NPs of similar composition, size, synthesis method and/or surface coating, to find analogies and differences to better comprehend (if possible) the interplay between NP properties and cellular responses. On the other hand, since the evaluation of nanoferrites' toxicity in vivo is relatively scarce (compared to in vitro assessment), this information is presented in a combined single table accounting for all co-ions (Table 8). Table 8 is more diverse than its precedent in vitro tables, refers to several distinct evaluation methods and contains a wide array of in vivo toxicological observations and experimental details.

3.1 Toxicity of Cobalt Nanoferrites

Cobalt ferrite nanoparticles (Co-FNPs) are among the most promising magnetic NPs (MNPs) derived from iron oxides. They have the general chemical formula $CoFe_2O_4$ and present an inverse spinel crystallographic structure. Also, Co-FNPs with varying amounts of Co ($Co_xFe_{3-x}O_4$, with $x < 1$) [143] have been intensively studied and will be considered in this section. Co-FNPs are usually hard magnetic materials that exhibit high Curie temperature (ca. 520 °C), large coercivity, moderate magnetic saturation (up to 80 emu/g), and high magnetic anisotropy [144]. In addition, they are chemically stable and present excellent mechanical hardness. Due to these properties, they possess an enormous potential for diverse applications in the biomedical field, like magnetic hyperthermia, MRI and magnetic drug delivery, among others [144, 145].

Among the different ferrite based-nanoparticles, the toxicity of Co-FNPs is the most studied in the literature [146]. Table 1 summarizes main results from representative works dealing with the in vitro toxicological characterization of Co-FNPs. This table focuses mainly on cytotoxicity results, whereas tests devoted to assessing other toxicity aspects, like oxidative stress or genotoxicity are briefly mentioned. As it can be seen, Co-FNPs cytotoxicity has been studied in a plethora of cell lines deriving from normal and cancerous tissues of several different organs. For instance, Horev-Azaria and co-workers reported IC_{50} values for commercial Co-FNPs of around 17 nm diameter in six different cell lines from diverse tissues (A549 and NCIH441, human lung; Caco-2, human colon; HepG2, human liver; MDCK, dog kidney; TK6, human lymphoblast), primary dendritic cells (mouse) and lung slices (rat) [147]. By using different cell viability assays, such as MTT, Alamar Blue, Neutral red uptake and WST-1, they showed that the Co-FNPs-induced cytotoxicity depended on the cell type, being TK6 cells the most affected ones, while A549 and HepG2 cells exhibited negligible changes.

Ahamed [148], Abudayyak [149], Zhao [150] and their co-workers have studied different biomarkers related to oxidative stress (ROS, MDA, GSH, among others) and shown that the latter plays an important role in Co-FNPs cytotoxicity. On the

Table 1 In vitro toxicity evaluation of cobalt nanoferrites

Author	Synthesis method	Size	Surface coating	Cell line(s)	Main results/observations
Hoque et al. [162]	Co-precipitation Different Co:Fe ratios	4–5 nm (XRD) ~7 nm (TEM) 95–160 nm (DLS)	PEG, Chitosan	• 9L	All NPs were not cytotoxic up to 2 mg/mL (Trypan blue assay)
Di Guglielmo et al. [163]	Commercial ferrite cores (Nanotex)	17 nm	Silica, Silica + Gold	• 3T3 • D3	Silica coated NPs: IC_{50} ~ 0.7 mg/mL on 3T3 cells and IC_{50} ~ 0.3 mg/mL on D3 cells. Silica + gold coated NPs: IC_{50} ~ 3.5 mg/mL on both cells (MTT assay) • Evaluation of embryotoxicity (EVCAM embryonic stem cell test)
Salunkhe et al. [151]	Combustion method	~ 35 nm (XRD)	PVA	• L929	Slight reduction of cell viability. Cytotoxicity of bare NP > PVA coated NP (Trypan blue assay)
Peeples et al. [152]	Co-precipitation	~ 11 nm (XRD) 5–10 nm (TEM)	APTES, Citric Acid	• RL-65	Slight reduction of cell viability. Cytotoxicity of bare NP > coated NP (MTT and Live/Dead assays)
Berger et al. [164]	Co-precipitation (with oleic acid)	Bare NPs: ~ 15 nm (XRD) ~ 12 nm (TEM) Coated NPs: ~ 160 nm (aggregates, TEM)	Silica (MCM-41 like)	• CRL-1840	No cytotoxic up to 0.2 mg/mL (MTS assay)
Nam et al. [165]	Thermal decomposition	6–19 nm (XRD) 6–21 nm (TEM) 19–61 nm (DLS)	PMAO	• Sarcoma 180	Slight reduction of cell viability (MTT assay)
Dutz et al. [166]	Co-precipitation Different Co:Fe ratios	7–12 nm (XRD) 8–12 nm (TEM) 90–110 nm (DLS)	Citrate	• HBMEC	Slight reduction of cell viability (studied up to 50 µg/cm^2) (Resazurin-based assay, Real-time cell analysis and Live/Dead assay)

(continued)

Table 1 (continued)

Author	Synthesis method	Size	Surface coating	Cell line(s)	Main results/observations
Ansari et al. [167]	Co-precipitation followed by hydrothermal treatment	~ 12 nm (XRD) ~ 12 nm (FE-SEM) ~ 10–12 (TEM) ~ 8.5 nm (SAXS) > 400 nm (DLS)	PEG	• A2780/CP70 • Human PBMC • Human RBC	Slight reduction of cell viability in A2780/CP70 and PBMC (MTT assay). Non-hemolytic up to 0.25 mg/mL
Pasukoniene et al. [168]	Co-precipitation	~ 1–15 nm (AFM)	Citric acid	• MiaPaCa2 • A2780	No cytotoxicity observed in MiaPaCa2. Mild to high cytotoxicity observed in A2780 (Live/Dead and clonogenic assays)
Ahamed et al. [148]	Commercial (Sigma-Aldrich)	~ 23 nm (XRD) ~ 23 nm (TEM) ~ 200–400 nm (DLS)		• HepG2	High cytotoxicity observed above 0.1 mg/mL (MTT and LDH assays) • Measurements of ROS (DCFH-DA assay) and GSH levels (Ellmann method), and of SOD activity • Evaluation of caspase -3 and -9 gene expression (PCR) and activity
Horev-Azaria et al. [147]	Polyol method	~ 6 nm (XRD) ~ 14 nm (TEM)		• A549 • NCIH441 • Caco-2 • HepG2 • MDCK • Murine PDC • TK6 • Rat Lung slices	IC_{50} ~ 0.9 mM in Caco2 cells. Slight decrease of cell viability in HepG2 cells. IC_{50} ~ 0.6–0.8 mM in MDCK cells. Slight decrease of cell viability in A549 cells. IC_{50} ~ 0.15–0.35 mM in TK6 cells. No cytotoxicity in dendritic cells up to 1 mM. IC_{50} ~ 0.5 mM in lung slices (MTT assay; NRU, Alamar Blue and WST-1 assay in selected cases) • Measurement of ROS levels (DCFH-DA assay)

Table 1 (continued)

Author	Synthesis method	Size	Surface coating	Cell line(s)	Main results/observations
Abudayyak et al. [149]	Commercial (Sigma-Aldrich)	~ 39 nm (TEM)		• HepG2 • A549 • Caco-2 • SH-SY5Y	Slightly cytotoxic in all cell lines tested (MTT and NRU assays). Increased cell death by apoptosis and necrosis [A549 > SH-SY5Y > Caco-2 ~ HepG2] (AnnexinV + PI assay) • Measurements of MDA, GSH, PC and 8-OHdG levels • Primary DNA damage assessed (Comet assay)
Lojk et al. [51]	Co-precipitation	~ 60 nm with PAA, ~ 80 nm with PAA + PEI (DLS)	PAA, PAA + PEI	• B16-F1 • Human MYO	No cytotoxicity observed for PAA coated NPs. For PAA-PEI coated NPs, IC$_{50}$ ~ 0.005–0.006 mg/mL (PI viability and Annexin-V assays) • Measurement of ROS levels (DCFH-DA assay) • Measurement of NF-kB levels (for PAA-PEI coated NPs in MYO cells)
Lojk et al. [169]	Co-precipitation	~ 80 nm (DLS)	PAA	• RT4 • T24 • Porcine urothelial model	No cytotoxicity observed in any of the cell lines used up to 0.1 mg/mL (Trypan blue assay)
Lojk et al. [57]	Co-precipitation	10–20 nm (TEM) ~ 250 nm (DLS)	PAA	• SH-SY5Y	No and slight cytotoxicity observed up to 0.1 mg/mL (Live/Dead assay). Evaluation of cell cycle (flow cytometry) and autophagy (LC3 conversion) • Measurements of ROS levels (DCFH-DA assay) and mitochondrial membrane potential

(continued)

Table 1 (continued)

Author	Synthesis method	Size	Surface coating	Cell line(s)	Main results/observations
Abudayyak et al. [170]	Commercial (Sigma–Aldrich)	~ 39 nm (TEM) ~ 180 nm (DLS)		• NRK-52E	No cytotoxic up to 1 mg/mL (MTT and NRU assays). Evaluation of induced apoptosis (AnnexinV-PI assay) • Assessment of primary DNA damage (Comet assay)
Medina-Ramirez et al. [171]	Microwave assisted thermal decomposition	~ 5 nm (XRD) ~ 5 nm (TEM) ~ 90 nm (aggregates, SEM)	Citrate, Glycine	• HepG2	Highly cytotoxic mainly above 0.5 mg/mL [Glycine coated > citrate coated > bare] (Trypan blue assay)
Asmatulu et al. [172]	Sol–gel process followed by oil-in-oil emulsion/solvent evaporation technique	15–25 nm	PLGA	• RAW 264.7	Cytotoxicity observed (MTT assay)
Ovejero et al. [173]	Electrochemical Synthesis	~ 9 nm (TEM) ~ 8 nm (XRD)	Citric acid	• HeLa	Slightly cytotoxic at 0.1 mg/mL (MTT assay)
Hong et al. [174]	Oxalate-based precursor method	~ 8 nm (TEM)	Silica	• Rat harvested myocytes	NPs do not affect myocyte survival. NPs increase myocyte's contractility
Mushtaq et al. [175]	Co-precipitation	20–60 nm (SEM, AFM, DLS)	Xanthan gun	• CHO • Huh7	Slightly cytotoxic in both cell lines above 1.0 mg/mL (MTT assay)
Zhao et al. [150]	Thermal decomposition	~ 3 nm (TEM)	PMAA-PTMP	• A549	Slightly and considerably cytotoxic after 24 h and 48 h of exposure, respectively (MTT assay, microscopic observation) • Measurements of ROS (DCFH-DA assay), GSH, and MDA levels and of SOD activity

(continued)

Table 1 (continued)

Author	Synthesis method	Size	Surface coating	Cell line(s)	Main results/observations
Mariani et al. [176]	Commercial (Colorobbia Italia S.p.A.)	~36 nm (in Diethylenglycol;DLS)		• BALB/3T3	IC_{50} ~ 38 μM from Colony Forming Efficiency assay IC_{50} ~ 120 μM from cell impedance measurement and IC_{50} ~ 100 μM from respiration rates (using a Bionas 2500 analyzing system)
Akhtar et al. [157]	Hydrothermal method (nanoparticles) Solvothermal method (nanospheres)	Nanoparticles: ~25 nm (SEM and TEM) Nanospheres: 80–100 nm (SEM and TEM)	PEG	• L-132 • THP-1	Both NPs cytotoxic above 0.15 mg/mL in L-132. Both NPs cytotoxic above 0.075 mg/mL in THP-1 [cytotoxicity of nanosphere > nanoparticles] (MTT assay) • Measurement of MDA levels • Measurement of T-AOC (nanosphere < nanoparticles) • Measurements of IL-6, IL-8 and TNF-α levels
Matsuda et al. [177]	Co-precipitation (using spermine)	~10 nm (TEM) ~8 nm (XRD)		• MCF-7	Slightly cytotoxic up to 0.8 mg/mL (Flow cytometry, cells labeled with PI and thiazole orange)
Ansari et al. [178]	Hydrothermal method	~9–11 nm (XRD) ~5 nm (SAXS) ~14 nm (SEM)		• MCF-7 • Human PBMC • Human RBC	Slightly cytotoxic (in both cell lines) up to 0.3 mg/mL (MTT assay). Negligible hemolytic activity
Lucht et al. [154]	Co-precipitation	Bare NPs: ~18 nm (TEM) Coated NPs: ~27 nm (TEM)	Silica	• Jurkat cells	No cytotoxicity observed up to 0.1 and 0.4 mg/mL after 24 h and 48 h of incubation, respectively (flow cytometry using PI and Annexin-V labeling) • Evaluation of mitochondrial potential (flow cytometry using DiIC1(5))

(continued)

Table 1 (continued)

Author	Synthesis method	Size	Surface coating	Cell line(s)	Main results/observations
Aşık et al. [56]	Co-precipitation	Bare NPs: 8–20 nm (TEM) Coated NPs: 11–24 nm (TEM)	Silica	• MDA-MB-231 • MCF-10A	Bare NPs: $IC_{50} \sim 0.44$ and ~ 0.97 mg/mL on MDA-MB-231 and MCF-10A, respectively. Coated NPs: $IC_{50} \sim 0.49$ and ~ 2.1 mg/mL on MDA-MB-231 and MCF-10A cells, respectively (XTT assay) • Evaluation of primary DNA damage (Comet assay) • Evaluation of aneugenic and clastogenic potential (micronucleus assay)
Primo et al. [179]	Co-precipitation Nanoemulsion containing nanoferrite	~ 200 nm (DLS)		• J774A.1	Slightly cytotoxic (MTT assay)
Finetti et al. [180]	Commercial (Colorobbia Italia S.p.A.)	~ 19 nm	APTMS	• HUVEC	Bare NPs no cytotoxic and coated NPs slightly cytotoxic at 0.25 mg/mL for 72 h (Cell counting with H-E staining and MTT assay). Evaluation of cell permeability (using dextran-FITC) • Measurement of ROS levels (DCFH-DA assay) • Measurement of caspase-3 levels • Determination of p53 and p21 levels • Measurements of iNOS and COX-2 levels

Table 1 (continued)

Author	Synthesis method	Size	Surface coating	Cell line(s)	Main results/observations
Hwang et al. [153]	Commercial (biterials) labeled with 68 Ga	Bare NPs: ~ 35 nm (TEM) Coated NPs: ~ 50 nm (TEM)	Silica + Amine + PEG	• Hep3B	Coated NPs slightly cytotoxic up to 20 µg/well and bare NPs considerably cytotoxic (MTT assay) • Evaluation of the regulation of 52 genes, 22 associated with oxidative stress, metabolic stress and DNA repair (quantitative real time PCR array)
Pradhan et al. [159]	Co-precipitation	9–11 nm (XRD) 9–10 nm (TEM) ~ 90 (DLS)		• BHK-21	Considerably cytotoxic above 0.2 mg/mL (SRB assay)

Abbreviations and Acronyms:

Characterization techniques: XRD X-ray diffraction, *TEM* Transmission electron microscopy, *SEM* Scanning electron microscopy, *FE-SEM* Field emission scanning electron microscopy, *DLS* Dynamic light scattering, *SAXS* Small angle X-ray scattering, *AFM* Atomic force microscopy

Surface Coatings: PEG Polyethyleneglycol, *PVA* Polyvinyl alcohol, *APTES* (3-aminopropyl)trietoxysilane, *APTMS* (3-aminopropyl)trimethoxysilane, *PEI* Polyethyleneimine, *PMAO* Poly(maleic anhydride-alt-1-octadecene), *PAA* Polyacrylic acid, *PLGA* Poly(lactic-co-glycolic) acid, *PMAA-PTMP* Thiol-functionalized poly(methacrylic acid)

Cell Lines: 9L Rat gliosarcoma, *NIH/3T3 and BALB/3T3* Mouse fibroblast, *D3* Mouse embryonic stem cell, *L929* Mouse fibroblast, *RL-65* Rat lung epithelial cell, *CRL-1840* Opposum kidney cell, *Sarcoma 180* Mouse sarcoma cancer cell, *HBMEC* Human brain microvascular endothelium cell, *A2780 and A2780/CP70* Human ovarian cancer cell, *MiaPaCa2* Human pancreatic cancer cell, *A549* Human lung carcinoma cell, *NCIH441* Human lung adenocarcinoma cell, *Caco-2* Human colon carcinoma cell, *HepG2* Human hepatocellular carcinoma cell, *MDCK* Dog kidney fibroblast, *TK-6* Human lymphoblast, *SH-SY5Y* Human neuroblastoma cell, *B16-F1* Mouse melanoma cell, *RT4* Human bladder papillary urothelial neoplasm cell, *T24* Human invasive urothelial neoplasm cell, *NRK-52E* Rat kidney epithelial cell, *RAW 264.7* Mouse macrophage, *HeLa* Human cervix adenocarcinoma cell, *CHO* Hamster ovary cell, *Huh7* Human liver carcinoma cell, *L-132* Human epithelial cell, *THP-1* Human monocyte, *MCF-7* Human breast cancer cell, *Jurkat Cells* Human T lymphocyte, *MDA-MB-231* Human breast cancer cell, *MCF-10A* Human breast epithelial cell, *J774A.1* Mouse monocyte/macrophage, *HUVEC* Human umbilical vein endothelial cell, *Hep3B* Human hepatocellular carcinoma, *BHK-21* Hamster kidney fibroblast

Primary cells and related: PBMC Peripheral blood mononuclear cells, *RBC* Red blood cell, *PDC* Primary dendritic cells, *MYO* Primary myocytes

Toxicological methods: IC50 Inhibition concentration 50%, *PI* Propidium iodide, *ROS* Reactive oxygen species, *GSH* Glutathione, *SOD* Superoxide dismutase, *MDA* Malondialdehyde, *DCFH-DA* 2′,7′-dichlorofluorescein diacetate, *T-AOC* Total antioxidant capacity, *iNOS* inducible nitric oxide synthase, *COX-2* cyclooxygenase-2, *SRB* Sulforhodamine B, *NRU* Neutral red uptake, *TNF* Tumor necrosis factor, *NF* Nuclear Factor, *IL* Interleukin, *H-E* Hematoxylin–eosin, *MTT* 3-(4,5-dimethylthiazol-2-yl)-2,5-diphenyltetrazolium bromide, *MTS* 3-(4,5-dimethylthiazol-2-yl)-5-(3-carboxymethoxyphenyl)-2-(4-sulfophenyl)-2H-tetrazolium, *XTT* 2,3-bis-(2-methoxy-4-nitro-5-sulfophenyl)-2H-tetrazolium-5-carboxanilide, *PC* Protein carbonyl, *LC3* Microtubule-associated protein 1A/1B-light chain 3, *DilCl* DilC1(5) (1,1′-dimethyl-3,3,3′,3′-tetramethylindodicarbocyanine iodide, *8-OHdG* 8-Hydroxy deoxyguanosine

other hand, genotoxic effects of Co-FNPs have been less frequently investigated than cytotoxicity and oxidative stress. For instance, Aşık et al. have demonstrated that Co-FNPs induced primary DNA damage and presented clastogenic activity in human breast cancerous (MDA-MB-231) and non-cancerous (MCF-10A) cells [56]. As it can be seen in Table 1, no clear trend between Co-FNP size or synthesis method and cytotoxicity can be deduced. Nanoparticle coating usually decreases Co-FNP cytotoxicity as long as the surface functionalization is biocompatible [151–153]. As an example, Fig. 1 depicts how a silica coating diminished the cytotoxicity of Co-FNPs of around 18 nm as determined by multiparametric flow cytometry [154]. On the contrary, when coatings with known toxic effects (such as PEI, polyethyleneimine) are used, coated Co-FNPs induced higher cytotoxic effects than bare ones [51].
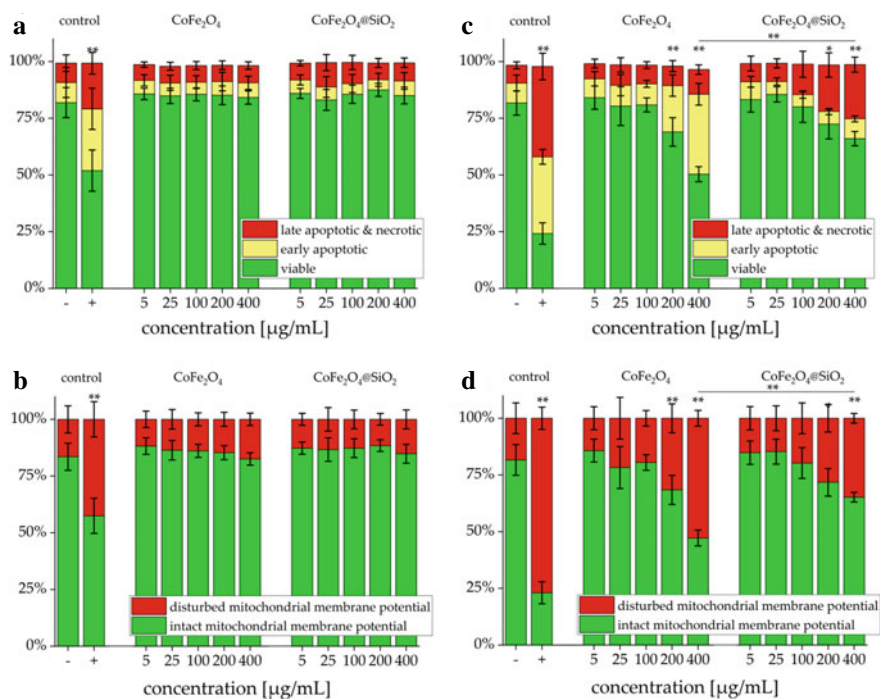
Fig. 1 Viability of Jurkat cells after incubation with increasing amounts of $CoFe_2O_4$ and $CoFe_2O_4@SiO_2$ nanoparticles for 24 h (**a, b**) or 48 h (**c, d**) and analyzed by multiparametric flow cytometry. Viability (**a, c**) was determined by Annexin V-FITC (AxV–FITC) and propidium iodide (PI) staining (first row), yielding the percentage of viable (Ax − PI −), early apoptotic (Ax + PI −) and late apoptotic and necrotic (PI +) cells. The status of the mitochondrial membrane potential (**b, d**) was analyzed by $DiIC_1(5)$ (1,1′-dimethyl-3,3,3′,3′-tetramethylindodicarbocyanine, iodide) staining and distinguishes cells with intact ($DiIC_1(5)$ positive) and depolarized ($DiIC_1(5)$ negative) membranes (second row). Positive controls contain 2% DMSO and negative controls represent the corresponding amount of solvent instead of ferrofluid. Concentrations are normalized to their respective particle concentrations, not to the magnetic content. Reproduced from Lucht et al. *Nanomaterials* 2019, *9*, 1713, with the permission of MDPI

Compared to in vitro toxicological characterization of Co-FNPs, much less works devoted to in vivo studies are found in the literature. Main results from representative toxicity reports investigating Co-FNPs together with ferrites based in other co-ions can be found in Table 8. Most of these works were performed using rodents (mice or rats) [153, 155–160] and some of them present both in vitro and in vivo results [153, 157, 159]. As shown in table 8, Co-FNPs usually tended to accumulate primarily in the liver and spleen when injected. Alterations in liver (e.g. AST, ALT or bilirubin), kidney (e.g. urea, BUN or creatinine) and/or blood (e.g. RBC, WBC or platelet count) parameters were commonly observed [156, 157, 159, 161]. However, they returned to normal values after relatively short times (8 days in the case of reference [159]). On the other hand, when Co-FNPs were intratracheally instilled, they induced an infiltration of neutrophils, lymphocytes and eosinophils in bronchoalveolar lavage fluid, among other alterations [158].

3.2 Toxicity of Copper Nanoferrites

Copper nanoferrites (Cu-FNPs) are considered suitable for biomedical applications since their constituents (copper, iron, oxygen) can be degraded by metabolic pathways in the body [181]. They exhibit high electronic conductivity, superparamagnetic behavior and high thermal stability, among other interesting properties [182], as well as the possibility to tune their size and shape using different synthetic approaches [183]. Regarding applications, Cu-FNPs are frequently designed for imaging applications [184, 185] and antibacterial treatments [186].

Table 2 summarizes representative articles studying Cu-FNPs' toxicity in vitro. The studies presented in the table used Cu-FNPs with sizes in the range 5–60 nm that were frequently not toxic up to 0.1 mg/mL. Among the different articles analyzed in this section, the one published by Ahmad and co-workers [187] presents a complete in vitro cytotoxicity analysis of Cu-FNP of ca. 35 nm on A549 and HepG2 cells. The authors showed that these Cu-FNPs reduce cell viability on both cell lines (MTT and NRU assays). In addition, they demonstrated that oxidative stress plays a key role in the cytotoxicity exerted by these nanoparticles (quantification of ROS, GSH and cell viability in the absence and presence of N-acetyl cysteine). Khanna et al. obtained similar results working with smaller Cu-FNPs and demonstrated that coating the ferrites with silica reduced their cytotoxicity [181].

Regarding in vivo studies, a recent work by Liu et al. exhaustively describes the synthesis and physicochemical properties of hemoglobin-functionalized Cu-FNPs (Hb-CFNPs; size around 13 nm) for antimicrobial and wound healing therapies and analyses their toxicity in vivo in mice [186]. Figure 2 displays in vivo results of biodistribution, body weight monitoring and histological evaluation of major organs after administration of the nanomaterial. In absence of any stimuli (like H_2O_2 or near infrared irradiation, NIR), Hb-CFNPs mainly accumulated in the heart, kidney, liver and scars and did not alter the histological structure of key organs. Moreover, the authors also performed in vitro studies and showed that Hb-CFNPs were negligible

Table 2 In vitro toxicity evaluation of copper nanoferrites

| Author	Method of synthesis	Size	Surface coating	Cell line(s)	Main results/observations
Kanagesan et al. [184]	Sol–gel self-combustion	~ 56 nm (TEM)		• MCF-7	IC_{50} ~ 0.415, 0.320 and 0.260 mg/mL after 24 h, 48 h and 72 h of incubation, respectively (MTT assay)
Ahmad et al. [187]	Commercial (Sigma-Aldrich)	~ 35 nm (TEM, XRD) ~ 450 nm in water (DLS)		• HepG2 • A549	Moderate to high cytotoxicity above 0.010 mg/mL in all cell lines tested (NRU, MTT and apoptosis caspase-3 assays) • Measurements of ROS (DCFH-DA assay) and GSH levels • Evaluation of cell cycle
Liu et al. [186]	Hydrothermal method	~ 13 nm (TEM)	Hemoglobin	• NIH-3T3 • Mouse RBC	Negligible cytotoxicity up to 0.1 mg/mL (MTT assay). Negligible hemolytic activity up to 0.03 mg/mL
Khanna et al. [181]	Sol–gel (followed by calcination)	~ 7 nm (XRD)	Silica	• J77 • A549	Bare NPs induce slight to negligible cytotoxicity up to 0.250 mg/mL. Similar results were found for coated NPs, though a slight increase in cell viability was observed (MTT assay, ATP luminescent test, cell flow cytometry)
Chakraborty et al. [185]	Co-precipitation Enriched with ^{65}Cu	~ 30 nm (TEM) ~ 175 nm in MEM media (DLS)		• WRL68	NPs with chemical composition $^{65}Cu_{0.143}Fe_{3.31}O_4$ resulted more toxic than those with $^{65}Cu_{0.088}7Fe_{2.085}O_4$ in a concentration range from 0.01 to 0.1 mg/mL (MTT assay) • Measurement of ROS levels (DCFH-DA assay)

Abbreviations and Acronyms:

Characterization techniques: *XRD* X-ray diffraction, *TEM* Transmission electron microscopy, *DLS* Dynamic light scattering

Cell Lines: NIH/3T3 Mouse fibroblast, *A549* Human lung carcinoma cell, *HepG2* Human hepatocellular carcinoma cell, *MCF-7* Human breast cancer cell, *WRL68* Human hepatic cell line (HeLa derivative cell), *J77* Human T lymphocyte

Primary cells and related: *RBC* Red blood cell

Toxicological methods: IC_{50} Inhibition concentration 50%, *ROS* Reactive oxygen species, *GSH* glutathione, *DCFH-DA* 2′,7′-dichlorofluorescein diacetate, *MTT* 3-(4,5-dimethylthiazol-2-yl)-2,5-diphenyltetrazolium bromide, *NRU* Neutral red uptake
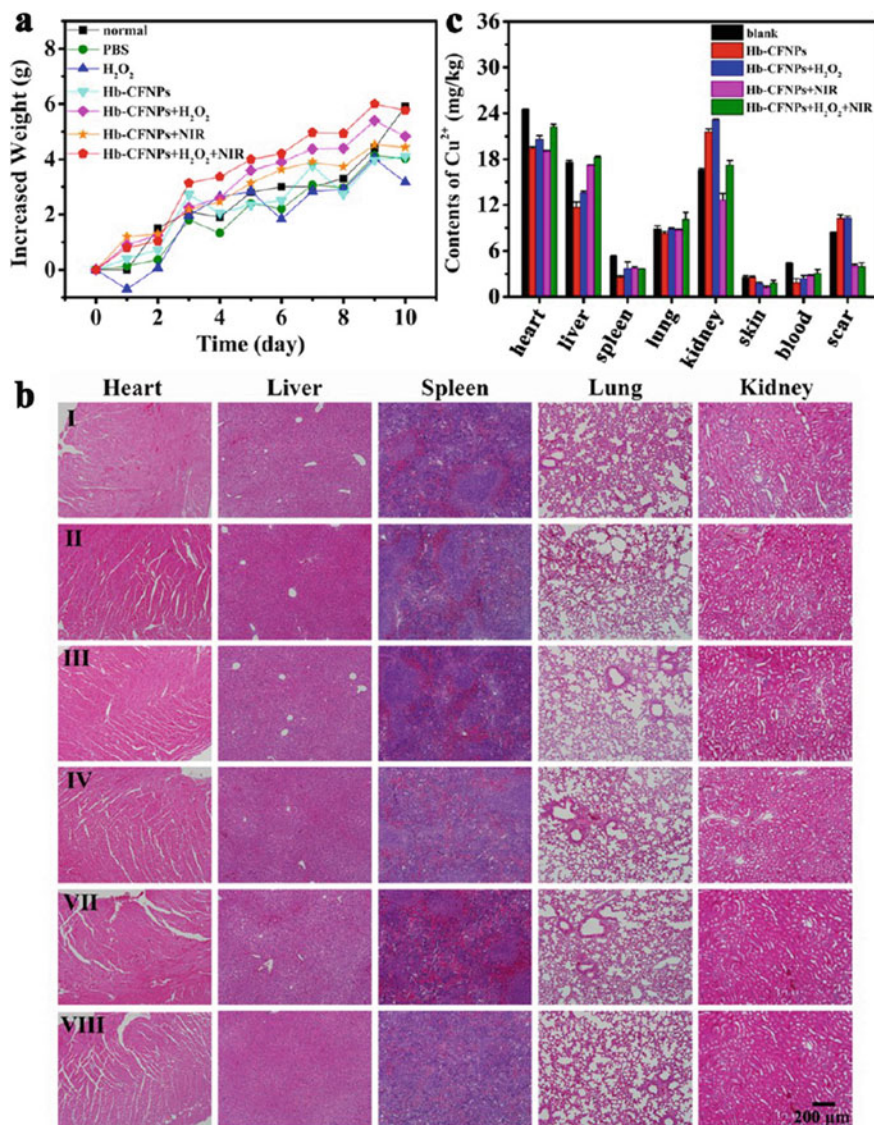
Fig. 2 In vivo toxicological assessment of Cu ferrite NPs in Kunming mice. Mice with a created subcutaneous abscess (*S. aureus*) were injected with the nanomaterial suspension (directly in the abscess). **a** Body weight change of mice in different groups as a function of time. **b** H&E-stained tissue slices from major organs (heart, liver, spleen, lung and kidney) of different treatment groups (I: PBS, II: H_2O_2 (1 mM), III: Hb-CFNPs (20 µg/mL), IV: Hb-CFNPs + H_2O_2, VII: Hb-CFNPs + NIR, and VII: Hb-CFNPs + H_2O_2 + NIR). Scale bar: 200 µm. **c** In vivo accumulation of Hb-CFNPs in mice after various treatments. Reproduced from Liu et al. ACS *Applied Materials and Interfaces* 2019, *11*, 31,649, with the permission of the American Chemical Society (ACS)

cytotoxic and hemolytic in NIH-3T3 cells and mouse red blood cells, respectively. Representative results from in vivo studies from other authors are summarized in Table 8.

3.3 Toxicity of Manganese Nanoferrites

Manganese ferrite nanoparticles (Mn-FNPs) exhibit some remarkable magnetic properties like higher SAR, saturation magnetization and relaxation times than magnetite (Fe_3O_4)-based nanoparticles [3, 116, 188]. In addition, they present good biocompatibility and low cytotoxicity [3, 136, 189, 190]. Due to this, Mn-FNPs are very promising platforms for biomedical and environmental applications, such as magnetic hyperthermia [118, 189], MRI [34, 191–194], water remediation [195, 196] and theranostics [136, 190, 191, 194, 197], among others. Furthermore, Mn can be found as part of ferrites containing mixed ions as it will be discussed in a separate subsection. These nanoferrites are usually synthesized using diverse methods, like wet chemical co-precipitation, thermal decomposition, electrochemical synthesis and hydrothermal processing, and different morphologies and sizes are obtained (from few nanometers to hundreds) [115, 150, 189, 191].

Table 3 presents representative results from in vitro toxicity studies concerning Mn-FNPs. These nanoferrites have been tested in a wide variety of cell lines including HeLa [118, 136, 190, 191], L929 [136, 191] and A549 [150], among others. Most of the works have shown that Mn-FNPs are not cytotoxic up to 0.1–0.2 mg/mL, mainly using MTT assay to test cell viability after exposure to the nanomaterial [34, 118, 150, 159, 189–191, 193]. Although less explored, oxidative stress and hemolytic activity of Mn-FNPs have been analyzed by many researchers. For instance, Zhao et al. studied the alteration of ROS, GSH, SOD, lipid peroxidation and MDA levels induced by a 5 nm Mn-FNP and showed that oxidative stress plays a central role on the nanoferrite's cytotoxicity [150]. On the other hand, Sharmiladevi and co-workers demonstrated that Mn-FNPs decorated with carbon dots exhibited negligible hemolysis in human red blod cells [194].

Representative work dealing with in vivo characterization of the toxicity induced by Mn-FNPs is summarized in Table 8. As it can be extracted from the table, most of the studies were carried out in mice and evaluated different parameteres, such as blood, liver and kidney related parameters, among other evaluations [136, 159, 191–193]. As an example, Fig. 3 presents the results obtained by Deng et al. with Mn-FNPs of ~ 16 nm diameter and decorated with PEG and a photosensitizer. Selected indicators of the function of critical organs, such as liver (Fig. 3c), kidney (Fig. 3d, e) and heart (Fig. 3f) are presented.

Table 3 In vitro toxicity evaluation of manganese nanoferrites

Author	Synthesis method	Size	Surface coating	Cell line(s)	Main results/observations
Pradhan et al. [159]	Co-precipitation	~ 10 nm (TEM)	Lauric acid	• BHK-21	Moderated cytotoxicity was observed from 0.2 to 0.6 mg/mL (SRB assay)
Ovejero et al. [118]	Electrochemical synthesis	~ 9 nm (TEM) ~ 10 nm (XRD)	Citric acid	• HeLa	No relevant cytotoxicity observed up to 0.1 mg/mL (MTT assay, Methylene blue)
Mazarío et al. [198]	Electrochemical synthesis	~ 18 nm (TEM)	Citric acid	• HeLa	No cytotoxic effects were detected for concentrations up to 0.2 mg/mL (MTT assay)
Pernia Leal et al. [34]	Seed-growth method (6 nm MnFe₂O₄ seeds)	Bare NPs: Different sizes from 6 to 14 nm (TEM) Coated NPs: From 20 to 32 nm (DLS)	PEG (3KDa)	• PC-3	No decrease in cell viability up to 0.1 mg/mL independently of NP size (MTT assay). Slight cytotoxicity was observed by means of LDH assay at 0.1 mg/mL. No evidence of apoptosis or necrosis (Flow Cytometry with PI)
Deng et al. [136]	Thermal decomposition	~ 16 nm (TEM)	PEG + photosensitizer	• HeLa • L929	No cytotoxicity was observed up to 0.2 mg/mL (MTT assay) • Measurement of ROS levels (DCFH-DA assay)
Yang et al. [191]	Thermal decomposition on graphene oxide (GO)	~ 5 nm (TEM, attached on GO nano-sheets)		• HeLa • L929 • Human RBCs	Negligible cytotoxicity was observed up to 0.2 mg/mL for all cell lines tested (MTT assay). No hemolytic effects were detected up to 0.4 mg/mL

(continued)

Table 3 (continued)

Author	Synthesis method	Size	Surface coating	Cell line(s)	Main results/observations
Pacchierotti et al. [192]	Mechanochemical processing (high-energy ball-milling)	~ 8 nm (TEM) ~ 60 nm (DLS)	Citric acid	• Balb/3T3	Cell viability was significantly decreased at concentrations of 0.05 and 0.1 mg/mL (MTT assay). Cell proliferation was significantly reduced in a dose-dependent manner starting from the 0.020 mg/mL concentration (Colony forming assay)
Zhao et al. [150]	Thermal decomposition	~ 5 nm (TEM)		• A549	Moderate toxicity was found with concentrations over 0.1 mg/mL (MTT assay). Similar results were found analyzing cell morphology changes for the same concentrations (Cell morphology analysis) • Measurements of ROS (DCFH-DA assay), GSH, SOD and MDA levels and lipid peroxidation
Lopez-Abarrategui et al. [199]	Inverse micelle method	~ 5 nm (TEM) 24–51 nm (DLS)	Citric acid + antifungal peptide Cm-p5	• RAW 264.7	Non-toxic at 0.250 mg/mL. Highly toxic above 0.5 mg/mL (MTT assay)

(continued)

Table 3 (continued)

| Author	Synthesis method	Size	Surface coating	Cell line(s)	Main results/observations
Sharmiladevi et al. [194]	Hydrothermal method	~ 142 nm (DLS)	Carbon Dots	• B16F10 • Human RBCs	Bare NPs exhibited moderate to high cytotoxicity up to 20 mM. Negligible toxicity was observed for coated NP (MTT assay, hemolytic activity test). Coated NPs were found non hemolytic
Iacovita et al. [189]	Polyol method	~ 83 nm (TEM)		• D047 • MW35 • B16F10 • A549	Negligible cytotoxicity observed in all cells up to 0.2 mg/mL (MTT assay). Microscopic evaluation of cellular features under NP exposure
Qian et al. [193]	Hydrothermal method Nanocomposite of reduced graphene oxide and $MnFe_2O_4$, labeled with ^{131}I		$C_{18}PMH$-PEG	• 4T1	Slight cytotoxicity at 200 μCi(^{131}I)/mL (MTT assay) while negligible at lower concentrations

Abbreviations and Acronyms:

Characterization techniques: *TEM* Transmission electron microscopy, *DLS* Dynamic light scattering, *XRD* X-ray diffraction

Surface Coatings: $C_{18}PMH$-*PEG* Poly(ethyleneglycol)-grafted poly(maleic anhydride-alt-1-octadecene)

Cell Lines: *BALB/3T3* Mouse fibroblast, *L929* Mouse fibroblast, *A549* Human lung carcinoma cell, *B16-F10* Mouse melanoma cell, *HeLa* Human cervix adenocarcinoma cell, *PC-3* Human prostate cancer cell, *BHK-21* Hamster kidney fibroblast, *D047* Hamster retinal pigment epithelial cell, *MW35* Human melanoma cell, *4T1* Murine breast cancer cell

Primary cells and related: *RBC* Red blood cell

Toxicological methods: *LDH* Lactate dehydrogenase, *PI* Propidium iodide, *ROS* Reactive oxygen species, *GSH* Glutathione, *SOD* Superoxide dismutase, *MDA* Malondialdehyde, *DCFH-DA* 2′,7′-dichlorofluorescein diacetate, *SRB* Sulforhodamine B, *MTT* 3-(4,5-dimethylthiazol-2-yl)-2,5-diphenyltetrazolium bromide
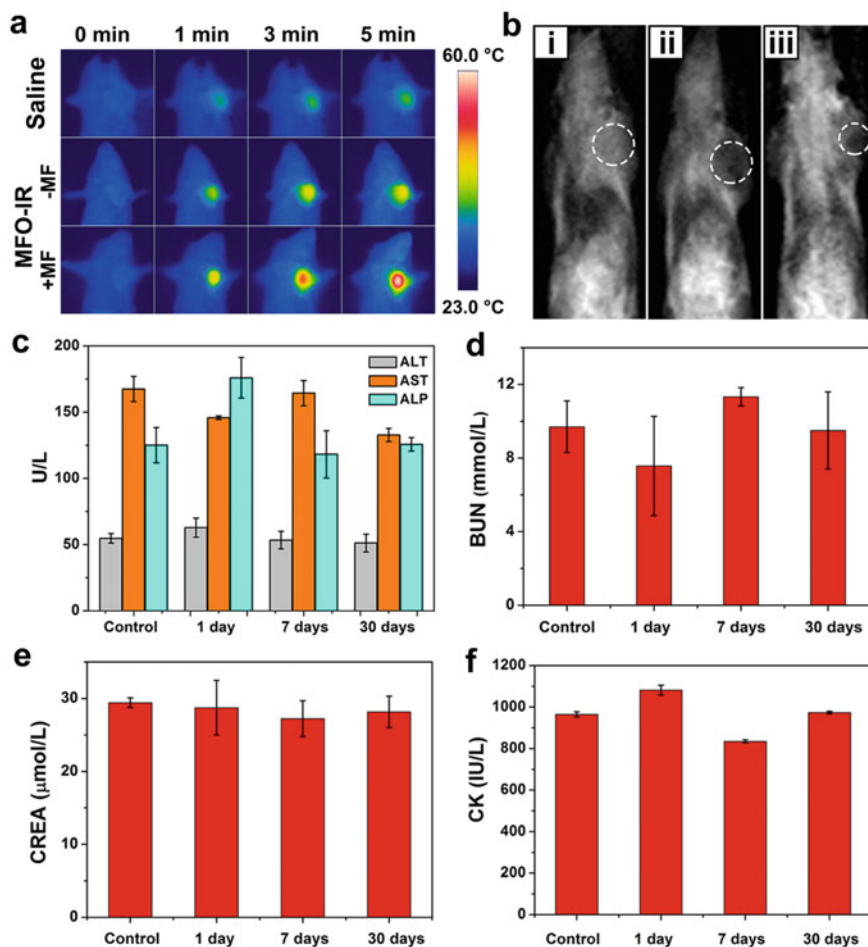
Fig. 3 In vivo IR/MRI imaging and long-term biocompatibility of Mn-FNPs of ~ 16 nm diameter and decorated with PEG and a photosensitizer (MFO-IR). **a** Full-body IR thermal images of tumor-bearing Balb/c mice after intravenous injection of saline and MFO-IR (dose 10 mg/kg) with or without magnetic field (+/-MF) under 808 nm laser irradiation (1.0 W/cm^2) taken at different time intervals. **b** T2-weighted MRI images of H22 tumor-bearing mice before injection (i), post intratumoral injection of MFO-IR (ii) and post intravenous injection of MFO-IR with an external magnetic field (iii). The tumors are highlighted by white circles. **c–f** Blood test parameters for control group and MFO-IR treated groups at different times after nanomaterial administration. **c** Liver function as determine by alanine transaminase (ALT), aspartate transaminase (AST) and alkaline phosphatase (ALP) activities. **d, e** Examination of kidney function through measurements of blood urea nitrogen (BUN) and creatinine (CREA), respectively. **f** Heart function as evaluated by creatinine kinase (CK). Reproduced from Deng et al. *Journal of Materials Chemistry B* 2017, *5*, 1803, with the permission of the Royal Society of Chemistry (RSC)

3.4 Toxicity of Nickel Nanoferrites

Nickel ferrite nanoparticles (Ni-FNPs) are well-known soft magnetic materials with an inverse spinel structure in which Fe^{3+} is equally located at tetrahedral and octahedral sites while Ni^{2+} is located at octahedral sites [2, 200]. Among all spinel ferrites, Ni and Ni-Zn ferrites are very promising nanomaterials due to their low cost, moderate saturation magnetization, good chemical and thermal stability, catalytic behavior and ferromagnetic properties [2, 200, 201]. As for other spinel ferrites, Ni-FNPs show paramagnetic to superparamagnetic behavior and have therefore found applications in MRI, magnetic hyperthermia, targeted drug delivery, cell labeling, photocatalysis, environmental remediation, among others [2, 48]. According to a recent survey by Kefeni et al., cobalt ferrites are the ones possessing the highest numbers of published papers among all ferrites in the biomedical field and are followed by Mn, Ni and Zn ferrites, with no substantial differences between these last three [200]. This survey highlights the relevance of Ni-FNPs as interesting NPs in the biomedical field, though this does not seem to correlate with the notorious lack of information about their toxicity, both in vitro and in vivo [201–203].

Nickel is considered a toxic material; its toxicological mechanism of action has been linked to mitochondrial dysfunctions and oxidative stress, though epigenetic alterations induced by nickel exposure were also found to perturb the genome [204]. Table 4 summarizes the main observations corresponding to a selection of scientific publications dealing with the in vitro toxicological assessment of Ni-FNPs. Multiple cell types have been considered, both cancerous or not, belonging to different tissues and organs. NP size, synthesis method and NP coating are various too. Worth a note in the table is the work from Ahamed et al. that expands the usual cell viability assessment commonly found in most of the literature to include genotoxicity, oxidative stress and the rational use of a series of methods aiming at unveiling the molecular cytotoxicity mechanisms [201, 202]. Working with either commercial or lab-made NPs of similar size, ~ 20 nm (TEM) and ~ 100 nm (DLS in cell medium), and with three human cancer cell lines, A549 (alveolar), HepG2 (liver) and MCF-7 (breast), they found significant viability reduction below 85% at concentrations above 25 μg/mL for A549 or above 5 μg/mL for HepG2 and MCF-7 measured with the MTT and NRU assays and confirmed by increased LDH production. Caspase 3 and 9 enzymatic activity and mRNA levels were also elevated above those concentrations (Fig. 4) and the mitochondrial membrane potential was reduced. Oxidative stress, the generation of ROS and depletion of GSH were also confirmed. Key apoptotic protein p53 and apoptotic genes were upregulated while anti-apoptotic proteins and genes like Bcl-2 were down-regulated.

Although adding a coating or ligand to NPs can oftentimes enhance cell viability, this was not the case for oleic acid (OA) around 10 and 150 nm size NPs as evaluated in Neuro 2A cells (mouse neuroblastoma) by the MTT assay [203]. NPs coated with OA resulted more cytotoxic than bare NPs. Furthermore, NPs coated with one layer of OA were more cytotoxic than those coated with two, and that for both NP sizes. Working with NPs of ~ 70–80 nm size (TEM) obtained by co-precipitation followed

Table 4 In vitro toxicity evaluation of nickel nanoferrites

Author	Synthesis method	Size	Surface coating	Cell line(s)	Main results/observations
Karunamoorthi et al. [206]	Co-precipitation followed by freeze-drying Nanocomposite containing Hydroxyapatite, HA	200–300 nm (TEM)		• HeLa	Pure Ni-ferrite showed high cytotoxicity compared to pure HA and the composite material. Composite exhibited slight cytotoxicity from 0.01 mg/mL onwards (MTT assay)
Ovejero et al. [118]	Electrochemical synthesis	~ 14 nm (TEM) ~ 12 nm (XRD)	Citric acid	• HeLa	Moderate to high cytotoxicity above 0.01 mg/mL (MTT assay)
Yin et al. [203]	Ball milling or polyol method	~ 10 nm (small NPs) and ~ 150 nm (large NPs) (TEM)	Oleic acid	• Neuro 2A	Bare NPs: slightly cytotoxic. Cytotoxicity independent of particle size. Coated NPs: Increased cytotoxicity. Large particles showed higher cytotoxicity than smaller particles (MTT assay)
Ahamed et al. [202]	Commercial (Sigma–Aldrich)	~ 26 nm (XRD) ~ 97 nm (DLS in cell medium)		• A549	Slightly cytotoxic from 0.025 mg/mL onwards (MTT, NRU and LDH assays). Determination of caspase-3 and -9 activities (LDH and enzyme activity test) • Measurement of ROS (DCFH-DA assay) and GSH levels (Ellman's method) • Evaluation of mRNA expression of p53, apoptotic and anti-apoptotic proteins

Table 4 (continued)

Author	Synthesis method	Size	Surface coating	Cell line(s)	Main results/observations
Ahamed et al. [201]	Co-precipitation	~ 21 nm (TEM) ~ 110 nm (DLS in cell medium)		• HepG2 • MCF-7	Slightly cytotoxic in both cell lines at a concentration of 0.005 mg/L (MTT, NRU and LDH assays). Increased activity of caspase 3 and caspase 9 and reduction of MMP (enzyme activity test and MMP assay) • Measurements of ROS (DCFH-DA assay), GSH (Ellman's method) and LPO levels • Evaluation of mRNA expression of p53, apoptotic and anti-apoptotic genes • Measurement of caspase-3 and -9 genes
Egizbek et al. [205]	Co-precipitation followed by thermal annealing	70–80 nm (TEM)		• HeLa • PC-3 • L929	Slightly cytotoxic up to 0.1 mg/mL in all cell lines (MTT assay)

(continued)

Table 4 (continued)

| Author	Synthesis method	Size	Surface coating	Cell line(s)	Main results/observations
Martinez-Rodriguez et al. [207]	Commercial (Nanoshel®-UK Ltd.)	< 30 nm		• Human RBC • Human PBMC	No cytotoxicity observed up to 0.2 mg/mL in PBMC (Trypan blue and MTT assays). No hemolysis induced in RBC up to 0.2 mg/mL • Catalase and GST activities tested in hemolyzed sample's supernatant

Abbreviations and Acronyms:

Characterization techniques: *XRD* X-ray diffraction, *TEM* Transmission electron microscopy, *DLS* Dynamic light scattering

Cell Lines: *HeLa* Human cervical cancer cell line, *A549* Human alveolar basal epithelial cancer cell line, *MCF-7* Human breast cancer cell line, *HepG2* Human liver cancer cell line, *PC-3* Human prostate cancer cell line, *Neuro 2A* Mouse neuroblastoma cancer cell line, *L929* Mouse fibroblasts

Primary cells and related: *RBC* Red blood cells, *PBMC* Peripheral blood mononuclear cells

Toxicological methods: *ROS* Reactive oxygen species, *GSH* Glutathione, *MTT* 3-(4,5-dimethylthiazol-2-yl)-2,5-diphenyltetrazolium bromide, *NRU* Neutral red uptake, *LDH* Lactate dehydrogenase, *MMP* Mitochondrial membrane potential, *DCFH-DA* 2',7'-dichlorofluorescein diacetate, *GST* Glutathione S-transferase, *LPO* lipid peroxidation
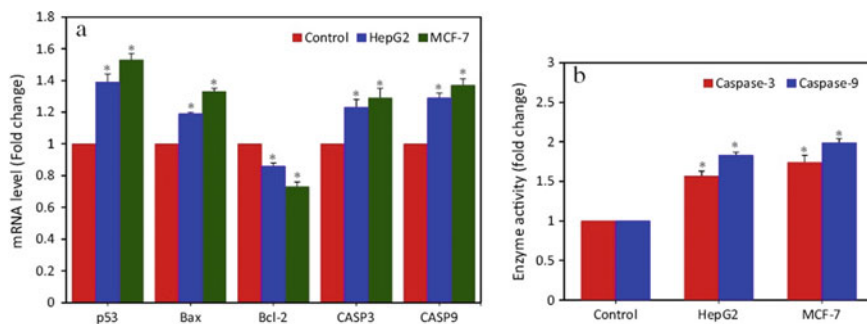
Fig. 4 Nickel ferrite NPs induce apoptosis in HepG2 and MCF-7 human cancer cells. **a** mRNA levels of relevant apoptotic (p53, Bax, CASP3, CASP9) and anti-apoptotic (BCl-2) genes after cell exposure to 10 μg/mL of nickel ferrite NPs during 24 h as determined by quantitative real-time PCR. **b** Caspase 3 and caspase 9 enzyme activity levels after cell exposure to 10 μg/mL of nickel ferrite NPs during 24 h. Data correspond to the mean ± SD of three identical experiments carried out in triplicate. *Significant difference compared to the controls ($p < 0.05$). Reproduced from Ahamed et al. *Chemosphere* 2015, *135*, 278 with the permission of Elsevier

by thermal annealing, Egizbek et al. found very promising viability results (> 85%) up to 0.1 mg/mL Ni-FNPs in the three cell lines evaluated (HeLa, PC-3 and L929) [205].

Finally, as for other ferrite co-ions, Table 8 presents a brief summary of in vivo evaluations of Ni-FNPs. As observed in the table, only a few reports could be found referring to this subject. This underlines the need for further investigations in this area applied to relevant model organisms.

3.5 Toxicity of Zinc Nanoferrites

The introduction of Zn^{+2} ions into the tetrahedral sites of the ferrite structure (replacing Fe^{+2} ions) reduces the magnetic properties (e.g. saturation magnetization and coercivity, among others) of the derived materials [208, 209]. Thus, it is very common to observe the use of Zn^{2+} in combination with other divalent ions to form mixed co-ion nanoferrites (see Sect. 3.7 below) [115, 210]. Zinc-based nanoferrites (Zn-FNTs) are mostly used in supercapacitors, electrodes for lithium batteries or for water splitting processing [115].

Table 5 summarizes representative articles reporting in vitro toxicity studies of Zn-FNPs. As it can be observed in the table, these studies were performed using synthesized NPs (thermal decomposition, polyol method, sol–gel process, among other strategies) as well as commercial ones [207, 211, 212], and a wide variety of cell lines and primary cells. For instance, Kanagesan et al. reported IC_{50} values in the range of 0.2–0.3 mg/mL for Zn-FNPs of ~ 56 nm diameter in contact with MCF-7 cells (MTT assay) and demonstrated that the higher the incubation time the lower the

Table 5 In vitro toxicity evaluation of zinc nanoferrites

Author	Synthesis method	Size	Surface coating	Cell line(s)	Main results/observations
Alhadlaq et al. [211]	Commercial (Sigma-Aldrich)	~ 44 nm (TEM) ~ 390 nm (DLS)		• A549 • A431 • HepG2	Moderate to high toxicity was observed above 0.01 mg/mL in all cells (roughly cytotoxicity in A549 cells > HepG2 cells > A431) (MTT and LDH assays) • Measurements of ROS (DCFH-DA assay) and GSH levels (Ellmann's method) and mitochondrial membrane potential • Measurements of apoptotic genes and enzymes (Reverse transcription PCR and colorimetric assay)
Lacovita et al. [189]	Polyol method	79 nm (TEM)		• D047 • MW35 • B16F10 • A549	Negligible cytotoxicity at 0.05 mg/mL in all cell lines. At higher concentrations (0.1 and particularly at 0.2 mg/mL) considerable toxicity is observed in MW35, B16F10 and A549 cells (MTT assay)

(continued)

Table 5 (continued)

Author	Synthesis method	Size	Surface coating	Cell line(s)	Main results/observations
Saquib et al. [212]	Commercial (Sigma-Aldrich)	40–85 nm (TEM) ~ 130 nm (DLS)		• WISH	Moderate to high reduction of cell viability at concentrations of 0.08 and 0.1 mg/mL after 72 h (MTT and NRU assays) with significant mitochondrial damage and apoptosis. Evaluation of cell cycle (Flow cytometry) • Measurements of ROS levels (DCFH-DA assay) and mitochondrial membrane potential • Measurements of caspase-3 levels and of p53, bax and bcl2 levels (Western blot) • Primary DNA damage assessed (Comet assay) • Evaluation of the regulation of 84 genes responsible for human stress and toxicity pathways (quantitative real time PCR assay)

(continued)

Table 5 (continued)

Author	Synthesis method	Size	Surface coating	Cell line(s)	Main results/observations
Kanagesan et al. [184]	Sol–gel self-combustion method	~ 68 nm (TEM)		• MCF-7	IC_{50} values were 0.310, 0.285 and 0.221 mg/mL after 24 h, 48 h and 72 h of incubation, respectively (MTT assay)
Hong et al. [174]	Oxalate-based precursor method	~ 8 nm (TEM)	Silica	Myocytes of Sprague–Dawley rats	NPs improved cell contraction after incubation with 0.1 mg/mL NP solution for 30 min (Video-sarcomere detection system IonOptix Corp.)
Martínez-Rodríguez et al. [207]	Commercial (Nanoshel)			• Human RBC • Human MNC	No cytotoxicity observed up to 0.2 mg/mL in PBMC (Trypan blue and MTT assay). No hemolysis induced in RBC up to 0.2 mg/mL • Catalase and GST activities tested in hemolyzed sample's supernatant
Wang et al. [117]	Solvothermal method	~ 180 nm (TEM) ~ 200 nm (DLS)		• HEK-293 T • HeLa • A549	Negligible to slight toxicity was found for concentrations up to 1 mg/mL in all tested cells (CCK-8 assay)

(continued)

Table 5 (continued)

Author	Synthesis method	Size	Surface coating	Cell line(s)	Main results/observations
Zou et al. [215]	Mineralization (in situ with silk fibroin (SF)) Nanoparticles (NP) and Nanorods (NR)	NRs: ~ 20–50 nm (TEM)	Silk-fibroin	• PC-12	NRs and NPs induced negligible reduction in cell viability up to 0.5 mg/mL after 48 h and 5 days (MTT assay). Mean length and number of neurites in PC12 cells were calculated from TEM images
Liu et al. [216]	Mineralization (in situ with silk fibroin (SF))	10-15 nm (XRD) 10–50 nm (TEM)	Silk-fibroin	• PC12	NPs induced negligible reduction in cell viability up to 0.5 mg/mL after 48 h and 5 days (MTT assay). Cell viability decreased with the concentration of NPs with/without SF. Compared to bare NPs, coated NPs enhanced the viability of cells at 0.25 and 0.5 mg/mL for 2 days and at 0.0625 mg/mL for 5 days (MTT assay, TEM images). Mean length and number of neurites in PC12 cells were calculated from TEM images

(continued)

Table 5 (continued)

Author	Synthesis method	Size	Surface coating	Cell line(s)	Main results/observations
Rivero et al. [214]	Electrochemical synthesis	~ 12 nm (TEM) ~ 160 nm (DLS)	Citric acid	• Caco-2 • HepG2 • MDCK • Calu-3 • Raw 264.7	Slightly cytotoxic in Caco-2, Calu-3 and HepG2 cells. Moderately cytotoxic in RAW 264.7 and MDCK cells (MTT assay)

Abbreviations and Acronyms:

Characterization techniques: *XRD* X-ray diffraction, *TEM* Transmission electron microscopy, *DLS* Dynamic light scattering

Cell Lines: *A549* Human lung carcinoma cell, *B16-F10* Mouse melanoma cell, *RAW 264.7* Mouse macrophage, *D047* Human retinal pigment epithelial cell, *MW35* Human melanoma cell, *MCF-7* Human breast cancer cell, *HepG2* Human hepatocellular carcinoma cell, *A431* skin epidermoid carcinoma cell, *Caco-2*: Human colon carcinoma cell, *MDCK* Dog kidney fibroblast, *WISH* Human amnion epithelial cell (HeLa derivative cell), *HeLa* Human cervix adenocarcinoma cell, *HEK-293 T* Human embryonic kidney cell, *PC-12* Rat pheochromocytoma cell, *Calu-3* Human lung adenocarcinoma

Primary cells and related: *RBC* Red blood cell, *MNC* Mononuclear cells

Toxicological methods: *IC$_{50}$* Inhibition concentration 50%, *LDH* Lactate dehydrogenase, *ROS* Reactive oxygen species, *GSH* Glutathione, *DCFH-DA 2',7'*-dichlorofluorescein diacetate, *CCK-8* Cell counting kit 9, *NRU* Neutral red uptake, *GST* Glutathione S-transferase

IC$_{50}$ [184]. Alhadlaq and co-workers showed that commercial Zn-FNPs of ca. 44 nm size can be very cytotoxic above 0.01 mg/mL for HepG2, A549 and A431 cells (MTT and LDH assays), increasing ROS and reducing GSH levels [211]. On the other hand, Saquib et al. performed an extensive study using commercial Zn-FNPs of 40–85 nm in size and WISH cells [212]. The authors demonstrated that the nanoparticles were cytotoxic above 0.060–0.080 mg/mL and induced primary DNA damage (comet assay). In addition, they found that Zn-FNPs significantly reduced mitochondrial potential ($\Delta\Psi$m) and increased intracellular ROS generation suggesting the role of these nanomaterials in the induction of oxidative stress leading to DNA damage (see Fig. 5).

Studies about the in vivo toxicological effects of Zn-FNPs are really scarce in the literature [213, 214]. Representative works can be found in Table 8. For instance, Hadrup and co-workers studied the effects of commercial Zn-FNPs (10–30 nm size) on mice intratracheally instilled with the nanomaterial and demonstrated that the NPs were slightly inflammogenic exhibiting neutrophil infiltration in bronchoalveolar lavage (BAL) fluid after 1 and 3 days of exposure [48].
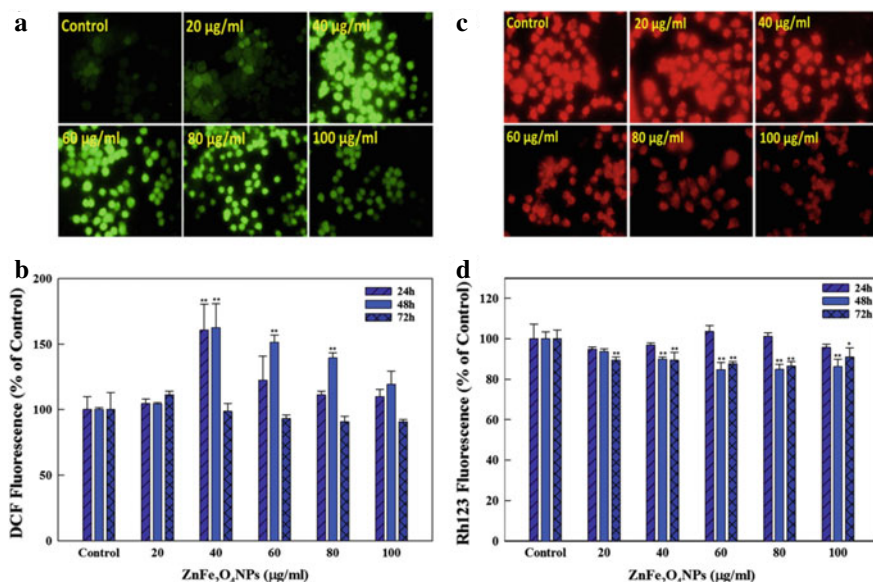
Fig. 5 Zn-FNPs mediate intracellular ROS generation. **a** Zn-FNPs concentration-dependent enhancement in DCF (dichlorodihydrofluorescein) green fluorescence in WISH cells due to ROS generation by ZnFe$_2$O$_4$ NPs after exposure for 48 h. **b** Comparative analysis of the fluorescence enhancement of DCF obtained by flow cytometry at various time points with increasing Zn-FNPs concentrations. **c** The effect of Zn-FNPs on the mitochondrial potential ($\Delta\Psi$m) of WISH cells measured as the change in the fluorescence intensity of rhodamine 123 (Rh123) after 48 h. **d** Flow cytometry measurements of $\Delta\Psi$m in WISH cells at different time points after cell exposure to increasing concentrations of Zn-FNPs. Reproduced from Saquib et al. *Toxicology and Applied Pharmacology* 2013, *273*, 289, with the permission of Elsevier

3.6 Toxicity of Nanoferrites Containing Other Co-Ions

Ferrites containing other co-ions than Co, Cu, Mn, Ni and Zn are here labeled as "other co-ion ferrites". Their representation in the biomedical scientific literature is far less prominent than that of the other ferrites [200], though possibly similarly represented as the mixed co-ions ferrites as inferred from the literature search onto which this chapter is based. Ba, Bi, Ca, Cu, Ga, Gd, Mg and Sr are examples of other co-ions included in this group.

Some co-ion ferrites have a crystalline structure that differs from the cubic spinel MFe_2O_4, though many are of that type, e.g. $CaFe_2O_4$, $CuFe_2O_4$, $GaFe_2O_4$ and $MgFe_2O_4$. For instance, barium ferrite is a hexagonal ferrite with the formula $BaFe_{12}O_{19}$ that is a permanent magnet with high Curie temperature, strong magnetization, high coercivity and chemical stability [142, 217]. Bismuth ferrites, $BiFeO_3$, have a perovskite crystal structure and are perhaps the only multiferroic material that is both ferromagnetic and ferroelectric at room temperature [218]. Bi ferrites have high photoelectric absorption and are therefore excellent candidates for radiation amplification, MRI and computed tomography [219]. Strontium ferrites, $SrFe_{12}O_{19}$, have a hexagonal crystal structure and are a typical hard magnetic material of high saturation magnetization, low cost and good chemical stability [220].

Concerning the cytotoxicity of other co-ion ferrites, it can be better than that of pure iron oxide NPs in as much as the co-ion in use is less toxic than Fe for the organism, i.e. participates less in the induction of ROS that inevitably leads to cell damage [123]. From the relevant literature analyzed in this section and summarized in Table 6, the work from Song et al. [221] is certainly worth a note, though the work from Rajaee et al. deserves a mention as they could obtain cell viabilities after 72 h higher than 85% up to a concentration of 1 mg/mL in MCF-7 (human breast cancer) cells treated with bismuth ferrites of 28 nm (SEM) size [219]. Viability was determined with the Cell Counting kit-8 (CCK-8), with and without posterior radiotherapy. Song and co-workers devoted a special attention to cell-NP interactions, both, after cells were already adhered to the culture plates and during the process of cell adhesion [221]. For the first, they observed that cell morphology and granularity were altered upon PC-12 cell exposure to the Bi-FNPs (30–90 nm (SEM)) at concentrations of 50 and 200 µg/mL, with higher concentrations linked to increase coverage of the cell membrane by the NPs. Such strong NP interaction with the cell membrane -and the consequent apparent coverage of the cell body by the NPs- was found to dilute over time as cell replication progressed. On the other hand, when cells were plated together with the NPs, their adhesion was remarkably affected, with 78% of cells displaying a round morphology after 24 h exposure to 50 µg/mL Bi-FNPs. These effects onto cell morphology and adhesion were afterwards found to correlate with the viability results: at 50 µg/mL, viability dropped to ~ 85% after 24 h incubation (MTT assay, Fig. 6a), though LDH increase was only substantial at this concentration after 48 h (i.e. there were no significant differences at 24 h in LDH production). The apoptosis/necrosis evaluation indicated that > 85% of cells remained viable up to 48 h incubation with 200 µg/mL Bi-FNPs; the other 15% of

Table 6 In vitro toxicity evaluation of other co-ion nanoferrites

Author	Co-Ion	Synthesis method	Size	Surface coating	Cell line(s)	Main results/observations
Rajaee et al. [219]	Bi	Sol–gel process	~ 28 nm (SEM)		• MCF-7	Slightly cytotoxic up to 1 mg/mL (72 h), with and without radiotherapy (CCK-8). Survival fraction as a function of radiation dose was assessed with a clonogenic assay
Song et al. [221]	Bi (BiFeO$_3$)	Sol–gel process	30–90 nm (SEM)		• PC-12	Moderate cytotoxicity at 0.5 mg/mL (MTT and LDH assays). Cell adhesion and morphology affected (microscopy). Evaluation of cell cycle distribution and apoptosis/necrosis (PI staining, Annexin V) • Measurement of ROS levels (DCFH-DA assay) • Evaluation of DNA damage
Mekonnen et al. [223]	Gd	Co-precipitation	~ 90 nm (DLS) ~ 92 nm (AFM)	PAMAM G4.5	• HeLa	Slightly cytotoxic at 0.1 mg/mL (MTT assay)

(continued)

Table 6 (continued)

| Author	Co-Ion	Synthesis method	Size	Surface coating	Cell line(s)	Main results/observations
Zioni et al. [141]	Sr ($SrFe_{12}O_{19}$)	Ultrasound	80–100 nm (TEM) 30–110 nm (DLS)	NPs dispersed in a cream	• Human skin organ cultures	The cream containing the NPs did not affect cell viability in skin cultures (MTT assay). Also, it reduced apoptosis (caspase-3 activity) and inflammatory cytokines levels

Abbreviations and Acronyms:

Characterization techniques: *TEM* Transmission electron microscopy, *SEM* Scanning electron microscopy, *DLS* Dynamic light scattering, *AFM* Atomic force microscopy

Surface Coatings: *PAMAM G4.5* Poly(amidoamine) dendrimer generation 4.5

Cell Lines: *HeLa* Human cervical cancer cell, *MCF-7* Human breast cancer cell, *PC-12* Rat pheochromocytoma cell

Toxicological methods: *CCK-8* Cell counting kit-8, *MTT* 3-(4,5-dimethylthiazol-2-yl)-2,5-diphenyltetrazolium bromide, *LDH* Lactate dehydrogenase, *PI* Propidium iodide, *ROS* Reactive oxygen species, *DCFH-DA* 2′,7′-dichlorofluorescein diacetate
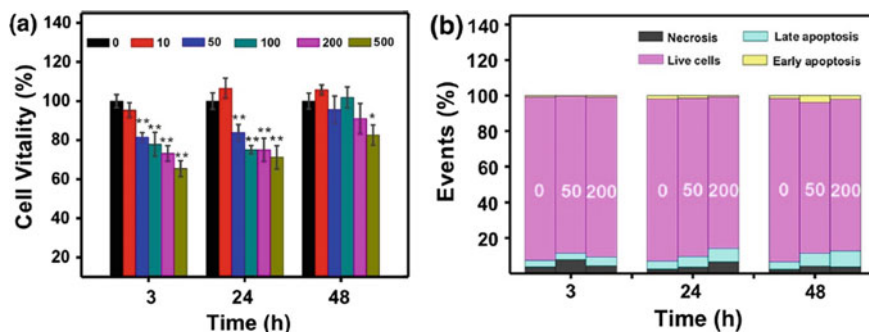
Fig. 6 Bismuth ferrite NPs and their interaction with PC-12 cancer cells. **a** Cell viability (MTT assay) of cells incubated with Bi-FNPs at various concentrations: 0–500 μg/mL during 3, 24 and 48 h. Data correspond to the mean ± SD ($n = 3$). *$p < 0.05$, **$p < 0.01$ versus the control group. **b** Stack columns summarizing results of apoptosis and necrosis of PC-12 cells exposed to 0, 50 and 200 μg/mL of Bi-FNPs during 3, 24 and 48 h. Necrotic cells are those stained with propidium iodide only. Cells stained with Annexin-V only correspond to early apoptosis. Dual staining corresponds to late apoptosis and no staining to viable cells. Reproduced from Song et al. *Journal of Nanoparticle Research* 2014, *16*, 2408, with the permission of Springer

cells underwent apoptosis and necrosis. Finally, although the authors reported ROS generation and DNA damage, they also stated that such damage is possibly within the range of the repairing capability of the cells, especially as time progresses and cells divide, alleviating then the insult resulting from the exposure of the cells to the NPs.

Table 8 assembles a series of in vivo evaluations of other co-ion ferrites. Of interest are the results from Park et al. [155] in rats with calcium ferrites and of Nikiforov et al. [222] in mice with gadolinium ferrites (Fe[$Gd_{0.1}Fe_{1.9}$]O_4). For the first, lethal dose 50% was 300 mg Fe/kg while for the second it was of 600 mg Fe/kg. The calcium ferrites were visualized in all organs investigated, with higher amounts in the spleen than in the liver, kidneys and lungs [155]. Gadolinium ferrites were observed in great extent in the liver. The authors state that the liver was completely black after 3 and 21 days [222].

3.7 Toxicity of Nanoferrites Containing Mixed Co-Ions

The synthesis of nanoferrites containing two or more metallic ions ($M_{(x-1)}N_xFe_2O_4$, for two ions, M and N) allows to engineer FNPs for different applications in the biomedical field, like magnetic hyperthermia therapy [197, 224, 225], MRI [119, 225, 226] and magnetic drug delivery [197, 225, 227]. By changing the molar ratio between co-ions, as well as the magnetic character of the divalent cations, the physical properties of the nanoferrites can be tuned and optimized for specific requirements, such as having a low Curie temperature with a strong temperature dependence of the

magnetization (valuable for MRI) [119] or possessing a high Specific Absorption Rate (SAR) (valuable for MHT) [225, 228].

Table 7 summarizes the main results from in vitro toxicity studies of nanoferrites containing mixed co-ions (Mix-FNPs). Within this category, the most studied are those containing Zn and another co-ion, mostly Co [197, 228–230], Mn [210, 225–228] and Ni [207, 228, 231]. On the contrary, works evaluating NPs composed of three co-ions (e.g. Ni-Zn-Cu) are very scarce [232]. As it can be seen, most of the studies evaluated cytotoxicity using tetrazolium-based cell viability assays [233]. To a lesser extent, oxidative stress [119, 207, 225, 226, 231], and genotoxicity were investigated [234].

Among these works, Al-Qubaisi et al. published two very comprehensive articles on the toxicity of a commercial Ni-Zn-FNP [231, 234]. They reported IC_{50} values for these NPs in four different human cell lines (HT29, MCF-7, HepG2 and MCF-10A) using different cytotoxicity assays including MTT, LDH and Trypan blue exclusion assay for cell viability and BrdU cell proliferation assay. They showed that the Ni-Zn-FNPs were able to decrease cell viability and proliferation in all cell lines, being MCF-10A the least sensitive. In addition, the authors measured ROS, GSH and MDA levels and demonstrated that the nanomaterial generated oxidative stress [231]. Furthermore, they also studied the apoptosis (caspase-3 and -9 activities [234], and Bax and p53 levels [231], among others), DNA fragmentation (diphenylamine assay) [234] and alterations in mitochondrial transmembrane potential [231] induced by Ni-Zn-FNPs.

The main results of the in vivo toxicity studies of Mix-FNPs are summarized in Table 8. All the works presented in the table use Mix-FNPs containing Zn [48, 197, 229]. Among them, the research by Hanini and co-workers is perhaps the most complete [229]. They studied the toxicity of Zn-Co-FNPs (of ~ 8 nm; see Fig. 7a) on rabbits intravenously injected and found no alterations in body temperature and red blood cell count (Fig. 7b). However, they observed increased white blood cell count, and organs such as lungs, liver and kidney, among others, presenting evidence of inflammatory processes under histological evaluation (Figs. 7b, c).

Table 7 In vitro toxicity evaluation of nanoferrites containing mixed ions ($M_{(x-1)}N_xFe_2O_4$)

Author	Co-ions	Synthesis method	Size	Surface coating	Cell line(s)	Main results/observations
Zachanowicz et al. [235]	Co–Mn (x = 0.2, 0.5 and 0.8)	Bradley's reaction (microwave-stimulated)	8–10 nm (XRD and TEM) 190–330 nm (DLS)		• J774.E • HTB • ASCs	Moderate to high cytotoxicity observed from 0.0002 mg/mL [cytotoxicity ASCs > J774.E > HTB] (Trypan blue assay)
Kim et al. [224]	Co–Ni (x = 0.1)	Sol–gel process			• L929	Slight to negligible cytotoxicity (MTT assay and Agar overlay test)
Kim et al. [232]	Co–Ni (x = 0.1)	Sol–gel process	~ 220 nm (SEM)		• L929	Slight to negligible cytotoxicity (MTT assay and Agar overlay test)
Shahbazi-Gahrouei et al. [230]	Co–Zn (x = 0.5)	Co-precipitation	Bare NPs: ~ 16 nm (TEM) Coated NPs: ~ 40 nm (TEM)	DMSA	• PC3 • DU145	Bare NPs do not affect and slightly reduce PC3 and DU145 cell viability, respectively. Coated NPs considerably reduce the cell viability of both cell lines at Fe concentrations above 1 mM (MTT assay)
Alghamdi et al. [119]	Cu–Zn (x = 0.65)	Standard ceramic technique (ball milling)	~ 720 nm (DLS in cell medium at 1/100)		• RAW 264.7	No influence on cell viability up to 0.24 mg/mL (MTS assay). However NPs triggered an inflammation response (IL-6 mRNA determination) • Measurement of ROS levels (CellROX® Green Reagent)
Alghamdi et al. [119]	Mg–Zn (x = 0.64)	Standard ceramic technique (ball milling)	~ 740 nm (DLS in cell medium at 1/100)		• RAW 264.7	No influence on cell viability up to 0.24 mg/mL (MTS assay). However, slight increase (not significant compared to untreated control) of inflammation response (IL-6 mRNA determination) • Measurement of ROS levels (CellROX® Green Reagent)

(continued)

Table 7 (continued)

Author	Co-ions	Synthesis method	Size	Surface coating	Cell line(s)	Main results/observations
Montha et al. [227]	Mn–Zn ($x = 0.1$)	Co-precipitation	Bare NPs: ~20–25 nm (TEM) Coated NPs: 45–50 nm (TEM)	PLGA	• HeLa	Below 0.125 mg/mL, the doxorubicin (DOX)-loaded NPs showed lower cytotoxicity than free DOX (24 h). At higher concentrations (0.250 mg/mL), DOX-loaded NPs showed high cytotoxicity, similar to free DOX (MTT assay)
Kim et al. [232]	Ni–Zn–Cu ($Ni_{0.65}Zn_{0.35}Cu_{0.1}Fe_{1.9}O_4$)	Sol–gel process	~210 nm (SEM)		• L929	Slight to moderate cytotoxicity (Agar overlay Test and MTT assay)
Herynek et al. [226]	Mn–Zn ($Mn_{0.61}Zn_{0.42}Fe_{1.97}O_4$)	Hydrothermal method	Bare NPs: ~10 nm (TEM) Coated NPs: ~30 nm (TEM), ~90 nm (DLS)	Silica	• BM-MSCs • C6 • AT-MSCs	No influence on AT-MSCs cells viability up to 0.2 mM. Reduction of cell viability in BM-MSCs and C6 cells at 0.55 mM (Trypan blue assay and real time cell proliferation analysis). Evaluation of apoptosis (APO-DIRECT™ Kit stained for TUNEL) • Measurement of ROS levels (CellROX® Deep Red Flow Cytometry Assay Kit)
Wang et al. [225]	Mn–Zn ($x = 0.4$)	Thermal decomposition method Silica-coated NPs dispersed in a polysaccharide hydrogel	Bare NPs: 7 nm (TEM) Coated NPs: 55 nm (TEM) Shell Thickness: 24 nm (TEM)	Silica	• 4T1	Reduction of cell viability (MTT assay) • Measurement of ROS levels (DCFH-DA assay)

(continued)

Table 7 (continued)

Author	Co-ions	Synthesis method	Size	Surface coating	Cell line(s)	Main results/observations
Al-Qubaisi et al. [231, 234]	Ni–Zn ($x = 0.5$)	Co-precipitation	~ 12 nm (XRD) ~ 11 nm (TEM) ~ 250 nm (DLS)		• MCF-7 • HT29 • HepG2 • MCF10A	The IC_{50} values at 72 h were ~ 0.0285 mg/mL (HepG2), ~ 0.0587 mg/mL (MCF-7), ~ 0.0311 mg/mL (HT29) and ~ 0.915 mg/mL (MCF10A) (MTT assay). Alterations in cell proliferation observed in HepG2 at 0.005 mg/mL (72 h) and 0.1 mg/mL (24 h). Alterations not observed in MCF-7 (48 h) and HT29 (24 h) up to 0.1 mg/mL and in MCF10A up to 1 mg/mL (72 h) (BrdU cell proliferation assay). Evaluation of membrane damage (LDH assay) • Measurements of ROS, GSH and MDA levels and lipid peroxidaton • Evaluation of Bcl-2, Bax, cytochrome C, p53, caspase-3 and caspase -9 levels • Determination of mitochondrial transmembrane potential (flow cytometry using Rh123) • Evaluation of DNA fragmentation (Diphenylamine assay)

(continued)

Table 7 (continued)

Author	Co-ions	Synthesis method	Size	Surface coating	Cell line(s)	Main results/observations
Martínez-Rodríguez et al. [207]	Ni–Zn (x = 0.5)	Commercial (Nanoshel)	< 30 nm		• Human RBC • Human PBMC	NPs at a concentration of 0.2 mg/mL induce hemolysis in RBCs. NPs did not reduce cell viability in PBMCs up to 0.2 mg/mL (MTT and Trypan blue assays) • Measurements of catalase and GST activities, and total protein content in RBC
Hanini et al. [229]	Zn–Co (x = 0.2)	Polyol method	~ 8 nm (XRD and TEM)		• HUVECs	NPs can induce high cytotoxicity at concentrations above 0.01 mg/mL after exposure times from 30 min onwards (MTT assay)
Basti et al. [228]	Zn–Co (x = 0.1)	Polyol method	Small NPs: ~ 5 nm (XRD, TEM) Large NPs: ~ 12 nm (XRD) ~ 11 nm (TEM)		• HUVECs	Both NPs were cytotoxic after 24 h of contact at high doses (0.1 mg/mL). Large NPs were highly cytotoxic even at low concentrations (0.01 mg/mL) and at short incubation times (30 min) (MTT assay)
Hamed et al. [236]	Zn–Cr (ZnCrFeO₄)	Sol–gel process	~ 8 nm (XRD) ~ 24 nm (TEM) ~ 49 nm (SEM) ~ 10 nm (AFM)	DMSA	• A375M	Negligible cytotoxicity at short incubation times (2 h) up to 0.2 mg/mL. Moderate toxicity at longer times
Wang et al. [197]	Core: Zn–Co (x = 0.6) Shell: Zn–Mn (x = 0.6)	Two-step pyrolysis Core–shell magnetic nanocubes, MNCs	Core: ~ 7 nm (TEM) Core-Shell MNC: ~ 11 nm (TEM)	HA-PEG	• HeLa	MNCs-PEG/HA NPs were not cytotoxic to HeLa cells (Flow cytometry and MTT assay)

(continued)

Table 7 (continued)

Author	Co-ions	Synthesis method	Size	Surface coating	Cell line(s)	Main results/observations
Basti et al. [228]	Zn–Mn (x = 0.1)	Polyol method	Small NPs: ~5 nm (XRD) ~4 nm (TEM) Large NPs: ~12 nm (XRD) ~11 nm (TEM)	Dopamine	• HUVEC	Bare NPs were cytotoxic mainly after 24 h at high doses (above 0.01 mg/mL, cytotoxicity small NP > large NP). Coated NPs exhibited similar behavior (MTT assay)
Basti et al. [228]	Zn–Ni (x = 0.1)	Polyol method	Small NPs: ~5 nm (XRD) ~3.5 nm (TEM) Large NPs: ~11 nm (XRD) ~9 nm (TEM)		• HUVEC	Small NPs were weakly cytotoxic. Large NPs were mildly cytotoxic (MTT assay)
Yao et al. [237]	Zn–Gd $(ZnGd_yFe_{(2-y)}O_4)$ (y = 0.02)	Co-precipitation	Bare NPs: ~13 nm (XRD) Coated NPs: 20–30 nm (TEM)	PEG	• HUVEC	Bare NPs reduced significantly cell viability at high concentration (4 mg/mL). Coated NPs did not affect cell viability at any of the concentrations (MTT assay)

Abbreviations and Acronyms:

Characterization techniques: *XRD* X-ray diffraction, *TEM* Transmission electron microscopy, *DLS* Dynamic light scattering, *SEM* Scanning electron microscopy, *AFM* atomic force microscopy

Surface Coatings: *DMSA* Meso-2,3-dimercaptosuccinic acid, *PLGA* Poly(lactic-co-glycolic acid), *HA* Hyaluronic acid, *PEG* Polyethyleneglycol

Cell Lines: *J774.E* Murine macrophage, *J774.E* Murine macrophage (active phagocytosis), *HTB* Human osteosarcoma cells, *L929* Mouse fibroblast, *PC3* Human prostate cancer cell, *DU145* Human prostate cancer cell, *RAW 264.7* Mouse macrophage, *HeLa* Human cervix adenocarcinoma cell, *C6* Rat glioblastoma cells, *4T1* Murine breast cancer cell, *MCF-7* Human breast cancer cell, *HT29* Human colorectal adenocarcinoma cell, *HepG2* Human hepatocellular carcinoma cell, *MCF-10A* Human breast epithelial cell, *HUVEC* Human endothelial cell, *A375M* Human skin melanoma cells

Primary cells and related: *RBC* Red blood cell, *PMMC* Peripheral blood mononuclear cells, *ASCs* Human adipose derived mesenchymal stromal stem cells, *BM-MSCs* Rat mesenchymal stem cells isolated from bone marrow, *AT-MSCs* Rat mesenchymal stem cells from the adipose tissue of genetically modified Lewis rats with ubiquitous expression of a gene for the luciferase enzyme (Lew–Tg(Gt(ROSA)26Sor-luc)11msk)

Toxicological methods: *MTT* 3-(4,5-dimethylthiazol-2-yl)-2,5-diphenyltetrazolium bromide, *MTS* 3-(4,5-dimethylthiazol-2-yl)-5-(3-carboxymethoxyphenyl)-2-(4-sulfophenyl)-2H-tetrazolium), *IL-6* Interleukin-6 as a marker of inflammation, *ROS* Reactive oxygen species, *TUNEL* Terminal deoxynucleotidyl transferase dUTP Nick-end labeling, *DCFH-DA* 2′,7′-dichlorodihydrofluorescein diacetate, *LDH* Lactate Dehydrogenase, *BrdU* Bromodeoxyuridine, *Rh123* Rhodamine 123, *GSH* Glutathione, *MDA* Malondialdehyde

Table 8 In vivo toxicity evaluation of nanoferrites

Author	Ion(s)	Synthesis method	Size	Surface coating	Animal model(s)	Main results/observations
Park et al. [155]	Co	Co-precipitation [61]Co used	~ 11 nm (TEM)	Lecithin	Sprague–Dawley rat	Rats were intravenously injected in the tail vein Acute toxicity (single dose): $LD_{50} \sim 300$ Fe–mg/kg. MTD ~ 374 Fe–mg/kg Ferrite nanoparticles detected in liver, lung, kidney and mainly in spleen (H-E and Prussian blue staining)
Şincai et al. [161]	Co		5–15 nm		Dog White rat	In dogs: Slight alteration in clinical signs (cardiac rhythm, pulmonary ventilation) and alteration in blood parameters (increment of erythrocyte sedimentation rate, leukocytosis, polycythemia, among others) at 100 mg/kg In rats: Clinical and hematological changes at doses above 364 mg/kg
Gökçe et al. [238]	Co	Co-precipitation	50–110 nm (SEM)		Daphnia magna	$LT_{50} \sim 64$ h (acute exposure) $LC_{50} \sim 0.04$ mg/mL (acute exposure) NPs induce minor morphological changes (length, width and spine length)

(continued)

Table 8 (continued)

Author	Ion(s)	Synthesis method	Size	Surface coating	Animal model(s)	Main results/observations
Akhtar et al. [156]	Co	Co-precipitation	Bare NPs: ~ 25 nm (XRD) 40–340 nm (SEM, mixture of shapes) ~ 79 nm (DLS) Coated NPs: ~ 530 nm (PEG, DLS) ~ 342 nm (citrate, DLS)	PEG, Citrate	Albino rats	Hepatic function (bilirubin, ALT, ALP, AST levels), blood parameters (hemoglobin levels and RBC, WBC and platelet count) and kidney function (BUN, creatinine, urea levels) altered 1 day after NP injection. Normal function is recovered after 8 days, except for bare NPs that still show slightly altered levels of some markers Toxicity of NPs can be ranked roughly as: bare > citrate coated > PEG Histological observations also performed
Mirzaee et al. [160]	Co	Co-precipitation	~ 23 nm (XRD) < 100 nm (clusters, SEM)	Sucrose	Wister rats	After one week of daily intraperitoneal injection of NPs at 40 mg/kg, slight modifications in hematological parameters (e.g. increased WBC) were observed while no substantial alteration in liver function (ALT, AST and ALP) was detected

(continued)

Table 8 (continued)

Author	Ion(s)	Synthesis method	Size	Surface coating	Animal model(s)	Main results/observations
Akhtar et al. [157]	Co	Hydrothermal method (nanoparticle) Solvothermal method (nanosphere) Nanomaterials were radioactively labeled with ^{99m}Tc	Nanoparticles: ~ 25 nm (SEM and TEM) Nanospheres: 80–100 nm (SEM and TEM)	PEG	Kunming SPF mice	Both nanoparticles and nanospheres were found in blood, liver, spleen, kidney, lung and heart. Nanoparticles were mainly located in spleen and heart while nanospheres were mainly in the spleen Nanoparticles and nanospheres were rapidly cleared from these organs (low dose remaining after 24 h). Nanospheres accumulated more than nanoparticles (measure of radioactivity with a gamma counter) Both materials (nanosphere > nanoparticle) affect liver (ALT, AST and bilirubin levels) and kidney function (creatinine, BUN, etc.) Histopatological observations also performed
Hwang et al. [153]	Co	Commercial (Biterials) Labeled with ^{68}Ga	Bare NPs: ~ 35 nm (TEM) Coated NPs: ~ 50 nm (TEM)	Silica + Amine + PEG	BALB/c-ν-mice	Bare and coated NPs presented higher accumulation in liver (50-fold) than in muscle Bare nanoparticles induced upregulation of genes related to cellular stress in liver. Coated NP did not induced upregulation of the mentioned genes (quantitative real time PCR analysis) Other genes were evaluated

(continued)

Table 8 (continued)

Author	Ion(s)	Synthesis method	Size	Surface coating	Animal model(s)	Main results/observations
Billing et al. [158]	Co	Hydrothermal method Different Co:Fe ratios used	< 40 nm (TEM) Also DLS data from agglomerates		C57BL/6 J BomTac mice	NPs administered by intratracheal instillation NPs induced infiltration of neutrophils (after 1 day), lymphocytes (after 3 days) and eosinophils (only late response; correlated with increasing Co content) in bronchoalveolar lavage fluid (BALF) NPs induced increased expression of acute phase gene Saa3 (after 1 day), increased LDH (after 3 days) and total protein levels in BALF NPs induced increased levels of DNA strand primary damage in BALF, lungs and liver Detailed information on extensive proteome analysis performed on BALF is available
Pradhan et al. [159]	Co	Co-precipitation	9–11 nm (XRD) 9–10 nm (TEM) ~ 90 nm (DLS)		Swiss mice	After injection of NPs at 400 mg/kg (24 h) no substantial alteration of hematological parameters and BUN was observed, while ALT levels slightly increased (not significantly though) No histopathological changes were observed in liver, lung, spleen, heart and kidney NPs accumulated preferentially in liver, lung and spleen while they did not accumulate in kidneys and heart (Prussian blue staining)

Table 8 (continued)

Author	Ion(s)	Synthesis method	Size	Surface coating	Animal model(s)	Main results/observations
Liu et al. [186]	Cu	Hydrothermal method	~ 13 nm (TEM)	Hemoglobin	Kunming mice	No appreciable inflammatory lesion, injury, or necrosis observed in heart, liver, spleen, lung, and kidney tissues (histological examination using H-E) No appreciable changes in body weight NPs were mainly accumulated in heart, liver, and kidney (cleared after NIR irradiation)
Gökçe et al. [238]	Cu	Co-precipitation	50–110 nm (SEM)		*Daphnia magna*	After 96 h, LC_{50} was 1.45 mg/L NPs also had a negative effect on the morphological development of neonates (body length, width, and spine length) High mortality was observed between 1–10 mg/L
Park et al. [155]	Cu	Co-precipitation ^{67}Cu used		Lecithin	Sprague–Dawley rat	Rats were intravenously injected in the tail vein Acute toxicity (single dose): $LD_{50} \sim 300$ Fe–mg/kg. MTD ~ 374 Fe–mg/kg Ferrite nanoparticles detected in liver, lung, kidney and mainly in spleen (H-E and Prussian Blue staining)

Table 8 (continued)

Author	Ion(s)	Synthesis method	Size	Surface coating	Animal model(s)	Main results/observations
Pradhan et al. [159]	Mn	Co-precipitation	~ 10 nm (TEM)	Lauric acid	Swiss mice	No substantial alteration of hematological parameters (e.g. RBC, WBC, among others), ALT and BUN was observed after injection of NPs at 400 mg/kg (24 h) No histopathological changes were observed in liver, lung, spleen, heart and kidney NPs accumulated preferentially in liver, lungs and spleen, but not in kidney and heart (Prussian blue staining)
Coppola et al. [195, 196]	Mn	Oxidative hydrolisis	~ 75 nm (TEM) ~ 6000 nm (DLS in salt water)		*Mytilus galloprovincialis*	After 24 h exposure to 0.05 mg/mL, no significant changes in metabolic parameters were observed (electron transport system activity, glycogen and total protein) Compared to the control, there was a slight increase in ROS parameters (SOD, Lipid peroxidation, GSH/GSSG ratio) and moderate neurotoxicity (AchE activity) was observed

(continued)

Table 8 (continued)

Author	Ion(s)	Synthesis method	Size	Surface coating	Animal model(s)	Main results/observations
Nunes et al. [198]	Mn	Co-precipitation	8–22 nm (TEM) 87–90 nm (DLS)	Citrate, TPP	Wistar rats	Bare and coated NPs induced direct effects on the ventricular contractility and coronary vasomotricity of isolated hearts although no effect on heart rate or arterial blood pressure was observed in vivo (Blood pressure measurement) Bare NPs induced a more pronounced effect on contractility of the isolated hearts when compared with coated nanoparticles (Coronary perfusion pressure measurements, mechanical contractility of aortic rings)
Pernia Leal et al. [34]	Mn	Seed-growth method (6 nm MnFe$_2$O$_4$ seeds)	Bare NPs: 6–14 nm (TEM) Coated NPs: 20–32 nm (DLS)	PEG (3KDa)	Balb/c mice	The total clearance from the body was 24 h and 48 h for the 6 nm and 14 nm NPs, respectively (MRI)

(continued)

Table 8 (continued)

Author	Ion(s)	Synthesis method	Size	Surface coating	Animal model(s)	Main results/observations
Deng et al. [136]	Mn	Thermal decomposition	~ 16 nm (TEM)	PEG + photosensitizer	Balb/c mice with H22 cell tumor	No significant weight loss was found in mice within 28 days Renal (BUN, creatinine), heart (CK) and liver (ALP, ALT, AST) functions were normal Half-life of NPs in blood circulation was ~ 0.73 h (Mn determined by ICP-MS)
Yang et al. [191]	Mn	Thermal decomposition on graphene oxide (GO)	~ 5 nm (TEM, attached on GO nano-sheets)		Kunming mice	After administration of 15 mg/kg of NPs, the treated mice showed no abnormal behavior over the entire study period, with normal shape and blood cells count Five days after intravenous injection, liver (ALT, AST, TBIL) and kidney (creatinine, BUN) parameters were normal NPs accumulated mainly in liver and spleen (Prussian blue staining) No obvious tissue damage, inflammation or lesions were detected in various organs (histological examination using H-E) NPs were mostly cleared after 50 h (ICP measurement of Fe in blood)

Table 8 (continued)

Author	Ion(s)	Synthesis method	Size	Surface coating	Animal model(s)	Main results/observations
Pacchierotti et al. [192]	Mn	Mechanochemical processing (high-energy ball-milling)	~ 8 nm (TEM) ~ 60 nm (DLS)	Citric acid	CD1 mice	After intravenous administration of NPs, the treated mice showed no abnormal behavior over the entire study period
						NPs accumulated mainly in liver and kidney, and less into spleen and brain 6–7 h post injection, and their retained amount decreased gradually until 21 h (Prussian blue, ICP measurements of Mn)
						No relevant changes in cell morphology were observed after long periods (histological examination using H-E)
Qian et al. [193]	Mn	Hydrothermal synthesis Nanocomposite of reduced graphene oxide and $MnFe_2O_4$, labeled with ^{131}I		C_{18}PMH-PEG	Balb/c mice bearing 4T1 tumor	NPs accumulated mainly in liver and spleen, and less in tumor and kidney (MRI, SPECT)
						Body weight was not significantly altered
						Liver and kidney function parameters were in normal range compared to the control group
						No obvious toxicity was found after 60 days in liver, spleen, kidney, heart and lungs (histological examination using H-E)

(continued)

Table 8 (continued)

Author	Ion(s)	Synthesis method	Size	Surface coating	Animal model(s)	Main results/observations
Park et al. [155]	Ni	Co-precipitation ^{65}Ni used		Lecithin	Sprague–Dawley rat	Rats were intravenously injected in the tail vein. Acute toxicity (single dose): $LD_{50} \sim 300$ Fe–mg/kg. MTD ~ 374 Fe–mg/kg. Ferrite nanoparticles detected in liver, lung, kidney and mainly in spleen (H-E and Prussian Blue staining)
Gökçe et al. [238]	Ni	Co-precipitation	50–110 nm (SEM)		*Daphnia magna*	Mortality rate and morphometric changes measured up to 96 h. $LC_{50} \sim 21.7$ mg/L and mortality was higher than 80% above 20 mg/L. The NPs drastically affected lifespan and growth
Kovriznych et al. [239]	Ni	Commercial (Sigma-Aldrich)	< 100 nm		Zebra fish *(Danio rerio)*	For adult fish and eggs, LC_{50} > 1.6 mg/mL (up to 96 h of exposure). Premature hatching was observed for eggs after 96 h exposure at 1.6 mg/mL. No yolk deformation, body shortening of the embryos or other malformations were observed

(continued)

Table 8 (continued)

Author	Ion(s)	Synthesis method	Size	Surface coating	Animal model(s)	Main results/observations
N. Hadrup et al. [48]	Ni	Commercial (NanoAmor)	~ 16 nm (XRD) ~ 180 nm (DLS in water with 2% mouse serum)		C57BL/6 J BomTac mice	Mice were dosed 0.014, 0.043 or 0.128 mg/kg by a single intratracheal instillation. Recovery periods were 1, 3 or 28 days. After one day of recovery, neutrophil influx into bronchoalveolar lavage fluid (BALF) was found at the two highest concentrations. It remained high for the highest concentration also after 28 days recovery (microscopic examination) Primary DNA damage was found in BALF at the highest NP concentration after one day, but not observed after 3 and 28 days No DNA damage was found in lung and liver (Comet assay)
Alvino et al. [142]	Ba (BaFe$_{12}$O$_{19}$)	Commercial (Sigma-Aldrich)	~ 32 nm (TEM) > 1000 nm (DLS in various cell media)		Caenorhabditis elegans	After 72 h of treatment, mortality at 0.5 mg/mL was around 60% and 50% for young and adult worms, respectively (microscopy) NPs significantly affected reproduction from 0.05 mg/mL onwards and increased ROS production from 0.015 mg/mL, both at 72 h (microscopy and DCFH-DA assay)

(continued)

Table 8 (continued)

Author	Ion(s)	Synthesis method	Size	Surface coating	Animal model(s)	Main results/observations
Kovriznych et al. [239]	Ba	Commercial (Sigma-Aldrich)	< 100 nm		Zebra fish (*Danio rerio*)	For adult fish and eggs, LC_{50} > 1.6 mg/mL (up to 96 h of exposure) Premature hatching was observed for eggs after 96 h exposure at 1.6 mg/mL. No yolk deformation, body shortening of the embryos or other malformations were observed
Park et al. [155]	Ca	Co-precipitation ^{47}Ca used		Lecithin	Sprague–Dawley rat	Rats were intravenously injected in the tail vein Acute toxicity (single dose): $LD_{50} \sim 300$ Fe–mg/kg. MTD ~ 374 Fe–mg/kg Ferrite nanoparticles detected in liver, lung, kidney and mainly in spleen (H-E and Prussian Blue staining)
Nikiforov et al. [222]	Gd		10–12 nm (TEM)		C57B1/6j mice BDF1 mice BALB/c mice	Two routes of administration were used: intravenous and intraperitoneal For $Fe[Gd_{0.1}Fe_{1.9}]O_4$, the LD_{50} was of 0.6 g/kg High NP accumulation was found in liver (histological examination using H-E and Prussian blue staining)

Table 8 (continued)

Author	Ion(s)	Synthesis method	Size	Surface coating	Animal model(s)	Main results/observations
Zioni et al. [141]	Sr ($SrFe_{12}O_{19}$)	Ultrasound	80–100 nm (TEM) 30–110 nm (DLS)	NPs dispersed in a cream	Humans	The NPs were dispersed in a cream, permanently magnetized and the cream (0.4 mL) applied to the forearm of human volunteers aged 18–60 year old. Moisturization of the upper epidermal layers was measured up to 8 h after cream application by electrical capacitance
Rivero et al. [214]	Zn	Electrochemical synthesis	~ 12 nm (TEM) ~ 160 nm (DLS)	Citric acid	*Xenopus laevis*	NPs were evaluated up to 2 mg/mL. NPs induced decrease in survival factors (dose dependent), phenotypic abnormalities and alteration of Fe and Zn metabolisms in embryos/tadpoles
Hadrup et al. [48]	Zn	Commercial (NanoAmor)	~ 10 nm (XRD) ~ 98 nm (DLS)		C57BL/6 J BomTac mice	Mice were dosed 0.014, 0.043 or 0.128 mg/kg by a single intratracheal instillation. Recovery periods were 1, 3 or 28 days. After one day of recovery, neutrophil influx into bronchoalveolar lavage fluid (BALF) was found at the two highest concentrations. It remained high for the highest concentration also on recovery day 3 (microscopic examination). Primary DNA damage was found in BALF after one day, but not observed after 3 and 28 days. No DNA damage was found in lung and liver (Comet assay)

(continued)

Table 8 (continued)

Author	Ion(s)	Synthesis method	Size	Surface coating	Animal model(s)	Main results/observations
Zhu et al. [213]	Zn	Co-precipitation followed by solvothermal treatment	~ 11 nm (TEM) 20–25 nm (DLS in biological fluids)	DMSA	Mice	After daily intragastric administration for 30 days, no abnormal symptoms, body weight modification, or remarkable alterations of kidney (e.g. BUN) and liver (e.g. AST) biochemical parameters were observed Histopathological observations, oxidative stress and Zn content in liver and kidney were also studied
Hanini et al. [229]	Zn-Co (x = 0.2)	Polyol method	~ 8 nm (XRD and TEM)		New Zealand rabbits	Rabbits were intravenously injected in the jugular vein. No substantial alteration of rectal temperature, heart beat rate, behavior and RBC count after injection of NPs at 20 mg/kg (4 h) was observed. However, the presence of NPs increased WBC (+50%) indicating an inflammatory process. Perivascular inflammations in lungs, granulomas in liver, multiple congestions in kidneys and blackish particles in the interalveolar walls were observed (Histological observations)

(continued)

Table 8 (continued)

Author	Ion(s)	Synthesis method	Size	Surface coating	Animal model(s)	Main results/observations
Hadrup et al. [48]	Ni–Zn ($x = 0.5$)	Commercial (NanoAmor)	~ 12 nm (TEM) ~ 200 nm (DLS)		C57BL/6 J BomTac mice	Mice were dosed 0.014, 0.043 or 0.128 mg/kg by a single intratracheal instillation. Recovery periods were 1, 3 or 28 days. After one day of recovery, neutrophil influx into bronchoalveolar lavage fluid (BALF) was found at the highest concentration. After 3 days, there were not statistically significant levels. After 28 days recovery, neutrophil influx into BALF was elevated for NPs at the highest dose. Primary DNA damage was found in BALF at all NP concentrations after one day, but not observed after 3 and 28 days. No DNA damage was found in lung and liver (Comet assay)
Wang et al. [197]	Zn-Co ($x = 0.6$)	Two-step pyrolysis Core–shell magnetic nanocubes, MNCs	Core: ~ 7 nm (TEM) Core–Shell: ~ 11 nm (TEM)	HA-PEG	HeLa tumor-bearing mice	Mice were intravenously injected in the tail vein with MNCs-PEG/HA-DOX (Fe: 0.10 mmol/kg). The signal gradually darkened 0.5 to 3 h after administration and recovered after 4 h (MRI)

Abbreviations and Acronyms:

Characterization techniques: XRD X-ray diffraction, *TEM* Transmission electron microscopy, *DLS* Dynamic light scattering, *SEM* Scanning electron microscopy, *NIR* Near infrared, *ICP-MS* Inductively coupled plasma—mass spectroscopy, *MRI* Magnetic resonance imaging, *SPECT* Single photon emission computed tomography

Surface Coatings: DMSA Meso-2,3–dimercaptosuccinic acid, *HA* Hyaluronic acid, *PEG* Polyethyleneglycol, *TPP* Tripolyphosphate

Toxicological methods: LD$_{50}$ Lethal dose 50%, *LC$_{50}$* Lethal concentration 50%, *LT$_{50}$* Lethal time 50%, *MTD* Maximum tolerated dose, *ALT* Alanine aminotransferase, *AST* Aspartate aminotransferase, *ALP* Alkaline phosphatase, *RBC* Red blood cell count, *WBC* White blood cell count, *BUN* Blood urea nitrogen, *AchE* Acetylcholinesterase, *GSH/GSSG* Reduced / oxidized glutathione ratio, *H–E* Hematoxylin–eosin, *ROS* Reactive oxygen species, *DCFH-DA* 2,7′-dichlorodihydrofluorescein diacetate, *LDH* Lactate dehydrogenase, *GSH* glutathione, *SOD* Superoxide dismutase, *CK* Creatinine kinase, *TBIL* Total bilirubin
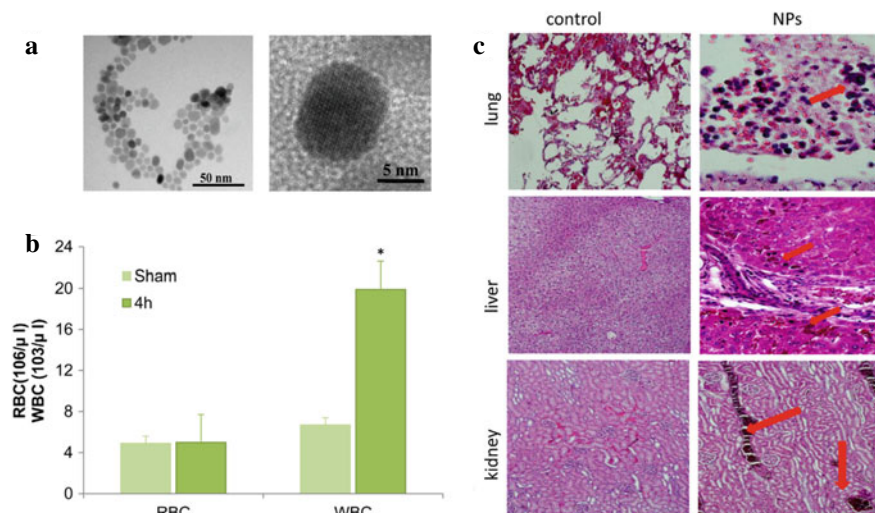
Fig. 7 **a** $Zn_{0.8}Co_{0.2}Fe_2O_4$ NPs morphology as observed by TEM in a collection of as-produced particles (left image). Zoom in one representative particle (right panel). **b**, **c** In vivo toxicity of $Zn_{0.8}Co_{0.2}Fe_2O_4$ nanoparticles: six New Zealand rabbits on each group received urethane (Sham, control group) or $Zn_{0.8}Co_{0.2}Fe_2O_4$ NPs (20 mg/kg) by intravenous injection. **b** Numbers of white (WBC) and red (RBC) blood cells were determined in the control group and in NPs-injected animals 4 h after administration. **c** Organs were collected 4 h post-treatment and processed for staining with hematoxylin and eosin; red arrows correspond to black regions and inflammations. Reproduced from Hanini et al. *Environmental Toxicology and Pharmacology* 2016, *45*, 321, with the permission of Elsevier

4 Concluding Remarks

Ferrites represent a class of versatile and very promising nanomaterials in the nanomedicine field. As previously noted, though most of the literature corresponds to cobalt ferrites, Mn, Ni and Zn as co-ions also gathered significant attention, with plentiful scientific publications devoted to the synthesis, characterization and toxicological evaluation of these nano-objects [200]. Ferrites possess a broad range of magnetic and physicochemical properties that depend upon the degree of substitution of the co-ion(s) and that enables the obtainment of nanomaterials with variable saturation magnetization, Curie temperature, crystalline structure, magnetic properties (e.g. ferromagnetic, ferroelectric), among others and, also, aptitude to interact with cells, tissues, organs and whole organisms in distinct ways. As it can be deduced from the tables in this chapter, most of the here covered literature is devoted to in vitro assays, and within them, to cytotoxicity and viability evaluations in cell lines. Genotoxicity and oxidative stress assessments are less common, though DNA techniques enable nowadays the unveiling of many molecular biology mechanisms, notably those behind cell cycle control and expression of, e.g. antioxidant enzymes and biomolecules. In vivo evaluations are scarce and are carried out in a wide variety of

animals and organisms, which makes any attempt to find relationships and/or trends between, for instance, NP composition and size and the outcome of the organism-NP interaction, almost inaccessible.

In analyzing the literature to carry out this work, we found that it was hard to compare NPs of a same co-ion in terms of their toxicological characteristics to attempt to extract any valuable information regarding, e.g. concentration ranges for safe use in vitro. As expected, it was even harder to compare ferrites of different co-ions among them, unless they were analyzed altogether in a unique work and had, at the least, similar sizes and synthesis methods. Fortunately, there are some research papers that suit these criteria and are worth a mention. For instance, Zhao et al. studied the cell viability and oxidative stress (ROS, GSH, MDA, SOD levels) in A549 cells exposed to $CoFe_2O_4$, $MnFe_2O_4$ and Fe_3O_4 ultrasmall nanoparticles (~3 nm) [150]. The authors demonstrated that Co-nanoferrites were more cytotoxic and induced higher oxidative stress than Mn-nanoferrites, and that these two were more toxic than the Fe_3O_4 NPs under study. In this same line, Pradhan and co-workers evaluated the effects of nanoparticles with similar composition but bigger sizes (9–11 nm) on BHK-21 cells and also found that cobalt-based ferrites were the most cytotoxic [159]. On the other hand, Ovejero et al. compared Fe_3O_4, $CoFe_2O_4$, $MnFe_2O_4$ and $NiFe_2O_4$ nanoparticles (8–13 nm) and showed that the latter presented the highest cytotoxicity towards HeLa cells producing an important decrease in cell viability, while the three formers were found slightly cytotoxic [173]. After 24 h cell incubation with 0.1 mg/mL of NPs, cell viability was of ~ 70% for $CoFe_2O_4$ onto both, A549 (Zhao et al.) and HeLa (Ovejero et al.) cells, showing here a concordance between two different works, but $NiFe_2O_4$ NPs had ~ 40% viability onto HeLa (Ovejero et al.) cells. Besides, Martínez-Rodríguez and co-workers studied the hemolytic activity of Ni-, Zn- and ZnNi-based nanoferrites (sizes < 30 nm) together with magnetite nanoparticles and found that only the mixed nanoferrite caused lysis to human red blood cells [207]. In addition, they also proved that none of the tested nanoparticles were cytotoxic for human peripheral blood mononuclear cells up to a concentration of 0.2 mg/mL. Nevertheless, Ovejero et al. found that $NiFe_2O_4$ NPs resulted in ~ 40% cell viability after 24 h incubation of HeLa cells with 0.1 mg/mL of NPs. So, a concentration of 0.1 mg/mL of $NiFe_2O_4$ NPs is highly toxic for HeLa cells but the double of that concentration is seemingly not toxic for human peripheral blood mononuclear cells. Certainly, the NP size is not the same in both cases, neither is it the surface coating (citric acid [173] vs. none [207]), so a straight comparison is possibly incorrect, but it nevertheless illustrates about the challenges in this area and their multi-parametric nature.

Establishing more standardized methods and model systems to evaluate in vitro and in vivo the interactions of nanoferrites (and nanomaterials in general) with cells, tissues, organs and whole organisms may be a laborious process whose outcome could provide the stepping stone to better understand these nanotoxicological phenomena and to promote a more rational design of nanomaterials for nanomedicine applications. Last but not least, the inclusion of all cell types that are expected to interact with the NPs in their journey through the body in the in vitro assays and a more dedicated evaluation of the NP stability in biological media and under biological

conditions (pH, ionic strength, presence of a multitude of biomolecules in solution, etc.) may provide a more robust assessment of the NP suitability for further in vivo studies.

References

1. Zhang W, Yu X, Li H, Dong D, Zuo X, Wu CW (2019) Magnetic nanoparticles with low curie temperature and high heating efficiency for self-regulating temperature hyperthermia. J Manag Manag Mater 489:165382. https://doi.org/10.1016/j.jmmm.2019.165382
2. Sharifi I, Shokrollahi H, Amiri S (2012) Ferrite-based magnetic nanofluids used in hyperthermia applications. J Magn Magn Mater 324(6):903–915. https://doi.org/10.1016/j.jmmm.2011.10.017
3. Kumar CSSR, Mohammad F (2011) Magnetic nanomaterials for hyperthermia-based therapy and controlled drug delivery. Adv Drug Deliv Rev 63(9):789–808. https://doi.org/10.1016/j.addr.2011.03.008
4. Sugimoto M (1999) The past, present, and future of ferrites. J Am Ceram Soc 82(2):269–280. https://doi.org/10.1111/j.1551-2916.1999.tb20058.x
5. Tasso M, Lago Huvelle MA, Diaz Bessone I, Picco AS (2020) Toxicity assessment of nanomaterials. In: Magnetic Nanoheterostructures. Diagnostic, Imaging and Treatment. Edited by Sharma S, Javed Y. Springer. pp 383–446. https://doi.org/10.1007/978-3-030-39923-8_13
6. Kunzmann A, Andersson B, Thurnherr T, Krug H, Scheynius A, Fadeel B (2011) Toxicology of engineered nanomaterials: focus on biocompatibility, biodistribution and biodegradation. Biochim Biophys Acta Gen Subj 1810(3):361–373. https://doi.org/10.1016/j.bbagen.2010.04.007
7. Kumar V, Sharma N, Maitra SS (2017) In vitro and in vivo toxicity Assessment of nanoparticles. Int Nano Lett 7(4):243–256. https://doi.org/10.1007/s40089-017-0221-3
8. Buzea C, Pacheco II, Robbie K Nanomaterials and nanoparticles: sources and toxicity. Biointerphases 2(4):MR17–MR71 (2007). https://doi.org/10.1116/1.2815690
9. Sharifi S, Behzadi S, Laurent S, Forrest ML, Stroeve P, Mahmoudi M (2012) Toxicity of nanomaterials. Chem Soc Rev 41(6):2323–2343. https://doi.org/10.1039/c1cs15188f
10. ISO/TS 80004-1:2015(en) Nanotechnologies—vocabulary—Part 1: core terms. https://www.iso.org/obp/ui/#iso:std:iso:ts:80004:-1:ed-2:v1:en. Accessed 29 Mar 2019
11. Auffan M, Rose J, Bottero J-Y, Lowry GV, Jolivet J-P, Wiesner MR (2009) Towards a definition of inorganic nanoparticles from an environmental. Health Safety Perspect Nat Nanotechnol 4(10):634–641. https://doi.org/10.1038/nnano.2009.242
12. Oberdörster G, Oberdörster E, Oberdörster J (2005) Nanotoxicology: an emerging discipline evolving from studies of ultrafine particles. Environ Health Perspect 113(7):823–839. https://doi.org/10.1289/ehp.7339
13. Nel A, Xia T, Mädler L, Li N (2006) Toxic potential of materials at the nanolevel. Sci (80):311(5761):622–627. https://doi.org/10.1126/science.1114397
14. Zhu M, Nie G, Meng H, Xia T, Nel A, Zhao Y (2013) Physicochemical properties determine nanomaterial cellular uptake, transport, and fate. Acc Chem Res 46(3):622–631. https://doi.org/10.1021/ar300031y
15. Pietroiusti A, Campagnolo L, Fadeel B (2013) Interactions of engineered nanoparticles with organs protected by internal biological barriers. Small 9(9–10):1557–1572. https://doi.org/10.1002/smll.201201463

16. Shvedova AA, Kagan VE, Fadeel B (2010) Close encounters of the small kind: adverse effects of man-made materials interfacing with the nano-cosmos of biological systems. Annu Rev Pharmacol Toxicol 50(1):63–88. https://doi.org/10.1146/annurev.pharmtox.010909.105819

17. Garnett, M. C.; Kallinteri, P. Nanomedicines and nanotoxicology: some physiological principles. Occup Med (Chic Ill) 56(5):307–311. https://doi.org/10.1093/occmed/kql052

18. Pankhurst QA, Connolly J, Jones SK, Dobson J (2003) Applications of magnetic nanoparticles in biomedicine. J Phys D Appl Phys 36(13):R167–R181. https://doi.org/10.1088/0022-3727/36/13/201

19. Banerjee R, Katsenovich Y, Lagos L, McIntosh M, Zhang X, Li C-Z (2010) Nanomedicine: magnetic nanoparticles and their biomedical applications. Curr Med Chem 17(27):3120–3141

20. Wu K, Su D, Liu J, Saha R, Wang J-P (2019) Magnetic nanoparticles in nanomedicine: a review of recent advances. Nanotechnol 30:502003. https://doi.org/10.1088/1361-6528/ab4241

21. Kreyling WG, Semmler-Behnke M, Seitz J, Scymczak W, Wenk A, Mayer P, Takenaka S, Oberdörster G (2009) Size dependence of the translocation of inhaled iridium and carbon nanoparticle aggregates from the lung of rats to the blood and secondary target organs. Inhal Toxicol 21(sup1):55–60. https://doi.org/10.1080/08958370902942517

22. Ali S, Rytting E (2014) Influences of nanomaterials on the barrier function of epithelial cells. Adv Exp Med Biol 811:45–54. https://doi.org/10.1007/978-94-017-8739-0_3

23. Busquets M, Espargaró A, Sabaté R, Estelrich J, Busquets MA, Espargaró A, Sabaté R, Estelrich J (2015) Magnetic nanoparticles cross the blood-brain barrier: when physics rises to a challenge. Nanomaterials 5(4):2231–2248. https://doi.org/10.3390/nano5042231

24. De Matteis V (2017) Exposure to inorganic nanoparticles: routes of entry, immune response, biodistribution and in vitro/in vivo toxicity evaluation. Toxics 5(4). https://doi.org/10.3390/TOXICS5040029.

25. Arami H, Khandhar A, Liggitt D, Krishnan KM (2015) In vivo delivery, pharmacokinetics, biodistribution and toxicity of iron oxide nanoparticles. Chem Soc Rev 44(23):8576–8607. https://doi.org/10.1039/c5cs00541h

26. Hume DA, Irvine KM, Pridans C (2019) The mononuclear phagocyte system: the relationship between monocytes and macrophages. Trends Immunol 40(2):98–112. https://doi.org/10.1016/j.it.2018.11.007

27. Chow A, Brown BD, Merad M (2011) Studying the mononuclear phagocyte system in the molecular age. Nat Rev Immunol 11(11):788–798. https://doi.org/10.1038/nri3087

28. Davies LC, Jenkins SJ, Allen JE, Taylor PR (2013) tissue-resident macrophages. Nat Immunol 14(10):986–995. https://doi.org/10.1038/ni.2705

29. Feng Q, Liu Y, Huang J, Chen K, Huang J, Xiao K (2018) Uptake, distribution, clearance, and toxicity of iron oxide nanoparticles with different sizes and coatings. Sci Rep 8(1):2082. https://doi.org/10.1038/s41598-018-19628-z

30. Gustafson HH, Holt-Casper D, Grainger DW, Ghandehari H (2015) Nanoparticle uptake: the phagocyte problem. Nano Today 10(4):487–510. https://doi.org/10.1016/j.nantod.2015.06.006

31. Owens DE, Peppas NA (2006) Opsonization, biodistribution, and pharmacokinetics of polymeric nanoparticles. Int J Pharm 307(1):93–102. https://doi.org/10.1016/J.IJPHARM.2005.10.010

32. Corbo C. Molinaro R, Parodi A, Toledano Furman NE, Salvatore F, Tasciotti E (2016) The impact of nanoparticle protein corona on cytotoxicity, immunotoxicity and target drug delivery. Nanomedicine 11(1):81–100. https://doi.org/10.2217/nnm.15.188

33. Aggarwal P, Hall JB, McLeland CB, Dobrovolskaia MA, McNeil SE (2009) Nanoparticle interaction with plasma proteins as it relates to particle biodistribution, biocompatibility and therapeutic efficacy. Adv Drug Deliv Rev 61(6):428–437. https://doi.org/10.1016/j.addr.2009.03.009

34. Pernia Leal M, Rivera-Fernández S, Franco JM, Pozo D, De La Fuente JM, García-Martín ML (2015) Long-circulating PEGylated manganese ferrite nanoparticles for MRI-based molecular imaging. Nanoscale 7(5):2050–2059. https://doi.org/10.1039/c4nr05781c

35. Foroozandeh P, Aziz AA (2018) Insight into cellular uptake and intracellular trafficking of nanoparticles. Nanoscale Res Lett 13(1):339. https://doi.org/10.1186/s11671-018-2728-6

36. Beddoes CM, Case CP, Briscoe WH (2015) Understanding nanoparticle cellular entry: a physicochemical perspective. Adv Colloid Interface Sci 218:48–68. https://doi.org/10.1016/j.cis.2015.01.007

37. Stern ST, Adiseshaiah PP, Crist RM (2012) Autophagy and lysosomal dysfunction as emerging mechanisms of nanomaterial toxicity. Part Fibre Toxicol 9(1):20. https://doi.org/10.1186/1743-8977-9-20

38. Appelqvist H, Wäster P, Kågedal K, Öllinger K (2013) The lysosome: from waste bag to potential therapeutic target. J Mol Cell Biol 5(4):214–226. https://doi.org/10.1093/jmcb/mjt022

39. Manke A, Wang L, Rojanasakul Y (2013) Mechanisms of nanoparticle-induced oxidative stress and toxicity. Biomed Res Int 2013:1–15. https://doi.org/10.1155/2013/942916

40. Azqueta A, Arbillaga L, López de Cerain A (2014) Genotoxicity of nanoparticles. In: Biointeractions of nanomaterials. Edited by Sutariya VB, Pathak Y. CRC Press. pp 353–363. https://doi.org/10.1201/b17191

41. Khanna P, Ong C, Bay B, Baeg G (2015) Nanotoxicity: an interplay of oxidative stress, Inflammation and cell death. Nanomaterials 5(3):1163–1180. https://doi.org/10.3390/nano5031163

42. Stevenson R, Hueber AJ, Hutton A, McInnes IB, Graham D (2011) Nanoparticles and inflammation. Sci World J 11:1300–1312. https://doi.org/10.1100/tsw.2011.106

43. Dixon SJ, Lemberg KM, Lamprecht MR, Skouta R, Zaitsev EM, Gleason CE, Patel DN, Bauer AJ, Cantley AM, Yang WS et al (2012) Ferroptosis: an iron-dependent form of nonapoptotic cell death. Cell 149(5):1060–1072. https://doi.org/10.1016/j.cell.2012.03.042

44. Huang G, Chen H, Dong Y, Luo X, Yu H, Moore Z, Bey EA, Boothman DA, Gao J (2013) Superparamagnetic iron oxide nanoparticles: amplifying ros stress to improve anticancer drug efficacy. Theranostics 3(2):116–126. https://doi.org/10.7150/thno.5411

45. Huang Y-W, Wu C, Aronstam RS (2010) Toxicity of transition metal oxide nanoparticles: recent insights from in vitro studies. Materials 3(10):4842–4859. https://doi.org/10.3390/ma3104842

46. Singh N, Manshian B, Jenkins GJS, Griffiths SM, Williams PM, Maffeis TGG, Wright CJ, Doak SH (2009) NanoGenotoxicology: the DNA damaging potential of engineered nanomaterials. Biomaterials 30(23–24):3891–3914. https://doi.org/10.1016/j.biomaterials.2009.04.009

47. Park EJ, Yoon J, Choi K, Yi J, Park K (2009) induction of chronic inflammation in mice treated with titanium dioxide nanoparticles by intratracheal instillation. Toxicology 260(1–3):37–46. https://doi.org/10.1016/j.tox.2009.03.005

48. Hadrup N, Saber AT, Kyjovska ZO, Jacobsen NR, Vippola M, Sarlin E, Ding Y, Schmid O, Wallin H, Jensen KA et al (2020) Pulmonary toxicity of Fe_2O_3, $ZnFe_2O_4$, $NiFe_2O_4$ and $NiZnFe_4O_8$ nanomaterials: inflammation and DNA strand breaks. Environ Toxicol Pharmacol 74. https://doi.org/10.1016/j.etap.2019.103303

49. Contini C, Schneemilch M, Gaisford S, Quirke N (2018) Nanoparticle–membrane Interactions. J Exp Nanosci 13(1):62–81. https://doi.org/10.1080/17458080.2017.1413253

50. Leroueil PR, Hong S, Mecke A, Baker JR, Orr BG, Banaszak Holl MM, Holl MMB (2007) Nanoparticle interaction with biological membranes: does nanotechnology present a janus face? Acc Chem Res 40(5):335–342. https://doi.org/10.1021/ar600012y

51. Lojk J, Strojan K, Miš K, Bregar BV, Bratkovič IH, Bizjak M, Pirkmajer S, Pavlin M (2017) Cell stress response to two different types of polymer coated cobalt ferrite nanoparticles. Toxicol Lett 270:108–118. https://doi.org/10.1016/j.toxlet.2017.02.010

52. Karlsson HL, Cronholm P, Hedberg Y, Tornberg M, De Battice L, Svedhem S, Wallinder IO (2013) Cell membrane damage and protein interaction induced by copper containing nanoparticles—importance of the metal release process. Toxicology 313(1):59–69. https://doi.org/10.1016/J.TOX.2013.07.012

53. Singh N, Nelson BC, Scanlan LD, Coskun E, Jaruga P, Doak SH (2017) Exposure to engineered nanomaterials: impact on DNA repair pathways. Int J Mol Sci 18(7). https://doi.org/10.3390/ijms18071515

54. Ahamed M, Alhadlaq HA, Alam J, Majeed Khan MA, Ali D, Alarafi S (2013) Iron oxide nanoparticle-induced oxidative stress and genotoxicity in human skin epithelial and lung epithelial cell lines. Curr Pharm Des 19(37):6681–6690. https://doi.org/10.2174/1381612811319370011

55. Alarifi S, Ali D, Alkahtani S, Alhader MS (2014) Iron oxide nanoparticles induce oxidative stress, DNA damage, and caspase activation in the human breast cancer cell line. Biol Trace Elem Res 159(1–3):416–424. https://doi.org/10.1007/s12011-014-9972-0

56. Aşık E, Akpınar Y, Güray NT, Đşcan M, Demircigil GÇ, Volkan M (2016) Cellular uptake, genotoxicity and cytotoxicity of cobalt ferrite magnetic nanoparticles in human breast cells. Toxicol Res (Camb) 5:1649–1662. https://doi.org/10.1039/C6TX00211K

57. Lojk J, Repas J, Veranič P, Bregar VB, Pavlin M (October 2019) Toxicity mechanisms of selected engineered nanoparticles on human neural cells in vitro. Toxicology 2020(432):152364. https://doi.org/10.1016/j.tox.2020.152364

58. Wang F, Salvati A, Boya P (2018) Lysosome-dependent cell death and deregulated autophagy induced by amine-modified polystyrene nanoparticles. Open Biol 8(4). https://doi.org/10.1098/rsob.170271

59. Oh N, Park JH (2014) Endocytosis and exocytosis of nanoparticles in mammalian cells. Int J Nanomedicine 9(Suppl 1):51. https://doi.org/10.2147/IJN.S26592

60. Crisponi G, Nurchi VM, Lachowicz JI, Peana M, Medici S, Zoroddu MA (2017) Toxicity of nanoparticles: etiology and mechanisms. Antimicrob Nanoarchitectonics 511–546. https://doi.org/10.1016/B978-0-323-52733-0.00018-5

61. Zhang X-Q, Xu X, Bertrand N, Pridgen E, Swami A, Farokhzad OC (2012) Interactions of nanomaterials and biological systems: implications to personalized nanomedicine. Adv Drug Deliv Rev 64(13):1363. https://doi.org/10.1016/J.ADDR.2012.08.005

62. Xie Y, Liu D, Cai C, Chen X, Zhou Y, Wu L, Sun Y, Dai H, Kong X, Liu P (2016) Size-dependent cytotoxicity of Fe_3O_4 nanoparticles induced by biphasic regulation of oxidative stress in different human hepatoma cells. Int J Nanomed 11:3557–3570. https://doi.org/10.2147/IJN.S105575

63. Vedantam P, Huang G, Tzeng TRJ (2013) Size-dependent cellular toxicity and uptake of commercial colloidal gold nanoparticles in DU-145 Cells. Cancer Nanotechnol. 4(1–3):13–20. https://doi.org/10.1007/s12645-013-0033-8

64. Kim T-H, Kim M, Park H-S, Shin US, Gong M-S, Kim H-W (2012) Size-dependent cellular toxicity of silver nanoparticles. J Biomed Mater Res Part A 100A(4):1033–1043. https://doi.org/10.1002/jbm.a.34053

65. Amstad E, Textor M, Reimhult E (2011) Stabilization and functionalization of iron oxide nanoparticles for biomedical applications. Nanoscale 3(7):2819. https://doi.org/10.1039/c1nr10173k

66. Barry SE (2008) Challenges in the development of magnetic particles for therapeutic applications. Int J Hyperth 24(6):451–466. https://doi.org/10.1080/02656730802093679

67. Moghimi SM, Simberg D (2018) Nanoparticle transport pathways into tumors. J Nanoparticle Res 20(6). https://doi.org/10.1007/s11051-018-4273-8

68. Huang X, Li L, Liu T, Hao N, Liu H, Chen D, Tang F (2011) The Shape Effect of mesoporous silica nanoparticles on biodistribution, clearance, and biocompatibility in vivo. ACS Nano 5(7):5390–5399. https://doi.org/10.1021/nn200365a

69. Gratton SEA, Ropp PA, Pohlhaus PD, Luft JC, Madden VJ, Napier ME, DeSimone JM (2008) The Effect of particle design on cellular internalization pathways. Proc Natl Acad Sci 105(33):11613–11618. https://doi.org/10.1073/PNAS.0801763105

70. Sargent LM, Shvedova AA, Hubbs AF, Salisbury JL, Benkovic SA, Kashon ML, Lowry DT, Murray AR, Kisin ER, Friend S et al (2009) Induction of aneuploidy by single-walled carbon nanotubes. Environ Mol Mutagen 50(8):708–717. https://doi.org/10.1002/em.20529

71. Ling D, Hyeon T (2013) Chemical design of biocompatible iron oxide nanoparticles for medical applications. Small 9(9–10):1450–1466. https://doi.org/10.1002/smll.201202111
72. Bresgen N, Eckl P, Bresgen N, Eckl PM (2015) oxidative stress and the homeodynamics of iron metabolism. Biomolecules 5(2):808–847. https://doi.org/10.3390/biom5020808
73. Thorek DLJ, Tsourkas A (2008) Size, charge and concentration dependent uptake of iron oxide particles by non-phagocytic cells. Biomaterials 29(26):3583–3590. https://doi.org/10.1016/j.biomaterials.2008.05.015
74. Salatin S, Dizaj SM, Khosroushahi AY (2015) Effect of the surface modification, size, and shape on cellular uptake of nanoparticles. Cell Biol Int 39:881–890. https://doi.org/10.1002/cbin.10459
75. Perton F, Tasso M, Muñoz Medina G, Ménard M, Blanco-Andujar C, Portiansky E, Fernandez van Raap M, Bégin D, Meyer F, Bégin-Colin S et al (2019) Fluorescent and magnetic stellate mesoporous silica for bimodal imaging and magnetic hyperthermia. Appl Mater Today 16:301–314. https://doi.org/10.1016/J.APMT.2019.06.006
76. Kim J, Kim HS, Lee N, Kim T, Kim H, Yu T, Song IC, Moon WK, Hyeon T (2008) multifunctional uniform nanoparticles composed of a magnetite nanocrystal core and a mesoporous silica shell for magnetic resonance and fluorescence imaging and for drug delivery. Angew Chemie Int Ed 47(44):8438–8441. https://doi.org/10.1002/anie.200802469
77. Lu A-H, Salabas EL, Schüth F (2007) magnetic nanoparticles: synthesis, protection, functionalization, and application. Angew Chemie Int Ed 46(8):1222–1244. https://doi.org/10.1002/anie.200602866
78. Bonvin D, Bastiaansen JAM, Stuber M, Hofmann H, Mionić Ebersold M (2017) Folic acid on iron oxide nanoparticles: platform with high potential for simultaneous targeting, MRI detection and hyperthermia treatment of lymph node metastases of prostate cancer. Dalton Trans 46(37):12692–12704. https://doi.org/10.1039/c7dt02139a
79. Huang Y, Mao K, Zhang B, Zhao Y (2017) superparamagnetic iron oxide nanoparticles conjugated with folic acid for dual target-specific drug delivery and MRI in cancer theranostics. Mater Sci Eng C 70:763–771. https://doi.org/10.1016/J.MSEC.2016.09.052
80. Li L, Gao F, Jiang W, Wu X, Cai Y, Tang J, Gao X, Gao F (2015) Folic acid-conjugated superparamagnetic iron oxide nanoparticles for tumor-targeting MR imaging. Drug Deliv 23(5):1726–1733. https://doi.org/10.3109/10717544.2015.1006404
81. Tasso M, Giovanelli E, Zala D, Bouccara S, Fragola A, Hanafi M, Lenkei Z, Pons T, Lequeux N (2015) Sulfobetaine-vinylimidazole block copolymers: a robust quantum dot surface chemistry expanding bioimaging's horizons. ACS Nano 9(11):11479–11489. https://doi.org/10.1021/acsnano.5b05705
82. Dembele F, Tasso M, Trapiella-Alfonso L, Xu X, Hanafi M, Lequeux N, Pons T (2017) Zwitterionic silane copolymer for ultra-stable and bright biomolecular probes based on fluorescent quantum dot nanoclusters. ACS Appl Mater Interfaces 9(21):18161–18169. https://doi.org/10.1021/acsami.7b01615
83. Trapiella-Alfonso L, Pons T, Lequeux N, Leleu L, Grimaldi J, Tasso M, Oujagir E, Seguin J, D'Orlyé F, Girard C et al (2018) Clickable-zwitterionic copolymer capped-quantum dots for in vivo fluorescence tumor imaging. ACS Appl Mater Interfaces 10(20):17107–17116. https://doi.org/10.1021/acsami.8b04708
84. Lundqvist M, Augustsson C, Lilja M, Lundkvist K, Dahlbäck B, Linse S, Cedervall T (2017) The nanoparticle protein corona formed in human blood or human blood fractions. PLoS One 12(4):e0175871. https://doi.org/10.1371/journal.pone.0175871
85. Nguyen VH, Lee B-J (2017) Protein corona: a new approach for nanomedicine design. Int J Nanomedicine 12:3137–3151. https://doi.org/10.2147/IJN.S129300
86. Yallapu MM, Chauhan N, Othman SF, Khalilzad-sharghi V, Ebeling C, Khan S, Jaggi M, Chauhan SC, States U, Falls S (2015) Implications of protein corona on physico-chemical and biological properties of magnetic nanoparticles. Biomaterials 46:1–12. https://doi.org/10.1016/j.biomaterials.2014.12.045.Implications
87. Goodman TT, Chee PN, Suzie HP (2008) 3-D tissue culture systems for the evaluation and optimization of nanoparticle-based drug carriers. Bioconjug Chem 19(10):1951–1959. https://doi.org/10.1021/bc800233a

88. Feliu N, Docter D, Heine M, del Pino P, Ashraf S, Kolosnjaj-Tabi J, Macchiarini P, Nielsen P, Alloyeau D, Gazeau F et al (2016) In Vivo degeneration and the fate of inorganic nanoparticles. Chem Soc Rev 45(9):2440–2457. https://doi.org/10.1039/c5cs00699f

89. Kumar A, Aileen Senapati V, Dhawan A (2018) Protocols for in vitro and in vivo toxicity assessment of engineered nanoparticles. In: Nanotoxicology: experimental and computational perspectives (issues in toxicology No. 35). Edited by Dhawan A, Anderson D, Shanker R. Royal Society of Chemistry. pp 94–132. https://doi.org/10.1039/9781782623922-00094

90. Mitjans M, Nogueira-Librelotto DR, Vinardell MP, Nogueira-Librelotto DR, Vinardell MP (2018) Nanotoxicity in vitro: limitations of the main cytotoxicity assays. In: Kumar V, Dasgupta N, Ranjan R (eds) Nanotoxicology: toxicity evaluation, risk assessment and management. CRC Press, pp 171–192. https://doi.org/10.1201/b21545-8

91. Niles AL, Moravec RA, Riss TL (2008) Update on in vitro cytotoxicity assays for drug development. Expert Opin Drug Discov 3:655–670

92. Jain MR, Bandyopadhyay D, Sundar R (2018) Scientific and regulatory considerations in the development of in vitro techniques for toxicology. In: In Vitro toxicology. Edited by Dhawan A, Kwon S. Elsevier. pp 165–185. https://doi.org/10.1016/B978-0-12-804667-8.00009-2

93. Horváth S (1980) Cytotoxicity of drugs and diverse chemical agents to cell cultures. Toxicology 16(1):59–66. https://doi.org/10.1016/0300-483X(80)90110-9

94. Sylvester PW (2011) Optimization of the tetrazolium dye (MTT) colorimetric assay for cellular growth and viability. In: Drug design and discovery: methods and protocols (Methods in Molecular Biology, vol 716). Edited by Satyanarayanajois S. Humana Press. pp 157–168. https://doi.org/10.1007/978-1-61779-012-6_9

95. Cory AH, Owen TC, Barltrop JA, Cory JG (1991) Use of an aqueous soluble tetrazolium/formazan assay for cell growth assays in culture. Cancer Commun 3(7):207–212. https://doi.org/10.3727/095535491820873191.

96. Mosmann T (1983) Rapid colorimetric assay for cellular growth and survival: application to proliferation and cytotoxicity assays. J Immunol Methods 65(1–2):55–63. https://doi.org/10.1016/0022-1759(83)90303-4

97. O'Brien J, Wilson I, Orton T, Pognan F (2000) Investigation of the Alamar Blue (resazurin) fluorescent dye for the assessment of mammalian cell cytotoxicity. Eur J Biochem 267(17):5421–5426. https://doi.org/10.1046/j.1432-1327.2000.01606.x

98. Twigg RS (1945) Oxidation-reduction aspects of resazurin. Nature 155(3935):401–402. https://doi.org/10.1038/155401a0

99. Riss TL, Moravec RA, O'Brien MA, Hawkins EM, Niles A (2006) Homogeneous multiwell assays for measuring cell viability, cytotoxicity and apoptosis. In: Handbook of assay development in drug discovery. Edited by Minor LK. CRC Press. pp 385–406. https://doi.org/10.1201/9781420015706

100. Riss TL, Moravec RA, Niles AL (2011) Cytotoxicity testing: measuring viable cells, dead cells, and detecting mechanism of cell death. In: Stoddart M (ed) Mammalian cell viability: methods and protocols. Humana Press, pp 103–114. https://doi.org/10.1007/978-1-61779-108-6_12

101. Bouhifd M, Bories G, Casado J, Coecke S, Norlén H, Parissis N, Rodrigues RM, Whelan MP (2012) Automation of an in vitro cytotoxicity assay used to estimate starting doses in acute oral systemic toxicity tests. Food Chem Toxicol 50(6):2084–2096. https://doi.org/10.1016/J.FCT.2012.03.046

102. Rodrigues RM, Bouhifd M, Bories G, Sacco M-G, Gribaldo L, Fabbri M, Coecke S, Whelan MP (2013) Assessment of an automated in vitro basal cytotoxicity test system based on metabolically-competent cells. Toxicol Vitr 27(2):760–767. https://doi.org/10.1016/J.TIV.2012.12.004

103. Skehan P, Storeng R, Scudiero D, Monks A, McMahon J, Vistica D, Warren JT, Bokesch H, Kenney S, Boyd MR (1990) New colorimetric cytotoxicity assay for anticancer-drug screening. J Natl Cancer Inst 82(13):1107–1112. https://doi.org/10.1093/jnci/82.13.1107

104. Vichai V, Kirtikara K (2006) Sulforhodamine B colorimetric assay for cytotoxicity screening. Nat Protoc 1(3):1112–1116. https://doi.org/10.1038/nprot.2006.179

105. Woolston C, Martin S (2011) Analysis of tumor and endothelial cell viability and survival using sulforhodamine B and clonogenic assays. In: Stoddart MJ (ed) Mammalian cell viability: methods and protocols. Methods in molecular biology, vol 740. Humana Press, pp 45–56. https://doi.org/10.1007/978-1-61779-108-6_7

106. Koh JY, Choi DW (1987) quantitative determination of glutamate mediated cortical neuronal injury in cell culture by lactate dehydrogenase efflux assay. J Neurosci Methods 20(1):83–90. https://doi.org/10.1016/0165-0270(87)90041-0

107. Decker T, Lohmann-Matthes M-L (1988) A quick and simple method for the quantitation of lactate dehydrogenase release in measurements of cellular cytotoxicity and tumor necrosis Factor (TNF) activity. J Immunol Methods 115(1):61–69. https://doi.org/10.1016/0022-1759(88)90310-9

108. Kohen R, Nyska A (2002) Oxidation of biological systems: oxidative stress phenomena, antioxidants, redox reactions, and methods for their quantification. Toxicol Pathol 30(6):620–650. https://doi.org/10.1080/01926230290166724

109. Olowe R, Sandouka S, Saadi A, Shekh-ahmad T (2020) Approaches for reactive oxygen species and oxidative stress quantification in epilepsy. Antioxidants 9(10):1–26. https://doi.org/10.3390/antiox9100990

110. Katerji M, Filippova M, Duerksen-Hughes P (2019) Approaches and methods to measure oxidative stress in clinical samples: research applications in the cancer field. Oxid Med Cell Longev 2019 (Article ID 1279250). https://doi.org/10.1155/2019/1279250

111. Aranda A, Sequedo L, Tolosa L, Quintas G, Burello E, Castell JV, Gombau L (2013) Dichlorodihydro-fluorescein diacetate (DCFH-DA) assay: a quantitative method for oxidative stress assessment of nanoparticle-treated cells. Toxicol. Vitr. 27(2):954–963. https://doi.org/10.1016/j.tiv.2013.01.016

112. Mesquita CS, Oliveira R, Bento F, Geraldo D, Rodrigues JV, Marcos JC (2014) Simplified 2,4-dinitrophenylhydrazine spectrophotometric assay for quantification of carbonyls in oxidized proteins. Anal Biochem 458:69–71. https://doi.org/10.1016/j.ab.2014.04.034

113. Kumar A, Dhawan A (2013) Genotoxic and carcinogenic potential of engineered nanoparticles: an update. Arch Toxicol 87(11):1883–1900. https://doi.org/10.1007/s00204-013-1128-z

114. Doak SH, Liu Y, Chen C (2017) Genotoxicity and cancer. In: Adverse effects of engineered nanomaterials: exposure, toxicology, and impact on human health (2nd edition). Edited by Fadeel B, Pietroiusti A, Shvedova AA. Academic Press, pp 423–445. https://doi.org/10.1016/B978-0-12-809199-9.00018-5

115. Shaikh SF, Ubaidullah M, Mane RS, Al-Enizi AM (2020) Types, synthesis methods and applications of ferrites. In: Spinel ferrite nanostructures for energy storage devices. Edited by Mane RS, Jadhav VV Elsevier, pp 51–82. https://doi.org/10.1016/b978-0-12-819237-5.00004-3

116. Desai I, Nadagouda MN, Elovitz M, Mills M, Boulanger B (2019) Synthesis and characterization of magnetic manganese ferrites. Mater Sci Energy Technol 2(2):150–160. https://doi.org/10.1016/j.mset.2019.01.009

117. Wang K, Yang P, Guo R, Yao X, Yang W (2019) Photothermal performance of MFe_2O_4 nanoparticles. Chinese Chem Lett 30(12):2013–2016. https://doi.org/10.1016/j.cclet.2019.04.005

118. Ovejero JG, Mayoral A, Cañete M, García M, Hernando A, Herrasti P (2018) Electrochemical synthesis and magnetic properties of MFe_2O_4 (M=Fe, Mn Co, Ni) nanoparticles for potential biomedical applications. J Nanosci Nanotechnol 19(4):2008–2015. https://doi.org/10.1166/jnn.2019.15313

119. Alghamdi N, Stroud J, Przybylski M, Żukrowski J, Cruz Hernandez A, Brown JM, Hankiewicz JH, Celinski Z (2019) Structural, magnetic and toxicity studies of ferrite particles employed as contrast agents for magnetic resonance imaging thermometry. J Magn Magn Mater 497(18):165981 https://doi.org/10.1016/j.jmmm.2019.165981

120. Eid R, Arab NTT, Greenwood MT (2017) Iron mediated toxicity and programmed cell death: a review and a re-examination of existing paradigms. Biochim Biophys Acta Mol Cell Res 1864(2):399–430. https://doi.org/10.1016/j.bbamcr.2016.12.002

121. Spinowitz BS, Kausz AT, Baptista J, Noble SD, Sothinathan R, Bernardo MV, Brenner L, Pereira BJG (2008) ferumoxytol for treating iron deficiency anemia in CKD. J Am Soc Nephrol 19(8):1599–1605. https://doi.org/10.1681/ASN.2007101156

122. Lima-Tenório MK, Gómez Pineda EA, Ahmad NM, Fessi H, Elaissari A (2015) Magnetic nanoparticles: in vivo cancer diagnosis and therapy. Int J Pharm 493(1–2):313–327. https://doi.org/10.1016/j.ijpharm.2015.07.059

123. Al-Rawi NN, Anwer BA, Al-Rawi NH, Uthman AT, Ahmed IS (2020) Magnetism in drug delivery: the marvels of iron oxides and substituted ferrites nanoparticles. Saudi Pharm J 28(7):876–887. https://doi.org/10.1016/j.jsps.2020.05.003

124. Thorat ND, Bohara RA, Tofail SAM, Alothman ZA, Shiddiky MJA, Hossain MS, Yamauchi Y, Wu KC-W (2016) Superparamagnetic Gadolinium Ferrite Nanoparticles with controllable curie temperature—cancer theranostics for MR-imaging-guided magneto-chemotherapy. Eur J Inorg Chem 2016(28):4586–4597. https://doi.org/10.1002/ejic.201600706

125. Mahmoudi M, Sant S, Wang B, Laurent S, Sen T (2011) Superparamagnetic iron oxide nanoparticles (SPIONS): development, surface modification and applications in chemotherapy. Adv Drug Deliv Rev 63(1–2):24–46. https://doi.org/10.1016/j.addr.2010.05.006

126. Paul W, Sharma CP (2010) Inorganic nanoparticles for targeted drug delivery. Biointegration Med Implant Mater 204–235. https://doi.org/10.1533/9781845699802.2.204

127. Price PM, Mahmoud WE, Al-Ghamdi AA, Bronstein LM (2018) Magnetic drug delivery: where the field is going. Front Chem 6:619. https://doi.org/10.3389/fchem.2018.00619

128. Chen S, Huang B, Pei W, Xu Y, Jiang Z, Li J, Wang L, Niu C (2019) Magnetically targeted nanoparticles for imaging-guided photothermal therapy of cancer. RSC Adv 9(65):38154–38164. https://doi.org/10.1039/c9ra08281f

129. Falconieri A, De Vincentiis S, Raffa V (2019) recent advances in the use of magnetic nanoparticles to promote neuroregeneration. Nanomedicine 14(9):1073–1076. https://doi.org/10.2217/nnm-2019-0103

130. Dobson J (2006) Magnetic micro- and nano-particle-based targeting for drug and gene delivery. Nanomedicine 1(1):31–37. https://doi.org/10.2217/17435889.1.1.31

131. Prosen L, Prijic S, Music B, Lavrencak J, Cemazar M, Sersa G (2013) Magnetofection: a reproducible method for gene delivery to melanoma cells. Biomed Res Int 2013:209452. https://doi.org/10.1155/2013/209452

132. Fang K, Liu P, Dong S, Guo Y, Cui X, Zhu X, Li X, Jiang L, Liu T, Wu Y (2016) magnetofection based on superparamagnetic iron oxide nanoparticle-mediated low LncRNA HOTAIR expression decreases the proliferation and invasion of glioma stem cells. Int J Oncol 49(2):509–518. https://doi.org/10.3892/ijo.2016.3571

133. Neuwelt EA, Hamilton BE, Varallyay CG, Rooney WR, Edelman RD, Jacobs PM, Watnick SG (2009) Ultrasmall superparamagnetic iron oxides (USPIOs): a future alternative magnetic resonance (MR) contrast agent for patients at risk for nephrogenic systemic fibrosis (NSF)? Kidney Int 75(5):465–474. https://doi.org/10.1038/ki.2008.496

134. Mulder WJ, Griffioen AW, Strijkers GJ, Cormode DP, Nicolay K, Fayad ZA (2007) Magnetic and fluorescent nanoparticles for multimodality imaging. Nanomedicine 2(3):307–324. https://doi.org/10.2217/17435889.2.3.307

135. Kwon Y.-S, Choi K-B, Lim H, Lee S, Lee J-J (2018) Preparation and characterization of alginate based-fluorescent magnetic nanoparticles for fluorescence/magnetic resonance multimodal imaging applications. Jpn J Appl Phys 57(6S1):06HE03. https://doi.org/10.7567/JJAP.57.06HE03

136. Deng K, Chen Y, Li C, Deng X, Hou Z, Cheng Z, Han Y, Xing B, Lin J (2017) 808 Nm light responsive nanotheranostic agents based on near-infrared dye functionalized manganese ferrite for magnetic-targeted and imaging-guided photodynamic/photothermal therapy. J Mater Chem B 5(9):1803–1814. https://doi.org/10.1039/C6TB03233H

137. Bell G, Balasundaram G, Attia ABE, Mandino F, Olivo M, Parkin IP (2019) Functionalised iron oxide nanoparticles for multimodal optoacoustic and magnetic resonance imaging. J Mater Chem B 7(13):2212–2219. https://doi.org/10.1039/C8TB02299B

138. Stafford S, Serrano Garcia R, Gun'ko Y, Stafford S, Serrano Garcia R, Gun'ko YK (2018) Multimodal magnetic-plasmonic nanoparticles for biomedical applications. Appl Sci 8(1):97. https://doi.org/10.3390/app8010097s

139. Tomitaka A, Kaushik A, Kevadiya BD, Mukadam I, Gendelman HE, Khalili K, Liu G, Nair M (2019) Surface-engineered multimodal magnetic nanoparticles to manage CNS diseases. Drug Discov Today 24(3):873–882. https://doi.org/10.1016/J.DRUDIS.2019.01.006

140. Hanini A, Kacem K, Gavard J, Abdelmelek H, Ammar S (2018) Ferrite nanoparticles for cancer hyperthermia therapy. In: Handbook of nanomaterials for industrial applications; Elsevier Inc., pp 638–661. https://doi.org/10.1016/B978-0-12-813351-4.00036-5

141. Zioni T, Perkas N, Wolfus Y, Soroka Y, Popov I, Oron M, Perelshtein I, Bruckental Y, Brégégère FM, Ma'or Z et al (2010) Strontium hexaferrite nanomagnets suspended in a cosmetic preparation: a convenient tool to evaluate the biological effects of surface magnetism on human skin. Ski Res Technol 16(3):316–324. https://doi.org/10.1111/j.1600-0846.2010.00435.x

142. Alvino L, Pacheco-Herrero M, López-Lorente ÁI, Quiñones Z, Cárdenas S, González-Sánchez ZI (2020) Toxicity evaluation of Barium Ferrite nanoparticles in bacteria. Chemosphere 254:126786. https://doi.org/10.1016/j.chemosphere.2020.126786

143. Fantechi E, Innocenti C, Albino M, Lottini E, Sangregorio C (2015) Journal of magnetism and magnetic materials influence of cobalt doping on the hyperthermic efficiency of magnetite nanoparticles. J Magn Magn Mater 380:365–371. https://doi.org/10.1016/j.jmmm.2014.10.082

144. Amiri S, Shokrollahi H (2013) The Role of cobalt ferrite magnetic nanoparticles in medical science. Mater Sci Eng C 33(1):1–8. https://doi.org/10.1016/j.msec.2012.09.003

145. Srinivasan SY, Paknikar KM, Bodas D, Virendra G (2018) Applications of cobalt ferrite nanoparticles in biomedical nanotechnology. Nanomedicine 13:1221–1238

146. Ahmad F, Zhou Y (2017) Pitfalls and challenges in nanotoxicology: a case of cobalt ferrite ($CoFe_2O_4$) nanocomposites. Chem Res Toxicol 30:492–507. https://doi.org/10.1021/acs.chemrestox.6b00377

147. Horev-azaria L, Baldi G, Beno D, Bonacchi D, Golla-schindler U, Kirkpatrick JC, Kolle S, Landsiedel R, Maimon O, Marche PN et al (2013) Predictive toxicology of cobalt ferrite nanoparticles: comparative in-vitro study of different cellular models using methods of knowledge discovery from data. Part Fibre Toxicol 10:32

148. Ahamed M, Javed M, Khan MAM, Alhadlaq HA (2016) cobalt iron oxide nanoparticles induce cytotoxicity and regulate the apoptotic genes through ROS in human liver cells (HepG2). Colloids Surf B 148:665–673. https://doi.org/10.1016/j.colsurfb.2016.09.047

149. Abudayyak M, Gurkaynak TA, Özhan G (2017) In vitro toxicological assessment of cobalt ferrite nanoparticles in several mammalian cell types. Biol Trace Elem Res 175:458–465. https://doi.org/10.1007/s12011-016-0803-3

150. Zhao H, Chen Z, Tao L, Zhu X, Lan M, Li Z (2015) In vitro toxicity evaluation of ultra-small MFe_2O_4 (M=Fe, Mn, Co) nanoparticles using A549 cells. RSC Adv 5:68454–68460. https://doi.org/10.1039/C5RA11013K

151. Salunkhe AB, Khot VM, Thorat ND, Phadatare MR, Sathish CI, Dhawale DS, Pawar SH (2013) Applied surface science polyvinyl alcohol functionalized cobalt ferrite nanoparticles for biomedical applications. Appl Surf Sci 264(3):598–604. https://doi.org/10.1016/j.apsusc.2012.10.073

152. Peeples B, Goornavar V, Peeples C, Spence D, Parker V, Bell C, Biswal D, Ramesh GT, Pradhan AK (2014) Structural, stability, magnetic, and toxicity studies of nanocrystalline iron oxide and cobalt ferrites for biomedical applications. J. Nanoparticle Res. 16:2290. https://doi.org/10.1007/s11051-014-2290-9

153. Hwang DW, Lee DS, Kim S (2012) Gene Expression Profiles for Genotoxic Effects of Silica-Free and Silica-Coated Cobalt Ferrite Nanoparticles. J Nucl Med 53(1):106–112. https://doi.org/10.2967/jnumed.111.088443

154. Lucht N, Friedrich RP, Draack S, Alexiou C, Viereck T, Ludwig F, Hankiewicz B (2019) Biophysical characterization of (silica-coated) cobalt errite nanoparticles for hyperthermia treatment. Nanomaterials 9:1713. https://doi.org/10.3390/nano9121713

155. Park SI, Lim JH, Hwang YH, Kim JH, Kim CG, Kim CO (2007) Enhancing radioactive magnetic properties in monodispersed MFE_2O_4 nanoparticles. Phys Status Solidi Appl Mater Sci 204(12):3913–3917. https://doi.org/10.1002/pssa.200777265

156. Akhtar K, Javed Y, Jamil Y, Muhammad F (2020) Functionalized cobalt ferrite cubes: toxicity, interactions and mineralization into ferritin proteins. Appl Nanosci 10(9):3659–3674. https://doi.org/10.1007/s13204-020-01484-x

157. Akhtar S, Khan Q, Anwar S, Ali G, Maqbool M, Khan M, Karim S, Gao L (2019) A comparative study of the toxicity of polyethylene glycol-coated cobalt ferrite nanospheres and nanoparticles. Nanoscale Res Lett 14:386. https://doi.org/10.1186/s11671-019-3202-9

158. Billing AM, Knudsen KB, Chetwynd AJ, Ellis LJA, Tang SVY, Berthing T, Wallin H, Lynch I, Vogel U, Kjeldsen F (2020) Fast and robust proteome screening platform identifies neutrophil extracellular trap formation in the lung in response to cobalt ferrite nanoparticles. ACS Nano 14(4):4096–4110. https://doi.org/10.1021/acsnano.9b08818

159. Pradhan P, Giri J, Samanta G, Sarma HD, Mishra KP, Bellare J, Banerjee R, Bahadur D (2007) Comparative evaluation of heating ability and biocompatibility of different ferite-based magnetic fluids for hyperthermia application. J Biomed Mater Res Part B Appl Biomater 81(1):12–22. https://doi.org/10.1002/jbm.b.30630

160. Mirzaee S, Bayrami A, Mirzaei Z (2020) Experimental and theoretical investigation of sugar-coated cobalt ferrite nanoparticles. J Aust Ceram Soc 56(3):1021–1028. https://doi.org/10.1007/s41779-019-00407-6

161. Şincai M, Deleanu L, Argherie D, Bica D (2002) The Effects of Magnetic Fluids on Blood Parameters in Dogs. J Magn Magn Mater 252:406–408. https://doi.org/10.1016/S0304-8853(02)00714-X

162. Hoque SM, Huang Y, Cocco E, Maritim S, Santin AD, Shapiro EM, Coman D, Hyder F (2016) Improved specific loss power on cancer cells by hyperthermia and MRI contrast of hydrophilic $Fe_xCo_{1-X}Fe_2O_4$ nanoensembles. Contrast Media Mol Imaging 11(6):514–526. https://doi.org/10.1002/cmmi.1713

163. Di Guglielmo C, Ramos López D, De Lapuente J, De Llobet Mallafre JM, Borràs Suarèz M (2010) Embryotoxicity of cobalt ferrite and gold nanoparticles: a first in vitro approach. Reprod Toxicol 30(2):271–276. https://doi.org/10.1016/j.reprotox.2010.05.001

164. Berger D, Georgescu D, Bajenaru L, Zanfir A, Stănică N, Matei C (2017) Properties of mesostructured silica coated $CoFe_2O_4$ versus Fe_3O_4-silica composites. J Alloys Compd 708:278–284. https://doi.org/10.1016/j.jallcom.2017.02.268

165. Nam PH, Lu LT, Linh PH, Manh DH, Thanh Tam LT, Phuc NX, Phong PT, Lee IJ (2018) Polymer-coated cobalt ferrite nanoparticles: synthesis, characterization, and toxicity for hyperthermia applications. New J Chem 42(17):14530–14541. https://doi.org/10.1039/c8nj01701h

166. Dutz S, Buske N, Landers J, Gräfe C, Wende H, Clement JH (2020) Biocompatible magnetic fluids of co-doped iron oxide nanoparticles with tunable magnetic properties. Nanomaterials 10:1019. https://doi.org/10.3390/nano10061019

167. Ansari SM, Sinha BB, Pai KR, Bhat SK, Ma Y, Sen D, Kolekar YD, Ramana CV (2018) Controlled surface/interface structure and spin enabled superior properties and biocompatibility of cobalt ferrite nanoparticles. Appl Surf Sci 459:788–801. https://doi.org/10.1016/j.apsusc.2018.08.063

168. Pasukoniene V, Mlynska A, Steponkiene S, Poderys V, Matulionyt M, Karabanovas V, Purvinien R, Aleksander J, Kurtinaitien M, Strioga M et al (2014) Accumulation and biological effects of cobalt ferrite nanoparticles in human pancreatic and ovarian cancer cells. Medicina (B. Aires) 50:237–244. https://doi.org/10.1016/j.medici.2014.09.009

169. Lojk J, Bregar VB, Strojan K, Hudoklin S, Veranič P, Pavlin M, Kreft ME (2018) Increased endocytosis of magnetic nanoparticles into cancerous urothelial cells versus normal urothelial cells. Histochem Cell Biol 149:45–59. https://doi.org/10.1007/s00418-017-1605-1

170. Abudayyak M, Gürkaynak TA, Özhan G (2017) In vitro evaluation of the toxicity of cobalt ferrite nanoparticles in kidney cell Kobalt Ferrit Nanopartiküllerinin Böbrek Hücresi Üzerine Güvenliğinin İn. Turkish J Pharm Sci 14(2):169–173. https://doi.org/10.4274/tjps.99609

171. Medina-Ramírez IE, Alejandra M, León DD, Ortega HM, Zapien JA, Betancourt I, Ortega HM, Zapien JA, Betancourt I, Santoyo-elvira N (2019) Development and assesment of nano-technologies: cytotoxicity and hyperthermia laboratory studies. Cancer Invest 38:61–84. https://doi.org/10.1080/07357907.2019.1698593

172. Asmatulu R, Garikapati A, Misak HE, Song Z, Yang S, Wooley P (2010) Cytotoxicity of magnetic nanocomposite spheres for possible drug delivery systems. Proc ASME - IMECE 2010 10:911–918. https://doi.org/10.1115/IMECE2010-40269

173. Ovejero JG, Mayoral A, Cañete M, García M, Hernando A, Herrasti P (2019) Electrochemical synthesis and magnetic properties of MFe_2O_4 (M=Fe, Mn Co, Ni) nanoparticles for potential biomedical applications. J Nanosci Nanotechnol 19:2008–2015. https://doi.org/10.1166/jnn.2019.15313

174. Hong NH, Raghavender AT, Ciftja O, Phan MH, Stojak K, Srikanth H, Zhang YH (2013) Ferrite nanoparticles for future heart diagnostics. Appl Phys A Mater Sci Process 112(2):323–327. https://doi.org/10.1007/s00339-013-7573-y

175. Mushtaq MW, Kanwal F, Islam A, Ahmed K, Jamil T, Imran M, Abbas SM, Huang Q (2017) Synthesis and characterisation of doxorubicin-loaded functionalised cobalt ferrite nanoparticles and their in vitro anti-tumour activity under an AC-magnetic field. Trop J Pharm Res 16(July):1663–1674. https://doi.org/10.4314/tjpr.v16i7.27

176. Mariani V, Ponti J, Giudetti G, Broggi F, Marmorato P, Gioria S, Franchini F, Rauscher H, Rossi F (2012) Online monitoring of cell metabolism to assess the toxicity of nanoparticles : the case of cobalt ferrite. Nanotoxicology 6(May):272–287. https://doi.org/10.3109/17435390.2011.572302

177. Matsuda S, Nakanishi T, Kaneko K, Osaka T (2015) Synthesis of cobalt ferrite nanoparticles using spermine and their effect on death in human breast cancer cells under an alternating magnetic Fi Eld. Electrochim Acta 183:153–159. https://doi.org/10.1016/j.electacta.2015.06.108

178. Ansari SM, Bhor RD, Pai KR, Sen D, Kolekar YD, Ramana CV, Sen D, Kolekar YD, Ramana CV (2016) Size and chemistry controlled cobalt-ferrite nanoparticles and their anti-proliferative effect against the MCF-7 breast cancer cells size and chemistry controlled cobalt-ferrite nanoparticles and their anti-proliferative effect against the MCF-7 breast C. ACS Biomater Sci Eng 2:2139–2152. https://doi.org/10.1021/acsbiomaterials.6b00333

179. Primo FL, Rodrigues MMA, Simioni AR, Lacava ZGM, Morais PC, Tedesco AC (2008) Photosensitizer-loaded magnetic nanoemulsion for use in synergic photodynamic and magne-tohyperthermia therapies of neoplastic cells. J Nanosci Nanotechnol 8(11):5873–5877. https://doi.org/10.1166/jnn.2008.476

180. Finetti F, Terzuoli E, Donnini S, Uva M, Ziche M, Morbidelli L (2016) Monitoring endothe-lial and tissue responses to cobalt ferrite nanoparticles and hybrid hydrogels. PLoS ONE 11:e0168727. https://doi.org/10.1371/journal.pone.0168727

181. Khanna L, Gupta G, Tripathi SK (2019) Effect of size and silica coating on structural, magnetic as well as cytotoxicity properties of copper ferrite nanoparticles. Mater Sci Eng C 97:552–566. https://doi.org/10.1016/j.msec.2018.12.051

182. Ahmed YMZ, Hessien MM, Rashad MM, Ibrahim IA (2009) Nano-Crystalline copper ferrites from secondary iron oxide (mill scale). J Magn Magn Mater 321(3):181–187. https://doi.org/10.1016/j.jmmm.2008.08.100

183. Masunga N, Mmelesi OK, Kefeni KK, Mamba BB (2019) Recent advances in copper ferrite nanoparticles and nanocomposites synthesis, magnetic properties and application in water treatment: review. J Environ Chem Eng 7(3):103179. https://doi.org/10.1016/j.jece.2019.103179

184. Kanagesan S, Hashim M, Aziz SAB, Ismail I, Tamilselvan S, Alitheen NB, Swamy MK, Chandra Rao BP (2016) Evaluation of antioxidant and cytotoxicity activities of copper ferrite ($CuFe_2O_4$) and zinc ferrite ($ZnFe_2O_4$) nanoparticles synthesized by sol-gel self-combustion method. Appl Sci 6(9):184. https://doi.org/10.3390/app6090184

185. Chakraborty S, Mahadevan BK, Shah J, Panse K, Malvi B, Balasubramanian C, Singh S, Misra SK (2020) Enhanced detection using stable isotope enriched 65Cu doped ferrite nanoparticles for tracing studies. J Alloys Compd 822:153502. https://doi.org/10.1016/j.jallcom.2019.153502

186. Liu Y, Guo Z, Li F, Xiao Y, Zhang Y, Bu T, Jia P, Zhe T, Wang L (2019) Multifunctional magnetic copper ferrite nanoparticles as Fenton-like reaction and near-infrared photothermal agents for synergetic antibacterial therapy. ACS Appl Mater Interfaces 11(35):31649–31660. https://doi.org/10.1021/acsami.9b10096

187. Ahmad J, Alhadlaq HA, Alshamsan A, Siddiqui MA, Saquib Q, Khan ST, Wahab R, Al-Khedhairy AA, Musarrat J, Akhtar MJ et al (2016) Differential cytotoxicity of copper ferrite nanoparticles in different human cells. J Appl Toxicol 36(10):1284–1293. https://doi.org/10.1002/jat.3299

188. Blanco-Andujar C, Walter A, Cotin G, Bordeianu C, Mertz D, Felder-Flesch D, Begin-Colin S (2016) Design of iron oxide-based nanoparticles for MRI and magnetic hyperthermia. Nanomedicine 11:1889–1910. https://doi.org/10.2217/nnm-2016-500

189. Iacovita C, Florea A, Scorus L, Pall E, Dudric R, Moldovan AI, Stiufiuc R, Tetean R, Lucaciu CM (2019) Hyperthermia, cytotoxicity, and cellular uptake properties of manganese and zinc ferrite magnetic nanoparticles synthesized by a polyol-mediated process. Nanomaterials 9(10):1489. https://doi.org/10.3390/nano9101489

190. Mazarío E, Sánchez-Marcos J, Menéndez N, Cañete M, Mayoral A, Rivera-Fernández S, De La Fuente JM, Herrasti P (2015) High specific absorption rate and transverse relaxivity effects in manganese ferrite nanoparticles obtained by an electrochemical route. J Phys Chem C 119(12):6828–6834. https://doi.org/10.1021/jp510937r

191. Yang Y, Shi H, Wang Y, Shi B, Guo L, Wu D, Yang S, Wu H (2016) Graphene oxide/manganese ferrite nanohybrids for magnetic resonance imaging, photothermal therapy and drug delivery. J Biomater Appl 30(6):810–822. https://doi.org/10.1177/0885328215601926

192. Pacchierotti F, Bellusci M, La Barbera A, Padella F, Mancuso M, Pasquo A, Grollino MG, Leter G, Nardi E, Cremisini C et al (2014) Biodistribution and acute toxicity of a nanofluid containing manganese iron oxide nanoparticles produced by a mechanochemical process. Int J Nanomedicine 9(1):1919. https://doi.org/10.2147/IJN.S56394

193. Qian R, Maiti D, Zhong J, Xiong SS, Zhou H, Zhu R, Wan J, Yang K (2019) T1/T2-weighted magnetic resonance imaging and SPECT imaging guided combined radioisotope therapy and chemotherapy using functionalized reduced graphene oxide-manganese ferrite nanocomposites. Carbon N. Y. 149:55–62. https://doi.org/10.1016/j.carbon.2019.04.046

194. Sharmiladevi P, Akhtar N, Haribabu V, Girigoswami K, Chattopadhyay S, Girigoswami A (2019) Excitation wavelength independent carbon-decorated ferrite nanodots for multimodal diagnosis and stimuli responsive therapy. ACS Appl Bio Mater 2(4):1634–1642. https://doi.org/10.1021/acsabm.9b00039

195. Coppola F, Tavares DS, Henriques B, Monteiro R, Trindade T, Soares AMVM, Figueira E, Polese G, Pereira E, Freitas R (2019) remediation of arsenic from contaminated seawater using manganese spinel ferrite nanoparticles: ecotoxicological evaluation in *Mytilus galloprovincialis*. Environ Res 175:200–212. https://doi.org/10.1016/j.envres.2019.04.008

196. Coppola F, Tavares DS, Henriques B, Monteiro R, Trindade T, Figueira E, Soares AMVM, Pereira E, Freitas R (2020) Can water remediated by manganese spinel ferrite nanoparticles be safe for *Marine bivalves*? Sci Total Environ 723:137798. https://doi.org/10.1016/j.scitotenv.2020.137798

197. Wang L, Yan Y, Wang M, Yang H, Zhou Z, Peng C, Yang S (2016) An Integrated nanoplatform for theranostics via multifunctional core-shell ferrite nanocubes. J Mater Chem B 4(10):1908–1914. https://doi.org/10.1039/c5tb01910a

198. Nunes ADC, Ramalho LS, Souza ÁPS, Mendes EP, Colugnati DB, Zufelato N, Sousa MH, Bakuzis AF, Castro CH (2014) Manganese ferrite-based nanoparticles induce ex vivo, but not in vivo, Cardiovasc Effects Int J Nanomed 9(1):3299–3312. https://doi.org/10.2147/IJN.S64254

199. Lopez-Abarrategui C, Figueroa-Espi V, Lugo-Alvarez MB, Pereira CD, Garay H, Barbosa JARG, Falcão R, Jiménez-Hernández L, Estévez-Hernández O, Reguera E et al (2016) The intrinsic antimicrobial activity of citric acid-coated manganese ferrite nanoparticles is enhanced after conjugation with the antifungal peptide Cm-P5. Int J Nanomed 11:3849–3857. https://doi.org/10.2147/IJN.S107561

200. Kefeni KK, Msagati TAM, Nkambule TT, Mamba BB (2020) Spinel ferrite nanoparticles and nanocomposites for biomedical applications and their toxicity. Mater Sci Eng C 107:110314. https://doi.org/10.1016/j.msec.2019.110314

201. Ahamed M, Akhtar MJ, Alhadlaq HA, Khan MAM, Alrokayan SA (2015) Comparative cytotoxic response of nickel ferrite nanoparticles in human liver HepG2 and Breast MFC-7 cancer cells. Chemosphere 135:278–288. https://doi.org/10.1016/j.chemosphere.2015.03.079

202. Ahamed M, Akhtar MJ, Siddiqui MA, Ahmad J, Musarrat J, Al-Khedhairy AA, AlSalhi MS, Alrokayan SA (2011) Oxidative stress mediated apoptosis induced by nickel ferrite nanoparticles in cultured A549 cells. Toxicology 283(2–3):101–108. https://doi.org/10.1016/j.tox.2011.02.010

203. Yin H, Too HP, Chow GM (2005) The Effects of particle size and surface coating on the cytotoxicity of nickel ferrite. Biomaterials 26(29):5818–5826. https://doi.org/10.1016/j.biomaterials.2005.02.036

204. Genchi G, Carocci A, Lauria G, Sinicropi MS, Catalano A (2020) Nickel: human health and environmental toxicology. Int J Environ Res Public Health 17(3):679. https://doi.org/10.3390/ijerph17030679

205. Egizbek K, Kozlovskiy AL, Ludzik K, Zdorovets MV, Korolkov IV, Marciniak BMJ, Chudoba D, Nazarova A, Kontek R (2020) Stability and cytotoxicity study of $NiFe_2O_4$ nanocomposites synthesized by co-precipitation and subsequent thermal annealing. Ceram Int 46(10):16548–16555. https://doi.org/10.1016/j.ceramint.2020.03.222

206. Karunamoorthi R, Suresh Kumar G, Prasad AI, Vatsa RK, Thamizhavel A, Girija EK (2014) Fabrication of a novel biocompatible magnetic biomaterial with hyperthermia potential. J Am Ceram Soc 97(4):1115–1122. https://doi.org/10.1111/jace.12746

207. Martínez-Rodríguez NL, Tavárez S, González-Sánchez ZI (2019) In Vitro Toxicity assessment of zinc and nickel ferrite nanoparticles in human erythrocytes and peripheral blood mononuclear cell. Toxicol Vitr 57:54–61. https://doi.org/10.1016/j.tiv.2019.02.011

208. Rodríguez Torres CE, Golmar F, Ziese M, Esquinazi P, Heluani SP (2011) Evidence of defect-induced ferromagnetism in $ZnFe_2O_4$ thin films. Phys Rev B Condens Matter Mater Phys 84(6):1–13. https://doi.org/10.1103/PhysRevB.84.064404

209. Tian Q, Wang Q, Xie Q, Li J (2010) Aqueous solution preparation, structure, and magnetic properties of nano-granular $Zn_XFe_{3-X}O_4$ ferrite films. Nanoscale Res Lett 5(9):1518–1523. https://doi.org/10.1007/s11671-010-9672-4

210. Thakur P, Chahar D, Taneja S, Bhalla N (2020) A review on MnZn ferrites: synthesis, characterization and applications. Ceram Int 46:15740–15763. https://doi.org/10.1016/j.ceramint.2020.03.287

211. Alhadlaq HA, Akhtar MJ, Ahamed M (2015) Zinc Ferrite nanoparticle-induced cytotoxicity and oxidative stress in different human cells. Cell Biosci 5(1):55. https://doi.org/10.1186/s13578-015-0046-6

212. Saquib Q, Al-Khedhairy AA, Ahmad J, Siddiqui MA, Dwivedi S, Khan ST, Musarrat J (2013) Zinc ferrite nanoparticles activate IL-1b, NFKB1, CCL21 and NOS2 signaling to induce mitochondrial dependent intrinsic apoptotic pathway in WISH cells. Toxicol Appl Pharmacol 273(2):289–297. https://doi.org/10.1016/j.taap.2013.09.001

213. Zhu S, Xu X, Rong R, Li B, Wang X (2016) Evaluation of zinc-doped magnetite nanoparticle toxicity in the liver and kidney of mice after sub-chronic intragastric administration. Toxicol Res (Camb) 5:97–106. https://doi.org/10.1039/c5tx00292c

214. Rivero M, Gutiérrez L, Wheeler GN (2019) Toxicity and biodegradation of zinc ferrite nanoparticles in *Xenopus laevis*. J Nanoparticle Res 21:181. https://doi.org/10.1007/s11051-019-4631-1

215. Zou Y, Huang Z, Deng M, Yin G, Chen X, Liu J, Wang Y, Yan L, Gu J (2013) Synthesis and neuro-cytocompatibility of magnetic Zn-ferrite nanorods via peptide-assisted process. J Colloid Interface Sci 408(1):6–12. https://doi.org/10.1016/j.jcis.2013.07.017

216. Liu J, Deng M, Huang Z, Yin G, Liao X, Gu J (2013) Preparation of $ZnFe_2O_4$ nanoparticles in the template of silk-fibroin peptide and their neuro-cytocompability in PC12 Cells. Colloids Surfaces B 107:19–26. https://doi.org/10.1016/j.colsurfb.2013.01.072

217. Iqbal S, Kotnala G, Shah J, Ahmad S (2019) Barium ferrite nanoparticles: a highly effective EMI shielding material. Mater Res Express 6(5): 055018. https://doi.org/10.1088/2053-1591/ab02a4

218. Catalan G, Scott JF (2009) Physics and applications of bismuth ferrite. Adv Mater 21(24):2463–2485. https://doi.org/10.1002/adma.200802849

219. Rajaee A, Wensheng X, Zhao L, Wang S, Liu Y, Wu Z, Wang J, Si-Shen F (2018) Multifunctional bismuth ferrite nanoparticles as magnetic localized dose enhancement in radiotherapy and imaging. J Biomed Nanotechnol 14(6):1159–1168. https://doi.org/10.1166/jbn.2018.2553

220. Xia A, Zuo C, Chen L, Jin C, Lv Y (2013) Hexagonal $SrFe_{12}O_{19}$ Ferrites: hydrothermal synthesis and their sintering properties. J Magn Magn Mater 332:186–191. https://doi.org/10.1016/j.jmmm.2012.12.035

221. Song Q, Liu Y, Jiang Z, Tang M, Li N, Wei F, Cheng G (2014) The Acute Cytotoxicity of bismuth ferrite nanoparticles on PC12 cells. J Nanopart Res 16(5):1–11. https://doi.org/10.1007/s11051-014-2408-0

222. Nikiforov VN, Ivanov AV, Brusentsov NA, Gendler TS, Irkhin VY (2017) Magnetically sensitive nanoparticles for magnetically controlled thermochemotherapy. Int J Nanotechnol 14(7–8):646–653. https://doi.org/10.1504/IJNT.2017.083439

223. Mekonnen TW, Birhan YS, Andrgie AT, Hanurry EY, Darge HF, Chou H-Y, Lai J-Y, Tsai H-C, Yang JM, Chang Y.-H (2019) Encapsulation of gadolinium ferrite nanoparticle in generation 4.5 poly(amidoamine) dendrimer for cancer theranostics applications using low frequency alternating magnetic field. Colloids Surf B 184:110531. https://doi.org/10.1016/j.colsurfb.2019.110531

224. Kim DH, Kim KN, Kim KM, Shim IB, Lee YK (2004) Necrosis of carcinoma cells using Co (1–x) Ni (x) Fe (2) O (4) and Ba (1–x) Sr (x) Fe/12/O/19/ ferrites under alternating magnetic field. IEEE Trans Magn 40(4):2985–2987. https://doi.org/10.7868/S0367676513060082

225. Wang C, Zhao N, Huang Y, He R, Xu S, Yuan W (2020) coordination of injectable self-healing hydrogel with Mn-Zn Ferrite@mesoporous silica nanospheres for tumor mr imaging and efficient synergistic magnetothermal-chemo-chemodynamic therapy. Chem Eng J 401:126100. https://doi.org/10.1016/j.cej.2020.126100

226. Herynek V, Turnovcová K, Gálisová A, Kaman O, Mareková D, Koktan J, Vosmanská M, Kosinová L, Jendelová P (2019) Manganese-zinc ferrites: safe and efficient nanolabels for cell imaging and tracking in vivo. ChemistryOpen 8(2):155–165. https://doi.org/10.1002/open.201800261

227. Montha W, Maneeprakorn W, Buatong N, Tang IM, Pon-On W (2016) Synthesis of doxorubicin-PLGA loaded chitosan stabilized (Mn, Zn)Fe_2O_4. Mater Sci Eng C 59:235–240. https://doi.org/10.1016/j.msec.2015.09.098

228. Basti H, Hanini A, Levy M, Ben Tahar L, Herbst F, Smiri LS, Kacem K, Gavard J. Wilhelm C, Gazeau F et al (2015) Size tuned polyol-made Zn0.9M0.1Fe2O4 (M=Mn, Co, Ni) ferrite nanoparticles as potential heating agents for magnetic hyperthermia: from synthesis control to toxicity survey. Mater Res Express 1(4). https://doi.org/10.1088/2053-1591/1/4/045047

229. Hanini A, El Massoudi M, Gavard J, Kacem K, Ammar S, Souilem O (2016) Nanotoxicological study of polyol-made cobalt-zinc ferrite nanoparticles in rabbit. Environ Toxicol Pharmacol 45:321–327. https://doi.org/10.1016/j.etap.2016.06.010

230. Shahbazi-Gahrouei D, Ghasemian Z, Abdolahi, M, Manouchehri S, Javanmard haghjooy S, Dana N (2013) In vitro evaluation of cobalt-zinc ferrite nanoparticles coated with DMSA on human prostate cancer cells. J Mol Biomark Diagn 4(3):1000154. https://doi.org/10.4172/2155-9929.1000154

231. Al-Qubaisi MS, Rasedee A, Flaifel MH, Ahmad SH, Hussein-Al-Ali S, Hussein MZ, Zainal Z, Alhassan FH, Taufiq-Yap YH, Eid EEM et al (2013) Induction of apoptosis in cancer cells by NiZn ferrite nanoparticles through mitochondrial cytochrome C release. Int J Nanomed 8:4115–4130. https://doi.org/10.2147/IJN.S50061

232. Kim DH, Lee SH, Kim KN, Kim KM, Shim IB, Lee YK (2005) Cytotoxicity of ferrite particles by MTT and agar diffusion methods for hyperthermic application. J Magn Magn Mater 293(1):287–292. https://doi.org/10.1016/j.jmmm.2005.02.078

233. Berridge MV, Herst PM, Tan AS (2005) Tetrazolium dyes as tools in cell biology: new insights into their cellular reduction. Biotechnol Annu Rev 11 (Suppl.):127–152. https://doi.org/10.1016/S1387-2656(05)11004-7

234. Al-Qubaisi MS, Rasedee A, Flaifel MH, Ahmad SHJ, Hussein-Al-Ali S, Hussein MZ, Eid EEM, Zainal Z, Saeed M, Ilowefah M et al (2013) Cytotoxicity of nickel zinc ferrite nanoparticles on cancer cells of epithelial origin. Int J Nanomedicine 8:2497–2508. https://doi.org/10.2147/IJN.S42367

235. Zachanowicz E, Zięcina A, Mikołajczyk PA, Rogacki K, Małecka M, Marycz K, Marędziak M, Poźniak B, Nowakowska M, Tikhomirov M et al (2016) Cytotoxic effects of $Co_{1-x}Mn_xFe_2O_4$ ferrite nanoparticles synthesized under non-hydrolytic conditions (Bradley's reaction)—in vitro. Eur J Inorg Chem 2016(34):5315–5323. https://doi.org/10.1002/ejic.201600720

236. Hamed A, Fitzgerald AG, Wang L, Gueorguieva M, Malik R, Melzer A (2013) Synthesis, characterization and surface modification of $ZnCrFeO_4$ nanoparticles. Mater Sci Eng C 33(3):1623–1628. https://doi.org/10.1016/j.msec.2012.12.071

237. Yao A, Ai F, Wang D, Huang W, Zhang X (2009) Synthesis, characterization and in vitro cytotoxicity of self-regulating magnetic implant material for hyperthermia application. Mater Sci Eng C 29(8):2525–2529. https://doi.org/10.1016/j.msec.2009.07.021

238. Gökçe D, Köytepe S, Özcan İ (2020) Assessing short-term effects of magnetite ferrite nanoparticles on daphnia magna. Environ Sci Pollut Res 27(25):31489–31504. https://doi.org/10.1007/s11356-020-09406-8

239. Kovrižnych JA, Sotńikóva R, Zeljenková D, Rollerová E, Szabová E, Wimmerová S (2013) Acute toxicity of 31 different nanoparticles to zebrafish (*Danio rerio*) tested in adulthood and in early life stages—comparative study. Interdiscip Toxicol 6(2):67–73. https://doi.org/10.2478/intox-2013-0012

Spinel Nanoferrites: A Versatile Platform for Environmental Remediation

Komal, Sneha Singh, Sandeep Bansal, and Sonal Singhal

Abstract Owing to remarkably promising applications and distinctive characteristics, spinel nanoferrites have gained immense research interest in the latest period. Being magnetically separable nanocatalysts, spinel ferrites have revolutionized the idea of environmental decontamination to a great extent. The present chapter highlights the most recognizable feature of nanospinels, i.e., their versatility in terms of ease of degradation of diverse pollutants, specifically organic pollutants. A deep structural insight and the detailed mechanism of pollutant degradation through distinct routes has been discussed. A considerable attention has been paid toward miscellaneous modifications being recently followed for enhancing the applicability of spinel nanoferrites such as substitution at the active sites, surface functionalization, and composting with different scaffolds. Such beneficial modifications make spinel nanoferrites a commercially exploitable and tunable platform for environmental remediation.

Keywords Spinel nanoferrites · Organic pollutants · Degradation · Oxidation · Magnetically separable

1 Introduction

The world has witnessed massive progress in the fields of industrial development and urban modernization in twenty-first century. Apart from the numerous advantages, the growing industrialization and urbanization has also left our environment polluted

Komal · S. Singh · S. Singhal (✉)
Department of Chemistry & Centre of Advanced Studies in Chemistry, Panjab University, Chandigarh, India
e-mail: sonal@pu.ac.in

S. Bansal
Department of Science and Technology, New Delhi, India

S. Singhal
Department of Chemistry, Panjab University, Chandigarh 160014, India

in the most brutal way. Over a few decades, the scientific advancements have alleviated the quality of day-to-day life to a great extent. These scientific advancements besides proving beneficial are also slowly hollowing us from inside by introducing a large number of contaminants which are fatal to ecosystem. These contaminants are introduced into the environment in the form of industrial, agricultural, or domestic wastes [1–3]. This introduction of contaminants through waste is the leading cause of increase in all types of pollution, i.e., water, air, and soil either directly or indirectly, making environmental pollution a matter of serious concern for scientific community. Among the various problems emerging from environment pollution, these contaminants are the root cause of water pollution as these contaminants are directly disposed off in to the water bodies without any prior treatment [4, 5]. Water bodies are relentlessly getting polluted with different effluents released from various sources as depicted in Fig. 1.

Scientific literature discloses heaps of reports concerned with the urgent issue of wastewater treatment. Jones et al. [6] have reported the contamination of water bodies in urban areas due to medicinal plants which constitute a potential risk for the ecosystems and living beings for long terms. Robinson et al. [7] have reported the adverse effect of chemical reagents, inorganic, and organic compounds in textile industries on the environment. Wang et al. [8] have studied the contamination caused by mercury in aquatic systems and reported industrial wastes and agricultural materials as the main source of contamination. Gregory McIsaac [9] has reported the industrially manufactured nitrogen fertilizers as the leading cause of surface water pollution. Thus, the pollution of water bodies is becoming a major global problem owing to the constant increase in the demand of freshwater supply due to the alarming rise in human population rates.

Fig. 1 Different contaminants polluting water resources

1.1 Water Pollution Current Status and Scenario

Clean water is an indispensable requirement for achieving human survival and well-being, from an individual to the international level. The current status of water consumption and water pollution around the globe can put any individual in a deep shock. Water is the most stressed resource, and its consumption has been increasing worldwide by about 1% per year and is expected to rise at similar rate until 2050, which will account for an overall increase of 20–30% water consumption [10]. According to recent water pollution statistics, humans dump approximately 1.2 trillion gallons of untreated wastewater into the water bodies each year. Across the world, an average of 1.5 million children under the age of five die as a consequence of waterborne diseases [11]. Currently, more than 20% of the entire population on the earth is unable to get adequate access to safe water. With the increasing slope of the graph of water pollution, it is anticipated that by 2050, about 47% inhabitants out of a total population of around 8 billion will have to face the situations of water scarcity [12].

Low-income countries typically treat only 8% of the total wastewater generated by various activities, whereas the high income countries like USA, Canada, Germany, and Japan are able to treat up to 70% of their respective wastewater. A recent report by the world bank suggests that the release of pollutant streams in the environment directly affects the economy of a region, especially in middle income regions like India, where the impact of pollution has led to an approximate reduction of one half in the growth of GDP. According to a recent report by world economic forum, it has been estimated that around 70% of the ground surface water in India is unsafe for direct consumption. Each day, approximately 40 million liters of wastewater is being discharged into the rivers and other water sources with only a minuscule portion acceptably treated [11]. Besides the huge expenditure on the treatment of wastewater, the annual cost of health maintenance in regard to water pollution alone has been estimated to be around INR 470–610 billion ($ 6.7–8.7 billion).

1.2 Major Water Pollutants and Sources

Water pollutants cause the most pivotal environmental problems by directly affecting the sustainable development of a country. The major water pollutants released from different sectors can be categorized as:

(i) **Pathogens**: The disease causing pathogenic organisms such as bacterium, virus, or other microorganism majorly enter the water bodies through sewage discharge or sometimes due to the wastewater generated from slaughterhouses. Such wastewater can lead to several waterborne diseases like cholera, diarrhea, typhoid, hepatitis, etc.

(ii) **Nutrients**: The wastewater produced from fertilizer industries or generated through agricultural run-off is often rich in nutrients like nitrogen and phosphorous. Such water may stimulate the growth of aquatic weeds like algae or may cause skin and eye irritation, vomiting or other gastric problems when consumed by human beings.

(iii) **Macroscopic pollutants**: These comprise of plastics, shipwrecks, papers, nurdles, sand, silt, etc. They emerge in the water bodies through surface runoff during rainy seasons, domestic activities, or through municipal sewerage waters. The macroscopic pollutants act as a hurdle for the sunlight to penetrate the water which eventually affects the aquatic life.

(iv) **Inorganic pollutants**: Contaminants such as ammonia, heavy metals, cyanides, nitrites, mineral acids, nitrates, sulfates, fall in this category, out of which the high concentrations of heavy metals such as Hg, As, Cu, Pb, Cd, and Se are predominantly known for their toxic effects. Several activities of mining, transportation, agriculture, and industries are responsible for their discharge in to the water sources.

(v) **Organic pollutants**: Although all the pollutants have detrimental effects on water bodies, but among the various pollutants, organic pollutants are considered to be the predominant contributors of water pollution. There are several types of organic pollutants such as insecticides, defoliants, volatile organic compounds, detergents, food processing wastes, fuel additives, pharmaceuticals, paints, plastics, synthetic fibers, dyes, and solvents.

Organic pollutants (OPs) have been a cause of great apprehension due to their presence in a high concentration even in remote ecosystems despite the government bans on the production and usage [13]. OPs are one of the vicious and worst water pollutants which are creating huge pressure on the remedial waste water recycling units. The industrial organic effluents vary in their corresponding molecular composition, color, and chemical oxygen demand. Direct release of these noxious pollutants in to the water bodies result in the formation of toxic compounds under oxidative conditions and in turn contaminate the ground water resources as well as water employed for the irrigation purposes. Such contaminants persist in the environment for long durations as these are not removed or decomposed by natural microbial or degradation action of mother nature. These OPs can also be called as emerging contaminants as for these no regulations have been established till date owing to which their addition to the environment is neither questioned nor checked by the government. The primary sources through which the organic pollutants enter the ecosystem include municipal and domestic sewage, pulp and paper mills, distilleries, slaughter houses, or through manmade activities such as production and applications of different organic compounds or through their spillage or leakage during transportation [14].

Among the various synthetic organic compounds, textile dyes are one of the major groups of organic compounds to cause hazardous effects on the environment as reported by Konstantinou and Albanis [15]. Mainly dyes are colored materials having specific affinity toward substrates such as plastic, paper, hair, and textiles. Dyes have emerged as a major concern among the researchers due to their variety

and complex structures. In comparison with other wastes, removal of dyes from the wastewater is often considered important because even a very small concentration of dye is clearly visible and considerably affects the water environment [16]. They are vastly used in textile industries, pharmaceutical industries, paper and pulp industries, bleaching industries, and dyes and dye intermediates industries. Large amounts of variety of dyes are annually produced making them foremost contributor of water pollution.

1.3 Need for Environmental Remediation

Perilous water proves fatal to more people every year than any form of warfare and violence combined.

In past half century, vigorous development of mankind, society, science and technology, industrial, and agricultural sectors have led to the use of chemicals which are potentially toxic contaminants when released into the environment [17–20]. Unregulated discharge of such effluents from the distinct sources into the aquatic water bodies has not only led to the formation of mixed pool of aquatic toxins, but also it poses detrimental effect on human and aquatic life. Hence, it is necessary to treat wastewater rich in chemicals before releasing in such a way so that it does not have any adverse effect on the environment. These compounds when get entered into the food chain have high toxic effects on humans, aquatic animals, and plantations. Their persistence for long periods of time in the environment and property of accumulating and passing from one species to the next through the food chain make them a major global concern [21]. OPs have adverse effects on gastrointestinal, genito-urinary, and cardiovascular system of human body and also have been reported to be carcinogenic. Most of these compounds are toxic and resistant to microbial/bacterial degradation. The presence of these pollutants in water make it unfit for plants, animals, and humans. A number of these compounds are considered as environmental hormones and are reported to have adversarial effects on the human and wildlife reproductive cycles. Paris et al. [22] have reported endocrine disruptors (steroids, polychlorinated biphenyls, and dioxins) as the chemicals that mimic the natural hormones and interfere with the normal functioning of the organisms. The presence of antibiotics in drinking water bodies have been detected as the cause of development of resistant pathogens or the development of allergic responses in humans as reported by Zuccato et al. [23]. A number of organic-based pesticides are reported to have carcinogenic effects on human bodies by various researchers. DDT, an organochlorine compound, readily accumulates in human adipose tissues and cause toxic effects in human bodies, animals, and plants. Similarly, dioxins, furans, and polychlorinated biphenyls have been reported to cause harmful effects to the environment [24]. The toxic and carcinogenic effects of organic dyes along with hindrance in photocatalytic activities of aquatic plants have been reported by Akpan and Hameed [25].

1.4 Various Tools and Recent Developments in Wastewater Remediation

The intricacy of the growing effects of water pollution necessitate the development and appliance of novel technology in order to control the pollution of ground and surface water and, eventually, to assure the security of drinking water. In recent years, various research cohorts, present worldwide, are putting in continuous and dedicated efforts to prioritize new methods and technologies for the effective removal of organic pollutants. Different techniques have been developed to minimize the concentration of pollutants to permissible limits prior to dumping them into the water bodies which will assure the restoration and improvement of overall water quality. Generally, wastewater treatment is classified into four different levels viz. primary, secondary, tertiary, and quaternary with each level focused to remove specific class of contaminant [26]. In primary treatment, suspended solids are removed from wastewater using simple physical processes. The soluble materials are eliminated in secondary treatment while tertiary and quaternary methods are designed to remove specific contaminant that was not eradicated in previous steps. Besides these methods, various technologies that have been adopted until now for wastewater abatement have been listed in Table 1.

Amongst these, advanced oxidation processes (AOPs) have emerged as a robust and cleaner alternative for the remediation of polluted wastewater. Primarily, AOPs are free radical mediated chemical oxidation processes that have the ability to successfully treat strenuous pollutants into nontoxic CO_2, H_2O, and inorganic salts. Basically, it involves in situ generation of hydroxyl radical (·OH) using oxidants such as O_3, H_2O_2, and O_2 at near-ambient temperature and pressure; thereby exploiting high reactivity of ·OH as a driving force for oxidation of wide variety of organic contaminants. The efficiency of AOPs is based on generation of highly reactive and unselective ·OH which is a powerful oxidant ($E^o = -2.8$ V) as compared to common oxidizing agents (O_3 ($E^o = -2.0$ V) and H_2O_2 ($E^o = -1.8$ V). Hydroxyl radical is the second-strongest oxidant next to fluorine ($E^o = -3.03$ V) and hence can

Table 1 Techniques used for treatment of organic pollutants from wastewater

Physical	Biological	Chemical	Electro-chemical	AOPs
Filtration [27]	Microorganisms [31]	Oxidation [7]	Electro-coagulation [33]	Photolysis [38]
Coagulation [28]	Enzymes [32]		Electro-flotation [34]	Ozonation [39]
Adsorption [29, 30]			Electro-oxidation [35]	Wet air oxidation [40]
			Electro-reduction [36]	Photocatalysis [41]
			Electro-disinfection [37]	Fenton [42]

non-selectively degrade variety of micropollutants with high rate constants (106–109 mol^{-1} s^{-1}). Owing to noteworthy advantages of AOPs, i.e., high reaction rates, high oxidation potential of OH and indiscriminate oxidation of wide range of organic contaminants; this technique is widely applied to treat wastewater, ground water, remediation of soil and sediments, conditioning of municipal sludge, destruction of volatile organic compounds, etc. [43].

Conventional AOPs only involve use of oxidants (O_3, H_2O_2, and O_2) for the eradication of high concentration obstinate toxic waste. However, there are huge piles of reports present in literature which support the fact that the introduction of transition metal salts (such as Fe^{2+}) and radiation sources (UV, visible, γ-rays, ultrasound, etc.) into the system greatly improves the rate of oxidation by enhancing the production of ·OH [44]. On the basis of these modifications, AOPs can be broadly classified under following categories: ozonation, photolysis, wet air oxidation, photocatalysis, and Fenton's process.

1.5 Fenton's Process

Fenton's method is one of the most promising AOPs for oxidation and mineralization of wide range of OPs [45]. The process is widely used due to its simpler substrates and easy application ruling out the use of any special equipment for the reaction. Its operation under normal temperature and pressure conditions also makes it an economical process for wastewater treatment. The catalytic decomposition of oxidizing agents in the presence of Fe^{2+} ions to generate ·OH is the core of Fenton Chemistry and is often referred as **Fenton's reaction**. In addition, to greatly improve the efficiency of regular Fenton's process, researchers have incorporated light (λ > 250 nm) as an additional component into typical Fenton's reaction for production of more ·OH and this process is widely known as **Photo-Fenton process**. This process turns out to have edge over classical Fenton process because the presence of light photochemically aids in reduction of excess Fe^{3+} into Fe^{2+} thereby regenerating the catalyst quickly.

Another crucial parameter while talking of the Fenton/photo-Fenton process is the choice of Fenton catalyst or the source of Fe^{2+} ions. The recent researches in the era of AOPs mostly focus on the use of environmentally benign magnetically recoverable nanocatalysts (MRNCs) as a Fenton catalyst, which possess advantages such as low preparation cost, high activity, great selectivity, high stability, efficient recovery, and good recyclability. Where, the extraction of conventional nanocatalysts such as metal nanoparticles, metal oxides, silica, clay, metal organic frameworks, zeolites, alumina, titania, grapheme, and carbon nanotubes is a tedious task owing to the extremely small particle size and high dispersive nature, the use of MRNCs has emerged as a savior [46]. They not only offer stable and high catalytic performance, but also decrease the use of energy, effort and time required for their separation [47]. These MRNCs possess inherent magnetic character so can easily be separated out

of the reaction mixture after the completion of the catalytic reaction with the aid of an external magnet as illustrated in Fig. 2.

Among various magnetically recoverable nanocatalysts probed so far, nanoferrites have emerged as proficient catalysts to aid in the oxidation of noxious pollutants. Importance of nanoferrites as catalysts lies in their cost effectiveness, facile synthetic methodologies, stability, inert nature toward harsh conditions, and their submissive character toward further modifications (Fig. 3).

Nanoferrites are actually ceramic magnetic materials which are majorly composed of Fe_2O_3 combined chemically to one or more other metallic elements. On the basis of structural characteristics, nanoferrites can be garnet, hexagonal, and spinel [48]. Spinel nanoferrites are the most widely employed class of nanoferrites from the point of view of catalysis. Spinel nanoferrites have the basic formula of MFe_2O_4. Here 'M' represents the divalent metal ions of Co, Ni, Cu, Zn, Mg, Cu, Ca, etc. Spinel nanoferrites have been extensively exploited to address numerous environmental applications. The catalytic activity of spinel nanoferrites is greatly affected by the nature and the mutual synergistic interactions of the metal ions present in the catalytically active sites [49].

Fig. 2 Facile separation of MRNCs using an external magnet
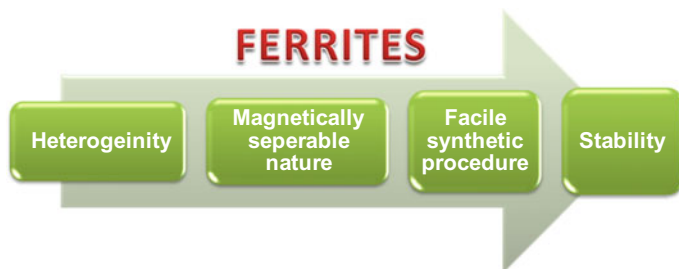
Fig. 3 Remarkable features of spinel nanoferrites

The present chapter is aimed at critical and detailed investigation of spinel nanoferrites as potential catalysts for environmental detoxification while also focusng on the future scope of these nanospinels.

2 Spinel Nanoferrites: A Versatile Tool for Environmental Remediation

Spinel nanoferrites have gained much interest as heterogeneous catalyst for the removal of pollutants owing to their unique properties, i.e., low cost, facile synthetic procedure, stability at wider pH range, non-toxicity, and inherent magnetic character. The emergence of spinel nanoferrites as potential candidates toward environmental remediation could also be attributed to their higher surface area as compared to their bulk counterparts. The aspects contributing toward the versatility of spinel nanoferrites for the removal of organic and inorganic pollutants and the reason for their inherent magnetic character could be better understood by gaining an insight into their crystal structure.

2.1 An Insight into the Crystal Structure of Spinel Nanoferrites

Spinel nanoferrites are ceramic magnetic oxides with the general formula, MFe_2O_4 where M is a divalent cation (M =Fe, Co, Ni, Cd, Mg, Zn etc.). In the crystal structure of spinel nanoferrites, oxide ions (O^{2-}) are arranged in face-centered cubic closed lattice, thus generating two different sites, i.e., tetrahedral (A) and octahedral (B) for the cations to occupy. The spinel crystal structure has Fd-3 m space group and the unit cell comprises of 32 oxygen (O^{2-}), 8 divalent metal ions (M^{2+}), and 16 trivalent iron (Fe^{3+}). Typical spinel structure of nanoferrites has been illustrated as Fig. 4. Each unit cell consists of 64 tetrahedral (A) sites and 32 octahedral (B) sites; out of which only 8 tetrahedral and 16 octahedral sites are occupied [50]. The crystal chemistry of spinel nanoferrites can be best described using the general formula, $(M^{2+}_{1-x}Fe^{3+}_x)_A [M^{2+}_x Fe^{3+}_{2-x}]_B O_4$, where x is the inversion parameter which depends on factors such as method of synthesis, different site preferences of metal ions, crystal field stabilization energy (CFSE), and covalent bonding effects [51].

Depending upon the distribution of cations over A and B sites, spinel nanoferrites can be classified into three classes:

(a) **Normal Spinel ($x= 0$)**: In this structure, all M^{2+} ions occupy A sites and all Fe^{3+} ions are found at B sites. Normal spinel nanoferrites can be structurally represented as $(M^{2+})_A [Fe_2^{3+}]_B O_4$, e.g., zinc ferrite, $(Zn^{2+})_A [Fe_2^{3+}]_B O_4$ belongs to this class [52].
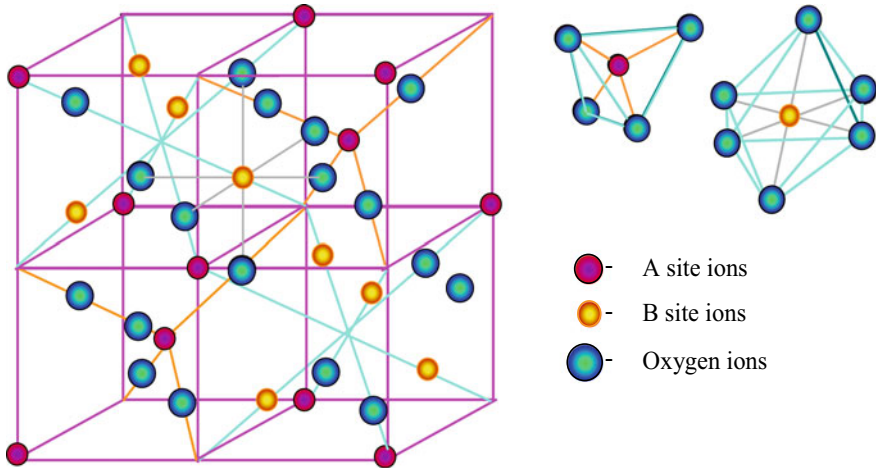
Fig. 4 Crystal structure of spinel nanoferrites

(b) **Inverse Spinel ($x= 1$)**: In case of inverse spinel nanoferrites, Fe^{3+} ions are equally distributed among A and B sites with consequent migration of all M^{2+} ions into A sites. $NiFe_2O_4$ and $CoFe_2O_4$ possess inverse spinel structure and their structural formula is $(Fe^{3+})_A [M^{2+} Fe^{3+}]_B O_4$ [53].

(c) **Mixed Spinel ($0 < x < 1$)**: In most spinels, all M^{2+} ions and Fe^{3+} ions tend to occupy both A and B sites resulting in mixed spinel structures. $MnFe_2O_4$ is an example of such type of structure with inversion parameter of $x = 0.2$ and the resulting structural formula is $(Mn^{2+}_{0.8}Fe^{3+}_{0.2})_A [Mn^{2+}_{0.2}Fe^{3+}_{1.8}]_B O_4$ [54].

Therefore, to sum up, if the value of x is 0, then the ferrite is normal spinel, if its value is one, then the ferrite is inverse spinel; and if its value is between 0 and 1, then the ferrite has a mixed spinel structure.

2.2 Inherent Magnetic Character of Spinel Nanoferrites

The journey of magnetic materials started with the discovery of a mineral called magnetite (Fe_3O_4), the first magnetic material known to mankind. This magnetite or lodestone is itself a ferrite or can be called as iron ferrite [55]. The inherent magnetic character possessed by nanoferrites is due to their ionic structure, *i.e.,* the constituent magnetic moment of metal ions presents in the lattice sites contribute to net magnetic moment possessed by nanoferrites. Nanoferrites are not ferromagnetic materials as the total magnetism acquired by them is quite less than sum total of magnetization of metal ions present in the lattice structure [56, 57].

Neel, for the first time suggested that magnetism attained by nanoferrites was distinctly different from any other magnetic material. The magnetism of nanoferrites

can be explained based upon Neel's assumption [58] that exchange force acting between the metal ions present in the two lattice sites, i.e., the octahedral sites and the tetrahedral sites, was negative just like anti-ferromagnetic materials. Such that lattices ions present in tetrahedral sites are magnetized in one direction and those present in octahedral site are magnetized in opposite direction [59]. Unlike anti-ferromagnetic materials, the magnetization possessed by metal ions present in the two kinds of sites is not equal, so there is some net magnetization left for nanoferrites to behave as magnets. According to Neel's two sub-lattice model, the magnetic moment per formula unit in Bohr magneton $n_B^N(\chi)$ is expressed as:

$$n_B^N(\chi) \; = \; M_B(\chi) - M_A(\chi)$$

where M_B and M_A are magnetization of B and A sub-lattices, respectively.

3   Pure Spinel Nanoferrites as Catalyst for Environmental Remediation

Owing to its stability and fascinating magnetic and catalytic properties, spinel nanoferrites have been extensively employed as catalyst in reactions such as biodiesel production [60], dehydrogenation of hydrocarbons [61], hydroxylation of benzene [62], and reduction of carbondioxide [63]. Apart from numerous other applications, spinel nanoferrites having a band gap capable of absorbing visible light can be widely utilized as photocatalyst for the degradation of pollutants. Organic pollutants such as dyes, detergents, pharmaceuticals, and solvents have been reported to resist microbial degradation, thus posing serious threat to the aquatic environment. The role of magnetically separable nanoferrites has been widely extended toward environmental remediation. Due to their ease of synthesis and non-toxicity, various research cohorts have devoted their studies toward exploring the role of spinel nanoferrites in catalytic abatement of toxic pollutants.

Dey et al. [64] have synthesized copper nanoferrites which possess good catalytic activity for the reduction of 4-nitrophenol, which is one among the harmful aromatic compounds that affect not only the environment but also human health. Fardood et al. [65] reported the green synthesis of magnesium ferrite nanoparticles using tragacanth gel by sol–gel method. The synthesized ferrite displayed high catalytic activity for the removal of malachite green dye under visible light showing recyclability efficiency up to fifth cycle. Lassoued et al. [66] have evaluated the catalytic capability of nickel nanoferrites synthesized at different temperature (25, 50, 80 °C) using chemical co-precipitation method for the photodecomposition of methyl orange. Results showed that $NiFe_2O_4$ synthesized at 80 °C degraded 83% of the dye in 140 min of irradiation. Sharma et al. [67] have investigated the potential of four spinel nanoferrites (MFe_2O_4; M=Co, Cu, Ni, Zn) as photo-Fenton catalyst for the deterioration of different phenolic

compounds such as o/m/p-nitrophenol, o/m/p-chlorophenol, 2,4-dinitrop-henol, 2,4-dichlorophenol, and 2,4,6-trinitrophenol using two different inorganic oxidants, i.e., hydrogen peroxide (HP) and peroxymonosulfate (PMS). These ferrites possess high activity and remarkable stability for the removal of aforementioned organic pollutants thus proved to be promising materials for wastewater treatment. Ibrahim et al. [68] examined and compared the catalytic activity of spinel nanoferrites (MFe_2O_4; M = Co, Cu, Ni, Zn) for the reduction of nitroarenes. The results demonstrated that the reduction reaction followed pseudo first-order kinetics and best catalytic activity was exhibited by $MnFe_2O_4$ that revealed 100% conversion into the corresponding amino derivatives in 270 s.

3.1 Factors Affecting the Catalytic Activity of Spinel Nanoferrites

(i) **Cation Distribution**: The distribution and concentration of cations present at the tetrahedral and octahedral sites of the spinel lattice largely governs the structural, optical, electrical, and magnetic properties of nanostructured ferrites which significantly affects their catalytic activity. The surface sites contribute majorly to the catalytic activity and in spinel structure the octahedral sites are exposed to surface, while the tetrahedral sites are present in the bulk [69] as shown in Fig. 5. Also the metal ions in the octahedral sites are placed at comparatively larger distances providing sufficient room for the reactant molecules to interact freely. So the catalytic activity of spinel nanoferrites is greatly affected
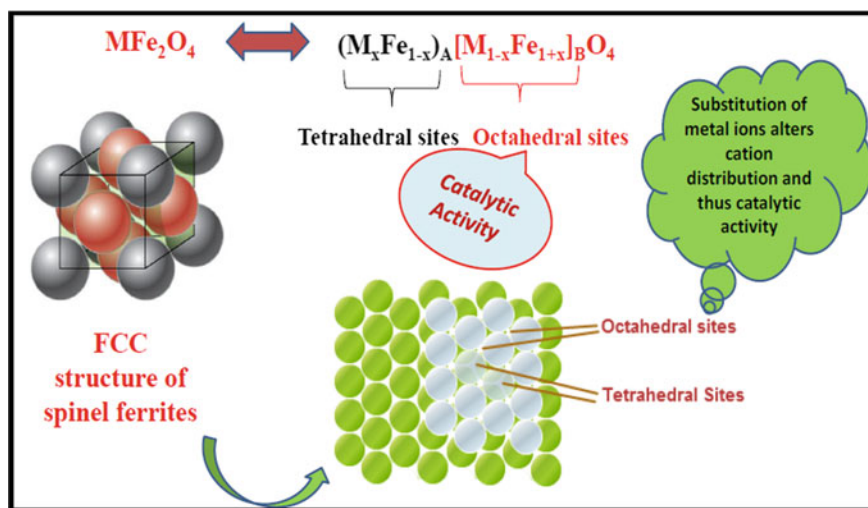
Fig. 5 Effect of cation distribution on catalytic activity in spinel nanoferrites

by the nature and the mutual synergistic interactions of the metal ions present in the catalytically active octahedral sites. The distribution of cations at different sites is influenced by various other factors such as ionic radii of metal ion, ionic charge, octahedral site preference energy, and crystal field stabilization energy. The preference order of some transition metal ions for octahedral site, based upon the above-discussed factors and as suggested by Miller is $Cr^{2+} > Ni^{2+} > Mn^{3+} > Al^{3+} > Fe^{2+} > Co^{2+} > Fe^{3+} > Mn^{2+}$ [70].

(ii) **Particle Size**: The particle size of spinel nanoferrites is another important parameter that determines their catalytic behavior. As the size of the particles decreases, an increase in the ratio of surface to bulk atoms is there as depicted in Fig. 6. It is well known that large surface areas of the nanocatalysts allow the increased exposure of the active sites leading to dramatic enhancement in the contact of reactants and catalyst and thereby enhancing the rate of the reaction [71]. The variation in the particle size of nanoferrites depends upon the method of synthesis as well as the annealing temperature, i.e., the heat treatment given to the sample. Various research cohorts have focused on this parameter and reported the effect of particle size on the catalytic performance of nanoferrites. Goyal et al. [72] have studied the effect of decreased particle size on the catalytic activity of Al substituted $NiFe_2O_4$ and $CoFe_2O_4$ for the reduction of nitrophenols. Kapoor et al. [73] reported drastic enhancement in the catalytic
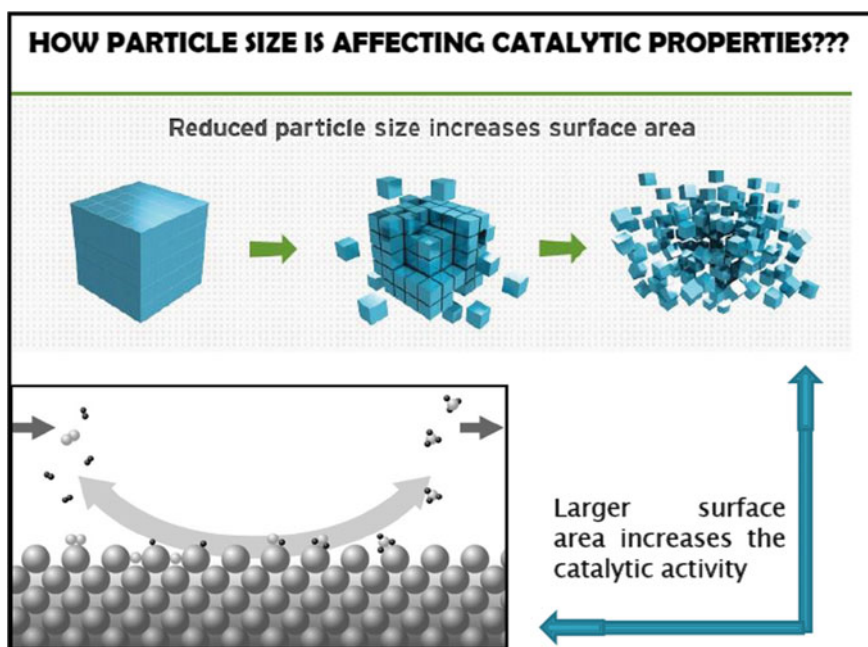
Fig. 6 Effect of particle size on the catalytic activity of spinel nanoferrites

activity of Bi doped cobalt ferrite for the oxidative degradation of organic dyes owing to their small crystallite size and octahedral site preference of Bi ions. Ziarati et al. [74] have reported high reactivity of Eu doped nickel nanoferrites for the synthesis of benzimidazole, benzoxazoles, and benzothiazoles on the basis of small grain size and high surface area. Singh et al. [75] have reported the enhanced catalytic activity of zinc ferrite nanoparticles in comparison with cobalt ferrite nanoparticles for the degradation of dyes and have correlated this increased catalytic activity with the smaller particle size of zinc ferrite nanoparticles.

(iii) **Particle Shape/Morphology**: Spinel nanoferrites with different shapes and morphology can be obtained by adopting different synthetic methodologies such as sol–gel auto combustion method [76], hydrothermal technique [77], co-precipitation method [78], and ball milling method [79]. Morphology control helps to enhance the surface features and local exchange interactions; thus, it is beneficial to synthesize multi-dimensional ferrite nanostructure, such as one-dimensional wires, rods, and fibers [80, 81], two-dimensional nanoflakes or nanoplatelets [82, 83], and three-dimensional nanospheres [84]. Tuning particle morphology is an important method to improve the catalytic property of nanoferrites. The effect of variable morphology on the catalytic activity of spinel nanoferrites has been presented in Fig. 7.

Dhiman et al. [85] successfully fabricated four different morphologies of $ZnFe_2O_4$ viz. nanoflowers, nanorods, microspheres, and nanoparticles and studied their
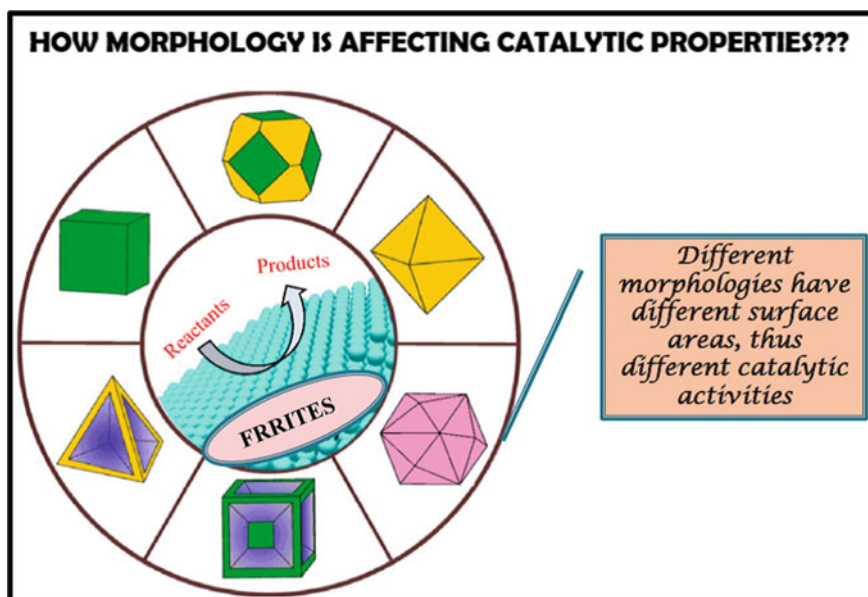
Fig. 7 Effect of variation in morphology of spinel nanoferrites on the catalytic properties

catalytic performance for the photo-oxidative degradation of toxic dyes—Safranin-O and Remazol brilliant yellow. The order of catalytic activity was found to be nanorods > nanoparticles > nanoflowers > microspheres. The maximum degradation efficiency of nanorods was attributed to greater surface area, greater band gap, and better delocalization of charged species along length of the rods. Wu et al. [86] studied the variation in morphology of cobalt ferrite from sphere to nanorods with increasing concentration of Pr and reveal the effect of particle morphology on the adsorption capacity of nanoferrites.

All the above-discussed factors, whether it is cation distribution, particle size, or particle morphology are mutually dependent on each other and modulate the physical and chemical properties of spinel nanoferrites, thus affecting their catalytic activity. Thus, extensive research has been devoted toward fabricating modified spinel nanoferrites with improved properties and utilizing them as efficient heterogeneous catalysts in a variety of water purification processes.

3.2 Possible Modifications in Spinel Nanoferrites

As already discussed above, pure spinel nanoferrites can be effectively used as catalysts for the treatment of contaminated wastewater, but despite being versatile catalysts they possess a limitation of being aggregated due to magnetic dipolar interactions which affects their catalytic activity. The nanoparticles tend to agglomerate which reduces their specific surface area and thus hinders the catalytic activity [87]. Thus, many scientists have been working effortlessly toward the modification of spinel nanoferrites in order to enhance their catalytic activity. The catalytic activity of pure nanoferrites can be enhanced by varying their physicochemical properties such as cation distribution, particle size, surface area, and morphology. Modification in ferrites can be done either by incorporating different metal/non-metal ions into the ferrite lattice, surface functionalization via ligand exchange reactions, polymer coating or silica coating, and heterojunction formation with various other semiconducting materials (CdS, ZnO, TiO_2, etc.).

These modifications in nanoferrites can be broadly classified into following three categories, which are further discussed in detail.

(i)   Substitution by different metal/non-metal ions
(ii) Composite formation with organic and inorganic moieties
(iii) Surface functionalization.

3.2.1 Substitution of Metal/non-Metal Ions at Different Sites

The substitution of different metal ions into the ferrite lattice results in the redistribution of cations into the tetrahedral and octahedral sites according to the respective site preferences of the substituted ions, thus affecting the catalytic property of nanoferrites. According to the basic structure of spinel ferrite, i.e., MFe_2O_4, substitution can

be done in two ways, i.e., the dopant metal ion either replaces the ions at iron site, i.e., substitution for 'Fe' or at the metal site, i.e., substitution for metal 'M'. The effect of doping on the catalytic properties of a photocatalyst depends on several factors such as fabrication method, type and concentration of dopant, and other physic-chemical properties of the catalyst. The substituted ion could belong to any block of the periodic table. Several research reports confirmed that substituted spinel nanoferrites based catalyst possesses great potential for enhancing visible-light-responsive photocatalytic activity. Thus, plethora of metals/non-metals has been explored as dopants for modifying the structural properties of spinel nanoferrites which eventually affects their photodegradation capacities against toxic environmental pollutants.

Lassoued et al. [88] reported the synthesis of Al substituted nickel ferrite ($NiAl_xFe_{2-x}O_4$; $x = 0.00, 0.05, 0.10$, and 0.15) and investigated the effect of substituting Al^{3+} on the structural, morphological, optical, and magnetic properties. The synthesized nanoferrite have been utilized for the degradation of methyl orange and the results showed that $NiAl_{0.15}Fe_{1.85}O_4$ sample exhibited the best photocatalytic activity owing to its lowest crystallite size and improved light harvesting capability. Dhiman et al. [89] fabricated solar-active Mg substituted Zn nanoferrites ($Zn_{1-x}Mg_xFe_2O_4$; $x = 0, 0.2, 0.4$) which worked efficiently as catalyst for the removal of sulfonamide drug, sulfadiazine. The dopant metal ion and oxygen vacancies facilitates electron flow and reduces the recombination rate of e^-/h^+ pairs thereby enhancing the catalytic activity, 99% sulfadiazine degradation was reported in 90 min. Co-doping of two or more heteroatoms into spinel nanoferrites have a synergistic effect on the band structures (conduction band and valence band) of the system that leads to modified morphological characteristics or improved photocatalytic redox ability and selectivity that enhances the visible light response behavior. Kirankumar and sumathi [90] studied the photocatalytic performance of copper and cerium co-doped cobalt ferrite nanoparticles for the removal of Congo red (CR) dye and Bisphenol A (BPA) from aqueous medium. They reported that co-doping of Cu^{2+} and Ce^{3+} showed marked effect on the structural, optical, magnetic, and photocatalytic activity. High removal rate of CR and BPA (99.09% and 99.33%) was observed within 30 min and 180 min using $Co_{0.5}Cu_{0.5}Fe_{1.95}Ce_{0.05}O_4$. Wang et al. [91] employed Ag doped $MnFe_2O_4$ as catalyst for the degradation of dibutyl phthalate by ozone treatment. Ag doped spinel nanoferrites exhibited enhanced catalytic performance due to reduced reduction potential and efficient cycling of electrons between Ag and Mn on the surface that leads to production of more hydroxyl radicals by ozone. Nair et al. [92] investigated the role of Cr substituted Zn ferrite nanocomposites for the catalytic abatement of 4-chlorophenol, 2, 4-dichlorophenol, and 2, 4-dichlorophenoxyacetic acid present in water. Doping of Cr increases the surface area and oxidizing power of zinc ferrite catalyst making it a good oxidation catalyst for the degradation of pollutants. Sharma et al. [93] reported the synthesis of yttrium-doped cobalt ferrite with composition $CoY_xFe_{2-x}O_4$ ($x = 0.0, 0.1, 0.2, 0.3$) by sol–gel method. Effect of Y^{3+} on the catalytic activity of cobalt ferrite was studied in the photo-Fenton degradation of RBY and RB5 dyes using two different oxidants (H_2O_2 and PMS) under visible light irradiation. Best catalytic results were obtained for $CoY_{0.2}Fe_{1.8}O_4$ ($x = 0.2$) and were attributed to the octahedral site preference,

reduced band gap, and high surface area as compared to pristine cobalt ferrite. Rashmi et al. [94] have reported the preparation of Sm^{3+} doped $MnFe_2O_4$ ($MnSm_xFe_{2-x}O_4$) nanoparticles via co-precipitation method, and the effect of doping on the photocatalytic activity was studied for the degradation of rose Bengal (RB) dye under sunlight irradiation. Maximum activity was observed for $MnFe_{0.5}Sm_{1.5}O_4$, which was attributed to its small particle size and efficient separation of charge carriers. From the above literature, it is clear that interesting and noteworthy enhancement in the catalytic performance of spinel nanoferrites can be achieved via substituting different metal ions at different lattice sites.

3.2.2 Composite Formation with Organic and Inorganic Moieties

Although pure spinel nanoferrites are promising photocatalysts, but due to inherent magnetic character, they tend to agglomerate which reduces their stability as well as the catalytic activity. Formation of composites or heterostructures of spinel nanoferrites using various organic or inorganic materials is one such approach that not only stabilizes them against aggregation but also improves their photostability by keeping the redox reactions at two different sites. Various C-based materials such as carbon nanotubes (CNTs), graphene, fullerenes, carbon dots, and semiconducting materials such as CdS, ZnS, ZnO, SiO_2, TiO_2, and Al_2O_3 have been widely explored to be coupled with nanoferrites for improved structural and catalytic properties as shown in Fig. 8. Such coupled systems promotes the seperation of photogenerated electron–hole pairs through different charge-transfer pathways and exhibit enhanced visible light photocatalytic activity. Also, the photocatalytic performance of these coupling systems is also related to the shape, size, and surface area of the heterostructure. Several studies have witnessed the efficiency and strong photocatalytic capacity of spinel ferrite nanocomposites for the removal of organic pollutants.

Naghshbandi et al. [95] studied the catalytic efficiency of graphene quantum dots/MFe_2O_4 (M=Ni, Co) nanocomposites for the reduction of 4-nitrophenol. $NiFe_2O_4$/GQD exhibited superior catalytic activity which could be due to several factors such as reduced band gap, particle size, morphology, and distribution of cations in the nanocomposite. Chen et al. [96] investigated the potential of $CoFe_2O_4$-graphene oxide as catalyst for the degradation of norfloxacin via oxone treatment. Graphene oxide possesses excellent adsorption capacity for organic compounds via $\pi-\pi$ interactions. Moreover, surface oxygen species at defective sites of GO played a critical role in the degradation process. Boutra et al. [97] successfully fabricated $MnFe_2O_4$/Tannic acid/ZnO nanocomposites for the photocatalytic degradation of Congo red dye.

The coupling of $MnFe_2O_4$ with ZnO and tannic acid facilitates charge transfer by reducing (e^-/h^+) recombination, enhances light absorption capability, and increases the amount of active sites for pollutant adsorption, thus boosting the photocatalytic performance of the nanocomposites for the elimination of organic pollutants. Nawaz et al. [98] incorporated multiwalled carbon nanotubes (MWCNTs) into $NiFe_2O_4$, and the photo-Fenton efficiency of the synthesized composite was assessed for
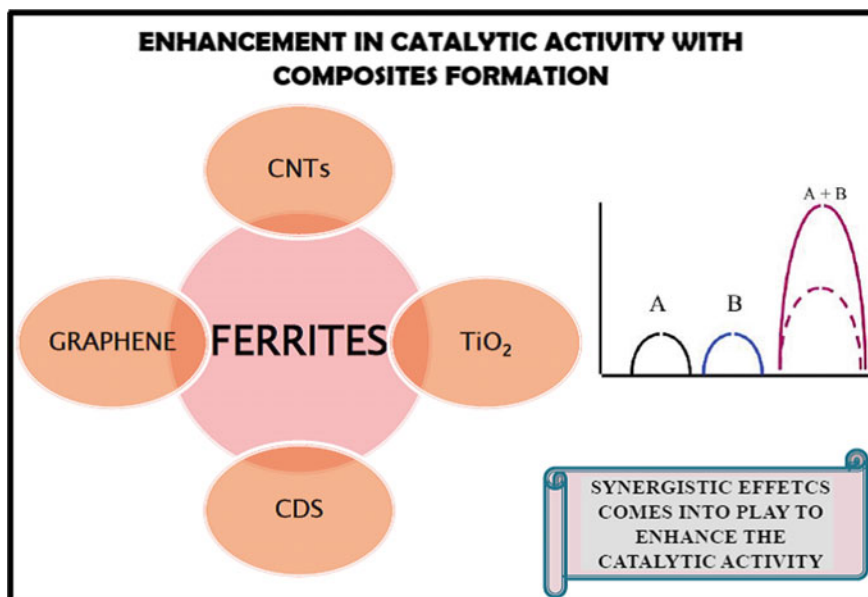
Fig. 8 Effect of composite formation on the catalytic activity of spinel nanoferrites

the degradation of sulfamethoxazole. MWCNTs possess high specific surface area, which retains the photogenerated charge carriers for longer time, thus exhibiting high photocatalytic performance by generating more hydroxyl radicals. Thus, the synergistic effect between $NiFe_2O_4$ and CNTs resulted in complete degradation of drug within 2 h using 25wt% CNT-$NiFe_2O_4$ composite. Farhadi and Siadatnasab [99] have reported the synthesis of cadmium sulfide-cobalt ferrite (CdS/CFO) nanocomposites by one-step hydrothermal decomposition of cadmium diethyldithiocarbamate complex on CoFe2O4 nanoparticles at 200 °C. The catalytic efficiency was evaluated for the degradation of MB, MO, and RhB dyes in the presence of H_2O_2 as oxidant. The nanocomposites exhibited excellent photoactivity as compare to pure CdS and $CoFe_2O4$ and degraded all three dyes in less than 10 min. Hassani et al. [100] have reported the synthesis of monodisperse $CoFe_2O_4$ nanoparticles composite with g-C_3N_4 via thermal decomposition method, and the synthesized nanocomposites were utilized for the photocatalytic degradation of MB, RhB, and acid orange 7 dyes under UV light irradiation. The photocatalytic performance of $CoFe_2O_4$/mpg-C_3N_4 nanocomposite was 1.2 times higher than that of pristine mpg-C_3N_4 and was attributed to the synergistic effect between mpg-C_3N_4 and $CoFe_2O_4$ nanoparticles which improved the separation of photogenerated e^-/h^+ pairs. Reports have also been available on the photocatalytic activity of the nanocomposites of pure ferrite with multiple heterojunctions. Li et al. [101] have reported the synthesis of Fe_2O_3/ZnO/$ZnFe_2O_4$ composites toward the photocatalytic degradation of RhB and MO dyes under visible light irradiation. The synthesized nanocomposites showed high photocatalytic activity toward the degradation of dye molecules. Sohail et al.

[102] have studied the photocatalytic activity of $TiO_2/CNTs@CoFe_2O_4$ nanocomposites toward the UV light-assisted degradation of MB dye. The nanocomposites exhibited high catalytic activity as compared with bare TiO_2. Thus, it has been very well established from the above studies that composites of spinel nanoferrites have some advantageous properties over pristine ferrites and are suitable to be used as photocatalyst for wastewater remediation.

3.3 Surface Functionalization

As already mentioned, pristine spinel nanoferrites tend to aggregate into large clusters and lose their distinctive properties linked to their single domains. Thus, different surface functionalization can be performed for ferrite nanoparticles to retain their nanoscale properties which improve the dispersability and stability of the ferrite nanostructures. These surface coatings can be inorganic metal oxides such as silica, alumina, and titania; organic moieties such as dopamine, cellulose, chitosan, and glutathione; polymers such as polyethylene glycol (PEG), polyvinyl alcohol (PVA), and polyvinyl pyrrolidone (PVP), which can be used as such or further functionalized with acidic or basic moieties. Also these can be used as sites for the immobilization of metal nanoparticles or other active catalysts to generate core–shell structures to be used as catalyst where synergy of each component contributes toward the catalytic performance. A variety of core–shell nanostructures having ferrites as cores have been synthesized by different research cohorts and widely utilized as photocatalyst for the removal of organic pollutants from wastewater.

Jiang et al. [103] studied the application of $MgFe_2O_4$/conjugated polyvinyl chloride (CPVC) nanocomposite as magnetically recoverable, high performance visible light catalyst for the treatment of Cr-VI polluted water. Conjugated polymers proved to be efficient modifiers for enhancing the photocatalytic activity of semiconducting materials like ferrites. They have band structures comparable to that of ferrites and possess outstanding visible light absorbing ability, thus producing additional charge carriers under visible light irradiation. The synthesized $MgFe_2O_4$/CPVC nanocomposite showed improved photocatalytic activity as compared to pristine ferrites for Cr VI reduction with good stability and facile recovery from the aqueous suspension. Tanwar et al. [104] reported the functionalization of Ni-Zn nanoferrites by cystamine ligand and studied their photocatalytic application for the degradation of Brilliant Blue G dye and Bisphenol A. The results conveyed that $Ni_{0.5}Zn_{0.5}Fe_2O_4$@cystamine exhibited superior catalytic activity as compared to bare ferrites. The cystamine functionalization not only prevents the agglomeration of Ni-Zn nanoferrites but also enhances the catalytic activity of the reaction by providing more adsorption and reaction sites. Singh et al. [105] fabricated the core–shell structure of silica-coated nanoferrites ($SiO_2@MFe_2O_4$;M=Zn, Co, Ni) through stobber's method. The effect of silica on the photocatalytic activity of nanoferrites was very well scrutinized using Rhodamine B dye as model pollutant. It was found that silica coating on nanoferrites imparts hydrophilicity due to the presence of Si-OH group on the
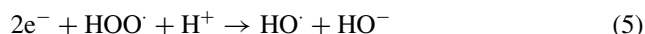
surface which improves their dispersibility. The dispersion stability of silica-coated nanocomposites plays significant role in the reactant transfer processes which makes them potential candidates for photocatalytic applications. Also, the thickness of silica shell significantly controls the photocatalytic behavior of nanoferrites. Malakootian et al. [106] reported the synthesis of $ZnFe_2O_4$@CMC nanobiocomposite as a new magnetic photocatalyst for the degradation of ciprofloxacin. Carboxymethyl cellulose carbohydrate (CMC), a derivative of cellulose, is an anionic biopolymer which plays an important role in improving the structural and catalytic properties of nanoferrites owing to its non-toxicity, optimal mechanical strength, and high adsorption capacity. The removal efficiency of $ZnFe_2O_4$@CMC was observed to be higher than $ZnFe_2O_4$ due to the synergistic effect of narrow band gap and larger surface area. Goyal et al. [107] synthesized transition metal functionalized core–shell nanostructures (M@Dop@CoFe; M=Cr, Mn, Fe, Co, Ni, Cu, Zn) having cobalt ferrite as core and dopamine as organic shell. The catalyst was explored for the activation of PMS for the oxidative degradation of nitrophenols. The hydroxyl groups present in dopamine enhances the activation of PMS and terminal amine groups facilitate the loading of different metal nanoparticles. Co@Dop@CoFe proved to be the most efficient catalytic system which degraded the organic pollutants within 2-3 min in which all the three components, i.e., the core, the shell, and functionalized transition metal, all assist synergistically to activate PMS for the degradation of nitrophenols. Bashir et al. [108] successfully synthesized a core–shell nanoferrite composite ($PANI/MgFe_2O_4$) and its hybrid composite with silica gel ($PANI/MgFe_2O_4/SiO_2$). Both the composites were studied as photocatalyst for the decontamination of water, and their catalytic activity was tested by evaluating their efficiency to photodegrade water-soluble carcinogenic indigo carmine dye in aqueous solution. The authors reported that the single-coated $PANI/MgFe_2O_4$ composite proved as efficient photocatalyst by presenting higher photodegradation percentage (97.52%) as compared to hybrid nanoferrite composites (94.36%).

4 Proposed Pathway for Degradation of Pollutants Using Spinel Nanoferrites

Before discussing the detailed mechanism for the photodegradation of organic pollutants, some salient features of visible-light-responsive photocatalytic system need to be focused on. First is the band gap or the optical properties of the system which determines the visible light absorbing ability of the photocatalyst. The band gap of the system needs to be in the visible range, for the photons to be excited upon visible light irradiation. The second important feature is the crystallinity of the sample; highly crystalline nanoferrites possess less crystalline defects, which would be beneficial for reducing the recombination rate of photogenerated charge carriers (electrons and holes). Surface area of nanoferrites is another significant factor that effects the chemical reactions taking place on the surface of catalyst such as oxidation by holes and

reduction by electrons. In general, the visible-light-activated photocatalytic system should consist of a light harvesting antenna and other active species that induce the degradation of pollutants.

When irradiated with light (hν), spinel nanoferrites generate electron–hole pairs (e^-/h^+), due to photoexcitation of electron from valence band (VB) to conduction band (CB) leaving hole behind. These e^-/h^+ pairs could easily move to the surface of catalyst and initiate redox reactions. The chain reactions occurring on the surface of the catalyst and in aqueous medium are in accordance with Eqs. (1–5).

$$Ferrites + hv \rightarrow e^- + h^+ \tag{1}$$

$$h^+ + H_2O \rightarrow H^+ + HO^{\cdot} \tag{2}$$

$$h^+ + HO^- \rightarrow HO^{\cdot} \tag{3}$$

$$e^- + O_2 \rightarrow HOO^{\cdot} \tag{4}$$

$$2e^- + HOO^{\cdot} + H^+ \rightarrow HO^{\cdot} + HO^- \tag{5}$$

The photocatalytic degradation of pollutants involves three main active species: a hydroxyl radical ($^{\cdot}OH$), photogenerated holes (h^+), and a superoxide radical ($^{\cdot}O_2^-$).The photogenerated hole (h^+) reacts with water and hydroxide ion (HO^-) to generate $HO^{\cdot}$. Also, the electron (e^-) in conduction band reacts with dissolved oxygen to create superoxide radical anion (O_2^-) which combines with H^+ to produce $HOO^{\cdot}$ and finally decomposes to $HO^{\cdot}$. Hydroxyl radical acts as primary oxidant for the oxidation of organic pollutants.

$$HO^{\cdot} + Organic\ pollutant \rightarrow removal\ intermediates \rightarrow CO_2 + H_2O$$

5 Use of Magnetic Spinel Ferrites as Photo-Fenton Catalyst Using Diverse Oxidants

Apart from the photo-energy-driven photocatalysis of spinel nanoferrites and their capability to generate reactive oxygen species, various research groups have taken an initiative to further increase the catalytic activity of the MFe_2O_4 using different oxidizing agents such as hydrogen peroxide (HP), potassium peroxymonosulfate (PMS), potassium bromate (PB), and potassium peroxodisulfate (PDS). The reactive species produced for degradation of organic pollutants depend on type of oxidizing agent used. Addition of oxidizing agents significantly enhance the generation of

active oxygen-containing species by converting it into photo-Fenton type system, where Fe^{2+} or M^{2+} ions of spinel nanoferrite reacts with the oxidizing agent using the cyclic electron transfer mechanism as detailed below.

(i) **Hydrogen Peroxide (HP) as oxidant**

Hydrogen peroxide is the most widely used inorganic oxidant in Fenton's process for degradation of wide range of organic contaminants at ambient temperature and pressure. According to Haber and Weiss [109], the key active species generated while activation of HP using spinel nanoferrites are the free radicals (OH· and HOO·), and the generalized equation of Fenton's process in presence of HP is given below:

$$M^{n+} + H_2O_2 \rightarrow M^{(n+1)+} + HO^{\cdot} + HO^{-} \quad (M = Fe, Mn, Cu, Co \, etc.) \quad (6)$$

Entire mechanism along with the reaction rates (k) as reported in literature is outlined below [110]:

$$Fe^{2+} + H_2O_2 \rightarrow Fe^{3+} + {}^-OH + \cdot OH \quad k_1 = 51 \; mol^{-1}s^{-1} \quad (7)$$

Equation 7 is known as Fenton's reaction and indicates the oxidation of Fe^{2+} to Fe^{3+} to dissociate H_2O_2 to (·OH). This equation is generally reflected as the basic of Fenton's chemistry.

To understand the whole process, other reactions should also be studied. The Fe^{3+} ions generated in Eq. 7 can undergo reaction with H_2O_2 to again form Fe^{2+} and radical species, thus leading to a cyclic mechanism.

$$Fe^{3+} + H_2O_2 \rightarrow Fe^{2+} + \cdot OOH + H^+ \quad k_2 = 2 \times 10^{-3} \; mol^{-1} \; s^{-1} \quad (8)$$

$$Fe^{2+} + \cdot OH \rightarrow Fe^{3+} + {}^-OH \quad k_3 = 3.2 \times 10^8 \; mol^{-1} \; s^{-1} \quad (9)$$

$$Fe^{2+} + \cdot OOH \rightarrow Fe^{3+} + {}^-OOH \quad k_4 = 1.3 \times 10^6 \; mol^{-1} \; s^{-1} \quad (10)$$

$$Fe^{3+} + \cdot OOH \rightarrow Fe^{2+} + O_2 + H^+ \quad k_5 = 7.8 \times 10^5 \; mol^{-1} \; s^{-1} \quad (11)$$
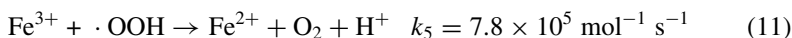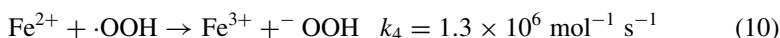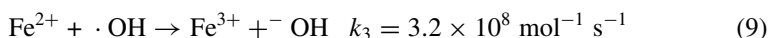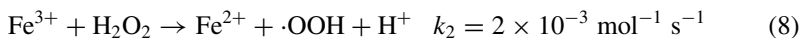
Equations (8) to (11) are the rate limiting steps as H_2O_2 is being consumed in the reactions and cyclic process of conversion of Fe^{3+} to Fe^{2+} is taking place. The hydroperoxyl radicals (·OOH) thus produced may also attack the organic contaminants but are less reactive in comparison with ·OH. This reaction is known as Fenton's like reaction, and its rate of reaction is slower than Fenton's reaction (Eq. 7).

$$\cdot OH + \cdot OH \rightarrow H_2O_2 \quad k_6 = 5.2 \times 10^9 \; mol^{-1} \; s^{-1} \quad (12)$$

$$\cdot OH + H_2O_2 \rightarrow \cdot OOH + H_2O \quad k_7 = 3.3 \times 10^7 \; mol^{-1} \; s^{-1} \quad (13)$$

$$\cdot OOH + \cdot OOH \rightarrow H_2O_2 + O_2 \quad k_8 = 2.3 \times 10^6 \ mol^{-1} \ s^{-1} \tag{14}$$

$$\cdot OH + \cdot OOH \rightarrow H_2O + O_2 \quad k_9 = 7.1 \times 10^9 \ mol^{-1} \ s^{-1} \tag{15}$$
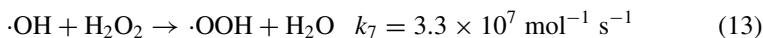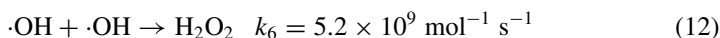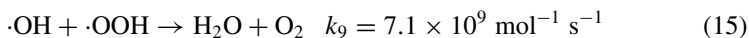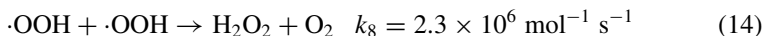
Equations (12)–(15) show the radical–radical reactions and H_2O_2-radical reactions. All the equations from (7) to (15) imply toward the complexity of Fenton's process. The production of anticipated ·OH takes place through a chain reaction. But the generated ·OH can undergo scavenging by Fe^{2+} ions (Eq. 9), H_2O_2 (Eq. 13), OOH radicals (Eq. 15) or may even undergo auto-scavenging (Eq. 12).

$$\cdot OH + R - H \rightarrow H_2O + R \cdot \quad k_{10} = > 10^8 - 10^9 \ mol^{-1} \ s^{-1} \tag{16}$$
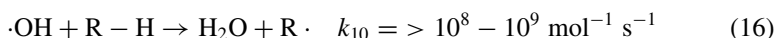
The ·OH thus generated can react with the organic compounds (represented as R-H) present in wastewater leading to their mineralization into simpler compounds (Eq. 16). The mechanistic pathway for the degradation of organic pollutants using spinel nanoferrites is given as Fig. 9.

The mechanism clearly indicates that the mixture of Fe^{2+} and H_2O_2 promotes initiation of a series of chain reactions leading to generation of free radicals which are responsible for degradation of organic substrates. Various research cohorts have directed their interest in utilizing spinel nanoferrites along with H_2O_2 as an oxidant for the treatment of recalcitrant organic pollutants. Li et al. [111] successfully synthesized metal-doped $ZnFe_2O_4$ from metal-rich industrial waste (pickling waste
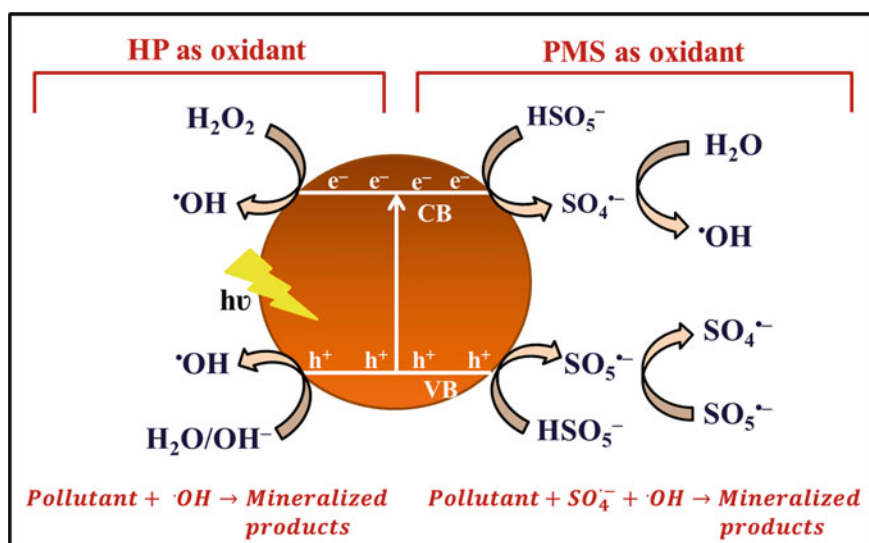
Fig. 9 Mechanism of oxidation of pollutants in the presence of spinel nanoferrites as catalyst and HP or PMS as oxidant under light irradiation

liquor and electroplating wastewater) and pure $ZnFe_2O_4$ from chemical reagents via microwave-assisted hydrothermal method. The catalytic activity was evaluated for the degradation of Congo red (CR) dye. The authors observed best catalytic performance at pH 6 with 0.8 g/L catalyst dosage in presence of 0.1 M H_2O_2. The reason behind the degradation was studied, and it was due to the generation of $OH^{\bullet}$ radicals due to photogenerated charge carriers and H_2O_2 oxidation via metal ions present on the catalyst surface. Hassani et al. [112] employed $CoFe_2O_4$-rGO nanocomposites for the elimination of organic dyes under ultrasonic irradiation. Out of four different studied dyes, the nanocomposites were found to be effective for the removal of AO7 dye. The removal efficiency was found to be 90.5% in 120 min of reaction time at pH 3, 3 mM H_2O_2, 0.08 g/L catalyst dosage, and 10 mg/L AO7 dye concentration. The mechanistic study suggested that superoxide anion radicals were the major reactive oxygen species in the sonocatalytic degradation process for the removal of AO7 dye.

Yao et al. [113] synthesized $CuFe_2O_4@C_3N_4$ core–shell photocatalysts for the degradation of Orange II dye in the presence of H_2O_2 under visible light. The degradation studies revealed that $CuFe_2O_4@C_3N_4$ (mass ratio: 2@1) exhibited enhanced catalytic activity in comparison with pure counterparts, i.e., $CuFe_2O_4$ and g-C_3N_4, as well as to the mixture of $CuFe_2O_4$ and g-C_3N_4. Dhiman et al. [114] reported the synthesis of rare earth metal (RE)-doped cobalt ferrite nanoparticles. The synthesized nanoparticles were utilized for the degradation of both anionic and cationic dyes in the presence of H_2O_2. The authors observed enhanced photocatalytic activity for rare-earth-doped cobalt ferrite in comparison with pure cobalt ferrite nanoparticles. Sundararanjan et al. [115] synthesized zinc-doped cobalt ferrite, $Co_{1-x}Zn_xFe_2O_4$ (where $0 \leq x \leq 0.5$) via microwave combustion method. The synthesized samples were used as catalyst for the photocatalytic degradation of rhodamine B (RhB) dye at optimized conditions of pH 2 and 6 mg/L initial dye concentration in presence of H_2O_2. It was observed that among all the synthesized doped samples, $Co_{0.6}Zn_{0.4}Fe_2O_4$ exhibited best catalytic efficiency and degraded 99.9% of dye within 210 min of light exposure.

(i) **Sulfate radical-based oxidants**

The conventional Fenton oxidants generate hydroxyl radicals as the only foremost reactive species and exhibit higher effectiveness in acidic conditions. Thus, it is highly desired to use such an oxidant in Fenton's process which can work at neutral pH. Apart from $\cdot OH$, sulfate radical ($SO_4^{\cdot-}$) is also a very strong oxidant that can degrade organic contaminants. Hence, the use of sulfate radical-based advanced oxidation processes (SR-AOPs) for chemical mineralization of different organic pollutants is being explored by researchers nowadays.

Among all the sulfate radical-based oxidants, **peroxymonosulfate** salts have been extensively chosen for oxidation of environmental contaminants owing to their application at broader pH range and production of greater number of reactive oxygen species such as superoxide anion radical, hydroxyl radical, sulfate radical, and singlet oxygen. PMS is commercially available in the form of a versatile and environmentally benign triple salt named oxone ($2KHSO_5.KHSO_4.K_2SO_4$). For the production of reactive sulfate radicals, PMS can be activated by means of distinct routes such as

thermal activation, light irradiation, ultrasound, and with the help of metals catalysts [116–118]. Literature encompasses a variety of reports where spinel nanoferrites have been exploited for the activation of PMS. Porous $CuFe_2O_4$ was used by Guan et al. [119] to activate PMS for the degradation of atrazine. The authors observed 98% of atrazine removal within 15 min at 1 mM PMS and 0.1 g/L $CuFe_2O_4$. Ding et al. [120] prepared $CuFe_2O_4$ nanoparticles using sol–gel combustion method and characterized it using diverse techniques. The magnetic catalyst effectively catalyzed PMS to generate SO_4^- for the degradation of tetrabromobisphenol A. The pollutant (10 mg/L) was completely degraded in 30 min when 0.2 mmol/L PMS and 0.1 g/L $CuFe_2O_4$ were used as oxidant and catalyst, respectively. Substantially high activity was ascribed to activation of PMS by both Cu(II) and Fe (III) in $CuFe_2O_4$. Another spinel ferrite tested by researchers for PMS activation is $CoFe_2O_4$. Deng et al. [121] used magnetic nanoscale $CoFe_2O_4$ for degradation of dichlofenac. The authors studied the effect of varying calcination temperature, initial pH, catalyst, and PMS dosage on degradation process. The obtained results demonstrated $CoFe_2O_4$ annealed at 300 °C exhibited best catalytic performance as complete dichlofenac was degraded within 15 min. $MnFe_2O_4$ has been recently used by Pang and Lei [122] for PMS activation. The authors prepared the catalyst by co-precipitation method and evaluated the degradation of p-nitrophenol under varying conditions. The authors used microwave (MW) radiations for enhancing catalytic activity, and observed 97.2% of nitrophenol was degraded within 2 min using PMS/$MnFe_2O_4$/MW. Ren et al. [123] prepared magnetic ferrospinel MFe_2O_4 (M =Co, Cu, Mn and Zn) by sol–gel process and used it as catalyst for di-n butyl phthalate (DBP) degradation in water. The sequence of catalytic effect for degradation process followed the order $CoFe_2O_4 > CuFe_2O_4 > MnFe_2O_4 > ZnFe_2O_4$.

The chemical reactions occurring during PMS activation via metal ions present at the catalytically active octahedral sites of spinel nanoferrites are as follows:
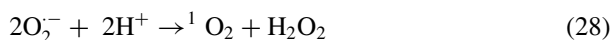
$$Fe^{2+} + HSO_5^- \rightarrow Fe^{3+} + SO_4^- + HO^- \tag{17}$$

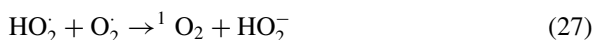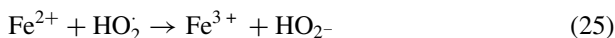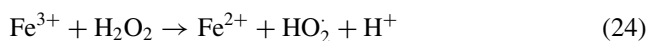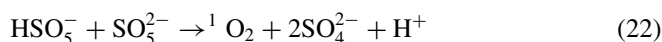$$Fe^{3+} + HSO_5^- \rightarrow Fe^{2+} + SO_5^{\cdot-} + H^+ \tag{18}$$
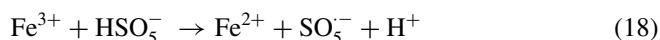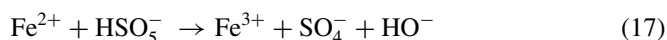
When the oxidative degradation takes place via PMS activation, the active species is $SO_4{}^{\cdot-}$, which then reacts with water (H_2O) and generates hydroxyl radicals (HO$^\cdot$) as illustrated below:

$$SO_4^{\cdot-} + H_2O \rightarrow HO^\cdot + SO_4^{2-} + H^+ \tag{19}$$
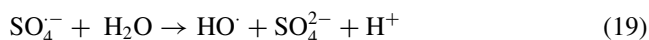
The $SO_5{}^{\cdot-}$ radical so generated reacts with water (H_2O) and leads to the production of singlet oxygen ($^1O_2$) as given:

$$2SO_5^{\cdot-} + H_2O \rightarrow 1.5\,{}^1O_2 + 2HSO_4^- \tag{20}$$
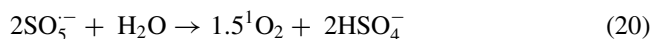
The various other reactions occurring sideways are given below.

$$HSO_5^- \rightarrow SO_5^{2-} + H^+ \tag{21}$$

$$HSO_5^- + SO_5^{2-} \rightarrow\, ^1O_2 + 2SO_4^{2-} + H^+ \tag{22}$$

$$HSO_5^- + H_2O \rightarrow H_2O_2 + HSO_4^- \tag{23}$$

$$Fe^{3+} + H_2O_2 \rightarrow Fe^{2+} + HO_2^{\cdot} + H^+ \tag{24}$$

$$Fe^{2+} + HO_2^{\cdot} \rightarrow Fe^{3+} + HO_{2^-} \tag{25}$$

$$HO_2^{\cdot} \rightarrow O_2^{\cdot} + H^+ \tag{26}$$

$$HO_2^{\cdot} + O_2^{\cdot} \rightarrow\, ^1O_2 + HO_2^- \tag{27}$$

$$2O_2^{\cdot-} + 2H^+ \rightarrow\, ^1O_2 + H_2O_2 \tag{28}$$

The produced $SO_4^{\cdot-}$, $O_2^{\cdot}$, and $^1O_2$ are the primary active radicals which aid in the oxidative degradation of noxious pollutants.

Besides PMS, potassium peroxodisulfate (PDS, $K_2S_2O_8$) and persulfate ($S_2O_8^{2-}$) are the alternative SR-AOPs that have recently been examined by researchers in context of their activation by spinel nanoferrites for the degradation of various pollutants [124–126].

6 Conclusion and Future Perspective

Recent years have witnessed a drastic upsurge in the environmental pollution levels as a result of flourishing urbanization and industrialization. In this regard, nano-ferrites are gaining immense global momentum and are presenting enormous path-ways to revolutionize environmental remediation due to their remarkable features. In this chapter, we have comprehensively detailed the current progress in nanofer-rites as catalysts for the degradation of distinct environmental pollutants, specifically focusing on organic pollutants. The fundamentals of photodegradation using ferrites, the effect of structural modifications, and the regulatory mechanism of pollutant degradation have been discussed in detail. To extend the photocatalytic response of nanoferrites, a variety of routes such as doping, exploring novel nanocomposites of ferrites with organic/inorganic moieties, changes in morphology, etc., have been adopted by various research cohorts. Such modifications prove to be beneficial in terms of ease of degradation of variety of pollutants in lesser time. The magneti-cally recoverable nature of the nanoferrites is their inherent advantage. Therefore,

nanoferrites offer a significant promise for further growth of sustainable and environmentally affable nanomaterials to ensure future environment safety. A brighter prospect for environmental detoxification is anticipated through the integration of multi-technology features using nanoferrites as the base for developing plenty of magnetically separable nanostructures.

References

1. Verma R, Vinoda KS, Papireddy M, Gowda ANS (2016) Toxic pollutants from plastic waste—a review. Procedia Environ Sci 35:701–708
2. Thomaidi VS, Stasinakis AS, Borova VL, Thomaidis NS (2015) Is there a risk for the aquatic environment due to the existence of emerging organic contaminants in treated domestic wastewater? Greece as a case-study. J Hazard Mater 283:740–747
3. Rivera MB, Giraldez MI, Fernandez-Caliani JC (2016) Assessing the environmental availability of heavy metals in geogenically contaminated soils of the Sierra de Aracena Natural Park (SW Spain). Is there a health risk? Sci Total Environ 560:254–265
4. Ramazani A, Oveisi M, Sheikhi M, Gouranlou F, Hanifehpour Y, Joo SW, Aghahosseini H (2018) A review on the destruction of environmentally hazardous chlorinated aromatic compounds in the presence (or without) of nanophotocatalysts. Curr Org Chem 22:1554–1572
5. Bilal M, Iqbal HM, Barcelo D (2019) Persistence of pesticides-based contaminants in the environment and their effective degradation using laccase-assisted biocatalytic systems. Sci Total Environ 695:133896
6. Jones OAH, Voulvoulis N, Lester JN (2005) Human pharmaceuticals in wastewater treatment processes. Crit Rev Env Sci Tec 35:401–427
7. Robinson T, McMullan G, Marchant R, Nigam P (2001) Remediation of dyes in textile effluent: a critical review on current treatment technologies with a proposed alternative. Bioresour Technol 77:247–255
8. Wang Q, Kim D, Dionysiou DD, Sorial GA, Timberlake D (2004) Sources and remediation for mercury contamination in aquatic systems—a literature review. Environ Pollut 131:323–336
9. McIsaac G (2003) Surface water pollution by nitrogen fertilizers. Encycl Water Sci 950
10. Burek P, Satoh Y, Fischer G, Kahil MT, Scherzer, A, Tramberend S, Nava LF, Wada Y, Eisner S, Florke M, Hanasaki N, Magnuszewski P, Cosgrove B, Wiberg D (2016) The water futures and solutions initiative of IIASA. 23–26. http://pure.iiasa.ac.at/id/eprint/13872/1/Proceedings_extended_abstract_IDRiM%202016%2032.pdf
11. https://www.weforum.org/agenda/2019/10/water-pollution-in-india-data-tech-solution/
12. https://www.globewater.org/facts/water-pollution-statistics/
13. Bakir A, Rowland SJ, Thompson RC (2014) Enhanced desorption of persistent organic pollutants from microplastics under simulated physiological conditions. Environ Pollut 185:16–23
14. https://scetcivil.weebly.com/uploads/5/3/9/5/5395830/m8_l10
15. Konstantinou IK, Albanis TA (2004) TiO$_2$-assisted photocatalytic degradation of azo dyes in aqueous solution: kinetic and mechanistic investigations: a review. Appl Catal B-Environ 49:1–14
16. Padhi BS (2012) Pollution due to synthetic dyes toxicity & carcinogenicity studies and remediation. Int J of Environ Sci 3:940–955

17. Sharma S, Basu S (2020) Highly reusable visible light active hierarchical porous WO_3/SiO_2 monolith in centimeter length scale for enhanced photocatalytic degradation of toxic pollutants. Sep Purif Technol 231:115916

18. Guleria A, Kumari G, Lima EC (2020) Cellulose-g-poly-(acrylamide-co-acrylic acid) polymeric bioadsorbent for the removal of toxic inorganic pollutants from wastewaters. Carbohydr Polym 228:115396

19. Kumar AKR, Saikia K, Neeraj G, Cabana H, Kumar VV (2020) Remediation of bio-refinery wastewater containing organic and inorganic toxic pollutants by adsorption onto chitosan-based magnetic nanosorbent. Water Qual Res J 55:36–51

20. Ali N, Ali F, Sheikh ZA, Bilal M, Ahmad I (2020) Photocatalytic performance of Zinc Ferrite Magnetic nanostructures for efficient eriochrome black-T degradation from the aqueous environment under unfiltered sunlight. Water Air Soil Poll 231:59

21. Ren J, Wang X, Wang C, Gong P, Wang X, Yao T (2017) Biomagnification of persistent organic pollutants along a high-altitude aquatic food chain in the Tibetan Plateau: processes and mechanisms. Environ Pollut 220:636–643

22. Paris F, Jeandel C, Servant N, Sultan C (2006) Increased serum estrogenic bioactivity in three male newborns with ambiguous genitalia: a potential consequence of prenatal exposure to environmental endocrine disruptors. Environ Res 100:39–43

23. Zuccato E, Calamari D, Natangelo M, Fanelli R (2000) Presence of therapeutic drugs in the environment. Lancet 355:1789–1790

24. Li QQ, Loganath A, Chong YS, Tan J, Obbard JP (2006) Persistent organic pollutants and adverse health effects in humans. J Toxicol Env Heal A 69:1987–2005

25. Akpan UG, Hameed BH (2009) Parameters affecting the photocatalytic degradation of dyes using TiO_2-based photocatalysts: a review. J Hazard Mater 170:520–529

26. Ziajahromi S, Neale PA, Rintoul L, Leusch FD (2017) Wastewater treatment plants as a pathway for microplastics: development of a new approach to sample wastewater-based microplastics. Water Res 112:93–99

27. Verma AK, Dash R, Bhunia P (2012) A review on chemical coagulation/flocculation technologies for removal of color from textile wastewaters. J Environ Manage 93:154–168

28. Huang H, Schwab K, Jacangelo JG (2009) Pretreatment for low pressure membranes in water treatment: a review. Environ Sci Technol 43:3011–3019

29. Belaid KD, Kacha S, Kameche M, Derriche Z (2013) Adsorption kinetics of some textile dyes onto granular activated carbon. J Environ Chem Eng 1:496–503

30. Njoku VO, Foo KY, Asif M, Hameed BH (2014) Preparation of activated carbons from rambutan (Nephelium lappaceum) peel by microwave-induced KOH activation for acid yellow 17 dye adsorption. Chem Eng J 250:198–204

31. Junghanns C, Krauss G, Schlosser D (2008) Potential of aquatic fungi derived from diverse freshwater environments to decolourise synthetic azo and anthraquinone dyes. Bioresour Technol 99:1225–1235

32. Chen H, Hopper SL, Cerniglia CE (2005) Biochemical and molecular characterization of an azoreductase from Staphylococcus aureus, a tetrameric NADPH-dependent flavoprotein. Microbiology 151:1433–1441

33. Taweel YAE, Nassef EM, Elkheriany I, Sayed D (2015) Removal of Cr (VI) ions from waste water by electrocoagulation using iron electrode. Egypt J Pet 24:183–192

34. Khelifa A, Aoudj S, Moulay S, Wery MDP (2013) A one-step electrochlorination/electroflotation process for the treatment of heavy metals wastewater in presence of EDTA. Chem Eng Process 70:110–116

35. Barrios JA, Becerril E, Leon CD, Barrera-Diaz C, Jimenez B (2015) Electrooxidation treatment for removal of emerging pollutants in wastewater sludge. Fuel 149:26–33

36. Koparal AS, Ouguteven UB (2002) Removal of nitrate from water by electroreduction and electrocoagulation. J Hazard Mater 89:83–94

37. Mook WT, Aroua MK, Issabayeva G (2014) Prospective applications of renewable energy based electrochemical systems in wastewater treatment: a review. Renew Sust Energ Rev 38:36–46

38. Sanches S, Leitao C, Penetra A, Cardoso VV, Ferreira E, Benoliel MJ, Crespo MTB, Pereira VJ (2011) Direct photolysis of polycyclic aromatic hydrocarbons in drinking water sources. J Hazard Mater 192:1458–1465

39. Xing S, Lu X, Liu J, Zhu L, Ma Z, Wu Y (2016) Catalytic ozonation of sulfosalicylic acid over manganese oxide supported on mesoporous ceria. Chemosphere 144:7–12

40. Monteros AE, Lafaye G, Cervantes A, Angel GD, Barbier J Jr, Torres G (2015) Catalytic wet air oxidation of phenol over metal catalyst (Ru, Pt) supported on TiO_2–CeO_2 oxides. Catal Today 258:564–569

41. He Y, Sutton NB, Rijnaarts HHH, Langenhoff AAM (2016) Degradation of pharmaceuticals in wastewater using immobilized TiO_2 photocatalysis under simulated solar irradiation. Appl Catal B-Environ 182:132–141

42. Kakavandia B, Takdastan A, Jaafarzadeh N, Azizi M, Mirzaei A, Azari A (2016) Application of Fe_3O_4@C catalyzing heterogeneous UV-Fenton system for tetracycline removal with a focus on optimization by a response surface method. J Photochem Photobiol A Chem 314:178–188

43. Domeno C, Rodríguez-Lafuente A, Martos J, Bilbao R, Nerin C (2010) VOC removal and deodorization of effluent gases from an industrial plant by photo-oxidation, chemical oxidation, and ozonization. Environ Sci Technol 44:2585–2591

44. Toki T, Nakamura K, Kurauchi M, Kanno T, Katsuda Y, Ikai H, Hayashi E, Egusa H, Sasaki K, Niwano Y (2015) Synergistic interaction between wavelength of light and concentration of H_2O_2 in bactericidal activity of photolysis of H_2O_2. J Biosci Bioeng 119:358–362

45. Ebrahiem EE, Al-Maghrabi MN, Mobarki AR (2017) Removal of organic pollutants from industrial wastewater by applying photo-Fenton oxidation technology. Arab J Chem 10:S1674–S1679

46. Lu AH, Salabas EE, Schuth F (2007) Magnetic nanoparticles: synthesis, protection, functionalization, and application. Angew Chem Int Ed 46:1222–1244

47. Yoon TJ, Lee W, Oh YS, Lee JK (2003) Magnetic nanoparticles as a catalyst vehicle for simple and easy recycling. New J Chem 27:227–229

48. Al-Nesraway SH, Al-Maamori MH, Al-Issawe JM (2018) Preparation of a rubber nanocomposite (silicone rubber-ferrite) for protect human from bioeffects of microwave emitted from mobile devices. J Bionanosci 12:645–651

49. Velinov N, Koleva K, Tsoncheva T, Paneva D, Manova E, Tenchev K, Kunev B, Genova I, Mitov I (2014) Copper-cobalt ferrites as catalysts for methanol decomposition. Open Chem 12:250–259

50. Reddy DHK, Yun YS (2016) Spinel ferrite magnetic adsorbents: alternative future materials for water purification? Coord Chem 315:90–111

51. Ghodake UR, Chaudhari ND, Kambale RC, Patil JY, Suryavanshi SS (2016) Effect of Mn^{2+} substitution on structural, magnetic, electric and dielectric properties of Mg–Zn ferrites. J Magn Magn Mater 407:60–68

52. Birgani AN, Niyaifar M, Hasanpour A (2015) Study of cation distribution of spinel zinc nano-ferrite by X-ray. J Magn Magn Mater 374:179–181

53. Streckova M, Hadraba H, Bures R, Faberova M, Roupcova P, Kubena I, Medvecky L, Girman V, Kollar P, Fuzer J, Cizmar E (2015) Chemical synthesis of nickel ferrite spinel designed as an insulating bilayer coating on ferromagnetic particles. Surf Coat 270:66–76

54. Zhang XY, Xu J, Li ZZ, Qi WH, Tang GD, Shang ZF, Ji DH, Lang LL (2014) Experimental evidence for the magnetic moment directions of Cr^{2+} and Cr^{3+} cations in the spinel ferrites $Cu_{x1}Cr_{x2}Fe_{3-x1-x2}O_4$.Physica B Condens Matter 446:92–99

55. Harris VG, Geiler A, Chen Y, Yoon SD, Wu M, Yang A, Chen Z, He P, Parimi PV, Zuo X, Patton CE (2009) Recent advances in processing and applications of microwave ferrites. J Magn Magn Mater 321:2035–2047

56. Mathew DS, Juang RS (2007) An overview of the structure and magnetism of spinel ferrite nanoparticles and their synthesis in microemulsions. Chem Eng J 129:51–65

57. Valenzuela R (2012) Novel applications of ferrites. Phys Res Int. http://doi.org/10.1155/2012/591839

58. Yafet Y, Kittel C (1952) Antiferromagnetic arrangements in ferrites. Phys Rev 87:290
59. Munir A, Ahmed F, Saqib M, Anis-ur-Rehman M (2016) Partial correlation of electrical and magnetic properties of Nd substituted Ni–Zn nanoferrites. J Magn Magn Mater 397:188–197
60. Sano N, Yamada K, Tsunauchi S, Tamon H (2017) A novel solid base catalyst for transesterification of triglycerides toward biodiesel production: carbon nanohorn dispersed with calcium ferrite. Chem Eng J 307:135–142
61. Kiyokawa T, Ikenaga N (2017) Oxidative dehydrogenation of but-1-ene with lattice oxygen in ferrite catalysts. Appl Catal A-Gen 536:97–103
62. Al-Sabagh AM, Yehia FZ, Eshaq G, ElMetwally AE (2017) Eclectic hydroxylation of benzene to phenol using ferrites of Fe and Zn as durable and magnetically retrievable catalysts. ACS Sustain Chem Eng 5:4811–4819
63. Karim KMR, Ong HR, Abdullah H, Yousuf A, Cheng CK, Khan MMR (2018) Photoelectrochemical reduction of carbon dioxide to methanol on p-type $CuFe_2O_4$ under visible light irradiation. Int J Hydrogen Energ 43:18185–18193
64. Dey C, De D, Nandi M, Goswami MM (2020) A high performance recyclable magnetic $CuFe_2O_4$ nanocatalyst for facile reduction of 4-nitrophenol. Mater Chem Phys 242:122237.
65. Taghavi Fardood S, Moradnia F, Mostafaei M, Afshari Z, Faramarzi V, Ganjkhanlu S (2019) Biosynthesis of $MgFe_2O_4$ magnetic nanoparticles and its application in photo-degradation of malachite green dye and kinetic study. Nanochem Res 4:86–93
66. Lassoued A, Lassoued MS, Dkhil B, Ammar S, Gadri A (2018) Photocatalytic degradation of methyl orange dye by $NiFe_2O_4$ nanoparticles under visible irradiation: effect of varying the synthesis temperature. J Mater Sci Mater Electron 29:7057–7067
67. Sharma R, Singhal S (2018) Spinel Ferrite Mediated Photo-Fenton Degradation of Phenolic Analogues: A Detailed Study Employing Two Distinct Inorganic Oxidants. Clean-Soil Air Water 46:1700605
68. Ibrahim I, Ali IO, Salama TM, Bahgat AA, Mohamed MM (2016) Synthesis of magnetically recyclable spinel ferrite (MFe_2O_4, M=Zn Co, Mn) nanocrystals engineered by sol gel-hydrothermal technology: High catalytic performances for nitroarenes reduction. Appl Catal B Environ 181:389–402
69. Jauhar S, Singhal S (2014) Substituted cobalt nano-ferrites, $CoM_xFe_{2-x}O_4$ (M=Cr^{3+}, Ni^{2+}, Cu^{2+}, Zn^{2+}; $(0.2 \leq x \leq 1.0)$ as heterogeneous catalysts for modified Fenton's reaction. Ceram Int 40:11845–11855
70. Miller A (1959) Distribution of cations in spinels. J Appl Phys 30:S24–S25
71. Li J, Chen W, Zhao H, Zheng X, Wu L, Pan H, Zhu J, Chen Y, Lu J (2017) Size-dependent catalytic activity over carbon-supported palladium nanoparticles in dehydrogenation of formic acid. J Catal 352:371–381
72. Goyal A, Bansal S, Chudasama B, Tikoo KB, Kumar V, Singhal S (2017) Augmenting the catalytic performance of spinel nanoferrites ($CoFe_2O_4$ and $NiFe_2O_4$) via incorporation of Al into the lattice. New J Chem 41:8320–8332
73. Kapoor S, Goyal A, Bansal S, Singhal S (2018) Emergence of bismuth substituted cobalt ferrite nanostructures as versatile candidates for the enhanced oxidative degradation of hazardous organic dyes. New J Chem 42:14965–14977
74. Ziarati A, Sobhani-Nasab A, Rahimi-Nasrabadi M, Ganjali MR, Badiei A (2017) Sonication method synergism with rare earth based nanocatalyst: preparation of $NiFe_{2-x}Eu_xO_4$ nanostructures and its catalytic applications for the synthesis of benzimidazoles, benzoxazoles, and benzothiazoles under ultrasonic irradiation. J Rare Earth 35:374–381
75. Singh C, Jauhar S, Kumar V, Singh J, Singhal S (2015) Synthesis of zinc substituted cobalt ferrites via reverse micelle technique involving in situ template formation: a study on their structural, magnetic, optical and catalytic properties. Mater Chem Phys 156:188–197
76. Al Maashani MS, Khalaf KA, Gismelseed AM, Al-Omari IA (2020) The structural and magnetic properties of the nano-$CoFe_2O_4$ ferrite prepared by sol-gel auto-combustion technique. J Alloys Compd 817:152786
77. Shen W, Zhang L, Zhao B, Du Y, Zhou X (2018) Growth mechanism of octahedral like nickel ferrite crystals prepared by modified hydrothermal method and morphology dependent magnetic performance. Ceram Int 44:9809–9815

78. Nasrin S, Chowdhury FUZ, Hoque SM (2019) Study of hyperthermia temperature of manganese-substituted cobalt nano ferrites prepared by chemical co-precipitation method for biomedical application. J Magn Magn Mater 479:126–134

79. Ahsan MZ, Khan MFA, Islam MA (2019) Influence of milling time on structural and electromagnetic properties of manganese doped cobalt ferrite nanoparticles. Int J Mater Sci Eng 7:199

80. Chen HD, Xu JK, Wei JQ, Wang PF, Han YB, Xu JC, Hong B, Jin HX, Jin DF, Peng XL, Li J (2019) Mesoporous $CoFe_2O_4$ nanowires: Nanocasting synthesis, magnetic separation and enhanced catalytic degradation for ciprofloxacin. J Phys Chem Solids 132:138–144

81. Jung HR, Kim KN, Lee WJ (2019) Heterostructured $Co_{0.5}Mn_{0.5}Fe_2O_4$-polyaniline nanofibers: highly efficient photocatalysis for photodegradation of methyl orange. c J Chem Eng 36:807–815

82. Gao G, Shi L, Lu S, Gao T, Li Z, Gao Y, Ding S (2018) Ethylene glycol-mediated rapid synthesis of carbon-coated $ZnFe_2O_4$ nanoflakes with long-term and high-rate performance for lithium-ion batteries. Dalton Trans 47:3521–3529

83. Wu C, Tu J, Tian C, Geng J, Lin Z, Dang Z (2018) Defective magnesium ferrite nano-platelets for the adsorption of As (V): the role of surface hydroxyl groups. Environ Pollut 235:11–19

84. Reddy MP, Mohamed AMA (2015) One-pot solvothermal synthesis and performance of mesoporous magnetic ferrite MFe_2O_4 nanospheres. Microporous Mesoporous Mater 215:37–45

85. Dhiman M, Sharma R, Kumar V, Singhal S (2016) Morphology controlled hydrothermal synthesis and photocatalytic properties of $ZnFe_2O_4$ nanostructures. Ceram Int 42:12594–12605

86. Wu X, Wang W, Song N, Yang X, Khaimanov S, Tsidaeva N (2016) From nanosphere to nanorod: tuning morphology, structure and performance of cobalt ferrites via Pr^{3+} doping. Chem Eng 306:382–392

87. Sakthivel K, Mani G, Chen SM, Lin SH, Muthumariappan A, Mani V (2018) A novel synthesis of non-aggregated spinel nickel ferrite nanosheets for developing non-enzymatic reactive oxygen species sensor in biological samples. J Electroanal Chem 820:161–167

88. Lassoued A, Lassoued MS, Dkhil B, Ammar S, Gadri A (2019) Substituted effect of Al^{3+} on structural, optical, magnetic and photocatalytic activity of Ni ferrites. J Magn Magn Mater 476:124–133

89. Dhiman P, Dhiman N, Kumar A, Sharma G, Naushad M, Ghfar AA (2019) Solar active nano-$Zn_{1-x}Mg_xFe_2O_4$ as a magnetically separable sustainable photocatalyst for degradation of sulfadiazine antibiotic. J Mol Liq 294:111574.

90. Kirankumar VS, Sumathi S (2019) Copper and cerium co-doped cobalt ferrite nanoparticles: structural, morphological, optical, magnetic, and photocatalytic properties. Environ Sci Pollut Res 26:19189–19206

91. Wang Z, Ma H, Zhang C, Feng J, Pu S, Ren Y, Wang Y (2018) Enhanced catalytic ozonation treatment of dibutyl phthalate enabled by porous magnetic Ag-doped ferrospinel $MnFe_2O_4$ materials: performance and mechanism. Chem Eng J 354:42–52

92. Nair DS, Kurian M (2018) Chromium-zinc ferrite nanocomposites for the catalytic abatement of toxic environmental pollutants under ambient conditions. J Hazard Mater 344:925–941

93. Sharma R, Kumar V, Bansal S, Singhal S (2017) Boosting the catalytic performance of pristine $CoFe_2O_4$ with yttrium (Y^{3+}) inclusion in the spinel structure. Mater Res Bull 90:94–103

94. Rashmi SK, Naik HSB, Jayadevappa H, Sudhamani CN, Patil SB, Naik MM (2017) Influence of Sm^{3+} ions on structural, optical and solar light driven photocatalytic activity of spinel $MnFe_2O_4$ nanoparticles. J Solid State Chem 255:178–192

95. Naghshbandi Z, Arsalani N, Zakerhamidi MS, Geckeler KE (2018) A novel synthesis of magnetic and photoluminescent graphene quantum dots/MFe_2O_4 (M=Ni, Co) nanocomposites for catalytic application. Appl Surf Sci 443:484–491

96. Chen L, Ding D, Liu C, Cai H, Qu Y, Yang S, Gao Y, Cai T (2018) Degradation of norfloxacin by $CoFe_2O_4$-GO composite coupled with peroxymonosulfate: a comparative study and mechanistic consideration. Chem Eng J 334:273–284

97. Boutra B, Güy N, Özacar M, Trari M (2020) Magnetically separable $MnFe_2O_4/TA/ZnO$ nanocomposites for photocatalytic degradation of congo red under visible light. J Magn Magn Mater 497:165994

98. Nawaz M, Shahzad A, Tahir K, Kim J, Moztahida M, Jang J, Alam MB, Lee SH, Jung HY, Lee DS (2020) Photo-Fenton reaction for the degradation of sulfamethoxazole using a multi-walled carbon nanotube-$NiFe_2O_4$ composite. Chem Eng J 382:123053

99. Farhadi S, Siadatnasab F (2016) Synthesis and structural characterization of magnetic cadmium sulfide–cobalt ferrite nanocomposite, and study of its activity for dyes degradation under ultrasound. J Mol Struct 1123:171–179

100. Hassani A, Eghbali P, Ekicibil A, Metin Ö (2018) Monodisperse cobalt ferrite nanoparticles assembled on mesoporous graphitic carbon nitride ($CoFe_2O_4/mpg-C_3N_4$): a magnetically recoverable nanocomposite for the photocatalytic degradation of organic dyes. J Magn Magn Mater 456:400–412

101. Li X, Jin B, Huang J, Zhang Q, Peng R, Chu S (2018) $Fe_2O_3/ZnO/ZnFe_2O_4$ composites for the efficient photocatalytic degradation of organic dyes under visible light. Solid State Sci 80:6–14

102. Sohail M, Xue H, Jiao Q, Li H, Khan K, Wang S, Feng C, Zhao Y (2018) Synthesis of well-dispersed $TiO_2/CNTs@CoFe_2O_4$ nanocomposites and their photocatalytic properties. Mater Res Bull 101:83–89

103. Jiang Z, Chen K, Zhang Y, Wang Y, Wang F, Zhang G, Dionysiou DD (2020) Magnetically recoverable $MgFe_2O_4$/conjugated polyvinyl chloride derivative nanocomposite with higher visible-light photocatalytic activity for treating Cr (VI)-polluted water. Sep Purif Technol 236:116272.

104. Tanwar R, Kumari R, Mandal UK, Kar KK (2020) Catalytic activity of surface-functionalized nanoscale nickel zinc multiferrites: potential vector for water purification. J Chem Technol Biotechnol 95:739–750

105. Singh C, Goyal A, Bansal S, Singhal S (2017) $SiO_2@MFe_2O_4$ core-shell nanostructures: efficient photocatalysts with excellent dispersion properties. Mater Res Bull 85:109–120

106. Malakootian M, Nasiri A, Asadipour A, Kargar E (2019) Facile and green synthesis of $ZnFe_2O_4@CMC$ as a new magnetic nanophotocatalyst for ciprofloxacin degradation from aqueous media. Process Saf Environ 129:138–151

107. Goyal A, Sharma R, Bansal S, Tikoo KB, Kumar V, Singhal S (2018) Functionalized core-shell nanostructures with inherent magnetic character: outperforming candidates for the activation of PMS. Adv Powder Technol 29:245–256

108. Bashira A, Hanifb F, Yasmeena F, Maboodc F, Hussaind A, Abbasa N, Yousafe AB, Aamira M, Manzoora S (2019) Polyaniline based magnesium nanoferrite composites as efficient photocatalysts for the photodegradation of Indigo Carmine in aqueous solutions. Desalin Water Treat 164:368–377

109. Haber F, Weiss JJ (1934) The catalytic decomposition of hydrogen peroxide by iron salts. Proc Roy Soc London Ser A 147:332–351

110. Duesterberg CK, Cooper WJ, Waite TD (2005) Fenton-mediated oxidation in the presence and absence of oxygen. Environ Sci Technol 39:5052–5058

111. Li Y, Chen D, Fan S, Yang T (2019) Enhanced visible light assisted Fenton-like degradation of dye *via* metal-doped zinc ferrite nanosphere prepared from metal-rich industrial wastewater. J Taiwan Inst Chem E 96:185–192

112. Hassani A, Celikdag G, Eghbali P, Sevim M, Karaca S, Metin O (2018) Heterogeneous sono-Fenton-like process using magnetic cobalt ferrite-reduced graphene oxide ($CoFe_2O_4$-rGO) nanocomposite for the removal of organic dyes from aqueous solution. Ultrason Sonochem 40:841–852

113. Yao Y, Lu F, Zhu Y, Wei F, Liu X, Lian C, Wang S (2015) Magnetic core–shell $CuFe_2O_4@C_3N_4$ hybrids for visible light photocatalysis of Orange II. J Hazard Mater 297:224–233

114. Dhiman M, Chudasama B, Kumar V, Tikoo KB, Singhal S (2019) Augmenting the photocatalytic performance of cobalt ferrite via change in structural and optical properties with the introduction of different rare earth metal ions. Ceram Int 45:3698–3709

115. Sundararajan M, Sailaja V, Kennedy LJ, Vijaya JJ (2017) Photocatalytic degradation of rhodamine B under visible light using nanostructured zinc doped cobalt ferrite: kinetics and mechanism. Ceram Int 43:540–548

116. Wang J, Wang S (2018) Activation of persulfate (PS) and peroxymonosulfate (PMS) and application for the degradation of emerging contaminants. Chem Eng J 334:1502–1517

117. Liu G, Lv H, Sun H, Zhou X (2018) Fabrication of tube like Co_3O_4 with superior peroxidase-like activity and activation of PMS by a facile electrospinning technique. Ind Eng Chem Res 57:2396–2403

118. Khan MAN, Klu PK, Wang C, Zhang W, Luo R, Zhang M, Qi J, Sun X, Wang L, Li J (2019) Metal-organic framework-derived hollow Co_3O_4/carbon as efficient catalyst for peroxymonosulfate activation. Chem Eng J 363:234–246

119. Guan YH, Ma J, Ren YM, Liu YL, Xiao JY, Lin LQ, Zhang C (2013) Efficient degradation of atrazine by magnetic porous copper ferrite catalyzed peroxymonosulfate oxidation via the formation of hydroxyl and sulfate radicals. Water Res 47:5431–5438

120. Ding Y, Zhua L, Wang N, Tang H (2013) Sulfate radicals induced degradation of tetra-bromobisphenol A with nanoscaled magnetic $CuFe_2O_4$ as a heterogeneous catalyst of peroxymonosulfate. Appl Catal B-Environ 129:153–162

121. Deng J, Shao Y, Gao N, Tan C, Zhou S, Hu X (2013) $CoFe_2O_4$ magnetic nanoparticles as a highly active heterogeneous catalyst of oxone for the degradation of diclofenac in water. J Hazard Mater 262:836–844

122. Pang Y, Lei H (2016) Degradation of p-nitrophenol through microwave-assisted heterogeneous activation of peroxymonosulfate by manganese ferrite. Chem Eng J 287:585–592

123. Ren Y, Lin L, Ma J, Yang J, Feng J, Fan Z (2015) Sulfate radicals induced from peroxymono-sulfate by magnetic ferrospinel MFe_2O_4 (M=Co, Cu, Mn, and Zn) as heterogeneous catalysts in the water. Appl Catal B-Environ 165:572–578

124. Rodriguez S, Santos A, Romero VF (2012) Kinetic of oxidation and mineralization of priority and emerging pollutants by activated persulfate. Chem Eng J 213:225–234

125. Ahmed MM, Chiron S (2014) Solar photo-Fenton like using persulfate for carbamazepine removal from domestic wastewater. Water Res 48:229–236

126. Pan X, Yan L, Li C, Qu R, Wang Z (2017) Degradation of UV-filter benzophenone-3 in aqueous solution using persulfate catalyzed by cobalt ferrite. Chem Eng J 326:1197–1209

New Chemical Modified of Rice Straw with CoFe$_2$O$_4$ Ferrite Nanocomposite for Heavy Metal Ions Adsorption from Wastewater

Sara M. Younes, Alaa E. Ali, Waheed M. Salem, and Aml Z. Elabdeen

Abstract Different types of contaminants are released to wastewater with the rapid increase in industrial activities, such as heavy metal ions, organics, and hazard organisms which are serious harmful to human health. Heavy metal ions, like Pb^{2+}, Cd^{2+}, Zn^{2+}, and Hg^{2+} can cause severe health problems in animals and human for its highly toxic nature. The use of agricultural by-products has been widely investigated as an efficient alternative for current costly methods of removing heavy metals from wastewater. Chemical composition of Rice Straw contains cellulose (32–47%), hemicellulose (19–27%) and lignin (5–24%). Rice Straw has several characteristics to predict the functional groups on the surface of the biomass that make it a potential adsorbent with binding sites capable of taking up metals from aqueous solutions. In our study, the active sites of Rice Straw were modified using CoFe$_2$O$_4$ nanoparticles which cause increasing their metal-binding capacity. Adsorption experiments were carried out using modified Rice Straw to absorb some heavy metals ions like Fe^{3+}, Mn^{2+}, Cu^{2+}, Cd^{2+}, Zn^{2+}, Ni^{2+} and Pb^{2+} from aqueous solution. The prepared samples were characterized using different analytical techniques. Our results of adsorption indicated that Rice Straw treated with CoFe$_2$O$_4$ spinel ferrite nanoparticles appeared to be more efficient to remove heavy metal ions from wastewater.

Keywords Rice Straw · Cobalt ferrite nanoparticles · Agricultural waste and wastewater treatment

S. M. Younes (✉)
Chemical Engineering Department, Borg El Arab Higher Institute Engineering and Technology, Alexandria, Egypt

A. E. Ali · W. M. Salem
Chemistry Department, Faculty of Science, Damanhur University, Beheria, Egypt

A. Z. Elabdeen
Damanhur Joint Lab, Ministry of Health, Beheria, Egypt

349

1 Introduction

Change of physical, chemical and biological properties of water can be defined as "Water Pollution" which restricts its use in the various applications [1]. It occurs when undesirable effluents disperse in water systems and so water quality changes. There is heavy metal contamination in wastewater streams from various industries such as metallic coatings, mining, wire drawing, printed circuit boards, as well as agricultural sources where fertilizers and fungicides are widely used [2]. One of the lignocellulosic malignant wastes in the world is Rice Straw. In terms of total production, rice is the third most important grain crop in the world after wheat and maize. In terms of chemical composition, steroids often contain cellulose (32–47%), hemicellulose (19–27%), lignin (5–24%) [3]. Black cloud phenomenon is released from burning of Rice Straw and affects on human health, visibility, and global climate by emitting gaseous pollutants. Rice Straw has binding sites that can able to remove of metal from aqueous solution by adsorption [4]. Functional groups on the surface of Rice Straw have binding characteristics capable to tack up metals from aqueous solutions. Rice Straw an alternative low-cost biosorbent in the removal of heavy metals from aqueous solutions [5].

Recently, fabrication of nanomaterial with large surface-to-volume ratios is very important in treatment of pollutants in our life. Nanotechnology is playing an important role in our environment, by providing new materials, sensors and remediation/treatment techniques and for monitoring purposes [6]. For water purification, removal of toxic contaminants from the environment to a safe level is occurred so rapidly, efficiently and within a reasonable costs framework. Thus, the development of novel nanomaterials with increased capacity, affinity, and selectivity for heavy metals. The nanoparticles (NPs) are ultrafine particles in the size of nanometer range typically from 1 to 100 nm. The nano-sized magnetic materials show many novel physio-chemical properties, especially, magnetization behavior different from the bulk counterpart. Recently, the use of nano-sized magnetic material as adsorbents has attracted increasing interest due to their high surface area and unique superparamagnetism behavior. These properties lead to high adsorption efficiency and high removal rate of contaminants [7]. The stability of magnetic nanoparticles is utmost important for their applications. This can be greatly improved by preventing their oxidation and aggregation. Modification of the surface of magnetic nanoparticles by attaching organic or inorganic materials is proven to be greatly enhance the stability and prevents aggregation. Further, these attached groups provide specific functionalities that can be selective for ion uptake [8].

Recently, several reports on magnetic oxides, especially Fe_3O_4, acting as nano-adsorbents for the removal of various toxic metal ions from wastewater, such as Ni^{2+}, Cu^{2+}, Cr^{3+}, Co^{2+}, As^{3+}, Pb^{2+} and Hg^{2+} [9]. The main properties of magnetic nanoparticles are large surface /volume ratio, easily bind with chemicals and then be manipulated using a magnet. In water contamination, nanoparticles are especially interesting and useful for removing water contaminants including bacteria, viruses, and hazardous heavy metals like arsenic, nickel, chromium, etc. [10, 11].

Cobalt ferrites (CoFe$_2$O$_4$) have been the subject of intensive research interest due to its high saturation magnetization and coercivity. CoFe$_2$O$_4$ materials are known to exhibit very high cubic magneto-crystalline anisotropy. The excellent magnetic properties of CoFe$_2$O$_4$ are known to be mainly attributed to the Co ions in a spinal lattice [12]. CoFe$_2$O$_4$ belongs to inverse spinel structure in which half of Fe^{3+} ions occupy tetrahedral sites and the other half occupy the octahedral sites along with Co^{2+} ions. In the inverse spinel structure, the magnetic moment of Fe^{3+} in the tetrahedral sites is aligned in opposite direction to that of Fe^{3+} in the octahedral sites and hence the net magnetic moment produced from Fe^{3+} is zero. So the net magnetic moment of CoFe$_2$O$_4$ is due to the magnetic moment of Co^{2+} in the octahedral sites [13].

Many synthetic methods to prepare highly crystalline and uniformly sized magnetic nanoparticles of CoFe$_2$O$_4$ have been reported such as the precipitation method [14], the solvothermal method [15], the co-precipitation method [14], the hydrothermal method [16] and the sol–gel method [17]. Sol–gel is a simple way to produce ultrafine powders due to their simple synthesis equipment and process. The reason behind studying and opting for this sol–gel route is that the reactants used for the process are cost-effective, safe and environmentally friendly [18].

Adsorption capacities of native plant materials usually show lower maximum. Nevertheless, these capacities can be significantly increased with a suitable method such as treatment with various hydroxides, acids; carbonization and hydrolysis have been reported recently. Combination of non-magnetic powdered material with magnetic nano or microparticles results in a formation of magnetically responsive (bio) composites which exhibit response to external magnetic field [19].

2 Materials and Methods

2.1 Materials

All the chemicals were of analytical reagent (AR) grade and used without further purification. Ferric chloride FeCl$_3$.6H$_2$O was obtained from (Applichempan-reac), cobalt chloride CoCl$_2$.2H$_2$O was obtained from (Oxford Lab Chem), citric acid C$_6$H$_8$O$_7$ was obtained from (Almasria), ammonia solution NH$_4$OH, sodium hydroxide NaOH and hydrochloric acid HCl were obtained from (Adwic), nitric acid HNO$_3$ was obtained from (SDFCL) and ethyl alcohol C$_2$H$_5$OH, 95% was obtained from (Egyptian company for chemical trading. All stages of the synthesis used deionized water for the reactions.

Fig. 1 **a** Photograph of raw Rice Straw. **b** Calcined $CoFe_2O_4$ nanoparticles and **c** prepared Rice Straw-$CoFe_2O_4$ nanocomposites

2.2 Preparation of Adsorbent Materials

2.2.1 Rice Straw

By-product Straw remained after Rice being harvested was gathered from local market, washed well to remove water soluble and dirt substances via soaking suitable amount of Rice Straw into a detergent solution for 50 min, followed by extensive washing 4–5 times with tap water for 1 h and left till next day in tab water, finally washed with deionized water and squeezed. The Rice Straw then cut to small pieces, dried in an oven at 65 °C until remains constant weight as shown in Fig. 1a. For preservation, the Rice Straw was kept in plastic bags and preserved in desiccators until the time of use to minimize contact with humidity [20]. The raw Rice Straw was characterized using different techniques such as FTIR and SEM.

2.2.2 Synthesis of Cobalt-Ferrites Nanoparticles

The synthesis of $CoFe_2O_4$ nanoparticles was carried out as: 10.8 g of $FeCl_3 \cdot 6H_2O$ was mixed with 3.3 g of $CoCl_2 \cdot 2H_2O$ and dissolved in 50 ml deionized water (Fe^{3+}: Co^{2+} ions, 2:1 molar ratio) according to the stoichiometric proportion of Co and Fe in $CoFe_2O_4$. 1.28 g of citric acid was added as gelling agent (Co^{2+} ions: citric acid, 3:1 molar ratio) [21]. 4.0 M ammonia solution (NH_4OH) was added in order to keep the pH of the solution to 7.0 with continuous stirring using a magnetic stirrer. After continuous stirring for 9 h at 85 °C, the clear sol was completely turned into a gel. Finally, it was dried in oven at 80 °C till constant weight and grinded to fine powder. After that, the powder was calcined at 550 °C for 5 h in furnace under air atmosphere. Magnetic black nanoparticles in different size were synthesized as shown in Fig. 1b [12]. The prepared nanoparticles were studied in terms of structure, morphology, size and surface area using different techniques such as XRD, FTIR, SEM and TEM. Rice Straw $CoFe_2O_4$ Nanocomposite used in the adsorption study was characterized by using (FTIR) and (SEM).

2.2.3 Preparation of Rice Straw-CoFe$_2$O$_4$ Ferrite Nanocomposite

In order to increase the adsorption capacities of adsorbent used Rice Straw in modified form, 5 g of Rice Straw was added to 0.5 g of CoFe$_2$O$_4$ nanoparticles and then refluxed with 30 ml ethyl alcohol and 30 ml NaOH (2.5%) at 85 C° for 3 h, filtered and washed for several times with HCl (0.1 N) then by deionized water. Later, the modified Rice Straw was dried at 105 °C until till constant weight [22]. A photograph of prepared Rice Straw-CoFe$_2$O$_4$ nanocomposite is shown in Fig. 1c.

3 Characterization Methods and Instrumentation

3.1 Fourier Transform Infrared Spectroscopy (FTIR)

For identification of functional groups responsible for metal adsorption was done using FTIR spectroscopy. CoFe$_2$O$_4$ nanoparticles and the Rice Straw before and after modification was characterized by using (Bruker Tensor 37 FTIR) to predict the functional groups on the surface of the biomass responsible for the adsorption process and to reveal the systematic changes in the spectral features upon activation with CoFe$_2$O$_4$ nanoparticles.

3.2 X-ray Diffraction (XRD)

The X-ray diffraction is a good tool to study the nature of the crystalline substances. CoFe$_2$O$_4$ nanoparticles were characterized by using powder X-ray Diffraction (Lab. XRD-6100 shimadzu). The instrument located at Egypt-Japan University of Science and Technology (E-JUST).

3.3 Scanning Electron Microscopy (SEM)

Scanning electron microscopy is useful for identifying the surface studies of metals, biological materials and composites for both topography as well as compositional analysis. CoFe$_2$O$_4$ nanoparticles and the Rice Straw before and after modification were characterized by using (JEOL JSM-6360LA) Analytical Scanning Electron Microscope. The instrument located at The City of Scientific Research and Technological Applications (SRTA-City), Borg Al Arab.

3.4   Transmission Electron Microscopy (TEM)

Transmission electron microscopy (TEM) is one important technique for observing the morphology and measures the size of synthesized nanoparticles. $CoFe_2O_4$ nanoparticles were characterized by using (FEI TECNAI SPIRIT) Transmission Electron Microscope. The instrument located at central laboratory in National Institute for Oceanography and Fisheries.

3.5   Atomic Absorption Spectroscopy (AAS)

In quantitative analysis for metals in the range (0.1–100 ppm), AAS technique is the most widely used technique to detect various materials. For this, first preparing a series of standard solutions for concentration range of the sample to be analyzed and a standard curve is obtained by plotting absorbance versus concentration of the samples by applying Beer–Lambert Law for the analysis. The concentrations of the samples can be obtained from the plot using the value absorbance of sample. The concentration of heavy metals in water samples before and after treatment were measured by using Atomic Absorption Spectrometer (AAS) model [PerkinElmer (PinAAcle 900 T)].

3.6   Method of Treatment-Removal of Heavy Metals:

The sewage water samples were collected from Zarkon channel. The samples were transferred to laboratory in closed bottles and then filtered to remove any suspended materials, distributed in sixteen 2-L beakers, each of them had 1-L water volume. Beakers were subdivided into 4 treatments with each adsorbent for 24 h and 4 treatments with each adsorbent for 72 h. The investigated polluted water (sewage water) was mixed with varying adsorbent weight (1–4 g) to investigate the effect of adsorbent weight on removal efficiencies of different metals and contact time (24–72 h) to investigate the effect of contact period on removal efficiencies of different investigated metals. Samples were placed in a shaker for 24 or 72 h at 120 rpm at room temperature [23].

Adsorption was performed for initial heavy metal concentrations of 1.9 and 1.0 mg/L for Fe, 0.53 and 0.3 mg/L for Mn, 0.013 and 0.015 mg/L for Cu, 0.01 and 0.008 mg/L for Cd, 0.18 and 0.1 mg/L for Zn, 0.12 and 0.1 mg/L for Ni as well as 0.163 and 0.1 mg/L for Pb. Metal ions remaining in aqueous solution were determined by AAS. The amount of metal ion adsorbed was calculated as:

$$\% \textbf{ Adsorption} = ((\textbf{C}_i - \textbf{C}_f)/\textbf{C}_i) \times \textbf{100}$$

where C$_i$ and C$_f$ are the initial and final concentrations of the metal ions in the solution (mg/L).

3.7 Desorption and Reusability

Regeneration is a process in which adsorbent loaded agricultural wastes are eluted by using appropriate solvent to recover a small volume of concentrated pollutants (especially metals). One of the important industrial applications of adsorption is recovery of loaded pollutants from the adsorbent and simultaneous regeneration of the adsorbent for reuse. Nanocomposites (RS/CoFe$_2$O$_4$) are undergoing under several investigation as reusability of the adsorbent, regeneration and desorption. Adsorbent was separated from adsorption process is performed into process which includes: (i) washing with deionized water to remove any unadsorbed metal ions; (ii) mixing the resultant metal-loaded adsorbent with 20 mL of 0.10 M HNO$_3$, (iii) stripping agent in water shaker bath for one hour, and (iv) drying adsorbent. These steps were repeated three times [24].

4 Results and Discussion

4.1 Characterization of Biosorbent: FTIR Study of CoFe$_2$O$_4$ Nanoparticles

Figure 2 shows that the FTIR spectrum of CoFe$_2$O$_4$ has two distinct absorption bands around 469 and 608 cm^{-1}. The absorption band at 469 cm^{-1} exhibits the stretching vibration frequency of the metal–oxygen at the octahedral site from the stretching vibration of the metal–oxygen at the tetrahedral site which has absorption band around 608 cm^{-1}. These two metal–oxygen vibrational bands are the characteristic bands of CoFe$_2$O$_4$ [25, 26]. The 1639 cm^{-1} band is due to the deformation mode of absorbed H$_2$O molecules, assigned to the bending vibration. At 3417 cm^{-1} stretches of hydroxyl groups is assigned due to water molecules and hydrogen-bonded hydroxyl groups in cobalt and iron hydroxide [27].

4.2 FTIR of Rice Straw Before and After Treatment

Figure 3 shows the FTIR spectra of raw Rice Straw while Fig. 4 shows the FTIR spectra of Rice Straw-CoFe$_2$O$_4$ ferrite nanocomposites. Figure 3 comprises bands assigned to the main components of Rice Straw, such as cellulose, hemicellulose. The bands at 3436, 2921, 1643 and 1430 cm^{-1} belong to vibration of O–H, C–H
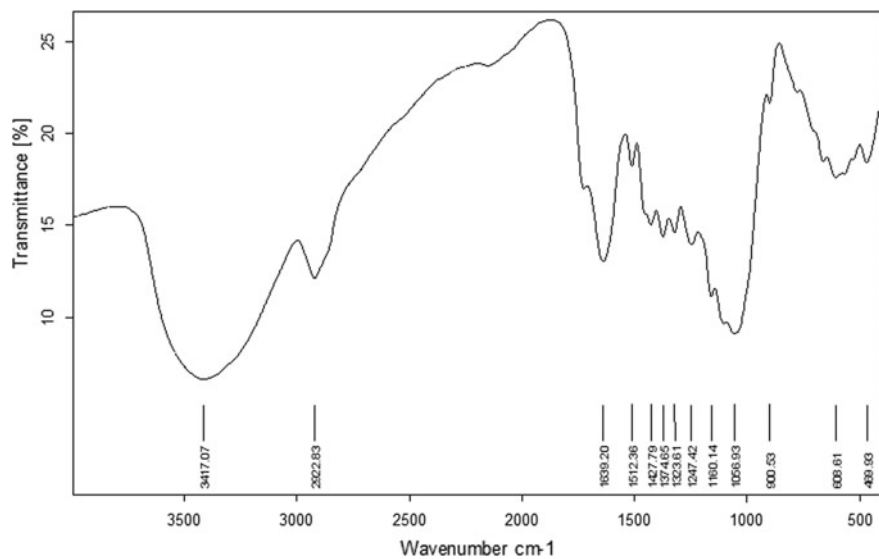
Fig. 2 FTIR for $CoFe_2O_4$ nanoparticles
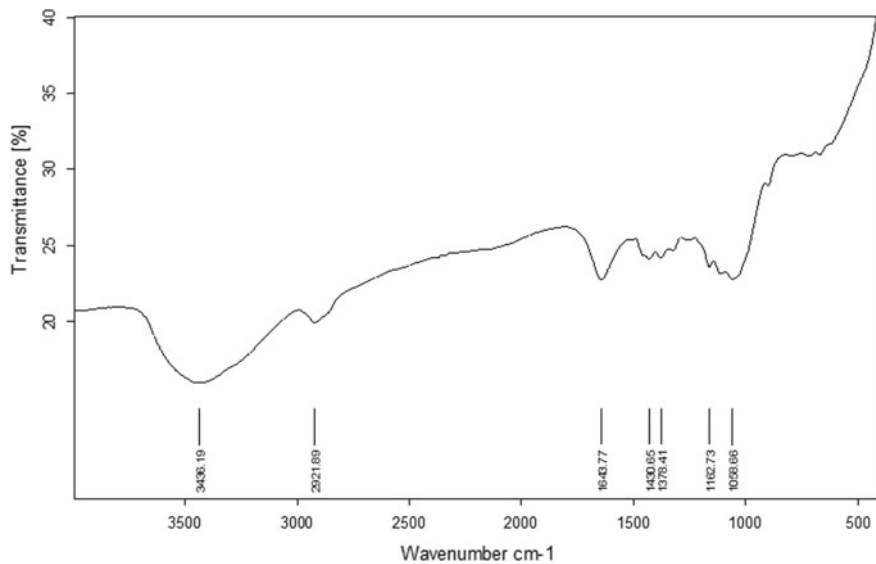
Fig. 3 FTIR for raw Rice Straw
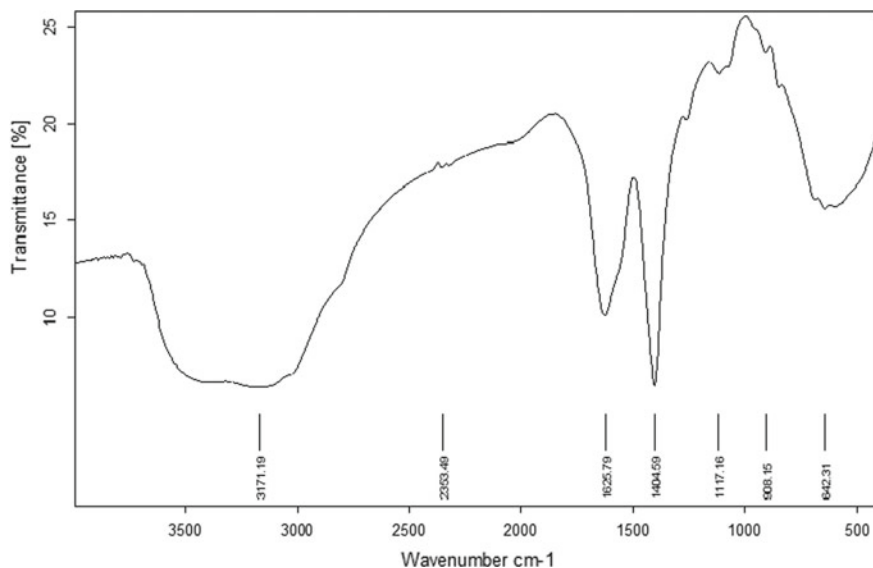
Fig. 4 FTIR for Rice Straw—CoFe$_2$O$_4$ nanocomposite (modified Rice Straw)

stretching, vibration of –C=O and CH$_2$ bending, respectively. The band at 1378 cm^{-1} can be ascribed to CH$_2$ wagging vibrations in cellulose, while the band at 1162 cm^{-1} is representative of the antisymmetric bridge stretching of C–O–C groups in cellulose. Also, the band near 1058 cm^{-1} can be connected to the existence of valence vibration of –C–O of carboxylic acids. Generally, the spectrum indicates that carbonyl and hydroxyl groups are appeared, these groups are the most important sites for the binding of heavy metals. In general, some differences were also detected in Fig. 6 in terms of intensity of the bands and disappearance of bands after treatment. However, slight changes were found for some functional groups. For instance, a broad absorption band at 3436 cm^{-1} in Fig. 5 became more broad in Fig. 4 and shifted to a lower wave number value 3171 cm^{-1}. Also, strong sharp peaks appeared at 1625 and 1404 cm^{-1}. Absorption band appear at 642 cm^{-1} which belongs to the stretching vibration of the metal–oxygen. This difference indicated that the structure of Rice Straw was changed after treatment which indicate the successful modification process.

4.3   X-ray Diffraction

Figure 5 shows the XRD pattern for the calcinated CoFe$_2$O$_4$ nanoparticles. This pattern matches well with the standard diffraction data of CoFe$_2$O$_4$ crystals and showing the single-phase cubic spinel structure. All the peaks of the prepared samples and its position at 2θ scale are completely compatible with the characteristic peaks
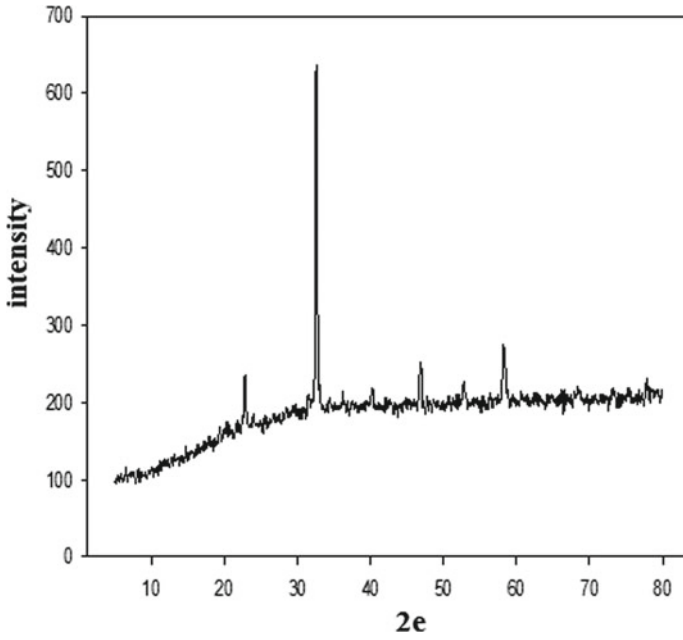
Fig. 5 XRD pattern for CoFe$_2$O$_4$ Nanoparticles

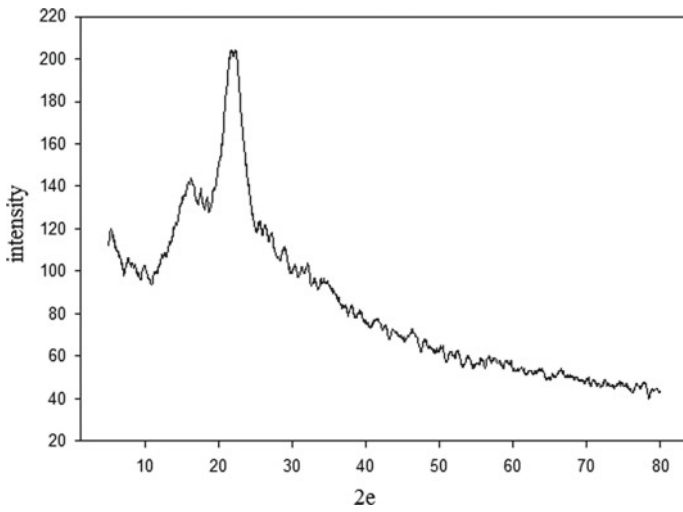**Fig. 6** XRD pattern for Rice Straw-CoFe$_2$O$_4$ ferrite nanocomposite

of cubic spinel CoFe$_2$O$_4$ and they are matched with the XRD card no. 22–1086. The CoFe$_2$O$_4$ peaks are particularly sharp. Other oxides or secondary impurity phases were not detected which indicate that we have pure cubic spinel CoFe$_2$O$_4$ [18]. While Fig. 6 shows the XRD pattern of Rice Straw-CoFe$_2$O$_4$ ferrite nanocomposite.

4.4 Scanning Electron Microscopy

The structural morphology of cubic spinel CoFe$_2$O$_4$ nanoparticles and Rice Straw before and after modification were investigated through SEM. Figure 7a shows the SEM images of CoFe$_2$O$_4$ nanoparticles. The SEM images show that the CoFe$_2$O$_4$ nanoparticles prepared by sol–gel method were mainly consisting of spherical rods. Some moderately agglomerated particles as well as separated particles were also seen.

Figure 7b shows the SEM images of raw Rice Straw which appear in the shape of fibers. By magnification, the pores appear which are responsible for adsorbtion process. Figure 7c shows the SEM images of Rice Straw-CoFe$_2$O$_4$ nanocomposite. SEM images show that the CoFe$_2$O$_4$ nanoparticles are presented on the surface of Rice Straw.

4.5 Transmission Electron Microscopy

The TEM images presented in Fig. 8 reveals slightly agglomerate pseudo spherical particles with a grain size ranging from 43 to 87 nm. The particles have generally two different shapes; spherical and elongated as shown in the TEM images.

5 Removal Efficiency of Heavy Metals by Using Raw and Modified Rice Straw

The concentrations of different metals were measured in sewage water samples before and after treatment with different dosages of Rice Straw-CoFe$_2$O$_4$ nanocomposites along with their removal efficiencies and the results are given below.
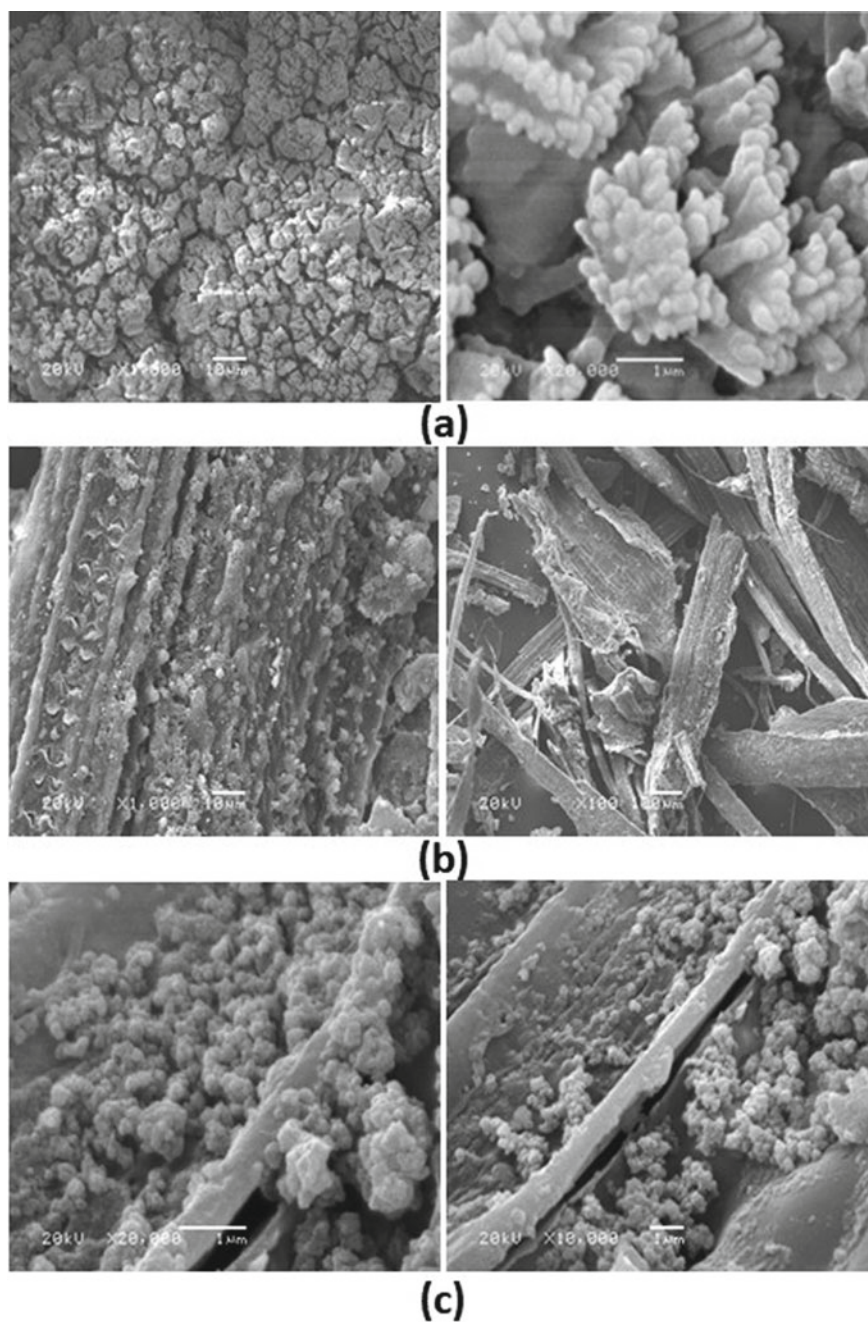
Fig. 7 SEM images of **a** CoFe$_2$O$_4$ nanoparticles, **b** raw Rice Straw, **c** Rice Straw-CoFe$_2$O$_4$ nanocomposite
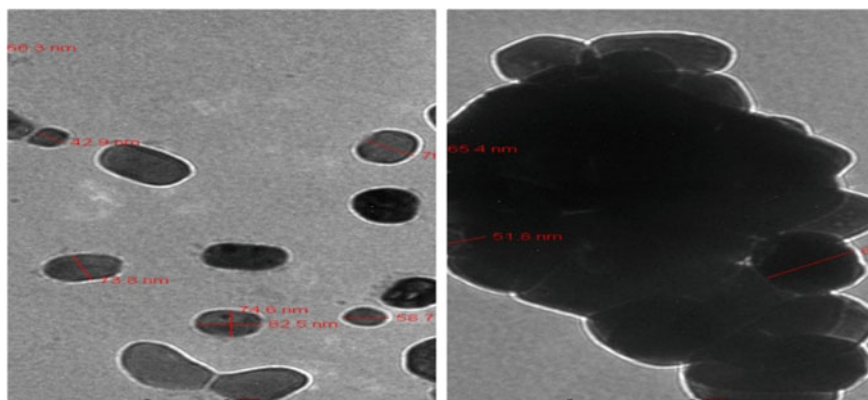
Fig. 8 TEM images of the CoFe$_2$O$_4$ nanoparticles at a scale of 100 nm

5.1 Iron (Fe)

Iron concentration in non-treated water samples was the highest among the different tested metals in the present study (1.9 and 1.0 mg/L for sample 1 and 2, respectively). The investigated practice of applying different concentrations of raw Rice Straw as a low-cost by-product and the modified Rice Straw kept in contact with the samples of polluted water for different periods, showed a significant reduction in iron concentration. Removal efficiencies influenced by adsorbent concentration as well as contact period. Table 1 which illustrated the obtained removal efficiencies of iron showed that the modified Rice Straw was more efficient than the raw Rice Straw. The highest iron % removed from water was 48.42% by raw Rice Straw comparing

Table 1 Removal efficiencies of Fe metal ion by raw and modified Rice Straw

Fe metal ion					
Weight of adsorbent (g)		Percentage of removal (%) by Rice Straw		Percentage of removal (%) by Rice Straw-CoFe$_2$O$_4$ ferrite nanocomposite	
		24 h (%)	72 h (%)	24 h (%)	72 h (%)
Sample 1	1.0	4.1	6.84	12.97	20.45
	2.0	8.42	10.53	22.45	30.58
	3.0	15.79	21.58	38.58	44.53
	4.0	21.05	23.68	40.45	51.05
Sample 2	1.0	6.84	10.53	24.21	35.26
	2.0	11.74	21.26	41.05	73.68
	3.0	21.58	40.53	73.68	84.21
	4.0	38.42	48.42	74.1	84.25

as compared to 84.25% of iron removed from sewage water by modified Rice Straw. After 24 h of contacting period with 1, 2, 3 and 4 g of both adsorbents: raw Rice Straw and modified Rice Straw, respectively, the iron percentages removed were 4.1, 8.42, 15.79 and 21.05% from sample 1 while, 6.84, 11.74, 21.58 and 38.42% of iron was removed from sample 2 by raw Rice Straw. The iron percentages removed by modified Rice Straw were 12.97, 22.45, 38.58 and 40.45% for sample 1 and 24.21, 41.05, 73.68 and 74.1% of iron for sample 2, respectively.

Extending the contact period to 72 h with different concentrations of both adsorbents increased removal efficiencies of iron. The removal efficiencies for raw Rice Straw were 6.84, 10.53, 21.58 and 23.68% for sample 1 and 10.53, 21.26, 40.53 and 48.42% for sample 2, respectively, while these values for modified Rice Straw were 20.45, 30.58, 44.53 and 51.05% for sample 1 and 35.26, 73.68, 84.21 and 84.25% for sample 2, respectively.

5.2 Manganese (Mn)

Manganese concentration in non-treated water samples was 0.53 and 0.3 mg/L, respectively. By applying different concentrations of raw Rice Straw and modified Rice Straw kept in contact with the samples of polluted water for different periods, the removal efficiencies were influenced by both adsorbent concentration as well as contact period. Table 2 which illustrated the obtained removal efficiencies of Mn showed that the modified Rice Straw was more efficient than the raw Rice Straw. The highest Mn % removed from water was 66.04% by raw Rice Straw as compared to 92.45% of Mn removed from water sample by modified Rice Straw.

Table 2 Removal efficiencies of Mn metal ion by raw and modified Rice Straw

Mn metal ion					
Weight of adsorbent (g)		Percentage of removal (%) by Rice Straw		Percentage of removal (%) by Rice Straw-CoFe$_2$O$_4$ ferrite nanocomposite	
		24 h (%)	72 h (%)	24 h (%)	72 h (%)
Sample 1	1.0	12.97	21.58	22.45	30.4
	2.0	23.3	29.05	35.23	54.53
	3.0	35.79	47.17	68.58	73.58
	4.0	40.45	48.68	70.45	81.05
Sample 2	1.0	15.09	26.42	32.08	33.96
	2.0	26.42	33.96	63.58	64.91
	3.0	47.17	52.83	81.13	86.79
	4.0	50.94	66.04	84.91	92.45

After 24 h of contacting period with 1, 2, 3 and 4 g of both adsorbents: raw Rice Straw and modified Rice Straw, respectively, the % of Mn removed were 12.97, 23.3, 35.79 and 40.45% for sample 1 and 15.09, 26.42, 47.17 and 50.94% for sample 2 by raw Rice Straw. These values were 22.45, 35.23, 68.58 and 70.45% for sample 1 and 32.08, 63.58, 81.13 and 84.91% for sample 2 by modified Rice Straw, respectively.

Extending the contact period to 72 h with different concentrations of both adsorbents increased the removal efficiencies of Mn. The removal efficiencies for raw Rice Straw were 21.58, 29.05, 47.17 and 48.68% for sample 1 and 26.42, 33.96, 52.83 and 66.04% for sample 2, respectively, while these values for modified Rice Straw were 30.4, 54.53, 73.58 and 81.05% for sample 1 and 33.96, 64.91, 86.79 and 92.45% for sample 2, respectively.

It was observed that the removal efficiencies of Mn metal ion increased as both adsorbent dosage and contact period increase. So, the optimum adsorbent weight from the modified Rice Straw for the removal of Mn metal ion was 4.0 g and the optimum contact time was 72 h.

5.3 Copper (Cu)

Cu concentration in non-treated water samples was 0.013 and 0.015 mg/L, respectively. In the present investigated practice of applying, Rice Straw for heavy metal removal from sewage water was potentially effective with Cu detected in the water. Potentiality of the investigated practice was influenced by absorbent dosage as well as period of contact between the absorbent and the tested polluted water. Cu removal efficiencies in water samples after treatment were given in Table 3.

Table 3 Removal efficiencies of Cu metal ion by raw and modified Rice Straw

Cu metal ion					
Weight of adsorbent (g)		Percentage of removal (%) by Rice Straw		Percentage of removal (%) by Rice Straw-CoFe₂O₄ ferrite nanocomposite	
		24 h (%)	72 h (%)	24 h (%)	72 h (%)
Sample 1	1.0	23.08	84.6	92.3	100
	2.0	31.77	92.3	100	100
	3.0	37.46	100	100	100
	4.0	46.15	100	100	100
Sample 2	1.0	21.22	84.6	92.3	100
	2.0	30.77	92.3	100	100
	3.0	37.56	100	100	100
	4.0	44.45	100	100	100

The percentages of Cu removal efficiencies from polluted water sample after 24 h of contact with 1, 2, 3 and 4 g of raw Rice Straw were 23.08, 31.77, 37.46 and 46.15% for sample 1, and 21.22, 30.77, 37.56 and 44.45% for sample 2, respectively. After 72 h, the removal percentages were 84.6, 92.3, 100 and 100%, for the two samples, whereas after 24 h of contacting with the modified Rice Straw, the removal % were 92.3, 100, 100 and 100% for the two samples. Prolonging of contact period with any of the tested dosage of the modified Rice Straw to 72 h, removed all sewage water copper.

It was observed that the removal efficiencies of Cu metal ion increased as both adsorbent dosage and contact period increased. So, the optimum adsorbent weight from the modified Rice Straw for the removal of Cu metal ion was 4.0 g and the optimum contact time was 72 h.

5.4 Cadmium (Cd)

Cadmium exists in water in low concentrations, and its values were 0.01 and 0.008 mg/L, respectively. This low concentration greatly affected by applying of Rice Straw. When non-treated water samples kept in contact with 1, 2, 3 and 4 g of raw Rice Straw for 24 h; 9, 15, 28 and 48% for sample 1 and 12, 21, 40 and 66% for sample 2 of Cd were detected. When the contact period prolonged to 72 h; the removal efficiencies of Cd increased to 14.6, 22, 50, 80% and 15, 33, 60, 85% for sample 1 and 2, respectively.

Table 4 reveals that the tested practice of applying the modified Rice Straw to polluted water samples removed 58, 84.6, 90, 100% and 65, 90, 93, 100% of its detected cadmium from sample 1 and 2, respectively when kept in contact with 1,

Table 4 Removal efficiencies of Cd metal ion by raw and modified Rice Straw

Cd metal ion					
Weight of adsorbent (g)		Percentage of removal (%) by Rice Straw		Percentage of removal (%) by Rice Straw-CoFe$_2$O$_4$ ferrite nanocomposite	
		24 h (%)	72 h (%)	24 h (%)	72 h (%)
Sample 1	1.0	9	14.6	58	100
	2.0	15	22	84.6	100
	3.0	28	50	90	100
	4.0	48	80	100	100
Sample 2	1.0	12	15	65	100
	2.0	21	33	90	100
	3.0	40	60	93	100
	4.0	66	85	100	100

2, 3 and 4 g of the modified Rice Straw for 24 h. However, prolonging the contact period with any of the tested dosage of the modified Rice Straw to 72 h, removed all water cadmium.

It was observed that the removal efficiencies of Cd metal ion increased as both adsorbent dosage and contact period increased. So, the optimum adsorbent weight from the modified Rice Straw for the removal of Cd metal ion was 4.0 g and the optimum contact time was 72 h.

5.5   Zinc (Zn)

Zinc concentrations in non-treated water samples were 0.18 and 0.1 mg/L, respectively. As given in Table 5, the investigated practice efficiently reduced zinc in water. This reduction occurred in zinc values significantly influenced by the different adsorbent concentrations as well as its period of contact with the investigated polluted waters. Zinc removal efficiencies from polluted water after 24 h of contact with 1, 2, 3 and 4 g of raw Rice Straw were 26.67, 38.56, 45.89, 50% and 35,45.45, 63.89, 70% for sample 1 and 2, respectively. However, keeping these concentrations of raw Rice Straw in contact with water for 72 h, removed 45.56, 53.89, 65.56 and 71.67% of its zinc for sample 1 and 55, 73,80 and 84.66% of its zinc for sample 2, respectively.

These values for modified Rice Straw after 24 h of contact period were 55, 70.56, 83.33 and 100% for sample 1 and 75,100, 100 and 100% for sample 2, respectively; while after 72 h of contacting period with the mentioned modified Rice Straw concentrations; 70, 95, 100 and 100% of water zinc were removed from sample 1, while all water zinc was removed from sample 2 by any weight of the modified Rice Straw.

Table 5 Removal efficiencies of Zn metal ion by raw and modified Rice Straw

Zn metal ion					
Weight of adsorbent (g)		Percentage of removal (%) by Rice Straw		Percentage of removal (%) by rice Straw-COFE₂O₄ ferrite nanocomposite	
		24 h (%)	72 h (%)	24 h (%)	72 h (%)
Sample 1	1.0	26.67	45.56	55	70
	2.0	38.56	53.89	70.56	95
	3.0	45.89	65.56	83.33	100
	4.0	50	71.67	100	100
Sample 2	1.0	35	55	75	100
	2.0	45.45	73	100	100
	3.0	63.89	80	100%	100
	4.0	70	84.66	100	100

It was observed that the removal efficiencies of Zn metal ion increased as both adsorbent dosage and contact period increased. So, the optimum adsorbent weight from the modified Rice Straw for the removal of Zn metal ion was 4.0 g and the optimum contact time was 72 h.

5.6   Nickel (Ni)

Nickel concentrations in non-treated water samples were 0.12 and 0.1 mg/L, respectively. As given in Table 6, the investigated practice efficiently reduced Ni in water. This reduction occurred in Ni values significantly influenced by the different adsorbent concentrations as well as its period of contact with the investigated polluted waters. Nickel removal efficiencies from polluted water after 24 h of contact with 1, 2, 3 and 4 g of raw Rice Straw were 20.63, 35.67, 50.43 and 55.29% for sample 1, while Ni removal efficiencies were 28.33, 41.67, 57.5 and 65% for sample 2, respectively. However, keeping these concentrations of raw Rice Straw in contact with water for 72 h removed 35, 53.23, 72.81 and 75% of Ni in sample 1 and 45, 63.33, 75.17 and 83.33% in sample 2, respectively.

These values for modified Rice Straw after 24 h of contact period were 35.67, 65, 85 and 89.33% for sample 1 and 41.67, 74.17, 95.83 and 99.17% for sample 2, respectively; while after 72 h of contacting period with the mentioned modified Rice Straw concentrations, 62.5, 85, 100 and 100% of water Nickel was removed from sample 1 and 72.5, 95, 100 and 100%of water Nickel was removed from sample 2, respectively. The obtained data revealed that efficiency toward Ni removal by the modified Rice Straw was higher than that of non-modified Rice Straw in water.

Table 6 Removal efficiencies of Ni metal ion by raw and modified Rice Straw

Ni metal ion					
Weight of adsorbent (g)		Percentage of removal (%) by Rice Straw		Percentage of removal (%) by Rice Straw-$CoFe_2O_4$ ferrite nanocomposite	
		24 h (%)	72 h (%)	24 h (%)	72 h (%)
Sample 1	1.0	20.63	35	35.67	62.5
	2.0	35.67	53.23	65	85
	3.0	50.43	72.81	85	100
	4.0	55.29	75	89.33	100
Sample 2	1.0	28.33	45	41.67	72.5
	2.0	41.67	63.33	74.17	95
	3.0	57.5	75.17	95.83	100
	4.0	65	83.33	99.17	100

Table 7 Removal efficiencies of Pb metal ion by raw and modified Rice Straw

Pb metal ion					
Weight of adsorbent (g)		Percentage of removal (%) by Rice Straw		Percentage of removal (%) by Rice Straw-CoFe$_2$O$_4$ Ferrite Nanocomposite	
		24 h (%)	72 h (%)	24 h (%)	72 h (%)
Sample 1	1.0	10.43	14.78	33.7	51. 3
	2.0	18.88	32.3	56.2	85
	3.0	27.54	46.93	75.8	91
	4.0	34.6	55.09	80	100
Sample 2	1.0	15.52	27.78	41.1	71.17
	2.0	29.86	57.3	73.62	95.09
	3.0	40.54	66.93	95.7	100
	4.0	54.6	65.09	99.14	100

It was observed that the removal efficiencies of Ni metal ion increased as both adsorbent dosage and contact period increased. So, the optimum adsorbent weight from the modified Rice Straw for the removal of Cu metal ion was 4.0 g and the optimum contact time was 72 h.

5.7 Lead (Pb)

Lead concentrations in non-treated water samples were 0.163 and 0.1 mg/L, respectively. El-Nabawi et. al (1987) reported that agricultural, beside industrial discharges are primary sources of lead pollution in Egypt [28].

As shown in Table 7, remained Pb in the investigated polluted water sample, significantly influenced by both absorbent dosage as well as contact period. Lead removal efficiencies after applying 1, 2, 3 and 4 g of raw Rice Straw were 10.43, 18.88, 27.54 and 34.6% for sample 1 and 15.52, 29.86, 40.54 and 54.6% for sample 2, respectively. When contact period increased to 72 h, the removal efficiency was highly increased. These values were 14.78, 32.3, 46.93 and 55.09% for sample 1 and 27.78,57.3,66.93 and 65.09% for sample 2, respectively. These percentages after 24 h of contacting with the modified Rice Straw were 33.7, 56.2, 75.8 and 80%for sample 1 and 41.1, 73.62, 95.7 and 99.14% for sample 2, respectively.

Prolonging of contact period to 72 h, the removal efficiencies were 51.3, 85, 91 and 100% for sample 1 and 71.17, 95.09, 100 and 100% for sample 2, respectively. The highest efficiencies obtained after applying 3 and 4 g of the modified Rice Straw for 72 h with all Pb was removed from investigated water samples.

It is observed that the Pb removal efficiency obtained after 72 h by applying 4 g of raw Rice Straw to water sample was lower than that obtained after applying 3 g only. This means that some of lead captured by the adsorbent released again into the water.

So, the optimum adsorbent weight from raw Rice Straw and modified Rice Straw for the removal of Pb metal ion was 3.0 and 4.0 g, respectively and the optimum contact time was 72 h for both adsorbents.
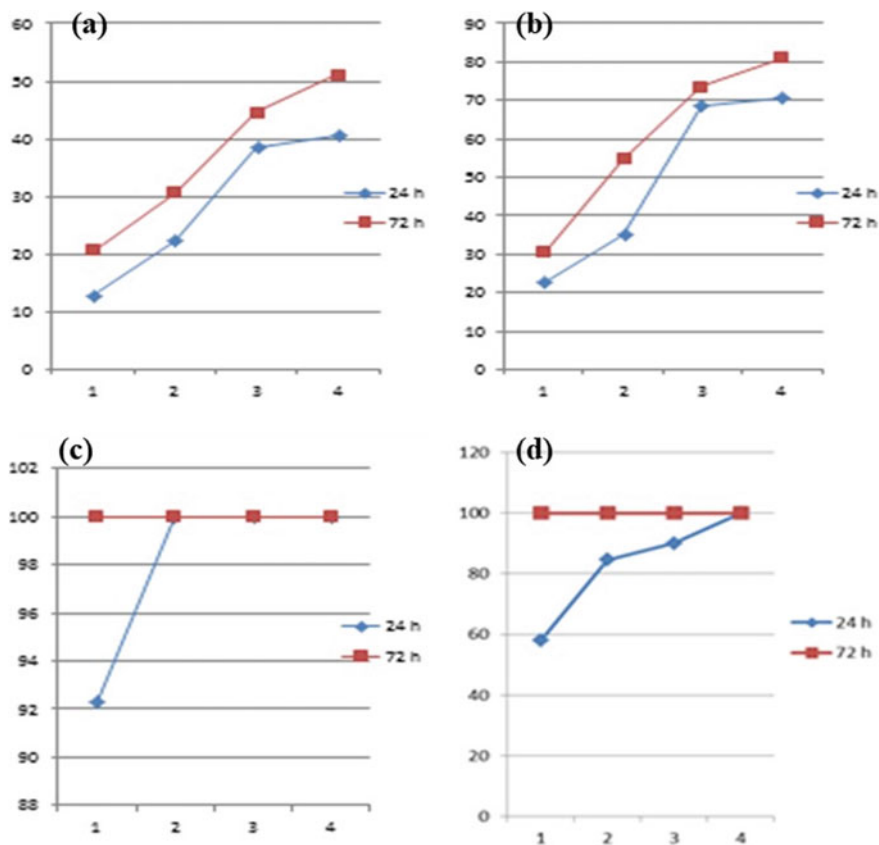
6 Effect of Adsorbent Weight

The adsorbent weight is an important parameter in adsorption studies because it determines the capacity of adsorbent for a given initial concentration of metal ion solution. The amount of adsorbent decides the extent of available surface binding sites for adsorption. Hence, the % removal of adsorbate increases with adsorbent dosage. The effect of variation of adsorbent amount on the removal of metal ions by raw and modified Rice Straw was studied by varying adsorbent amount from (1 to 4 g). It is apparent that the metal ion concentration in solution decreases with increasing adsorbent amount for a given initial metal concentration [29].

7 Effect of Contact Time

The removal of metal ions from solution in equilibrium time is effective factor. Increasing of the contact time is accompanied with enhancing of uptake of both metal ions due to the decreased coefficient of mass transfer for diffusion controlled reaction between the metal ions and the adsorbent [30]. Equilibrium time for the removal of metal ions is released from several experiments which were carried in aqueous solution at initial concentration. The contact time varied from 24 to 72 h and the observed relation between contact time and removal efficiency is in linearly proportion [20]. The rate of ion sorption is faster for metal ion at initial stage as cause to large number of available sorption sites for adsorption. For the initial blank surface, adsorption proceeded with a high rate. At the end, the adsorption rate is slower probably due to active sites become saturated and equilibrium is stabilized [31]. The effect of adsorbent weight and contact time on removal efficiencies of heavy metals by Rice Straw-$CoFe_2O_4$ Ferrite Nanocomposite is shown in Figs. 9 and 10.

In adsorption process, the most important factor which has a great impact is surface area. This is due to the fact that decrease in a particle size is accompanied with more number of binding sites for adsorption. Waste surface of agriculture is porous and which contain mesoporous, micro-pores, and macro-pores. Along with volume, area and diameter of pores are also influencing factors. Degree or extent of diffusion is determined by volume and diameter of pore for pollutant molecules into the pores. Diffusion is depended on the pore diameter and size of the molecule. If the diameter of adsorbate molecule is smaller than the pore diameter, then the molecule diffuses deeper into the pore. From that finding, the surface area is influenced on the number of sorption site [32].
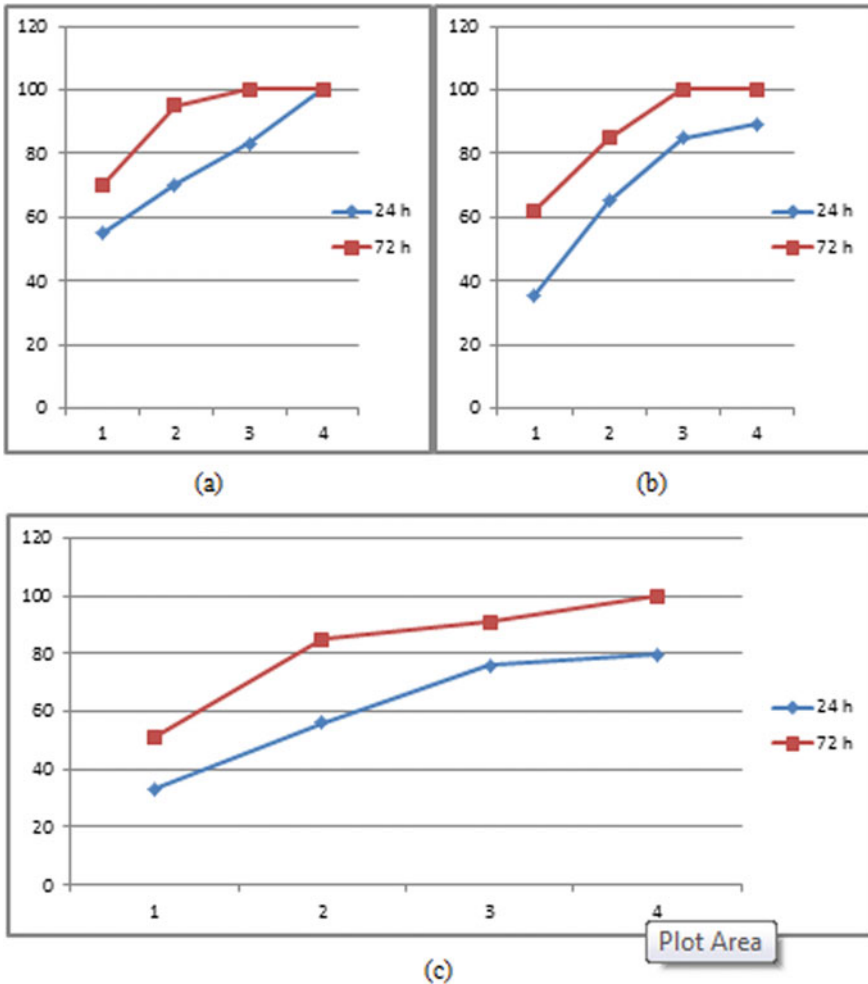
Fig. 9 Effect of adsorbent weight (*x*-axis) and contact time on removal efficiency (*Y*-axis) of **a** Fe metal ion, **b** Mn metal ions, **c** Cu metal ions and **d** Cd metal ions by modified Rice Straw

Cellulose of Rice Straw can provide binding sites for heavy metals, so it is potential adsorbent for heavy metals when used as adsorbent without coating the CoFe₂O₄, but the yield of removal is low and difficult separation of adsorbent from solution. Other site removal of heavy metal with Rice Straw-coating CoFe₂O₄ nanoparticles is higher yield of heavy metals because of the high surface area to volume ratio of Rice Straw-CoFe₂O₄ nanocomposites [33].

8 Adsorption Mechanism

It can be seen in Fig. 11 that -OH groups of the Rice Straw have negative dipole moments, and the surface of CoFe₂O₄ nanoparticles has a partial positive charge, hence these different charges, negative and positive, can attract each other [33].

Fig. 10 Effect of adsorbent weight (on *x*-axis) and contact time on removal efficiency (on *y*-axis) of **a** Zn metal ions, **b** Ni metal ions and **c** Pb metal ions

On the other hand, for adsorption of heavy metal ions by RS/CoFe$_2$O$_4$ nanocomposite, CoFe$_2$O$_4$ nanoparticles act as a magnet when the metal ions approach the composite, their surface change from positive charge to a negative charge as CoFe$_2$O$_4$ nanoparticles is acted as temporary dipole, it means there will be cationic interaction between CoFe$_2$O$_4$ nanoparticles and metal ions. Therefore, the interaction is physical interaction.

The suitable dispersion of nanoparticles as well as superior accessible active sites could be of interesting for the higher removal of metal ions by RS/ CoFe$_2$O$_4$ nanocomposite than with raw RS. The dispersion of nanoparticles sites on the surface of RS is better which provides more available adsorption for heavy metal ions. After
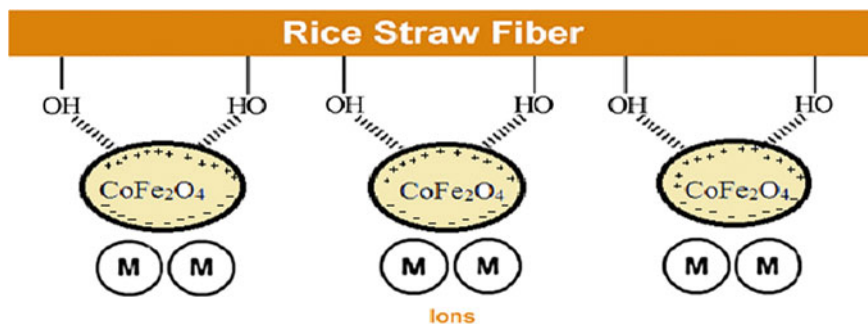
Fig. 11 Schematic illustration of adsorption process for heavy metals by Rice Straw-CoFe$_2$O$_4$ nanocomposite

adsorption, the CoFe$_2$O$_4$ nanoparticles on the surface of RS separated to adsorbent superparamagnetism as magnetic separation [24].

9 Conclusion

This study shows that the adsorption of metal ions by the modified Rice Straw was suitable as compared with the unmodified adsorbent from wastewater. Modification of Rice Straw with (CoFe$_2$O$_4$) nanoparticles, and practically use on adsorption ions from wastewater, as it gives higher adsorption than unmodified Rice Straw. The adsorption study showed that physically attraction between different charges was responsible for metal ions removal. The results have shown that RS/CoFe$_2$O$_4$ nanocomposite exhibiting elimination with highly efficiency for of heavy metal ions as good adsorbent from wastewater. From these studies, we have obtained the optimum conditions for the removal by adsorption mechanism involved mainly is of electrostatic attraction.

References

1. Taha A, El-Mahmoudi A, El-Haddad I (2004) Pollution sources and related environmental impacts in the new communities southeast Nile Delta. Egypt, Emirates Journal for Engineering Research 9:35–49
2. Kadirvelu K, Thamaraiselvi K, Namasivayam C (2001) Removal of heavy metals from industrial wastewaters by adsorption onto activated carbon prepared from an agricultural solid waste. Biores Technol 76:63–65
3. Saha BC (2003) Hemicellulose bioconversion. J Ind Microbiol Biotechnol 30:279–291
4. El-Sayed G, Dessouki H, Ibrahim S (2010) Biosorption of Ni (II) and Cd (II) ions from aqueous solutions onto rice straw. Chem Sci J 9:1–11
5. Osman HE, Badwy RK, Ahmad HF (2010) Usage of some agricultural by-products in the removal of some heavy metals from industrial wastewater. J Phytol 2:51–62

6. Hillie T, Munasinghe M, Hlope M, Deraniyagala Y (2006) Nanotechnology, water and development. Meridian Institute, Washington

7. Ambashta RD, Sillanpää M (2010) Water purification using magnetic assistance: a review. J Hazard Mater 180:38–49

8. Girginova PI, Daniel-da-Silva AL, Lopes CB, Figueira P, Otero M, Amaral VS, Pereira E, Trindade T (2010) Silica coated magnetite particles for magnetic removal of Hg^{2+} from water. J Colloid Interface Sci 345:234–240

9. Feng J, Zhang D-D, Liu Y-F, Bai Y, Chen Q-D, Liu S-Y, Sun H-B (2010) Magnetic nanofilm of Fe_3O_4 for highly efficient organic light-emitting devices. J Phys Chem C 114:6718–6721

10. Hu J, Lo IM, Chen G (2007) Comparative study of various magnetic nanoparticles for Cr (VI) removal. Sep Purif Technol 56:249–256

11. Wang X, Zhao C, Zhao P, Dou P, Ding Y, Xu P (2009) Gellan gel beads containing magnetic nanoparticles: an effective biosorbent for the removal of heavy metals from aqueous system. Biores Technol 100:2301–2304

12. Balakrishnan P, Veluchamy P (2015) Synthesis and Characterization of $CoFe_2O_4$ Magnetic Nanoparticles using Sol-Gel Method. Int J ChemTech Res 8:271–276

13. Zhang D, Zhang X, Ni X, Song J, Zheng H (2006) Synthesis and characterization of $CoFe_2O_4$ octahedrons via an EDTA-assisted route. J Magn Magn Mater 305:68–70

14. Houshiar M, Zebhi F, Razi ZJ, Alidoust A, Askari Z (2014) Synthesis of cobalt ferrite ($CoFe_2O_4$) nanoparticles using combustion, coprecipitation, and precipitation methods: a comparison study of size, structural, and magnetic properties. J Magn Magn Mater 371:43–48

15. Baykal A, Deligöz H, Sozeri H, Durmus Z, Toprak MS (2012) Triethylene glycol stabilized $CoFe_2O_4$ nanoparticles. J Supercond Novel Magn 25:1879–1892

16. Zhao D, Wu X, Guan H, Han E (2007) Study on supercritical hydrothermal synthesis of $CoFe_2O_4$ nanoparticles. The Journal of supercritical fluids 42:226–233

17. Sivakumar M, Kanagesan S, Babu RS, Jesurani S, Velmurugan R, Thirupathi C, Kalaivani T (2012) Synthesis of $CoFe_2O_4$ powder via PVA assisted sol–gel process. J Mater Sci: Mater Electron 23:1045–1049

18. Bortnic R-A, Goga F, Mesaroş A, Nasui M, Vasile BS, Roxana D, Avram A (2016) Synthesis of cobalt ferrite nanoparticles via a sol-gel combustion method. Stud Univ Babes-Bolyai, Chem 61:213–222

19. Yavuz CT, Prakash A, Mayo J, Colvin VL (2009) Magnetic separations: from steel plants to biotechnology. Chem Eng Sci 64:2510–2521

20. Al-Nagaawy A, Shalaby N (2009) Efficiency of two agricultural wastes for removing copper and lead from wastewater. In: Proceedings of the 2nd global fisheries and aquaculture research conference, Cairo International Convention Center, 24–26 October 2009, Massive Conferences and Trade Fairs, pp 39–51

21. Sharma H, Singh N, Singh SB, Devi T (2014) Synthesis and characterization of cobalt ferrite ($CoFe_2O_4$) nanoparticles by sol-gel autocombustion method. Invertis J Sci Technol 7:78–84

22. Mostafa KM, Samarkandy AR, El-Sanabary AA (2012) Harnessing of chemically modified rice straw plant waste as unique adsorbent for reducing organic and inorganic pollutants. Int J Org Chem 2:143–153

23. Parker C (1972) Water analysis by atomic absorption spectroscopy. Varian techtron

24. Khandanlou R, Ahmad MB, Masoumi HRF, Shameli K, Basri M, Kalantari K (2015) Rapid adsorption of copper (II) and lead (II) by rice straw/Fe_3O_4 nanocomposite: optimization, equilibrium isotherms, and adsorption kinetics study. PLoS ONE 10:1–19

25. Wu X, Yu H, Dong H, Geng L (2014) Enhanced infrared radiation properties of $CoFe_2O_4$ by single Ce^{3+} doping with energy-efficient preparation. Ceram Int 40:5905–5911

26. Vasundhara K, Achary S, Deshpande S, Babu P, Meena S, Tyagi A (2013) Size dependent magnetic and dielectric properties of nano $CoFe_2O_4$ prepared by a salt assisted gel-combustion method. J Appl Phys 113:194101–194110

27. Trad TM, Alvarez RM, McCumiskey EJ, Taylor CR (2011) Capped $CoFe_2O_4$ nanoparticles: non-hydrolytic synthesis, characterization, and potential applications as magnetic extractants and in ferrofluids. Ceram Trans 229:155–162

28. El Nabawi A, Heinzow B, Kruse H (1987) As, Cd, Cu, Pb, Hg, and Zn in fish from the Alexandria region, Egypt. Bull Environ Contam Toxicol 39:889–897
29. Elham A, Hossein T, Mahnoosh H (2010) Removal of Zn (II) and Pb (II) ions using rice husk in food industrial wastewater. J Appl Sci Environ Manag 14:159–162
30. Buasri A, Chaiyut N, Ponpatcharasakul N, Artsalee P, Potisook S (2007) Factors affecting the removal of copper (II) and zinc (II) from aqueous solutions with clinoptilolite. J Res Eng Technol 4:1–17
31. Pehlivan E, Altun T, Parlayıcı S (2009) Utilization of barley straws as biosorbents for Cu^{2+} and Pb^{2+} ions. J Hazard Mater 164:982–986
32. Nguyen T, Ngo H, Guo W, Zhang J, Liang S, Yue Q, Li Q, Nguyen T (2013) Applicability of agricultural waste and by-products for adsorptive removal of heavy metals from wastewater. Biores Technol 148:574–585
33. Ding Y, Jing D, Gong H, Zhou L, Yang X (2012) Biosorption of aquatic cadmium (II) by unmodified rice straw. Biores Technol 114:20–25

Magnetic Ferrites-Based Hybrids Structures for the Heavy Metal Removal

Muhammad Khawar Abbas, Effat Yasin, Muhammad Munir Sajid, Naveed Akhtar Shad, Kanwal Akhtar, Anita Manhas, Surender K. Sharma, and Yasir Javed

Abstract Adsorption is a major process for heavy metal removal and the research trend is focused toward the applications of new technologies in order to intensify the already existing processes. Intrinsic properties of magnetic materials (arrangement and surface-to-volume ratio) of adsorbate and adsorbent are critical for satisfactory results. Magnetic field strength plays an important role as it indicates the alignment of spins with the magnetic field to provide adsorbate mobility and generate heterogeneity at adsorbent surface. Applications of magnetic field for intensification of adsorption process provide environment friendly, safe and economic alternative. This chapter describes different types of magnetic ferrites-based hybrids for heavy metal removal. Surface modification of magnetic nanohybrids through different surface modification strategies and general adsorption mechanisms for different types of pollutants are discussed comprehensively. Major thrust of this chapter is to provide information about different features of magnetic ferrites for their potential application as adsorbent for heavy metal removal.

Keywords Ferrites · Heavy metals · Adsorption kinetics · Adsorption isotherms

1 Introduction

Water is enlisted among the essentials for living things and is needed in all kind of activities including domestic cares, industry and agriculture; consequently, its

M. K. Abbas · E. Yasin · K. Akhtar · Y. Javed (✉)
Magnetic Materials Laboratory, Department of Physics, University of Agriculture, Faisalabad, Pakistan

M. K. Abbas · E. Yasin · M. M. Sajid · N. A. Shad
Department of Physics, Government College University, Faisalabad, Pakistan

A. Manhas
Department of Physics, H.P. University, Shimla, H.P. 171005, India

S. K. Sharma
Department of Physics, Federal University of Maranhao, Sao Luis, Brazil

Department of Physics, Central University of Punjab, Bathinda 151401, India

quality influences human life in food, energy, health and economy. Development of affordable and efficient techniques is needed to access healthy water to humanity as harmless water to drink is our basic need to protect our life [1]. Worldwide water pollution is one of the serious health and environment problems. The types of pollutants include microbial and radioactive species, heavy metals, organic and inorganic materials. The quality of water may be affected by agricultural activates, industrial discharge and mismanagement of hazardous materials, etc. Many approaches are being used for water purification such as precipitation [2], particle trade oxidation [3], electrochemical medications [4], buoyancy [5], adsorption [6], invert osmosis [7], filtration [8] and biosorption [9]. However, there are certain pollutants which cannot be removed completely by the above-mentioned methods, and there is also plenty of room available for work on the present techniques of water purification [1].

Nano-magnetism is of a great interest for various potential applications. It is important for general miniaturization of devices as well as physical properties are drastically changed from bulk-size magnetic material [10]. For example, iron is ferromagnetic materials in bulk form, whereas at nanoscale, presented superparamagnetic behavior. In magnetic NPs, the facts are more interesting as NPs have size comparable to magnetic domains [11, 12]. On the basis of above discussion, two kinds of behavior in nanoparticles are observed named as;

(a) single-domain ferromagnetism NPs
(b) superparamagnetic NPs

An assembly of single-domain NPs also showed hysteresis (magnetization vs field dependence) loop. Bulk conventional ferromagnets (multi-domain) holds direct proportionality between magnetization and applied field because domain walls movement enlarges the domain size which leads to increase net magnetization. Whereas in the case of an array of single-domain nanoparticles, the magnetic moments of different particles interact with each other and aligned all in the direction of the applied field.

In recent years, water treatment using technology has arisen as an important area of research due to its fast and economical process. Researchers have investigated the potential of different nanomaterials for water purification. This includes removal of heavy metals or degradation of organic dyes from the textile effluents [13]. From inorganic nanomaterials, magnetic NPs have emerged as an important candidate in water purification and enormous studies have been reported in the literature. In magnetic nanomaterials, iron oxide and iron oxide-based nanomaterials are very encouraging for water decontamination especially from heavy metals and organic dyes as magnetic NPs can be separated easily by external magnetic field as shown in Fig. 1 [14, 15]. Moreover, magnetic NPs have large surface area and high level of stability. Ferrites are the most influential class of iron oxide-based nanomaterials and being explored extensively during the last two decades for their properties, structure and applications [16, 17]. This chapter will cover basic concepts about magnetic materials, ferrites, their structures and applications for the removal of heavy metals.
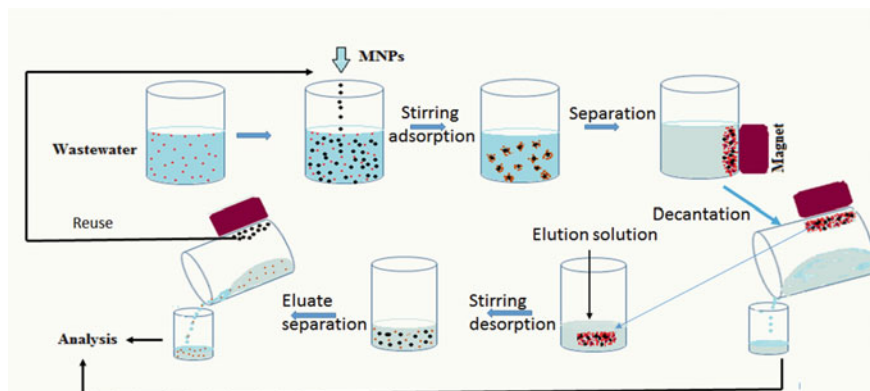
Fig. 1 Schematic representation of magnetic nanoparticles utilization for pollutant adsorption and desorption. Reprinted with permission from [15]

2 Magnetic Materials

The amount of magnetization for bulk material is increased by domain walls nucleation and rotation. Magnetization vector rotates away from the easy axis of magnetization; moreover, only coherent magnetization rotation is observed as domain walls movement is not possible for single-domain sample. In a single-domain range, coercivity varies as a function of particle diameter ranges 10–100 nm [18]. Sometimes for the specific anisotropic materials, the limit of single domain can be extended up to several hundred nanometers. However, the magnetization would not be stable, and the particle is referred as superparamagnetic if the thermal energy is sufficiently larger to overcome the anisotropy energy. Multiple NPs with each having own magnetic moment can simply get saturated in the presence of external field. However, the thermal fluctuations (both M_r and H_c are zero) results in magnetization returning to zero after the removal of external field [19, 20]. The term "superparamagnetism" refers to this behavior, which is like conventional paramagnets, but with a difference that it is joint magnetic moment of the whole particle rather than the individual electronic spins featuring this fluctuating response. Blocking temperature is considered the most important quantity to define the magnetic behavior of the assembly of particles due to its general transition from ferromagnetism to superparamagnetism. At small particle volume, thermal fluctuation became dominant. Development of synthesis routes for high anisotropic materials is a way to control these fluctuations. High saturation magnetization along with low-saturation field and no remnant magnetization have confirmed superparamagnetic materials as an ideal candidate for biomedical applications [21, 22]. Ferrites are an important class of materials, have applications in biomedical, catalysis and other fields.

2.1 Ferrites

Ferrites are basically ceramics, mixed metal oxide having general chemical composition $M^{2+} Fe_2^{3+} O_4^{2-}$ where M is a divalent metal ion, i.e., manganese (Mn^{2+}), copper (Cu^{2+}), nickel (Ni^{2+}), cobalt (Co^{2+}), magnesium (Mg^{2+}) and zinc (Zn^{2+}), etc. In general, any ferromagnetic ceramic material can be termed ferrite. Both soft and hard ferrites are needed in an ever-expanding industry due to their remarkable electrical and magnetic properties which is evident from the intimated world of ferrites production [23, 24].

To understand the phenomenon of magnetism in ferrites, the knowledge of spin coupling of unpaired metal ions in oxides is essential. The oxide ions can mediate the coupling of spins by super-exchange if it is shared by two metals ion. Depending on the symmetry of orbitals involved and orbital filling, coupling can be antiferromagnetic or ferromagnetic. The Goodenough-Kanamori rules prognosticate super-exchange coupling of electron spins in transition metal ions that results in local magnetic ordering (ferromagnetic vs antiferromagnetic). The strongest coupling in ferrites is between ions on neighboring tetrahedral and octahedral sites. These two sites have reliably antiferromagnetic order of spin [25, 26].

In spinel or/and inverse spinel crystal, all tetrahedral and octahedral sites are coupled together. It is worth to quote that ions will have same orientation on tetrahedral sites, whereas will have opposite orientation on octahedral sites. If the number of spins at two sites is the same, the material will be antiferromagnetic as in the case of Fe_3O_4, $CoFe_2O_4$ and $NiFe_2O_4$, whereas if the spins have an unequal number, then the material will be ferromagnetic [27]. This can be illustrated for Fe_3O_4 (magnetite or magnetic oxide) where spins of Fe^{3+} (ferric cation) sites cancel each other because half of them are down and half is up. However, for ferromagnetic, four unpaired electrons are aligned in crystal in the same way [28, 29].

Ferrites can be classified into following types on the basis of their crystal structure and magnetic properties;

(a) Spinel: general formula, MFe_2O_4, while M = can be any metal (Mn, Fe, Co, Ni, Co, Zn and etc.), (b) Garnet: general formula, $M_3Fe_5O_{12}$, while M is rare-earth cation [27].

(b) Hexaferrite: For example, $SrFe_{12}O_{19}$ and $BaFe_{12}O_{19}$ and (d) orthoferrite, $MFeO_3$, M is rare-earth cation. Among all mentioned types, special attention has been given to spinel ferrite NPs [30].

Spinel ferrites have cubic structure, with no preferred direction of magnetization. Through the application of external magnetic field, it can be relatively easy to change magnetization as they exhibit magnetically soft character [31]. Most common example of ferrite is Fe_3O_4 which has complex unit cell and its subunits can be understood as shown in Fig. 2. The subunit shows that four oxygen atoms are present at four vertices of each of the cubes form complete unit cell. There are two types of sites which the transition metal ions can occupy, tetrahedral sites (A) and octahedral sites (B). In the spinel unit cell, only eight out of 64 possible tetrahedral sites are
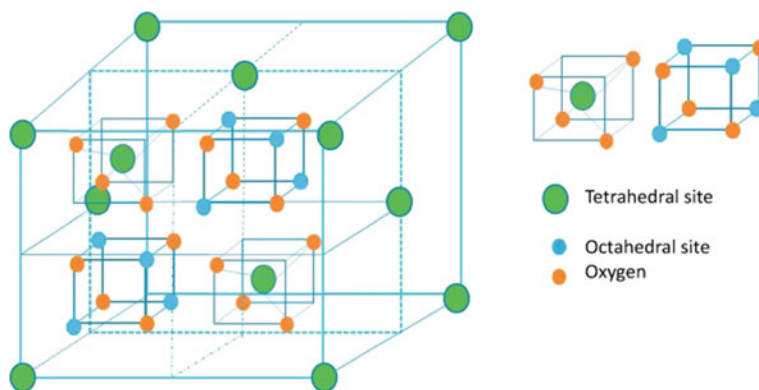
Fig. 2 Spinel structure of transition metal sites that are octahedral- and tetrahedral- coordinated by oxygen anions. Reprinted with permission from [15]

engaged and 16 out of 32 possible octahedral sites are occupied. Therefore, one A site and two B sites are occupied, in each formula unit of Fe_3O_4 [29, 32].

According to observations, the moment of Fe_3O_4 is 4pB per formula unit**.** The interaction between the three moments may not be clear; however, assuming to trivalent moments cancel each other as in antiferromagnetic Fe_2O and the net moment of divalent iron is FeO. The reason behind seeking special intention by spinel ferrites NPs is its tremendous magnetic properties and versatility of applications in numerous areas including water and wastewater management, catalyst, biomedical and electronic devices [33]. Its simple chemical composition is another add on benefit among many. These composites are stable, easy to generate and can be reused in repetitions without losing properties so reduces treatment cost for water purification and wastewater treatment [34, 35].

3   Synthetic Routes of Preparation of Magnetic NPs

In the recent development, several approaches for synthesizing NPs became a range of research in the arena of nanotechnology. These approaches considered mechanisms for controlling shape, size and chemical composition of NPs [36].

3.1   Mechanical Milling Method

In this method, production of powders is basically associated with the mechanical milling, in which bulk material is reduced to NPs. This happens by rubbing small surfaces with one another in the presence of agitators or jets having high speeds to

produce friction and huge pressure. During the whole process, the parent bulk material has to suffer elastic strain, structural defects, chemical disorders, which results in nanostructures. There are different ferrite NPs produced by ball milling method [37]. Ding et al. [38] prepared ultra-fine nickel ferrite ($NiFe_2O_4$) particles by combining co-precipitation and mechanical alloying methods. Pure nickel ferrite phase was observed by directly using mechanical milling of hydroxide precursor. Ultra-fine particles with a size of 10 nm have shown soft magnetic and superparamagnetic character. Baghbaderani et al. [39] synthesized $Fe_{45}Co_{45}Ni_{10}$ alloy, investigated magnetic properties and mechanism of nanostructure formation. A simultaneous increase in dislocation density and low-angle grain boundaries formation was suggested. After milling for 20–35 h, nanostructures have grain size, lattice parameter, saturation magnetization and coercivity values of 10 nm, 0.28512 nm, 186 emu/g and 32 Oe, respectively. Rashidi and Ataie [40] synthesized single-phase cobalt ferrite/polyvinyl alcohol composites with a size of 20 nm via mechanical alloying method and embedded into polymer matrix by intensive milling. By increasing polyvinyl alcohol concentration and milling time, cobalt ferrite dispersed more homogenously in the polymer matrix. Evaluation of magnetic properties of nanocomposite showed continuous decrease in anisotropy, coercivity and saturation magnetization compared to pure cobalt ferrite. But due to domain wall mechanism, coercivity was enhanced by increasing amount of polyvinyl alcohol. Hosseini and Bahrami [41] studied magnetic and structural properties of nanocrystalline powders of Fe–Si–Ni alloys. Mechanical alloying process was used. Characterization of samples with different chemical ratio and milling time revealed grain size variation from 8 to 19 nm. Crystallite size and coercivity decreased by increasing mechanical alloying time. $Fe_{87}Si_{10}Ni_5$ composition was obtained after 70 h milling time with highest saturation magnetization. Waje et al. [42] prepared spinel cobalt ferrite NPs using mechanically ball milling method. Variation in parameters such as milling time, ball-to-powder weight ratio and sintering temperature revealed that milling time and ball-to-powder ratio played a vital role in crystallite size. However, for the sintered samples, saturation and coercivity showed inverse relation. Rashidi and Ataie [43] synthesized cobalt ferrite NPs by mechanical alloying of α-Fe_2O_3 and $CoCO_3$ powder using ball milling method in air. Milling time affected the morphology, phase composition and magnetic properties of the prepared powder. Single-phase $CoFe_2O_4$ NPs of mean size 15 nm, saturation magnetization 52.19 emu/g and coercivity 831.95 Oe were observed after 25 h milling time. Uhm et al. [44] prepared nanocrystalline Ni-doped TiO_2 by mechanical alloying. Three phases of TiO_2 were observed, i.e., rutile, anatase and brookite in the powder. Magnetic hysteresis loops were measured at room temperature and showed increase in coercivity with the addition of Ni concentration.

3.2 Co-precipitation Method

Co-precipitation is the simplest, economical and productive technique for the synthesis of NPs with high yield. This is a pH-dependent reaction where pH of the

solution varies to basic level and metal precursors react and form NPs. This reaction is eco-friendly as no toxic gases evaporate into the air. Size and shape of the NPs can be controlled by changing precursor concentration, pH, reaction time, stirring time, etc. The tendency to agglomerate particles is the major problem to prepare magnetic NPs (MNP) by co-precipitation method. Salavati-Niasari et al. [45] prepared magnetite (Fe_3O_4) nanocrystals by chemical co-precipitation method assisted by surfactant (octanoic) and reported the size range of 25 nm with ferromagnetic properties. Matei et al. [46] synthesized magnetic iron oxide NPs by co-precipitation and characterize for removal of heavy metals from wastewater. Zhao et al. [47] produced Fe_3O_4 NPs for localized hyperthermia applications by a co-precipitation method. Agglomeration was controlled by using dodecylbenzene sulfonic acid. The synthesized NPs were spherical in shape with sizes range from 10 to 30 nm. Surendra et al. [48] synthesized magnetic NPs with sizes from 6 to 14 nm by varying the precursor to surfactant concentration in co-precipitation method. Wang et al. [49] prepared monodispersed Fe_3O_4 magnetic NPs (12 nm) by co-precipitation method using oleic acid and tween 80 as surfactants. Co-precipitation method is widely used for the preparation of ferrite NPs because of its ease of implementation and less-hazardous materials and procedures.

3.3 Sol–Gel Method

This procedure uses chemicals for the formation of gel. The steps performed after mixing of chemical are precipitation and calcination, respectively. A fluid suspension of a colloidal solid or aggregates, usually metal hydroxyl particles in a liquid called sol, is used for the casting of gel. Capping agents are added to avoid aggregates. Factors considered important in sol–gel are hydrolysis and condensation which influence structure, morphology and properties of the nanomaterials (Fig. 3). Surface
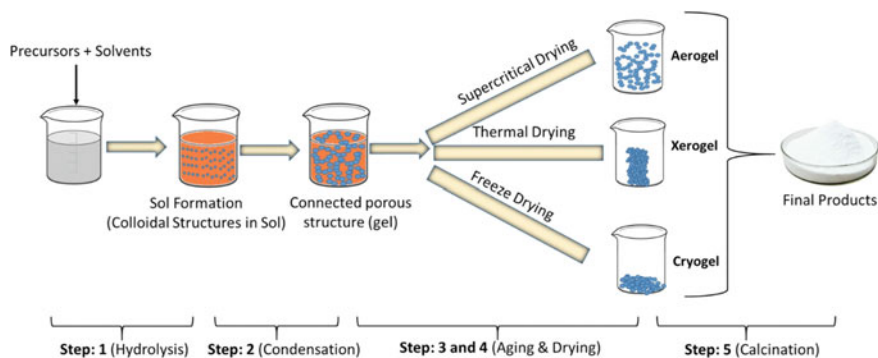
Fig. 3 Different steps involved in the sol–gel synthesis method. Reprinted with permission from [55]

properties of newly build materials are greatly affected by the variation in the value of pH because this can change the porosity in the gel. Saldivar-Ramirez et al. [50] prepared magnetic nanoparticles by sol–gel method and reported potential applications in cancer therapy by heating process. Chen and He [51] prepared $NiFe_2O_4$ NPs by the sol–gel method and used polyacrylic acid (PAA) as a chelating agent. Characteristic revealed that pure spinel structure with diameter 5–30 nm and specific surface area of 20–55.2 m^2/g can be achieved when gel precursor with different ratios of poly acrylic acid is calcined at 300 °C in air for two hours. Poly acrylic contributed not only as chelating agent, but its combustion heat also worked to increase the crystallinity of $NiFe_2O_4$ NPs, as molar ratio of polyacrylic to total metal ion has inverse relation with particle size but direct relation with crystallinity. Demonstration of its magnetic analysis showed $NiFe_2O_4$ NPs as superparamagnetic with saturation magnetization value of 0.19 emu/mol at 298 K. Goerge et al. [52] synthesized nickel ferrite through sol–gel procedure with variable grain size. $NiFe_2O_4$ attained maximum coercivity at grain size of 15 nm and hold inverse relation with further increase in grain size. Thota and Kumar et al. [53] synthesized nickel oxide NPs sizes ranging from 4 to 22 nm via sol–gel process. Precursors nickel acetate tetrahydrate and oxalic acid involve in gel formation at 110 °C for 24 h to form nickel oxalate dehydrate, while ethanol was taken as solvent. NiO powder yields after calcination at 300 °C. NiO showed absence of spin glass behavior and presented ferromagnetic behavior. The increase in blocking temperature (T_B) as well as energy band gap (E_g) was observed with decreasing particle size. Guan et al. [54] prepared magnetic silica particles coated with hydroxy-terminated multi-walled carbon nanotubes (MWCNTs–OH) via sol–gel method. Results proved sol–gel as a simple, effective and feasible technique. Extraction efficiencies of different estrogens were calculated as diethylstilbestrol (95.9%), estrone (93.9%) and estriol (52.4%) under optimum conditions.

3.4 Polyol Method

In this technique, fine metallic particles can be produced by the reduction of dissolved metallic salt and direct metal precipitation in polyol solution at elevated temperatures. In the polyol process, ethylene glycol (poly) acts as a solvent. Solubility of metal reactants in polyols can be high or low. After this, stirred solution is heated to boiling temperature of polyol to induce reaction under inert gas environment. At the time of precipitation, controlling the kinetics leads to well-defined size and shape of the NPs. Park et al. [56] synthesized silica-coated magnetic nanoparticle via polyols technique and reported labeling human cord-blood-derived mesenchymal stem cells. Results demonstrated that MNPs@SiO_2 were biocompatible and useful tools for human MSC labeling and bioimaging. Shen et al. [57] prepared Fe_3O_4 magnetic NPs by combining co-precipitation and polyol method for surface functionalization, possessed different size range 8, 12 and 32 nm. It was found that with the decrease in particle size, surface area also increased and consequently adsorption capacity of Fe_3O_4 improved. The factors influencing the adsorption of metal ions were pH,

temperature, amount of adsorbent and contacting time. Laurent et al. [58] coated the surface of the nanoparticle with hydrophilic polyol ligands. An easy dispersion in water media and other polar solvents were observed. Narrower size distribution of the NPs was observed than traditional methods. Cai et al. [59] had been successfully synthesized magnetite NPs at elevated temperature in liquid polyols. It was proven that for determining the morphology and colloidal stability of NPs, polyol solvent played a crucial role. Characterization showed that these NPs were highly crystalline, monodisperse and superparamagnetic at room temperature. Due to coating of hydrophilic polyol ligands layer on NPs, they dispersed easily in aqueous media and other polar solvents. Caruntu et al. [60] prepared well-dispersed Fe_3O_4 NPs with size 6.6 and 17.8 nm in the non-aqueous solution of polyols. Investigation revealed that smaller nanocrystals showed superparamagnetism whereas biggest particles behaved like ferromagnetic at room temperature. Disordered spin configuration on the surface affected the saturation magnetization. Couto et al. [61] synthesized nickel NPs as protective agent via modified polyols route (poly N-vinilpyrrolidone). Sodium borohydride acts as a reducing agent. Obtained sample of different ratios of nickel indicated face-centered cubic structure with the diameter (3.8 nm). Dipolar magnetic coupling between particles caused single-domain non-ideal superparamagnetism.

3.5 Green Synthesis

Other techniques for the formation of NPs are bound to many constraints as being expensive, high temperature and pressure requirement, toxic chemicals production, etc. Due to these disadvantages, researchers are focusing on synthesizing magnetic NPs by using plants and their extracts, and this technique is called green synthesis. In this approach, one can control morphology, range of particle size and assembly. Its benefits include cost-effectiveness and the process is environment friendly. In green synthesis of NPs, organisms such as bacteria, plant and fungi play important roles during the reaction. Plant extracts from different species and parts can be taken such as flowers, seeds, leaves and stems for the synthesis of NPs as these contain biomolecules such as terpenoids, enzymes, vitamins, flavonoids, protein, alkaloids, amino acid and phenolic acids. (Fig. 4). These biomolecules act as reducing agent. The reducing agent can mold metal ions for production of NPs of different sizes and shapes. For example, Pelargonium graveolens extract and Trigonella foenumgraecum extract cut ions of gold into NPs of size 20–40 nm and 15–25 nm, respectively. Phenolate ions from plants are useful as it can transfer electrons to metal ions in the process of synthesizing nanoparticle. For example, bioreduction of $AgNO_3$ and $HAuCl_4$ to form NPs with eugenol, a leading phenolic of clove extract. Formation of NPs because of bioreduction by extracts of plants also depends on many other parameters such as reaction temperature and pH value. It is found that metal ions nucleate slowly at low-pH solutions and cause agglomeration which produce larger particles. On the other hand, higher pH value helps in the growth of nanosized
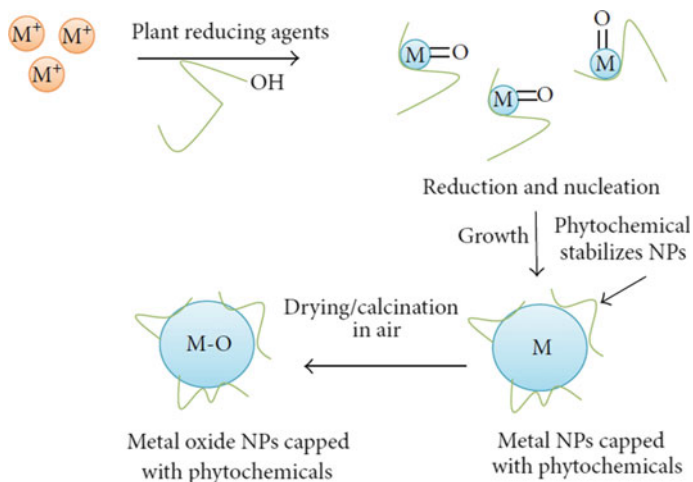
Fig. 4 Different kinetics involved in green synthesis for metal and metal oxide nanomaterials [65]

particles. The shape of NPs is also pH dependent. On higher pH, NPs became spherical and decahedral. Kumar et al. [62] reported synthesis of different shapes such as hexagonal, spherical and triangular with sizes 15–25 nm of Au NPs via the *Cassia auriculata* leaf extracts. At ambient temperature, $HAuCl_4 \cdot 3H_2O$ reduced in 10 mins and characteristic surface plasmon resonance was observed at 536 nm in UV–Vis spectrum. Arunachalam et al. [63] reported one pot green synthesis of Au NPs of size 50 nm using olive (*Olea europaea*) leaf hot-water extracts. It was observed that precursor takes about 20 min for the bioreduction due to high phenolic contents at room temperature. Ahmed et al. [64] synthesized purple-colored 22–35 nm size Au NPs from leaves aqueous extract of Salicornia brachiate and assessed their antibacterial efficiency toward *Pseudomonas aeruginosa*, *Escherichia coli*, *Salmonella typhi* and *Staphylococcus aureus*. Moreover, these particles in the presence of sodium borohydride reduced methylene blue dye.

4 Purification of Water from Heavy Metals

Heavy metals (Al, As, Cd, Pb, Cr, Hg, Cu, Co, Se, Mo, Ni and Zn) are the elements having atomic weights ranging from (63.546 to 200.590 g mol^{-1}) and density factor greater than 4.00 g/cm^3 and toxic in nature even in low concentrations. These metals occur in the earth's crust and are non-biodegradable in nature [66]. Although these are essential for the metabolic activities in animals and human beings in very trace amounts, their concentration above the safe level determined by World Health Organization (WHO) causes serious threats to human health. Heavy metals have the property of bioaccumulation. Their toxic nature appears by forming protein complexes,
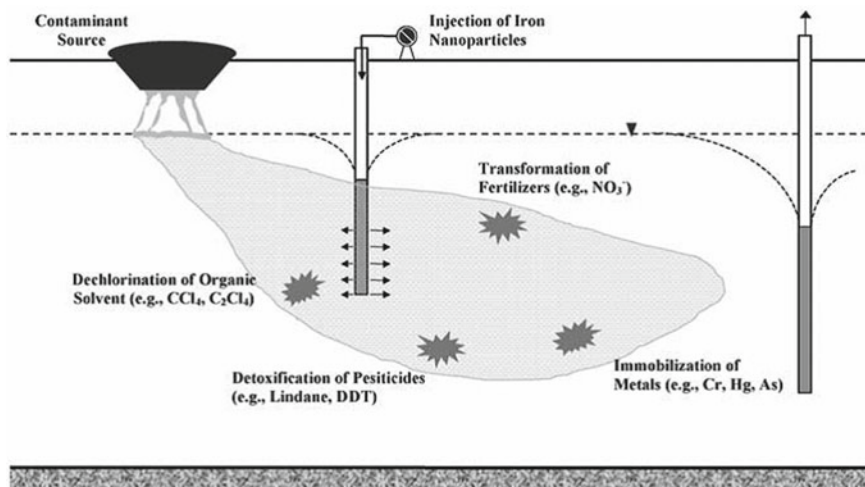
Fig. 5 Schematic representation of in situ treatment using iron particles for ground water. Reprinted with permission from [69]

where they have CA (carboxylic acid "–COOH"), thiol "–SH" and amine "–NH$_2$" groups. These mutant biomolecules start malfunctioning and result in breakdown or cell death as shown in Fig. 5 [67, 68].

Quality of surface water has been compromised over the years because of extensive farming, over-population and industrialization. Improper disposal of agricultural, domestic and industrial effluents makes water reservoirs more vulnerable to the toxic non-biodegradable contents, i.e., heavy metals. Moreover, some natural phenomenon like volcanic eruption, erosion of minerals within sediments and leaching of ore deposits also contributes to the addition of heavy metals in water [70, 71]. Heavy metals possess distinct chemical properties and are largely used in the field of electronics, mechatronics and high technological applications; consequently, they can enter the water reservoirs from various anthropogenic as well as natural geochemical sources. Once these metals dissolve in water, they can infiltrate into the food chain and become fetal to humans and animals. The other main sources include contaminated mining waste, municipality wastewater drainage, industrial waste aquatic products, urban wastewater and chiefly from electroplating and metal finishing factory zones. The new coming generations of machines can create serious problems for proper disposal of waste products containing heavy metallic contents. Aquatic sources are also facing higher concentrations of these metals [72, 73].

Heavy metals are extremely dangerous to the infants and can dent brain memory, interrupt the functioning of red blood cells (RBCs) and central nervous system (CNS) and sometimes induce psychological and physiological disorders. Higher toxicity from these metals can cause different types of cancers. Plants being irrigated by the water having higher concentration of heavy metals are observed to have morphological changes and their growth has been limited due to reduced photosynthetic

rate. Genetic mutations have also been reported in some species of plants. Exposure to heavy metallic ions can cause chlorosis, nutrient deficiencies, bleaching and oxidation stress in plants by affecting the mitochondrial functions [71, 74].

Long-term exposure of aluminum concentration (more than 50 mg/L) can cause skin damage. It is also a major factor promoting the "Alzheimer" and "Parkinson" diseases along with senile and presenile dementia [75]. Cadmium (Cd) is one of the most toxic heavy metals utilized for Ni–Cd batteries, pigments and plastics. Cd can be transmitted into atmosphere and earth by phosphate fertilizers and dumping of different wastes. Toxicity induced by Cd can cause lung cancer, bone softening in humans and animals and increase blood pressure. Cigarette smoking is a prime cause of Cd poisoning in humans. Cd concentration above 5 μg/L is considered carcinogen reported by WHO and may also cause hypertension and arteriosclerosis [76]. Chromium is widely used in the tanning industries, metal alloys and pigments for papers, rubbers, paints and cements. Low-level exposure of Cr is observed to cause ulceration and skin irritation, whereas high concentration exposure can cause kidney and liver damage. It also affects the CNS severely. Lead is also another human carcinogen metal above 10 μg/L [77]. Mercury is poisonous and is associated with mental deterioration, hearing loss, visual impairment and muscular disorder. High concentration of lead and mercury may also result "autoimmunity syndrome": a situation when immune system attacks its own cells. Chromium is also a carcinogen associated with gastrointestinal and lung cancer. Copper (Cu) plays an important role in activating some enzymes during photosynthesis; however, photosynthesis retards significantly at the higher concentration of Cu in water used by plants [78]. In human beings, harmful effects on health have been reported. Exposure of higher concentration of Cu dust can produce irritation in mouth, nose and eyes. Long-term exposure can affect kidneys severely. Even with low concentration, Cu is found to be toxic for various aquatic animals. High concentrations of Cu in water can be neurotoxin and results in Alzheimer's disease. Arsenic (As) poisoned the blood and CNS, can cause skin and lung cancer, especially in third world countries, its presence in drinking water is causing serious effects, anthropogenic sources such as metal processing, pesticides manufacturing and their waste products are increasing the level of As in drinking water [79]. Higher concentration of iron (Fe) and manganese (Mn) in drinking water can be very toxic to newly born babies. Although their presence in trace amount in body is essential for the synthesis of hemoglobin and cell functioning. Human intestinal tract rapidly absorbs the Fe and higher concentration causes toxic effects to liver, kidneys and heart. On the other hand, higher level of Mn in water causes neurological imbalances and muscle malfunctioning. Zinc (Zn) is another important component of our food. However, its higher concentration can be health hazardous. Too much amount of Zn in water can cause queasiness, anemia and cardiovascular problems in humans [79, 80].

4.1 Pseudo-Kinetic Models and Adsorption Isotherms

For better understanding of liquid/solid adsorption behaviors of hybrid materials, basic models of kinetics and adsorption are discussed here briefly.

4.1.1 Adsorption Kinetics

The mechanism in which solute molecules are attached to the adsorbent's surface is called adsorption. This phenomenon is carried out in column or batch set up. Adsorption of different composites is usually investigated as a potential tool for the sanitization of contaminated water as well as industrial and domestic effluents. In situations where we are dealing with the treatment of wastewater, adsorption is a viable method. Adsorption kinetics has become an important factor to be comprehended before applying adsorbents. To explain the process of adsorption, linear and non-linear analysis of kinetics is used. A curve or line describing the retention rate of solute in aqueous medium to solid-phase interface at doses of adsorbents, temperature, pH and flow rate is known as adsorption kinetics. Two major reactions take part in adsorption process: physisorption (physical) and chemisorption (chemical) reactions. Physisorption is due to Van der Waals forces (interaction of weak forces) and chemisorption results from strong bonding forces between adsorbent and solute that indicate the transfer of electrons.

4.1.2 Pseudo-First-Order (PFO) Model

This is also called Lagergren kinetic model as the equation was initially introduced by Lagergren [81]. PFO model explains the adsorption of liquid–solid phase systems based on adsorption capacity. Equation 1 describe the adsorption rate of solute onto the adsorbent followed the first-order mechanism [82].

$$\frac{dq_t}{dt} = (k_1)(q_e - q_t) \tag{1}$$

where

q_t: adsorbate adsorbed (mg g^{-1}) onto adsorbent at given time t.
q_e: equilibrium adsorption capacity (mg g^{-1}).
k_1: rate constant (1/min).

The integral of Eq. (1) with boundary conditions ($t = 0$, $t = t$) and ($q_t = 0$, $q_t = q_t$) provides the linear form of Pseudo-first order expression:

$$\text{Ln}(q_e - q_t) = \text{Ln}(q_e) - k_1 t$$
$$\frac{q_t}{q_e} + \text{Ln}(q_e - q_t) = \text{Ln}\, q_e - k_1 t \tag{2}$$

Equation (2) can also be written as:

$$q_t = q_e\big[1 - \exp(-k_1 t)\big] \tag{3}$$

The value of rate constant is obtained by plotting L.H.S of Eq. (2) vs time t. If q_e is calculated by experiment, then the fractional uptake can be determined:

$$F_{(t)} = q_t/q_e \tag{4}$$

It has been found that the rate constant (k_1) is inversely proportional to the initial concentration (C_o) of the solute as more time is needed for high solute concentration (initially).

Experimental conditions affect the control mechanism; therefore, the validity of PFO model is varied under Henry regime adsorption and high sorbent dosage. In order to account experimental difference, PFO model can be modified as:

$$\frac{dq_t}{dt} = \frac{q_e}{q_t}[\, k_1(q_e - q_t)] \tag{5}$$

In linear form,

$$\frac{q_t}{q_e} + \text{Ln}(q_e - q_t) = \text{Ln}\, q_e - k_1 t \tag{6}$$

Plotting L.H.S of Eq. (6) vs time t provides better fit model as compared to Lagergren model [83].

4.1.3 Pseudo-Second Order (PSO) Model

Pseudo-second order model depends on the adsorption capability of the solid phase. This model considers that adsorption rate of solute is directly proportional to the availability of sites on the adsorbent and rate of reaction depends on the concentration of solute on the adsorbent's surface. PSO model is used to calculate the initial solute uptake and adsorbent's adsorption capacity [83].

As deriving force is directly proportional to the available active sites on the adsorbent:

$$\frac{dq_t}{dt} = k_2(q_e - q_t)^2 \tag{7}$$

Equation (7) represents the curvilinear form of PSO model; here k_2 is the rate constant. Integrating over the limits $(t = 0, t = t)$ and $(q_t = 0$ to $q_t = q_t)$, the linear form obtained is given as:

$$q_t = \frac{t}{\frac{1}{k_2}\left(\frac{1}{q_e}\right)2 + \frac{t}{q_e}} \tag{8}$$

Equation (8) can be written as:

$$\frac{t}{q_t} = \left[\frac{1}{k_2(q_e)2}\right] + \frac{t}{q_e} \tag{9}$$

Dividing by "t"

$$\frac{1}{q_t} = \frac{1}{t}\left[\frac{1}{k_2(q_e)2}\right] + \frac{1}{q_e} \tag{10}$$

Further simplification can lead us to the

$$q_t = q_e - \left[\frac{1}{k_2q_e}\right] \times \frac{q_t}{t} \tag{11}$$

Finally

$$\frac{q_t}{t} = k_2(q_e)^2 - k_2q_eq_t \tag{12}$$

Using the above mathematics, curvilinear function of PSO model is linearized to measure the distribution of error function of the same kinetic model. Among these linearized equations, Eq. (9) provides better fit results as compared to others. Second order constants can be found by plotting the term "$\frac{t}{q_e}$" vs time "t" [84].

4.2 Adsorption Isotherms

To present the quantity of solute absorbed per unit weight of "adsorbent" as a function of equilibrium concentration at fixed temperature, adsorption isotherms are used. Adsorption isotherms indicate a sequence of adsorption calculations done at fixed temperature and obtained results are plotted between adsorbed and non-adsorbed quantities. The structure of isotherms contains very valuable information related to the nature of adsorption phenomenon, analyzing the adsorption capacity of adsorbents. Langmuir, Freundlich and Sips models are used for the determination of adsorption isotherms [85, 86].

4.2.1 Langmuir Model

Langmuir isotherms were introduced in 1918. It is generally appropriate for the description of chemisorption process when transfer of electrons takes place between adsorbent and adsorbate. This model anticipates an asymptotic approach to monolayer surface coverage as the partial pressure of adsorbate reaches to saturation; once all the active sites of adsorbent are filled, there is no further adsorption over these sites [87]. In linear form, Langmuir model can be represented as:

$$\frac{C_e}{q_e} = \frac{1}{bq_m} + \frac{C_e}{q_m} \tag{13}$$

Here

q_e: Adsorbent's equilibrium adsorption capacity in mg g^{-1}.
C_e: Adsorbate's equilibrium concentration in mg L^{-1}.
q_m: Saturated single layer adsorption capacity in mg g^{-1}.
b: Equilibrium adsorption constant.

4.2.2 Freundlich Model

Freundlich equation is an empirical equation established between solute concentration over the adsorbent surface to the solute concentration in liquid with which it has contact. Herbert Freundlich put this model in 1909; it helps to explain the isothermal variation in quantity adsorbed by unit mass of solid adsorbent with the change in pressure of the system for a given temperature in non-ideal sorption case. The base of the model is on the multilayered adsorption [87, 88]. Its linear form can be written as:

$$q_e = KC_e^{1/n} \tag{14}$$

Equation can also be written as:

$$\text{Ln } q_e = \text{Ln}\left(K_f C_e^{1/n}\right) \tag{15}$$

$$\text{Ln } q_e = \text{Ln}K_f + \frac{1}{n}\text{Ln}C_e \tag{16}$$

Here

K_f: Freundlich constant (index of adsorption capacity).
n: another Freundlich constant (index of adsorption intensity or surface heterogeneity).
q_e: Adsorbent's equilibrium adsorption capacity in (mg g^{-1}).
C_e: Adsorbate's equilibrium concentration in (mg L^{-1}).

4.2.3   Sips Model

Sometimes a situation arises where we are dealing to estimate the heterogeneous adsorption systems, then Sips model is used instead of Langmuir and Freundlich models. The Sips model is a combination (hybrid) model of Langmuir and Freundlich models. The Sips model is reduced to Freundlich model when adsorbate concentration is low, whereas at higher adsorbate concentration, the Sips model anticipates the monolayer sorption capacity characteristics of Langmuir model [89]. This hybrid (Sips) model is represented as:

$$q_e = q_m (K_s C_e)^{\text{ns}} 1 + (K_S C_e)^{\text{ns}} \tag{17}$$

Here
q_m: Sips max adsorption capacity (mg g^{-1}).
K_s: Langmuir equilibrium constant (L mg^{-1}).
n_S: ($n_S = 1/n_F$) factor comparable to Freundlich heterogeneity.

5   Magnetic Hybrid Ferrites as Adsorbent

Existence of life on Earth owes to the provision of safe water. Although water does not contain any nutrients, it is essential for all the metabolic activities in living organisms. Maintaining the balanced ecosystem for future generations is only possible when the water resources are preserved. For this purpose, development of water purification techniques can help to use the water which has to be disposed due to the addition of some contaminants; consequently, pressure on available water resources can be reduced. In recent years, magnetic hybrid ferrites are being used for the removal of heavy metals from contaminated water as they are chemically stable, less toxic, can be synthesized easily and possess good recycling ability. There are many methods to synthesize composite materials, but successful application lies in the stability of the NPs when introduced in solutions having different pH range, recovery time and responses to external magnetic fields. Adsorbent-based hybrid ferrites can be used for the purification of contaminated water with high precision [90, 91].

Removal of heavy metals from contaminated water using hybrid ferrites is a better option than traditional purification methods like reverse osmosis, ion exchange, membrane separation and filtration due to the cost-effectiveness and ease of use. It has been observed that traditional adsorption techniques are limited in their use because of the hindrance in filtration and regeneration of specific adsorbents. However, this problem can be overcome by using magnetic materials, but nanometal ferrites have shown poor stability in aqueous medium. This issue has been investigated by synthesizing hybrid magnetic ferrites, e.g., hybrid composite of magnetic ferrite and graphene oxide synthesized by hydrothermal method enhanced the adsorption level of heavy metals due to the presence of carboxylic, epoxy and hydroxyl functions at the graphene oxide layer [92, 93].

To remove lead (Pb) from the contaminated water, manganese-based nanoferrites (hybrid) capped with carboxymethylated biopolymers can be used [94]. The properties of the hybrid ferrites were optimized by the pH variation. All the nanosorbents have shown the elimination of Pb from the contaminated water samples nearly 100% after the contact time of half an hour. Following the pseudo-second-order model with adsorption capabilities in the range of 34–46 mg g^{-1} formulated by Sips model, it was found that the adsorption had been more effective at pH 5.5. The nanosorbents can be retrieved and reused for the extraction of Pb from the contaminated water as shown in Fig. 6. Recently, the hybrid ferrite NPs having singled layer of GO with manganese have shown excellent adsorption features to remove the Pb and arsenic from contaminated water. The adsorption data fitted well to the Langmuir isotherm, confirming the highest adsorption capability. In order to estimate the enthalpy and free energy of adsorption, temperature-dependent adsorption studies were made. Sustainability, easy magnetic separation, high surface area and high removal efficiency made these hybrid magnetic ferrites smart for commercial scale [95]. Extraction of Pb from contaminated water was successfully made by using $NiFe_2O_4/MnO_2$ hybrids with three-dimensional hierarchical floral and core-shell-like structure prepared by simple hydrothermal process. To study the effects of pH, primary Pb concentration and doses of absorbents were studied using batch experiments. $NiFe_2O_4/MnO_2$ nanocomposites indicated the rapid Pb adsorption; the optimum adsorption capacity of 85.78 mg/g was recorded. The results of isothermal experiments showed that the Langmuir model was better fitted rather than the Freundlich model which was evident from the monolayer adsorption process for Pb onto the composite surface. Six times regeneration capacity of the hybrid magnetic ferrite from the solution and maintaining the removal efficiency of 80% made the smart composite a new adsorbent for heavy metals [96].

To remove arsenic (As) ions from contaminated water, two newly synthesized hybrid ferrites, i.e., GO-manganese ferrites and titanium nanotube-manganese ferrites were successfully tested. These composites work on adsorption mechanism and were characterized by different tools prior to employ in the adsorption method. The optimum adsorption capacities for As were 102 mg/g and 80.8 mg/g using GO and Titania nanotube-based hybrids, respectively, when tested for contaminated

Fig. 6 Digital images of lead ion solution with $Fe_3O_4@SiO_2$ composites before (**a**), after (**b**) applying external magnetic field. Reprinted with permission from [99]
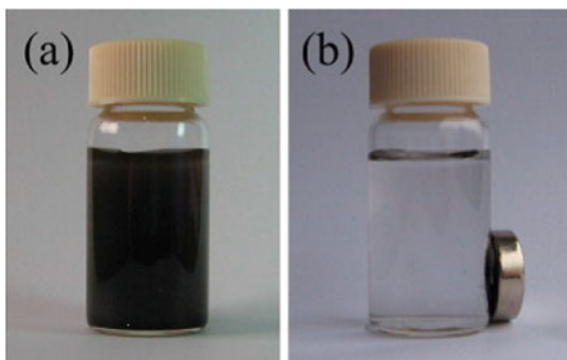
water having (As) concentration of 400 ppm. The adsorption capabilities of GO and Titania nanotube-based hybrids were enhanced 27% and 6%, respectively, than manganese ferrites. This enhancement was owing to the large surface area and higher number of oxygenated groups. On the surface of hybrid materials, these characteristics increased dispersion stability and number of active sites for As [97]. Chandra et al. [98] synthesized 10 nm (average size) superparamagnetic magnetite/rGO composites through chemical reaction which showed 99% adsorption capacity for the removal of Arsenic. Zhang and his colleagues prepared magnetic ferro-hydroxide and GO for the adsorption of As from contaminated water. They observed As removal at different pH levels and various arsenate concentration levels (0.5 from 20 ppm) in polluted water.

Some inorganic and organic pollutants such as acid black (AB 1) and chromium (Cr) from contaminated water have been removed by silica-based hybrid cobalt ferrites $SiO_2@CoFe_2O_4$ functionalized with GO. In order to measure the highest adsorption capacity of dye (AB 1) and Cr ions as function of contact time, pH and adsorbent dosage, the batch mode investigations were made with the hybrid material. The experimental results were fitted well to the Langmuir isothermal model. Adsorption capacity was affected by pH of the solution which was observed maximum at pH 2 for AB 1 dye and pH 1 for Cr ions. Detailed kinetic investigations showed that the process followed pseudo-second-order kinetic model for both contaminants. Desorption studies indicated the stable reusability of the sorbent, hence, making it a suitable choice on the commercial scale [100]. $CoFe_2O_4$/NOM (natural organic matter) synthesized by green method (s–gel) using enriched water with natural organic matter was successfully used to remove the chromium at natural pH of the contaminated water especially of industrial effluent. The hybrid ferrites could remove 80–90% Cr from the contaminated water within half an hour. Investigation of the kinetics indicated the flexibility of the material, and it can be reused for up to five cycles [101].

The porous magnetic ferrite nanowires having $MnFe_2O_4$ and Mn-doped Fe_3O_4 were prepared through thermal decomposition of organometallic compound using nitrilotriacetic acid as a chelating agent to match with different ratios of iron (Fe II) and manganese (Mn II) ions. The resulting nanostructures were found superparamagnetic in nature, having magnetic saturation values of 45.9 and 48.7 emug^{-1}, respectively. The Brunauer Emmett Teller explicit surface area for the $MnFe_2O_4$ was 37.8 m^2/g and 45.4m^2/g for Mn-doped Fe_3O_4. Nanomaterials hybrid ferrites showed great capacity to remove heavy metal ions along with organic pollutants from contaminated water [102]. Surface modification by Stober method of mercaptopropyl-coated cobalt ferrite ($CoFe_2O_4$) NPs prepared by co-precipitation process proved efficient adsorbent for Hg^{2+} ions from contaminated water. It was observed that the pH of the solution, mass of adsorbent, time of contact and temperature affected the adsorption of heavy metal. At pH 7 the maximum removal efficiency of about 97% was obtained [103]. In order to remove Zn(II) from contaminated water, magnetic hybrid silica-based core shell NPs (Fe_3O_4–SiO_2) have been prepared and tested as a nanosorbent. These hybrid composites were synthesized by using co-precipitation and sol–gel method. The maximum adsorption capacity of the hybrid material for the removal of

Zn (II) was measured at 25 °C to be 119 mg/g using the Langmuir isothermal model. Using the regeneration solution (1.0 M: HCl), the nanosorbent was easily separated by applying magnetic field. Leaching of Fe_3O_4 was very less due to the presence of Silica as a shell on the Fe_3O_4 nanomaterials [104]. The cadmium ions (Cd^{2+}) were removed from water by hybrid ferrites synthesized at different pH values. Such prepared composites had shown excellent magnetism, when they were uniformly distributed at nanoscale, which helped for liquid–solid separation. The optimum pH value for the adsorption of cadmium ions was 8.0. The adsorption mechanism followed the pseudo-second-order kinetics. Langmuir's isothermal model suggested the uniform distribution of active sites for cadmium ions adsorption with monolayer coverage [105].

6   Conclusion

Magnetic properties of Ferrite NPs have been explored for variety of applications such as biomedical, industry, sensing and heavy metal removal from water. Higher surface area of nanoparticles provides adsorption sites for heavy metal ions which results in their removal from wastewater and drinking water. Separation of ferrite nanoparticles is easy from the solution which increases its reusability. Although many reports based on magnetic nanoparticles for heavy matter removal are presented in the literature, however, most of the ferrite nanoparticles are tested at laboratory stage. Limitations still needed to be addressed particularly are cost effectiveness and technical handling. These issues can be solved by making a coordination between different stakeholders such as society, government and industries.

References

1. Savage N, Diallo MS (2005) Nanomaterials and water purification: opportunities and challenges. J Nanopart Res 7(4–5):331–342
2. Koh GY, Chou G, Liu Z (2009) Purification of a water extract of Chinese sweet tea plant (*Rubus suavissimus* S. Lee) by alcohol precipitation. J Agric Food Chem 57(11):5000–5006
3. Choi H et al (2010) TiO2-based advanced oxidation nanotechnologies for water purification and reuse. Sustain Sci Eng 2:229–254
4. Vuorensola K, Sirén H, Karjalainen U (2003) Determination of dopamine and methoxy-catecholamines in patient urine by liquid chromatography with electrochemical detection and by capillary electrophoresis coupled with spectrophotometry and mass spectrometry. J Chromatogr B 788(2):277–289
5. Raza MQ, Kumar N, Raj R (2016) Surfactants for bubble removal against buoyancy. Sci Rep 6:19113
6. Jiuhui Q (2008) Research progress of novel adsorption processes in water purification: a review. J Environ Sci 20(1):1–13
7. Burrows BD (1986) Purified water reverse osmosis reservoir. Google Patents
8. Nehls BL, Nehls KA (2002) Filter media containing powered cellulose and immobilized lipase for swimming pool and spa water filteration. Google Patents

9. Fomina M, Gadd GM (2014) Biosorption: current perspectives on concept, definition and application. Biores Technol 160:3–14

10. Zhongming LZZYR, Kang D (2006) Preparation of anisotropy nano-magnetism material. Shanghai Metals 1

11. Lisfi A et al (2014) Nano-magnetism of magnetostriction in $Fe_{35}Co_{65}$. Appl Phys Lett 104(9):092401

12. Mosca Conte A (2007) Quantum mechanical modeling of nano magnetism: new tools based on density-functional-theory with case applications to solids, surfaces, wires, and molecules. PhD dissertation. https://iris.sissa.it/handle/20.500.11767/3935#.YPCCEe1R3IU

13. Ghaly A et al (2014) Production, characterization and treatment of textile effluents: a critical review. J Chem Eng Process Technol 5(1):1–19

14. Ahmed M et al (2013) Effective dye removal and water purification using the electric and magnetic Zn0. 5Co0. 5Al0. 5Fe1. 46La0. 04O4/polymer core–shell nanocomposites. J Alloys Compd 578:121–131

15. Kefeni KK, Mamba BB, Msagati TA (2017) Application of spinel ferrite nanoparticles in water and wastewater treatment: a review. Sep Purif Technol 188:399–422

16. Reddy DHK, Yun Y-S (2016) Spinel ferrite magnetic adsorbents: alternative future materials for water purification? Coord Chem Rev 315:90–111

17. Ambashta RD, Sillanpää M (2010) Water purification using magnetic assistance: a review. J Hazard Mater 180(1–3):38–49

18. O'handley RC (2000) Modern magnetic materials: principles and applications. Wiley

19. Cullity BD, Graham CD (2011) Introduction to magnetic materials. Wiley

20. Buschow KHJ (2003) Handbook of magnetic materials. Elsevier

21. Spaldin NA (2010) Magnetic materials: fundamentals and applications. Cambridge University Press

22. Coey JM (2010) Magnetism and magnetic materials. Cambridge University Press

23. Sugimoto M (1999) The past, present, and future of ferrites. J Am Ceram Soc 82(2):269–280

24. Pardavi-Horvath M (2000) Microwave applications of soft ferrites. J Magn Mater 215:171–183

25. Rezlescu N, Rezlescu E (1974) Dielectric properties of copper containing ferrites. Physica Status Solidi (a) 23(2): 575–582

26. Amiri M, Salavati-Niasari M, Akbari A (2019) Magnetic nanocarriers: evolution of spinel ferrites for medical applications. Adv Coll Interface Sci 265:29–44

27. Baltz V et al (2018) Antiferromagnetic spintronics. Rev Modern Phys 90(1):015005

28. Trukhanov A et al (2018) Control of electromagnetic properties in substituted M-type hexagonal ferrites. J Alloy Compd 754:247–256

29. Tatarchuk T et al (2017) Structural characterization and antistructure modeling of cobalt-substituted zinc ferrites. J Alloy Compd 694:777–791

30. Vinnik D et al (2020) Influence of titanium substitution on structure, magnetic and electric properties of barium hexaferrites $BaFe_{12}-xTi_xO_{19}$. J Magnetism Magnetic Mater 498:166117

31. Mashuri X et al (2018) Preparation and microwave absorbing properties in the X-band of natural ferrites from iron sands by high energy milling. Mater Res Express 5(1):014003

32. Trukhanov S et al (2018) Polarization origin and iron positions in indium doped barium hexaferrites. Ceram Int 44(1):290–300

33. Das R et al (2014) Carbon nanotube membranes for water purification: A bright future in water desalination. Desalination 336:97–109

34. Le Pivert M et al (2020) Smart ZnO decorated optimized engineering materials for water purification under natural sunlight. Constr Build Mater 257:119592

35. Yu H et al (2020) Weak-reduction graphene oxide membrane for improving water purification performance. J Mater Sci Technol 39:106–112

36. Ali A et al (2016) Synthesis, characterization, applications, and challenges of iron oxide nanoparticles. Nanotechnol Sci Appl 9:49

37. Suwanboon S et al (2013) Optical and photocatalytic properties of La-doped ZnO nanoparticles prepared via precipitation and mechanical milling method. Ceram Int 39(3):2811–2819

38. Ding J et al (2000) Ultrafine ferrite particles prepared by coprecipitation/mechanical milling. Mater Lett 44(1):19–22
39. Baghbaderani HA, Sharafi S, Chermahini MD (2012) Investigation of nanostructure formation mechanism and magnetic properties in Fe45Co45Ni10 system synthesized by mechanical alloying. Powder Technol 230:241–246
40. Rashidi S, Ataie A (2016) Structural and magnetic characteristics of PVA/CoFe$_2$O$_4$ nano-composites prepared via mechanical alloying method. Mater Res Bull 80:321–328
41. Hosseini HM, Bahrami A (2005) Preparation of nanocrystalline Fe–Si–Ni soft magnetic powders by mechanical alloying. Mater Sci Eng B 123(1):74–79
42. Waje SB et al (2010) Sintering temperature dependence of room temperature magnetic and dielectric properties of Co0. 5Zn0. 5Fe2O4 prepared using mechanically alloyed nanoparticles. J Magnetism Magnetic Mater 322(6):686–691
43. Rashidi S, Ataie A (2014) One-step synthesis of CoFe$_2$O$_4$ nano-particles by mechanical alloying. In: Advanced materials research. Trans Tech Publication
44. Uhm YR et al (2006) The characterization of magnetic and photo-catalytic properties of nanocrystalline Ni-doped TiO$_2$ powder synthesized by mechanical alloying. J Magn Magn Mater 304(2):e781–e783
45. Salavati-Niasari M, Mahmoudi T, Amiri O (2012) Easy synthesis of magnetite nanocrystals via coprecipitation method. J Cluster Sci 23(2):597–602
46. Matei E et al (2013) Characterization and application results of two magnetic nanomaterials. J Environ Qual 42(1):129–136
47. Zhao D-L et al (2006) Inductive heat property of Fe$_3$O$_4$/polymer composite nanoparticles in an ac magnetic field for localized hyperthermia. Biomed Mater 1(4):198
48. Surendra MK et al (2014) Magnetic hyperthermia studies on water-soluble polyacrylic acid-coated cobalt ferrite nanoparticles. J Nanopart Res 16(12):2773
49. Wang Y et al (2011) Synthesis of Fe$_3$O$_4$ magnetic fluid used for magnetic resonance imaging and hyperthermia. J Magn Magn Mater 323(23):2953–2959
50. Saldívar-Ramírez M et al (2014) Study on the efficiency of nanosized magnetite and mixed ferrites in magnetic hyperthermia. J Mater Sci Mater Med 25(10):2229–2236
51. Chen D-H, He X-R (2001) Synthesis of nickel ferrite nanoparticles by sol-gel method. Mater Res Bull 36(7–8):1369–1377
52. George M et al (2006) Finite size effects on the structural and magnetic properties of sol–gel synthesized NiFe$_2$O$_4$ powders. J Magn Magn Mater 302(1):190–195
53. Thota S, Kumar J (2007) Sol–gel synthesis and anomalous magnetic behaviour of NiO nanoparticles. J Phys Chem Solids 68(10):1951–1964
54. Guan Y et al (2010) Preparation of multi-walled carbon nanotubes functionalized magnetic particles by sol–gel technology and its application in extraction of estrogens. Talanta 83(2):337–343
55. Parashar M, Shukla VK, Singh R (2020) Metal oxides nanoparticles via sol–gel method: a review on synthesis, characterization and applications. J Mater Sci Mater Electron 31(5):3729–3749
56. Park K-S et al (2010) Characterization, in vitro cytotoxicity assessment, and in vivo visualization of multimodal, RITC-labeled, silica-coated magnetic nanoparticles for labeling human cord blood–derived mesenchymal stem cells. Nanomed Nanotechnol Biol Med 6(2): 263–276
57. Shen Y et al (2009) Tailoring size and structural distortion of Fe$_3$O$_4$ nanoparticles for the purification of contaminated water. Biores Technol 100(18):4139–4146
58. Laurent S et al (2008) Magnetic iron oxide nanoparticles: synthesis, stabilization, vectorization, physicochemical characterizations, and biological applications. Chem Rev 108(6):2064–2110
59. Cai W, Wan J (2007) Facile synthesis of superparamagnetic magnetite nanoparticles in liquid polyols. J Colloid Interface Sci 305(2):366–370
60. Caruntu D, Caruntu G, O'Connor CJ (2007) Magnetic properties of variable-sized Fe$_3$O$_4$ nanoparticles synthesized from non-aqueous homogeneous solutions of polyols. J Phys D Appl Phys 40(19):5801

61. Couto GG et al (2007) Nickel nanoparticles obtained by a modified polyol process: synthesis, characterization, and magnetic properties. J Colloid Interface Sci 311(2):461–468

62. Kumar VG et al (2011) Facile green synthesis of gold nanoparticles using leaf extract of antidiabetic potent *Cassia auriculata*. Colloids Surf, B 87(1):159–163

63. Arunachalam K et al (2014) One step green synthesis of phytochemicals mediated gold nanoparticles from *Aegle marmales* for the prevention of urinary catheter infection. Int J Pharm Pharm Sci 6(1):700–706

64. Ahmed KBA et al (2014) Preparation of gold nanoparticles using Salicornia brachiata plant extract and evaluation of catalytic and antibacterial activity. Spectrochim Acta Part A Mol Biomol Spectrosc 130:54–58

65. Imran Din M, Rani A (2016) Recent advances in the synthesis and stabilization of nickel and nickel oxide nanoparticles: a green adeptness. Int J Anal Chem 3512145

66. Kryvoruchko A, Yurlova L, Kornilovich B (2002) Purification of water containing heavy metals by chelating-enhanced ultrafiltration. Desalination 144(1–3):243–248

67. Momodu M, Anyakora C (2010) Heavy metal contamination of ground water: the surulere case study. Res J Environ Earth Sci 2(1):39–43

68. Savage N, Diallo MS (2005) Nanomaterials and water purification: opportunities and challenges. J Nanopart Res 7(4):331–342

69. Zhang W-X (2003) Nanoscale iron particles for environmental remediation: an overview. J Nanopart Res 5(3):323–332

70. Fane AG, Wang R, Hu MX (2015) Synthetic membranes for water purification: status and future. Angew Chem Int Ed 54(11):3368–3386

71. Saleh TA (2017) Advanced Nanomaterials for water engineering, treatment, and hydraulics. IGI Global

72. Werber JR, Osuji CO, Elimelech M (2016) Materials for next-generation desalination and water purification membranes. Nat Rev Mater 1(5):16018

73. Si Y et al (2012) Synthesis of mesoporous magnetic Fe_3O_4@carbon nanofibers utilizing in situ polymerized polybenzoxazine for water purification. J Mater Chem 22(11):4619–4622

74. Oosthuizen, J., Environmental Health: Emerging Issues and Practice. 2012: IntechOpen.

75. Moore JW (2012) Inorganic contaminants of surface water: research and monitoring priorities. Springer, New York

76. Rahman Z, Singh VP (2019) The relative impact of toxic heavy metals (THMs) (arsenic (As), cadmium (Cd), chromium (Cr)(VI), mercury (Hg), and lead (Pb)) on the total environment: an overview. Environ Monit Assess 191(7):419

77. Dorris J, Atieh BH, Gupta RC (2002) Cadmium uptake by radishes from soil contaminated with nickel-cadmium batteries: toxicity and safety considerations. Toxicol Mech Methods 12(4):265–276

78. Gaur N et al (2014) A review with recent advancements on bioremediation-based abolition of heavy metals. Environ Sci Process Impacts 16(2):180–193

79. Bundschuh J et al (2008) Natural arsenic in groundwaters of Latin America. Taylor & Francis

80. Tchounwou PB, Centeno JA, Patlolla AK (2004) Arsenic toxicity, mutagenesis, and carcinogenesis—a health risk assessment and management approach. Mol Cell Biochem 255(1):47–55

81. Simonin J-P (2016) On the comparison of pseudo-first order and pseudo-second order rate laws in the modeling of adsorption kinetics. Chem Eng J 300:254–263

82. Bergmann CP, Machado FM carbon nanomaterials as adsorbents for environmental and biological applications. Springer International Publishing, Berlin

83. Wang A et al (2019) Novel approaches to design eco-friendly Materials based on natural nanomaterials. Frontiers Media SA

84. Naddeo V, Balakrishnan M, Choo KH (2019) Frontiers in water-energy-nexus—nature-based solutions, advanced technologies and best practices for environmental sustainability: proceedings of the 2nd WaterEnergyNEXUS conference, November 2018, Salerno, Italy. Springer International Publishing, Berlin

85. Rhoades DS (1995) Interpretation of empirical adsorption isotherms in terms of surface heterogeneity for the system CO on Pt foil. University of California, San Diego

86. Dobbs RA et al (1980) Carbon adsorption isotherms for toxic organics. Municipal Environmental Research Laboratory, Office of Research and Development, U.S. Environmental Protection Agency

87. Bethke CM (2007) Geochemical and biogeochemical reaction modeling. Cambridge University Press

88. Figura L, Teixeira AA (2007) Food physics: physical properties—measurement and applications. Springer, Berlin Heidelberg

89. SenGupta AK (1995) Ion exchange technology: advances in pollution control. Taylor & Francis

90. Hu A, Apblett A (2014) Nanotechnology for water treatment and purification. Springer International Publishing, Berlin

91. Naushad M (2018) A new generation material graphene: applications in water technology. Springer International Publishing

92. Saleh HEDM, Aglan R (2018) Heavy metals. IntechOpen

93. Abd-Elsalam KA, Mohamed MA, Prasad R (2019) Magnetic nanostructures: environmental and agricultural applications. Springer International Publishing, Berlin

94. Perez T et al (2019) Efficient removal of lead ions from water by magnetic nanosorbents based on manganese ferrite nanoparticles capped with thin layers of modified biopolymers. J Environ Chem Eng 7(1):102892

95. Kumar S et al (2014) Graphene oxide–$MnFe_2O_4$ magnetic nanohybrids for efficient removal of lead and arsenic from water. ACS Appl Mater Interfaces 6(20):17426–17436

96. Xiang B et al (2017) 3D hierarchical flower-like nickel ferrite/manganese dioxide toward lead (II) removal from aqueous water. J Hazard Mater 325:178–188

97. Shahrin S et al (2018) Adsorptive removal of As (V) Ions from Water using graphene oxide-manganese ferrite and titania nanotube-manganese ferrite hybrid nanomaterials. Chem Eng Technol 41(11):2250–2258

98. Chandra V et al (2010) Water-dispersible magnetite-reduced graphene oxide composites for arsenic removal. ACS Nano 4(7):3979–3986

99. Hu H, Wang Z, Pan L (2010) Synthesis of monodisperse Fe3O4@silica core–shell microspheres and their application for removal of heavy metal ions from water. J Alloy Compd 492(1):656–661

100. Santhosh C et al (2017) Magnetic SiO_2@ $CoFe_2O_4$ nanoparticles decorated on graphene oxide as efficient adsorbents for the removal of anionic pollutants from water. Chem Eng J 322:472–487

101. Cruz DR et al (2017) Green synthesis of a magnetic hybrid adsorbent ($CoFe_2O_4$/NOM): removal of chromium from industrial effluent and evaluation of the catalytic potential of recovered chromium ions. J Hazard Mater 334:76–85

102. Cui H-J et al (2013) Synthesis of porous magnetic ferrite nanowires containing Mn and their application in water treatment. J Mater Chem A 1(19):5902–5907

103. Viltužnik B, Lobnik A, Košak A (2015) The removal of Hg (II) ions from aqueous solutions by using thiol-functionalized cobalt ferrite magnetic nanoparticles. J Sol-Gel Sci Technol 74(1):199–207

104. Emadi M, Shams E, Amini MK (2013) Removal of zinc from aqueous solutions by magnetite silica core-shell nanoparticles. J Chem 2013

105. Chen K et al (2017) Removal of cadmium and lead ions from water by sulfonated magnetic nanoparticle adsorbents. J Colloid Interface Sci 494:307–316

Ferrites as an Alternative Source of Renewable Energy for Hydroelectric Cell

Mohan Chandra Mathpal, Gopal Niraula, Promod Kumar, Mahesh Chand, Manish Kumar Singh, Surender K. Sharma, Maria A. G. Soler, and H. C. Swart

Abstract There are many conventional ways of producing energy at large scales such as fossil fuels, hydroelectric power station, wind energy, solar cell plants, marine energy, etc., but most of these require bulky plantation, huge manpower, wide land occupation and are non-portable and expensive to handle too. In the twenty-first century, there is still a huge gap between worldwide energy supply and its demand. The advances in the technology sector have also increased the consumption of energy, but the sources of generating the renewable energy remain limited. In order to account for these problems in recent years, several methods have been adopted and a significant research in this direction has been made by the invention of the hydroelectric cell by Dr. R. K. Kotnala's group in 2016. Instead of using the magnetic character in the ferrite nanostructures, these nanomaterials were first time effectively exploited for direct energy harvesting application by using their capability to dissociate the absorbed water molecules on its porous surface. This allows the production of ions, which is then followed by the charge transfer of hydronium, hydroxyl and hydrogen ions between the electrodes of the ferrite nanostructures and results in the generation of an electric current across the circuit. The concept of the hydroelectric cell is new, and these cells are easily portable, inexpensive, biodegradable and eco-friendly in

M. C. Mathpal (✉) · M. A. G. Soler (✉)
Institute of Physics, University of Brasilia, Brasilia, DF 70910900, Brazil
e-mail: mohanmathpal@unb.br

M. A. G. Soler
e-mail: soler@unb.br

G. Niraula · S. K. Sharma
Department of Physics, Federal University of Maranhao, Sao Luis, Brazil

P. Kumar (✉) · H. C. Swart
Department of Physics, University of the Free State, Bloemfontein 9300, ZA, South Africa

M. Chand
Nano Lab, Faculty UnB Planaltina Campus, University of Brasília, Brasília, DF 73300-000, Brazil

M. K. Singh (✉)
Department of Physics, The LNM Institute of Information Technology, Jaipur 302031, India

S. K. Sharma
Department of Physics, Central University of Punjab, Bathinda 151401, India

nature. This chapter provides an insight on the concept of spinel ferrite nanostructures for the application in the hydroelectric cell.

Keywords Spinel ferrite · Iron oxide · Green energy · Hydroelectric cell · Porosity · Electrical resistance · Magnesium ferrite

1 Introduction

The mankind have a huge dependency on natural resources of energies, which can be obtained from different sources and then converted into the desired form of energy. The different natural resources that are popularly known for the generation of electricity are wind energy, hydro energy, fossil fuels, marine energy, solar energy, fuel cell, photovoltaic cell, hydrogen energy, geothermal energy and biomass energy [1–20]. The extensive use of traditional sources such as oil, coal, natural gas and other fossil fuels which not only make the environment unhealthy for living but also has raised several questions such as continuous carbon emissions, global warming, climate change, greenhouse effect and rapid depletion of natural resources of energy [10, 14, 17, 21]. With the increasing comfort level of mankind by a myriad of technologies in several areas including home, industrial and travel appliances, the consumption of energy has also increased, whereas there is no remarkable worldwide progress or strategy to fill the gap between the supply and demand of clean energy. Among various renewable sources with their pros and cons, the hydropower, wind energy, hydrogen energy, fuel cells and solar energy are considered the most environmental friendly but some of these require large land occupation, heavy infrastructure installation, expending time and money as well along with several geographical and environmental restrictions [2, 5, 6, 8, 10, 13, 14, 21–24]. For example, the fabrication of highly efficient solar cells is expensive and most of the materials used for the fabrication such as silicon, glass, dyes, polymers and electrolytes are also hazardous. In fact, the recycling of the wastage components of solar cell and commercially available batteries is also expensive. Similarly, the fuel cell requires the supply of fuels, an electrostatic separator with efficient oxidation and reduction processes to be useful for applications [25].

Nowadays, the efforts for inexpensive, portable, long lasting and sustainable clean energy sources at small scales are being made in several countries to replace the consumption of fossil fuels. Widely studied sources of literature can be found for the production of hydrogen energy by the means of several methods [6, 23, 26–38]. The hydrogen energy is a non-polluting fuel which can be generated from renewable resources and can also be stored and transported. Q. Yuan et al. theoretically reported the generation of hydroelectric voltage for nano-power cell applications for the first time in water-filled single-walled carbon nanotube (SWCNT), which developed a voltage of 17.2 mV at the two opposite ends of the tube [39]. The polarity of the water molecules plays an important role to form a weak coupling between free charge carriers and water dipoles in the nanotubes to induce a voltage difference

between the two ends. Miljkovic et al. have shown that the jumping of the water droplets from a hydrophobic copper oxide to the surface of the hydrophilic can develop an electric power of about 15 pW/cm^2 [40]. Wei et al. have used graphene oxide to develop a cell that can generate a maximum power of 2 μW within an active area of 0.1 cm^2 by the use of an electrolyte and humidity [41]. The direct sunlight can also be used to split the water molecules and to produce the hydrogen gas. Recently, it has been shown that Zn-doped CdS and hematite (α-Fe$_2$O$_3$) can also split the water molecules to produce the energy [26, 30]. Chandrasekhar et al. have developed a spheroidal hybrid generator-based renewable energy source for harvesting the energy from water waves by using the power from solar light [42]. The device was in fact enabled with a self-powered position tracking system, which is very useful for ocean navigation system. In a similar study, Liu et al. have developed a blue energy harvester to scavenge the water wave energy with an aim of all-weather internet-of-things (IoT)-based device applications by using the sunlight [43]. The direct generation of hydroelectric voltage in ceramic nanostructures without using an electrolyte or sunlight radiation has been challenging so far [20, 22, 30, 33–36, 38, 44, 45]. The electrolyte-based energy converting and storage devices are hydrophilic, chemically active and thermally unstable which may hinder their performance under certain solvents and atmosphere.

In order to overcome these challenges, a new concept of producing energy has been developed in the last decade by the use of hydroelectric cells (HECs) [25, 34, 46–61]. The hydroelectric cells are electrolytic free and generate electricity by the dissociation of absorbed water molecules on the surface of a porous ceramic/semiconducting material [33, 58, 60]. The HECs were first invented by Dr. Kotnala's group at National Physical Laboratory (NPL), New Delhi, India, in 2016 [54]. The first HEC developed by their group relied on the use of Li-doped magnesium ferrite nanomaterials. The ferrite materials are well known for the production of hydrogen gas by splitting the water molecules under the presence of sunlight [30, 38]. The splitting of water molecules at room temperature was rigorously addressed by Parkinson et al. in 2011 on the surface of a synthetic magnetite (Fe$_3$O$_4$ (001)) single crystal [50]. Magnesium ferrite, a highly resistive spinel ferrite material has been the focus of intense research due to its soft magnetic properties and porous microstructure that has been widely studied for humidity and gas sensing applications due to its high surface reactivity and oxygen deficient stoichiometry [58, 62–64]. The general structural formula of spinel ferrite materials is AB$_2$O$_4$, where A is a divalent transition-metal cation and B is a trivalent cation. Magnetic ferrites display mainly two groups of crystal structures such as the cubic comprising pure ferrites such as magnetite (Fe$_3$O$_4$) and maghemite (γ-Fe$_2$O$_3$) and mixed ferrites AFe$_2$O$_4$, where A = Co, Cu, Mg, Ni and Zn [65–69]. The A and B sites of the spinel structure occupy the tetrahedral and octahedral position, respectively, in the surrounded oxygen. There are eight molecules in a unit cell of spinel ferrite which are accommodated in 16 octahedral sites with divalent metal ions and eight tetrahedral sites with trivalent metal ions, therefore hosting a total of 24 metal ions in a unit cell. So, when the water molecules are absorbed on the surface of these porous ferrite nanostructures or a ceramic oxide nanomaterial, then it has the capability to dissociate it into the hydroxide and hydronium ions. These ions are

collected by an anode of Zn/Al and a cathode of Ag electrodes at two opposite ends, respectively, to produce the electricity [25, 54, 70]. A single water molecule can be dissociated into its constituents with 1.23 V of potential energy. This energy can be provided externally in the form of thermal, UV/catalysis, photons and biochemical techniques at room temperature. The nanoporous surface as a main host of ferrite and ceramic oxide materials are highly reactive sites for the dissociation of water molecules, which is in fact even possible at room temperature. So far, only a few ferrite nanomaterials and semiconductor nanostructures have been investigated for the application in HECs. As of now, there is a lack of literature for the deep physical insight on HEC as only a few groups of researchers have shown their interest to develop the HECs. This chapter provides a comprehensive state of art of the hydro-electric cell with an overview of efficient materials and signifies the importance of resistive type spinel ferrite nanostructures in energy harvesting. The chapter is aimed to boost the understanding and motivate the new energy researchers to develop a low-cost hydroelectric cell as an alternate source of renewable green energy. The readers of this chapter are also encouraged to read an excellent review article by Das et al. [60].

2   Concept of Hydroelectric Cell

The HEC materials are solid in nature and their preparation is neither sophisticated nor expensive as compared to other cell materials and storage devices. These are easily portable and compact in structure for flexible operation. The processing of HEC involves simple and low-cost preparation technology by the use of acid and alkali free, electrolyte free and environment friendly nanomaterials, which lead to an effort to reduce the effect of greenhouse gases, CO_2 emissions and other hazardous emissions to the environment [34, 53, 55, 61, 71]. The HEC based on Li-doped magnesium ferrite has been also proposed to be useful for light emitting diode (LED) applications and for the non-polluting production of hydrogen gas without using the electrolytes and solar energy [34, 56]. Ferrite-based HECs can instantly start working at room temperature without any external input except deionized water (DI).

The HEC works on the principle of conversion of energy released due to the dissociation of water molecules to the electric energy. It is a non-photocatalytic technique to split the water molecules to generate green energy. It has no external input or biasing except the deionized water molecules to generate the electricity. The key components of a HEC are a nanoporous pellet made of ferrite nanomaterials or metal oxide nanostructures, two electrodes consisting of zinc anode and a cathode based on silver paste. Figure 1 shows the schematic diagram of a magnesium ferrite-based HEC [49, 60, 70]. Two electrodes that consist of an anode of zinc (Zn) sheet and a cathode of interdigitated silver (Ag) paste are generally fabricated to collect the charge ions species at the end of two opposite faces of the pellets made of a ceramic material.
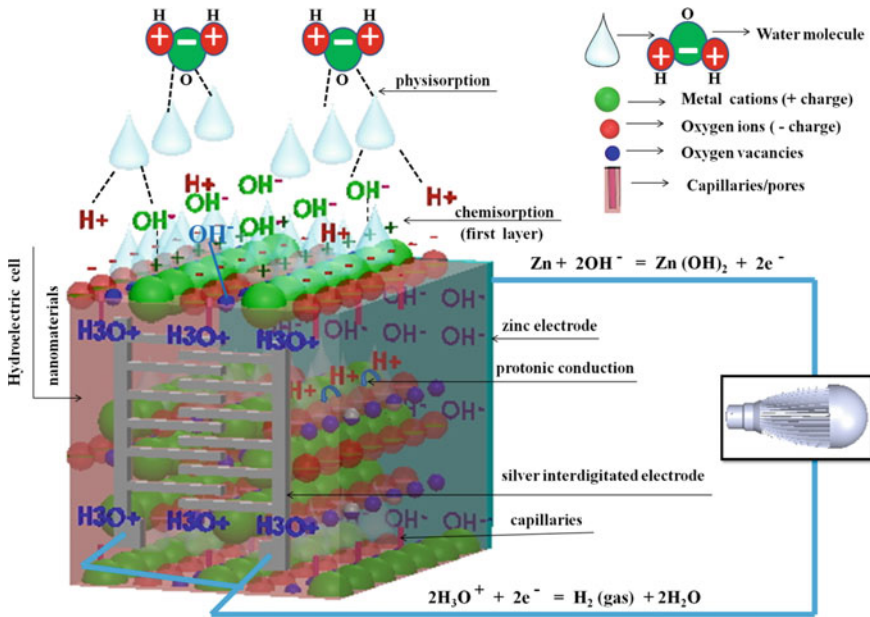
Fig. 1 Schematic presentation of working principle of hydroelectric cell

The materials are prepared under special conditions in order to control their porosity, oxygen deficiency and unsaturated surface cations to dissociate the water molecules. These materials split the water molecules into H_3O^+ and OH^- ions at room temperature which results in the ionic conduction on the surface and within the HEC. The OH^- ions start migration toward the zinc anode, where these ions oxidize the zinc to zinc hydroxide ($Zn(OH)_2$), and as a result, two electrons are released at the anode. On the other hand, the H_3O^+ ions migrate toward the inter-digitated silver electrode and collect the electrons from anode, which results in the release of hydrogen gas and water molecules at cathode [60]. The water splitting in a HEC mainly involves two steps, namely (i) chemidissociation or chemisorption and (ii) physidissociation or physisorption. The transportation of these dissociated ions toward the anode and cathode takes place through both surface cations and capillary diffusion (pink tubes in Fig. 1) of water molecules in porous microstructure of the HEC.

The presence of oxygen vacancies and unsaturated surface cations plays an important role in the absorption and splitting of water molecules at room temperature. The trapped charge electrons in the oxygen vacancies generate high electric field, which easily captures the OH^- ions of the water molecules. Meanwhile, the strong Coulomb interaction between the surface metal cations and the negatively charged oxygen of the water molecules also takes place, which results in the formation of hydrogen bonding that weakens the O–H covalent bonds of water molecules. Therefore, the

first layer formed on the surface of the HEC material by water molecules is dominated by OH^- ions. This adsorption of first layer of water molecules on HEC surface is popularly known as chemisorption process. Figure 1 illustrates this process clearly where the positively charged unsaturated metal surface cations (green balls) and the trapped charges at oxygen vacancies (blue balls) attract the OH^- ions due to high electro negativity of oxygen and its highly polar nature in the water molecules. As a result, a spontaneous process for the dissociation of water molecules occurs over the surface cations and vacancies. These metal cations have high charge density and strong electrostatic fields; therefore, during this process, many hydrogen ions (H^+) are also released which are free to migrate within the surface lattice through the natively present oxygen ions (red balls) in the lattice. This makes the protons mobile at the surface or within the lattice as shown in Fig. 1 [72, 73]. Now, these mobile protons move from one site to another site due to strong electrostatic fields and react with the nearest oxygen ions (O^{2-}) at surface to form another hydroxyl (OH^-) group. In this situation, the protons are tunneled from one molecule of water vapor to other through hydrogen bonding. This process is well known as Grotthuss mechanism for the diffusion of hydrogen (H^+) and hydroxide ions (OH^-) [73–76]. Therefore, diffusion of hydrogen (H^+) ions also take place in water molecules at the material surface [77, 78]. The diffusion and mobility of hydroxide ions (OH^-) play an important role in protonic conduction. In fact, the self-ionization or surface collision of water molecules results in the quick separation of protons (H^+) and hydroxide ions (OH^-). This process can be compensated by the use of a single water molecule or double water molecules as expressed follows [25, 77, 78].

$$H_2O \Leftrightarrow H^+ + OH^- \ldots eq^n \qquad (1)$$
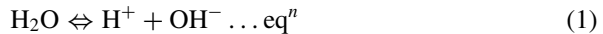
Now, this released hydrogen ions immediately protonate another water molecule to form a hydronium ion (H_3O^+).

$$H_2O + H_2O \Leftrightarrow H_3O^+ + OH^- \ldots eq^n \qquad (2)$$
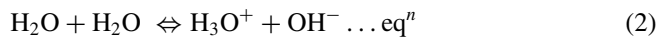
The dissociated hydrogen ions (H^+) can also form the bonding with the surface lattice oxygen atom (O_o) and create the hydroxyl groups ($OH)^-$ as

$$H^+ + O_o \leftrightarrow OH^-, \ldots eq^n \qquad (3)$$
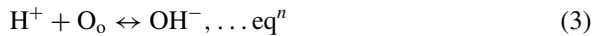
Now, the hydroxyl groups at the surface can react with the metal ion species and generate more free electrons. The generation of more free electrons increases the conductivity with increasing water adsorption at HEC surface [79];

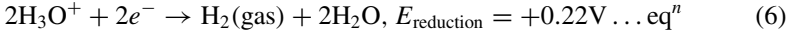$$[OH]^- + (Fe/Mg)^{++} \leftrightarrow [OH{-}Fe/Mg] + e^- \ldots eq^n \qquad (4)$$
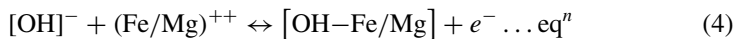
The layer formed by hydroxyl groups provides a channel for the formation of hydrogen bonding to attach the further water molecules. After chemisorption of first

layer of water molecules, further addition of water molecules results in physidissociation or physisorption of the water molecules in the first layer of hydroxyl ions. Once the first layer of physisorbed water vapors is completed, then another layer of water molecules is physisorbed via double hydrogen bonding with two neighboring hydroxyl groups [72, 73]. And this process of physisorption is continued to dissociate the water molecules and release more H^+ ions which start hopping in the second layer of physisorbed water molecules. Thus, the production of OH^- ions and H_3O^+ ions keeps going on during the process of water splitting. On the other hand, the presence of nanopores (~50 nm) on the surface also plays a vital role to trap these H_3O^+ ions that develop an electrostatic potential of the order of 10^4 V/cm to further rapidly dissociate the water molecules [60]. The chemisorption and then the physisorption of water molecules on the surface of HEC lead to H_3O^+ ion hopping and then protonic hopping by H^+ ions through the porous structure of the lattice. These H_3O^+ ions and OH^- ions are collected at anode and cathode, respectively, where it goes under reduction and oxidation mechanism, and therefore, a voltage in HEC is developed across two electrodes [47, 60]. The reactions that take place at two electrodes are written as follows [60]:

At anode (Zn plate),

$$Zn + 2OH^- \rightarrow Zn(OH)_2 + 2e^-, E_{oxidation} = -0.76 \text{ V} \dots eq^n \tag{5}$$
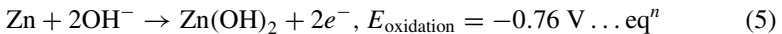
And at cathode (silver paste),

$$2H_3O^+ + 2e^- \rightarrow H_2(gas) + 2H_2O, E_{reduction} = +0.22V \dots eq^n \tag{6}$$

and also,

$$2H^+ + 2e^- \rightarrow H_2 \text{ (gas)} \dots eq^n \tag{7}$$
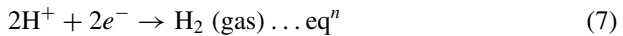
So, the total voltage developed across the hydroelectric cell of a 1-inch square pellet is equal to $0.22 - (-0.76) = 0.98$ V with a current of about 8 mA for Li-doped magnesium ferrite and about 77 mA for Co-doped SnO_2 nanomaterials [57, 60, 70]. This process develops enough electric potential that can continuously dissociate the physisorbed water molecules to regulate the current in HEC. The spontaneous reactions at the electrodes generate cell potential that allows the flow of electric current to the external circuit of HEC. A significant progress has been made to improve the performance of ferrite-based HEC cell.

3 Preparation and Characterizations of the Hydroelectric Cell

The main process of HEC development is to control its microstructure properties and optimize the synthesis of spinel ferrites or metal oxide nanomaterials. A pellet based on ferrite or metal oxide nanostructures has to be prepared for cell applications. The formation of a pellet or compact disk can easily be done after preparing the powder sample by one of the popularly known techniques such as sol–gel, mechanical ball-milling, solid-state reaction, co-precipitation, hydrothermal and solvothermal methods [60, 72, 80–88]. Now, these as-prepared powder samples can be compressed to form a pellet or a compact shape of circular disk, by uniform compression under a hydraulic pressing machine for half an hour at 4–8 tons of load pressure. The pellet dimensions can be varied from sample to sample and as per requirements for HEC applications. Depending on the material, the powder samples are pre-sintered or annealed twice at the desired temperatures so that a nanoporous surface with maximum oxygen deficiency can be obtained in order to enhance its performance for the maximum dissociation of the water molecules. In accordance with the chosen HEC, these pellets can be heat treated either in ambient conditions or in a different gaseous atmosphere in a wide range of temperature from 400 to 1200 °C for 2–8 h in order to maintain the porosity, oxygen concentration and the desired microstructure [60, 62, 86, 89, 90]. Here, the important factor is to optimize the annealing atmosphere, time and temperature of the HEC material because the annealing at higher temperature (>800 °C) in certain ferrites and metal oxide nanomaterials can results in structural instability and sample hardness, and therefore, the cell materials lose their porosity and the surface reactivity [91].

The main characteristics features of HEC materials can be probed by using X-ray diffraction (XRD), Raman spectroscopy (RS), Fourier-transform infrared spectroscopy (FTIR), high-resolution transmission electron microscopy (HRTEM) and secondary electron microscopy (SEM) for analyzing their structural, morphological, chemical and surface properties in order to optimize the cell performance. The control of microstructure properties (particles shape, size, distribution, surface roughness, etc.,) is the key consideration in order to maximize the dissociation of water molecules in the HECs. Energy-dispersive X-ray spectroscopy (EDX) and X-ray photoelectron spectroscopy (XPS) are very useful to confirm the presence of elements and analyze the surface properties and composition of the cell material. Brunauer–Emmett–Teller (BET) surface analyzer is useful to get information about pore size distribution and specific surface area, which provides an idea about the physical adsorption of water on HEC surface. Nitrogen adsorption–desorption isotherms can be recorded with high-purity nitrogen gas as adsorbate at 77 K by using an instrument like Micromeritics Gemini VII surface area and porosity system. The specific surface area can be estimated by the five-point or multiple-point Brunauer–Emmett–Teller (BET) method, and the pore size distribution can be derived from the desorption branch of the isotherms by using the method of Barrett–Joyner–Halenda (BJH) analysis [83]. The porosity (*p*) of the HEC pellets made of cubic spinel ferrite

sample can be calculated from the relation $p = 1 - d_{exp}/d_{th}$, where d_{exp} is known as the experimental density (d_{exp} = mass/volume) and d_{th} is known as the theoretical density ($d_{th} = 8M/a^3N_A$) for a spinel ferrite [60, 92]. Here, M is the molecular weight, a is the lattice constant and N_A is the Avogadro's constant. The specific surface area (A_s) can be calculated by using the equation ($A_s = s/Vd_{exp}$), where s and V are particle surface area and volume, respectively. The HEC performance can be measured by fabricating Zn anode electrode and an interdigitated silver paste-based cathode electrode at two opposite faces of the pellet/disks [60]. The impedance and electrical measurements can be performed by using different digital meters such as LCR meter LCR-8110G, Keithley 2400 and 2450 source meters and model DMM4050 made by Tektronix. The Nyquist plots by using electrochemical impedance spectroscopy (EIS) can provide the useful information about ionic conduction in the HEC device because it comprises of equivalent electrical circuits that consist of resistance, capacitance and inductance. The ionic diffusion in the HECs can be explained by the presence of distinct semicircle bands in different frequency ranges from 20 Hz to 120 MHz of Nyquist plots in wet and dry conditions at a minimum voltage (~10 mV) [60]. The important parameter to analyze the HEC performance is to examine the different loss regions in the cell by using voltage–current (V–I) polarization curve. The V–I polarization curve of HEC has been measured by using Keithley 2430 1 kW pulse source meter [60]. It gives useful information about the voltage loss due to potential barrier formation at electrode (or activation polarization loss), voltage loss due to resistance by charge transport (known as ohmic polarization loss) and voltage loss due to mass transport (also known as concentration polarization loss) in electrochemical reaction at the electrode surface. The V–I polarization curve can be directly fitted to empirical Eq. (8) to understand the contribution of losses in different regions for the amount of current flowing through the pellet [71]. Total output voltage (V_{out}) in HEC can be expressed by using Eq. (8);

$$V_{out} = E_{oc} - B \ln\left(\frac{I}{I_0}\right) - IR - m\left(\ln\left(1 - \frac{I}{I_l}\right)\right) \ldots eq^n \qquad (8)$$

where activation polarization loss,

$$V_{act} = B \ln\left(\frac{I}{I_0}\right) \ldots eq^n \qquad (9)$$

and ohmic polarization loss,

$$V_{ohm} = IR \ldots eq^n \qquad (10s)$$

and concentration polarization loss,

$$V_{conc} = m\left(\ln\left(1 - \frac{I}{I_l}\right)\right) \ldots eq^n \qquad (11)$$

Here, E_{oc} is the open-cell voltage of HEC; B is the Tafel slope; I_o is exchange current; R is the ohmic resistance; m is a fitting constant and I_1 is the limiting current in the cell [71]. Tafel equation (9) is useful to estimate the rate of electrochemical reaction of anode and cathode (Ag/Zn) with dissociated ions in HEC. In the intermediate current regions, the resistive losses are prominent, whereas in high-output current regions, the concentration losses are dominant on both electrodes. In order to evaluate the efficiency of a HEC, the voltage–current (V–I) characteristic curve is plotted for the flow of current across its electrodes for an externally applied or internally generated voltage through the device [57, 60]. The calculation of fill factor (F_{HEC}) could be important for an assessment of the performance of HEC as a better performance can be indexed with the higher fill factor. The fill factor is defined as the ratio of the maximum useful power to the ideal power of the HEC [57, 60],

$$\text{Fill Factor} \ (F_{HEC}) = \frac{P_{max}}{V_{oc} \times I_{sc}} = \frac{V_m \times I_m}{V_{oc} \times I_{sc}} \ldots \text{eq}^n \tag{12}$$

here the maximum useful power is,

$$(P_{max}) = V_m \times I_m \ldots \text{eq}^n \tag{13}$$

and the maximum theoretical ideal power is,

$$(P_{theory}) = V_{oc} \times I_{sc} \ldots \text{eq}^n \tag{14}$$

where V_m and I_m are maximum voltage and maximum current, respectively, at the maximum useful power. V_{oc} is the maximum open-circuit emf voltage generated by the cell under the condition if there is no current flowing through the device. I_{sc} is defined as the short-circuit current at zero resistance in the circuit [57, 60]. If there is zero resistance, then the current flowing through the cell would be maximized and the voltage will drop to zero. The number of unpaired electrons that are responsible for the dissociation of water molecules in the HEC can be calculated by using electron spin resonance (ESR). Mott Schottky (MS) plot gives an idea about carrier density in HEC [71]. Electron density can be calculated from MS plot by using the slope in quasilinear region with following Eq. (15) [71]:

$$N_d \ \left(\text{in cm}^{-3}\right) = \frac{2}{e\varepsilon\varepsilon_o \frac{d\left(\frac{1}{C^2}\right)}{d(V)}} \ldots \text{eq}^n \tag{15}$$

Here, N_d is the donor density, e is the electron charge, ϵ denotes the dielectric constant of HEC pellet (for hematite 80), ϵ_o is the permittivity of vacuum and V is the applied potential at electrode surface. A positive MS slope would mean an n-type semiconductor-based HEC with electrons as the majority charge carriers [71].

4 Overview of Different Materials for Hydroelectric Cell

The different materials for HECs that have been studied so far are CuO, NiO, CeO_2, TiO_2, MgO, SnO_2, ZnO, Cr_2O_3, Fe_3O_4, Fe_2O_3, Sc_2O_3, $MgFe_2O_4$, SiO_2, V_2O_5, $LiFe_2O_4$, Co_3O_4, Mn_3O_4, $Al_{2-x}Mg_xO_3$ (where $x = 0$–0.5) etc. [46, 47, 50–53, 56, 57, 60, 70, 93]. It is well known that most of these oxides are porous ceramic materials in nature and have been widely studied for humidity sensing and gas sensing applications of different gases because of their low cost, easy fabrication, moderate sensitivity and simple measurements techniques [72, 94–107]. The most common feature behind these sensing properties is the chemisorption properties of water and gas molecules at room temperature with high sensitivity on the porous surface microstructure of these metal oxides due to the presence of high concentration of unsaturated surface charge species [60]. The development of HEC based on different metal oxide semiconductors also relies on a similar mechanism for the absorption of water molecules on the surface and in the bulk of the porous ferrite or metal oxide nanomaterials.

Titanium dioxide (TiO_2) is a popularly known porous wide band gap metal oxide semiconductor material with 3.2 eV band gap of anatase phase and 3.0 eV of most stable rutile phase [108–110]. It has been widely studied due to its water-splitting nature and high photocatalytic activity under direct sunlight radiation [111–116]. The photocatalytic activity can take place by exciting the electron of titanium dioxide in UV region which generates the electron–hole pairs that are useful to split the water molecules. Unfortunately, the large rapid recombination of electron and hole at the scale of 10 ns makes the process inefficient [12, 117]. Recently, Shukla et al. exploited the concept of water splitting and prepared a TiO_2-based HEC cell by solid-state reaction method. The effect of different dopants on the cell performance was measured after the substitution of Li, Mg and Fe doping in the TiO_2 [55]. The dopants were taken in a molar ratio of 0.1:0.9 with respect to TiO_2. The HEC performance was recorded by fabricating the zinc and silver electrode on two opposite faces of a square shaped-pellet. The addition of water on the cell surface quickly dissociates it into H^+ ions and OH^- ions without using any external source. This leads to the movement of ions toward silver and zinc electrodes where it forms zinc hydroxide and hydrogen, respectively. This redox reaction between two electrodes makes the cell functional by developing a potential that allows the flowing of the current in an external circuit. The results showed that the Li and Mg doping increased the cell current in TiO_2, whereas the Fe doping has drastically reduced the cell current. The maximum short-circuit current of 6 mA was recorded for Mg-doped TiO_2 with an open-cell voltage of 0.925 V. The enhanced cell performance was attributed to the increased porosity, increased oxygen vacancies and improved specific surface area of the TiO_2 nanostructures, which help in the splitting of more water molecules at the TiO_2 surface [55].

SnO_2 is a well-known wide band gap semiconductor with a tetragonal rutile phase (P42/mnm space group), which has high chemical and thermal stability and widely studied for transparent conducting oxides (TCO) due to its transparency in the

visible region, dilute magnetic semiconducting (DMS) properties, water purification, photocatalytic properties and solar cell applications [60, 118–122]. There are four oxygen ions (O^{2-}) and two tin (Sn^{4+}) ions in a unit cell. The Sn ions occupy the octahedral position surrounded by six oxygen ions in the corners. The oxygen ions are surrounded by three tin ions sitting at the corners of three equilateral triangles [57, 60, 123–127]. Recently, SnO_2 has received huge attention among other metal oxide semiconductors for HEC applications due to its high defect density, porous nature, low bulk resistance and water dissociation properties [25, 47, 57]. Gaur et al. have used sol–gel method to prepare nanoporous SnO_2 materials for HEC application [57]. In order to improve the HEC conversion efficiency, SnO_2 nanomaterials were doped with magnesium and cobalt ions. The interstitial substitution of Mg and Co doping in SnO_2 nanomaterials was confirmed by XRD. The average particles sizes of 16 and 12 nm were calculated by using TEM images for Co- and Mg-doped SnO_2 samples, respectively. These were in good agreement with the crystalline size calculated from Debye Scherrer formula by using XRD pattern. The square pellets of an area of 4.08 cm^2 were prepared for HEC device applications and the pellets are shown in Fig. 2a–b. The zinc and silver electrodes were fabricated on two opposite faces of the HEC device. Figure 2c shows the maximum current flowing through the Mg- and Co-doped SnO_2-based HEC devices. The basic mechanism for water dissociation at doped SnO_2 surface remains the same as discussed in the previous section. It is primarily governed by the chemisorption of OH^- ions to the Sn cations and to the trapped sites created by the oxygen vacancies which act as the unsaturated/dangling bond. A maximum short-circuit current of 77.52 mA was observed for Co-doped SnO_2-based HEC device with an open-circuit voltage of 0.454 V and off-load output power of 35.19 mW. In the case of Mg-doped SnO_2-based HEC device, the short-circuit current was 41.69 mA with an open-circuit voltage of 0.787 V and off-load output power of 32.81 mW. Figure 3a–d shows the BET plot, *V*–*I* polarization, cyclic voltammetry (CV) graph and Nyquist curve, respectively, for the Co-doped SnO_2-based HEC device. The surface area was calculated by using BET curves, whose values are 46.22 and 46.81 m^2/g for Mg- and Co-doped SnO_2 nanomaterials, respectively, with an average pore radius of ∼3 nm. The EIS was used to study the charge transfer mechanism in Mg- and Co-doped SnO_2 nanomaterials. The Nyquist curves confirmed the ionic diffusion of H_3O^+ and OH^- ions in the wet pellets in comparison to their dry state (Fig. 3d). The resistance was suddenly dropped in wet pellets from ∼10^6 Ω to ~26 Ω and ~54 Ω, respectively, for Co- and Mg-doped SnO_2-based HECs after soaking in distilled water. CV was used to understand the nature of electrochemical reactions taking place at the surface of two different electrodes. The peaks for anodic potential and cathodic potential were observed at 0.254 V and 0.139 V, respectively, for Co-doped SnO_2-based HEC device. The redox reactions were confirmed by the presence of these cathodic and anodic peaks in CV plot (Fig. 3c). The *V*–*I* polarization curve (Fig. 3b) was plotted to understand the cell voltage in terms of operating current in HEC. The *V*–*I* polarization curve is mainly categorized into four types of control segments. The main segments are attributed to the internal loss, activation loss at low current density, ohmic losses and the concentration loss in the high current density regions. The Co-doped SnO_2 has shown
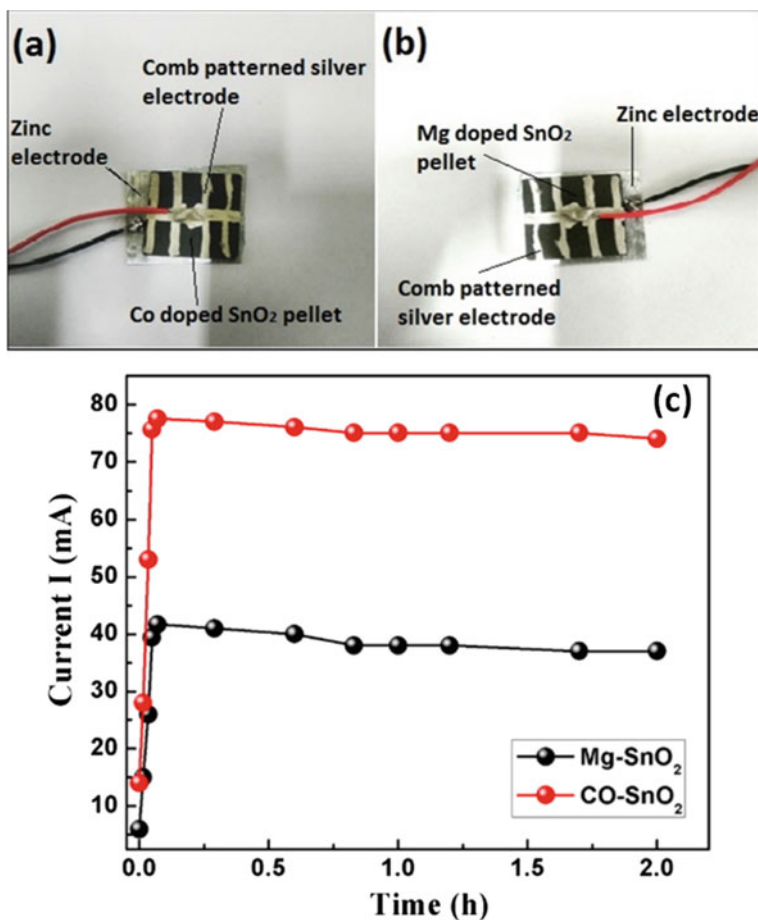
Fig. 2 HEC device fabrication for **a** Co-doped SnO_2 nanomaterials, and **b** Mg-doped SnO_2 nanomaterials and **c** current versus time (I–t) response of Mg and Co-doped SnO_2 nanomaterials. Open access journal; Reproduced under copyright 2020, ACS Omega [57]

promising behavior than other non-ferrite source of materials for HEC application as an alternate of green energy [57].

In an interesting work, Solanki et al. have presented the dissociation of water molecules in a SnO_2-based hydroelectric cell by using a thin aluminum foil of 11 μm thickness as an anode and silver paste as a cathode [25]. The cell has generated a high potential difference of ~1000 ± 20 mV between the electrodes at room temperature by using 50 ml of DI water [25]. The cell has high stability of more than 3500 h. In this case, the OH^- ions released the electron after reaction with the Al electrode instead of the Zn electrode. The most impressive job that this HEC device can do is generation of the electricity by using the moisture from the atmosphere with the help of a moisture-absorbing layer of chlorinated porous CuO with a size of
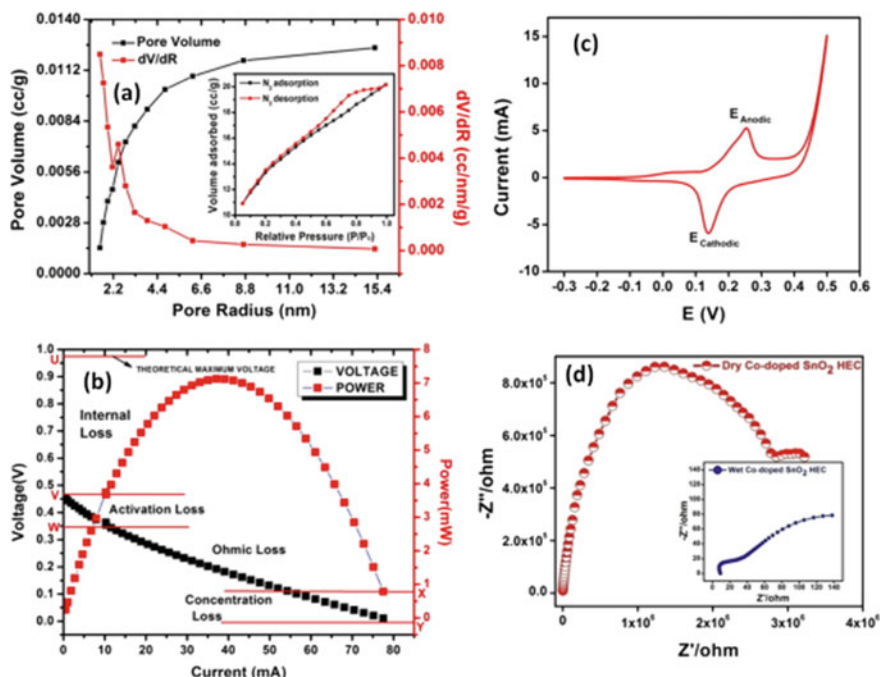
Fig. 3 Different graphs of HEC device for Co-doped SnO_2 nanomaterials **a** BET plot, **b** V–I polarization curve, **c** cyclic voltammetry graph and **d** Nyquist curve. Open access journal; Reproduced under copyright 2020, ACS Omega [57]

6–8 nm. BET was used to confirm the porosity of the CuO, which has a specific BET surface area of 6.95 m²/g and an average pore size of 6.6 nm. The composite material of porous SnO_2 for the HEC device was prepared by a green route hydrothermal method that involves elemental de-alloying by thermal-assisted sequential removal of highly mobile elements at high sintering temperatures [25]. The generation of the hydroxyl radical for splitting the water molecules was confirmed by the UV–visible absorbance and PL spectra of terephthalic acid (TA) degradation at the different time intervals. The formation of $Al(OH)_3$ at anode during the process of water splitting was also confirmed by the XRD pattern recorded for the deposited residual that was present over the Al electrode [25]. The various metal oxides of SnO_2, Al_2O_3, ZnO, TiO_2, MgO, and SiO_2-based HEC were developed by Kotnala et al. by solid-state reaction method followed by their sintering in different ranges of temperatures in two stages in order to obtain a nanoporous structure [47]. The cell performance was compared and a maximum power of ~16.6 mW was observed for a SnO_2-based HEC with a highest current of 22.2 mA generated by a pellet of an area 4.48 cm² [47]. The observed current was much higher than the magnesium ferrite-based HEC developed by their group. The BET analysis confirmed the distribution of nanopores within the size ranging from 3 to 6 nm in all the samples. The minimum porosity

of 6.22% was observed in SnO_2, whereas a maximum porosity of 38.4% for TiO_2 was calculated by Archimedes principle. The calculated values of power densities are: 6.4 mW for Al_2O_3, 4.5 mW for ZnO, 2.07 mW for TiO_2, 1.41 mW for MgO, and 1.05 mW for SiO_2. The observed values of current densities are ~0.79 $\mu A/cm^2$ in SnO_2, 0.62 $\mu A/cm^2$ in Al_2O_3, 0.587 $\mu A/cm^2$ in ZnO, 0.168 $\mu A/cm^2$ in TiO_2, 0.142 $\mu A/cm^2$ in MgO and 0.119 $\mu A/cm^2$ in SiO_2, respectively. Similarly, the potential difference between the electrodes was measured, whose values are 0.75 V for SnO_2, 0.93 V for Al_2O_3, 0.90 V for TiO_2 and ZnO, 0.94 V for MgO, and 0.96 V for SiO_2, respectively [47]. Figure 4 shows the different morphology of some metal oxides, and Fig. 5 shows the $V–I$ polarization curves at room temperature whereas Fig. 6 displays the complex impedance plots of dry metal oxide-based HECs. The insets in Fig. 6 show the curve fitting of wet HECs for the complex impedance spectra of metal oxides.

The defects concentration has been found to play a key role in water dissociation in HEC. Gupta et al. have recently shown that increasing the Mg doping concentration in the host lattice of alumina (Al_2O_3)-based HEC has significantly increased the number of defects density in nanoporous $Al_{2-x}Mg_xO_3$ ($x = 0$–0.5) from ~1.45×10^{15} cm^{-3} (for $x = 0.1$) to 5.4×10^{16} cm^{-3} (for $x = 0.5$) [46]. The polycrystalline Mg-doped alumina-based HECs were fabricated by a solid-state reaction method followed by low-temperature thermal treatments. The pellets for HECs were prepared into a dimension of 2 cm $\times$ 2 cm with a thickness of 0.1 mm and then finally annealed at 850 °C for 2 h. The HECs performance was recorded after fabricating the Zn and Ag electrodes at two opposite faces. The bare Al_2O_3 (for $x = 0$)-based HEC has a current density of 1.12 mA/cm^2, which was remarkably increased after Mg
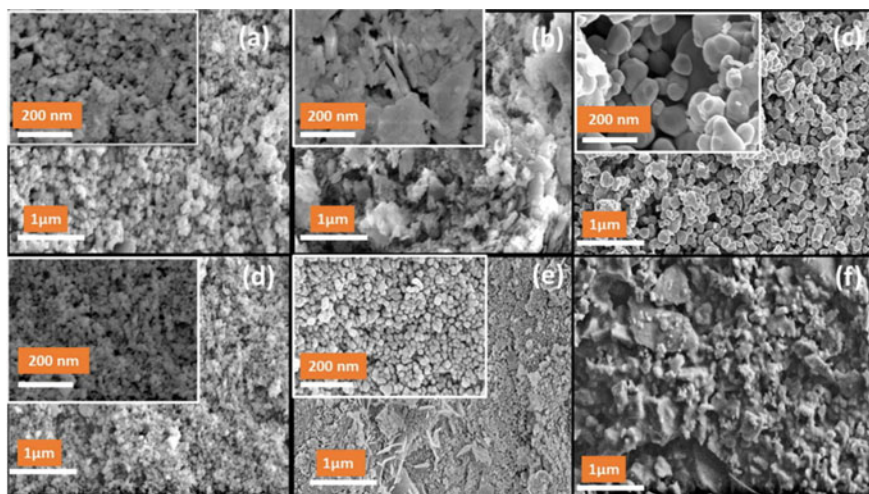
Fig. 4 SEM images of different metal oxide samples fabricated for HEC application **a** SnO_2, **b** Al_2O_3, **c** ZnO, **d** TiO_2, **e** MgO and **f** SiO_2, respectively. Reprinted (adapted) with permission from Ref. [47]. Copyright © (2018) American Chemical Society
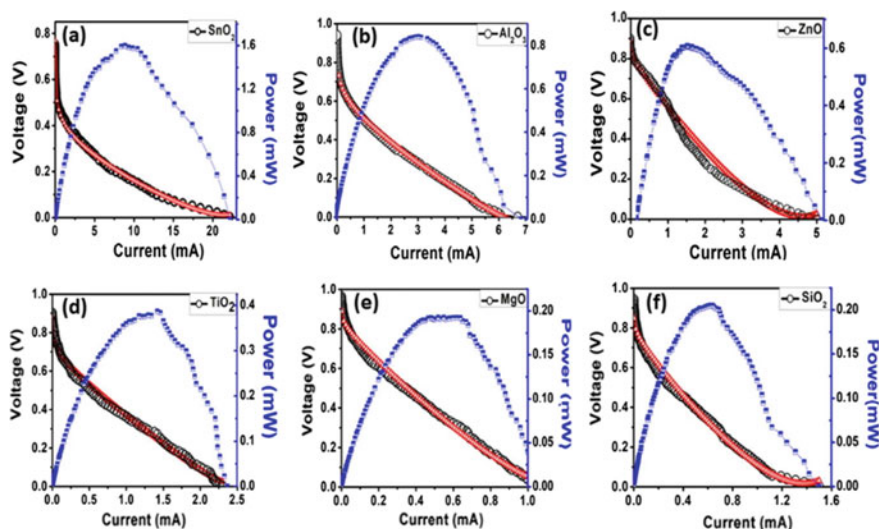
Fig. 5 Voltage–current (*V–I*) polarization curves with different polarization regions of various metal oxide samples fabricated for HEC application **a** SnO$_2$, **b** Al$_2$O$_3$, **c** ZnO, **d** TiO$_2$, **e** MgO, and **f** SiO$_2$, respectively. Reprinted (adapted) with permission from Ref. [47]. Copyright © (2018) American Chemical Society
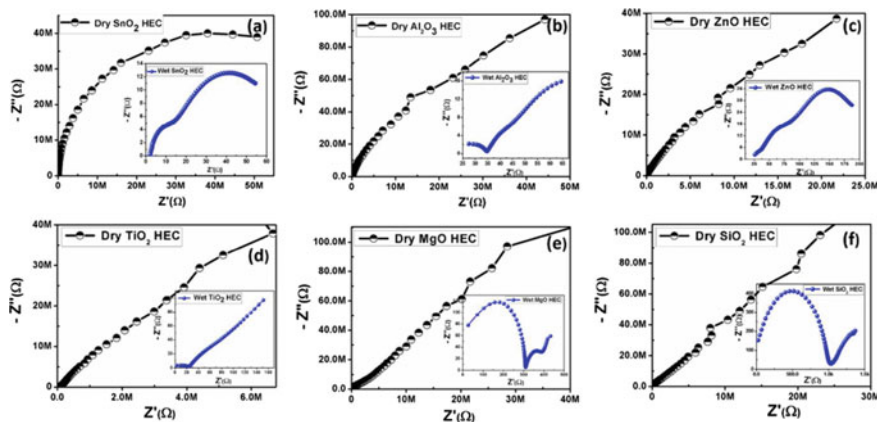
Fig. 6 Complex impedance plots of different dry metal oxide samples fabricated for HEC application **a** SnO$_2$, **b** Al$_2$O$_3$, **c** ZnO, **d** TiO$_2$, **e** MgO and **f** SiO$_2$, respectively. Reprinted (adapted) with permission from Ref. [47]. Copyright © (2018) American Chemical Society

doping with increasing the defects concentration from 1.75 mA/cm^2 (for $x = 0.1$) to 3.75 mA/cm^2 (for $x = 0.5$).

The maximum current of 15 mA was achieved for the highest concentration of Mg substitution ($x = 0.5$) with a maximum output power of 13.5 mW, which was higher

than the output power (4.95 mW) of bare alumina-based HEC [46]. The Nyquist spectra confirmed the ion–solid interaction in HEC during the process of charge transportation. A small contribution from polaron-mediated ionic charge transportation was observed in the nanoporous Mg-doped alumina-based HECs, which reduces the internal resistance and increases the ionic conduction of the HEC [46].

5 Ferrites-Based Hydroelectric Cell and Its Applications

Iron oxide nanoparticles and ferrites nanomaterials are widely used to modulate magnetic and electric properties and have applications in spintronics, biomedical science, magnetic field sensors, LPG sensors, gas sensors, hydroelectric cell and humidity sensors [62, 98, 99, 128–137]. In spite of having interesting magnetic properties, the ferrites nanomaterials show special characteristics such as their oxygen vacancy and porous nature, which make them suitable for humidity, gas sensing and hydroelectric cell applications wherein their magnetic properties are not utilized [47, 89]. The main idea of the generation of electricity by using the concept of hydroelectric cell was originated from the moisture/water absorption properties of the porous magnesium ferrite nanostructures, which make it a strategic material for humidity sensor applications [70, 138, 139]. The presence of oxygen vacancies and unsaturated surface cations/dangling bonds at the porous surface improves the surface reactivity of the ferrite samples. Before exploiting the magnesium ferrite for HEC application, it has displayed the utility for the humidity and gas sensor applications [64, 86, 140, 141]. For these applications, the porosity in ferrite nanomaterials is most important which can be controlled by doping and metallic particle incorporation or by preparing composite nanostructures and controlling the process and synthesis conditions. The change in pore size distribution can increase the resistance to the order of gega ohm in ferrite nanomaterials. The HEC performance can be largely affected by surface morphology and surface modifications, dopants, and adding catalyst.

The HECs based on ferrite materials have received significant attention due to their promising alternate for green and eco-friendly behavior for energy harvesting. The first practical HEC developed by Kotnala et al. was based on Li-substituted magnesium ferrite synthesized by a simple solid-state reaction method [70]. The powder of the precursor materials were firstly mixed and grounded for about 2 h in a pestle mortar and then heat-treated in ambient conditions at 850 °C for 10 h. The low temperature for synthesis is necessary in order to generate the nanopores in the microstructure of ferrite-based HEC. The thermally treated powder was grinded again for 30 min and then pressed into a pellet of volume $2.2 \times 2.2 \times 0.1$ cm^3 and a disk of 4.6 cm diameter with 0.1 cm of thickness [70]. These prepared pellets and circular disks were annealed to solidify at 1050 °C for 6 h in the presence of air atmosphere. Now, a 0.3 mm thick plate of the Zn electrode as anode was attached to one face of the pellet surface, whereas the other opposite face of the pellet was coated with a comb electrode of silver with thickness of 0.1 μm to act as a cathode. The circular disk was made bigger in size than the rectangular. The HEC pellets with

three different dimensions with effective areas of 1.1, 4.8 and 17 cm^2 were prepared to study the scalability of the cell for large-scale applications. The electrostatic force microscopy of Bruker Multimode AFM was used to confirm the generation of charges at the ferrite surface. XRD, SAED, SEM and TEM were used to confirm the desired structural properties and to analyze the particle shape and size. The BET measurement of pellet was performed by using Quanta Chrome instrument (NOVA 2000e USA) to analyze the porosity in terms of pore size distribution and specific surface area from the nitrogen physisorption graph. Keithley 2430 1 kW pulse source meter was mainly used to record the cell performance by measuring the current versus voltage measurements of the HEC pellet. The Wayne-Kerr Impedance Analyzer 6500B (UK) was used to record the data of Nyquist plot of the HEC to confirm the ionic diffusion in the cell in a dry and wet state by applying an AC voltage of 10 mV in a range from 20 Hz to 120 MHz [70]. In dry condition, the HEC pellet showed a high reactance of 10^8 Ω, which was drastically reduced to approximately 100 Ω after partially dipping in DI water with resistance of 16 MΩ. As the HEC was dipped in DI water, the dangling bonds of unsaturated cations and oxygen vacancies at the surface facilitate the separation of H_3O^+ and OH^- ions at room temperature. As a result, some of these H_3O^+ ions are trapped into the nanopores which generate an electric field of the order 2.16×10^4 V/cm, which is high enough for further dissociation of physisorbed water molecules. During the process of ionic conduction, the oxidation at Zn electrode takes place by hydroxide ion that converts the Zn metal partially into $Zn(OH)_2$, and a reduction reaction takes place at Ag electrode by H_3O^+/H^+ which produces a clean and green H_2 gas through the cell. This is a continuous process that develops voltage and current in cell, and the flow of the ionic current increases with increase in the physidissociation of the water molecules in the HEC. The HEC exhibited a short-circuit current of 82 mA and a maximum emf of ~0.920 mV with a maximum output power of 74 mW for a cell with an area of 17 cm^2. It was confirmed that the electrodes played a negligible role for the ionic conduction of DI water as compared to the pellet in HEC. The cost of preparation of the HEC is low and the performance displayed by Li-substituted magnesium ferrite was repetitive, eco-friendly and stable over a long time [70]. Up to date, the Li-doped magnesium ferrite-based HEC can deliver a maximum voltage of 0.98 V with a current of about 17 mA/cm^2 which is highly comparable to solar cell output power and other portable energy sources which do not use any electrolyte/acid/alkali except water [47, 58, 60, 70].

An optimized composition of lithium-substituted magnesium ferrite ($Mg_{0.8}Li_{0.2}Fe_2O_4$) pellet-based HEC has been typically used for the production of the hydrogen gas [34]. The generation of the H_2 gas in ferrites by using HEC is a non-photocatalytic technique, and it can be performed anywhere in dark or light, which does not require any separator, electrolyte, membrane, and catalyst. The continuous production of the H_2 gas through HEC just requires DI water and external source of DC voltage. The typical laboratory setup for the production of hydrogen gas from $Mg_{0.8}Li_{0.2}Fe_2O_4$ pellet-based HEC is shown in Fig. 7 [34]. The collection of hydrogen gas was done through a gas outlet in a sealed system, where the HEC was partially dipped into the DI water. The produced H_2 gas was collected via a silicon tube in an upside-down measuring cylinder tube that is filled with DI
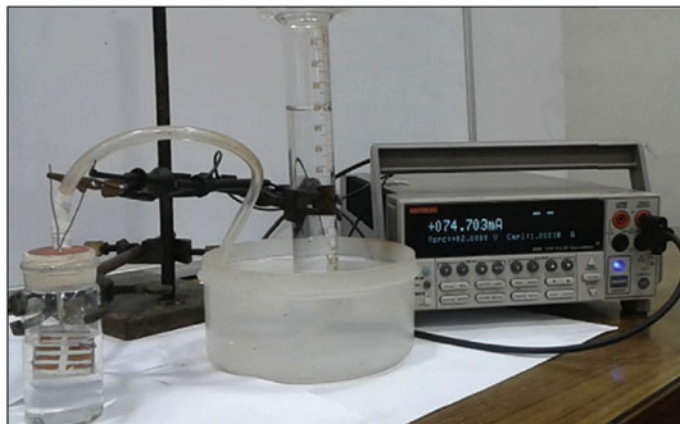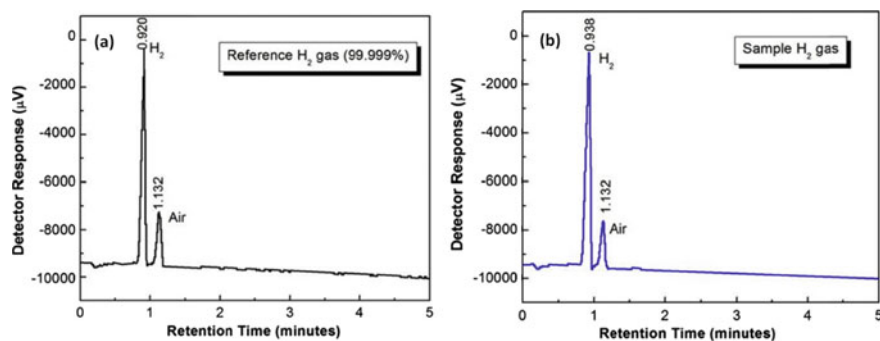
Fig. 7 The typical laboratory setup for the production of hydrogen gas from $Mg_{0.8}Li_{0.2}Fe_2O_4$ pellet-based HEC. Reproduced with permission from Ref. [34]. Copyright 2017, Elsevier B. V

water. The anode and the cathode of the HEC were connected to voltage source through conducting wires. The gas production was recorded for different voltages by using separate pellets in the range from 1 to 4 V and the production of H_2 gas increases with an increasing external applied voltage. A large quantity of H_2 gas was produced that was increased from 1.426 mmol/h to 1.856 mmol/h for increasing an applied voltage from 1 to 4 V, respectively. The results are comparable to other techniques of producing H_2 gas [34]. The XRD, surface morphology along with nitrogen adsorption and desorption curve of $Mg_{0.8}Li_{0.2}Fe_2O_4$ pellet is shown in Fig. 8a–d [34]. The N_2 adsorption–desorption isotherm showed an average nanopore size distribution of 3.8 nm. The TEM image displayed that the majority of the particles have rectangular shape with rounded corners, whose size is in the range of 50–200 nm, which are consistent to those observed in SEM images. Figure 9a, b shows the gas chromatography (GC) test for the collected H_2 gas from the HEC in comparison to the reference H_2 gas diluted with air [34]. The GC analysis confirms the gas produced by HEC is a high-purity hydrogen gas with a retention time of 0.938 min, whose position was similar to that observed for a reference hydrogen peak with a retention time of 0.919 min. Another intense peak observed in GC graph with a retention time of 1.132 min is due to ambient air including nitrogen. The details of GC measurements can be found elsewhere [34].

In fact, Shah et al. also reported the green route synthesis of zinc oxide (ZnO) nanoparticles by using the same composition of a nanoporous Li-doped magnesium ferrite ($Mg_{0.8}Li_{0.2}Fe_2O_4$)-based hydroelectric cell [48]. When the water molecules were dipped into the HEC, the porous Li-doped magnesium ferrite pellet splits the water molecules into hydronium and hydroxide ions. The hydroxide ions were collected at the zinc electrode, where it forms the zinc hydroxide and the hydronium ions react at the silver electrode to form the H_2 gas as discussed above. After the experiment, the residual of zinc hydroxide was collected from the Zn anode, which
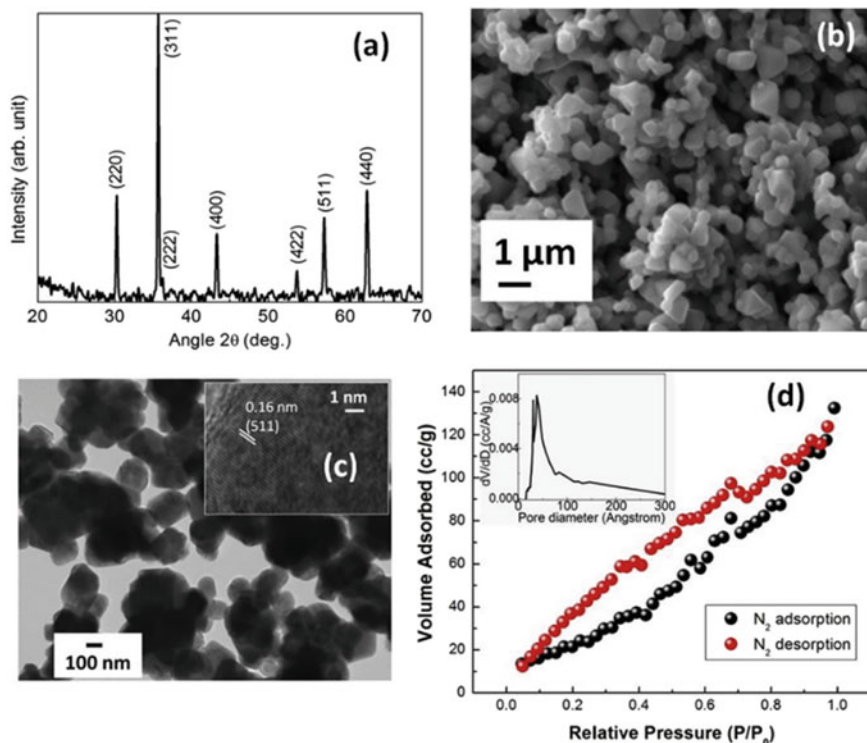
Fig. 8 Different characterizations of $Mg_{0.8}Li_{0.2}Fe_2O_4$ pellet-based HEC **a** XRD, **b** SEM image of porous surface, **c** TEM image and inset shows the d-spacing for (511) plane and **d** N_2 adsorption–desorption isotherm curve with an inset for pore size distribution. Reproduced with permission from Ref. [34]. Copyright 2017, Elsevier B. V

Fig. 9 Gas chromatography test **a** reference H_2 gas diluted with air and **b** collected H_2 gas from $Mg_{0.8}Li_{0.2}Fe_2O_4$-based HEC. Reproduced with permission from Ref. [34]. Copyright 2017, Elsevier B. V

was subsequently thermally treated at 250 °C for the formation of ZnO nanoparticles [48]. The structural, morphological, and optical properties of the ZnO nanoparticles were confirmed and thoroughly analyzed by using XRD, Raman spectroscopy, high-resolution transmission electron microscopy (HRTEM), UV–Vis spectroscopy, and PL spectroscopy [48].

Jain and Shah et al. demonstrated that the magnetite (Fe_3O_4), maghemite (γ-Fe_2O_3) and hematite (α-Fe_2O_3) nanoparticles synthesized by a chemical co-precipitation method can produce plenty of oxygen deficiency and work in a similar fashion as Li-doped magnesium ferrite for HEC application [51, 71, 93]. In these samples, the Fe cations, oxygen vacancies, and trapped charges inside the pores promote the dissociation of water molecules. A typical magnetite-based HEC with a cathode of silver comb electrode and an anode of zinc electrode is shown in Fig. 10a [93]. The V–I polarization curve and power produced by the magnetite-based HEC after dipping in DI water are shown in Fig. 10b. Nyquist plot of magnetite for dry and wet conditions shown in Fig. 10c, d has confirmed the ionic diffusion of dissociated water molecules in magnetite-based HEC by the presence of a diffusion tail in wet conditions [93]. The HEC resistance was drastically reduced to ~80 Ω from ~10^5 Ω
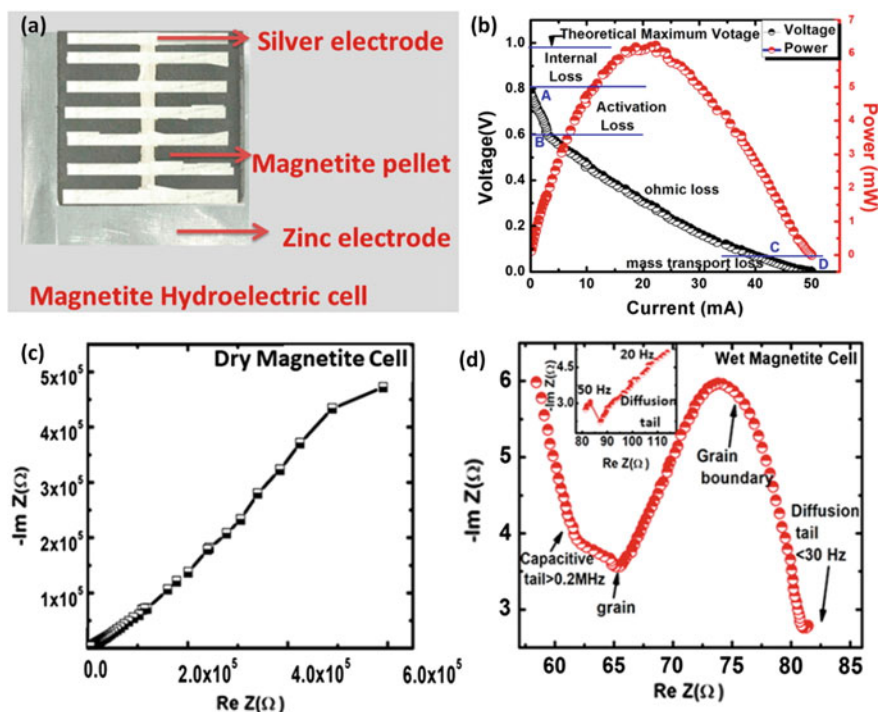
Fig. 10 Magnetite-based HEC; **a** fabrication of cell, **b** V–I polarization curve after absorbing water, **c** Nyquist plot in dry condition and **d** in wet condition. Reprinted (adapted) with permission from Ref. [93]. Copyright © (2018) American Chemical Society

after placing the cell into DI water. The hopping of Fe^{2+}/Fe^{3+} ions in the magnetite was found to be responsible to reduce the contribution from ohmic loss that resulted in a net increase in the cell current. HEC based on magnetite with an area of 4.8 cm^2 generates an emf of 0.77 V and a maximum current of 50 mA with a maximum output power of 38.5 mW. However, the peak power calculated by using the *V–I* polarization graph is 6.4 mW [93]. On the other hand, a hematite (α-Fe_2O_3)-based HEC can produce a current of 30 mA with an emf of 0.92 V by consuming approximately 500 µL of DI water [71]. HEC based on hematite with an area of 4.84 cm^2 has produced a maximum off-load output power of 27.6 mW which is apparently ~3.5 times higher than that reported of 7.84 mW for Li-substituted magnesium ferrite [70, 71]. The formation of $Zn(OH)_2$ at the zinc anode during the redox reaction in magnetite-based HEC was confirmed by XRD and the evolution of the H_2 gas at the Ag electrode was detected by using an MQ-8 H_2 gas sensor. The continuous operation of the cell resulted in deposition of an orange-brownish color of material over black magnetite surface which was identified as α-FeOOH (goethite) by Raman spectra as a result of oxidation of Fe^{2+} ions (Eq. 16) [93]. Moreover, the electrochemical reactions occurring on the magnetite surface were confirmed by cyclic voltammetry.

$$Fe_3O_4 + 4OH^- \rightarrow 3FeOOH + 2H_2O + e^- \tag{16}$$
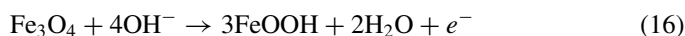
The ionic states of iron and oxygen vacancies in magnetite were rigorously studied by using X-ray photoelectron spectroscopy, which revealed a partial oxidation of Fe_3O_4 to γ-Fe_2O_3 that might have occurred during the synthesis. The presence of unsaturated/dangling bonds in Fe_3O_4 due to the existence of unpaired electrons with a high spin density of 8.37×10^{24} spins/g was confirmed by electron spin resonance (ESR) spectrum. This represents that a large number of active sites are available in magnetite-based HEC surfaces for the dissociation of water molecules.

The mesoporous nature of the magnetite was confirmed from field emission scanning electron microscopy images (FESEM), atomic force microscopy (AFM) topography, and N_2 adsorption–desorption isotherm curve from BET measurements. These images and graphs are shown in Fig. 11a–d. The FESEM images confirm the grain size distribution in the range of 9–20 nm, with an average of 11 nm. The average pore size calculated from SEM is about 10.0 nm, which corroborates well with AFM observation. The mesopores observed in the images have a size of less than 50 nm. Some distribution of macropores was also observed over the surface with a size greater than 50 nm. The specific surface area of 89.78 m^2/g and an average pore diameter of 9.8 nm were estimated by using BET for magnetite-based HEC [93]. In the case of hematite-based HEC, an average grain size of 18.8 nm was calculated by using SEM/TEM with a distribution in the range from 11 to 27 nm [71]. The specific surface area of hematite 72.2 m^2/g was estimated from N_2 desorption isotherm curve from multipoint BET measurements. The Barrett-Joyner-Halenda (BJH) method was used to record the pore size distribution curve of hematite, which resulted in an average pore size of 16.8 nm [71].

In a similar study, Gaur et al. have also synthesized the pure Fe_3O_4 and porous Li-doped Fe_3O_4 ($Li_{0.4}Fe_{2.6}O_4$) by chemical co-precipitation method [53]. The BET
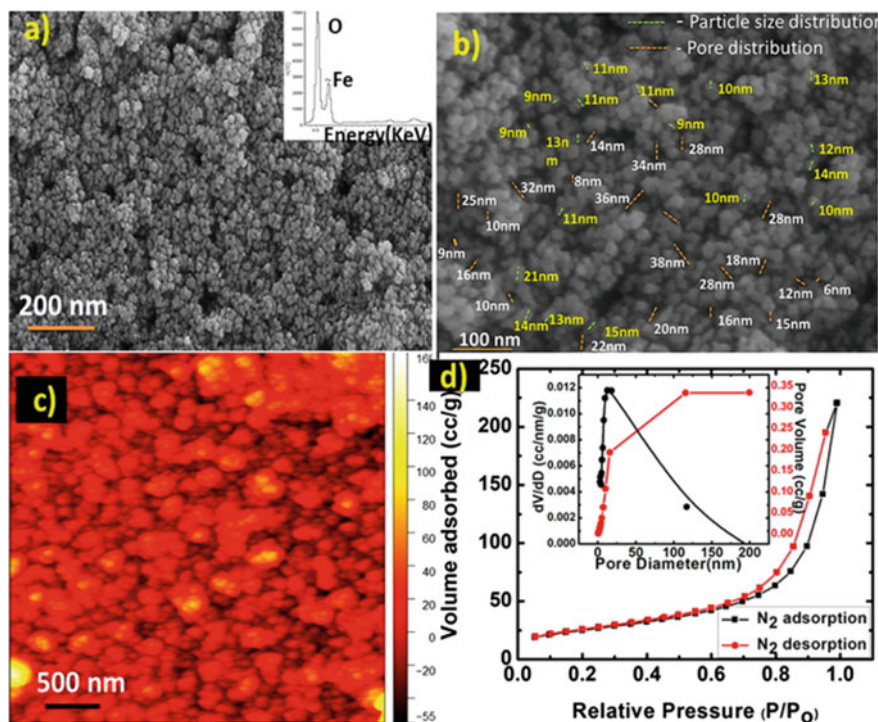
Fig. 11 **a** porous morphology of magnetite at 200 nm scale by FESEM; the inset shows the EDX spectrum, **b** high resolution FESEM image for pore and particle size distribution, **c** AFM 2D topography of magnetite shows the pore size ranging from 2 to 18 nm and **d** N_2 adsorption–desorption isotherm curves with an inset for pore size distribution. Reprinted (adapted) with permission from Ref. [93]. Copyright © (2018) American Chemical Society

measurements of Li-doped Fe_3O_4 showed a specific surface area of 45 m^2/g with an average pore radius of ~4 nm. HEC based on Li-doped Fe_3O_4 with an area of 4.08 cm^2 has generated a current of 44.91 mA, open-circuit voltage of 0.68 V, and a maximum of off-load output power of 30.80 mW, whereas the pure Fe_3O_4-based HEC has shown an output power of 3.31 mW [53]. However, the on-load peak power estimated by using V–I polarization curve for Fe_3O_4 is 0.917 mW, whereas for Li-doped Fe_3O_4 is 5.39 mW [53]. The CV measurement was used to confirm the enhanced redox reactions at cathode and anode. Nyquist curve was plotted for both pure and Li-doped Fe_3O_4-based HEC to confirm the ionic diffusion in the cells. In the case of Fe_3O_4-based HEC, the resistance jump from 10^3 Ω (dry condition) to 2000 Ω after spraying the DI water over the surface. On the other hand, Li-doped Fe_3O_4-based HEC exhibited a drastic drop from 10^3 Ω (dry condition) to 71 Ω under identical conditions [53].

In a latest report, maghemite (γ-Fe_2O_3) nanoparticles were synthesized by co-precipitation method by Shah et al. for HEC application [51]. The magnetite powder

was annealed at 300 °C for 2 h to obtain maghemite powder, which was then grounded and pressed into a pellet of dimension $2.48 \times 2.48 \times 0.1$ cm^3 followed by subsequent thermal annealing at 350 °C for 2 h. During the synthesis process, the vacancies of oxygen (V^O) and iron (V^{Fe}) were developed in maghemite nanoparticles which were analyzed by using XPS, PL, and Raman spectroscopy. The XPS, PL, and HRTEM images of the sample are displayed in Fig. 12a–d. The TEM showed oval-shaped nanograins with an average size of 13.1 nm and a distribution ranging between 9 and 17 nm. XPS study suggests that the V^{Fe} sites are preferable sites for water adsorption. A low concentration of iron in Fe^{2+} ionic state was also observed, which was attributed to the reduction of few Fe^{3+} ions in the inert atmosphere and believed to be responsible for decreasing the concentration of cation vacancy (V^{Fe}) in maghemite-based HEC. The study revealed that the association of water molecules with V^{Fe} sites in maghemite hinders the dissociation of OH^- and H^+ ions, which lower the performance of maghemite HEC in comparison to magnetite HEC. The presence of oxygen and iron vacancies is also evidenced by the presence of different emission peaks in PL spectroscopy. The dielectric measurements were conducted to understand the mechanism of ionic transport in the cell. The maghemite cell of 4.84 cm^2 area has generated a maximum current of 19 mA, an emf of 0.85 V with a maximum
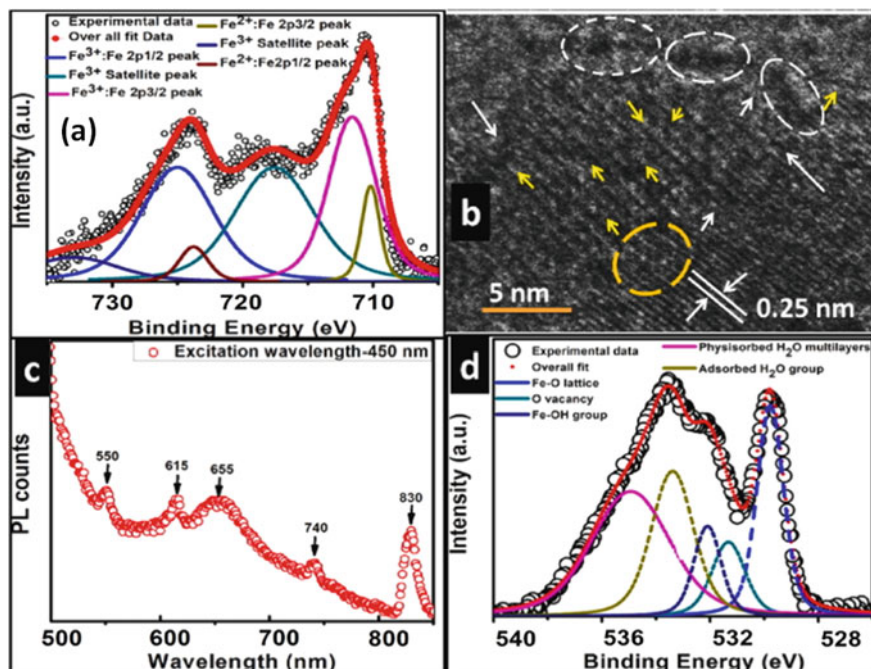
Fig. 12 **a** Deconvolution of Fe 2p XPS spectra of maghemite, **b** HRTEM image showing the (311) lattice and defects regions of maghemite, **c** PL spectra of maghemite and **d** deconvolution of O 1s XPS spectra of maghemite for identification of oxygen vacancies. Reproduced with permission from Ref. [51]. Copyright 2021, Elsevier B. V

output power of 16.15 mW by using 200 µL water, which is 0.58 and 0.42 times lower than magnetite- and hematite-based HECs, respectively, as discussed above [51]. The study revealed that the prominence of hydrophobic V^{Fe} sites, low concentration of oxygen vacancies and a large average pore size of ~10.8 nm are the key factors for lower performance of maghemite-based HEC as compared to other iron oxide-based HECs [51]. The BET measurement showed a high surface-to-volume ratio of maghemite pellet with a specific surface area of 90.37 m^2/g and a maximum pore size of 120 nm. The reactance of the maghemite was remarkably dropped from 10 MΩ to KΩs from its dry state to wet state. The EIS measurements and V–I polarization graphs of maghemite-based HEC are shown in Fig. 13a–d.

The electrical conductivity has increased mainly due to the ionic conduction after dissociation of water molecules by unsaturated surface ions and defect species. The
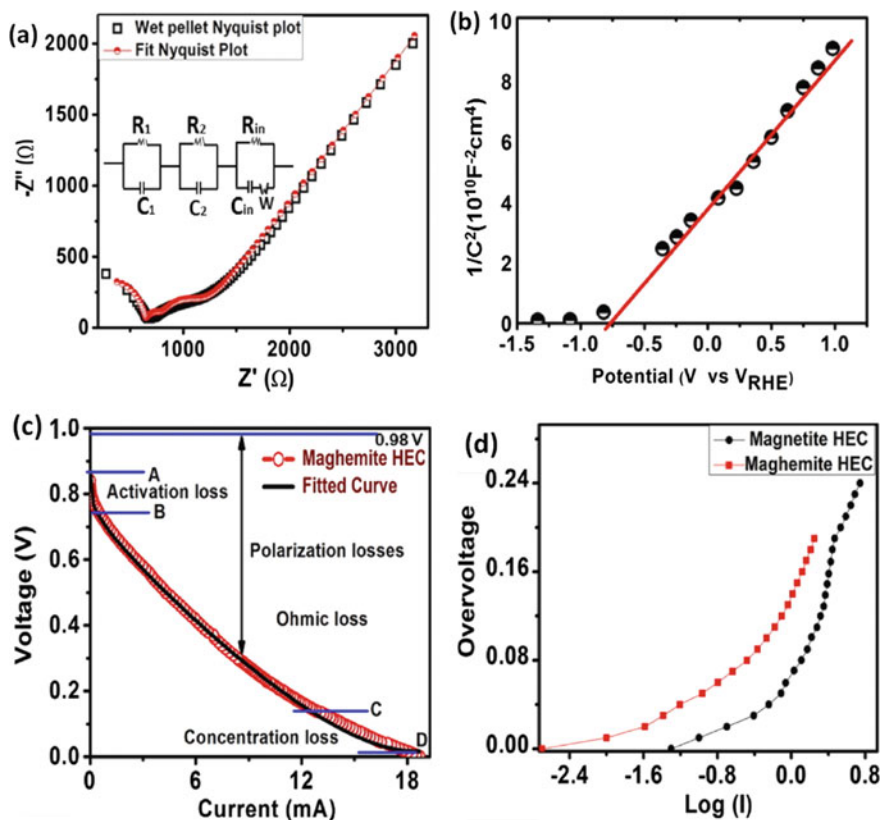

Fig. 13 **a** Nyquist plot of wet maghemite HEC and its fitting with an equivalent circuit shown in the inset, **b** Mott Schottky plot of maghemite pellet as working electrode in 0.1M KOH solution, **c** V–I polarization curve of maghemite-based HEC and black line is the fitted curve and **d** Tafel plots of magnetite and maghemite-based HEC. Reproduced with permission from Ref. [51]. Copyright 2021, Elsevier B. V

Nyquist plot shown in Fig. 13a was fitted to an equivalent electronic circuit diagram as shown in the inset to understand the mechanism of charge transfer. The circuit shown in the inset is a parallel RC circuit, which has a contribution from the bulk region ($R_1 \| C_1$), charge transfer through the grain boundaries of the crystallite ($R_2 \| C_2$), and an electrode interface region at low frequencies (($R_{in} + W) \| C_{in}$) due to their differing relaxation time constants [51]. Mott-Schottky analysis (Fig. 13b) was used to calculate the electron density of maghemite as working electrode, and its value 1.23 × 10^{18}/cm^3 is lower than the other phase of iron oxide (magnetite ~1.17 × 10^{19}/cm^3, and hematite ~4.86 × 10^{19}/cm^3, respectively) [51]. The fitting of V–I polarization graph (Fig. 13c) of maghemite-based HEC in the presence of different loads has confirmed the three operating current regions that correspond to the activation losses (AB region), ohmic losses (BC region), and concentration polarization losses (CD region). The slope in the Tafel plot (Fig. 13d) helps in understanding the initial voltage drop due to weak electrochemical kinetics in spinel ferrite-based HECs. Tafel graph suggests that activation of over-voltage-related electrochemical kinetics in magnetite and maghemite HEC is dominated by anode activity, and the higher slope in magnetite is because of high activation over-voltage drop [51].

In an attempt to improve the porosity and oxygen defects in HEC, a composite material of a multiferroic compound BaTiO$_3$ (BTO) and cubic CoFe$_2$O$_4$ (CFO) was prepared at low temperatures by Shah et al. to increase the dissociation of water molecules [52]. The different concentrations (x) of the BTO to CFO were chosen in a ratio of (1−x) BTO: xCFO [where x = 0.0 (BTO), 1.0 (CFO), 0.85 (BTO85), 0.75 (BTO75), 0.65 (BTO65), and 0.55 (BTO55)]. The XRD and HRTEM results confirmed that BTO–CFO composite nanocomposite has a compressive lattice strain due to a lattice strain in BTO as a result of lattice mismatch between two phases.

The surface morphology of the nanocomposite was found to be varying with the ratio of the composition. PL spectroscopy was used to assess the information about defect states. The porosity (p) of the pellets of nanocomposite was estimated by Archimedes principle, whose values are 2.3%, 7.8%, 10.8%, 7.15%, 6.18%, and 5.54% for BTO, CFO, BTO85, BTO75, BTO65, and BTO55, respectively. FESEM images showed a porous microstructure with a grain size distribution in the range of 66–300 nm. A typical laboratory setup for measuring the HEC performance of BTO: CFO nanocomposites is shown in Fig. 14a, and the V–I polarization graphs are shown in Fig. 14b [52]. Figure 14c, d shows the Nyquist plot and it is fitting in dry and wet conditions for complex impedance of BTO85- and BTO75-based HECs [52]. The current generated by BTO: CFO nanocomposites in wet state at room temperature as a function of time is displayed in Fig. 15 [52]. This graph demonstrates that the current initially fluctuates and then becomes constant for all BTO–CFO HECs over a long period of time. This confirms that the redox reaction at the electrodes and dissociation of water molecules can sustain for a long period. The fixed load current value of 1.2, 0.9, 7.9, and 5.9 mA have been estimated for BTO, CFO, BTO85-, and BTO75-based HECs, respectively. The composite material of BTO–CFO-based HEC generated more current and voltage than an individual BTO or CFO compound. The composite HEC consists of 0.85 BTO: 0.15 CFO (BTO85) with zinc and silver electrodes with an area of 4.5 cm^2 in the shape of circular
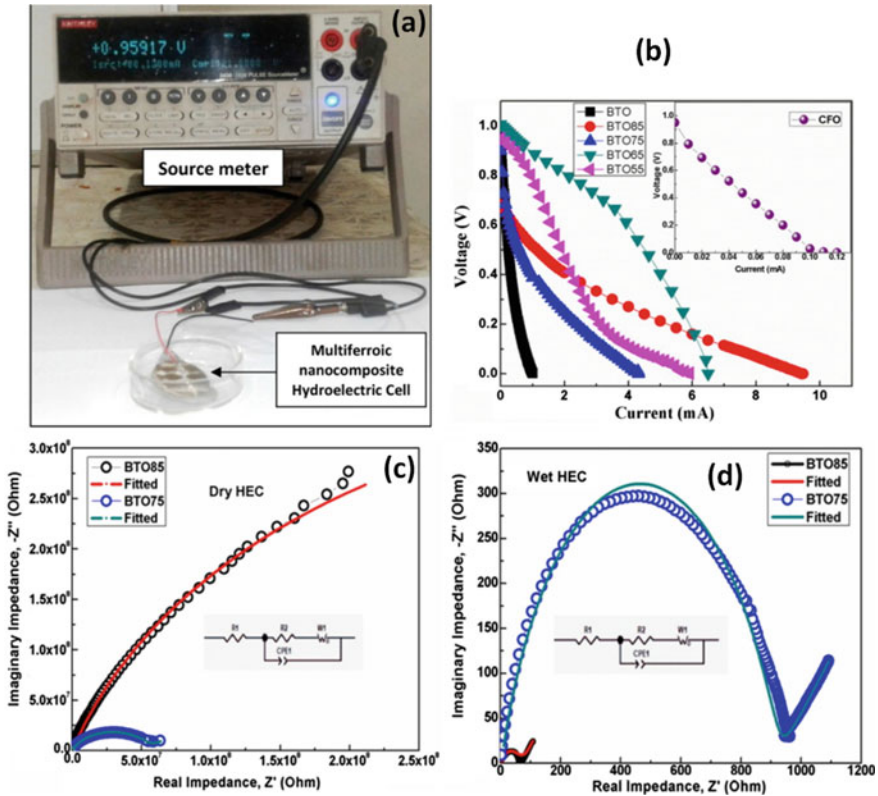
Fig. 14 **a** A typical laboratory setup for recording the $V-I$ graph of HEC by using a source meter, **b** $V-I$ polarization curve of different BTO:CFO nanocomposites-based HECs, **c** Nyquist plot of BTO:CFO nanocomposites-based HECs and the fitted curve (solid line) in dry condition and **d** in wet condition. Reproduced with permission from Ref. [52]. Copyright 2020, Elsevier B. V

disk has generated a voltage of 0.7 V with a maximum current of 7.93 mA and a maximum output power of 5.55 mW [52]. The high performance of BTO85-based HEC was attributed to the presence of highest porosity and high defect concentration for enhanced dissociation of water molecules as confirmed by PL spectroscopy. The $V-I$ polarization curve showed that the cell voltage was reduced due to activation polarization loss at low current to overcome against the initial potential barrier of dissociated ions at electrode–material interface [52].

In order to promote the hydroelectric cell for renewable energy source, Saini et al. have prepared an oxygen-deficient nanoporous material based on Ni-substituted lithium ferrite (termed as LNFO with composition $Li_{0.3}Ni_{0.4}Fe_{2.3}O_4$) by following the solid-state reaction method [61]. The pre-sintering temperature was varied in order to control the defect concentration in the LNFO. The pre-sintering of the samples was done at 750 and 800 °C for 8 h, whereas the final sintering was done at 950 °C for 2 h. These samples are referred to as LNFO-1 and LNFO-2, respectively.
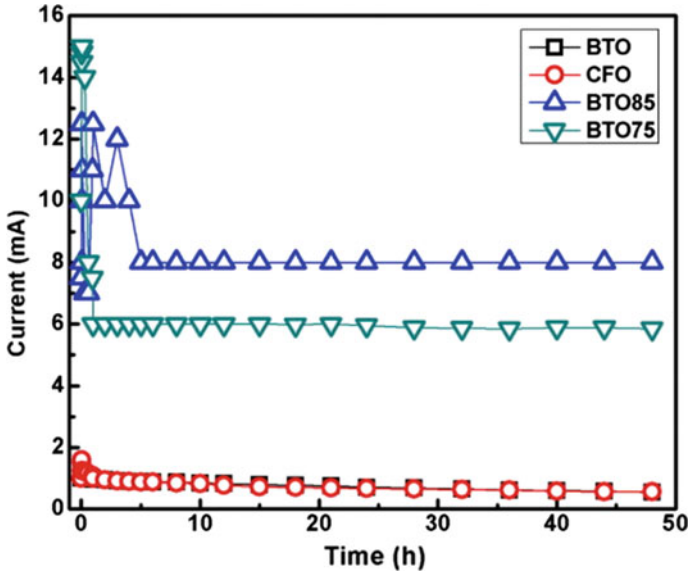
Fig. 15 The current generated by BTO:CFO nanocomposites in wet condition at room temperature as a function of time. Reproduced with permission from Ref. [52]. Copyright 2020, Elsevier B. V

The structural properties and porous microstructure were confirmed by characterization like XRD, FTIR, FESEM, BET, DFT, XPS and PL measurements. XPS and PL measurements corroborate the existence of defects states, whose concentration decreases with increasing the pre-sintering temperature; therefore, LNFO-1 has higher defects than LNFO-2. The two different morphologies were observed in FESEM image (Fig. 16) for LNFO-1 pellet. The average grain size calculated for LNFO-1- and LNFO-2-based HEC is 475 nm and 488 nm, respectively [61]. It has been observed that by increasing the pre-sintering temperature, the component of lattice oxygen has also increased which is responsible for the stability of ferrite lattice [61]. The V–I polarization curve and Nyquist plots in dry and wet conditions of LNFO-1- and LNFO-2-based HEC are shown in Figs. 17a, b and 18a, b, respectively. The V–I polarization curve confirms the smooth flow of ionic current in the LNFO-1-based HEC. The calculated activation potential loss in LNFO-1 and LNFO-2 HEC is 0.23 V and 0.32 V, respectively.

The maximum offload output power estimated for LNFO-1- and LNFO-2-based HECs was 13.77 mW and 14.36 mW, respectively. Maximum offload current and open-cell voltage of LNFO-1- and LNFO-2-based hydroelectric cells were measured as 15.3 mA, 0.9 V and 14.5 mA, 0.99 V, respectively. The impedance of the hydroelectric cell was rapidly dropped from ~10^8 Ω (for both LNFO-1 and LNFO-2 HECs) to few ohms after pouring the few drops of water into the cell. The current densities of LNFO-1 and LNFO-2 pellets with an area of 4 cm^2 are 3.8 mA/cm^2 and 3.6 mA/cm^2, respectively, which are approximately two times higher than that reported for Li-doped magnesium ferrite-based HEC (1.7 mA/cm^2) [61].
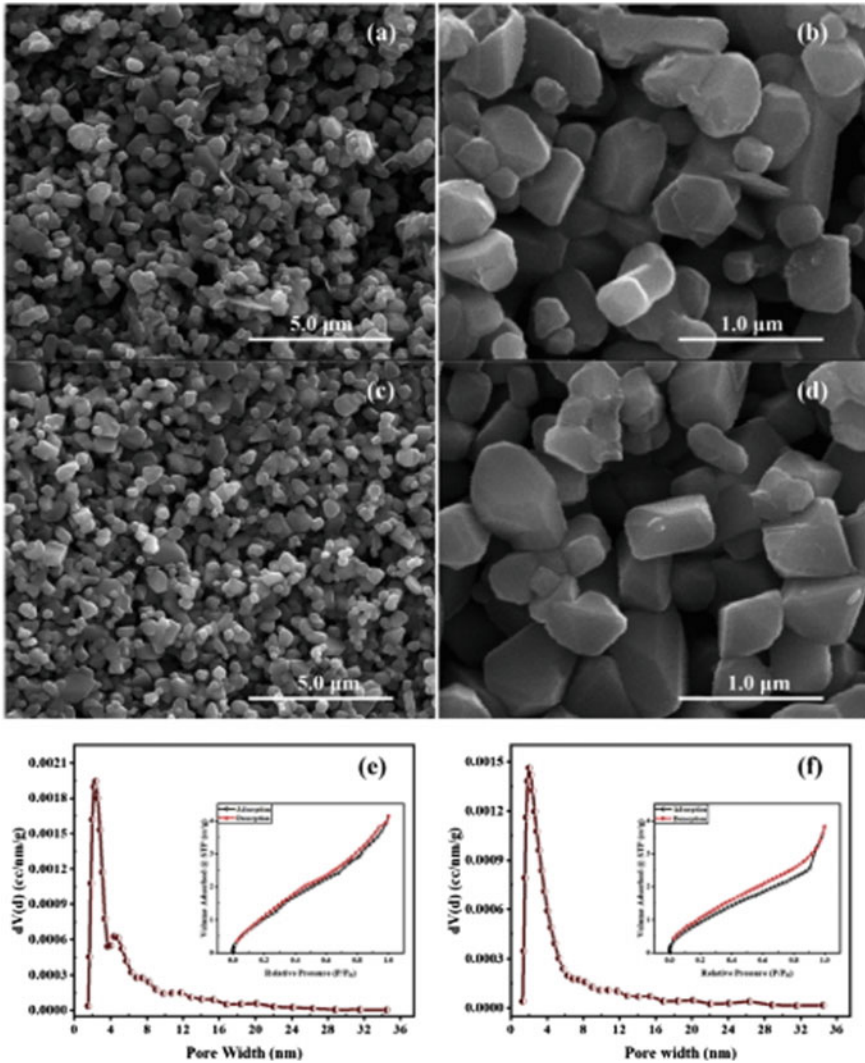
**Fig. 16 a, b** FESEM images of LNFO-1, **c, d** FESEM images of LNFO-2, **e** Pore size distribution curve of LNFO-1 and inset shows its BET isotherm, **f** Pore size distribution curve of LNFO-2, and inset shows its BET isotherm. Reproduced with permission from Ref. [61]. Copyright 2020, Elsevier B. V

6 Summary and Future Directions

The state of the art of the research herein highlighted shows that hydroelectric cells are a promising alternative for clean renewable energy sources, which would be especially viable for military applications and to provide energy in rural and remote areas.
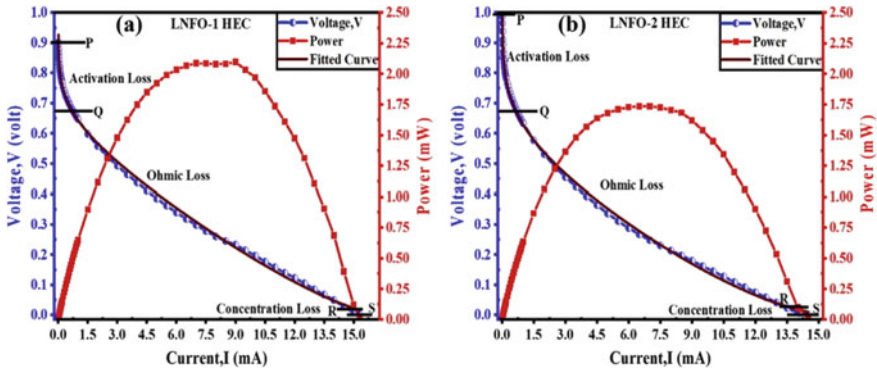
Fig. 17 *V–I* polarization curves after absorbing the water, **a** LNFO-1-based HEC, **b** LNFO-2-based HEC. Reproduced with permission from Ref. [61]. Copyright 2020, Elsevier B. V
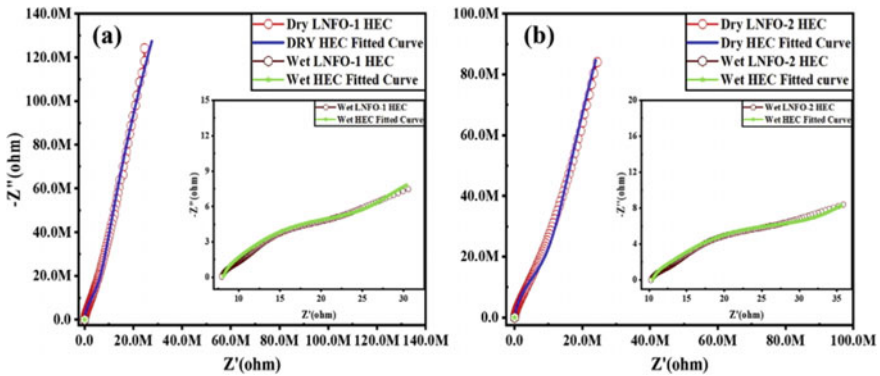
Fig. 18 Nyquist plots of Ni-doped lithium ferrite in dry and wet condition at room temperature, **a** LNFO-1-based HEC, **b** LNFO-2-based HEC. Reproduced with permission from Ref. [61]. Copyright 2020, Elsevier B. V

For reaching this goal of large application, it would be mandatory to focus on different ferrite and metal oxide-based semiconductors for their potential application as HEC owing to their high surface reactivity, high porosity with high oxygen deficiency in order to promote the splitting of the water molecules. In addition, the investigation on optimization of process parameters such as choice of preparation technique, control of pH value, stoichiometric composition, control over morphology, reaction time, reaction temperature and environment, surface functionalities, hybrid nanocomposites, annealing temperature and atmosphere, deposition methods, electrode choice, etc., certainly will contribute to optimize the HEC devices. Among several reports, the outcome of some of the remarkable ferrite/iron oxide-based HECs is summarized in Table 1.

Table 1 Summary of some remarkable HEC's based on ferrite nanomaterials, NA-not available

Reference No. and year	HEC Ferrite material name	Maximum emf voltage (V), current (mA), maximum power (mW) generation, and area	Specific surface area (in m^2/g) and average pore size (in nm) from BET analysis	Preparation methods
[54, 70] 2016	Li-doped magnesium ferrite $Mg_{0.8}Li_{0.2}Fe_2O_4$	8 mA, 0.98 V, 7.8 mW (area 4.8 cm^2) And, 82 mA, 0.92 V, 74 mW (area 17 cm^2)	165 m^2/g ~4.2 nm	Solid-state reaction
[93] 2018	Magnetite (Fe_3O_4)	50 mA, 0.77 V, 38.5 mW (area 4.8 cm^2)	89.78 m^2/g ~9.8 nm	Chemical co-precipitation method
[71] 2019	Hematite (α-Fe_2O_3)	30 mA, 0.92 V, 27.8 mW (area 4.8 cm^2)	72.2 m^2/g ~16.8 nm	Chemical co-precipitation method
[53] 2020	Li-doped $Fe_3O_4(Li_{0.4}Fe_{2.6}O_4)$	44.91 mA, 0.68 V, 30.80 mW (area 4.08 cm^2)	45 m^2/g ~4 nm	Chemical co-precipitation method
[52] 2020	Composite $BaTiO_3$ (BTO) and cubic $CoFe_2O_4$ (CFO)	7.93 mA, 0.7 V, 5.55 mW (area 4.5 cm^2)	NA	Sol–gel process
[52] 2020	Cubic cobalt ferrite $CoFe_2O_4$ (CFO)	0.9 mA, 0.95 V, 0.85 mW (area 4.5 cm^2)	NA	Sol–gel process
[61] 2020	Ni-substituted lithium ferrite ($Li_{0.3}Ni_{0.4}Fe_{2.3}O_4$)	15.3 mA, 0.9 V, 0.85 mW (area 4.0 cm^2)	NA ~2.5/4.6 nm	Solid-state reaction
[51] 2021	Maghemite (γ-Fe_2O_3)	19 mA, 0.85 V, 16.15 mW (area 4.84 cm^2)	90.37 m^2/g ~10.78 nm	Chemical co-precipitation method

HEC does not require any external source (such as other chemicals like acid/alkali/electrolyte) except DI water to produce the electricity. In fact, it is demonstrated that a copper layer in HEC can act as a pump for moisture absorption in the surrounding environment to generate electricity. Interestingly, the end electrodes of Zn and Ag at two opposite faces are pretty useful in the production of $Zn(OH)_2$/ZnO and a high purity H_2 gas (99.9%), respectively. The byproducts of the HEC are also non-hazardous, bio-compatible and reusable. Indeed the challenges remain unbeaten to produce the unique hydroelectric cells with high voltage and high current output which would not only reduce the cost but are also space and eco-friendly with high

durability, field replaceable and, importantly, the fabrication of compact devices for practical utility.

References

1. Dincer I (2018) Exergy, 1–5
2. MacEachern C, Yildiz I (2018) Wind energy, 1–5
3. Dincer I, Ozcan H (2018) Geothermal energy, 1–5
4. Xu C, Liao B, Pang S, Nazari L, Mahmood N, Tushar MSHK, Dutta A, Ray MB (2018) Biomass energy. Compr Energy Syst 1–5:770–94
5. Yildiz I (2018) Solar energy. Compr Energy Syst 1–5:638–64
6. Acar C, Dincer I (2018) Hydrogen energy, 1–5
7. Bagher AM, Vahid M, Mohsen M, Parvin D (2015) Hydroelectric energy advantages and disadvantages Am. J Energy Sci 2:17–20
8. Şen Z (2018) Energy innovation, 1–5
9. Ahmadi P, Dincer I (2018) Energy optimization, 1–5
10. Wang Z (2018) Energy air pollution, 1–5
11. Khademi F, Yildiz I (2018) Energy solid wastes, 1–5
12. Mathpal MC, Kumar P, Aragón FH, Soler MAG, Swart HC (2020) Basic concepts, engineering, and advances in dye-sensitized solar cells. In: Sharma SK, Ali K (eds) Solar cells: from materials to device technology. Springer, pp 185–234
13. Şen Z (2018) Hydro energy, 1–5
14. Yildiz AC (2018) Energy law and emerging legal issues, vol 1–5. Elsevier Ltd.
15. Yildiz I, Liu Y (2018) Energy units, conversions, and dimensional analysis Compr. Energy Syst 1–5:1–23
16. Ilhami Y, MacEachern C (2018) Historical aspects of energy. Compr. Energy Syst 1–5:24–48
17. Turner JA (1999) A realizable renewable energy future. Science 80(285):687–689
18. Yildiz I, MacEachern C (2018) Food and energy. Compr Energy Syst 1–5:850–74
19. Dincer I, Zamfirescu C (2018) Thermodynamic aspects of energy, vol 1–5
20. Thounthong P, Davat B, Raël S, Sethakul P (2009) Fuel cell high-power applications IEEE Ind. Electron Mag 3:32–46
21. Sweet ML (2016) The American association of petroleum geologists. AAPG Mem 111:iii
22. Blaabjerg F, Ionel DM (2015) Renewable energy devices and systems-state-of-the-art technology, research and development, challenges and future trends Electr. Power Compon Syst 43:1319–1328
23. Kayfeci M, Keçebaş A, Bayat M (2019) Hydrogen production
24. Pros HE (2020) Hydropower pros and cons. How hydroelectric energy works, 1–6
25. Solanki V, Krupanidhi SB, Nanda KK (2020) Harvesting energy via stimuli-free water/moisture dissociation by mesoporous SnO_2–based hydroelectric cell and CuO as a pump for atmospheric moisture Int. J Energy Res 44:1276–1283
26. del Valle F, Ishikawa A, Domen K, Villoria de la Mano JA, Sánchez-Sánchez MC, González ID, Herreras S, Mota N, Rivas ME, Álvarez Galván MC, Fierro JLG, Navarro RM (2009) Influence of Zn concentration in the activity of Cd1−xZnxS solid solutions for water splitting under visible light Catal. Today 143:51–56

27. Li H, Dong W, Xi J, Li Z, Wu X, Ji Z (2017) Hydropowered photoelectrochemical water splitting solar cell for hydrogen production. J Alloys Compd 691:750–754
28. Li FF, Qiu J, Wei JH (2018) Multiobjective optimization for hydro-photovoltaic hybrid power system considering both energy generation and energy consumption Energy Sci. Eng 6:362–370
29. Gobara HM, Nassar IM, El Naggar AMA, Eshaq G (2017) Nanocrystalline spinel ferrite for an enriched production of hydrogen through a solar energy stimulated water splitting process. Energy 118:1234–1242
30. Sivula K, Le FF, Grätzel M (2011) Solar water splitting: progress using hematite (α-Fe_2O_3) photoelectrodes. ChemSusChem
31. Armaroli N, Balzani V (2011) The hydrogen issue. ChemSusChem 4:21–36
32. Zografi G (1988) States of water associated with solids DRUG Dev. Ind Pharm 14:1905–1926
33. Dutta S (1990) Technology assessment of advanced electrolytic hydrogen production Int. J Hydrogen Energy 15:379–386
34. Shah J, Jain S, Shukla A, Gupta R, Kotnala RK (2017) A facile non-photocatalytic technique for hydrogen gas production by hydroelectric cell. Int. J Hydrogen Energy 42:30584–30590
35. Hauch A, Ebbesen SD, Jensen SH, Mogensen M (2008) Highly efficient high temperature electrolysis. J Mater Chem 18:2331–2340
36. Kanan MW, Nocera DG (2008) In situ formation of an oxygen-evolving catalyst in neutral water containing phosphate and Co_{2+}. Science 321:1072–1075
37. Chong L, Colón BC, Ziesack M, Silver PA, Nocera DG (2016) Water splitting–biosynthetic system with CO_2 reduction efficiencies exceeding photosynthesis. Science 352:1210–1213
38. Tamaura Y, Ueda Y, Matsunami J, Hasegawa N, Nezuka M, Sano T, Tsuji M (1999) Solar hydrogen production by using ferrites Sol. Energy 65:55–57
39. Yuan Q, Zhao Y (2009) Hydroelectric voltage generation based on water-filled single-walled carbon nanotubes. J Am Chem Soc 131:6374–6376
40. Miljkovic N, Preston DJ, Enright R, Wang EN (2014) Jumping-droplet electrostatic energy harvesting. Appl Phys Lett 105
41. Wei D (2015) Writable electrochemical energy source based on graphene oxide Sci. Rep 5:1–8
42. Chandrasekhar A, Vivekananthan V, Kim SJ (2020) A fully packed spheroidal hybrid generator for water wave energy harvesting and self-powered position tracking. Nano Energy 69:104439
43. Liu L, Shi Q, Lee C (2020) A novel hybridized blue energy harvester aiming at all-weather IoT applications. Nano Energy 76:105052
44. Bard AJ, Fox MA (1995) Artificial photosynthesis: solar splitting of water to hydrogen and oxygen Acc. Chem Res 28:141–145
45. Glanz K (2010) Using behavioral theories to guide decisions of what to measure, and why Int. J Hydrogen Energy 27:991–1022
46. Gupta R, Shah J, Das R, Saini S, Kotnala RK (2021) Defect-mediated ionic hopping and green electricity generation in $Al2-xMgxO_3$-based hydroelectric cell. J Mater Sci 56:1600–1611
47. Kotnala RK, Gupta R, Shukla A, Jain S, Gaur A, Shah J (2018) Metal oxide based hydroelectric cell for electricity generation by water molecule dissociation without electrolyte/acid. J Phys Chem C 122:18841–18849
48. Shah J, Kumar Kotnala R (2017) Rapid green synthesis of ZnO nanoparticles using a hydroelectric cell without an electrolyte. J Phys Chem Solids 108:15–20
49. Kotnala RK (2018) Invention of hydroelectric cell : a green energy groundbreaking revolution. J Phys Res Appl 2:2–5
50. Parkinson GS, Novotný Z, Jacobson P, Schmid M, Diebold U (2011) Room temperature water splitting at the surface of magnetite. J Am Chem Soc 133:12650–12655
51. Shah J, Jain S, Gahtori B, Sharma C, Kotnala RK (2021) Water splitting on the mesoporous surface and oxygen vacancies of iron oxide generates electricity by hydroelectric cell. Mater Chem Phys 258:123981
52. Shah J, Verma KC, Agarwal A, Kotnala K (2020) Novel application of multiferroic compound for green electricity generation fabricated as hydroelectric cell. Mater Chem Phys 239:122068

53. Gaur A, Kumar P, Kumar A, Shah J, Kotnala RK (2020) An efficient green energy production by Li-doped Fe_3O_4 hydroelectric cell. Renew. Energy 162:1952–1957
54. Kotnala RK, Shah J (2016) Lithium-substituted magnesium ferrite material based hydroelectric cell and process for preparation thereof. Patent Application Publication No.: US 2016/0271610 A1. 1, 1–5
55. Shukla A, Das R, Agrawal R, Kotnala G, Jain S, Gupta R, Shah J (2019) Substitution in Titanium Dioxide Hydroelectric Cell Induces Higher Green Energy AKGEC Int. J Technol 10:1–4
56. Chauhan SS, Gaur A, Kotnala RK (2019) Application of hydroelectric cell for LED Lamp 2019 Innov. Power Adv Comput Technol i-PACT 2019:1–4
57. Gaur A, Kumar A, Kumar P, Agrawal R, Shah J, Kotnala RK (2020) Fabrication of a SnO_2-based hydroelectric cell for green energy production. ACS Omega 5:10240–6
58. Kotnala RK, Shah J (2018) Magnetic materials, vol 2–5
59. Kharbanda P, Madaan T, Sharma I, Vashishtha S, Kumar P, Chauhan A, Mittal S, Bangruwa JS, Verma V (2019) Ferrites: magnetic materials as an alternate source of green electrical energy. Heliyon 5:e01151
60. Das R, Shah J, Sharma S, Sharma PB, Kotnala RK (2020) Electricity generation by splitting of water from hydroelectric cell: an alternative to solar cell and fuel cell. Int. J Energy Res 44:11111–11134
61. Saini S, Shah J, Kotnala R K and Yadav K L 2020 Nickel substituted oxygen deficient nanoporous lithium ferrite based green energy device hydroelectric cell *J. Alloys Compd.* **827** 154334
62. Kotnala RK, Shah J (2015) Ferrite materials: nano to spintronics regime vol 23. Elsevier
63. Kotnala RKK, Shah J, Mathpal MC, Verma KCC, Singh S, Lovkush (2011) Influence of annealing on humidity response of RF sputtered nanocrystalline $MgFe_2O_4$ thin films. Thin Solid Films 519:6135–6.39
64. Kotnala RK, Shah J, Mathpal MC, Gupta D, Purohit LP, Kishan H (2009) Study of humidity sensing property of LiCe substituted magnesium ferrite Sens. Lett 7:1051–1056
65. Soler MAG, Paterno LG (2017) Magnetic nanomaterials. Elsevier Inc.
66. Cullity BD, Graham CD (2008) Introduction to magnetic materials. Introduction to magnetic material
67. Letti CJ, Costa KAG, Gross MA, Paterno LG, Pereira-da-Silva MA, Morais PC, Soler MAG (2017) Synthesis, morphology and electrochemical applications of iron oxide based nanocomposites Adv. Nano Res 5:215–230
68. Soler MAG, Da Silva SW, Garg VK, Oliveira AC, Azevedo RB, Pimenta ACM, Lima ECD, Morais PC (2005) Surface passivation and characterization of cobalt-ferrite nanoparticles. Surf. Sci 575:12–16
69. Melo TFO, da Silva SW, Soler MAG, Lima ECD, Morais PC (2006) Investigation of surface passivation process on magnetic nanoparticles by Raman spectroscopy. Surf. Sci 600:3642–3645
70. Kotnala RK, Shah J (2016) Green hydroelectrical energy source based on water dissociation by nanoporous ferrite. Int. J Energy Res 33:23–40
71. Jain S, Shah J, Negi NS, Sharma C, Kotnala RK (2019) Significance of interface barrier at electrode of hematite hydroelectric cell for generating ecopower by water splitting. Int. J Energy Res 43:4743–4755
72. Farahani H, Wagiran R, Hamidon MN (2014) Humidity sensors principle, mechanism, and fabrication technologies: a comprehensive review, vol 14
73. Babu Reddy LP, Megha R, Chethan B, Raj Prakash HG, Ravikiran YT, Ramana CHVV, Kim D (2018) Role of molybdenum trioxide in enhancing the humidity sensing performance of magnesium ferrite/molybdenum trioxide composite. Inorg. Chem Commun 98:68–74
74. Agmon N (1995) The Grotthuss mechanism. Chem Phys Lett 244:456–462
75. Fischer SA, Gunlycke D (2019) Analysis of correlated dynamics in the Grotthuss mechanism of proton diffusion. J Phys Chem B 123:5536–5544

76. Conway BE, Bockris JOM, Linton Ü (1956) Proton conductance and the existence of the $H_3\dot{O}$ ion. J Chem Phys 24:834–850

77. Wraight CA (2006) Chance and design-Proton transfer in water, channels and bioenergetic proteins. Biochim. Biophys Acta Bioenerg 1757:886–912

78. Mccafferty E, Zettlemo AC (1971) Adsorption of water vapour on a-Fe_2O_3. Discuss. Faraday Soc 52:239

79. Ashok BG, Tukaram JS, Pramod NV (2013) Role of sm3+ addition on humidity sensing of nanocrtsyallite Mg-Cd ferrites. Adv. Mater Res 645:160–163

80. Pedroza RC, Da Silva SW, Soler MAG, Sartoratto PPC, Rezende DR, Morais PC (2005) Raman study of nanoparticle-template interaction in a $CoFe_2O_4/SiO_2$-based nanocomposite prepared by sol-gel method. J Magn Magn Mater 289:139–141

81. Manikandan V, Sikarwar S, Yadav BC, Vigneselvan S, Mane RS, Chandrasekaran J, Mirzaei A (2019) Rapid humidity sensing activities of lithium-substituted copper-ferrite (Li−$CuFe_2O_4$) thin films Mater. Chem Phys 229:448–452

82. Sandu I, Presmanes L, Alphonse P, Tailhades P (2006) Nanostructured cobalt manganese ferrite thin films for gas sensor application. Thin Solid Films 495:130–133

83. Zhao J, Liu Y, Li X, Lu G, You L, Liang X, Liu F, Zhang T, Du Y (2013) Highly sensitive humidity sensor based on high surface area mesoporous $LaFeO_3$ prepared by a nanocasting route. Sens Actuators. B Chem 181:802–809

84. Capraro S, Le Berre M, Chatelon J P, Joisten H, Mery E, Bayard B, Rousseau J J and Barbier D 2004 Properties of barium ferrite sputtered films *Sensors Actuators A Phys.* **113** 382–6

85. Jeseentharani V, George M, Jeyaraj B, Dayalan A, Nagaraja KS (2013) Synthesis of metal ferrite (MFe_2O_4, M = Co, Cu, Mg, Ni, Zn) nanoparticles as humidity sensor materials. J Exp Nanosci 8:358–370

86. Kotnala RK, Shah J, Mathpal MC, Verma KC, Singh S (2011) Influence of annealing on humidity response of RF sputtered nanocrystalline $MgFe_2O_4$ thin films. Thin Solid Films 519:6135–6139

87. Shaikh SF, Ubaidullah M, Mane RS, Al-Enizi AM (2020) Types, synthesis methods and applications of ferrites. Elsevier Inc.

88. Tripathy A, Pramanik S, Cho J, Santhosh J, Osman NAA (2014) Role of morphological structure, doping, and coating of different materials in the sensing characteristics of humidity sensors Sensors (Switzerland) 14:16343–16422

89. Gopal Reddy CV, Manorama SV, Rao VJ (2000) Preparation and characterization of ferrites as gas sensor materials. J Mater Sci Lett 19:774–778

90. Shah J, Kotnala RK (2012) Humidity sensing exclusively by physisorption of water vapors on magnesium ferrite. Sens Actuators. B Chem 171–172:832–837

91. Doroftei C, Popa PD, Rezlescu N (2010) The influence of the heat treatment on the humidity sensitivity of magnesium nanoferrite. J Optoelectron Adv Mater 12:881–884

92. Rezlescu N, Doroftei C, Rezlescu E, Popa PD (2006) Structure and humidity sensitive electrical properties of the Sn4+ and/or Mo6+ substituted Mg ferrite. Sens Actuators. B Chem 115:589–595

93. Jain S, Shah J, Dhakate SR, Gupta G, Sharma C, Kotnala RK (2018) Environment-friendly mesoporous magnetite nanoparticles-based hydroelectric cell. J Phys Chem C 122:5908–5916

94. Tulliani JM, Bonville P (2005) Influence of the dopants on the electrical resistance of hematite-based humidity sensors. Ceram. Int 31:507–514

95. Pan M, Sheng J, Liu J, Shi Z, Jiu L (2020) Design and verification of humidity sensors based on magnesium oxide micro-arc oxidation film layers. Sensors (Switzerland) 20

96. Nagarajan V, Thayumanavan A, Chandiramouli R (2017) Magnesium ferrite nanostructures for detection of ethanol vapours—a first-principles study. Process. Appl Ceram 11:296–303

97. Shaheen K, Shah Z, Khan B, Adnan OM, Alamzeb M, Suo H (2020) Electrical, photocatalytic, and humidity sensing applications of mixed metal oxide nanocomposites. ACS. Omega 5:7271–7279

98. Morán-Lázaro JP, López-Urías F, Muñoz-Sandoval E, Blanco-Alonso O, Sanchez-Tizapa M, Carreon-Alvarez A, Guillén-Bonilla H, Olvera-Amador M de la L, Guillén-Bonilla A,

Rodríguez-Betancourtt VM (2016) Synthesis, characterization, and sensor applications of spinel $ZnCo_2O_4$ nanoparticles. Sensors (Switzerland) 16

99. Jain A, Baranwal RK, Bharti A, Vakil Z, Prajapati CS (2013) Study of Zn-Cu ferrite nanoparticles for LPG sensing. Sci World J

100. Wang C, Yin L, Zhang L, Xiang D, Gao R (2010) Metal oxide gas sensors: sensitivity and influencing factors. Sensors 10:2088–2106

101. Dey A (2018) Semiconductor metal oxide gas sensors: a review. Mater. Sci Eng B 229:206–217

102. Bârsan N, Weimar U (2003) Understanding the fundamental principles of metal oxide based gas sensors; the example of CO sensing with SnO_2 sensors in the presence of humidity. J Phys Condens Matter 15

103. Liu X, Cheng S, Liu H, Hu S, Zhang D, Ning H (2012) A survey on gas sensing technology. Sensors (Switzerland) 12:9635–9665

104. Pelino M, Cantalini C, Faccio M (1994) Principles and applications of ceramic humidity sensors. Act. Passiv Electron Compon 16:69–87

105. Shaheen K, Suo H, Shah Z, Khush L, Arshad T, Khan SB, Siddique M, Ma L, Liu M, Cui J, Ji YT, Wang Y (2020) Ag–Ni and Al–Ni nanoparticles for resistive response of humidity and photocatalytic degradation of Methyl Orange dye. Mater Chem Phys 244:122748

106. Chethan B, Raj Prakash HG, Ravikiran YT, Vijaya Kumari SC, Manjunatha S, Thomas S (2020) Humidity sensing performance of hybrid nanorods of polyaniline-Yttrium oxide composite prepared by mechanical mixing method. Talanta 215:120906

107. Crochemore GB, Ito ARP, Goulart CA, de Souza DPF (2018) Identification of humidity sensing mechanism in $MgAl_2O_4$ by impedance spectroscopy as function of relative humidity. Mater Res 21

108. Mathpal MC, Tripathi AK, Singh MK, Gairola SP, Pandey SN, Agarwal A (2013) Effect of annealing temperature on Raman spectra of TiO_2 nanoparticles. Chem. Phys Lett 555:182–186

109. Mathpal MC, Kumar P, Balasubramaniyan R, Chung JS, Tripathi AK, Singh MK, Ahmad MM, Pandey SN, Agarwal A (2014) Ag/TiO_2/graphene stacking for plasmonic metamaterial-based transparent semiconducting thin films. Mater. Lett 128:306–309

110. Tripathi AK, Mathpal MC, Kumar P, Singh MK, Mishra SK, Srivastava RK, Chung JS, Verma G, Ahmad MM, Agarwal A (2014) Synthesis based structural and optical behavior of anatase TiO_2 nanoparticles. Mater. Sci Semicond Process 23:136–143

111. Mathpal MC, Tripathi AK, Kumar P, Balasubramaniyan R, Singh MK, Chung JS, Hur SH, Agarwal A (2014) Polymorphic transformations and optical properties of graphene-based Ag-doped titania nanostructures. Phys. Chem Chem Phys 16:23874–23883

112. Mathpal MC, Tripathi AK, Kumar P, Agrahari V, Singh MK, Agarwal A (2014) Distortion induced band gap and phase transformation in $Ti-x\ Ag(1–x)O_2$ system. Chem. Phys Lett 614:162–166

113. Iwasaki M, Hara M, Kawada H, Tada H, Ito S (2000) Cobalt ion-doped TiO_2 photocatalyst response to visible light. J Colloid Interface Sci 224:202–204

114. Xu P, Huang T, Huang J, Yan Y, Mallouk TE (2018) Dye-sensitized photoelectrochemical water oxidation through a buried junction. Proc. Natl Acad Sci 115:6946–6951

115. Park N-GG, van de Lagemaat J, Frank A, Frank AJ (2000) Comparison of dye-sensitized rutile- and anatase-based TiO_2 solar cells. J Phys Chem B 104:8989–8994

116. Tripathi AK, Singh MK, Mathpal MC, Mishra SK, Agarwal A (2013) Study of structural transformation in TiO_2 nanoparticles and its optical properties.pdf. J Alloys Compd 549:114–120

117. Grätzel M, Huang SY, Schlichthörl G, Nozik AJ, Frank AJ (2002) Charge recombination in dye-sensitized nanocrystalline TiO_2 solar cells. J Phys Chem B 101:2576–2582

118. Agrahari V, Gaur LK, Mathpal MC, Agarwal A (2017) Structural, optical and dilute magnetic semiconducting properties of Gd doped SnO_2 nanoparticles. J Nanosci Nanotechnol 17:8752–8762

119. Agrahari V, Mathpal MC, Kumar S, Kumar M, Agarwal A, Chandra M, Sachin M, Mahendra K (2016) Cr modified Raman, optical band gap and magnetic properties of SnO_2 nanoparticles. J Mater Sci Mater Electron 27:6020–6029

120. Agrahari V, Mathpal MC, Kumar S, Agarwal A, Chandra M, Kumar S, Agarwal A (2016) Low field room temperature magnetism and band gap modifications in Sm doped SnO_2. J Mater Sci Mater Electron 27:3053–3064

121. Singh MK, Mathpal MC, Agarwal A (2012) Optical properties of SnO_2 quantum dots synthesized by laser ablation in liquid. Chem. Phys Lett 536:87–91

122. Agrahari V, Mathpal MC, Kumar M, Agarwal A (2015) Investigations of optoelectronic properties in DMS SnO_2 nanoparticles. J Alloys Compd 622:48–53

123. Guillen-Baca YB, Vilca Huayhua CA, Paz Corrales KJ, Carlos-Chilo AF, Aragón FFH, Mathpal MC, da Silva SW, Coaquira JAH, Sucasaire W, Guerra JA, Pacheco-Salazar DG (2019) Lattice strain effects on the structural properties and band gap tailoring in columnarly grown Fe-doped SnO_2 films deposited by DC sputtering. J Phys D Appl Phys 52:465306

124. Zhou P, Wu J, Tu Y, Zhen M, Huo J, Wei Y, Lan Z (2016) Tin oxide nanosheets as efficient electron transporting materials for perovskite solar cells. Sol. Energy 137:579–584

125. Al-Hamdi AM, Rinner U, Sillanpää M (2017) Tin dioxide as a photocatalyst for water treatment: a review. Process Saf. Environ Prot 107:190–205

126. Alcantara GB, Paterno LG, Fonseca FJ, Pereira-Da-Silva MA, Morais PC, Soler MAG (2013) Dielectric properties of cobalt ferrite nanoparticles in ultrathin nanocomposite films. Phys. Chem Chem Phys 15:19853–19861

127. Alcantara G, Paterno L, Fonseca F, Pereira-da-Silva M, Morais P, Soler MG (2013) Layer-by-layer assembled cobalt ferrite nanoparticles for chemical sensing. J Nanofluids 2:175–183

128. Thankachan S, Kurian M, Nair DS, Xavier S, Mohammed EM (2014) Effect of rare earth doping on structural, magnetic, electrical properties of magnesium ferrite and its catalytic activity. Int. J Eng Sci Innov Technol 3:529–537

129. Rivera LMR, Paterno LG, Chaves NL, Gregurec D, Báo SN, Moya SE, Jain M, Azevedo RB, Morais PC, Soler MAG (2019) Biocompatible superparamagnetic carriers of chondroitin sulfate. Mater Res Expr 6

130. Afiune LAF, Ushirobira CY, Barbosa DPP, de Souza PEN, Leles MIG, Cunha-Filho M, Gelfuso GM, Soler MAG, Gratieri T (2020) Novel iron oxide nanocarriers loading finasteride or dutasteride: Enhanced skin penetration for topical treatment of alopecia. Int J Pharm 587

131. Gumbi SW, Mkwae PS, Kortidis I, Kroon RE, Swart HC, Moyo T, Nkosi SS (2020) Electronic and simple oscillatory conduction in ferrite gas sensors: gas sensing mechanisms, long-term gas monitoring, heat transfer and other anomalies. ACS Appl. Mater Interfaces 12:43231–43249

132. Chen Z, Lu C (2005) Humidity sensors: a review of materials and mechanisms. Sens. Lett 3:274–295

133. Koli PB, Kapadnis KH, Deshpande UG (2019) Nanocrystalline-modified nickel ferrite films: an effective sensor for industrial and environmental gas pollutant detection. J Nanostruct Chem 9:95–110

134. Sn P, Am P, Jd D, Bp L (2017) Comparative study of ferrite based humidity sensor for smart sensor module design. Int Res J Sci Eng 203–209

135. Kant R, Jhabarmal J, Mann AK (2018) A review of doped magnesium ferrite nanoparticles: introduction, synthesis techniques and applications. 2018 Ijsrset 4:646–660

136. Ortiz-Quiñonez JL, Pal U, Villanueva MS (2018) Structural, magnetic, and catalytic evaluation of spinel Co, Ni, and Co-Ni ferrite nanoparticles fabricated by low-temperature solution combustion process. ACS. Omega 3:14986–15001

137. Rivera LMR, Machado JG, Chandra Mathpal M, Chaves NL, Gregurec D, Báo SN, Paterno LG, Moya SE, Azevedo RB, Soler MAG (2020) Functional glucosamine-iron oxide nanocarriers. J Mater Res 1–12

138. Kotnala RK, Shah J, Singh B, kishan H, Singh S, Dhawan SK, Sengupta A (2008) Humidity response of Li-substituted magnesium ferrite. Sens Actuators B Chem 129 909–914

139. Kotnala RK, Shah J, Kishan H, Singh B (2017) Resistive type humidity sensor based on porous magnesum ferrite pellet 1–10

140. Kotnala RK, Shah J, Mathpal MC, Gupta D, Puohit LP, Kishan H (2009) Role of modified active surface sites of magnesium ferrite for humidity sensing. J Optoelectron Adv Mater 11:296–301

141. Jaiswal AK, Sikarwar S, Singh S, Dey KK, Yadav BC, Yadav RR (2019) Fabrication of nanostructured magnesium ferrite polyhedrons and their applications in heat transfer management and gas/humidity sensors. J Mater Sci Mater Electron 31:80–89

State of Art of Spinel Ferrites Enabled Humidity Sensors

Check for updates

Mohan Chandra Mathpal, Gopal Niraula, Mahesh Chand, Promod Kumar, Manish Kumar Singh, Surender K. Sharma, Maria A. G. Soler, and H. C. Swart

Abstract Controlling the moisture level in air and gases is an important aspect in defense, weather station, industry, laboratory and healthcare systems. The accurate measurement and sensing of the humidity/moisture level in the surrounding environment can help to maintain the temperature level for ideal living conditions; from a safety point of view, it can help to prevent the virus/disease transmission; importantly, it can protect expensive equipment, electronic devices and optical devices against damage which are sensitive to high humidity in the atmosphere. The controlled monitoring, regulation and management of humidity necessarily require humidity sensors with high sensitivity, high stability and low response time. Currently, there are various types of humidity sensors available in the market, but there are always limitations on the practical applications as the main problems are associated with their eco-friendly nature, cost, sensitivity, response time (rapid action) and lifetime. Aiming to address these issues, the spinel ferrite nanostructures arise as promising nanomaterials due to their moderate semiconducting features with high resistance, porous nature and high surface activities enabling easy fabrication of the humidity

M. C. Mathpal (✉) · M. A. G. Soler (✉)
Institute of Physics, University of Brasilia, Brasilia, DF 70910900, Brazil
e-mail: mohanmathpal@unb.br

M. A. G. Soler
e-mail: soler@unb.br

G. Niraula · S. K. Sharma
Department of Physics, Federal University of Maranhao, Sao Luis , Brazil

M. Chand
Nano Lab, UnB Planaltina Campus, University of Brasília, Brasília, DF 73300-000, Brazil

P. Kumar (✉) · H. C. Swart (✉)
Department of Physics, University of the Free State, Bloemfontein 9300, ZA, South Africa
e-mail: SwartHC@ufs.ac.za

M. K. Singh
Department of Physics, The LNM Institute of Information Technology, Jaipur 302031, India

S. K. Sharma
Department of Physics, Central University of Punjab, Bathinda 151401 , India

sensors. This chapter provides an overview of the role of spinel ferrite nanostructures for their applications in humidity sensors.

Keywords Spinel ferrite · Iron oxide · Humidity sensor · Relative humidity · Electrical resistance

1 Introduction

The content of water molecules in air or any gaseous environment is termed as humidity. Humidity sensors are mandatory from a safety point of view, which find their various applications for indoor air quality monitoring, humidifiers/dehumidifiers, nebulizers, medical instruments, optical instruments, computer components, air conditioning, domestic appliances, food processing and defogging controlling devices [1–7]. If generated, then the combination of moisture with harmful gas at a certain temperature in the open atmosphere or in its surrounding can cause pollution, breathing problems, skin problems and even major accidents and disasters. For instance, it was found that at certain temperature and humidity conditions, certain viruses can exist in the form of aerosol and thus it can spread and transmit easily from human to human and can be airborne in the hall with close air circulation or in the rooms equipped with air-conditioner [8–12]. Therefore, the speedy accurate measurement of the moisture content in the environments becomes essential. There are various types of humidity and temperature sensors commercially available. However, there are always limitations and the key issues are their cost, selectivity, sensitivity response time (rapid action) and lifetime of the sensors. Different types of humidity and temperature sensing technologies are available, and the scientific efforts are directed to overcome these problems for precise humidity measurements. There are different categories of humidity sensors based on their working principle such as change in electrical properties (resistive and capacitive sensors), change in optical properties (absorbance, reflectance, fluorescence, refractive index, transmittance, etc.), change in mass and crystal frequency (mainly gravimetric sensors based on quartz crystal microbalance), and change in mechanical-optoelectronic properties [6, 13, 14]. The different humidity sensors which have been widely considered so far include a sensing elements mainly made of the organic polymers, electrolytes and porous ceramics materials [3–6].

The bare polymer and polymer-based composite structures have emerged as promising humidity sensor because of their excellent physical and chemical properties. Several polymeric materials are also commercially available nowadays at low cost, but these sensors are not adequate to work at high temperatures and most of them are not stable with the exposure to the chemical attack. Their response and mechanical stability in the presence of gaseous and corrosive environment become suspicious. Especially in some cases, these are water soluble and become unstable at low-humidity ($\leq$20% RH) levels. On the other hand, the electrolyte-based humidity

sensors are hydrophilic, chemically active, unable to perform in the presence of ammonia or organic solvents and are thermally unstable [15].

In the recent years, the porous ceramic materials have drawn significant interest in the development of resistive type humidity sensors to overcome some of these difficulties. Among these transition metal oxides and their composite-based semiconductors comprising $MgAl_2O_4$, Fe_2O_3, TiO_2, MgO, ZrO_2-MgO, Cr_2O_3, SnO_2, ZnO, $ZnCr_2O_4$, $ZnCo_2O_4$, V_2O_5, Y_2O_3, VO_2, WO_3, Ag–Ni and Al–Ni metal oxides nanoparticles have been widely studied because of their low cost, easy fabrication, moderate sensitivity and simple measurements techniques for both humidity and gas-sensing applications [4, 5, 16–27]. As for instance, recently Chethan et al. have yielded high-density nanorods of polyaniline/yttrium oxide (PYO) composites (Y_2O_3/PANI) by mechanical mixing for humidity sensing applications with a response and recovery time of 3 s and 4 s, respectively, [24]. Li et al. reported on the ultra-high sensitivity humidity sensor based on MoS_2/Ag composite films [16]. Late et al. experimentally studied the single and multiple layers of crystalline MoS_2 sheets to fabricate a transistor-based gas-sensing platform. The sensing performance of these transistors for NO_2, NH_3, and humidity with and without gate bias and light irradiation has been investigated to study the role of layered structures in gas–solid interaction [17]. However, various semiconductors, ceramics materials and their composite structure-based materials have shown good humidity response, temperature and gas-sensing behavior but some of these require heating treatment and suffer with imperfect contacts with metal electrodes which prevent their potential application for eco-friendly and flexible devices [7, 28–30]. The ceramic materials or metal oxide-based semiconductor sensors are relatively expensive and display low sensitivity at room temperature not favoring their applications. The positive aspect of these ceramic sensors is their mechanical stability and these can withstand and are sensitive at high temperature. Therefore, a heater can be coupled to the sensor, which can quickly desorb the moisture from the sensor surface and restart the physical adsorption of water molecules, hence increasing its stability, accuracy and lifetime [2]. Though, the sensors which can operate only at high temperatures also consume high energy. Overall, there are different disadvantages one over the other such as poor selectivity, high fabrication costs, long-time instability, miniaturization of devices, irreversibility issues, aging effect, operation in certain chemical environment, in space applications and risk of poisoning.

Consequently, a sensor material fulfilling most of the above criteria's, with sufficient moisture absorption properties, high surface to volume ratio, high specific surface area and environment friendly which can be operated in entire temperature range (from room temperature to high temperature) is highly desirable. In the search of such materials, the spinel ferrite nanostructures have gained a huge interest due to their moderate semiconducting features with high resistance, porous nature and high surface activities for easy fabrication of the humidity sensors.

The spinel ferrite structure presents a general formula AB_2O_4, where A is a divalent transition-metal cation and B is a trivalent cation. Magnetic ferrites display mainly two groups of crystal structures such as the cubic comprising pure ferrites such as magnetite (Fe_3O_4) and maghemite (γ-Fe_2O_3), and mixed ferrites AFe_2O_4,

where A=Co, Cu, Mg, Ni and Zn. Special attention is drawn to those produced with the transition metals such as Fe, Co, Ni and their alloys. The second group is of hexagonal structure, where the most important compounds are barium and strontium ferrites [31, 32]. In particular, nanoferrites are widely employed to modulate magnetic and electric properties of devices and have a large range of applications such as in spintronics, biomedical science, magnetic field sensors, LPG sensors, gas sensors, chemical sensors and humidity sensors [7, 17, 18, 33–44]. Moreover, spinel nanoferrites are emerging fascinating material with huge attention to explore its structural, magnetic and sensing properties as well as the interaction of the materials with substrates for future nanodevices applications [45]. The ferrite nanostructures possess electric, mechanical and thermal properties, and in fact, few of these have potential in gas sensing for selected gases with high sensitivity, stability and good response time due to their high surface-to-volume ratio [46, 47]. In spite of having interesting magnetic properties, the ferrites nanomaterials show special characteristics such as their oxygen vacancy and porous nature, which make them suitable for humidity and gas-sensing applications wherein their magnetic properties are not utilized [30].

In the last two decades, among various AB_2O_4 spinel ferrites researchers have studied several highly resistive ferrite nanomaterials for humidity sensing applications such as Ni ferrite [48], Al–Cd ferrite [49], Co–Mg nanocomposite ferrite [50], polyhedrons shaped magnesium ferrite thin film [51], Co–Ni ferrites [52], Mn doped Ni ferrite ($Mn_{0.2}Ni_{0.8}Fe_2O_4$ nanoparticles) [53], Neodymium-doped iron oxide ($Nd_xFe_{2-x}O_3$) nanoparticles [54], set of $CuFe_2O_4$, $CoFe_2O_4$, $ZnFe_2O_4$ and $NiFe_2O_4$ [30], $MgFe_2O_4$ [55, 56], Ce substituted magnesium ferrites ($MgCe_xFe_{2-x}O_4$, with $x = 0.00, 0.02$, and 0.04) [57], copper-zinc-tungsten spinel ferrite ($Cu_{0.5}Zn_{0.5}W_{0.3}Fe_{1.7}O_4$) [58], $ZnFe_2O_4$ [59], Ca, Ti substituted Mg ferrites ($CaMgFe_{1.33}Ti_3O_{12}$) [60], Y^{3+} doped $CdFe_2O_4$ [61], Sm^{3+} added Mg–Cd ferrite ($Mg_{1-x}Cd_x$ Fe_2O_4, with $x = 0, 0.2, 0.4, 0.6, 0.8$ and 1) [1], cerium oxide added $MgFe_2O_4$ [62], Ni–Zn ferrite [63], magnesium ferrite/molybdenum trioxide composite [64], Fe_3O_4 [65], bismuth substituted copper ferrite nanoparticles ($Bi_xCuFe_{2-x}O_4$, with $x = 0.0, 0.1, 0.2, 0.3, 0.4$ and 0.5) [66], Mg–Zn ferrites ($Mg_xZn_{1-x}Fe_2O_4$, with $x = 0.2, 0.4, 0.6$ and 0.8) [14, 41], set of copper, cobalt and copper–cobalt ferrite ($Cu_xCo_{1-x}Fe_2O_4$ with $x = 0, 0.5$ and 1.0) [67]. The particular candidates of interest for ceramics humidity sensors based on spinel nanoferrite magnetic materials are $MgFe_2O_4$, $NiFe_2O_4$, $ZnFe_2O_4$, $CuFe_2O_4$, $MnFe_2O_4$, $CoFe_2O_4$ and $CdFe_2O_4$ due to their porosity, high sensitivity, mechanical stability and operation capability over wide humidity range [7, 13, 61, 64, 68, 69].

Nowadays, most of the humidity and gas sensors rely on the principle of change in electrical properties (resistance, capacitance, etc.) of the sensing material. Measuring the resistance in the ceramic sensors materials is straightforward and much easier than measuring the capacitance. It can be measured in terms of the dew point where at a particular temperature and pressure the gas starts to condense into the liquid form. The humidity in an environment at a particular temperature can be expressed by either relative humidity (% RH) or absolute humidity (AH in g/m^3). The most employed technique to express the humidity is to measure the relative humidity (%

RH). The RH value is measured as the ratio of the vapor pressure (H_{vp}) of moisturized air to its saturated vapor pressure (H_{svp}) at a given temperature and is expressed as [6]:

$$\text{RH (in \%)} = \frac{H_{vp}}{H_{svp}} \times 100\% \tag{1}$$

The absolute humidity (g/m^3) is expressed as the ratio of the amount of water vapor to the unit volume of dry air. In ceramic sensors, the change of air humidity with the variation of resistance $R(r_h)$ at relative humidity (RH) under a specific humid condition r_h follows a logarithmic equation, which can be represented by Eq. (2) [6]:

$$\log\left(\frac{R(r_h)}{R_0}\right) = \frac{\log a - \log r_h^n}{1 + b/r_h^n} \tag{2}$$

where R_0 is the resistance at zero humidity, and a and b are the constants. The humidity sensing response (S_R) of a sensor material can be measured by using Eq. (3) [6]:

$$S_R = \frac{R_h - R_0}{R_0} \times 100\% \tag{3}$$

where R_h represents the resistance at certain humidity and R_0 refers to the sensor resistance in air at ~3% RH.

The humidity response can be largely affected by the surface morphology, dopants, adding catalyst and surface coating. In iron-based materials, it was observed that the humidity sensing in the low RH range becomes less sensitive in the high-frequency region, whereas in the low-frequency region (10 and 100 Hz) it has high sensitivity and good linearity. This happens due to the fact that at the high frequency the absorbed water cannot be polarized, and the dielectric phenomena disappear [6, 70]. Therefore, to get high sensitivity and good linearity, a low-frequency region is always desirable in most of the resistive and capacitive type humidity sensors. In practice, the basic principle behind most of the commercial humidity sensors is to either observe the change in the impedance through ionic conduction (mainly in polymers) or to measure the change in the capacitance or resistance of the sensor materials after the physisorption of water molecules. The capacitance-based change in impedance involves complex electronic circuits to measure the humidity response, and it is not a common feature of all ferrite nanomaterials, whereas measuring the resistance is straight forward in spinel nanoferrite. This chapter provides an insight for the basic concept of humidity sensors and a discussion about the key parameters and the importance of resistive type spinel ferrite nanostructures in developing humidity sensors. Moreover, a summary about recent developments of spinel ferrite humidity sensors is presented.

2 Basic Mechanism of Humidity Sensing in Ceramic Sensors

The main mechanism of detecting the moisture level in ceramic sensors is to observe a change in the resistance by the adsorption of water vapors from the environment. In contrast, upon exposure to air/non-humid or an inert environment, the moisture is desorbed from the surface of sensing materials, and the sensor resistance goes back to their original state [39]. This change in the sensor resistance is due to the transfer of electrons (donation of electron) from the water molecules after adsorption on the surface of a semiconductor oxide material. After surface adsorption, the conductivity of the sensor material can either increase or decrease depending upon the semiconductors that are either *n*-type or *p*-type [28]. The performance of a humidity sensor depends on the interaction between moisture and reactivity of the surface species of the metal oxide nanomaterials, sensor preparation methods, porosity, surface morphology, particle and grain size distribution, surface composition and electrical conductivity (resistivity) [28]. Importantly, the surface with the grain in the nanometer regime offers a high surface area for the adsorption and detection of water molecules as compared to the grains in the micrometer regime at the surface of the metal oxide semiconductor materials. The factors that influencing the humidity sensing properties (selectivity, sensitivity and response time) of the spinel ferrite nanostructures are their dimension; porosity; electronic structure at the surface; type of charge carrier; high surface-to-volume ratio; number of edges; highly exposed surface area (high specific surface area) that makes them highly sensitive to the adsorption of water molecules; kinks and corner atoms which increase the number of chemisorbed water molecules for adsorption at the surface [7, 13, 15, 39]. The signal of humidity response is collected through the two electrodes by applying an external DC voltage ranging from $+0.5$ to $+5.0$ V. In the bulk sample, the electrodes are usually developed at the ends of the samples, whereas in the thick/thin films the electrodes are developed on the top surface. The conduction starts mainly due to the polarization of charges at the sensor surface, which involves either migration of H^+ ions from the physisorption layer of the water molecules into the metal electrode contacts or due to the electron migration from the metal contacts to any conducting species at the surface. Hence, the positive charges are collected at the metal contacts and a cation layer is developed between the sensor surface species and the metal electrodes [6]. This conduction mechanism can be understood by Grotthuss reaction for protonic conduction as discussed in the next section.

3 Protonic Conduction in Spinel Ferrite Humidity Sensors

The concept of moisture adsorption in the spinel ferrite-based humidity sensors is due to their ceramic nature and porous structure, which allows the molecules of water vapors for chemical adsorption (chemisorption), physical adsorption (physisorption)

and/or the capillary condensation on the surface. This mechanism is illustrated in Fig. 1 for a surface of magnesium ferrite nanostructures (showing Mg^{2+}, $Fe^{2+/3+}$, O_2^- ions) that are exposed to the moisture. The process is further explored with a chemically bonded structure in Fig. 2. This is the basics for humidity sensing of all ceramic materials which shows electronic conduction, capacitive type, solid
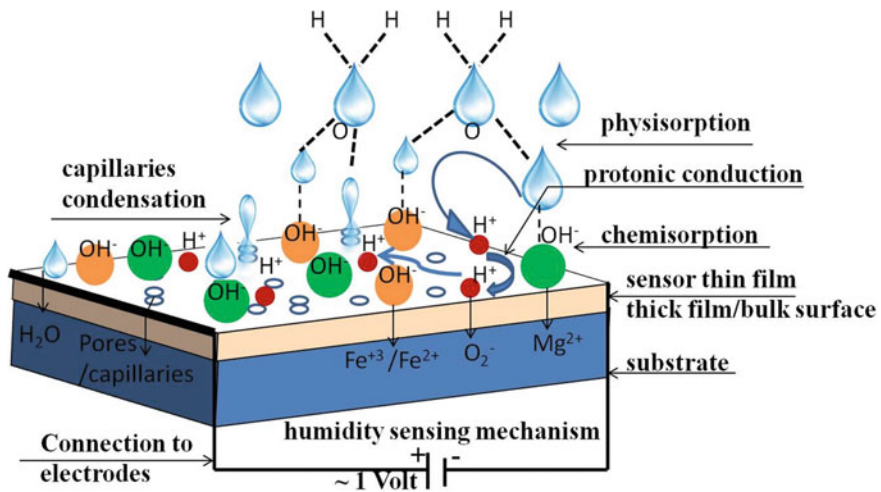

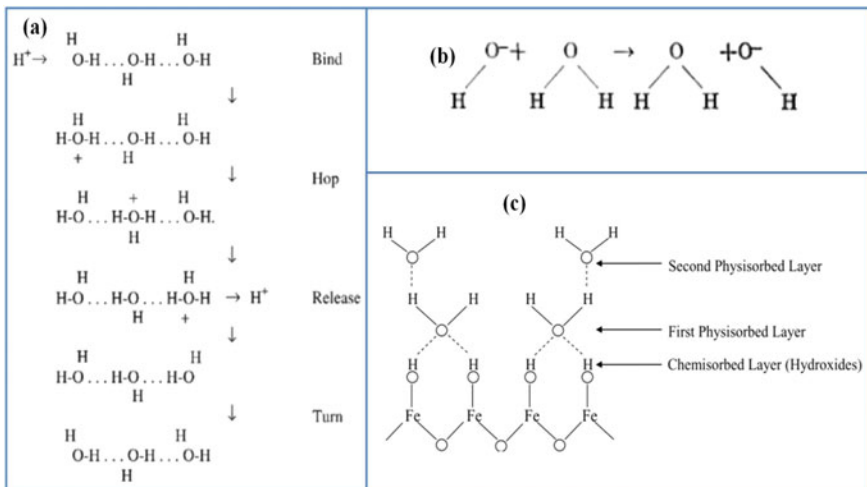**Fig. 1** Illustration of the working mechanism of a humidity sensor

Fig. 2 **a** Mechanism of proton conduction in a hydrogen-bonded network between water molecules [74], **b** mechanism of proton transfers in hydroxide ions (OH^-) [75] and **c** the adsorption of moisture on ferrite surface in the form of multilayers. Open access journal, figure is reproduced under copyright 2014, sensors [4]

electrolyte and ionic conduction. In the porous structure, the ionic conduction takes place where the conductivity increases with increasing the adsorption of water vapors and thus it increases the dielectric constant of the sensor material [4].

Under equilibrium, the mobility of proton in water or moisture is very high and thus accumulation of water molecules further increases the proton concentration at the surface. In this situation, the protons are tunneled from one to another molecule of water vapor through hydrogen bonding as shown in Fig. 2a. This process is well-known as the Grotthuss mechanism for the diffusion of hydrogen (H^+) and hydroxide ions (OH^-) [64, 71–73]. Therefore, the diffusion of hydrogen (H^+) ions takes place in the condensed water molecules at the material surface and conduction starts by these protons [74, 75].

Indeed, the electrical conductivity is predominated by the protons conduction after exposing the sensor to the humid environment. On the other hand, the diffusion and mobility of the hydroxide ions (OH^-) play an important role for the protonic conduction as shown in Fig. 2b. At low-humidity levels, the sensor surface is partially covered with moisture and dissociated hydroxyl functional groups. The self-ionization or surface collision of water molecules results into the quick diffusion of protons (H^+) and hydroxide ions (OH^-), which leads to the separation of water molecules in H^+ and OH^- ions:

$$H_2O <=> H^+ + OH^- \tag{4}$$

The released hydrogen nucleus immediately protonates another H_2O molecule to form a hydronium ion (H_3O^+),

$$H_2O + H_2O <=> H_3O^+ + OH^- \tag{5}$$
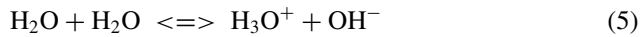
In a humid environment, the surface of the ceramic sensor material is covered by hydroxyl groups, which provides a channel for the formation of hydrogen bonding to absorb the water vapors. The first layer of water molecules is chemically adsorbed (chemisorption) on the activated sites of metal cations on the sensor surface and forms the hydroxyl groups. These metal cations have high charge density and strong electrostatic fields, which make the protons mobile at the surface as shown in Fig. 1 [4, 64]. Now, these mobile protons move from one site to another site due to strong electrostatic fields and react with the nearest oxygen ions (O^{2-}) at the surface to form another hydroxyl (OH^-) group. In this process, the first layer of the moisture on the surface is a chemisorbed layer which will not change by further exposure to the moisture in the environment [4]. After the chemisorption of a monolayer of water molecules, the further exposure to the moisture results in physical adsorption (physisorption) of the water molecules on the first layer of hydroxyl ions. Once the first layer of physisorbed water vapors is completed, then another layer of water molecules is physisorbed via a double hydrogen bonding with two neighboring hydroxyl groups as shown in Fig. 2c [4, 64]. And this process of physisorption is continuous to form the multilayer of water molecules until it is exposed to the humid environment. During the multilayer formation in physisorbed layers, the water vapors are less ordered than

the first physisorbed layer, which results in the singly bonding of some hydrogen to the water molecules and formations of the continuous dipoles and electrolyte layers between the electrodes. The formation of electrolyte layers increases the dielectric constant and bulk conductivity of the sensor materials due to the synergic effect of water protonation and protonic conduction at the surface [4, 64]. Importantly, the physisorption of water vapor molecules usually takes place below a temperature of 100 °C, whereas the chemisorption process can occur up to 400 °C.

4   Main Parameters of Humidity Sensors

Besides considering the cost of the fabrication, it is important to take into account the key parameters for developing an efficient humidity sensor. These parameters are presented as follows.

(i) Humidity Response and Selectivity One of the main issues in most of the ceramic sensor materials is their selectivity. Selectivity of a sensor means that it is not sensitive to the presence of other gaseous species in the measuring environment. This becomes a challenge for humidity sensing since many metal oxide materials are optically active, and also, sensitive to different gases present in the atmosphere, which hampers their practical utility for core humidity sensing. Therefore, in order to develop a core humidity sensor, the material should be exposed to different gaseous atmosphere and the obtained results should be compared with the exposure to a bare moisture-containing environment or in any standard source of generating humidity. For example, magnesium ferrite can also detect different gases such as LPG, methane, ethanol, NH_3, CO_2, acetone and CO in different operating range of the temperatures [51].

(ii) Reproducibility and Repeatability The material can reproduce easily and the response measured by a set of sensors of a material should generate the same signal under identical conditions irrespective of its time and location. It means that the response from a single sensor material should not drift apart in each set of measurement of the resistance or capacitance. The sensor should follow its own calibration graph at each point of RH for reliable measurements.

(iii) Humidity Hysteresis and Reversibility The humidity hysteresis is defined as the difference or drift in the humidity response plot when the measurements are repeated in reverse order under identical conditions. For practical application, the sensor should follow the same path, so the hysteresis becomes zero or a minimum. The humidity hysteresis generally arises due to presence of defects and non-uniform morphology across the sample, and these differences vary from sample to samples. So, if the resistance of the sensors after measurements on increasing order of RH from 20 to 80% is different than that measured on decreasing order from 80 to 20%, then the sensor is said to have the humidity hysteresis. It indicates that the sensor

has different adsorption and desorption rate of water molecules. The hysteresis error (H_E) is defined as [68]:

$$H_E \;=\; \pm\; \frac{\Delta R_{\max}}{2 F_{FS}} \tag{6}$$

where $\Delta R_{\max}$ is the difference in the humidity response during the adsorption and desorption process, and F_{FS} is the full-scale output.

(iv) Response and Recovery Time The time taken by the sensor during the adsorption process of water molecules to achieve 90% of the total change of resistance/or capacitance is known as response time, whereas the recovery time is defined for the desorption process of the water molecules under identical conditions. Though depending upon the desired application range, some researchers calculate the response time in a particular RH range. In other words, it is the degree of sensitivity that how quickly a sensor can respond to the highest (response time) or lowest (recovery time) level of change in resistance. The response time and recovery time of a humidity sensor are sensitive to its structure and morphology. It is a very important property for humidity sensors because as low, as quick and as accurate is the response time; their commercial utility will increase and will become much reliable. In practice, the change is resistance from ~30 to ~70% RH values are recorded to attain its 90% resistance at 70% RH during the adsorption and 30% RH during the desorption process. For a porous magnesium ferrite pellet, the response and recovery time measured by Kotnala et al., at 70 and 30% RH were 140 s and 180 s, respectively, [15].

(v) Linearity An ideal humidity sensor response must be linear during the entire range of measurements starting from the chemisorption process to the physisorption process. In general, the change in resistance is slow at the low-humidity range and sharp (higher slope) in the high humidity range. This depends on the amount of chemisorbed and then importantly physisorbed water molecules by the pores on the surface of the sensor materials. The pore size distribution can be changed by controlling the synthesis condition and its annealing time and temperature. A nonlinear response at different humidity levels reflects that the sensor cannot accurately measure the adsorbed water vapors, though in some cases the sensor may have two different linear regions corresponding to the chemisorption and the physisorption process, respectively.

(vi) Porosity The porosity is an important parameter in a resistive type known humidity sensors. The change in pore size distribution increases the resistance to the gega ohm order of the sensor materials, which is difficult to measure at low-humidity levels; therefore, the sensor becomes insensitive or shows nonlinear response in low range of humidity. In ferrite-based humidity sensors, the most suitable range of electrical resistance is in the range of mega ohm at the low-humidity level (~10–30% RH). Moreover, it is also complex for sensors to measure the high resistance by a simple electronic circuit. The porosity in ferrite nanomaterials can be controlled by

doping and metallic particle incorporation or by preparing composite nanostructures and controlling the process condition. However, the effect of different dopants and composite structure on the humidity sensing properties of spinel ferrite nanoparticles are not yet fully understood and still the subject of deep investigation. The role of pore size distribution can be understood from the Kelvin equation, where the response of a resistive type humidity sensor is based on the condensation of adsorbed water molecules in the pores in the form of capillaries (capillary condensation). If the pores are of a cylindrical shape with one end close, then all the pores are in the stage of condensation with a radius up to the "Kelvin radius" expressed by Eq. (7) [2, 3]:
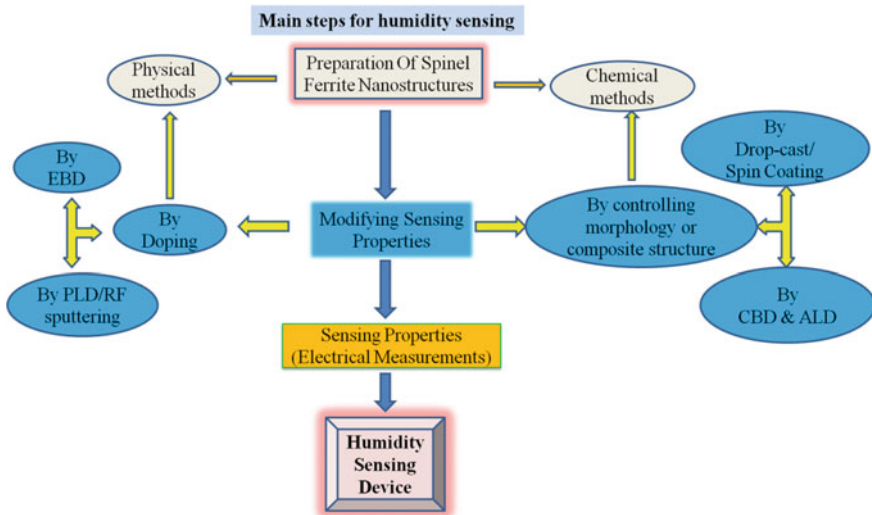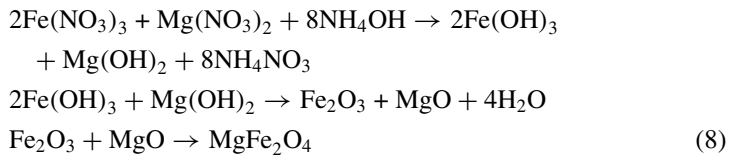
$$r_K = \frac{2\gamma M}{\rho R T \ln(P_s/P)} \tag{7}$$

where r_K stands for the Kelvin radius, γ, ρ and M for the surface tension, density and molecular weight of water, respectively, and P and P_s for water vapor pressures in the surrounding environment and at saturation, respectively, [3]. Therefore, the pores with small dimensions are filled with condensed water before than the large radii, which leads to the impedance variations at a low moisture (low RH) contents [2]. The water condensation occurs in all the pores with radius up to $r_K/2$, at a given temperature and constant pressure. For a smaller r_K value, or a lower temperature, water vapor condensation occurs in the capillaries more easily [4].

(vii) Stability The sensor response should be stable against the various gaseous species, corrosive environment, aging effect, smoke test, oil test and water resistance test at each point of a fixed relative humidity. The thermal and mechanical stability are also important to avoid any physical damage of the sensor.

(viii) Lifetime The fluctuation in the humidity response of a ferrite sensor over a long period of time should be zero or a minimum so that the sensor functionality is not interrupted to work over the years. Therefore, the humidity response of the sample at different relative humidity must be measured with respect of time of, say 1 week, 2 week, 1 month, 2 months, 4 months, 8 months, 1 year and 2 years, respectively. A systematic drift in the electrical resistance at a specific humidity of 2–4% of the sample over a period of 1 year can be acceptable. If the drift is not analogous at all specific humidity levels, then the sensor is no longer good for humidity sensing applications.

5 Basic Synthesis and Characterizations Techniques for Humidity Sensors

The key point in the development of a humidity sensor based on spinel nanoferrites is the optimization of the process parameters for the synthesis of spinel ferrites. A typical schematic for the process of development of ferrite-based humidity sensors is shown in Fig. 3. The pellet and thick film-based ferrite nanostructures for humidity sensor applications can be prepared by sol-gel, solid-state reaction, mechanical ball milling, co-precipitation, hydrothermal and solvothermal methods, whereas the thin film of ferrite nanostructures can be deposited via various techniques such as spin coating, spray coatings, radio frequency (RF) magnetron sputtering of metal oxide targets and pulse laser deposition (PLD) [4, 70, 76–82]. Tripathy et al. have listed the various type of humidity sensing materials and their preparation methods [6]. For example, the popular humidity sensing material based on magnesium ferrite can be prepared by using nitrate precursor with the following simple chemical reaction [28]:

$$2Fe(NO_3)_3 + Mg(NO_3)_2 + 8NH_4OH \rightarrow 2Fe(OH)_3$$
$$+ Mg(OH)_2 + 8NH_4NO_3$$
$$2Fe(OH)_3 + Mg(OH)_2 \rightarrow Fe_2O_3 + MgO + 4H_2O$$
$$Fe_2O_3 + MgO \rightarrow MgFe_2O_4 \tag{8}$$

Fig. 3 A typical schematic for the development of ferrite nanostructures-based humidity sensor device

The as-prepared powder samples can be compressed to form a pellet or a compact disk shape, by uniform compression under a hydraulic pressing machine at pressure of 5–8 kN. This compact disk is usually heat treated in the range of 700–1100 °C for 4–6 h, in a furnace to control its microstructure and retain its porous structure [7, 30, 80, 83]. Here, the important key is to optimize the annealing temperature of the sensor material because the annealing at higher temperature may not be suitable for humidity sensing applications as it can results into sample hardness, which reduces the porosity and the surface reactivity and the samples also lose their grain size distribution in the nano regime [84].

All the as-prepared sensor materials can be basically characterized by X-ray diffraction (XRD), Raman spectroscopy (RS), Fourier-transform infrared spectroscopy (FTIR) high resolution transmission electron microscopy (HRTEM), secondary electron microscopy (SEM) and atomic force microscopy (AFM) for analyzing the structural, morphological, chemical and surface properties in order to optimize the humidity sensing properties. The microstructure behavior (particles shape, size, distribution and surface roughness) and cross-section (for growth orientation and thickness) are the key parameters to optimize for humidity sensing. Energy dispersive X-ray spectroscopy (EDX) and X-ray photoelectron spectroscopy (XPS) are very useful to confirm the presence of elements, surface properties and detect any impurities that can unintentionally persist in the samples. The film thickness of thin films can also be determined by using a surface profiler (Tencor P-10). Brunauer–Emmett–Teller (BET) surface analyzer is useful to get information about pore size distribution and specific surface area, which provides an idea about the physical adsorption of water and gas molecules on a solid surface. Nitrogen adsorption–desorption isotherms can be measured by using a Micromeritics Gemini VII surface area and porosity system with high purity nitrogen gas as adsorbate at 77 K. The specific surface area can be estimated by the five-point BET method, and the pore size distribution can be derived from the desorption branch of the isotherms by using the Barrett–Joyner–Halenda (BJH) analysis [70]. The porosity ($p = 1 - d_{exp}/d_{th}$) in the pellets made of powder samples of spinel ferrite can be calculated from the relation of experimental density (d_{exp} = mass/volume) and the theoretical density ($d_{th} = 8 M/a^3 N_A$) [28]. Here, M is the molecular weight, a is the lattice constant and N_A is the Avogadro's constant. The specific surface area (A_s) can be calculated by using the equation ($A_s = s/V d_{exp}$), where s and V are the particle surface area and volume, respectively. In case of thin film, the surface roughness/porosity can be approximately measured using AFM.

The electrical properties of the sensor materials in the form of a pellet can be measured by making silver electrodes, or Platinum electrodes, or Ag/Pd electrodes or by applying silver paste at two opposite faces of the pellet/disk [2, 4, 6, 13, 70]. The platinum electrodes are expensive but considered as the primary choice due to their low contact resistance, fast collection of charge carriers and high stability and sensitivity to read out the impendence changes [2]. In the case of a thin film with low thickness or in a layered structure, the electrodes at two ends on the top surface for measuring the electrical properties of the thin film of the humidity sensor device can be fabricated by depositing the combination of two metal electrodes of

Au/Cr (200/5 nm) or Ti/Au (10/40 nm) by electron beam deposition /or a thermal evaporation technique by using a shadow mask [85–87]. Recently, Zak et al. reported the porous Fe_3O_4 nanoparticle prepared by a solvothermal method for humidity sensing in the range of 10–70% RH. The sensor was fabricated on RCA cleaned Si–P silicon wafers [65]. They developed chromium and gold metal contacts of 20 nm and 100 nm thicknesses over silicon, respectively, by using thermal evaporation technique followed by photolithography. The best method to measure the humidity response of a ferrite thick/thin film is to fabricate the interdigitated electrodes (comb electrode) made of gold or platinum on the top of film surface as shown in Fig. 4a–c [2, 4, 6]. The impedance measurements at low frequency (~100 to 1 kHz) are essential to study the humidity sensing properties that change with the change in concentration of the moisture level in the surrounding of the sensor. The impedance and electrical measurements can be performed by using different digital meters such as a LCR meter LCR-8110G, Keithley 2400 and 2450 source meters and model DMM4050 made by Tektronix.

All the humidity sensing measurements should be performed under the identical conditions at room temperature or in the range of different working temperature.
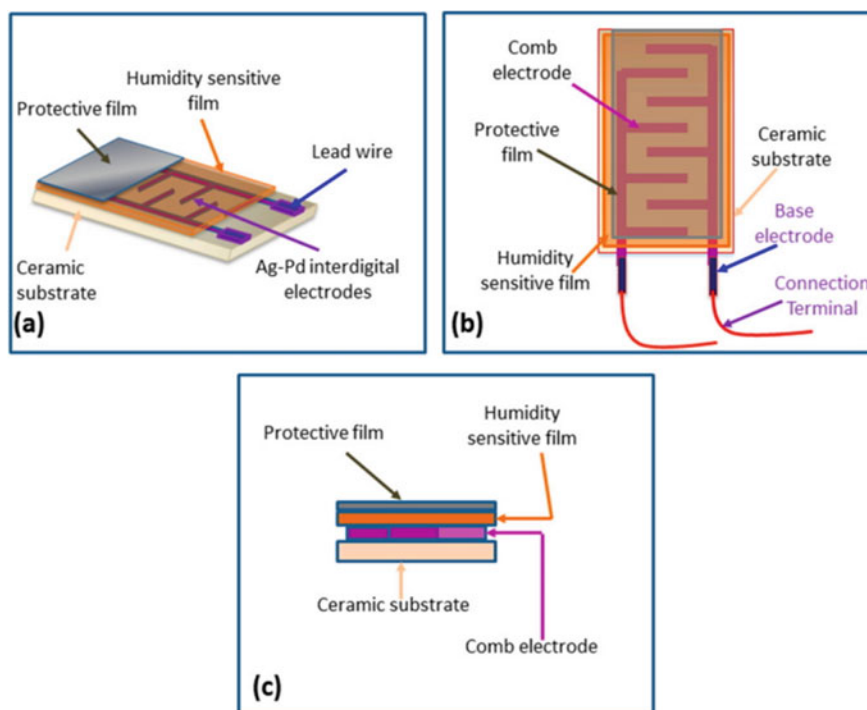

Fig. 4 Different views of interdigitated electrodes on the top surface of humidity sensor thin film: **a** isometric view; **b** top view; **c** cross-sectional (side) view. Open access journal, figure is reproduced under copyright 2014, sensors [6]

The humidity sensing measurements can be done inside a commercially available standard humidity generator such as an Aditi Associate Model ASC-10, Thunder Scientific 2500 series, digital CEM DT-615 hygrometer and in a humidity chamber, provided by Gayatri Scientific, Mumbai. On the other hand, due to economic reasons, one can follow a standard chart of saturated salts and their constant humidity values given in Table 1 to get the desired range of RH [28]. A simplest schematic diagram for measuring humidity sensing properties at low cost by using the method of saturated salts is shown in Fig. 5 [64, 88, 89].

Table 1 Relative humidity RH above saturated salt solutions at 20 °C

Salt	Relative humidity (%)
LiCl	11.3
K(CH₃COO)	22.7
MgCl₂	33.1
K₂CO₃	43.2
Mg(NO₃)₂	53.0
CoCl₂	64.0
NaCl	75.7
KCl	85.1
K₂SO₄	97.6
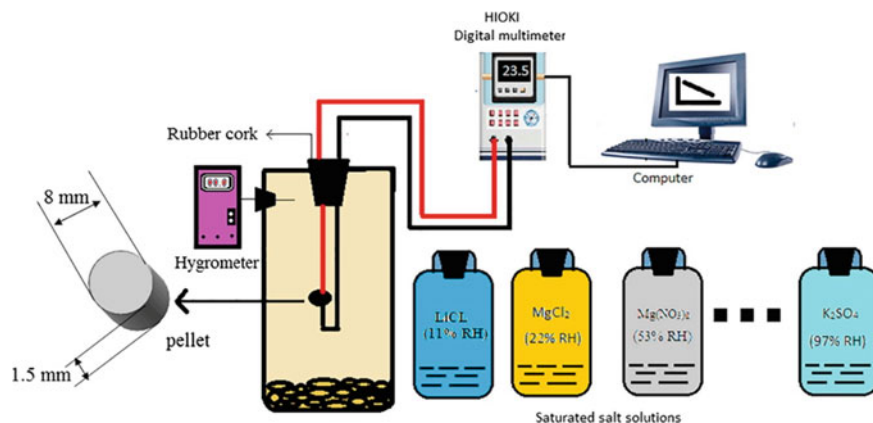
Fig. 5 Schematic for a humidity sensor setup by using saturated salt solutions. Reproduced with permission from Ref. [64]. Copyright 2018, Elsevier B. V

6   Spinel Nanoferrites for Humidity Sensors

Doroftei and Rezlescu et al. have demonstrated the partial substitutions of two ions, Sn^{4+} and Mo^{6+}, with different ionic sizes and charge states by Mg and/or Fe in magnesium ferrite ($MgFe_2O_4$) [28, 90]. Their results showed that the electrical resistivity is heavily dependent on the surface composition, crystallite size, surface area and pore size distributions (porosity) of the samples. The humidity sensitivity was enhanced after the substitution Sn doping where Sn ions partially replace (~10%) the Mg ions in the $MgFe_2O_4$ [28]. The Mo^{6+} substitution in magnesium ferrite yielded the smallest resistivity, whereas the Sn^{4+} substitution resulted in the highest resistivity among all the samples. The high resistivity in Sn doped $MgFe_2O_4$ was attributed to the fact that partial substitution of the tetravalent Sn ions in octahedral Mg sites localize the octahedral Fe^{2+} ions. This leads to the hopping conduction mechanism in ferrites due to the electronic jumps between Fe^{2+} and Fe^{3+} ions and a net reduction in the resistivity at room temperature [28].

Gadkari et al. studied the effect on humidity sensing properties of Sm^{3+} ions doping in of Mg–Cd ferrites prepared by the oxalate co-precipitation technique [1]. The shortest humidity response time of 160 s with a recovery time of 279 s was observed for Sm^{3+} doped Cd-ferrite sensor over a range of 40–90% RH. The physical adsorption of water molecules on the surface of a ferrite material leads to the dissociation of hydrogen ions. The dissociated hydrogen ions (H^+) form the bonding with the surface lattice oxygen atoms (O_o) and create the hydroxyl groups (OH) as,

$$H^+ + O_o \leftrightarrow [OH], \tag{9}$$

Now, the hydroxyl groups at the surface react with the metal ions species and generate the free electrons. The generation of more freer electron increases the conductivity with increasing moisture adsorption at the material surface [1]:

$$[OH]^- + Fe/Mg \leftrightarrow \left[OH-Fe/Mg\right] + e^- \tag{10}$$
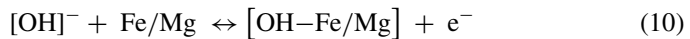
The role of molybdenum trioxide (MoO_3) in magnesium ferrite/molybdenum trioxide nanocomposite for humidity sensing at room temperature was explored by Reddy et al. [64]. The basic setup used by their group for humidity measurement is shown in Fig. 5. They prepared the sample by using a mechano-chemical mixing method and measured the humidity in the range of 11–97% RH at room temperature.

The active adsorption sites for water vapors were enhanced after MoO_3 incorporation to $MgFe_2O_4$. The nanocomposite structure showed the best response of 45 s and a recovery time of 74 s, respectively, whereas the bare magnesium ferrite showed a response and recovery time of 225 s and 364 s, respectively. The nanocomposite sample showed a stable humidity sensing ability and a low-humidity hysteresis. The nanocomposite material was compressed into a cylindrical pellet, and then, a conducting silver paste was coated on the opposite circular faces to act as electrodes
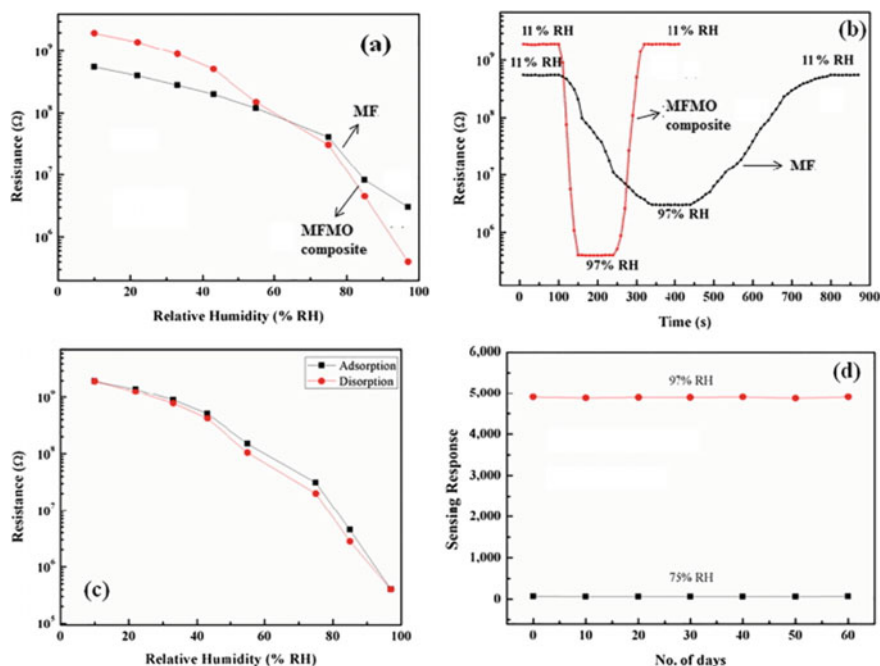
Fig. 6 a Electrical resistance as a function of relative humidity of MgFe$_2$O$_4$ (MF) and MgFe$_2$O$_4$@MoO$_3$ (MFMO) nanocomposites, **b** response and recovery time, **c** MFMO humidity hysteresis graph and **d** MFMO sensing stability. Reproduced with permission from Ref. [64]. Copyright 2018, Elsevier B. V

to measure the electrical resistance of the sensors. The variation of the electrical resistance as a function of relative humidity of MgFe$_2$O$_4$ (MF) and MgFe$_2$O$_4$@MoO$_3$ nanocomposites (MFMO) composite is shown in Fig. 6a, whereas their response and recovery time graphs, humidity hysteresis and sensing stability of MFMO composite are shown in Fig. 6b–d [64]. It is important to note that the humidity sensing response of the composite samples (MFMO) was highly stable even after 2 months, when measured at 75% RH and 97% RH, respectively.

In a comparative study by Patil et al., the Ni–Zn and Mn–Zn ferrites (Ni$_x$Zn$_{1-x}$Fe$_2$O$_4$ and Mn$_x$Zn$_{1-x}$Fe$_2$O$_4$ with $x = 0.20, 0.40, 0.60$ and 0.80) were synthesized by a chemical route to study their humidity sensing properties and observed that the thick film sensor deposited over ceramic substrates consisting of Ni–Zn ferrites are more suitable for designing the smart sensor module (SSM) [14, 41]. In their study, they also revealed and discussed about two regions of humidity sensing due to the nonlinear humidity sensitivity in the entire range of 30–95% RH corresponding to the chemisorption and physisorption process of water molecules.

Copper ferrite is a *p*-type metal oxide semiconductor which has found its application in organic synthesis as a catalyst [88]. Muthurani et al. reported the nanostructured copper ferrite, cobalt ferrite and mixture of copper-cobalt ferrite

($Cu_xCo_{1-x}Fe_2O_4$) synthesized by auto-combustion method [67]. All the materials were exposed to different humidity levels, among which cooper ferrite showed the best humidity response. All the samples showed two linear regions instead of a single linearity in the entire range of humidity sensing measurement. For instance, in copper ferrite region (i) in the range of 38–58% RH, with poor sensitivity was observed, and region (ii) in the range of 65–84% RH with relatively faster sensitivity in comparison to region (i) was observed. Overall, 17-fold increased in the total conductivity was realized in the entire range of 38–64% RH [67]. These results suggest that copper ferrite and their composite with cobalt ferrite do not possess remarkable sensitivity to be considered for their practical applications. Sathisha et al. reported the humidity sensing properties of Eu doped $CuFe_2O_4$ nanoparticles with a composition of $CuFe_{(2-x)}Eu_xO_4$ (where $x = 0.00, 0.01, 0.02, 0.03$) with best sensing properties for $x = 0.03$ in the range of 11% to 97% RH [88]. The best response and recovery time of 63 s and 164 s were recorded, respectively, for $x = 0.03$ sample, when the sensor was switched from 11% RH to 97% RH. In another recent study, Sathisha et al. reported the humidity sensing properties of 3 mol% Bi substituted $CuFe_2O_4$ nanoparticles [89]. They measured the humidity response at room temperature in the range of 11% to 97% RH and observed a slow desorption process as compared to the adsorption process. The sensing response and recover time were 73 s and 36 s, respectively, in the range of 11–97% RH. In fact, the sample showed high stability up to 54 days at relative humidity of 99% RH and 33% RH. The humidity sensing properties of Bi-doped copper ferrites showed better response and linearity than that of previously discussed for copper ferrite reported by Muthurani et al. [67]. This may be due to the fact that with increasing bismuth doping concentration the particle size has decreased and the porosity was enhanced.

Chavan et al. reported the humidity sensing properties of bismuth-doped copper oxide ($Bi_xCuFe_{2-x}O_4$, with $x = 0.0, 0.1, 0.2, 0.3, 0.4$ and 0.5) nanoparticles and observed the best sensitivity factor of 925.64 for $Bi_{0.1}CuFe_{1.9}O_4$ nanoparticles in the range of 10% to 90% RH at room temperature [66]. The electrical resistance measurement was performed by applying a DC bias voltage of 1 V $\pm$ 0.0001 across the electrodes of the pellet. Interestingly, with increasing concentration of the bismuth substitution, the sensitivity factor has continuously decreased. This is due to the fact that the presence of metal ions contributes for the conduction of electrons in ferrites resulting into the change in local charge density on the pellet surface for the adsorbed water molecules. Thus, bismuth ions uptake oxygen ions from the copper ferrites by leaving Cu^{2+} ions in the bulk form and adsorption sites give the increased surface charge [66]. Moreover, the lowest humidity sensitivity for $Bi_{0.5}CuFe_{1.5}O_4$ was assigned to the less porosity, larger grains size and lower surface charge.

In earlier studies by Kotnala et al., they have performed rigorous studies on humidity sensors and measured the humidity sensing properties of Li doped $MgFe_2O_4$, carbon-doped $MgFe_2O_4$, Pr doped $MgFe_2O_4$, Li–Ce co-doped $MgFe_2O_4$, $CeO_2@MgFe_2O_4$ composite and bare $MgFe_2O_4$ thin film deposited by RF magnetron sputtering [7, 15, 62, 80, 83, 91–94]. For Ex-magnesium ferrite, cobalt ferrites have a good sensing property toward humidity depending on physical and electrical properties of ferrite materials. Most of the ceramic humidity sensor which is being widely

used in the market are capacitance based and are good sensitive to high humidity range in atmosphere, but the Kotnala et al. group has developed a resistive type humidity sensor based on magnesium ferrite material which can work in the entire range of 10–90% RH. Shah et al. reported the Pr doped (0.1 and 0.3 mol% concentration) magnesium ferrite in the range of 10% to 90% RH for enhancing the humidity sensing properties [91]. The concentration of the spin density/dangling bond as calculated by electron paramagnetic resonance (EPR) was increased from 8.15×10^{20} to 15.6×10^{20} for 0.3 mol% Pr doped in comparison with the bare magnesium ferrite sample. Interestingly, the bulk porosity (from 8.4 to 34%) and sensitivity factor (from 24 to 113) were drastically increased after Pr doping. The humidity hysteresis was drastically decreased after Pr doping as compared to the bare magnesium ferrite sample. During the adsorption process, the heat is exchanged because of the chemisorption and physisorption of water molecules. This heat energy can be obtained by calculating the isosteric heat of adsorption, and its magnitude is useful to explore the adsorption process. The isosteric heat of sorption is a measurement of the energy or intermolecular bonding between the water molecules and absorbing surfaces [83]. The direct calorimetry method or by fitting the Clausius–Clapeyron heat equation to the isothermal data one can determine the adsorption energy [7]. The expression for isosteric heat of adsorption (q_{st}) can be calculated from the Clausius–Clapeyron Eq. (11) and written as follows [83]:

$$\log P = \frac{-q_{st}}{R}\left(\frac{1}{T}\right) \tag{11}$$

where $P = p/p_0$ is the ratio of vapor pressure at different temperature $T(p)$ and the vapor pressure at initial temperature (p_0) and R is the gas constant. Shah et al. have confirmed the conduction of water molecules due to mainly a physisorption process on magnesium ferrite by measuring the isosteric heat of adsorption (<0.1 eV) [83]. Their results based on a multilayer adsorption model showed that magnesium ferrite follows the Freundlich isotherm with an exponential decrease in the isotherm.

The humidity sensing properties of ferrite-based nanomaterials can be mainly affected by annealing temperature, measuring environment, measurement frequency and surface morphology. The following sub-sections explore the particular physical characteristics which affect the humidity sensing properties of several ferrites nanostructures.

**(i) Effect of Temperature/annealing Temperature on Measurements**
It was shown by Seki et al. that ferrite can also be used as temperature-sensitive humidity sensors [29]. Doroftei et al. have shown that by changing the temperature and time of the heat treatment the grain size and surface morphology can be changed of bare $MgFe_2O_4$ samples prepared by a method of self-combustion [84]. Their study showed the high humidity sensitivity with a response time of about 70 s of $MgFe_2O_4$ in the range 0–98% RH for the sample with thermal treatment in air at 1000 °C for 30 min [84]. They observed a huge difference in electrical resistivity measurements of bare $MgFe_2O_4$ samples after heat treatment at different temperatures and time.

In a similar study, by their coworkers N. Rezlescu et al. have reported the synthesis of $MgFe_2O_4 + 1$ wt% CaO and $MgFe_{1.8}Mn_{0.2}O_4$ by a self-combustion method (SCM) using metal nitrates, whereas $Mg_{0.5}Cu_{0.5}Fe_{1.8}Ga_{0.2}O_4$ and $Mg_{0.5}Zn_{0.5}Fe_2O_4 + 1$ wt% KCl, were prepared by using ceramic technology (CT) based on solid-state reaction of oxide powders [56]. Figure 7 shows the comparison of electrical resistivity measurements and response time of these ferrites samples [56]. The humidity response drastically changes for the MgZn ferrite + KCl sample after annealing at two different temperatures of 1050 and 1100 °C. The long response time over 5 min [see right panel in Fig. 7] with a change of about two orders of magnitude in resistivity was recorded for the Mn-doped Mg ferrite sample, which has a large number of pores below 1 μm in diameter. On the other hand, a short response time was recorded for the MgZn ferrite + KCl sample annealed at 1100 °C, which has a few micropores below 1 μm in diameter. These results showed that annealing at different temperature affects the porosity, pores-size distribution which results in the change of sensitivity and response time of a ferrite-based humidity sensor [56, 84].

Shah et al. investigated the adsorption–desorption of water vapors on a magnesium ferrite pellet surface by calculating the activation energy for charge conduction from an Arrhenius equation by measuring the conductivity in the range for 0–90% RH at different temperatures from 25 to 45 °C with an interval of 5 °C [83]. There were small changes observed in the activation energy with increasing RH. The BET measurement was performed to measure the average pore radius, sample porosity and specific surface area of the particles, which were about to be 16.3 Å, 38% and 72
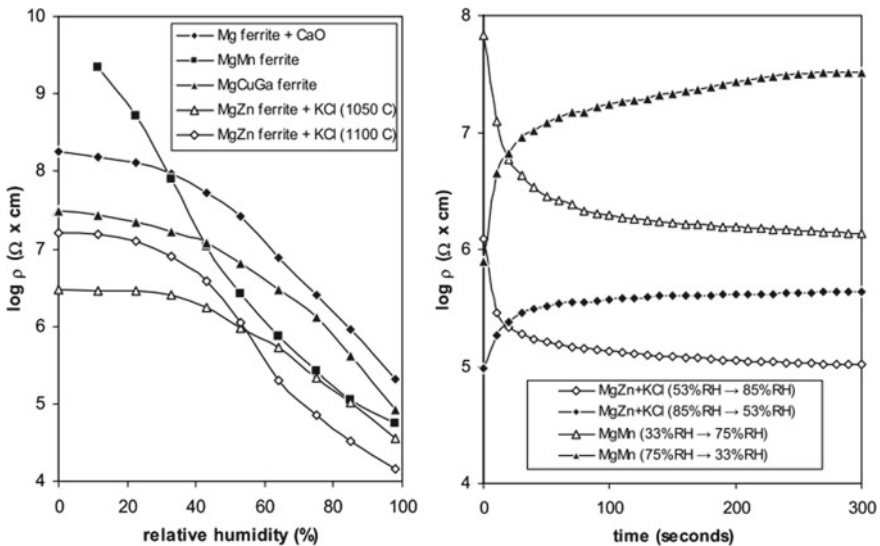
Fig. 7 In left panel, humidity response of different Mg ferrite-based humidity sensor and right panel show their response time. Open access journal; Reproduced under copyright 2015, Institute of Physics Publishing [56]
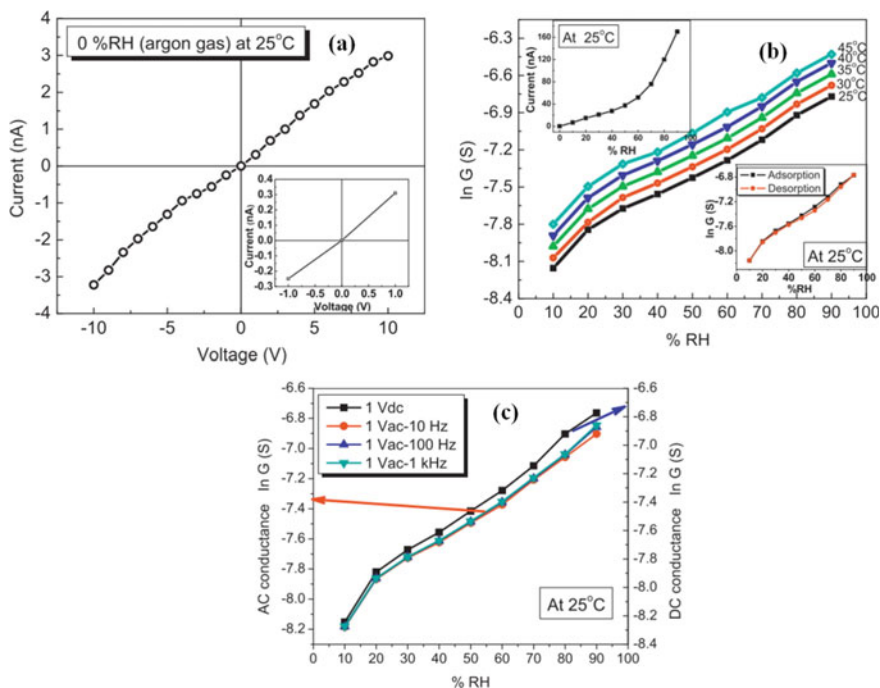
Fig. 8 **a** I–V characteristic of the electrodes in MgFe$_2$O$_4$ pellet, **b** DC conductance measurement at different temperatures and **c** AC conductance measurement at different frequency. Reproduced with permission from Ref. [83]. Copyright 2012, Elsevier B. V

m^2/g, respectively. The sensor showed a fast recovery time of 44 s as compared to its response time of 80 s. In order to measure the humidity response, the ohmic contact was made by using a silver paste at two opposite ends and their ohmic nature was confirmed by measuring the I–V characteristic within ±10 V as shown in Fig. 8a. The conductivity measurements of the magnesium ferrite pellet were done in the range of 10–90% RH at 1 V DC and also at 1 V AC at different frequencies 10, 100 Hz, and 1 kHz to ensure that there is no polarization effect in water molecules at the electrode interface and water electrolysis. The results of conductance measurements in the range of 10–90% RH at different temperatures and working frequency are shown in Fig. 8b–c [83]. The measured values of the AC conductance were slightly lower than the corresponding DC conductance values due to dipole moment of water molecules adsorbed on the sensor surface [83]. The physisorption of water molecules was confirmed from the adsorption–desorption curve after complete recovery of the conductivity values.

The humidity sensing properties of magnesium ferrite thin film were firstly reported by Kotnala et al. [95]. They prepared the magnesium ferrite target material for RF magnetron sputtering by using mechanical ball milling, which was followed

by sintering. The films were deposited over on α-Al$_2$O$_3$ substrate by Ar$^+$ bombardment at a base pressure of 7 Pa for 2 h. These as grown films were further annealed at a temperature of 400, 600 and 800 °C for 2 h.

The humidity sensing for the polycrystalline and porous film annealed at 800 °C was highly sensitive with a linear log R (Ohm) response in the entire humidity range of 10–90%RH. The AFM was used to see the morphology and measure the surface root mean square roughness. The surface roughness increased with increasing annealing temperature and was in the range of 51–87 nm. The surface morphology, humidity sensing behavior and the graph of response and recovery time are shown in Fig. 9a–d, respectively. The sensor annealed at 800 °C showed the least drift in humidity hysteresis and good reversibility and repeatability toward humidity sensing. Table 2
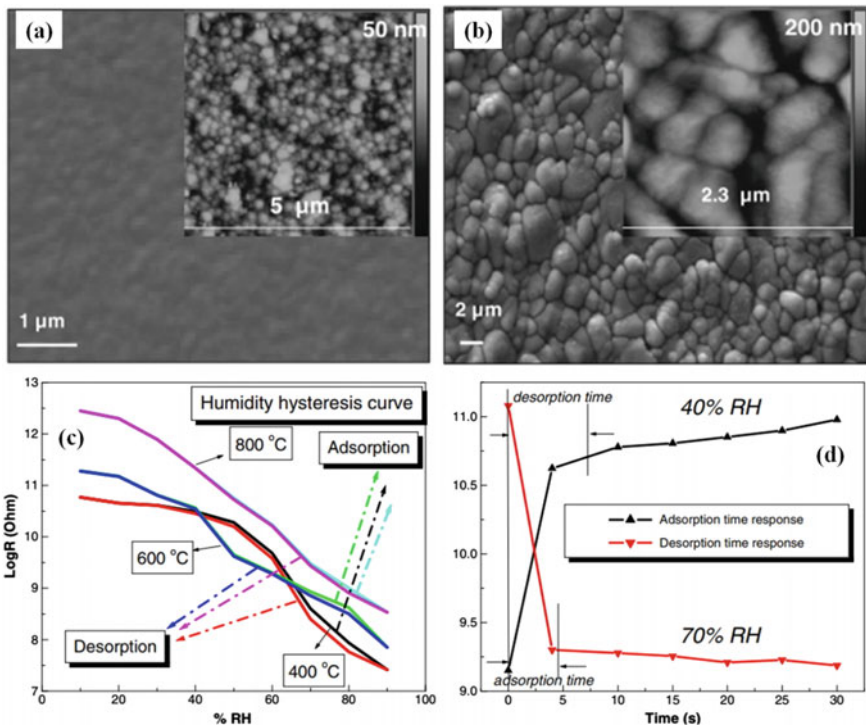
Fig. 9 Surface morphology by SEM and AFM (inset) images of MgFe$_2$O$_4$ thin film annealed at **a** 600 °C, and **b** 800 °C. The figure (**c**) shows the humidity hysteresis graphs and figure (**d**) shows the response and recovery time of MgFe$_2$O$_4$ thin film annealed at 800 °C. Reproduced with permission from Ref. [95]. Copyright 2011, Elsevier B. V

Table 2 Effect of annealing temperature on the surface morphology and humidity response of $MgFe_2O_4$ thin films [7, 95]

Annealing temperature (°C)	Pore size distribution (AFM) (μm)	RMS roughness (nm)	Sensitivity factor ($R_{10\%}/R_{90\%}$)	Response/Recovery time (s)
400	0.01–0.2	51	2269	10/16
600	0.05–0.3	64	9090	8/15
800	0.07–0.9	87	20,888	4/6

shows the various annealing temperature dependent parameters of magnesium ferrite thin films [7, 95].

(ii) Effect of Porosity/pore Size Distribution

Manikandan et al. have recently reported the highly sensitive thin films of lithium-substituted copper-ferrite ($Li_{0.2}Cu_{0.8}Fe_2O_4$) nanomaterials by using the spray pyrolysis technique [76]. The nanomaterials with particle size in the range of ∼1–31 nm were prepared by a chemical co-precipitation method, and the humidity sensing measurement was performed in the range of 10–99% RH. The plots of the humidity sensitivity, aging effect and response time are presented in Fig. 10a–d [76]. The humidity sensors have a sensitivity of 2.2 MΩ/% RH in the entire range of measurements with fast response/recovery time of 7/36 s. The porosity of the sample was analyzed by using BET at 77 K, and the plotted graphs are shown in Fig. 11a–c [76]. The nitrogen adsorption–desorption isotherms showed (see Fig. 11a) that with increasing pressure, the adsorption volume also increased which is attributed to the condensation of more nitrogen gas on the pores.

The calculation from the BET analysis showed that the specific surface area is 59.211 m^2/g, pore volume is 0.1360 cm^3/g and a mean of the pore radius is 36.71. The porosity of less than 50 nm in Li substituted $CuFe_2O_4$ confirms the micro-porous nature of the sample. In evidence of its chemical stability and mechanical robustness, the sensor has displayed ~99% reproducibility [76].

Tulliani et al. have reported the few alkali and alkaline-earth-doped hematite thick film-based humidity sensors by a screen printing technique onto α-Al_2O_3 substrates [2]. The samples were calcinated at different temperatures ranging between 850 and 950 °C. The humidity response in most of the samples was dependent on the porosity (microstructure) of the thick film rather than the ionic radius of the different dopants. The sensors doped with barium had no noticeable response, however, with Li doping the sensor showed a significant decrease over a limited RH range, and for other dopants, the materials showed a wider range of sensitivity. But in all the cases, these hematite-based compositions were insensitive below 40–50% RH, which is believed due to fact that the dopant cations increased the opened porosity but did not strongly influence the pore size distribution in the sensor materials [2]. The surface modification by doping with foreign elements and presence of dangling bond produced by oxygen vacancies can drastically improve the humidity sensing properties of the ferrite nanomaterials [7, 91, 92]. After Li substitution, the humidity
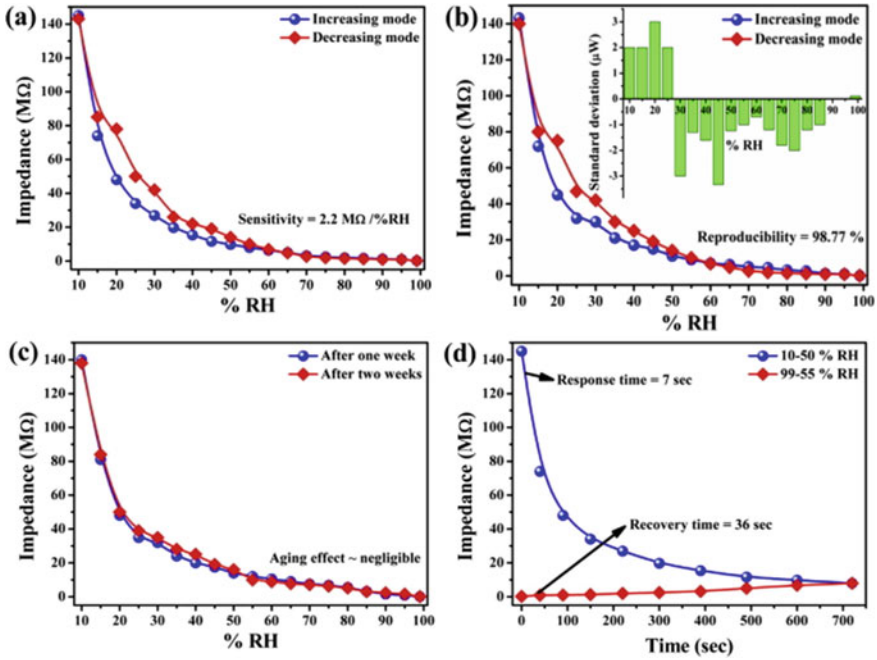
Fig. 10 **a** Humidity sensing response of LieCuFe$_2$O$_4$ film, **b** reproducibility, **c** the aging effect on humidity hysteresis graphs and **d** shows the response and recovery time. Reproduced with permission from Ref [76]. Copyright 2019, Elsevier B. V
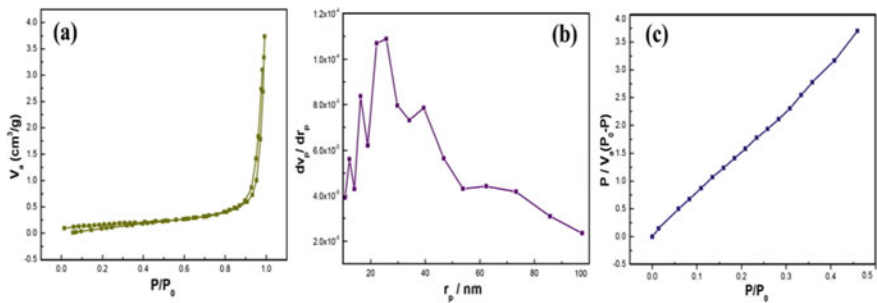
Fig. 11 **a** Nitrogen adsorption/desorption curve as a function of pressure, **b** relationship between the pore radius and change in the pore volume with pore radius and **c** BET plot used for the calculation of pore volume, surface area and pore-diameter. Reproduced with permission from Ref. [76]. Copyright 2019, Elsevier B. V

sensitivity of pure magnesium ferrite was increased, which was attributed to the high surface charge density, large surface area and open pores formed on the surface of the sensors. The easy dissolution of Li^+ ions in the magnesium ferrite lattice prompts the quick nucleation which results into the smaller grain size and pore size distribution [92, 96]. Magnesium ferrite is a potential candidate for resistive type humidity sensor due to its porous microstructure and high resistance of the order of 10^7 Ω, which is very crucial to measure the impedance in low humidity environment otherwise it is difficult to measure in the materials with low electrical resistivity. Ferrite-based humidity sensor can operate at a low DC voltage of 1–5 V and exhibit significantly good response time [7, 66]. By substituting and doping of alkali element, rare earth elements one can control the microstructure and surface activity of pure magnesium ferrite [7, 33]. This pore size distribution and unsaturated bonds provide the active surface sites for water vapors to adsorb on the material surface often decrease the resistance of the materials. The magnesium ferrite is porous in nature with high specific surface area and high electrical conductivity. Jyoti Shah et al. also reported that the addition of 4 wt% of cerium oxide to pure $MgFe_2O_4$ powder improved the porosity and increased the electrical resistance, which showed a good linearity in the entire range of humidity with an enhanced humidity sensitivity at low value of RH (<30% RH) [62].

(iii) Effect of Surface Morphology in Humidity Response

Cobalt ferrite nanoparticles ($CoFe_2O_4$ NPs) of different shape prepared by controlling the morphology via a solution route method were also tested for humidity sensing in the range of 8–97% RH at room temperature. Kumar et al. obtained spherical (CF-S), cubic (CF-C) and hexagonal shapes (CF-H) of $CoFe_2O_4$ NPs by tuning the growth conditions like amount of solvent and reaction time [68]. These $CoFe_2O_4$ NPs showed morphology dependent chemisorption properties and a fast recovery time as compared to the response time. $CoFe_2O_4$ hexagonal (CF-H) exhibited the highest humidity sensitivity among all with a value of 590 and a response/recovery time of 25/2.6 s at room temperature. The sensitivity of $CoFe_2O_4$ hexagonal (CF-H) was 2.15 and 1.41 times higher than that of the CF-C and CF-S NPs. The spinel ferrites have a lot of surface-activated water adsorption sites due to the presence of multi-cation sites; therefore, the surface behavior for the humidity sensing can be appropriately explained by the Freundlich adsorption isotherm process. This is a relationship between S (relative deviation in resistance as a function of solute adsorbed on the adsorbent) and C (percent relative humidity as a function of water vapor concentration), which is expressed as $S = k \times C^\alpha$, where k and α are the proportionality and exponent constants and represent the adsorption capacity and adsorption strength [68].

The experimental results obtained by Kumar et al. were well fitted to Freundlich adsorption isotherm model to understand the mechanism of surface adsorption for humidity sensing at room temperature in different shape of the $CoFe_2O_4$ NPs [68]. The different morphology that is used for humidity sensing is shown in Fig. 12.

The humidity response, sensitivity, hysteresis characteristics, response and recovery time, and a graph for relative deviation in resistance (ΔR_H) as a function of
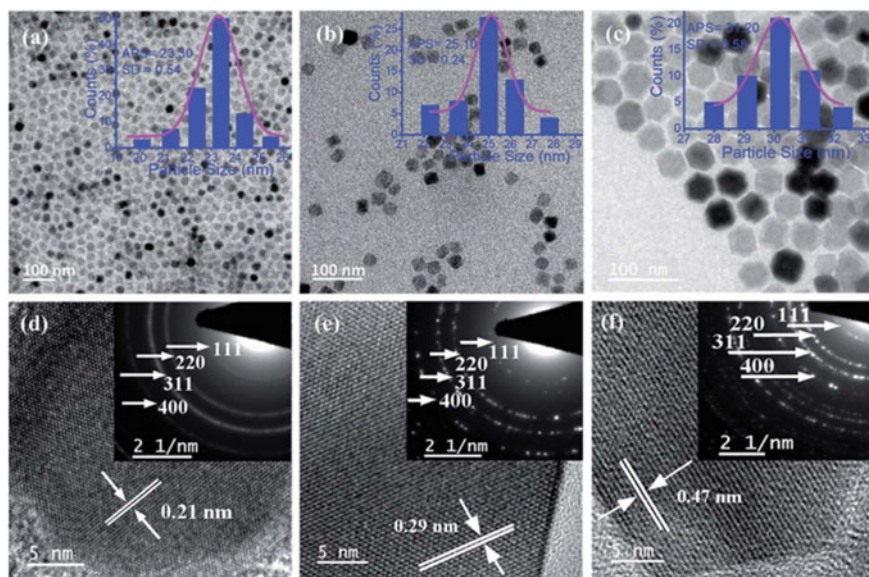
Fig. 12 Different surface morphology observed by TEM for $CoFe_2O_4$ nanoparticles. TEM images of **a** CF-S, **b** CF-C and **c** CF-H NPs (insets show size distribution histograms) and HRTEM images of **d** CF-S, **e** CF-C and **f** CF-H NPs (insets show the SAED patterns). Open access journal; reproduced under copyright 2017, RSC Advances [68]

applied relative humidity are shown in Fig. 13a–h, respectively. The lower response at low RH value was due to that fact that protons (H^+) cannot move freely in the chemisorbed water vapors and few initially physisorbed water layers over the sensor. The humidity response of all these samples was stable in different RH conditions even after 7–8 weeks.

(iv) Effect of Frequency on Humidity Response Measurements

Recently, Kuru et al. prepared a series of Mg–Zn–Cr ferrites and Al–Ni–Zn ferrite by using simple chemical co-precipitation method and studied their structural, optical and humidity sensing properties [97, 98]. The three different concentrations of Cr^{3+} dopants were used by maintaining the stoichiometry $Mg_{0.75}Zn_{0.25}Cr_xFe_{2-x}O_4$ (where $x = 0, 0.1, 0.3$) [97]. They recorded the humidity response by applying an operating voltage of 0.5 V at room temperature between 20% - 90% RH with the use of digital CEM 615 hygrometer. They explored the frequency dependent humidity sensing properties and showed that with increasing operating frequency the impedances of all the samples decreases at all RH values as shown in Fig. 14a–c [97]. It was demonstrated that at high frequencies the adsorbed water cannot be polarized, and the sensor is controlled by its geometric capacitance. On the other hand, with increasing RH value, the impedance decreases which are because the conduction occurred in the connected grains by the adsorption of water molecules. Likewise, as mentioned before in the case of copper ferrite, they have also observed two linear regions with
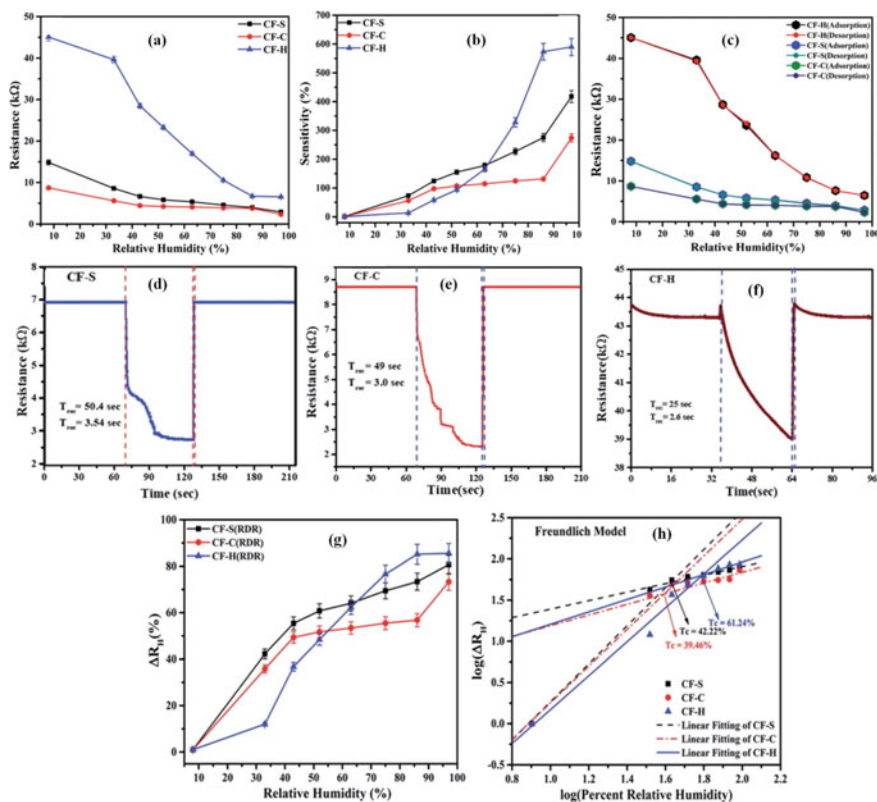
Fig. 13 The humidity measurements of different morphology of $CoFe_2O_4$ nanoparticles. **a** Humidity response, **b** sensitivity, **c** hysteresis characteristics, and **d**–**f** response and recovery times, and **g** relative deviation in resistance (ΔR_H) and **h** log–log plot of (ΔR_H) versus percent relative humidity for CF-S, CF-C, and CF-H. Open access journal; reproduced under copyright 2017, RSC Advances [68]

different sensitivity toward humidity, which were attributed to the chemisorption and physisorption process of water vapors in the crystal sites of Mg–Zn–Cr ferrites. Under an applied electric field during the chemisorption process the adsorbed water vapors on the surface gets ionized and produce hydronium ions, whose concentration increases with an increasing number of water molecules at increased RH levels. These hydronium ions serve as charge carriers therefore the areas with high concentration of hydronium ions has low impedance, and it has high impedance in the areas where the concentration of hydronium ions is low [97].

In addition, the low sensitivity with high impedance in the low-humidity region is attributed to the initial stage of adsorption of water molecules in the pores of the sample and the impedance decreases as the number of charge carriers increases.

On the other hand, in the high humidity region, the impedance decreases rapidly because of the fast adsorption of the water vapors by the pores. The influence of Cr^{3+}

Fig. 14 Humidity sensing behavior of $Mg_{0.75}Zn_{0.25}Cr_xFe_{2-x}O_4$ ferrites, and **a** $x = 0$, **b** $x = 0.1$ and **c** $x = 0.3$. Reproduced with permission from Ref. [97]. Copyright 2020, Elsevier B. V
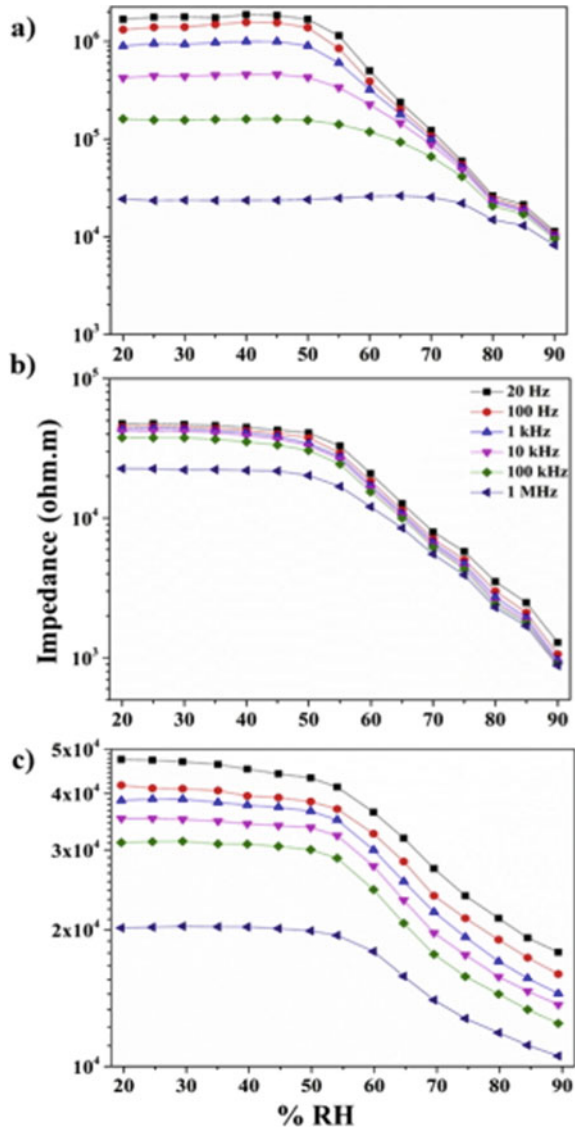
doping in Mg–Zn ferrites humidity sensitivity was clearly observed. The sensitivity decreases with increasing Cr^{3+} doping concentration which was because of transfer of charge density on the surface to water molecules as a result of uptake of oxygen ions from the Mg–Zn ferrites.

In an another report by T. S. Kuru et al., they studied the humidity sensing properties in the 15–90% range of RH at room temperature of Al–Cd ferrite synthesized by a chemical co-precipitation method [49]. They rigorously studied the frequency

dependent humidity response and observed that Al–Cd ferrite humidity sensor device has stable response at a working frequency of 1 MHz and even higher. Interestingly, the humidity response at 15% RH was 4 times greater than that of 90% RH at a frequency of 1 kHz. The sensor has a very fast response and recovery time of 5.5 s and 8 s, respectively. The humidity hysteresis curve was recorded for its reliability to check the difference between adsorption and desorption process under 1 V of potential and 1 kHz of frequency at room temperature. Al–Cd ferrite has shown a narrow humidity hysteresis with a maximum drift of 3% RH in the middle range of RH. The graph for humidity-frequency-impedance map, sensitivity as a function of frequency at different RH and humidity hysteresis curves of Al–Cd nanoparticle system are shown in Fig. 15a–c, respectively, [49].

7   Summary and Future Directions

The technological progresses of several areas from space to biomedical science demands the design and develop of novel humidity sensing materials with ultra-high surface-to-volume ratios and strong surface activities working in the entire range of humidity level by operating at a low or room temperature. The challenges are to produce unique humidity sensors which are cost effective, portable, space and eco-friendly, non-corrosive having high sensitivity, high selectivity and high durability with zero drift in reversibility. In this direction, significant research has carried out on the ferrite-based nanostructures. Among important reports available in the literature, the outcome from some of the strategic ferrite nanomaterials in the recent years is summarized in Table 3. The listed spinel ferrite-based humidity sensors are based on change in electrical resistivity, and their sensing material, working range and conditions, response/recovery time and preparation methods.

It is important to point out that the effect of doping and metallic nanoparticles incorporation in spinel nanoferrites thin films for humidity sensor applications is not yet fully explored as most of the available literature is based on bulk and/or pellet form/ thick films of ferrite nanomaterials. Therefore, optimizations of perfect stoichiometric composition, choices of various substrates, deposition technique and parameters are still a handy job to get the desired structure and morphology of thin film for further improving the humidity sensing mechanism and the geometry of its device fabrication. The continuous exposure to the humidity leads to the formation of stable chemisorbed OH^- ions on the ceramic sample surface, which requires an additional heater to remove these ions by heating at a temperature higher than 400 °C. The efforts can be directed to avoid the use of a heater and protect the sensor surface by environmental contamination also.

In addition, one can tune the structural and optical properties to look out for other readout methods such as change in absorbance and photoluminescence properties. The new theoretical models can be developed, and the outcome of the experimental results can be compared with theoretical values. Moreover, it is necessary to develop such humidity sensor devices which can itself discard the detection of other gases

Fig. 15 a Humidity-
frequency-impedance map of
Al–Cd nanoparticles system,
b humidity sensitivity versus
frequency in different
humidity levels and
c humidity hysteresis graph.
Reproduced with permission
from Ref. [49]. Copyright
2016, Elsevier B. V
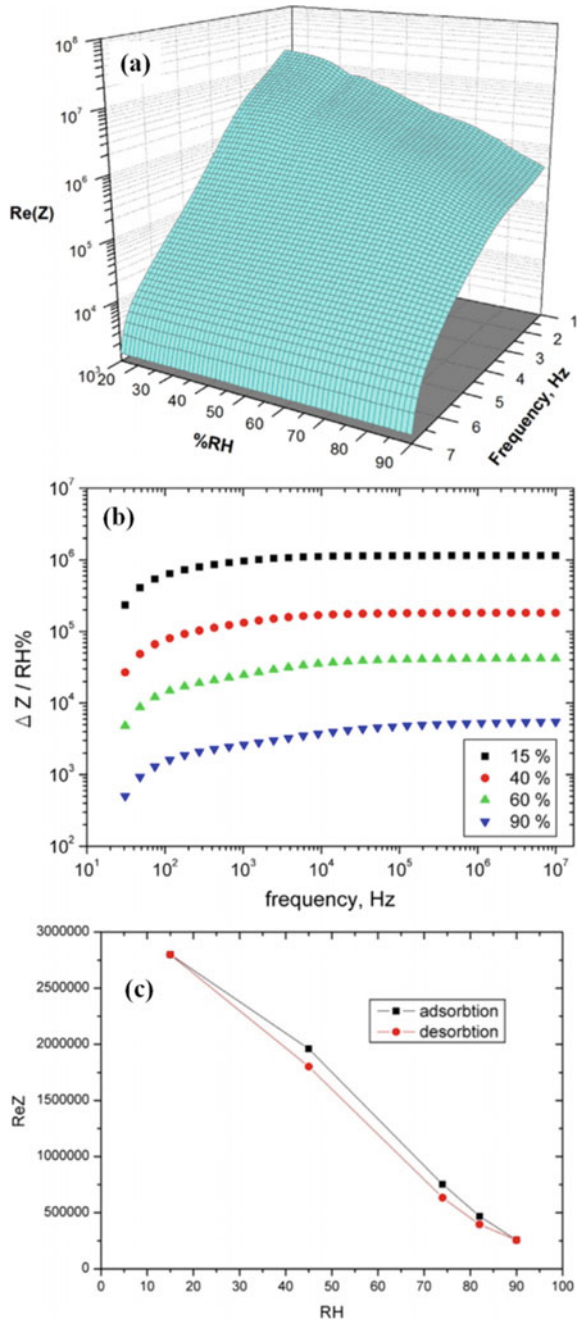
Table 3 Summary of some remarkable spinel ferrite-based humidity sensors developed in recent years, NA—Not available

Reference No. and year	Sensing ferrite material name and form of application (bulk or film and substrate type)	Working range and conditions	Response/Recovery time (time measurement range)	Preparation methods
[28] 2005	$Mg_{0.9}Sn_{0.1}Fe_2O_4$ ferrite. (pellet of Sn doped magnesium ferrite nanomaterial)	11–98% RH (Change in resistance)	3 min/NA (53–98% RH)	Combination of sol-gel and self-combustion
[2] 2005	Alkali and alkaline-earth-doped hematite (α-Fe_2O_3) thick film on to α-Al_2O_3 substrates	45–70% RH (Change in resistance)	NA	Screen-printed thick film
[62] 2007	Bare magnesium ferrite pellet 6 wt% CeO_2 added magnesium ferrite pellet	10–90% RH (Change in resistance at room temperature)	80 s/100 s 130 s/150 s (10–60% RH)	One step solid-state synthesis by wet mixing method
[92] 2008	Li doped magnesium ferrite pellet	10–80% RH (Change in resistance at room temperature)	180 s/605 s (40–70% RH)	Solid-state reaction
[84] 2010	Magnesium ferrite with thermal treatment at 1000 °C for 30 min (disk)	0–98% RH (Change in resistance)	70 s/NA	Self-combustion
[95] 2011	Magnesium ferrite thin film of 820–830 nm thickness by RF sputtering over α-Al_2O_3 substrate and thermal treatment at 800 °C	10–90% RH (Change in resistance at room temperature)	4 s/6 s (40–70% RH)	Magnesium ferrite target for sputtering was prepared by solid-state reaction and ball milling
[83] 2012	Magnesium ferrite pellet	10–90% RH (Change in resistance at room temperature)	80 s/44 s (40–70% RH)	By mechanical ball mill with zirconium balls
[1] 2013	Sm^{3+} doped Mg–Cd ferrite sensor (pellet type)	40–90% RH (Change in resistance)	160 s for Cd—ferrite/279 s (40–90% RH)	Oxalate co-precipitation method

(continued)

Table 3 (continued)

Reference No. and year	Sensing ferrite material name and form of application (bulk or film and substrate type)	Working range and conditions	Response/Recovery time (time measurement range)	Preparation methods
[53] 2013	Mn doped Ni ferrite ($Mn_{0.2}Ni_{0.8}Fe_2O_4$) thick film	(1000–8000 ppm) (RH range: NA) (Change in resistance at room temperature)	110 s/160 s (RH range: NA)	PEG assisted hydrothermal technique
[58] 2013	Copper–zinc–tungsten spinel ferrite ($Cu_{0.5}Zn_{0.5}W_{0.3}Fe_{1.7}O_4$) pellet	0–100% RH (Change in resistance and capacitance (both) at room temperature)	Fastest response time (both type ~50 s) (RH range: NA)	Nanoparticles by sol-gel auto-combustion technology,
[79] 2013	Bare Zn ferrite nanoparticles pellet	5–98% RH (sensitivity factor of 2895 and change in resistance at room temperature)	330 s/80 s (5–98% RH)	solid-state reaction of inorganic precursors
[48] 2015	Nickel ferrite disk	0–99% RH (Change in resistance at room temperature)	NA	Sol-gel auto-combustion method
[88] 2016	3 mol % Eu^{3+} doped $CuFe_2O_4$ nanoparticles pellet	11–97% RH (Change in resistance at room temperature)	63 s/164 s (11–97% RH)	Solution combustion method
[14] 2016	$Mn_xZn_{1-x}Fe_2O_4$ (Mn–Zn ferrite with x = 0.40) thick film of 0.25 mm on ceramic substrate	30–95% RH (Change in resistance)	for x = 0.40, 13 s/9 s (range 30–90% RH)	Co-precipitation method and then prepared paste for thick coating
[49] 2016	Al–Cd ferrite pellet ($Al_{0.5}Cd_{0.5}Fe_2O_4$)	15–90% RH (Change in resistance at room temperature at 1 kHz)	for x = 0.50, 5.5 s/8 s (range 15–95% RH)	Chemical co-precipitation method

(continued)

Table 3 (continued)

Reference No. and year	Sensing ferrite material name and form of application (bulk or film and substrate type)	Working range and conditions	Response/Recovery time (time measurement range)	Preparation methods
[60] 2016	Ca, Ti substituted Mg ferrites pellet ($CaMgFe_{1.33}Ti_3O_{12}$)	33–95% RH (Change in resistance at room temperature)	20 s/40 s (33–95% RH)	Solid-state reaction and ball milling and step-sintering
[68] 2017	Film of $CoFe_2O_4$ nanoparticles of different shape for humidity sensing	8–97% RH (Change in resistance at room temperature)	25 s/2.6 s (8–97% RH)	Solution-based technique to prepare NPs and drop cast method for film over ITO coated glass method for humidity sensing
[41] 2017	$Ni_xZn_{1-x}Fe_2O_4$ (Ni–Zn ferrite with x = 0.20 and 0.80) thick film on ceramic substrate	30–95% RH (measured change in resistance at 35 °C)	for x = 0.20, 10 s /5 s, and For x = 0.80, 14 s/6 s (range 30–90% RH)	Co-precipitation method and then prepared paste for thick coating
[41] 2017	$Mn_xZn_{1-x}Fe_2O_4$ (Mn–Zn ferrite with x = 0.20 and 0.40) thick film on ceramic substrate	30–95% RH (measured change in resistance at 35 °C)	for x = 0.20, 10 s/5 s, and For x = 0.40, 11 s/8 s (range 30%–90% RH)	Co-precipitation method and then prepared paste for thick coating
[64] 2018	Magnesium ferrite/molybdenum trioxide (MoO_3) nanocomposite by using pellet	11–97% RH (Change in resistance at room temperature)	45 s/74 s (11–97% RH)	Magnesium ferrite by sol–gel auto-combustion method and composite by me- chano chemical mixing method
[66] 2018	Bismuth substituted copper ferrite nanoparticles pellet ($Bi_{0.1}CuFe_{1.9}O_4$)	10–90% RH (Change in resistance at room temperature)	NA	Solution combustion route by using metal nitrates

Table 3 (continued)

Reference No. and year	Sensing ferrite material name and form of application (bulk or film and substrate type)	Working range and conditions	Response/Recovery time (time measurement range)	Preparation methods
[76] 2019	Lithium-substituted copper-ferrite ($Li_{0.2}$–$Cu_{0.8}Fe_2O_4$) thin film	10–99% RH (Change in resistance at room temperature)	7 s/36 s response range (10–50% RH) recovery range (99–55% RH)	Nanomaterials by co-precipitation method and thin film by using spray pyrolysis technique
[51] 2019	Polyhedrons shaped bare magnesium ferrite thin film by spin coating	10–99% RH (Average sensitivity 0.0237 MΩ/%RH) (Change in resistance at room temperature)	NA	Nanomaterials prepared by sol–gel method
[89] 2020	3 mol % Bi substituted $CuFe_2O_4$ nanoparticles pellet	11–97% RH (Change in resistance at room temperature)	73 s/36 s (11%–97% RH)	Solution combustion technique
[97] 2020	Cr^{3+} substituted Mg–Zn ferrite nanoparticles	20–90% RH (Change in resistance at room temperature)	NA	Co-precipitation method
[54] 2020	Neodymium-doped iron oxide, $Nd_xFe_{2-x}O_3$ nanoparticles ($x = 0.4$)	10–95% RH (Change in resistance at room temperature under corrosive environment)	for $x = 0.40$, 5 s/88 s, (range—NA)	Chemical co-precipitation route

present in the atmosphere with a high degree of sensitivity. The surface functionalities can be modified by doping and decorating with foreign elements and preparing new nanocomposite structures where the synergic effect of porosity, low hysteresis, sensitivity and selectivity can be easily addressed.

References

1. Ashok BG, Tukaram JS, Pramod NV (2013) Role of sm3+ addition on humidity sensing of nanocrtsyallite Mg–Cd ferrites. Adv Mater Res 645:160–163
2. Tulliani JM, Bonville P (2005) Influence of the dopants on the electrical resistance of hematite-based humidity sensors. Ceram Int 31:507–514
3. Yamazoe N, Shimizu Y (1986) Humidity sensors: principles and applications. Sens Actuat 10:379–398
4. Farahani H, Wagiran R, Hamidon MN (2014) Humidity sensors principle, mechanism, and fabrication technologies: a comprehensive review vol 14
5. Pelino M, Cantalini C, Faccio M (1994) Principles and applications of ceramic humidity sensors. Act Passiv Electron Compon 16:69–87
6. Tripathy A, Pramanik S, Cho J, Santhosh J, Osman NAA (2014) Role of morphological structure, doping, and coating of different materials in the sensing characteristics of humidity sensors Sensors (Switzerland) 14:16343–16422
7. Kotnala RK, Shah J (2015) Ferrite materials: nano to spintronics regime, vol 23. Elsevier
8. Morawska L, Cao J (2020) Airborne transmission of SARS-CoV-2: the world should face the reality. Environ Int 139:105730
9. Lakshmi Priyadarsini S, Suresh M (2020) Factors influencing the epidemiological characteristics of pandemic COVID 19: a TISM approach. Int J Healthc Manag 13:89–98
10. Srivastava A (2020) COVID-19 and air pollution and meteorology—an intricate relationship: a review. Chemosphere 263:128297
11. Regalado A (2020) Here's how long the coronavirus can live in the air and on packages. 1–9
12. Ahmed AT, Ghanem AS (2020) A statistical study for impacts of environmental conditions on the rapid spread of new corona virus. Int J Environ Sci Technol 17:4343–4352
13. Blank TA, Eksperiandova LP, Belikov KN (2016) Recent trends of ceramic humidity sensors development: a review. Sens Actuat B Chem 228:416–442
14. Patil SN, Pawar AM, Tilekar SK, Ladgaonkar BP (2016) Investigation of magnesium substituted nano particle zinc ferrites for relative humidity sensors. Sens Actuat A Phys 244:35–43
15. Kotnala RK, Shah J, Kishan H, Singh B (2017) Resistive type humidity sensor based on porous magnesum ferrite pellet. 1–10
16. Shaheen K, Shah Z, Khan B, Adnan OM, Alamzeb M, Suo H (2020) Electrical, photocatalytic, and humidity sensing applications of mixed metal oxide nanocomposites. ACS Omega 5:7271–7279
17. Morán-Lázaro JP, López-Urías F, Muñoz-Sandoval E, Blanco-Alonso O, Sanchez-Tizapa M, Carreon-Alvarez A, Guillén-Bonilla H, Olvera-Amador M de la L, Guillén-Bonilla A, Rodríguez-Betancourtt VM (2016) Synthesis, characterization, and sensor applications of spinel $ZnCo_2O_4$ nanoparticles Sensors (Switzerland) 16

18. Jain A, Baranwal RK, Bharti A, Vakil Z, Prajapati CS (2013) Study of Zn–Cu ferrite nanoparticles for LPG sensing Sci World J 2013
19. Chand M, Kumar S, Shankar A, Porwal R, Pant RP, Kumar A, Kumar S, Shankar A, Pant RP (2013) The size induced effect on rheological properties of Co-ferrite based ferrofluid. J Non Cryst Solids 361:38–42
20. Wang C, Yin L, Zhang L, Xiang D, Gao R (2010) Metal oxide gas sensors: sensitivity and influencing factors. Sensors 10:2088–2106
21. Dey A (2018) Semiconductor metal oxide gas sensors: a review. Mater Sci Eng B 229:206–217
22. Bârsan N, Weimar U (2003) Understanding the fundamental principles of metal oxide based gas sensors; the example of CO sensing with SnO_2 sensors in the presence of humidity J Phys Condens Matter 15
23. Shaheen K, Suo H, Shah Z, Khush L, Arshad T, Khan SB, Siddique M, Ma L, Liu M, Cui J, Ji YT, Wang Y (2020) Ag–Ni and Al–Ni nanoparticles for resistive response of humidity and photocatalytic degradation of methyl orange dye. Mater Chem Phys 244:122748
24. Chethan B, Raj Prakash HG, Ravikiran YT, Vijaya Kumari SC, Manjunatha S, Thomas S (2020) Humidity sensing performance of hybrid nanorods of polyaniline-yttrium oxide composite prepared by mechanical mixing method Talanta 215:120906
25. Crochemore GB, Ito ARP, Goulart CA, de Souza DPF (2018) Identification of humidity sensing mechanism in $MgAl_2O_4$ by impedance spectroscopy as function of relative humidity Mater Res 21
26. Pan M, Sheng J, Liu J, Shi Z, Jiu L (2020) Design and verification of humidity sensors based on magnesium oxide micro-arc oxidation film layers. Sensors (Switzerland) 20
27. Nagarajan V, Thayumanavan A, Chandiramouli R (2017) Magnesium ferrite nanostructures for detection of ethanol vapours—A first-principles study. Process Appl Ceram 11:296–303
28. Rezlescu N, Doroftei C, Rezlescu E, Popa PD (2006) Structure and humidity sensitive electrical properties of the Sn^{4+} and/or Mo^{6+} substituted Mg ferrite. Sens Actuat B Chem 115:589–595
29. Seki K, Shida J-I, Murakami K (1988) Use of a temperature-sensitive ferrite for temperature/humidity measurements. IEEE Trans Instrum Meas 37:468–470
30. Gopal Reddy CV, Manorama SV, Rao VJ (2000) Preparation and characterization of ferrites as gas sensor materials. J Mater Sci Lett 19:774–778
31. Soler MAG, Paterno LG (2017) Magnetic nanomaterials. Elsevier
32. Cullity BD, Graham CD (2008) Introduction to magnetic materials. Introd Magn Mater
33. Thankachan S, Kurian M, Nair DS, Xavier S, Mohammed EM (2014) Effect of rare earth doping on structural, magnetic, electrical properties of magnesium ferrite and its catalytic activity. Int J Eng Sci Innov Technol 3:529–537
34. Afiune LAF, Ushirobira CY, Barbosa DPP, de Souza PEN, Leles MIG, Cunha-Filho M, Gelfuso GM, Soler MAG, Gratieri T (2020) Novel iron oxide nanocarriers loading finasteride or dutasteride: enhanced skin penetration for topical treatment of alopecia. Int J Pharm 587
35. Rivera LMR, Paterno LG, Chaves NL, Gregurec D, Báo SN, Moya SE, Jain M, Azevedo R B, Morais PC, Soler MAG (2019) Biocompatible superparamagnetic carriers of chondroitin sulfate. Mater Res Express 6
36. Letti CJ, Costa KAG, Gross MA, Paterno LG, Pereira-da-Silva MA, Morais PC, Soler MAG (2017) Synthesis, morphology and electrochemical applications of iron oxide based nanocomposites. Adv Nano Res 5:215–230
37. Viali WR, Alcantara GB, Sartoratto PPC, Soler MAG, Mosiniewicz-Szablewska E, Andrzejewski B, Morais PC (2010) Investigation of the molecular surface coating on the stability of insulating magnetic oils. J Phys Chem C 114:179–188
38. Gumbi SW, Mkwae PS, Kortidis I, Kroon RE, Swart HC, Moyo T, Nkosi SS (2020) Electronic and simple oscillatory conduction in ferrite gas sensors: gas sensing mechanisms, long-term gas monitoring, heat transfer and other anomalies. ACS Appl Mater Interfaces 12:43231–43249
39. Chen Z, Lu C (2005) Humidity sensors: a review of materials and mechanisms. Sens Lett 3:274–295
40. Koli PB, Kapadnis KH, Deshpande UG (2019) Nanocrystalline-modified nickel ferrite films: an effective sensor for industrial and environmental gas pollutant detection. J Nanostruct Chem 9:95–110

41. Sn P, Am P, Jd D, Bp L (2017) Comparative study of ferrite based humidity sensor for smart sensor module design. Int Res J Sci Eng 203–209
42. Kant R, Jhabarmal J, Mann AK (2018) A review of doped magnesium ferrite nanoparticles: introduction, synthesis techniques and applications. IJSRSET 4:646–660
43. Ortiz-Quiñonez JL, Pal U, Villanueva MS (2018) Structural, magnetic, and catalytic evaluation of spinel Co, Ni, and Co-Ni ferrite nanoparticles fabricated by low-temperature solution combustion process. ACS Omega 3:14986–15001
44. Rivera LMR, Machado JG, Chandra Mathpal M, Chaves NL, Gregurec D, Báo SN, Paterno LG, Moya SE, Azevedo RB, Soler MAG (2020) Functional glucosamine-iron oxide nanocarriers J Mater Res 1–12
45. Alcantara GB, Paterno LG, Afonso AS, Faria RC, Pereira-Da-Silva MA, Morais PC, Soler MAG (2011) Adsorption of cobalt ferrite nanoparticles within layer-by-layer films: a kinetic study carried out using quartz crystal microbalance. Phys Chem Chem Phys 13:21233–21242
46. Alcantara GB, Paterno LG, Fonseca FJ, Pereira-Da-Silva MA, Morais PC, Soler MAG (2013) Dielectric properties of cobalt ferrite nanoparticles in ultrathin nanocomposite films. Phys Chem Chem Phys 15:19853–19861
47. Alcantara G, Paterno L, Fonseca F, Pereira-da-Silva M, Morais P, Soler MG (2013) Layer-by-layer assembled cobalt ferrite nanoparticles for chemical sensing. J Nanofluids 2:175–183
48. Dumitrescu AM, Lisa G, Iordan AR, Tudorache F, Petrila I, Borhan AI, Palamaru MN, Mihailescu C, Leontie L, Munteanu C (2015) Ni ferrite highly organized as humidity sensors. Mater Chem Phys 156:170–179
49. Şaşmaz Kuru T, Şentürk E (2016) Humidity sensing properties of ferrite based Al–Cd nanoparticles as a fast response sensor device. Sens Actuat A Phys 249:62–67
50. Şaşmaz Kuru T, Eyüpoğlu V (2018) Co-Mg ferrite nanocomposite as a humidity sensor device prepared by Co-precipitation method. Sak Univ J Sci 22:1–1
51. Jaiswal AK, Sikarwar S, Singh S, Dey KK, Yadav BC, Yadav RR (2019) Fabrication of nanostructured magnesium ferrite polyhedrons and their applications in heat transfer management and gas/humidity sensors. J Mater Sci Mater Electron 31:80–89
52. Virlan C, Tudorache F, Pui A (2017) Increased sensibility of mixed ferrite humidity sensors by subsequent heat treatment. Int J Appl Ceram Technol 14:1174–1182
53. Köseoğlu Y, Aldemir I, Bayansal F, Kahraman S, Çetinkara HA (2013) Synthesis, characterization and humidity sensing properties of $Mn_{0.2}Ni_{0.8}Fe_2O_4$ nanoparticles. Mater Chem Phys 139:789–793
54. Manikandan V, Mirzaei A, Petrila I, Kavita S, Mane RS, Denardin JC, Lundgaard S, Juodkazis S, Chandrasekaran J, Vigneselvan S (2020) Effect of neodymium stimulation on the dielectric, magnetic and humidity sensing properties of iron oxide nanoparticles. Mater Chem Phys 254:123572
55. Rezlescu N, Rezlescu E, Popa PD, Tudorache F (2005) A model of humidity sensor with a Mg-based ferrite. J Optoelectron Adv Mater 7:907–910
56. Rezlescu N, Rezlescu E, Doroftei C, Popa PD (2005) Study of some Mg-based ferrites as humidity sensors. J Phys Conf Ser 15:296–299
57. Zainuddin Z, Masri SA, Zaib WAW, Awang R, Jumali MHH (2017) Structure, humidity sensitivity and magnetic properties of Ce substituted magnesium ferrite. In: AIP conference proceedings, vol 1838
58. Petrila I, Tudorache F (2013) Humidity sensor applicative material based on copper-zinc-tungsten spinel ferrite. Mater Lett 108:129–133
59. Nikolic MV, Vasiljevic ZZ, Lukovic MD, Pavlovic VP, Krstic JB, Vujancevic J, Tadic N, Vlahovic B, Pavlovic VB (2019) Investigation of $ZnFe_2O_4$ spinel ferrite nanocrystalline screen-printed thick films for application in humidity sensing. Int J Appl Ceram Technol 16:981–993
60. Tripathy A, Pramanik S, Manna A, Shasmin HN, Radzi Z, Abu Osman NA (2016) Uniformly porous nanocrystalline $CaMgFe_{1.33}Ti_3O_{12}$ ceramic derived electro-ceramic nanocomposite for impedance type humidity sensor. Sensors (Switzerland) 16:1–18
61. Gadkari AB, Shinde TJ, Vasambekar, PN (2013) Humidity sensor using soft Y–Cd ferrite In: AIP conference proceedings, vol 1536, pp 1115–1116

62. Shah J, Kotnala RK, Singh B, Kishan H (2007) Microstructure-dependent humidity sensitivity of porous $MgFe_2O_4$–CeO_2 ceramic. Sensors Actuat B Chem 128:306–311
63. Ladgaonkar BP, Patil SN, Tilekar SK (2013) Development of Ni–Zn ferrite based smart humidity sensor module by using mixed signal programmable system-on-chip. Appl Mech Mater 310:490–493
64. Babu Reddy LP, Megha R, Chethan B, Raj Prakash HG, Ravikiran YT, Ramana CHVV, Kim D (2018) Role of molybdenum trioxide in enhancing the humidity sensing performance of magnesium ferrite/molybdenum trioxide composite. Inorg Chem Commun 98:68–74
65. Khorsand Zak A, Shirmahd H, Mohammadi S, Banihashemian SM (2020) Solvothermal synthesis of porous Fe_3O_4 nanoparticles for humidity sensor application. Mater Res Express 7
66. Chavan P, Naik LR (2018) Effect of Bi^{3+} ions on the humidity sensitive properties of copper ferrite nanoparticles. Sens Actuat B Chem 272:28–33
67. Muthurani S, Balaji M, Gautam S, Chae KH, Song JH, Padiyan DP, Asokan K (2011) Magnetic and humidity-sensing properties of nanostructured $Cu_xCo_{1-x}Fe_2O_4$ synthesized via autocombustion. J Nanosci Nanotechnol 11:5850–5855
68. Kumar Y, Sharma A, Shirage PM (2017) Shape-controlled $CoFe_2O_4$ nanoparticles as an excellent material for humidity sensing. RSC Adv 7:55778–55785
69. Rezlescu N, Doroftei C, Popa P (2007) Humidity-sensitive electrical resistivity of $MgFe_2O_4$ and $Mg_{0.9}Sn_{0.1}Fe_2O_4$ porous ceramics. Rom J Phys 52:353
70. Zhao J, Liu Y, Li X, Lu G, You L, Liang X, Liu F, Zhang T, Du Y (2013) Highly sensitive humidity sensor based on high surface area mesoporous $LaFeO_3$ prepared by a nanocasting route. Sens Actuat B Chem 181:802–809
71. Agmon N (1995) The Grotthuss mechanism. Chem Phys Lett 244:456–462
72. Fischer SA, Gunlycke D (2019) Analysis of correlated dynamics in the grotthuss mechanism of proton diffusion. J Phys Chem B 123:5536–5544
73. Conway BE, Bockris JOM, Linton Ü (1956) Proton conductance and the existence of the $H_3\dot{O}$ ion. J Chem Phys 24:834–850
74. Wraight CA (2006) Chance and design-proton transfer in water, channels and bioenergetic proteins. Biochim Biophys Acta Bioenerg 1757:886–912
75. Mccafferty E, Zettlemo AC (1971) Adsorption of water vapour on a-Fe_2O_3. Discuss Faraday Soc 52:239
76. Manikandan V, Sikarwar S, Yadav BC, Vigneselvan S, Mane RS, Chandrasekaran J, Mirzaei A (2019) Rapid humidity sensing activities of lithium-substituted copper-ferrite (Li−$CuFe_2O_4$) thin films Mater. Chem Phys 229:448–452
77. Sandu I, Presmanes L, Alphonse P, Tailhades P (2006) Nanostructured cobalt manganese ferrite thin films for gas sensor application. Thin Solid Films 495:130–133
78. Capraro S, Le Berre M, Chatelon JP, Joisten H, Mery E, Bayard B, Rousseau JJ, Barbier D (2004) Properties of barium ferrite sputtered films. Sens Actuat A Phys 1s13:382–386
79. Jeseentharani V, George M, Jeyaraj B, Dayalan A, Nagaraja KS (2013) Synthesis of metal ferrite (MFe_2O_4, M=Co, Cu, Mg, Ni, Zn) nanoparticles as humidity sensor materials. J Exp Nanosci 8:358–370
80. Kotnala RK, Shah J, Mathpal MC, Verma KC, Singh S (2011) Influence of annealing on humidity response of RF sputtered nanocrystalline $MgFe_2O_4$ thin films. Thin Solid Films 519:6135–6139
81. Shaikh SF, Ubaidullah M, Mane RS, Al-Enizi AM (2020) Types, synthesis methods and applications of ferrites. Elsevier
82. Chand M, Kumar A, Kumar S, Shankar A, Pant RP (2014) Synthesized by sol-gel and co-precipitation methods 4:1–6
83. Shah J, Kotnala RK (2012) Humidity sensing exclusively by physisorption of water vapors on magnesium ferrite. Sens Actuat B Chem 171–172:832–837
84. Doroftei C, Popa PD, Rezlescu N (2010) The influence of the heat treatment on the humidity sensitivity of magnesium nanoferrite. J Optoelectron Adv Mater 12:881–884
85. Kumar R, Goel N, Kumar M (2017) UV-activated MoS_2 based fast and reversible NO_2 sensor at room temperature ACS Sensors 2:1744–1752

86. McEvoy N, Duesberg GS, Hallam T, Gatensby R, Lee K (2013) High-performance sensors based on molybdenum disulfide thin films. Adv Mater 25:6699–6702
87. Kuru C, Choi C, Kargar A, Choi D, Kim YJ, Liu CH, Yavuz S, Jin S (2015) MoS_2 Nanosheet–Pd nanoparticle composite for highly sensitive room temperature detection of hydrogen. Adv Sci 2:1–5
88. Sathisha IC, Manjunatha K, Angadi VJ, Chethan B, Ravikiran YT, Pattar VK, Manjunatha SO, Matteppanavar S (2016) Enhanced humidity sensing response in Eu^{3+}-doped iron-rich $CuFe_2O_4$: a detailed study of structural, microstructural, sensing, and dielectric properties. Intech, pp 1–15
89. Sathisha IC, Manjunatha K, Bajorek A, Rajesh Babu B, Chethan B, Ranjeth Kumar Reddy T, Ravikiran YT, Jagadeesha Angadi V (2020) Enhanced humidity sensing and magnetic properties of bismuth doped copper ferrites for humidity sensor applications. J Alloys Compd 848:156577
90. Doroftei C, Rezlescu E, Rezlescu N, Popa PD (2006) Microstructure and humidity sensitive properties of $MgFe_2O_4$ ferrite with Sn and Mo substitutions prepared by selfcombustion method. J Optoelectron Adv Mater 8:1012–1015
91. Shah J, Arora M, Purohit LP, Kotnala RK (2011) Significant increase in humidity sensing characteristics of praseodymium doped magnesium ferrite. Sens Actuat A Phys 167:332–337
92. Kotnala RK, Shah J, Singh B, kishan H, Singh S, Dhawan SK, Sengupta A (2008) Humidity response of Li-substituted magnesium ferrite. Sens Actuat B Chem 129:909–914
93. Kotnala RK, Shah J, Mathpal MC, Gupta D, Purohit LP, Kishan H (2009) Study of humidity sensing property of LiCe substituted magnesium ferrite. Sens Lett 7:1051–1056
94. Verma V, Srivastava AK, Shah J, Kunchakara S (2016) Highly sensitive carbon doped magnesium ferrite humidity sensor 3:283–285
95. Kotnala RKK, Shah J, Mathpal MC, Verma KCC, Singh S, Lovkush (2011) Influence of annealing on humidity response of RF sputtered nanocrystalline $MgFe_2O_4$ thin films. Thin Solid Films 519:6135–6139
96. Kotnala RK, Shah J, Mathpal MC, Gupta D, Puohit LP, Kishan H (2009) Role of modified active surface sites of magnesium ferrite for humidity sensing. J Optoelectron Adv Mater 11:296–301
97. Kuru M, Kuru T Ş, Karaca E, Bağcı S (2020) Dielectric, magnetic and humidity properties of Mg–Zn–Cr ferrites. J Alloys Compd 836:155318 (1–11)
98. Şaşmaz Kuru T, Kuru M, Bağcı S (2018) Structural, dielectric and humidity properties of Al–Ni–Zn ferrite prepared by co-precipitation method. J Alloys Compd 753:483–490